Atmospheric and Oceanographic Sciences Library 48

Alexander Soloviev
Roger Lukas

The Near-Surface Layer of the Ocean

Structure, Dynamics and Applications

Second Edition

Springer

The Near-Surface Layer of the Ocean

ATMOSPHERIC AND OCEANOGRAPHIC SCIENCES LIBRARY

VOLUME 48

For further volumes:
http://www.springer.com/series/5669

Alexander Soloviev • Roger Lukas

The Near-Surface Layer of the Ocean

Structure, Dynamics and Applications

Springer

Alexander Soloviev
Nova Southeastern University
Oceanographic Center
Dania Beach
Florida
USA

Roger Lukas
Department of Oceanography
University of Hawaii at Manoa
Honolulu
Hawaii
USA

ISSN 1383-8601
ISBN 978-94-007-7620-3 ISBN 978-94-007-7621-0 (eBook)
DOI 10.1007/978-94-007-7621-0
Springer Dordrecht Heidelberg London New York

Library of Congress Control Number: 2013952814

Printed on acid-free paper

Springer is part of Springer Science+Business Media (www.springer.com)

Preface for the Second Edition

The first edition of our book, "The Near-Surface Layer of the Ocean" was the first monograph to provide a comprehensive account of the structures and dynamics of the near-surface layer of the ocean under different environmental conditions. The rationale for publishing a second edition is that this area of research continues to see remarkable advancement. Pioneering satellite missions by ESA and NASA to measure sea surface salinity have been launched. The newest generation of synthetic aperture radar (SAR) satellites has provided unprecedented, meter-scale horizontal resolution of fine features on the sea surface. In addition, the computational fluid dynamics (CFD) type models have recently been introduced for upper ocean research, opening new opportunities to understand processes involved in formation of fine scale features and their visibility to SAR. Passive acoustic methods for monitoring short sea surface waves (and potentially effects of surfactants) have obtained significant development due to pioneering works by Walter Munk with observations from deep-sea hydrophones. Study of the Deepwater Horizon oil spill in the Gulf of Mexico has generated unique data sets on fine scale structure and dynamics of the near-surface layer of the ocean.

In this second edition, we have preserved the overall structure of the monograph. As in the first edition, detailed treatment is given to the following topics: molecular sublayers, turbulence and waves, air-sea exchanges, buoyancy effects, fine thermohaline structure of the near-surface layer of the ocean, spatially-coherent organized motions and other processes having surface manifestations, and the high wind-speed regime.

Chapter 1 introduces the reader to the main theme of the book—the near-surface layer of the ocean as an element of the ocean-atmosphere system. This chapter has been supplemented with an overview of numerical methods for modeling mixing in the upper ocean including computational fluid dynamics (CFD) models, which are effective new tools for studying three-dimensional processes in the near-surface layer of the ocean and across the air-sea interface. Statistical description of surface waves has been extended to introduce wave form stress and kinetic energy flux to waves from wind.

The dynamics of the aqueous viscous, thermal, and diffusive sublayers at the air-sea interface are discussed in Chap. 2 updated with new developments in chemistry,

biology, and physics of surface films. CFD modeling of the viscoelastic properties of surface films due to presence of surfactants is another new topic in this chapter. In addition, we describe a new approach to studying the bacterial content of the sea surface microlayer using DNA analysis in conjunction with SAR remote sensing techniques.

Chapter 3 is devoted to upper ocean turbulence, which is the key to understanding many other processes that are responsible for the structure of the near-surface layer of the ocean. This chapter has been updated with the new results on wave-induced turbulence that emerged since the publication of the first edition. Progress in studying upper ocean turbulence is significantly hampered by technological challenges; we discuss this problem throuout the chapter. At this point, none of the existing sensor systems is capable of providing reliable measurements of turbulence levels within active wave breakers due to high concentrations of air bubbles. In fact, a significant part of the wave kinetic energy dissipates within wave breakers. In concluding remarks to Sect. 3.4 we discuss a possible new approach to address this problem using high-resolution 3D sonar technology.

Chapter 4 presents the fine thermohaline structure of the near-surface layer of the ocean. It has been updated with a discussion of new approaches to modeling the diurnal cycle of sea surface temperature (SST) using CFD. A somewhat more detailed consideration is now given to the near-surface layer of the ocean in polar seas.

Chapter 5 is devoted to spatially-coherent organized motions in the near-surface layer of the ocean. A new theoretical insight into physics of spiral structures on the sea surface has been added. The resonant interaction of density-driven currents in the near-surface layer of the ocean with ambient stratification has been reproduced with a CFD model. We have updated the section on Langmuir circulation and an alternate mechanism is now discussed.

Chapter 6 discusses the air-sea interface under tropical cyclone conditions. Dramatic development in this area of research is associated with the recent finding that whitecap coverage does not exceed 10% of the sea surface area even under very high wind speed conditions. New data support the mechanism of direct disruption of the air-sea interface under very high wind speed conditions, which was hypothesized in the first edition of our book. The resulting two-phase transition layer has been included in a unified parameterization for the drag coefficient.

The biggest changes in the second edition are in Chap. 7, which is a result of the rapid widening of potential applications of near-surface ocean research results. Sections on remote sensing of the ocean, ocean acoustics, air-sea gas exchange and climate studies have been significantly updated. The updates include interpretation of natural and artificial features on the sea surface in SAR imagery. A new section on remote sensing of oil spills has been added.

This book is mainly directed toward researchers in physical and chemical oceanography, marine biology, remote sensing, ocean optics, and ocean acoustics. We anticipate that more specialists will need to be prepared to work in this and related areas of research. We have therefore attempted to make it of value for graduate studies in oceanography and environmental sciences.

Acknowledgments for the Second Edition

We would like to thank Mark Donelan, Isaac Ginis, Greg Holland, Brian Haus, and Lynn Shay for their valuable insight and important discussions regarding the problem of air–sea interactions in hurricanes. Work on the remote sensing component of the new edition was inspired by the participation of the first author on the NASA Sea Surface Temperature Team, and collaboration with Hans Graber, Susanne Lehner, William Perrie, Stephan Brusch, and Maurizio Migliaccio on SAR oceanography. We are grateful to Atsushi Fujimura, Silvia Matt, Mikhail Gilman, and Michael McGauley for help with numerical simulations and to Bryan Hamilton, Cayla Dean, and Tatiana Solovieva for editing text and arranging literature references.

The second edition was significantly supported by the NOPP project "Advanced coupled atmosphere-wave-ocean modeling for improving tropical cyclone prediction models" (PIs: Isaac Ginis, URI and Shuyi Chen, UM), and by the Gulf of Mexico Research Initiative Consortium for Advanced Research on the Transport of Hydrocarbons in the Environment (PI: Tamay Özgökmen, UM).

Dean Richard Dodge of the Nova Southeastern University Oceanographic Center, and University President George Hanbury II granted sabbatical leave to the lead author for the work on the new edition of the monograph. The second author was also supported by the NOPP project, by National Science Foundation grant OCE-0926766 and by the State of Hawaii.

Preface for the First Edition

Until the 1980s, a tacit agreement among many physical oceanographers was that nothing deserving attention could be found in the upper few meters of the ocean. The lack of adequate knowledge about the near-surface layer of the ocean was mainly due to the fact that the widely used oceanographic instruments (such as bathythermographs, CTDs, current meters, etc.) were practically useless in the upper few meters of the ocean. Interest in the near-surface layer of the ocean rapidly increased along with the development of remote sensing techniques. The interpretation of ocean surface signals sensed from satellites demanded thorough knowledge of upper ocean processes and their connection to the ocean interior.

Despite its accessibility to the investigator, the near-surface layer of the ocean is not a simple subject of experimental study. Random, sometimes huge, vertical motions of the ocean surface due to surface waves are a serious complication for collecting quality data close to the ocean surface. The supposedly minor problem of avoiding disturbances from ships' wakes has frustrated several generations of oceanographers attempting to take reliable data from the upper few meters of the ocean. Important practical applications nevertheless demanded action, and as a result several pioneering works in the 1970s and 1980s laid the foundation for the new subject of oceanography—the near-surface layer of the ocean.

In 1988, K. N. Fedorov and A. I. Ginzburg published a monograph "The Near-Surface Layer of the Ocean", which summarized many of the new results but which was printed in limited numbers. In 1992, this book was translated into English. Since the publication of Fedorov's book, this area of research has dramatically advanced. Numerous exciting new experimental and theoretical results have been obtained. The idea of the importance of the ocean-atmosphere coupling on small scales found its practical realization in the TOGA COARE program which took place between 1992 and 1994. The concept of one-dimensional upper ocean dynamics has been enriched with the consideration of three-dimensional spatial structures. In particular, spatially coherent organized motions are attracting more attention.

Our book provides a comprehensive account of the structures and dynamics of the near-surface layer of the ocean under different environmental conditions. Fedorov's pioneering monograph attempted to achieve this objective, but it had

unfortunate gaps and redundancies. Now it is possible to provide a more coherent presentation of this important subject.

In this book, detailed treatment is given to the following topics: molecular sublayers, turbulence and waves, buoyancy effects, fine thermohaline structure of the near-surface layer of the ocean, spatially coherent organized motions having surface manifestations, and the high wind-speed regime. Although this selection of topics depends somewhat on the specific research interests of the authors, the monograph attempts to systematically develop its subjects from physical and thermodynamic principles. The accent on the analysis of the results from recent major air-sea interaction experiments (including the data collected by the authors) is our effort to ensure that the book comprises the most comprehensive and reliable sum of knowledge that has been obtained in this area of research. For the subjects that are related to the physics of the near-surface layer of the ocean but not covered in the book in sufficient detail (or not covered at all), the reader is referred to useful literature. Among these subjects are the biochemistry of surface films (*The Sea Surface and Global Change*, edited by P.S. Liss and R.A. Duce, 1997), surface wave dynamics (Donelan and Hui 1990), atmospheric boundary-layer dynamics (Stull 1988), mixed layer modeling (Kantha and Clayson 2000), air-sea fluxes (Businger and Kraus 1994; Csanady 2001), and coupled ocean-atmosphere systems (Godfrey et al. 1998).

Chapter 1 introduces the reader to the main theme of the book—the near-surface layer of the ocean as an element of the ocean-atmosphere system. A general discussion of upper ocean dynamics and thermodynamics sets the stage for the content of Chaps 2–7. This discussion introduces the different processes that mix and restratify the upper ocean.

Very close to the air-sea interface, turbulent mixing is suppressed and molecular diffusion appears to dominate the vertical property transport. Viscous, thermal, and diffusive sublayers close to the ocean surface exist as characteristic features of the air-sea momentum, heat, and mass transport. Their dynamics, discussed in Chap. 2, can be quite complex due to the presence of surface waves, capillary effects, penetrating solar radiation, and rainfall.

Chapter 3 provides insight into dynamics of the upper ocean turbulent boundary layer. The turbulence regime is the key to understanding many other processes in the near-surface layer of the ocean. Because methodological issues of turbulence measurements near the ocean surface are still not resolved, we start Chap. 3 with analysis of the existing experimental approaches. (The measurement of wave-enhanced turbulence is a very important but specialized topic.) Analyses of turbulence observations reveal different (sometimes contradictory) points of view on the role of surface waves. Recent observations obtained under a wide range of environmental conditions allows us to explain and, in some cases, to reconcile different points of view.

The wave-induced turbulence does not depend directly on stratification effects, and it is therefore reasonable to analyze the stratification effects separately. The analysis of stratification effects on turbulence in Chap. 3 is based on some analogy between the atmospheric and oceanic turbulent boundary layers. This analogy has been employed in the studies of Steve Thorpe and Michael Gregg. It may only be

observed starting from the depth where wave-breaking turbulence is not important. A discussion of the surface mixed layer versus the Ekman layer concept will illustrate the depth to which momentum supplied by the wind penetrates relative to where the base of the mixed layer is found.

Chapter 4 is devoted to the fine thermohaline structure of the near-surface layer. We consider the penetrative solar radiation and the impacts of the distribution of radiant heating on the mixed layer dynamics. Stable stratification in the near-surface ocean due to diurnal warming or rainfall can reduce the turbulence friction, which results in intensification of near-surface currents. Unstable stratification leads to convective overturning, which increases turbulent friction locally. In addition, discrete convective elements—analogs of thermals in the atmosphere—penetrate into the stably stratified layer below and produce non-local transport. Experimental studies at the equator have produced striking examples of local and non-local effects on the dynamics of the diurnal mixed layer and thermocline. The last section of this chapter demonstrates how the local (diffusive) and non-local (convective) transport can be parameterized and incorporated into one- or three-dimensional models. This chapter contains a few effective examples of spatial near-surface structures. These examples should motivate the reader to study in detail the relatively lengthy Chap. 5.

Chapter 5 is devoted to the coherent structures within the near-surface layer of the ocean. Spatially-coherent organized motions have been recognized as an important part of turbulent boundary layer processes. In the presence of surface gravity waves, the Ekman boundary layer becomes unstable to helical motions (Langmuir cells). "Wind-rows" can often be seen from space due to spray patches and have already been used in advanced remote sensing algorithms to determine the direction of near-surface winds. Ramp-like structures are a common feature of boundary layer flows; they are, however, oriented perpendicular to the wind direction, while Langmuir cells are roughly aligned with wind. The Langmuir cells and ramp-like structures entrain bubbles and can be traced with side-scan sonar. Other types of quasi-periodical structures in the near-surface ocean, such as freshwater lenses produced by rainfalls and near-inertial oscillations induced by moving storms may have distinct signatures in the sea surface temperature field. Sharp frontal interfaces are an intriguing example of self-organization. These interfaces are supposedly related to the subduction process and are of different nature in mid- and low-latitudes. Internal waves, resonant interactions between surface and internal modes, and billows in the diurnal thermocline also produce signatures on the ocean surface under certain conditions.

Chapter 6 addresses high wind speed conditions, when breaking waves intermittently disrupt the air-sea interface producing a two-phase environment—air-bubbles in water and sea spray in air. These two-phase mixtures alter the distribution of buoyancy forces, which may affect the air-sea dynamics. The volume nature of the buoyancy forces further complicates the dynamics. Sect. 6.2 describes air-bubbles in the near-surface layer of the ocean. Sect. 6.3 has extensive references to the works on sea-spray production. Effects of sea spray as well as air bubbles on air-sea exchanges in a tropical cyclone are the subjects of Sect. 6.4.

Chapter 7, the final chapter of this monograph, describes current and potential applications of the near-surface results. Among these applications are remote sensing of the ocean, marine optics, marine chemistry and biology, ocean acoustics, and air-sea gas exchange. The last section of this chapter contains possible application of the near-surface results to ocean general circulation and climate modeling.

The upper ocean processes obtain another level of complexity in coastal zones due to several possible additional factors, including river (and other freshwater) discharge, wider range of air-humidity and air-sea temperature differences, typically short wave fetch (for offshore winds), wave shoaling, refraction, and breaking, surface and bottom boundary layers merging approaching the coast, anthropogenic surfactants and other contaminants (sewage, nutrients). Suspended sediments (due to river outflows and to wave action) alter optical properties and stratification. Though some of the related issues are discussed throughout the book, no attempt is made in this book to present the near-surface processes of coastal zones in a systematic way.

This book is mainly directed toward research scientists in physical and chemical oceanography, marine biology, remote sensing, ocean optics, and acoustics. To broaden the potential audience, we have tried to make the book interesting and informative for people with different backgrounds. We also try to keep its style as close as possible to a textbook format to make it of value for graduate studies in oceanography and environmental sciences.

Acknowledgments for the First Edition

Collaborations and discussions with Nikolai Vershinsky (P.P. Shirshov Institute of Oceanology), Vladimir Kudryavtsev (MGI), Peter Schlüssel (EUMETSAT), Julian McCreary (NSU and UH), Mark Donelan (UM), Kristina Katsaros (AOML/NOAA), Eugene Terray (WHOI), and Hiroshi Matsuura (JAMSTEC) helped to motivate writing this book.

We are grateful to Michael Gregg (APL/UW), Anatoly Arjannikov (Granit), David Carlson (WHOI), Robert Weller (WHOI), Chris Fairall (ETL/NOAA), Robert Pinkel (SIO/UCSD), Peter Hacker (UH), Robert Weisberg (USF), Frank Bradley, and Stuart Godfrey (CSIRO) for fruitful collaboration during TOGA COARE, when many results discussed in this book were obtained. Several topics that later formed the foundation for this book were presented during the 1980s at the Theoretical Seminar of the P. P. Shirshov Institute of Oceanology led by Prof. Grigory Barenblatt (now with UC Berkley). Selected parts of this book were presented at the WHOI GFD Summer School during 2002 and 2003 and at the UM Applied Marine Physics laboratory during 2000–2005. Follow up discussions provided important feedback.

Dean Richard Dodge of the NOVA Southeastern University Oceanographic Center, and university President Ray Ferrero, granted sabbatical leave to the lead author during which the bulk of this monograph was undertaken. Support from the Office of Naval Research, NOAA, and NSF are also gratefully acknowledged. The second author was generously supported by the University of Hawaii and by the National

Science Foundation during the research leading up to this book, and during its production.

Technical help with the preparation of the manuscript by Nancy Paquin (UH), Kevin Kohler (NSU), Sharon DeCarlo (UH), Rebekah Walker (NSU) is gratefully acknowledged. Their important contributions and support were critical to the successful conclusion of this project.

Contents

Mathematical Notations

Symbol	Description
a	Wave amplitude
a_i	Weights corresponding to the spectrally distributed absorption coefficients α_i
a_0	Dimensionless constant in microlayer parameterization
A	Albedo
A_d	Parameter determining free-rising profiler dynamics
A_w	Wave age
A_0	Dimensionless coefficient in parameterization for gas transfer
b	Turbulent kinetic energy (TKE)
b_w	Surface wave kinetic energy
B	Dimensionless constant in Craig and Banner (1994) model
B_0	Vertical flux of buoyancy just below the sea surface
c	Phase speed of wave
c	Bubble-free sound speed
c_p	Phase speed at the spectral peak of wind waves
c_p	Specific heat capacity of water at constant pressure
c_{pr}	Specific heat of rain water
c_{pa}	Specific heat capacity of air at constant pressure
C	Conductivity of seawater
C	Volume concentration of bubbles
C_i	Concentration of tracer
C_w	Concentration of tracer in the bulk of water
C_0	Surface concentration of tracer
C_D	Drag coefficient
C_E	Bulk transfer coefficient for latent heat
C_T	Bulk transfer coefficient for sensible heat
C_u	Drag coefficient in the near-surface layer of the ocean
D_r	Diameters of dry particles
$e(k)$	Wavenumber spectrum of kinetic energy
E	Evaporation rate
E	Vertical flux of the kinetic energy
E_B	One-dimensional (horizontal) wavenumber spectrum of buoyancy
E_ρ	One-dimensional (horizontal) wavenumber spectrum of density
$E_u(k_x)$	One-dimensional wavenumber spectrum of turbulence
f	Coriolis parameter
f	Frequency in Hz
f_y	Horizontal component of the Coriolis parameter
f_V	Source function for penetrating rain

Symbol	Description
$f_R(z)$	Function characterizing the absorption of solar radiation with depth
$F_p(\omega_p)$	Longuett-Higgins pressure at the ocean floor
F_k	Flux of kinetic energy carried by rain droplets
F_0	Flux of kinetic energy to waves from wind
F_0	Total spray particle flux
g	Acceleration due to gravity
G_i	Flux of i-th component of tracer admixture
G_{Vi}	Volume source of i-th tracer
G_0	Net air-sea flux of gas
h	Layer depth, mixed layer depth, turbulent boundary layer depth
h_c	Penetration depth of convection
h_r	Rain-formed mixed layer depth
h_D	Diurnal mixed layer depth
h_E	Ekman layer depth
h_{TD}	Turbulent diffusion layer depth
$h_{w\text{-}s}$	Wave-stirred layer depth
h_0	Depth of the near-surface density anomaly
$H(k,\theta)$	Wave directionality function
H	Helicity
H_D	Depth of the bottom boundary of diurnal thermocline
ΔH_D	Thickness of the diurnal thermocline
H	Wave directionality function
H_r	Depth of the bottom boundary of rain-formed halocline
H_s	Significant wave height
I	Overlap integral
I_L	Net longwave irradiance
I_R	Volume source of heat due to absorption of solar radiation
I_Σ	Insolation (surface solar irradiance)
I_0	Solar constant
J	Salinity flux
J_{rV}	Volume source of freshwater due to the decay of raindrops
k	Wavenumber ($k=2\pi/\lambda$)
$\vec{k}$	Wavenumber vector with components k_x,k_y
K_b	Bubble-mediated transfer velocity
K_B	Turbulent diffusion coefficient for bubbles
K_D	Turbulent diffusion coefficient for droplets
K_h	Horizontal mixing coefficient
K_{int}	Interfacial (direct) transfer velocity
K_{Ci}	Diffusion coefficient for *i*-th tracer
Ke	Keulegan number
K_M	Kinematic viscosity
K_S	Diffusion coefficient for salinity
K_T	Thermal diffusion coefficient
K_μ	Gas transfer (piston) velocity
K_0	Mixing coefficient in the logarithmic boundary layer
Ko	Koga number
l	Characteristic length scale of turbulence
L	Width of frontal interface
L	Specific heat of vaporization for water
$L(z,\theta,\phi)$	Radiance in the direction defined by the zenith angle θ and azimuth angle ϕ, and z is the depth

Symbol	Description
L_c	Diameter of low-salinity lense
L_E	Ekman length scale
L_f	Baroclinic Rossby radius
L_G	Garwood et al. (1985) length scale
L_O	Oboukhov buoyancy length scale
L_p	Pressure-gradient length scales
L_β	Equatorial baroclinic Rossby radius
m_d	Mass of the free-ascending device
M_r	Cumulative precipitation
$n(r_0)$	Initial drop size distribution (at z = 0)
N	Brunt-Vaisala frequency
Nu	Nusselt number
p	Pressure
p_a	Gas partial pressure in air
p_w	Gas partial pressure in water
p_0	Atmospheric pressure
P	Precipitation rate
Pr	Prandtl number
q_a	Specific humidity of air
q	Turbulent velocity scale
$q_R(z)$	Scaled solar irradiance as a function of z
q_{R0}	Scaled solar irradiance just below the air-sea interface
q_0	Scaled net heat flux at the sea surface
Q	Heat flux
Q_E	Latent heat flux
Q_{rs}	Surface component of rain-induced heat flux
Q_{rV}	Volume component of rain-induced heat flux
Q_T	sensible heat flux
Q_v	Virtual cooling
Q_0	Net surface heat flux
r	Drop radius
r	Bubble radius
r_0	Initial drop radius
r_{80}	Radius of spray droplets in equilibrium at a relative humidity of 80 %
P_f	Nondimensional number characterizing surface film
R_{rs}	Remote sensing reflectance
R_s	Surface reflectance (traditional definition)
R_s	Surface reflectance (IOCCG, 2000 definition)
Ra	Rayleigh number
Ra_f	Flux Rayleigh number
Re	Reynolds number
Rf	Flux Richardson number
Rf_0	Surface Richardson number
Ri	Richardson number
Ri_{cr}	Critical Richardson number
Ro	Rossby number
R_w	Number associated with direct disruption of the air-sea interface under very strong wind speed conditions
S	Salinity
S_h	Shear
S_h	Bulk salinity of the mixed layer
S_M, S_q	Dimensionless constants in Craig and Banner (1994) model

Symbol	Description
S_r	Bulk salinity of the rain-formed mixed layer
$S_u(f)$	Frequency spectrum of turbulence
S_w	Bulk salinity
S_μ	Gas solubility
S_0	Sea surface salinity
S_0	Reference salinity
Sc	Schmidt number
Sc_T	Turbulent Schmidt number
t	Time, elapsed time
t_*	Renewal time
T	Thermodynamic temperature
T_h	Bulk temperature of the upper ocean mixed layer
T_r	Raindrop temperature
T_w	Bulk water temperature
T_D	Bulk temperature of the diurnal mixed layer
T_0	Sea surface temperature (SST)
T_0	Reference temperature
u, v, w	Mean velocity components in x, y, z directions, respectively
u_l	Typical velocity scale
u_S	Stokes surface drift
u_w	Current velocity of the bulk of water
u_{wd}	Wind-induced surface drift
u_0	Current velocity at the sea surface (relative to the background ocean current)
u_*	Friction velocity in the upper ocean boundary layer
u_{*a}	Friction velocity in the atmospheric boundary layer
u_{*l}	Local friction velocity
u_{*r}	Equivalent friction velocity scale induced in the upper ocean corresponding to the flux of kinetic energy carried by the rain
$\overline{\Delta u}$	Ensemble averaged velocity difference across the aqueous viscous sublayer
U_a	Mean wind speed relative to the ocean surface
U_0	Relative flow speed (towed or mean flow advection speed)
U_{10}	Wind speed at 10 m height
V_x	Longitudinal component of the bow velocity signal
w_b	Buoyant rise speed of bubbles
w_e	Entrainment velocity
w_i	Impact (terminal) velocity of raindrops
w_0	Nominal ascending speed of the free-rising profiler in still water
w_*	Convective velocity scale
W	Total squared vorticity (enstrophy)
W_c	Fraction of sea surface covered by oceanic whitecaps
We	Weber number
x, y, z	Cartesian coordinate system with origin at the sea surface (x directed eastward, y directed northward, z directed upward or downward)
z	Depth
z_c	Compensation depth
z_0	Surface roughness length scale
z_{0a}	Surface roughness length scale from the air side of the air-sea interface
z_+	The wall coordinate $z_+ = zu_*/v$
α	Ostwald solubility coefficient (dimensionless)
α	Polar angle
α_T	Thermal expansion coefficient of seawater

Symbol	Description
α_i	Spectrally distributed absorption coefficients
α_w	Proportionality coefficient for kinetic energy flux from wind to waves
β	Void fraction of entrained air
β_S	Coefficient of saline contraction
β_ω	ε-folding scale for the temporal growth of wave energy in the absence of nonlinear interactions and dissipation
γ	Dimensional parameter in nonlinear diffusion equation
δ	Solar declination angle
δ_ν	Thickness of the viscous sublayer
δ_μ	Thickness of the diffusion sublayer
Δ_e	Equilibrium supersaturation
ε	Viscous dissipation of the turbulent kinetic energy
$\varepsilon_{(0)}$	Viscous dissipation of the turbulent kinetic energy in water near the sea surface
ζ	Stability parameter in the Monin-Oboukhov theory
η	Surface wave displacement
η_D	Internal diffusivity length scale of turbulence
η_T	Internal thermal length scale of turbulence
η_ν	Kolmogorov's internal length scale of turbulence
θ	Zenith angle
θ	Wind direction
Θ	Potential temperature
κ	von Karman constant
κ_T	Molecular coefficient of thermal diffusivity
λ	Wavelength
λ_{IG}	Wavelength of equatorial inertia-gravity wave
λ_S	Nondimensional coefficient in cool-skin parameterization
Λ_0	Dimensionless constant in microlayer parameterization
μ	Molecular coefficient of kinematic tracer diffusivity (for gas, salinity etc.)
μ	Parameter relating to the vertical mixing process and horizontal buoyancy gradients
ν_a	Molecular kinematic viscosity of air
ν_T	Eddy viscosity in Benilov and Ly (2003) model
ξ	Solar elevation angle
ρ	Water density
ρ_0	Reference density
ρ_a	Air density
ρ_r	Density of rain water
σ_s	Surface tension of water covered with film
σ_w	Surface tension of pure water
σ_f	Film pressure($\sigma_f=\sigma_w-\sigma_s$)
σ_t	Sigma-t density
σ_*	Bubble decay rate
σ_η^2	Variance of surface wave elevation
τ	Relaxation time
τ_{ij}	Components of the viscous stress tensor (where i and j can be x, y, or z)
τ_{rs}	Surface component of rain-induced stress
τ_{rV}	Volume component of rain-induced stress
τ_r	Stress due to rain
τ_t	Tangential component of air-sea momentum flux
τ_ω	Wave form induced stress
τ_0	Magnitude of wind stress
Υ	Heat content
φ	Geographical latitude

Symbol	Description
ϕ	Potential function
$\Phi_{\eta}(\vec{k},\omega)$	Surface wave spectrum
$\Phi(\omega)$	Frequency spectrum of surface waves
$\Psi(\vec{k})$	Wavenumber spectrum of surface wave
ω	Frequency ($\omega = 2\pi/f$)
ω_p	Frequency of the wave spectrum peak
ω_0	Lowest eigenfrequency of a single bubble oscillation
Ω	Magnitude of the Earth's rotation vector

Chapter 1
Introduction

Abstract Chapter 1 introduces the reader to the main theme of the book—the near-surface layer of the ocean as an element of the ocean–atmosphere system. The chapter starts with the formulation of the equations of fluid mechanics and thermodynamics that govern the ocean–atmosphere boundary layers. Most of the theoretical results in subsequent chapters of this book are based on these equations. Surface heat, momentum, and freshwater fluxes provide boundary conditions for solving equations. Solar radiation and its absorption in the near-surface layer of the ocean must be treated as a body (volume) source of thermal energy. Rainfall contributes to the surface and volume freshwater, momentum, and heat fluxes. Elements of surface wave theory directly relating to the dynamics of the near-surface layer of the ocean are introduced in this chapter as well. Matching the dynamics and thermodynamics of the ocean and atmosphere occurs in planetary boundary layers. The existing mixing models are briefly reviewed in the context of the planetary boundary layer. This general discussion of upper ocean dynamics and thermodynamics sets the stage for the content of Chaps. 2–7.

Keywords Near-surface layer • Conservation equations • Turbulence • Air–sea fluxes • Solar radiation • Rain-induced fluxes • Wave dynamics • Planetary boundary layer • Mixing • Barrier layer

1.1 The Ocean Near-Surface Layer in the Ocean–Atmosphere System

The top 2–3 m of the ocean has the same heat capacity as the entire atmosphere above. Of the surface-penetrating solar radiation, 50 % is absorbed within the first 0.5 m of the ocean. Of the breaking surface wave kinetic energy, 50 % dissipates within 20 % of the significant wave height from the surface. These facts highlight the special role of the near-surface layer of the ocean in the ocean–atmosphere system.

Historically, standard oceanographic instruments (like Conductivity, Temperature, Depth (CTD) sensors, acoustic Doppler current profilers (ADCPs), and most types of turbulence profilers) have not produced high-quality measurements in the upper few meters of the ocean. As a result, important processes in the near-surface layer of the ocean, like the large diurnal warming event shown in Fig. 1.1, were largely

A. Soloviev, R. Lukas, *The Near-Surface Layer of the Ocean,* Atmospheric and Oceanographic Sciences Library 48, DOI 10.1007/978-94-007-7621-0_1,

missed. The aim of this monograph is to cover this gap to provide the reader with a more complete picture of the upper ocean, which is of increasing importance for certain practical applications such as remote sensing, climate modeling, and determining the global carbon cycle.

Since the publication of the first edition of this book, the new types of autonomous underwater vehicles (such as ocean gliders, wave gliders, and solar-powered gliders) and Argo floats have been under development. These amazing new instruments have usually been designed for studying deeper ocean layers and have limited capabilities near the sea surface. Development of the new generation of specialized instrumentation for the near-surface studies is ongoing.

We define the near-surface layer of the ocean as being immediately adjacent to the air–sea interface and dominantly influenced by the local fluxes of heat, moisture, momentum, and gas from the atmosphere. It is impossible to give a universal definition of this layer in meters because the mixing regime below the air–sea interface strongly depends on meteorological, radiation, and surface wave conditions. Instead, in this monograph the near-surface layer of the ocean is considered as an integral part of the ocean–atmosphere system. There are in fact some processes that are unique to the upper few meters (*e.g.*, wave breaking) or even for the upper few millimeters (*e.g.*, molecular transport) of the ocean. Other processes may be confined to the upper few meters of the ocean under certain conditions (*e.g.*, large diurnal warming events), but, for different environmental conditions, they will have depth scales of tens of meters. There are also processes that originate at the air–sea interface but extend to the overall depth of the upper ocean mixed layer (*e.g.*, Langmuir circulations and nighttime convection).

The variety of forcing factors, in combination with nonlinear feedbacks, result in different near-surface regimes. Fedorov and Ginzburg (1988) consider five regimes in the near-surface layer of the ocean:

1. intensive wind–wave mixing (wind speed at 10 m height above the ocean surface $U_{10} > 8$–10 m s^{-1});
2. intensive convection (nighttime, winter, or atmospheric cold fronts);
3. Langmuir circulations (U_{10} from 3 to 10 m s^{-1});
4. intensive solar heating under low wind and calm weather conditions (U_{10} from 0 to 3–5 m s^{-1}); and
5. near-surface freshening due to rain.

This classification is still valid in general and is useful for many practical applications. In particular, regimes 4 and 5 are consistent with the new results presented in Chaps. 3 and 4 of our book. At this point, however, Fedorov and Ginzburg's classification requires comment.

The near-surface ocean under regime 1 is usually well mixed. However, surface molecular sublayers, which are not included in this classification, may develop even under conditions of intensive wind–wave mixing though only between wave-breaking events (see Chap. 2).

The Langmuir circulations, which are considered as a separate regime (regime 3) by Fedorov and Ginzburg, are a type of spatially coherent organized motion in

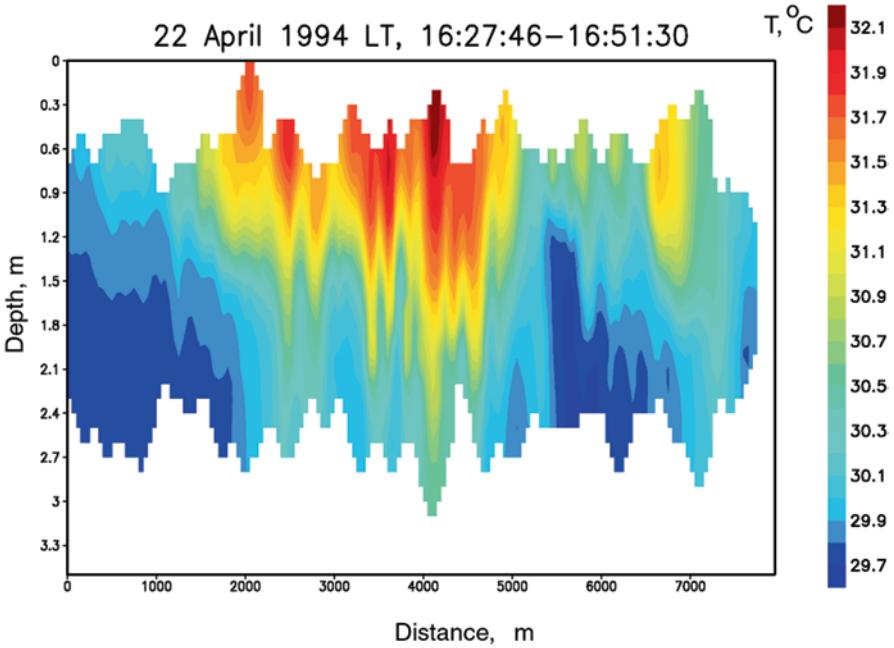

Fig. 1.1 High-resolution temperature section in the upper 3 m of the ocean during a large diurnal warming event in the equatorial Pacific Ocean, from measurements by bow-mounted sensors (see Sect. 3.3.5). Temperature is given by the color bar on the right. After Soloviev and Lukas (1997) by permission of Elsevier

the upper ocean. There are also other types of organized structures in the upper ocean, which are not included in the Fedorov and Ginzburg classification but widely observed in the near-surface ocean (see Chap. 5). These are ramp-like structures, surface streaks, large-amplitude internal waves (developing on a shallow diurnal thermocline or rain-formed halocline), sharp frontal interfaces, and penetrative convection.

Now, it is becoming clear that conditions of very high wind speeds (U_{10}>25–30 m s^{-1}) should be considered as a separate near-surface regime. In these extreme conditions, a two-phase environment with gradual transition from bubble-filled water to spray-filled air is formed (Chap. 6).

Before proceeding to the main subject of this book, the near-surface layer of the ocean, in Chap. 1 we provide a general discussion of the governing equations and air–sea interaction processes. The organization of the material in the rest of Chap. 1 is as follows.

Section 1.2 formulates the equations of fluid dynamics that govern the ocean–atmosphere boundary layers. Most of the equations for the near-surface ocean and the calculated results in this book are derived from these basic equations. Surface heat, momentum, and freshwater fluxes provide boundary conditions for equations formulated in Sect. 1.2. These surface boundary conditions are discussed in Sect. 1.3.

Section 1.4 considers solar radiation and its absorption in the near-surface layer of the ocean. This solar energy and its variations are the major forcing factor in the ocean–atmosphere system. For the near-surface layer of the ocean, it should be treated as a body (volume) source of thermal energy. Formally, this term does not enter the surface boundary condition for the heat budget. The rain contributions to the surface and volume heat fluxes are considered in Sect. 1.5.

Surface waves are the most important process distinguishing the near-surface layer of the ocean from its deeper layers. In Sect. 1.6, the elements of surface wave theory directly relating to the dynamics of the near-surface layer of the ocean are introduced as solutions for the equations of fluid mechanics.

Matching the dynamics and thermodynamics of the ocean and atmosphere occurs in the planetary boundary layers (PBL), which are the subject of Sect. 1.7.

1.2 Basic Equations of Fluid Mechanics and Useful Approximations

1.2.1 Mathematical Notation and Governing Equations

This book covers a variety of topics relating to different disciplines. Some reuse of symbols for different properties is therefore unavoidable. This is noted in the list of frequently used mathematical symbols given in the "Mathematical Notations". An attempt is made to avoid situations where a symbol with two different meanings would appear in the same section. Symbols that appear only locally in the text typically are not included in the list of frequently used mathematical symbols.

The main equations that govern the oceanic and atmospheric boundary layers, including the near-surface layer of the ocean, have been formulated and discussed in many scientific publications. The full system of equations includes conservation laws for mass, momentum, heat, energy, salt or moisture plus the equation of state. The transport equation for an arbitrary passive tracer can be easily included.

From the developments of LeBlond and Mysak (1978), Mellor (1996), and Müller (2006), the components of the *momentum equation* on a rotating sphere on the *f-plane* are as follows:

$$\rho\left(\frac{Du}{Dt} - fv + f_y w\right) = -\frac{\partial p}{\partial x} + \frac{\partial \tau_{xx}}{\partial x} + \frac{\partial \tau_{yx}}{\partial y} + \frac{\partial \tau_{zx}}{\partial z} \tag{1.1}$$

$$\rho\left(\frac{Dv}{Dt} + fu\right) = -\frac{\partial p}{\partial y} + \frac{\partial \tau_{xy}}{\partial x} + \frac{\partial \tau_{yy}}{\partial y} + \frac{\partial \tau_{zy}}{\partial z}, \tag{1.2}$$

$$\rho\left(\frac{Dw}{Dt} - f_y u\right) = -\rho g - \frac{\partial p}{\partial z} + \frac{\partial \tau_{xz}}{\partial x} + \frac{\partial \tau_{yz}}{\partial y} + \frac{\partial \tau_{zz}}{\partial z} \tag{1.3}$$

where ρ is the fluid density, and $\frac{D}{Dt} = u\frac{\partial}{\partial x} + v\frac{\partial}{\partial y} + w\frac{\partial}{\partial z} + \frac{\partial}{\partial t}$. The rectangular coordinate system has its origin at the sea surface, with x directed eastward, y directed northward, z directed upward, and u, v, and w represent the corresponding velocity components; t is time; $f = 2\Omega\sin\varphi$ and $f_y = 2\Omega\cos\varphi$, where Ω is the magnitude of the Earth's rotation vector and φ is the latitude; p is pressure; and g is the acceleration due to gravity. Symbol τ denotes the *stress tensor*, due to viscosity (and to fluctuating velocities if u, v, and w refer to ensemble mean quantities).

Seawater density cannot be measured directly in the ocean. It is determined from the equation of state, $\rho = function(T, S, p)$, which defines the ocean water density as a nonlinear function of temperature, salinity, and pressure. The Intergovernmental Oceanographic Commission (IOC) has recently adopted the Thermodynamic Equation Of Seawater – 2010 (TEOS-10). TEOS-10 exploits the thermodynamic equilibrium properties between seawater, ice, and humid air and provides very accurate properties such as freezing temperature, latent heat of evaporation, etc. (IOC et al. 2010). TESCO-10 replaces Practical Salinity with Reference Salinity, effective from January 1, 2010. The use of Practical Salinity in journal articles is being phased out over a 5-year transition period. We continue using Practical Salinity in our book since all sources referenced here reported salinity in Practical Salinity units.

For small changes of temperature and salinity, the equation of state can be approximated with the following linear function: $\rho = \rho_0 + \rho_0\left[-\alpha_T\left(T - T_0\right) + \beta_S\left(S - S_0\right)\right]$, where ρ_0 is the reference density, α_T is the thermal expansion coefficient of seawater, and β_S is the coefficient of saline contraction. Coefficients α_T and β_S are, however, functions of the reference temperature T_0, salinity S_0, and pressure p_0.

The system of equations (1.1)–(1.3) is complemented with the *continuity equation* for fluids,

$$\frac{D\rho}{Dt} + \frac{\partial u}{\partial x} + \frac{\partial v}{\partial y} + \frac{\partial w}{\partial z} = 0. \tag{1.4}$$

For oceanographic applications, water in general can be treated as an incompressible fluid. The water compressibility term has, however, to be taken into account for acoustic and other similar applications.

In the Boussinesq approximation, which is applicable to many oceanic conditions, the water compressibility term $(D\rho/Dt)$ in equation (1.4) and density changes in equations (1.1)–(1.3) can be neglected except in the gravity term entering (1.3) where ρ is multiplied by g. The Boussinesq approximation is not valid for acoustic applications and for two-phase environments like the surface wave breaker.

In the general case of an isotropic *Newtonian fluid*, the different components of the viscous stress tensor depend linearly on strain components (Mellor 1996):

$$\begin{bmatrix} \tau_{xx} & \tau_{yx} & \tau_{zx} \\ \tau_{xy} & \tau_{yy} & \tau_{zy} \\ \tau_{xz} & \tau_{yz} & \tau_{zz} \end{bmatrix} = \rho K_M \begin{bmatrix} 2\dfrac{\partial u}{\partial x} & \dfrac{\partial u}{\partial y}+\dfrac{\partial v}{\partial x} & \dfrac{\partial u}{\partial z}+\dfrac{\partial w}{\partial x} \\ \dfrac{\partial v}{\partial x}+\dfrac{\partial u}{\partial y} & 2\dfrac{\partial v}{\partial y} & \dfrac{\partial v}{\partial z}+\dfrac{\partial w}{\partial y} \\ \dfrac{\partial w}{\partial x}+\dfrac{\partial u}{\partial z} & \dfrac{\partial w}{\partial y}+\dfrac{\partial v}{\partial z} & 2\dfrac{\partial w}{\partial z} \end{bmatrix}, \tag{1.5}$$

where ρ is the water density that under the Boussinesq approximation can be treated as a constant property of the fluid, and K_M is the *kinematic viscosity*, which is also assumed to be a property of the fluid. (Note that Newtonian fluids are actually a relatively narrow class of fluids.)

1.2.2 Boundary-Layer Approximation

Adjacent to the air–sea interface, there are boundary layers in both the atmosphere and the ocean. Their thickness is much less than their horizontal dimension, which leads to the so-called *boundary-layer approximation*. Under this approximation, the motion and continuity equations (1.1)–(1.4) are as follows (Mellor 1996):

$$\frac{\partial u}{\partial t}+u\frac{\partial u}{\partial x}+v\frac{\partial u}{\partial y}+w\frac{\partial u}{\partial z}-fv=-\frac{1}{\rho}\frac{\partial p}{\partial x}+\frac{1}{\rho}\frac{\partial \tau_{zx}}{\partial z}, \tag{1.6}$$

$$\frac{\partial v}{\partial t}+u\frac{\partial v}{\partial x}+v\frac{\partial v}{\partial y}+w\frac{\partial v}{\partial z}+fu=-\frac{1}{\rho}\frac{\partial p}{\partial y}+\frac{1}{\rho}\frac{\partial \tau_{zy}}{\partial z}, \tag{1.7}$$

$$\frac{\partial p}{\partial z}=-\rho g, \tag{1.8}$$

$$\frac{\partial u}{\partial x}+\frac{\partial v}{\partial y}+\frac{\partial w}{\partial z}=0. \tag{1.9}$$

Note that the definition of this approximation may vary between different authors. Here, we follow the Mellor (1996) definition.

Under the boundary-layer approximation, the conservation equation for vertical momentum (1.3) reduces to the hydrostatic equation (1.8). This equation provides a substantial simplification of the governing system of equations because the vertical distribution of pressure can be determined from the density field, and it does not directly depend on the fluid motion.

The heat, salinity, and other material transport equations in the upper ocean under the boundary-layer approximation are as follows:

$$\rho c_p \left(\frac{\partial \Theta}{\partial t} + u \frac{\partial \Theta}{\partial x} + v \frac{\partial \Theta}{\partial y} + w \frac{\partial \Theta}{\partial z} \right) = - \frac{\partial Q}{\partial z} + \frac{\partial I_R}{\partial z} - \frac{\partial Q_{rV}}{\partial z}, \tag{1.10}$$

$$\rho \left(\frac{\partial S}{\partial t} + u \frac{\partial S}{\partial x} + v \frac{\partial S}{\partial y} + w \frac{\partial S}{\partial z} \right) = - \frac{\partial J}{\partial z} - \frac{\partial J_{rV}}{\partial z}. \tag{1.11}$$

$$\frac{\partial C_i}{\partial t} + u \frac{\partial C_i}{\partial x} + v \frac{\partial C_i}{\partial y} + w \frac{\partial C_i}{\partial z} = - \frac{\partial G_i}{\partial z} - \frac{\partial G_{Vi}}{\partial z} - \sigma_* C_i, \tag{1.12}$$

where c_p is the specific heat capacity, Θ is the *potential temperature*, S is the salinity, and C_i is the concentration of ith component of passive (neutrally buoyant) tracer admixture; Q, J, and G_i are the vertical fluxes of heat, salt, and ith component of tracer, respectively. I_R and Q_{rV} are the volume heat sources due to absorption of solar radiation and absorption of raindrops penetrating the sea surface; J_{rV} is the volume source of freshwater due to the absorption of raindrops; G_{Vi} is the volume source of material or gas (due to bubbles, biochemical reactions, etc.), and σ_* is the dissolution rate. Parameterizations for I_R, Q_{rV}, and J_{rV} are provided in Sects. 1.4 and 1.5. Parameterizations for G_{Vi} in application for gas transport are discussed in Sect. 7.8.1e

For most near-surface applications, Θ is practically equivalent to thermodynamic temperature, T; however, the difference between the potential and thermodynamic temperature becomes more important when a weakly stratified mixed layer is considered (Sect. 5.3.1).

The vertical heat flux is related to the gradient of temperature according to *Fourier's law*:

$$Q = -c_p \rho K_T \frac{\partial \Theta}{\partial z}, \tag{1.13}$$

where K_T is the coefficient of thermal diffusivity, assumed to be constant. The vertical salt and scalar tracer fluxes are related to the gradients of salinity and concentration according to *Fick's law:*

$$J = -\rho K_S \frac{\partial S}{\partial z}, \tag{1.14}$$

$$G_i = -K_{Ci} \frac{\partial C_i}{\partial z}, \tag{1.15}$$

where K_S and K_{Ci} are the constant diffusion coefficients for salt and an arbitrary scalar tracer, respectively.

1.2.3 Low Rossby Number Approximation

Further simplification of equations (1.6)–(1.7) is possible in the case of low *Rossby number*,

$$Ro = u_l / (Lf) \ll 1, \tag{1.16}$$

where u_l is the typical velocity scale, l is the length scale characteristic of horizontal variation of properties in the ocean, and f is the Coriolis parameter. Under the boundary layer and low Rossby number approximations, the advective terms in equations (1.6)–(1.7) disappear reducing these equations to

$$\frac{\partial u}{\partial t} - fv = -\frac{1}{\rho}\frac{\partial p}{\partial x} + \frac{1}{\rho}\frac{\partial \tau_{zx}}{\partial z}, \tag{1.17}$$

$$\frac{\partial v}{\partial t} + fu = -\frac{1}{\rho}\frac{\partial p}{\partial y} + \frac{1}{\rho}\frac{\partial \tau_{zy}}{\partial z}. \tag{1.18}$$

Equations (1.10)–(1.12) for the heat, salinity, and other substances are unaffected by the low Rossby number approximation since the Coriolis term does not enter into these scalar equations.

1.2.4 Turbulence and Turbulent Kinetic Energy Budget

In the ocean, diffusion is dominated by turbulence. Turbulence can occur because of local (shear or convective) flow instability or may be transported from a nonlocal source by advection, convection, or turbulent velocity and pressure fluctuations. An important source of turbulence in the upper ocean is surface wave breaking (Chap. 3).

The criterion for shear instability commonly used in hydrodynamics is the Reynolds number,

$$Re = u_l l / \nu \tag{1.19}$$

where u_l is the velocity scale, ν is the molecular coefficient of kinematic viscosity ($\nu = 1.1 \cdot 10^{-6}$ m^2 s^{-1} at $T = 20$°C and $S = 35$ psu), and l is the characteristic length scale. The transition from laminar to turbulent flow usually occurs at $\mathrm{Re}_{cr} \sim 10^3$.

Convective instability of the flow results from unstable temperature or salinity stratification. A relevant nondimensional criterion for thermal convection is the *Rayleigh number*,

$$Ra = -\alpha_T g \Delta T h^3 / (\kappa_T \nu), \tag{1.20}$$

where g is the acceleration of gravity, α_T is the thermal expansion coefficient of seawater ($\alpha_T = -2.6 \times 10^{-4}$ °C^{-1} at $T = 20$°C and $S = 35$ psu), ΔT is the vertical temperature difference between the top and bottom of the convecting layer, h is the layer thickness, and κ_T is the molecular coefficient of thermal diffusivity ($\kappa_T = 1.3 \times 10^{-7}$ m^2 s^{-1} at $T = 20$°C and $S = 35$ psu). The term, $\alpha_T \Delta T = \Delta\rho/\rho$, represents the fractional density difference between the top and bottom of the convective layer. The transition from laminar to turbulent convection is usually observed in the ocean for critical Rayleigh number $Ra_{cr} \sim 5 \times 10^4$ (Turner 1973).

The Reynolds numbers associated with ocean currents are very large, on the order of 10^7, and these currents are generally turbulent. Rayleigh numbers in the ocean are also very large (typically greater than 10^{14} for a temperature difference of 0.1°C over 10 m), so convection is usually turbulent. However, for strong stable stratification, Ra may drop below Ra_{cr}. In the near-surface ocean, such cases can occur under conditions of calm weather and strong insolation (Chap. 4).

Although originally derived for laminar flows, parameterization laws (1.5) and (1.13)–(1.15) are applicable for characterizing the turbulent transport of momentum and scalar properties like temperature, salinity, or gas. In the case of a turbulent flow, coefficients K_m, K_T, K_S, and K_C represent the turbulent eddy transport. The conservation equations for momentum, heat, salt, and passive tracers expressed in terms of turbulent eddy coefficients appear exactly in the same form as their laminar analogs (1.1)–(1.3) and (1.10)–(1.12) in the limiting case that K_m, K_T, K_S, and K_C do not vary in space. In a developed turbulent flow (*i.e.*, at large Reynolds numbers), K_m, K_T, K_S, and K_C are approximately equal, unlike the corresponding molecular diffusivities, though their differences may still matter.

Turbulent eddy coefficients depend on the flow, geometry, and stratification. In the simplest form, the turbulent eddy coefficient for momentum is parameterized based on Prandtl's mixing length hypothesis $K_m \sim l u_l$ and Kolmogorov's hypothesis $u_l \sim \sqrt{b}$, where l is the mixing length, and b is the turbulent kinetic energy (TKE). More sophisticated semi-empirical closure schemes are considered in Chaps. 3–5.

The individual components of the TKE budget are given in the form derived by Garwood (1977):

$$\frac{1}{2}\frac{\partial \overline{u'^2}}{\partial t} = -\overline{u'w'}\frac{\partial u}{\partial z} - \frac{\partial}{\partial z}\left(\frac{\overline{w'u'^2}}{2}\right) + \overline{\frac{p'}{\rho}\frac{\partial u'}{\partial x}} + f\overline{u'v'} - f_y\overline{u'w'} - \frac{\varepsilon}{3}, \tag{1.21}$$

$$\frac{1}{2}\frac{\partial \overline{v'^2}}{\partial t} = -\overline{v'w'}\frac{\partial v}{\partial z} - \frac{\partial}{\partial z}\left(\frac{\overline{w'v'^2}}{2}\right) + \overline{\frac{p'}{\rho}\frac{\partial v'}{\partial y}} - f\overline{u'v'} - \frac{\varepsilon}{3}, \tag{1.22}$$

$$\frac{1}{2}\frac{\partial \overline{w'^2}}{\partial t} = -\frac{g}{\rho}\overline{\rho' w'} - \frac{\partial}{\partial z}\left(\frac{\overline{w'^3}}{2} + \frac{\overline{w' p'}}{\rho}\right) + \frac{\overline{p'}}{\rho}\frac{\partial \overline{w'}}{\partial z} + f_y \overline{u' w'} - \frac{\varepsilon}{3}, \tag{1.23}$$

where ρ is treated as a constant density and ρ' is the density fluctuation, ε is the viscous dissipation, and primes denote the fluctuating components. Garwood and Gallacher (1985) studied the usually neglected horizontal Coriolis term $\left(f_y \overline{u' w'}\right)$ in the TKE budget. In this term, the Reynolds stress interacts with the northward component of planetary rotation to exchange TKE between horizontal and vertical components. In fact, the sum of equations (1.21)–(1.23) does not contain the horizontal Coriolis term:

$$\frac{\partial b}{\partial t} = \tau_{xz}\frac{\partial u}{\partial z} + \tau_{yz}\frac{\partial v}{\partial z} - \frac{g}{\rho}\overline{w' \rho'} - \frac{\partial E}{\partial z} - \varepsilon, \tag{1.24}$$

where $b = \overline{(u'^2 + v'^2 + w'^2)}/2$ and $b' = (u'^2 + v'^2 + w'^2)/2$ are the mean TKE and its fluctuation, respectively; $E = \overline{w'(b' + p'/\rho)}$ is the vertical flux of TKE; $\tau_{xz} = -\rho\overline{u' w'}$ and $\tau_{yz} = -\rho\overline{v' w'}$ are the components of the Reynolds stress. The term associated with buoyancy forces can be expressed in terms of the turbulent heat $(Q = c_p \rho \overline{\Theta' w'})$, salt $(J = \rho \overline{S' w'})$, and tracer concentration $(G_i = \overline{w' C_i'})$ fluxes as follows: $\frac{g}{\rho}\overline{\rho' w'} = \frac{\alpha_T g Q}{c_p \rho} + \frac{\beta_S g J}{\rho} + g\sum_i \frac{(\rho_i - \rho) G_i}{\rho}$, where α_T and β_S are the previously defined thermal expansion coefficient of seawater and coefficient of saline contraction, respectively; and, ρ_i is the density of *i*th tracer.

1.3 Boundary Conditions

In order to compute changes in the ocean–atmosphere system, it is necessary to know the appropriate conditions to apply at boundaries. Volume sources must also be specified. In this section, we consider the surface boundary conditions for the momentum, heat, and mass balance equations. The volume sources due to solar radiation and penetrating raindrops are discussed in Sects. 1.4 and 1.5, respectively. (Initial conditions are also required but are more problem specific and formulated individually for each case.)

Surface waves significantly complicate boundary conditions. The idealized discontinuity of density across the air–water interface works well in many situations. However, in the presence of breaking waves, the flux of kinetic energy (and ideally the flux of the momentum, heat, and mass) from the atmospheric boundary layer to the near-surface layer of the ocean has to be treated as a volume source (Rascle et al. 2013).

Under very high wind speed conditions, the breaking events produce a diffuse, two-phase layer (air bubbles in water and sea spray in air; see Chap. 6). In this regime, the oceanic and atmospheric boundary layers are strongly coupled via the spectrum of surface waves with different wavelengths and heights. As a result, setting of the boundary conditions using bulk-flux coefficients referred to 10 m above mean sea level may be a challenge.

1.3.1 Types of Surface Boundary Conditions

For the air–sea interface, boundary conditions are usually formulated in terms of velocity, temperature, and concentration or in terms of momentum, heat, and mass (gas) fluxes. In many practical situations, the detailed structure of the air–sea interface is difficult to resolve, in particular, due to the presence of molecular sublayers (see Chap. 2). As a result, a formulation of boundary conditions in terms of fluxes is often more suitable.

The surface boundary conditions for momentum balance equations (1.17) and (1.18) expressed in terms of fluxes are as follows:

$$\tau_{x0} = \tau_{xz}\big|_{z\to -0} \text{ and } \tau_{y0} = \tau_{yz}\big|_{z\to -0}, \tag{1.25}$$

where τ_{x0} and τ_{y0} are the east- and northward components of the surface stress, usually due to wind; and, $z \to -0$ denotes the one-sided limit from the water side. Alternatively, the wave- or rain-induced component of the momentum flux can be treated as a combination of surface flux and volume source of momentum in the near-surface layer of the ocean, which, however, requires the addition of the volume source term into the equation for momentum balance.

The surface boundary condition for the heat transport equation (1.10) in water is as follows:

$$Q_0 = Q\big|_{z\to -0} = Q_T + Q_E + I_L + Q_{rs}, \tag{1.26}$$

where Q_0 is the net surface heat flux; Q_T and Q_E are the sensible and latent heat fluxes, respectively; I_L is the net longwave radiative flux; Q_{rs} is the surface component of the rain-induced heat flux (see Sect. 1.5.4). Solar radiation does not enter the surface boundary condition because it is treated as a volume source of heat.

The surface boundary condition for the salinity transport equation (1.11) is associated with freshwater fluxes at the air–sea interface due to evaporation and precipitation. A vertical balance of freshwater flux across the ocean surface is as follows (Mellor 1996):

$$E - P + m_0 \cdot (1 - S_0) = 0, \tag{1.27}$$

where S_0 is the sea surface salinity; E is the evaporation rate, which is related to the latent heat flux as

$$Q_E = LE, \tag{1.28}$$

L is the specific volume heat of vaporization for water; P is the precipitation rate; and m_0 is the flux of freshwater to the sea surface (in units of volume of water per unit area per unit time). The factor $(1-S_0)$ accounts for the exclusion of salt from seawater during evaporation. The salt flux at the waterside of the air–sea interface in units of mass per unit area per unit time (kg m^{-2} s^{-1}) is

$$J_0 = J\big|_{z\to -0} = \rho S_0 m_0. \tag{1.29}$$

Combining (1.27) and (1.29) leads to the following boundary condition on the salt flux at the ocean surface:

$$J_0 = -(E-P)S_0/(1-S_0) \approx -(E-P)S_0 = -(Q_E/L - P)S_0. \tag{1.30}$$

Note that in the open ocean, $S_0 \approx 35$ psu $= 0.035$; therefore, factor $(1-S_0)$ is replaced with unity in (1.30). However, for calculating horizontal density gradients, the factor $(1-S_0)$ may still be of importance (IOC et al. 2010).

The salinity increases toward the ocean surface when evaporation exceeds precipitation ($E>P$) or decreases when precipitation exceeds evaporation ($E<P$) because of freshwater flux subtracted from or added to the surface water, respectively. Vertical salinity gradients developing in the near-surface layer of the ocean due to surface forcing are considered in Chap. 2 of this monograph in relation to the microlayer and in Chap. 4 in relation to diurnal warming and precipitation effects.

Due to generation and subsequent evaporation of spray droplets, salt crystals are transported into the atmosphere (see Chap. 6); however, only a relatively small mass of salt actually crosses the air–sea interface. The salt crystals left behind by evaporating spray play a role in the radiation balance and in cloud microphysics as condensation nuclei.

Fluxes of momentum, heat, and moisture at the air–sea interface can be estimated from eddy covariance and inertial-dissipation measurements in the atmospheric boundary layer (Smith et al 1996; Fairall et al. 2003). However, such direct flux measurements are a rather complicated experimental task, which is only performed during specialized field campaigns. For many practical purposes, the fluxes at the air–sea interface can be linked to the properties of the bulk of the atmosphere and ocean, and to the properties of the interface.

The balance of forces that act upon the air–sea interface constitutes the dynamic boundary condition in the potential theory of surface waves. This boundary condition is discussed in Sect. 1.6.1.

Implementation of non-hydrostatic, computational fluid dynamics (CFD) type models in the upper ocean research has opened new perspectives in three-dimensional (3-D) description of the upper ocean and its evolution in response to changing

environmental forcing (see, e.g., Matt et al. 2011; McWilliams et al. 2012; Soloviev et al. 2012). Boundary conditions for 3-D models have some specifics because of limited horizontal extent of the numerical domain. One approach is to use periodic lateral boundary conditions along the direction of the main flow. This approach may, however, cause spurious results in the presence of the Coriolis force, which has a tendency to change direction of the flow. The Coriolis effect results in some angle ($\alpha = 20°$ or so) between the wind–wave direction and the Langmuir cell axis direction, also changing with depth due to the Ekman spiraling. Setting periodicity in the numerical domain may result in an imposed periodicity in the transverse direction with length scale $L_y = L_0 \sin\alpha$, where L_0 is the length of the numerical domain along the flow direction. For $L_0 = 100$ m, $L_y = 34$ m, which is dangerously close to the transverse size of real Langmuir cells. As a result, the numerical simulation may produce an artifact, which will look like real Langmuir cells.

1.3.2 Bulk-Flux Formulation

The turbulent flux of property x is parameterized in bulk-flux algorithms as follows (Smith et al. 1996; Fairall et al. 2003):

$$\overline{w'\chi'} = c_\chi^{1/2} c_D^{1/2} U_a \Delta\chi = C_\chi U_a \Delta\chi, \tag{1.31}$$

where w is the vertical component of the wind velocity vector; χ can represent wind velocity components, temperature, specific humidity, or the mixing ratio of atmospheric gases (the prime sign denotes a fluctuation); c_χ is the bulk transfer coefficient for property χ; and $C_\chi = c_\chi^{1/2} c_D^{1/2}$ is the total transfer coefficient (symbol D is reserved for momentum).

The mean wind speed relative to the ocean surface U_a is composed of a mean vector part (u and v components) and a *gustiness* component (U_g) in the following way:

$$U_a = (u^2 + v^2 + U_g{}^2)^{1/2} \tag{1.32}$$

The air–sea difference in the mean value of χ is defined as follows:

$$\Delta\chi = \chi_{sea} - \chi(z) \tag{1.33}$$

Both U_a and $\Delta\chi$ are referenced to the specified height, z, of the mean quantities above the mean ocean surface (usually $z = 10$ m).

The bulk-flux formulation for the magnitude of wind stress $\tau_0 = (\tau_{x0}^2 + \tau_{y0}^2)^{1/2}$ following from (1.25) and (1.31) is as follows:

$$\tau_0 = C_D \rho_a (U_{10} - u_s)^2, \tag{1.34}$$

where C_D is the drag coefficient, ρ_a is the density of air, U_{10} is the wind speed at 10 m height ($z=10$ m), and u_S is the component of the surface current velocity in the wind direction. Traditionally, the ocean currents have been ignored in this parameterization because they are not generally known.

Sensible, Q_T, and latent, Q_E, heat fluxes are estimated from the following bulk formulations:

$$Q_T = c_{pa}\rho_a C_T U_{10}(T_0 - T_a) \tag{1.35}$$

$$Q_E = L\rho_a C_E U_{10}(q_0 - q_a) \tag{1.36}$$

where c_{pa} is the specific heat capacity of air at constant pressure, C_T is the bulk transfer coefficient for sensible heat, C_E is the bulk transfer coefficient for latent heat, T_0 is the sea surface temperature (SST), T_a is the air temperature at a reference height, q_0 is the saturation specific humidity of air at sea surface temperature, and q_a is the specific humidity of air. The reference height for the temperature and humidity data in the air is typically 2 m. Note that the definition of SST is somewhat problematic here due to temperature differences across the near-surface layer of the ocean (see Chaps. 2 and 4).

For order of magnitude estimates, $C_D \sim 1.1\times10^{-3}$ for $U_{10}=5$ m s^{-1}, while for wind speeds within the range, 6 m s$^{-1}<U_{10}<22$ m s^{-1}, Smith (1988) suggested a linear relationship:

$$C_D \approx 1\times10^{-3}\cdot(0.61+0.063U_{10}) \tag{1.37}$$

Smith (1988) also proposed empirical formulas for the sensible and latent heat transfer coefficients:

$$C_T = \begin{cases} 0.83\times10^{-3} \text{ for stable conditions} \\ 1.10\times10^{-3} \text{ for unstable conditions} \end{cases} \tag{1.38}$$

and

$$C_E = 1.5\times10^{-3}, \tag{1.39}$$

which are in reasonably good agreement with data in the wind speed range above.

Advanced bulk-flux algorithms are based on the Monin–Oboukhov similarity theory (see Sect. 1.7.2), representing the fluxes in terms of mean quantities. While there are many algorithms available today, we will restrict our discussion to the Coupled Ocean–Atmosphere Response Experiment (COARE) 3.0 bulk-flux algorithm (Fairall et al. 2003), because it is well documented, based on physics, and works well.

The transfer coefficients depend on the Monin–Oboukhov stability parameter $\zeta = |z| / L_O$:

$$c_\chi^{1/2}(\zeta) = c_{\chi 0}^{1/2} \Big/ \left[1 - c_{\chi 0}^{1/2} \kappa^{-1} \psi_\chi(\zeta)\right] \tag{1.40}$$

where z is the height of measurements, L_0 is the Oboukhov buoyancy length scale, $c_{\chi 0}^{1/2} = \kappa / \ln(z / z_{0\chi})$ is the transfer coefficient under neutral stratification ($\zeta = 0$), ψ_χ is a universal function of stability parameter ζ, κ is the von Karman constant (commonly used value $\kappa = 0.4$), and $z_{0\chi}$ is the *surface roughness length* for property χ under neutral stratification in the atmospheric boundary layer. The stability parameter is given by the formula of Zilitinkevich (1966):

$$\varsigma = \frac{-\kappa g |z|}{T} \frac{(\overline{w'\Theta'} + 0.61 T \overline{w'q'})}{(-\overline{w'u'})^{3/2}}, \tag{1.41}$$

where g is the acceleration of gravity and T is the absolute temperature in K.

It is convenient to define a velocity scaling parameter $u_{*a} = (-\overline{w'u'})^{1/2}$, which is known as the *friction velocity* (in the atmosphere, in this case) and respective scaling parameters for temperature $\Theta_{*a} = -\overline{w'\Theta'} / u_{*a}$, and humidity $q_* = -\overline{w'q'} / u_{*a}$. Here, $\overline{w'u'}$ denotes the streamwise component of the vertical momentum flux. The kinematic fluxes in (1.41) can then be replaced with u_{*a}, Θ_{*a}, and q_* obtained by iteration within the bulk algorithm.

The bulk model formulated in (1.31), (1.40), and (1.41) has to be completed with representations (parameterizations) of the roughness length (or, equivalently, the transfer coefficients) and the profile stability functions (ψ_χ). The roughness length can be parameterized with Charnock's (1955) velocity roughness formula plus a smooth flow limit expression from Smith (1988):

$$z_{0a} = \alpha_C u_{*a}^2 / g + 0.11 \nu_a / u_{*a} \tag{1.42}$$

where $\alpha_C = 0.011$ for the COARE 3.0 algorithm (Fairall et al. 2003) and ν_α is the kinematic molecular viscosity of the air.

The profile stability functions near neutral stratification conditions ψ_χ are known from accurate measurements over land, in particular, from the Kansas experiment (see Sect. 1.7.2). These functions have been extended theoretically for highly unstable (convective) conditions (Fairall et al. 1996). For highly stable conditions, the Kansas functions predict zero fluxes. Later, Beljaars and Holstlag (1991) found finite, but highly intermittent, values for fluxes in very stable conditions and corrected the Kansas functions for the stable stratification limit. Adopting the stability functions with improved convective and stable limits eliminates occasional pathological results obtained with earlier versions of the COARE algorithm (Fairall et al 1996).

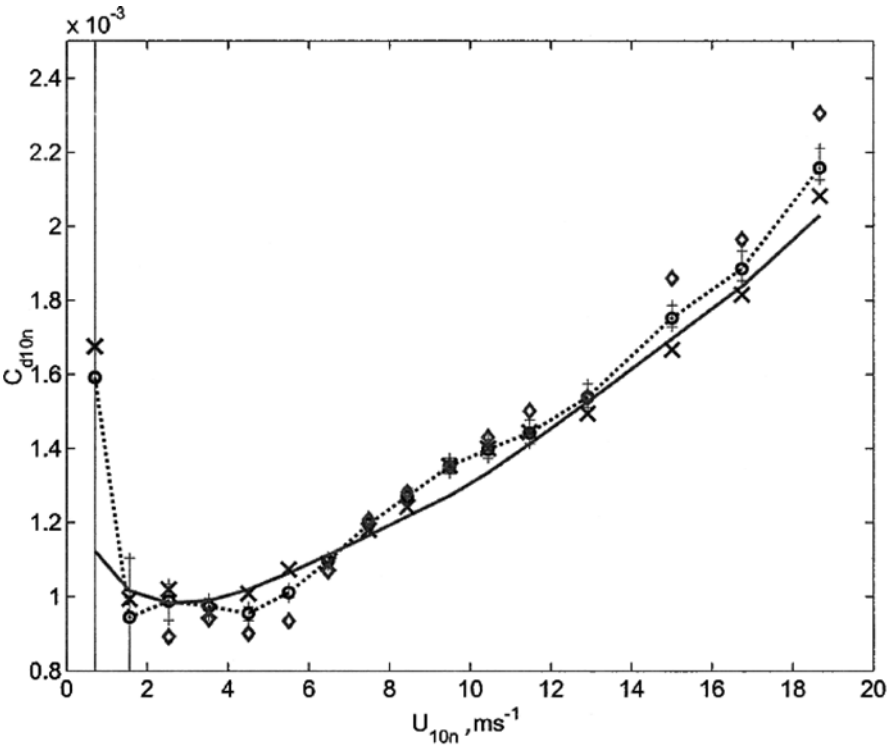

Fig. 1.2 Median 10 m neutral velocity transfer coefficient as a function of 10 m neutral wind. Error bars indicate the statistical uncertainty (one sigma) of the median based on the distribution within the mean wind speed bin. Results of different experimental techniques are also shown: O are the combined covariance and inertial dissipation estimates, X are the inertial dissipation estimates only, and ◊ are the covariance values only. After Fairall et al. (2003). Copyright © 2003 American Meteorological Society. Used with permission

The addition of gustiness provides finite scalar fluxes as the wind speed approaches zero. In the COARE algorithm, the gustiness is introduced using the convective velocity scale, w_*,

$$U_g = \beta_c w_* = \beta_c \left(\frac{g}{T} \overline{w' \Theta_v'} z_c \right)^{1/3}, \tag{1.43}$$

where z_c is the depth of the convective boundary layer; Θ_v is the virtual potential temperature, which is analogous to the potential temperature that removes the adiabatic temperature variations caused by changes in the ambient pressure of an air parcel but also accounts for humidity effects (Stull 1988); and β_c is an empirical coefficient ($\beta_e \approx 1.25$).

Figure 1.2 shows the comparison between measured and modeled (COARE bulk-flux algorithm) velocity transfer coefficients as a function of wind speed. Typically,

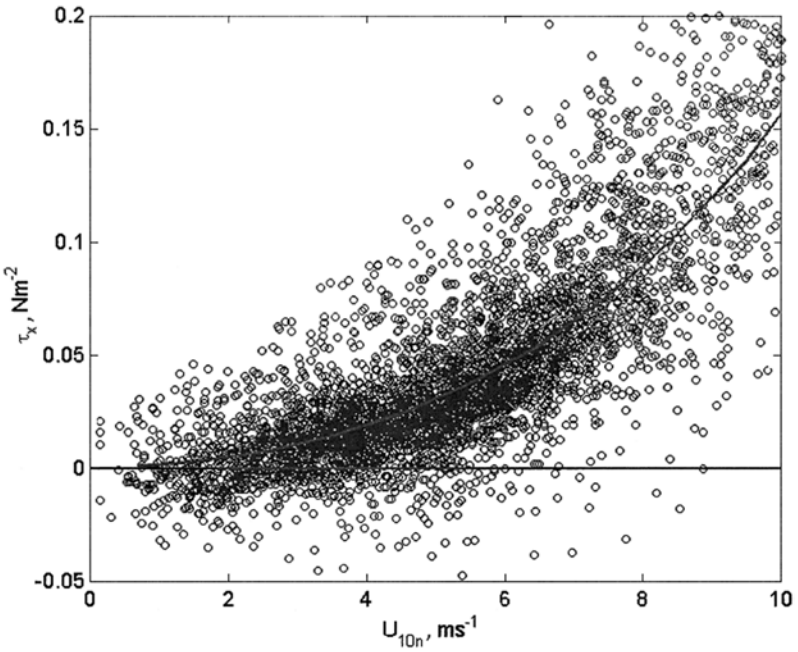

Fig. 1.3 Covariance measurements of the streamwise momentum flux (τ_x) as a function of 10 m neutral wind speed. The individual points are nominal 1-hour averages. The solid curve is the COARE 3.0 bulk flux algorithm. After Fairall et al. (2003). Copyright © 2003 American Meteorological Society. Used with permission

measurements or model output provide input atmospheric variables (U_a, T, q) and the surface properties (current vector, temperature) to a bulk-flux algorithm. The surface value for specific humidity is computed from the sea surface temperature and the vapor pressure of seawater. Strictly speaking, (1.31) requires the true interface temperature, T_0, and salinity, S_0, but usually only the temperature and salinity at some depth are available. The vapor pressure of seawater is approximately (at S = 35 psu) 0.98 times the vapor pressure of pure water (Kraus and Businger 1994). The dependence of the vapor pressure on the typical salinity changes in the near-surface layer is negligible (except during heavy rainfalls when S_0 may drop for as much as a few psu; see Chaps. 2 and 4). When it is not raining, the salinity diffusion sublayer implies that the true salinity is only a few tenths psu higher than the bulk water salinity near the surface.

In Fig. 1.3, a scatter plot of streamwise covariance stress measurements is shown together with the COARE bulk-flux algorithm prediction. Grachev and Fairall (2001) found that at very low winds there is a tendency for the streamwise component to average to a negative value; this could be interpreted as the return of momentum to the atmosphere by waves. Though the COARE 3.0 algorithm incorporates a dependence of the bulk coefficient on the wave age, the bulk algorithm

does not deal with negative momentum fluxes. This effect represents a difficulty in bulk-flux parameterizations.

The near-surface temperature gradients due to the cool or warm skin (see Chap. 2) and diurnal thermocline (Chap. 4) may have some effect on the bulk-flux parameterization. The cool or warm skin results in an interface temperature that is several tenths K cooler or warmer than the more easily measured bulk seawater near the surface. During light wind and sunny conditions, the upper few meters of the ocean may also warm up to several K. In such cases, calculation of heat and momentum air–sea fluxes with bulk-flux algorithms is a coupled ocean–atmosphere problem (see Chap. 4). In order to address these physics, the COARE algorithm incorporates sub-models that represent the millimeter-scale cool skin near the interface and the diurnal warm layer in the upper few meters of the ocean, which estimate T_0 from T_w.

The bulk coefficients C_D, C_T, C_E, and, especially, K_μ are poorly known for very high wind speeds. The COARE bulk-flux algorithm has been verified for wind speeds ranging from 0 to 20 m s^{-1}. There are indications that under very high wind speed conditions, starting from 35 or 40 m s^{-1}, the bulk coefficients may no longer be increasing with wind speed (Sect. 6.4.3).

The effects of sea spray, which are important under high wind speed conditions, have yet to be satisfactorily quantified. Sea spray enhances evaporation, influences atmospheric stratification, and also transports momentum. Sea-spray effects under very high wind speed conditions are discussed in Chap. 6.

Since many trace gases of practical importance (CO_2, O_2, etc.) are almost infinitely soluble in air, the main gradient in gas concentration is on the waterside of the air–sea interface (Bolin 1960). The bulk-flux formulation for air–sea gas exchange is therefore somewhat different from (1.31):

$$G_0 = G\big|_{z\to -0} = K_\mu \Delta C, \tag{1.44}$$

where ΔC is the effective air–sea gas concentration difference and K_μ is the gas transfer (piston) velocity. Expressed in terms of the gas partial pressure in water (p_w) and in air (p_a), and gas solubility (S_μ), formula (1.44) reads as follows:

$$G_0 = K_\mu S_\mu (p_w - p_a). \tag{1.45}$$

Strictly speaking, partial pressure in equation (1.45) should be replaced with gas fugacity (DOE 1994). The fugacity of an ideal gas is simply its partial pressure. In terms of fugacity, the thermodynamic relationships for real (nonideal) gases coincide with those established for ideal gases. An example of a nonideal gas is CO_2. For typical oceanic conditions, the difference between the CO_2 partial pressure and CO_2 fugacity is, however, only about 1 μatm, which is about 0.3 % of the CO_2 fugacity in seawater.

The air–sea gas transfer velocity K_μ is determined by the properties of the turbulent boundary layer and sea surface (Sect. 7.5.1), while simplified parameterization formulas imply that K_μ is a function of wind speed only. A complicating issue is

the bubble-mediated gas transport because it is a volume source, which depends on bubble dynamics (see Chaps. 6 and 7). Representation of the volume source term G_V in equation (1.12) involves such factors as the rate of bubble injection by breaking waves under different wind–wave conditions and gas solubility. The presence of surface-active materials on the sea surface may affect the air–sea gas exchange (as well as momentum, energy, mass, and heat exchanges), especially under low and moderate wind speed conditions (see Chap. 2).

1.4 Radiative Forcing

1.4.1 Definitions

Radiation in the atmosphere and ocean can be described in terms of *radiance*, which is the radiant energy per unit time arriving from a specific direction and passing through a unit area perpendicular to that direction. *Irradiance,* or *downwelling irradiance*, is defined as the radiant energy that passes through a unit horizontal area per unit time coming from all wavelengths and directions (Kraus and Businger 1994):

$$I_d = \int_{\phi=0}^{2\pi} \int_{\theta=0}^{\pi/2} L(z, \theta, \phi) \cos\theta \sin\theta d\theta d\phi, \tag{1.46}$$

where $L(z, \theta, \phi)$ is the radiance in the direction defined by the zenith angle θ and azimuth angle θ, and z is the depth. Zenith angle θ is defined so that the direction pointing vertically downward corresponds to zenith angle of zero. *Exitance* I_u, or upwelling irradiance, which is the irradiance from below the unit horizontal area, is defined by a similar integral but with the zenith angle limits corresponding to the hemisphere below the unit area:

$$I_u = \int_{\phi=0}^{2\pi} \int_{\theta=\pi/2}^{\pi} L(z, \theta, \phi) \cos\theta \sin\theta d\theta d\phi. \tag{1.47}$$

Certain applications considered in Chap. 7 require introduction of spectral irradiances and radiances. Following IOCCG (2000), the *spectral irradiance*, or the *spectral downwelling irradiance*, is defined as

$$E_d(\lambda, z) = \int_{\phi=0}^{2\pi} \int_{\theta=0}^{\pi/2} L(\lambda, z, \theta, \phi) \cos\theta \sin\theta d\theta d\phi, \tag{1.48}$$

where $L(\theta, \phi, \lambda, z)$ is now the *spectral radiance* and λ is the wavelength. Likewise, the *spectral exitance*, or the *spectral upwelling irradiance*, is defined here as follows:

$$E_u(\lambda, z) = \int_{\phi=0}^{2\pi} \int_{\theta=\pi/2}^{\pi} L(\lambda, z, \theta, \phi) \cos\theta \sin\theta d\theta d\phi. \tag{1.49}$$

The radiation budget at the sea surface consists of shortwave and longwave components. Shortwave solar radiation is one of the most important components of the air–sea energy budget, accounting for almost all of the heat transferred into the ocean. Penetrating solar radiation and its variability in space and time are important for both the physics and biology of the ocean surface layer. Biologically, the *photosynthetically available radiation* (PAR) portion of the solar irradiance spectrum (usually from 400 to 700 nm) regulates marine primary productivity and therefore the evolution of aquatic ecosystems.

About one-half of the penetrating solar radiation is absorbed within the upper half a meter of the ocean, while the longwave radiation is absorbed in or emitted from the top several μm of the ocean. Global circulation models of the ocean often consider the incident shortwave solar irradiance as a source of thermal energy applied directly to the ocean surface. For studying the near-surface layer of the ocean, however, the solar radiation is more appropriately treated as a volume source of energy (see equation (1.10)), which requires detailed knowledge of solar energy absorption as a function of depth. At the same time, the net longwave irradiance in most practical applications is considered as a source of energy applied to the ocean surface and thus entering boundary condition (1.26). However, actually it involves a layer several micrometers in thickness (Chap. 2).

Currently, models to predict upper ocean properties, such as temperature and primary productivity, use either shipboard measurements or climatological irradiance levels as input. *In situ* measurements, generally confined to process studies, are sparse while regional and seasonal averages produced from meteorological data collected aboard ships of opportunity are limited in both accuracy and coverage. Radiation fields from combined satellite data promise dramatic improvement in providing surface boundary conditions on global scales for upper ocean models.

1.4.2 Solar Constant and Insolation

The radiation from the Sun received at the top of the Earth's atmosphere on a surface oriented perpendicular to the Sun's rays (at the mean Earth–Sun distance), integrated over all wavelengths (hence total solar irradiance), is called the *solar constant*. It has been shown that the solar constant varies on time scales from minutes to decades (Fig. 1.4). The largest variations of up to a few tenths of a percent occur on time scales from days to several months and are related to the photospheric features of solar activity. Increases in the irradiance occur during the appearance of sunspots, due to bright faculae that are also present. The long-term modulation of the solar constant is associated with the well-known 11-year solar activity cycle and with less-studied longer term changes (Foukal 2003).

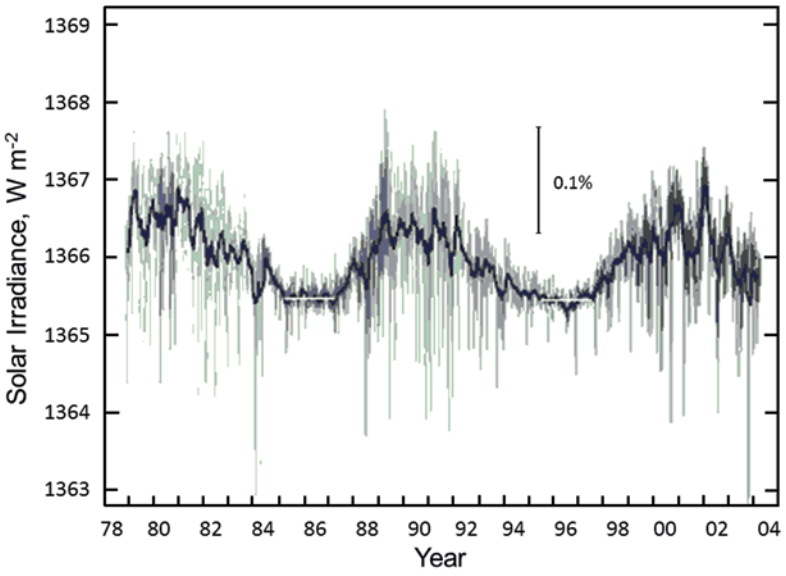

Fig. 1.4 Composite total solar irradiance at the top of the Earth's atmosphere (solar constant) monitored since 1978 with satellites. After Fröhlich (2000) by permission of Springer

The total (spectrally integrated) downwelling solar energy at the ocean surface, I_{Σ}, which is also called the surface solar irradiance or *insolation*, substantially depends on the latitude, season, time of day, and optical properties of the Earth's atmosphere. While satellites accurately measure the solar constant, the surface solar irradiance is much more difficult to assess. Passing through the Earth's atmosphere, the sunlight is absorbed and scattered. Absorption in the atmosphere occurs mainly in the ultraviolet and infrared bands and is weak in the visible band. The ultraviolet part of the solar radiation spectrum is absorbed essentially by ozone. The ozone absorption limits the solar irradiance at sea level to wavelengths greater than 0.29 μm. The infrared part of the solar spectrum is absorbed by greenhouse gases like CO_2 and even more strongly by water vapor.

Molecular scattering by gases in the atmosphere closely follows a *Raleigh law*, obeying a $\lambda^{-4.09}$ relationship, which mainly results from the anisotropy of the air molecules involved in the scattering. The solid particles suspended in the atmosphere scatter the light close to a λ^{-1} relationship, while the water droplets in clouds and fog scatter the light with no wavelength dependence. The water droplets, nevertheless, absorb strongly in the infrared part of the solar spectrum.

For the analysis of the solar radiation as a volume source of energy in the near-surface layer of the ocean, it is important to know the surface solar irradiance and its spectral distribution. The solar energy reaching the sea surface is essentially a function of the Sun's elevation (depending on the latitude, month of year, and time of day), cloudiness, the thickness of the section of atmosphere penetrated, and natu-

ral (*e.g.*, volcanic activity) or anthropogenic pollution. We first consider the case of clear skies and, then, the more complex problem of skies partially or totally covered by clouds.

1.4.3 Insolation Under Clear Skies

The surface solar irradiance I_{CLR} under a clear sky is proportional to $\cos\theta$, where θ is the zenith angle. This leads to the following formula (Lumb 1964):

$$I_{CLR} = m_a I_0 \cos\theta, \tag{1.50}$$

where I_0 is the solar constant and m_a is a factor determined by the optical properties of the atmosphere.

The zenith angle is dependent upon geographical latitude φ, solar declination angle δ, and time of day in the following way:

$$\theta = \cos^{-1}\left[\sin\varphi\sin\delta + \cos\varphi\cos\delta\cos\left(180^o \times \left(t - t_0\right)/t_0\right)\right],$$

where time of day t is given in *solar time* as the hour of the day from midnight, and $t_0 = 12$ hr. Solar declination angle δ is defined as a measure of how many degrees north (positive) or south (negative) of the equator the Sun is when viewed from the center of the Earth. The solar declination angle,

$$\delta = \varphi_\gamma \cos\left[2\pi\left(t_d - t_\gamma\right)/d_y\right], \tag{1.51}$$

varies from +23.44° at the (Northern Hemisphere) summer solstice in June to −23.44° at the winter solstice in December. Here, $\varphi_\gamma = 23.44°$ is the latitude of the tropic of Cancer; t_d is the year day; $t_\gamma = 173$ is the day of the summer solstice; and $d_y = 365.25$ is the average number of days per year.

Factor m_a depends strongly on atmospheric variables. Numerous formulas have been proposed to estimate this factor. Lumb (1964) found from an interpolation of the stationary weather ship data (52°30'N, 20°W) that, under virtually clear skies, $m_a \approx a_L + b_L \cos\theta$, where $a_L = 0.61$ and $b_L = 0.2$.

More sophisticated algorithms for m_a have since been developed. A relatively simple yet accurate analytical formula to compute surface irradiance and PAR at the ocean surface under clear skies was proposed by Frouin et al. (1989). Their formula represents a parameterization of the more complex radiative transfer model of Tanre et al. (1979) and requires inputs of date, solar zenith angle, visibility, aerosol type, and the vertically integrated concentrations of ozone and water vapor. When compared to the Tanre et al. (1979) model, the Frouin et al. (1989) formulation is accurate to 1–2% for solar zenith angles below 75°.

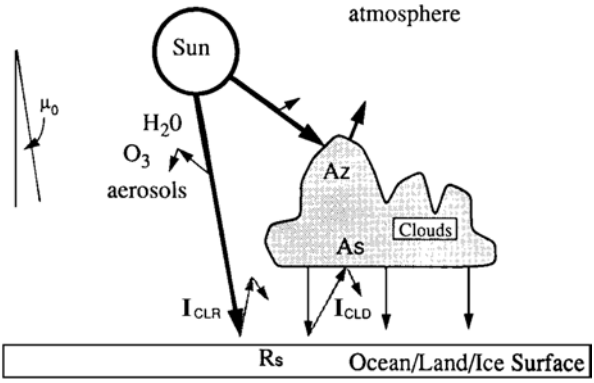

Fig. 1.5 Schematic representation of the components of the fast scheme for surface solar irradiance. After Bishop and Rossow (1991) by permission of John Wiley and Sons

1.4.4 Insolation Under Cloudy Skies

Bishop and Rossow (1991) developed a computationally effective scheme for computing the surface solar irradiance during cloudy conditions. The fast algorithm for surface solar irradiance (FAST) utilizes the solar zenith angle (θ), atmospheric water vapor profile (H_2O) and ozone column abundance (O_3), the cloud fraction and optical thickness, the visible surface reflectance (R_S), the surface type (land, water, coast, or ice), and the surface pressure. The main algorithm components are depicted in Fig. 1.5.

The cloudy sky component of the calculation, I_{CLD}, begins with the direct solar energy flux to the cloud top (I_{DIR}), which is I_{CLR} evaluated with zero surface reflectance and zero cloud fraction. A fraction of that flux is reflected back to space using a solar zenith angle dependent on cloud albedo A_Z. The remaining transmitted fraction exiting the cloud base, not absorbed by the surface (determined by surface reflectance, R_S), is reflected upward and is reflected downward again from the cloud base (determined by spherical cloud albedo, A_S).

Field measurements of radiative forcing in the presence of clouds have been done in a number of research cruises (*e.g.*, Fairall et al. 2008; de Szoeke et al 2012). Additionally, satellites can provide global coverage. The International Satellite Cloud Climatology Project (ISCCP) produced global surface solar irradiance fields for several years (beginning in July 1983) using data from a number of satellites. Data were temporally resolved every 3 hours and spatially resolved at $0.5^\circ \cdot 0.5^\circ$ latitude and longitude. The major input data set for the ISCCP contained information about clouds, the atmosphere, and the ocean surface at nominal 30 km resolution (4–8 km pixel size, randomly sub-sampled at 30 km resolution) collected every 3 hours from around the globe (Bishop et al. 1997). These data were then used to produce a 0.5 by 0.5 degree gridded product. The ISCCP data were available eight times per day for most of the globe (Fig. 1.6) but gaps in the data set were present over regions observed less frequently by polar orbiters rather than geostationary satellites. Validation of this remote-sensing approach to collecting radiation data has been done by Waliser et al. (1999) by comparisons between buoy-observed, satellite-derived,

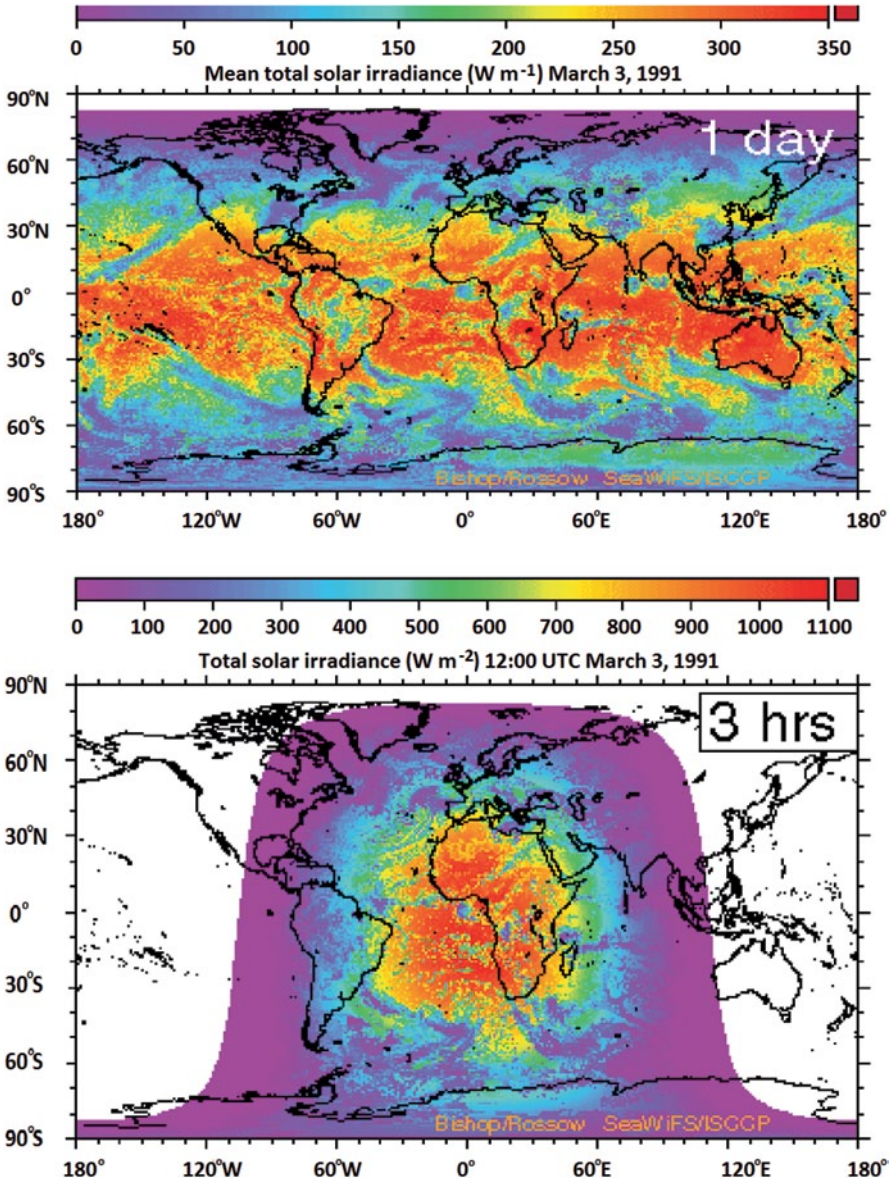

Fig. 1.6 Example: surface solar irradiance at 3 hourly and daily resolutions from ISCCP After Bishop et al. (2000)

and modeled surface shortwave flux over the subtropical North Atlantic for data collected during the Subduction Experiment. Fairall et al. (2008) combined the ship data, the TAO buoys, and ISCCP products to form a consensus observational data set for cloud, radiation, and surface forcing in the Equatorial Eastern Pacific.

1.4.5 Albedo of the Sea Surface

Albedo is the ratio of the amount of electromagnetic radiation reflected by the surface of a body to the amount incident upon it, commonly expressed as a percentage. The albedo of the sea surface is defined as follows (Ivanoff 1977):

$$A = I_u / I_d = (I_r + I_b) / I_d, \tag{1.52}$$

where I_d is the surface solar irradiance, I_r the solar irradiance reflected from the sea surface, and I_b is that part which is upward back-scattered from below the sea surface. Introducing the reflectance coefficient of the sea surface,

$$R_s = I_r / I_d, \tag{1.53}$$

the definition of albedo (1.52) can be rewritten as follows:

$$A = R_s + I_b / I_d, \tag{1.54}$$

while the flux absorbed by the sea is equal to

$$I_d - (I_r + I_b) = I_d(1 - A). \tag{1.55}$$

Fresnel's formula can be used for an idealized plane sea surface to calculate the reflectance coefficient, R_s, which is independent of absorption and scattering properties of the waters. Curve 1 in Fig. 1.7 corresponds to the idealized case of direct incident solar rays and flat ocean surface; curve 2 includes scattered solar radiation as well (cloudy sky). The reflectance coefficient typically lies in the range of 5–7% for a plane sea surface and an overcast sky, but can exceed 30% when the Sun is low on the horizon of a clear sky.

Cox and Munk (1956) and Saunders (1967a) studied reflectance calculations in more complicated situations including rough seas and low solar elevation. Their results are also shown in Fig. 1.7 (curve 3). Note that the solar elevation ξ and solar zenith angle θ are related by: $\xi = 90° - \theta$

For rough seas, the angle of incidence of direct solar rays varies with the slope of the waves. Difficulty arises again when the Sun is low on the horizon, giving rise to shadow zones and multiple reflections. For solar elevation greater than about 25°, surface roughness slightly increases the ocean surface reflectance. For lower angles, surface roughness results in a sharp reduction of the reflectance (Fig. 1.7).

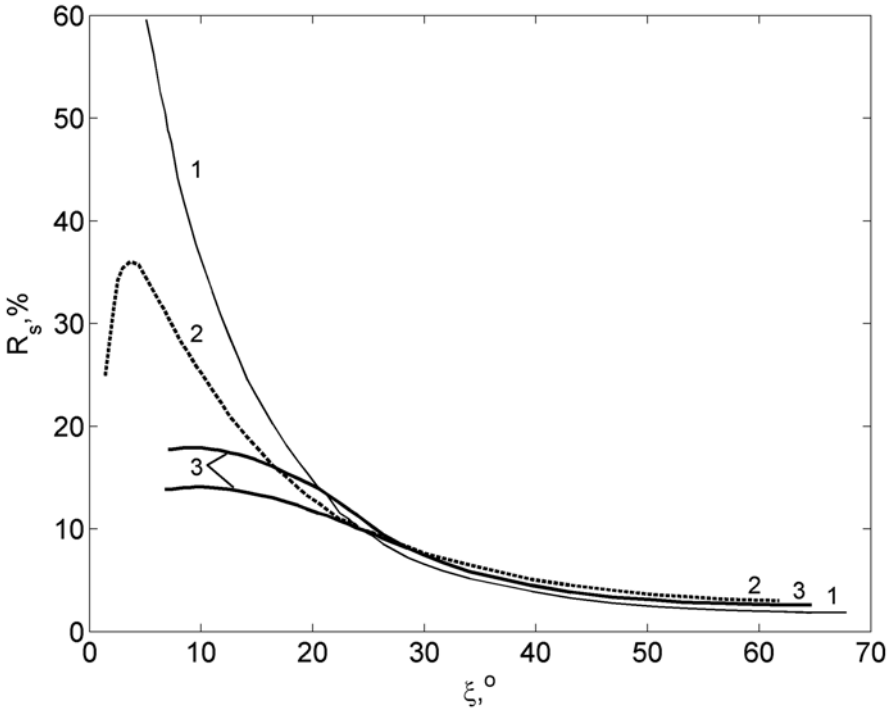

Fig. 1.7 Reflectance coefficient (R_s in our notation) as a function of the solar elevation ξ Here: curve 1 is the idealized case of direct incident solar rays and flat ocean surface; curve 2 the case of total (direct and scattered) solar rays and flat ocean surface; curves 3 the case of direct solar rays and rough seas. Curves 3 are calculated from the Cox and Munk (1956) data for two different assumptions regarding multiple reflections at low sun elevations. (After Ivanoff 1977) Copyright owner could not be found

The formula for albedo (1.54) contains the ratio of upward to downward irradiance, I_b/I_d. Its magnitude and spectral distribution vary considerably as the absorption and scattering properties of the water change (Jerlov 1976; Zaneveld 1989). In extremely clear water, the spectral ratio of the upward to downward irradiance can reach 10 % for $\lambda = 0.4$ mm wavelength, while, in strongly scattering water, this ratio can also reach 10 % for λ between 0.55 and 0.56 μm. The ratio I_b/I_d (remember that I_b and I_d are the integrals over all wavelengths) has a maximum of only 2 % (when the water is very clear or strongly scattering), though it does not exceed 0.5 % in typical situations. The upwelling light from the sea determines ocean color, which contains useful information about the upper ocean waters. The ocean color can be remotely sensed from satellites (see Sect. 7.5.2).

Experimental values of the albedo are very close to those shown above for the reflectance. Under clear skies, when solar elevation ξ exceeds 20–25°, the sea state plays a relatively minor role. The albedo of the sea can be roughly estimated from the Laevastu (1960) formula:

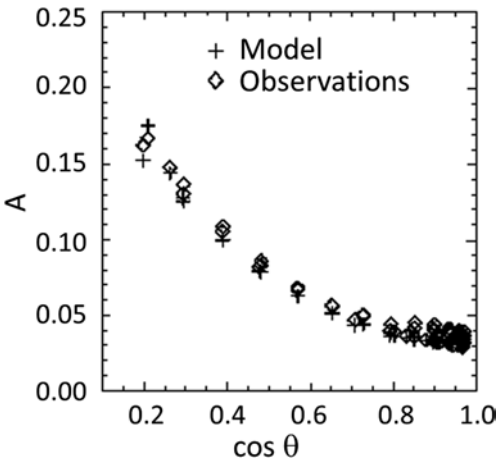

Fig. 1.8 Model-observation comparison for the sea surface albedo A as a function of solar zenith angle θ at a site 25 km east of Virginia in the Atlantic Ocean for 3 months from June to August 2000. The mean difference between model and observations is 0.44 %; standard deviation is 0.34 %. After Jin et al. (2002). Copyright © 2002 American Meteorological Society. Used with permission

$$A = 300 / \xi, \tag{1.56}$$

where ξ is in degrees and A is in %.

For angles $25° < \xi < 50°$, empirical formula

$$A = 250 / \xi \tag{1.57}$$

is more accurate than (1.56).

Payne (1972) parameterized sea surface albedo values from field data as a function of atmospheric transmittance (defined as the ratio of downward irradiance incident at the sea surface to irradiance at the top of the atmosphere) and solar zenith angle. A subsequent field study of Katsaros et al. (1985) and simulation with a radiation model by Ohlmann et al. (2000a) demonstrated good agreement with the Payne (1972) parameterization for solar elevation angles $\xi > 25°$.

For solar elevations $\xi < 25°$, the values obtained by different authors, however, differ greatly as a result of the strong influence of the sea state. This presents a serious problem when calculating the rate of solar energy absorption by the ocean in latitudes higher than 50° or 60°. For these latitudes, according to Payne (1972), mean values of albedo can be as high as 44 %, while Budyko (1963) suggested values that do not exceed 23 %.

The radiative models considered above treat radiative transfer in the atmosphere and ocean separately, often by regarding one medium as a boundary condition for the other. Coupled atmosphere–ocean radiative transfer models treat absorption and scattering by layers for both the atmosphere and the ocean explicitly and consistently. Such models are capable of more accurately calculating radiative flux and albedo over the ocean surface based on the optical properties of the atmosphere and ocean (Jin et al. 2002). The key input parameters in the Jin et al. (2002) model are aerosol optical depth, surface wind speed, and total precipitable water from *in situ* measurements. According to the results of the field test shown in Fig. 1.8, the mean model–

observation differences for the ocean surface albedo are generally less than 1 %. Sensitivity tests conducted by Jin et al. (2002) indicate that the incorporation of scattering effects by air bubbles and/or suspended material into the algorithms has the potential to further reduce the model–observation differences in the ocean surface albedo.

1.4.6 Attenuation of Solar Radiation in the Ocean

Similar to air, the attenuation of solar radiation in seawater involves both absorption and scattering. The absorption consists mainly of a conversion from radiant energy to heat, with some of the absorbed radiant energy being involved in chemical reactions such as photosynthesis. In reality, the portion of solar energy penetrating into the oceans and involved in photosynthesis is usually only of order 0.1 %. The scattering of solar radiation consists of changes in the direction of photons without losing energy. This process increases the path length of photons between the sea surface and the depth under consideration. As a result, scattering leads to increased absorption and an additional energy loss.

An optical property that is often used in models of light penetration is the diffusive attenuation coefficient for downwelling irradiance, or K_d, which defines the rate of decrease of downwelling irradiance with depth:

$$K_d(\lambda) = -\frac{1}{E_d(\lambda, z)} \frac{dE_d(\lambda, z)}{dz}. \tag{1.58}$$

It is one of the important geophysical variables that can in principle be derived from ocean-color data (see Sect. 7.5.2).

Following the classification of Preisendorfer (1976), the diffusive attenuation coefficient defined with (1.58) is an *apparent optical property*, because it can be modified both by the nature and quantity of substances present in the medium and by the zenith-angular structure of the incident light field. At the same time, *inherent optical properties*, according to Preisendorfer's classification, are the properties that are independent of variations in the angular distribution of the incident light field, and they solely depend on the type and concentration of substances present in the medium.

The attenuation coefficient (including both absorption and scattering) is defined for the idealized conditions of collimated, monochromatic flux incident normally on the water, and traversing an infinitesimally thin layer of the water. Absorption is caused by the water itself, by dissolved salts, organic substances in solutions, suspended matter, and by air bubbles, to some extent. The absorption coefficient for pure water increases rapidly toward long wavelengths and exceeds 2.3 m^{-1} for wavelengths greater than 0.8 μm. The absorption coefficient value in the ultraviolet is less known than for the visible spectrum.

Scattering is partially due to molecules of water and substances in solution, but mainly results from suspended matter. Scattering becomes less important compared

Table 1.1 Absorption of solar radiation in the top 1 m below the water surface

Depth (m)	Absorbed part of total solar radiation (%)	
	Bethoux (1968)	Pruvost (1972)
0.01	17	13
0.1	35	31
0.2	41	41
0.5	~50	–
1	–	56.5–65

to absorption as absorption increases toward longer wavelengths, eventually becoming negligible at wavelengths greater than 0.7–0.8 μm.

Air bubbles efficiently scatter sunlight in water (Sect. 7.5.4). The air bubble concentration and size distribution, however, significantly depend on weather conditions.

Investigation of the progressive attenuation of daylight with depth must simultaneously take into account the inherent properties of the water (absorbing and scattering) and the angular and spectral distributions of light incident on the sea surface. Numerous experimental and theoretical studies have been carried out with these aims, especially in relation to the remote sensing of the ocean color (see Sect. 7.5.2). In this chapter, we limit the following discussion to analysis of the solar energy absorption as a function of depth because this term enters the equation for the heat budget (1.10).

The attenuation of solar radiation with depth appears to follow a more or less exponential form depending on the wavelength or spectral band. Absorption of solar radiation in the top meter of the ocean (integrated over wavelength), according to measurements of Bethoux (1968) and calculations of Pruvost (1972), is given in Table 1.1. These data indicate that solar radiation is absorbed very unevenly in the upper ocean.

The absorption and scattering of light for wavelengths exceeding 0.7–0.8 μm mainly determine the transmission of solar radiation within the upper meter of the ocean. Chlorophyll, organic substances, or suspended matter do not affect the inherent optical properties of the oceanic water for these wavelengths. According to the radiative transfer model of Ohlmann et al. (2000a), a tenfold increase in chlorophyll concentration results in less than 1 % change in solar transmission for the upper ten centimeters of the ocean (Fig. 1.9).

For depths greater than 1 m, with a greater portion of the irradiance in the visible spectral region (i.e., for less than 0.7–0.8 μm wavelength), the dependence of solar irradiance on the inherent optical properties of the water is more evident. Respectively, Jerlov (1976) proposed an optical classification of oceanic surface waters by distinguishing three major water types—I, II, and III—and later adding two intermediate types—IA and IB—and coastal turbidity types—1, 3, 5, 7, and 9. (In the open ocean, chlorophyll concentration mainly determines inherent optical properties of water.)

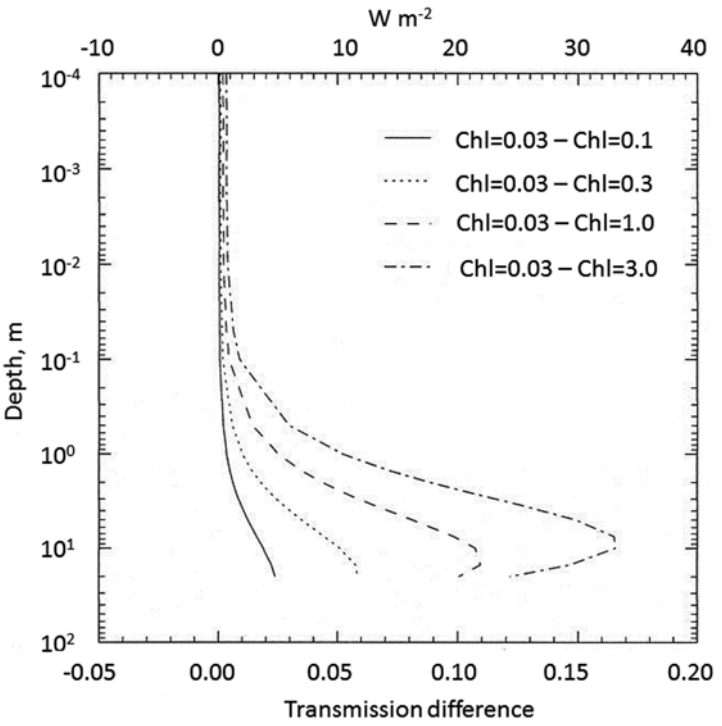

Fig. 1.9 Solar transmission differences between the base case (chl = 0.03 mg m^{-3}, $\theta = 0°$, clear skies) and cases of increased chlorophyll concentration (chl = 0.1, 0.3, 1.0, 3.0 mg m^{-3}). After Ohlmann et al. (2000). Copyright © 2000 American Meteorological Society. Used with permission

The absorption of solar radiation in the ocean can be expressed in the following way:

$$I_R(z) = (1 - A) I_\Sigma f_R(z), \tag{1.59}$$

where I_Σ is the surface solar irradiance (spectrally integrated), and function $f_R(z)$ characterizes the absorption of solar radiation with depth. Paulson and Simpson (1981) parameterized f_R as a sum of nine exponentials:

$$f_R(z) = \sum_{i=1}^{9} a_i \exp(\alpha_i z), \tag{1.60}$$

where a_i are the weights corresponding to the spectrally distributed absorption coefficients α_i. The absorption coefficients in this parameterization were determined for pure water only based on measurements of Schmidt (1908). The subsequent determination of the absorption coefficients in clear water by Pope and Fry (1997)

Table 1.2 Irradiance absorption coefficients α_i and spectral weighting coefficients a_i according to Paulson and Simpson (1981) and the modification of coefficient α_1 proposed by Soloviev and Schlüssel (1996), based on Jerlov's water-type classification

Wavelength (μm)			I		a_i			$\alpha_i(m^{-1})$		
0.2–0.6			1		0.2370			2.874×10^{-2}		
0.6–0.9			2		0.3600			4.405×10^{-1}		
0.9–1.2			3		0.1790			3.175×10^{1}		
1.2–1.5			4		0.0870			1.825×10^{2}		
1.5–1.8			5		0.0800			1.201×10^{3}		
1.8–2.1			6		0.0246			7.937×10^{3}		
2.1–2.4			7		0.0250			3.195×10^{3}		
2.4–2.7			8		0.0070			1.279×10^{4}		
2.7–3.0			9		0.0004			6.944×10^{4}		
Water type	I	IA	IB	II	III	1	3	5	7	9
α_1 (m^{-1})	0.066	0.076	0.088	0.132	0.382	0.49	0.70	1.00	1.09	1.60

produced similar results. The more recent studies of optical properties of the near-surface layer of the ocean as a part of the Radiance in a Dynamic Ocean (RaDyO) program (Dickey et al. 2012) are consistent with Schmidt (1908) and Pope and Fry (1997).

To extend the calculations to real ocean water, Soloviev and Schlüssel (1996) proposed a small modification of the Paulson and Simpson (1981) parameterization. For wavelengths smaller than 0.6 μm, the absorption is strongly modified by phytoplankton, suspended inorganic matter, and yellow substance (Jerlov 1976). These substances are not important at longer wavelengths because of a strong decrease of their absorption coefficients with wavelength. Therefore, taking Jerlov (1976) into account, Soloviev and Schlüssel (1996) replaced the absorption coefficient for the spectral band 0.2–0.6 μm by average values calculated from narrow-band spectral values for different types of water representing varying oceanic (types I, IA, IB, II, and III) and coastal turbidity (types 1, 3, 5, 7, and 9). Furthermore, they excluded the spectral range below 0.31 μm because of the strong absorption by atmospheric ozone. The absorption coefficients from Soloviev and Schlüssel (1996) are listed in Table 1.2. Verevochkin and Startsev (2005) have proposed to separate the spectral band 0.2–0.6 μm into two subranges, which provides a better approximation of the solar radiation absorption for the different types of oceanic water. This improvement, however, has only a marginal effect for the upper meters of the ocean.

Formulation (1.59)–(1.60) provides a convenient description for the volume source $\partial I_R / \partial z$ in equation (1.10). Dependence of the incident solar radiation in the infrared range on the water vapor content (Ivanoff 1977) may, however, affect values of the weight coefficients a_3–a_9 in Table 1.2.

1.4.7 Longwave Radiation

The longwave radiation is absorbed in and emitted from a surface layer of several micrometers (see the schematic diagram in Fig. 2.1). In many practical applications, the longwave radiation can be treated as a surface flux.

The longwave radiation emitted from the sea surface (longwave exitance) is nearly balanced by the downward longwave radiation (longwave irradiance) emitted primarily from moisture in the atmosphere. It is possible, however, for the difference to be significant. To compute longwave exitance, it is assumed that the ocean radiates as a gray body. This implies that the longwave exitance is proportional to the fourth power of the absolute sea surface temperature when expressed in degrees Kelvin (K).

The net longwave radiation flux is parameterized as follows:

$$I_L = \varepsilon_w \sigma T_0^4 - \varepsilon_w E_a, \tag{1.61}$$

where $\sigma = 5.67 \times 10^{-8} W \cdot m^{-2} K^{-4}$ is the Stefan–Boltzmann constant, T_0 is the sea surface temperature, $\varepsilon_w \approx 0.97$ is the infrared emissivity of water (fraction of blackbody radiation), and E_a is the longwave irradiance from the sky that can either be measured with an Eppley Precision Infrared Radiometer or be calculated with an existing algorithm (see Katsaros (1990) for a review). Note that the longwave irradiance depends on cloud type and coverage.

Ideally, the temperature difference across the millimeter-thick aqueous thermal diffusion sublayer (cool or warm skin) should be accounted for. Yet, the temperature profile in the top few millimeters of the ocean is extremely difficult to measure. In many locations of the ocean, the temperature in the upper few millimeters differs from the temperature at 0.5 m or more below the surface by less than 0.5 K. In some places and times, the difference can be as much as 4–5 K, making a correction to the bulk temperature necessary in order to closely approximate the skin temperature (Fairall et al. 1996). In these extreme cases, the aqueous thermal diffusion sublayer should be treated as a component of the coupled ocean–atmosphere system.

1.5 Rain Forcing

1.5.1 Dynamics of Raindrops at the Air–Sea Interface

This presentation is simplified for a limiting case of a flat surface at no wind and waves. Raindrops falling on to the sea surface behave differently depending on their size and impact velocity and they represent both a surface and a volume source of

freshwater (Schlüssel et al. 1997). Drops of rain typically reach the sea surface at their terminal velocities, the vertical velocity when the gravitational force equals the drag force. Small droplets with a low impact velocity cannot break the surface and thereby accumulate freshwater on top of the sea surface. Heavier drops with higher vertical velocities can coalesce into the sea surface with little or no splashing and generate a vortex ring that penetrates downward into the ocean (Katsaros and Buettner 1969; Rodriguez and Mesler 1988; Hsiao et al. 1988). Alternatively, they repel or splash with the formation of a Rayleigh jet (which is the jet-like column of fluid at the sea surface). The occurrence of the Rayleigh jet depends on the Weber number

$$We = w_i(\rho_r D / \sigma_s)^{1/2}, \tag{1.62}$$

where D is the drop diameter, w_i is the impact (terminal) speed, ρ_r the density of the drop, and σ_s the surface tension.

For small Weber numbers, the drop entering the ocean directly penetrates downward (or stays on the sea surface) without any prominent splash or jet production. For larger Weber numbers, a jet is produced and the vortex formation is deferred until a secondary drop breaking off the tip of the jet column makes its way into the ocean. There is a critical Weber number We_{cr} at which the transition from the direct coalescence to the production of a jet and/or splash takes place; according to Hsiao et al. (1988), $We_{cr} \approx 8$. Rodriguez and Mesler (1988) found that the submergence of large primary drops into the water is rather low due to their high impact velocities, in contrast to secondary ones that break off the Rayleigh-jet column and enter the ocean at lower velocities, allowing them to penetrate to deeper levels.

Remarkably, the formation of vortex rings is associated with drop oscillations. The best coalescence of an oscillating drop with the ocean occurs when the drop is spherical and changing from an oblate to a prolate spheroid at the moment of contact with the surface (Chapman and Critchlow 1967).

Natural rain is an ensemble of raindrops. The penetration depth of primary and secondary drops not only depends on the behavior of single events, as mostly analyzed in laboratory studies, but is also governed by the interaction of raindrops with the vortex rings and surface waves generated by them and preexisting waves. For natural rain, Maxworthy (1972) concluded that the depth z_p reached by the vortex rings is proportional to the initial drop radius r_0. The constant of proportionality is large $(a_1 = z_p / r_0 \approx 300)$ for single drops but decreases to $a \approx 100$ for a drop ensemble (Manton 1973).

The kinetic energy of a falling drop entering the ocean is large compared with the potential energy reached at z_p; respectively, the buoyancy effects on the penetration depth can be ignored. The freshwater flux due to rain decreases the near-surface salinity and, thereby, further (though only slightly) reduces the buoyancy effect on the submerging drops.

1.5.2 Partition Between Surface and Submerged Fractions of Freshwater Due to Rain

The total volume of the rainwater as defined by Schlüssel et al. (1997) is

$$V_0 = V_u \int_0^\infty \frac{4}{3}\pi r_0^3 n(r_0) dr_0 \tag{1.63}$$

where $V_u = 1\ \mathrm{m}^3$ is the unit volume included for dimensional correctness of the equation and $n(r_0)$ is the raindrop distribution expressed in the number of drops per (volume) unit of air per equivalent drop radius. The dimension of $n(r_0)$ is $\mathrm{m}^{-3}\ \mathrm{m}^{-1}$ and is commonly described by the Marshall–Palmer distribution (Marshall and Palmer 1948):

$$n(r_0) = \frac{dN}{dr_0} = n_0 \exp(-2\Lambda r_0), \tag{1.64}$$

where $n_0 = 8\ \mathrm{m}^{-3}\ \mathrm{m}^{-1}$ and $\Lambda = 4.1\times10^3 (3.6\times10^6 P)^{-0.21}$ (in m^{-1}) are parameters describing the distribution, P is the rain rate (in $\mathrm{m\ s}^{-1}$), and N is the particle density (in m^{-3}).

Natural rain can exhibit more complicated drop size distributions (Ulbrich 1983). In particular, (1.64) does not capture "instantaneous" raindrop size distributions. Remote sensing of reflectivity and attenuation with the dual-wavelength radar technique, or the reflectivities at horizontal and vertical polarization with the polarimetric radar, opens new opportunities in the measurement of rain parameters (Zhang et al. 2003). At this point, the use of the Marshall–Palmer dependence is "justified" only by the fact that the rain rate has nearly always been the only rain parameter measured.

From (1.63) and (1.64), the total volume of rainwater is

$$V_0 = V_u \frac{4}{3}\pi n_0 \int_0^\infty r_0^3 \exp\left(-2\Lambda r_0\right) dr_0 = V_u \frac{\pi n_0}{2\Lambda^4}. \tag{1.65}$$

Surface tension prevents drops with smaller than critical radius r_c from entering the water body, since they do not have sufficient energy to overcome the surface tension. These drops stay on the sea surface and lead to a surface flux rather than a volume flux. The critical radius below which raindrops do not penetrate the ocean surface has been observed to be $r_c = 0.4$ mm by Oguz and Prosperetti (1991) and about $r_c = 0.75$ mm by Green and Houk (1979). However, the latter result was obtained in a laboratory experiment at rather low impact velocities.

The volume of freshwater that does not submerge but stays at the surface is determined as follows:

$$V_s = V_u \int_0^{r_c} \frac{4}{3}\pi n_0 r_0^3 \exp\left(-2\Lambda r_0\right) dr_0 = V_0 \frac{8\Lambda^4}{3} \int_0^{r_c} r_0^3 \exp\left(-2\Lambda r_0\right) dr_0. \tag{1.66}$$

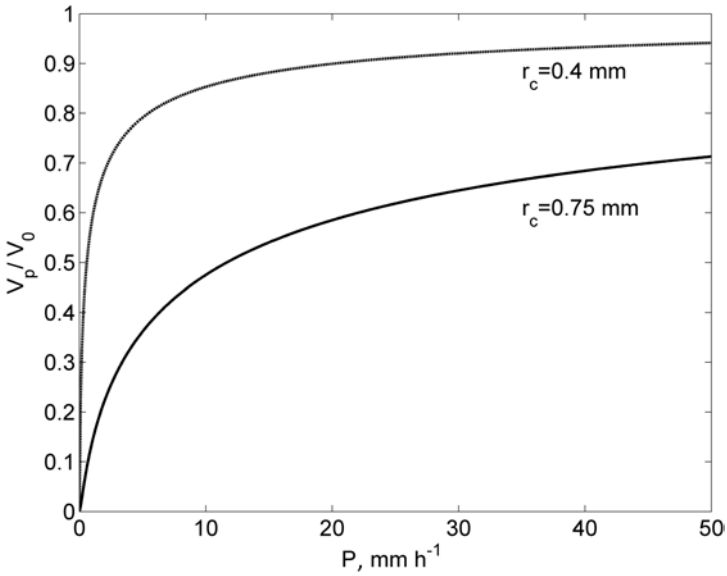

Fig. 1.10 Volume fraction of rain that submerges into the ocean as function of rain rate for critical radii of $r_c = 0.4$ mm and $r_c = 0.75$ mm. After Schlüssel et al. (1997) by permission of Springer

Schlüssel et al. (1997) obtained the following solution to (1.66):

$$V_s = V_0\left[1-\left(1+2\Lambda r_c+\frac{4\Lambda^2 r_c^2}{2}+\frac{8\Lambda^3 r_c^3}{6}\right)\exp\left(-2\Lambda r_c\right)\right]. \tag{1.67}$$

The volume of freshwater due to rain submerging into the ocean is

$$V_p = V_0 - V_s = V_0\left(1+2\Lambda r_c+2\Lambda^2 r_c^2+\frac{4}{3}\Lambda^3 r_c^3\right)\exp(-2\Lambda r_c). \tag{1.68}$$

Fig. 1.10 shows dependence (1.68) for two critical radii.

1.5.3 Volume Source of Freshwater Due to Rain

Following Schlüssel et al. (1997), we assume that the volume of a drop decays exponentially with depth, which results in the following parametric dependence:

$$V_r(z) = V_0 \exp\left(\frac{z}{ar_0}\right), \quad z<0, \tag{1.69}$$

where V_0 is the initial volume of the drop. Respectively, the drop radius r changes with depth as follows:

$$r^3(z) = r_0^3 \exp\left(\frac{z}{ar_0}\right) \text{ or } r(z) = r_0 \exp\left(\frac{z}{3ar_0}\right). \tag{1.70}$$

The drop-size distribution at depth z changes according to

$$n_z(r) = \frac{\partial N}{\partial r} = \frac{\partial N}{\partial r_0}\frac{\partial r_0}{\partial r}, \tag{1.71}$$

which, with (1.70) and (1.64), leads to

$$n_z(r) = n_0 \exp\left(-2\Lambda r_0 + \frac{z}{3ar_0}\right) / \left(1 - \frac{z}{3ar_0}\right). \tag{1.72}$$

The freshwater volume at depth z is given by integral

$$V(z) = V_u \int_{r_c}^{\infty} \frac{4}{3}\pi r^3 n_z(r) dr. \tag{1.73}$$

Substituting (1.70) and

$$dr = \exp\left(\frac{z}{3ar_0}\right)\left(1 - \frac{z}{3ar_0}\right) dr_0 \tag{1.74}$$

into (1.73) results in the following integral:

$$V(z) = \frac{8\Lambda^4}{3} V_0 \int_{r_c}^{\infty} r_0^3 \exp\left(\frac{z}{ar_0} - 2\Lambda r_0\right) dr_0, \tag{1.75}$$

which is equivalent to

$$V(z) = \frac{8\Lambda^4}{3} V_0 \int_0^{\infty} r_0^3 \exp\left(\frac{z}{ar_0} - 2\Lambda r_0\right) dr_0 - \int_0^{r_c} r_0^3 \exp\left(\frac{z}{ar_0} - 2\Lambda r_0\right) dr_0 \tag{1.76}$$

With the first integral on the right side of (1.76) expressed via the MacDonald function (or modified Bessel function) K_4 (see Gradshteyn and Ryzhik 2000), the source function for penetrating rain in the near-surface layer of the ocean due to penetrating raindrops can be represented as follows:

$$V(z) = V_0 f_V(z), \tag{1.77}$$

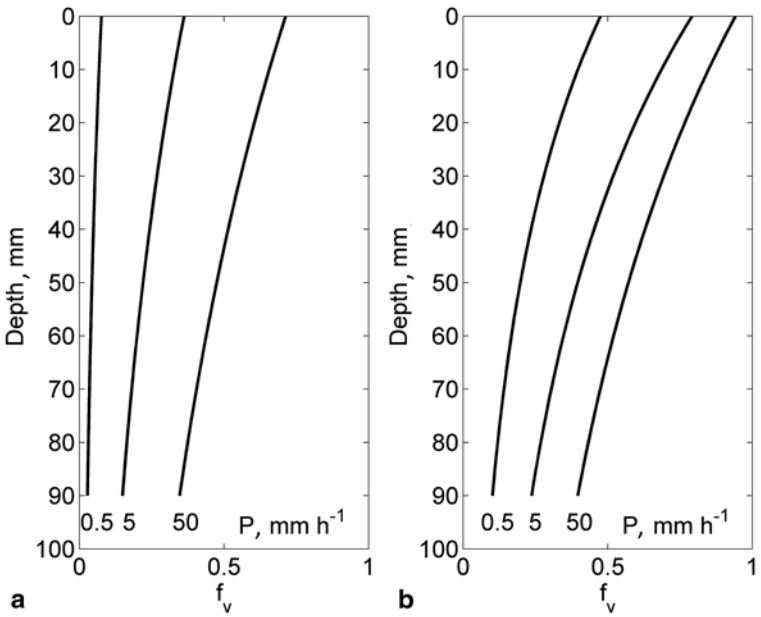

Fig. 1.11 Decay function of the freshwater volume in the upper ocean due to rain f_v for two critical droplet radii: **a** $r_c = 0.75$ mm and **b** $r_c = 0.4$ mm. The rain rate P is given below each curve. After Schlüssel et al. (1997) by permission of Springer

where

$$f_V(z) = \frac{4}{3}\frac{\Lambda^2 z^2}{a_r{}^2} K_4\left(\sqrt{-\frac{8\Lambda z}{a_r}}\right) - \frac{8\Lambda^4}{3}\int_0^{r_c} r_0^3 \exp\left(\frac{z}{a_r r_0} - 2\Lambda r_0\right) dr_0. \qquad (1.78)$$

Figure 1.11 shows dependence (1.78) as a function of depth for a number of rain rates and for two critical radii, $r_c = 0.75$ mm and $r_c = 0.4$ mm. The ratio between penetration depth and drop radius is taken as $a_1 = z_p / r_0 = 100$.

1.5.4 Rain-Induced Heat Flux

Since the surface volume flux density is the surface rain rate, $P = d^2V_0 / dA_s dt$, the heat flux related to rain is defined as follows (Schlüssel et al. 1997):

$$Q_{rV} = \frac{d^2V_r}{dA_s dt} c_{pr} \rho_r (T_w - T_r), \qquad (1.79)$$

where A_s is the area, t is the time, c_{pr} is the specific heat, ρ_r is the density of rain water, T_r is the raindrop temperature, and T_w is the temperature of the upper ocean

(which is a function of depth in the general case). The raindrop temperature is usually taken as the sea-level wet-bulb temperature. However, large raindrops may not have sufficient time to adjust to the change of the air temperature with altitude and can be cooler than the sea-level wet-bulb temperature. For the tropical warm pool conditions, the difference between the raindrop temperature and the sea-level wet-bulb temperature can reach 0.2 K. Gosnell et al. (1995) developed a microphysical model to correct for this effect.

The heat flux density produced by drops not submerging into the ocean is then determined from (1.67) and (1.79) as follows:

$$Q_{rs} = Pc_{pr}\rho_r\left(T_0 - T_r\right)\left[1 - f_V\left(0\right)\right] =$$
$$Pc_{pr}\rho_r\left(T_0 - T_r\right)\left[1 - \left(1 + 2\Lambda r_c + \frac{4\Lambda^2 r_c^2}{2} + \frac{8\Lambda^3 r_c^3}{6}\right)\exp\left(-2\Lambda r_c\right)\right] \tag{1.80}$$

where T_0 is the sea surface temperature. This surface heat flux enters boundary condition (1.26).

The heat flux related to the freshwater volume flux following from (1.77) and (1.79) is

$$Q_{rV}(z) = Pc_{pr}\rho_r(T_w - T_r)f_V(z), \tag{1.81}$$

where decay function $f_V(z)$ is determined by (1.78). Formula (1.81) provides a parameterization for the volume source due to rain, $\partial Q_{rv}/\partial z$, entering equation (1.10).

1.5.5 Surface Stress Due to Rain

Wind accelerates the raindrops horizontally as they fall. The horizontal momentum acquired by the drops on their way from clouds to the ocean surface is released in the near-surface layer of the ocean producing tangential stress. Caldwell and Elliott (1971) parameterized this additional stress in the following way (ignoring the effect of raindrops penetrating the sea surface and ignoring the tilts of the sea surface due to waves):

$$\tau_r = \gamma\rho_r U_{10} P \tag{1.82}$$

where U_{10} is the wind speed at 10 m, γ is an empirically determined factor that varies between 0.8 and 0.9 in most cases except for situations where only very small drops are involved, and P is the rain rate given by the volume rate of water accumulation per unit surface area. For heavy rainfall, raindrops may provide an appreciable contribution to the momentum flux at the air–sea interface as well as modify the surface wave spectrum. of the TKE generation in the near-surface layer of the ocean due to rainfall is considered in Chap. 2.

In addition to raindrops, the contribution of sea-spray droplets to the momentum flux may become significant for hurricane force winds (Chap. 6).

Similar to (1.81), the rain-induced momentum flux can be decomposed into the surface τ_{rs} and volume τ_{rv} components as follows:

$$\tau_{rv} = \gamma \rho_r U_{10} P f_V(z), \tag{1.83}$$

and

$$\tau_{rs} = \gamma \rho_r U_{10} P\left[1 - f_V(0)\right] = \gamma \rho_r U_{10} P\left[1 - \left(1 + 2\Lambda r_c + \frac{4\Lambda^2 r_c^2}{2} + \frac{8\Lambda^3 r_c^3}{6}\right)\exp\left(-2\Lambda r_c\right)\right] \tag{1.84}$$

1.6 Surface Waves

The theory of surface gravity waves is one of the oldest areas of hydrodynamics. In particular, wave motion was one of the first applications for which classical potential theory was developed. There is extensive literature covering various aspects of this phenomenon (cf. Phillips 1977 and LeBlond and Mysak 1978 for review). The aim of this section is to describe the main properties of surface waves important for understanding the near-surface processes.

Because there are numerous assumptions required to find wave-like analytical solutions to the Navier–Stokes equations, there are limits to their applicability in the real world. These are pointed out along the way in this section, and some areas are investigated in detail in Chap. 6. Despite simplifications provided by potential flow theory, generally only linear and weakly nonlinear analytical wave solutions can be found due to complex boundary conditions. Wave-breaking cannot be described by solutions to these simplified equations. Nor can the complex and chaotic sea state driven by surface winds be described by these solutions. However, important statistics of the wavy sea surface and breaking events can be predicted across a remarkable range of conditions (LeMéhauté 1976).

1.6.1 Potential Approximation

The dynamics of surface gravity waves are a large Rossby number problem. According to (1.16), for typical wave orbital velocity $u_l = 1$ m s^{-1}, wavelength $\lambda = 100$ m, and Coriolis parameter $f = 10^{-4}$ s^{-1}, the Rossby number estimate is $Ro = 10^2 \gg 1$. The Coriolis force, therefore, is neglected. Vertical velocity components are comparable to the horizontal velocity components, invalidating the boundary-layer approximation (1.6)–(1.9). In particular, the hydrostatic approximation (in general)

is not valid. Density variations, except across the air–sea interface, are neglected. (This is a problem under very high winds—see Chap. 6.)

In the application to unidirectional surface waves, the equations of hydrodynamics (1.1), (1.3), and (1.4) can then be written in an inviscid form as follows:

$$\frac{\partial u}{\partial t}+u\frac{\partial u}{\partial x}+w\frac{\partial u}{\partial z}=-\frac{1}{\rho}\frac{\partial p}{\partial x}, \tag{1.85}$$

$$\frac{\partial w}{\partial t}+u\frac{\partial w}{\partial x}+w\frac{\partial w}{\partial z}=-\frac{1}{\rho}\frac{\partial p}{\partial z}-g, \tag{1.86}$$

$$\frac{\partial u}{\partial x}+\frac{\partial w}{\partial z}=0. \tag{1.87}$$

The presence of advective and acceleration terms on the left side of (1.86) means that the flow is not hydrostatically constrained.

In addition to large Rossby number approximation (neglecting Coriolis terms), the solution to equations (1.85)–(1.86) is specified as 2-D, since short ocean waves are nearly 2-D and the x, z coordinate system can be aligned to correspond to the direction of propagation. Therefore, all derivatives with respect to y and the velocity component v are assumed to be zero. The density is constant and viscous terms are neglected.

Differentiating (1.85) with respect to z, and (1.86) with respect to x, and finally subtracting the second result from the first, one eliminates the pressure. After invoking incompressibility equation (1.87), this results in

$$\frac{D\omega_y}{Dt}=0, \tag{1.88}$$

where $\omega_y=\frac{\partial u}{\partial z}-\frac{\partial w}{\partial x}$ is the vorticity component in the x, z plane. If at some initial time all the velocity fields are zero, ω_y is initially zero and according to (1.88)

$$\omega_y=\frac{\partial u}{\partial z}-\frac{\partial w}{\partial x}=0 \tag{1.89}$$

for all time thereafter. This eliminates further consideration of turbulent motions, which are admitted (but poorly described) by equations (1.85) and (1.86). Therefore, equations (1.85) and (1.86) can be replaced by the much simpler equation (1.89). Together with equation (1.87), we have two equations with two unknowns, u and w. It is then possible to reduce these to one equation for a potential function

$$u=\frac{\partial \phi}{\partial x},\quad w=\frac{\partial \phi}{\partial z}, \tag{1.90}$$

satisfying (1.89).

When dealing with a free surface boundary condition, use of the potential function is more convenient. By stipulating (1.90) and inserting the expression into (1.87), we obtain Laplace's equation

$$\frac{\partial^2 \phi}{\partial x^2} + \frac{\partial^2 \phi}{\partial z^2} = 0. \tag{1.91}$$

Equation (1.91) is useful if solving for flows bounded by solid surfaces. For example, if n is a local coordinate normal to the solid surface and the velocity normal to the solid surface is zero, $\partial \phi / \partial n = 0$ will also be equal to zero. Since the bottom is a solid surface and we have excluded viscous terms, $\omega = \partial \phi / \partial z = 0$, at the bottom.

Since the free surface is exposed to the atmosphere, the dynamic free-surface condition is imposed by the requirement that the difference of pressure on two sides of the interface,

$$\Delta p = p - p_0, \tag{1.92}$$

is balanced by the effect of surface tension. For constant atmospheric pressure p_0, the boundary condition at $z = \eta$ is then derived from (1.85)–(1.86) in the form of Bernoulli's equation (see, for example, Debnath 1994):

$$\phi_t(x, \eta, t) + \frac{1}{2}\left[\phi_x(x, \eta, t)^2 + \phi_z(x, \eta, t)^2 \right] +$$
$$g\eta(x,t) = \frac{\sigma_s}{\rho} \eta_{xx}(x,t) \tag{1.93}$$

where σ_S is the surface tension ($\sigma_s \approx 7 \times 10^{-2}$ N m^{-1} for "clean" seawater surface).

Note that, for compactness, a subscript notation has been adopted here such that, for example, $\phi_x \equiv \partial \phi / \partial x$. Equation (1.91) then becomes

$$\phi_{xx} + \phi_{zz} = 0. \tag{1.94}$$

Equation (1.93) is the *dynamic boundary condition*; it relates the surface elevation to the velocity field through the velocity potential ϕ. A second surface boundary condition is the *kinematic boundary condition*:

$$\phi_z(x, \eta, t) = \phi_x(x, \eta, t)\, \eta_t(x,t) + \eta_t(x,t). \tag{1.95}$$

At the bottom, $z = -h_b$, the kinematic bottom boundary condition is as follows:

$$\phi_z(x, -h_b, t) = 0. \tag{1.96}$$

Equations (1.93)–(1.96) complete the formulation for irrotational gravity waves, except for stipulating initial and lateral boundary conditions.

1.6.2 Linear Waves

In classical linear wave theory, the amplitude is assumed to be small when compared to the wavelength. Nonlinear boundary conditions (1.93) and (1.95) are replaced with their linear approximations as follows:

$$\phi(x,0,t) + g\,\eta(x,t) = \sigma_s \rho^{-1} \eta_{xx}, \tag{1.97}$$

$$\phi_z(x,0,t) = \eta_t(x,t). \tag{1.98}$$

For an elementary solution of this system in the form of 2-D plane harmonic waves,

$$\eta = a\cos(kx - \omega t), \tag{1.99}$$

the velocity potential is as follows:

$$\phi = \frac{\omega a \cosh k(z + h_b)}{k \sinh kh_b} \sin(kx - \omega t). \tag{1.100}$$

The frequency ω and wave number k are related to each other via the dispersion relationship

$$\omega(k) = [(gk + \sigma_s k^3/\rho)\tanh kh_b]^{1/2}. \tag{1.101}$$

For deepwater waves, $kh_b \gg 1$, and expression (1.100) reduces to

$$\phi = k^{-1} a\,\omega \exp(kz)\sin(kx - \omega t), \tag{1.102}$$

with dispersion relationship

$$\omega(k) = (gk + \sigma_s k^3/\rho)^{1/2}. \tag{1.103}$$

For very short surface waves, where $\sigma_s k^2 \gg \rho g$, gravity becomes negligible compared to surface tension; waves of this type are known as *capillary waves*. On the other hand, when $\sigma_s k^2 \ll \rho g$, surface tension is negligible and the dynamics are dominated by gravity.

The phase speed of deepwater waves following from dispersion relationship (1.103) is as follows:

$$c = \omega/k = (g/k + \sigma_s k/\rho)^{1/2}. \tag{1.104}$$

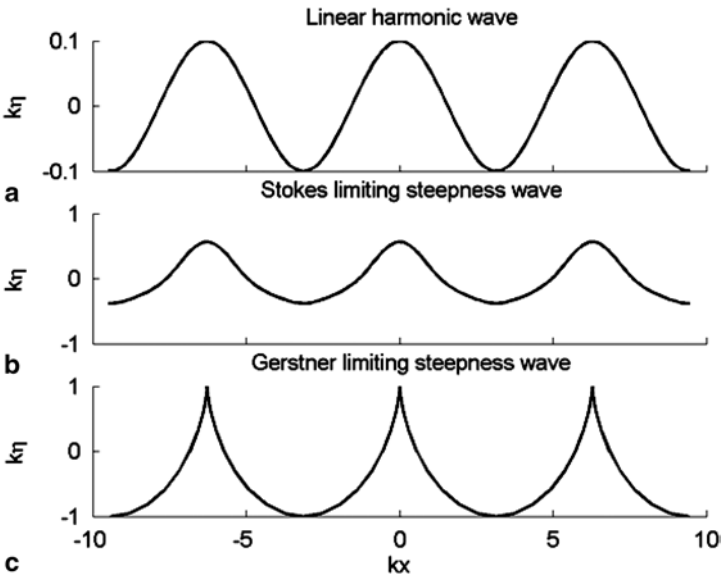

Fig. 1.12 The surface elevation profile of linear (**a**) and nonlinear (**b**, **c**) waves

Analysis of (1.104) shows that the phase speed has a minimum $c = c_m = (4g\sigma_s/\rho)^{1/4} \approx 0.23\text{ms}^{-1}$ at $\kappa = \kappa_m = (g\rho/\sigma_s)^{1/2} \approx 370\text{m}^{-1}$, where gravity and surface tension are equally important. The phase speed of gravity waves $(k \ll k_m)$ increases with wavelength $\lambda = 2\pi/k$ or with decreasing wave number k. The phase speed of capillary waves $(k \gg k_m)$ decreases with wavelength λ or with increasing wave number k. The minimum phase speed corresponds to a 1.7 cm wavelength.

1.6.3 Nonlinear Waves

A solution for the nonlinear system (1.93)–(1.96) is the plane steady nonlinear wave in the form $\eta(\vec{x},t) = \eta(x - ct)$ propagating along axis $x = x_i$ with a constant speed c. Stokes (1880) showed that the surface wave elevation of a plane wave train in deepwater can be expanded in powers of a small parameter $\varepsilon = ak \ll 1$. The third order result is as follows:

$$\eta = a\cos\theta + \frac{1}{2}ka^2\cos 2\theta + \frac{3}{8}k^2a^3\cos 3\theta + ..., \tag{1.105}$$

where the phase $\theta = kx - \omega t$ and

$$\omega^2 = gk\left(1 + a^2k^2 + \frac{5}{4}a^4k^4 + ...\right). \tag{1.106}$$

Equation (1.105) is the Fourier series for the wave displacement η. As illustrated in Fig. 1.12b, the wave profile described by solution (1.105) is no longer sinusoidal. It has a flattened trough and a peaked crest. In finite amplitude waves, fluid particles no longer trace closed orbits, but undergo a slow drift in the direction of wave propagation; this is the so-called *Stokes drift*.

As originally described by Stokes (1880), the maximum possible wave amplitude is $a_{\max} = 0.07\lambda$, at which point the crest forms a 120° angle. Attempts at generating waves of larger amplitude result in instability at the wave crest.

The system of equations (1.93)–(1.96) considered above describes a potential (*i.e.*, an irrotational) approximation of the surface gravity wave theory. Gerstner (1802), however, found an exact solution of the equations of hydrodynamics (1.85)–(1.87) in Lagrangian coordinates in the form of steady, plane vorticity waves of finite amplitude on the free surface of an infinitely deep ideal fluid. According to his solution, illustrated in Fig. 1.12c, coordinates (x, z) of the fluid particle (in the absence of waves located at (x_1, z_1)) are the following function of time:

$$x = x_1 - a \exp kz_1 \sin\left[k\left(x_1 - ct\right)\right], \tag{1.107}$$

$$z = z_1 + a \exp kz_1 \cos\left[k\left(x_1 - ct\right)\right], \tag{1.108}$$

where k is the wave number, $c=(g/k)^{1/2}$, and a is the wave amplitude at $z_1=0$. This is a closed orbit trajectory with the rotation in the opposite direction to the particle path (LeMéhauté 1976).

1.6.4 Wave Breaking

If the ratio of wave amplitude to wavelength increases (due to wind work, for example), the waves are gradually deformed, become unstable, and eventually break, with the surface disrupted and air entrained forming a whitecap. Wave breaking and the subsequent formation of whitecaps, bubbles, and spray droplets are complicated hydrodynamic processes. The full problem involves the wave dynamics before breaking, the development of turbulence, the transition of the one-phase medium to a two-phase mixture (bubbles in water and water droplets in air), and the hydrodynamics of the two-phase mixture. Improved knowledge of the wave breaking is vital for a better understanding of air–sea interactions from micro- to global scales (Melville 1996).

The study of wave instabilities goes back to the classical works of Stokes (1880) and Michell (1893). Stokes suggested that wave-breaking inception occurs when the wave profile reaches the limiting wave steepness, and the water speed at the crest is equal to the phase speed of the wave. Theory suggests that the limiting steepness is achieved when the crest angle attains 120° and $a_{max}/\lambda=0.07$. However, observations show that waves usually break before achieving the limiting Stokes

form. One possible reason is that a limiting wave, with a 120° angle at the crest, has less energy than in a lower, symmetric wave with a smooth crest (Longuet-Higgins and Fox 1978). Another reason is that the vorticity at the crest of the wave induced by the generating wind stress reduces the limit on wave steepness (Debnath 1994). As a result, deep-sea wind waves with steepness larger than 0.10 are rarely encountered. Vorticity of the opposite sign theoretically increases the limiting wave steepness. This can be observed when the wave travels opposite to the wind direction. According to the closed-orbit Gestner theory, the maximum limiting steepness is 0.31, while the vorticity at the crest tends to infinity. Wave breaking is a complicated nonlinear phenomenon with wide variations in type and conditions. A general rotational wave theory including the mass transport due to wind action has yet to be finalized. An experimental demonstration of the limiting form of the wave appears to be difficult, even though considerable empirical studies on the breaking process are available.

Furthermore, surface wave instability in deepwater is in general a 3-D problem. McLean et al. (1981) found two types of 3-D instability of finite-amplitude surface waves. Su (1982) later reported experimental evidence of these types of instabilities.

Mason (1952) distinguished two types of breaking waves, *spilling* and *plunging* breakers, applying to most situations in the open ocean. The transition from one kind to another is gradual, so such classification is more qualitative than quantitative. Galvin (1972) extended this empirical classification by introducing also *collapsing* and *surging* breakers, which is applicable to the shoreline.

In the open ocean, when the wave height reaches its maximum value, breaking first appears as foam and bubbles on the crests of the steepest waves. This is a spilling breaker according to the Galvin (1972) classification. It is usually accompanied by a relatively small amount of kinetic energy dissipation, and the wave crest for this type of breaker is almost symmetric.

When the front face of the wave becomes steep, the crest curls over the front face and falls into the base of the wave producing a large splash. This plunging breaker type is not unusual for wave breaking on beaches but is much less frequent for deepwater waves (at least for not very high winds).

Spilling breakers are typical for deepwater (open ocean) conditions. A characteristic property of a spilling breaker is that, as it breaks gently at the crest, it traps enough air bubbles for the resulting air–water mixture to be significantly lighter than the water below it. This density difference inhibits mixing with the face of the wave, so that the whitecap rides on top of the sloping sea surface. Accordingly, Longuet-Higgins and Turner (1974) proposed treating a spilling breaker as a turbulent gravity current riding down the forward slope of a wave in the same way a turbulent gravity current rides down a solid sloping boundary (Fig. 1.13). As the flow continues, the turbulence leads to the entrainment of "extra water" and "extra air," especially near the front of the whitecap.

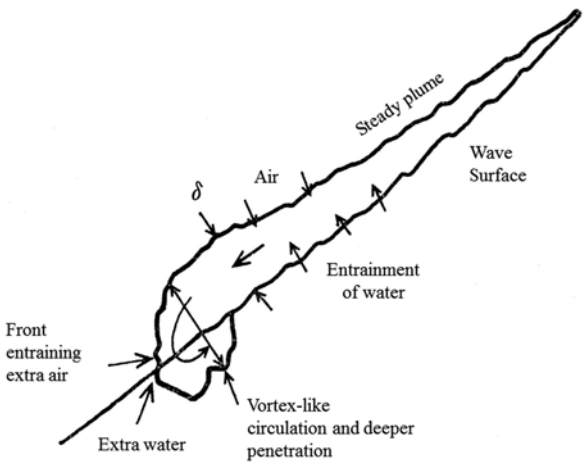

Fig. 1.13 Schematic representation of advancing spilling breaker. The wave is moving from right to left and has a whitecap on its forward face. Here δ is the thickness of the whitecap. After Longuet-Higgins and Turner (1974) by permission of Cambridge University Press

In the Longuet-Higgins and Turner (1974) model, the mean thickness of the whitecap δ increases proportionally to distance from the wave crest, while the whitecap accelerates down the slope. To maintain the stationary state of the wave breaker corresponding to the limiting Stokes wave with a 120° angle at the crest ($\theta = 30°$), the density of the air–water mixture ρ' should be at least 8 % less than water density ρ.

Limitations of the Longuet-Higgins and Turner (1974) model include the assumption of constant density of the air–water mixture in the whitecap as well as the Boussinesq approximation assuming small density differences. To the best of our knowledge, a more comprehensive model of spilling breakers is, however, still pending its development.

The appearance of the spilling breaker depends on wavelength. For long waves, the wave-breaking processes result in the appearance of a turbulent patch of fluid on the forward slope of the wave (as schematically shown in Fig. 1.13). For short waves ($\lambda < 10$ cm), the wave-breaking process is greatly influenced by surface tension; the turbulent bore is replaced with a capillary wave train that can break down without overturning of the water surface (see Fig. 1.14). This process resembles the microscale wave breaking that is described in Sect. 2.3.2 in relation to the sea surface microlayer. The effect of surface tension on the dynamics of the air–sea interface appears to be of greater importance than previously appreciated, for example, to understand the regime of the air–sea interaction in hurricane conditions (see Chap. 6).

1.6.5 Statistical Description of Surface Waves

The detailed configuration of the ocean surface generally varies irregularly in time and space due to a broad spectrum of plane surface waves. Ocean waves can there-

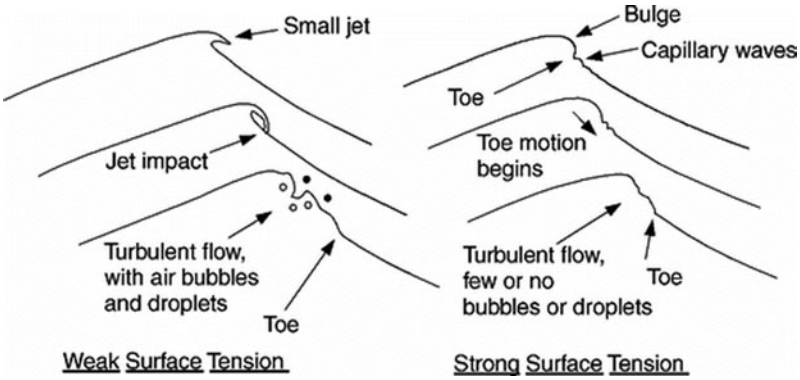

Fig. 1.14 Schematic showing three phases of spilling breaking for weak and strong surface tension effects. After Duncan (2001)

fore be treated as a random process and analyzed with statistical methods. A stationary, random surface elevation $\eta(\vec{x},t)$ can be represented in terms of a Fourier–Stieltjes integral,

$$\eta(\vec{x},t) = \int_{\vec{k}}\int_{\omega} dZ_{\eta}(k,\omega)\exp\left[i\left(\vec{k}\cdot\vec{x}-\omega t\right)\right], \tag{1.109}$$

where the integration is over all time and wave number space. Fourier–Stieltjes coefficients are defined as follows:

$$dZ_{\eta}(\vec{k},\omega)dZ_{\eta}^{*}(\vec{k}',\omega') = \begin{cases} 0 \text{ at } \vec{k},\omega \neq \vec{k}',\omega' \\ \Upsilon(\vec{k},\omega)d\vec{k}d\omega \text{ at } \vec{k}=\vec{k}',\ \omega=\omega' \end{cases} \tag{1.110}$$

where $\Upsilon(\vec{k},\omega)$ is the surface wave spectrum.

The wavenumber spectrum is obtained by integrating all frequencies:

$$\Psi\left(\vec{k}\right) = \int_{-\infty}^{\infty}\Upsilon\left(\vec{k},\omega\right)d\omega, \tag{1.111}$$

and the frequency spectrum by integrating all wave numbers

$$\Phi(\omega) = \int_{-\infty}^{\infty}\Upsilon\left(\vec{k},\omega\right)d\vec{k}. \tag{1.112}$$

It is possible to show that, for a stationary wave field, $\Phi(\omega)$ is real and is symmetrical with respect to $\omega=0$. Often, only positive frequencies are therefore considered, so that

$$\Phi(\omega) = 2\int_0^\infty \Upsilon(\vec{k}, \omega)\, d\vec{k}. \tag{1.113}$$

The root mean square elevation

$$H_{rms} = \sqrt{\langle \eta^2 \rangle} \tag{1.114}$$

is related to the frequency spectrum as follows:

$$\langle \eta^2 \rangle = \int_0^\infty \Phi(\omega) d\omega \tag{1.115}$$

The significant wave height H_S is defined as the mean of the highest one-third of the waves. In the absence of swell, it is related to H_{rms} by

$$H_S = 4H_{rms}. \tag{1.116}$$

The sea is fully developed when the waves have grown to their maximum amplitude for a given wind speed. This implies that the shore is far away (*i.e.*, the sea is not fetch limited) and the wind has been blowing for a long time so that the wave spectrum has become saturated and no more energy can be added.

In fully developed seas, the factors that are expected to be important for describing the surface wave spectrum are the wave frequency ω, wind speed U_a, and acceleration of gravity g (Kitaigorodskii 1962). Standard dimensional analysis leads to the following dependence:

$$\Phi(\omega) g^3 / U_a^5 = \phi_1(U_a \omega / g), \tag{1.117}$$

where ϕ_1 is a universal function. Pierson and Moskowitz (1964) plotted several field spectra for saturated conditions according to scaling (1.117) and proposed an interpolation formula

$$\frac{\Phi(\omega) g^3}{U_a^5} = 4.05 \times 10^{-3} \left(\frac{U_a \omega}{g}\right)^{-5} \exp\left[-0.74 \left(\frac{U_a \omega}{g}\right)^{-4}\right] \tag{1.118}$$

where U_a is the wind speed at 19.5 m height. This formula became known as the *Pierson–Moskowitz spectrum*.

Two useful relations following from (1.118) are

$$gH_S / U_a^2 \approx 0.2 \text{ and} \tag{1.119}$$

$$U_a \omega_p / g \approx 0.88, \tag{1.120}$$

where ω_p is the frequency of the spectral peak.

For a saturated wave number spectrum, in the analysis leading to equation (1.117), frequency ω is replaced with wave number vector k, which results in the following dependencies (Phillips 1977):

$$\Psi(\vec{k}) = \Psi(\vartheta, k) = k^{-4} \phi_2(\vartheta, k u_*^2 / g), \tag{1.121}$$

$$\Psi_a(k) = k^{-3} B(k u_*^2 / g), \tag{1.122}$$

where ϕ_2 and B are universal functions, ϑ is the wave direction, and u_* is the friction velocity. The wave number modulus spectrum, Ψ_a, is defined as follows:

$$\Psi_a(k) = \int_{-\pi}^{\pi} \Psi(\vartheta, k) k d\vartheta \tag{1.123}$$

The high wave number range of the surface wave spectrum has been a subject of substantial interest (see, e.g., Elfouhaily et al. 1997). The short gravity–capillary waves contribute in the momentum exchange between the atmosphere and the ocean (Munk 2009). These waves have other practical significance in air–sea heat and gas exchange, and are also important in remote sensing (Chap. 7).

Figure 1.15 demonstrates the Elfouhaily et al. (1997) model for wave curvature spectrum B at different wind speeds. This curvature spectrum has a peak at wavelength $\lambda = 0.017$ m, which is the wavelength of the phase speed minimum. This peak is related to the surface tension force. The high-wave-number portion of the curvature spectrum has a tendency to saturate under high wind speed conditions. This is consistent with the saturation of the microwave signal scatter by the sea surface under strong winds (Apel 1994; Donelan et al. 2004). The Elfouhaily et al. (1997) spectrum is considered in more detail in Chap. 6 in relation to the problem of air–sea momentum flux in hurricane conditions.

1.6.6 Wave form Stress and Kinetic Energy Flux to Waves from Wind

The wave form stress arises from the form of the waves and depends on wave steepness—steeper waves induce larger form stress. The spectral wave components that may have the phase speed close to the wind speed do not substantially contribute to the wave form stress. The main contribution to the wave form stress comes from the spectral components propagating much slower than the wind. As a result, short gravity–capillary waves, which have small phase speeds relative to the wind speed, can induce appreciable wave form stress.

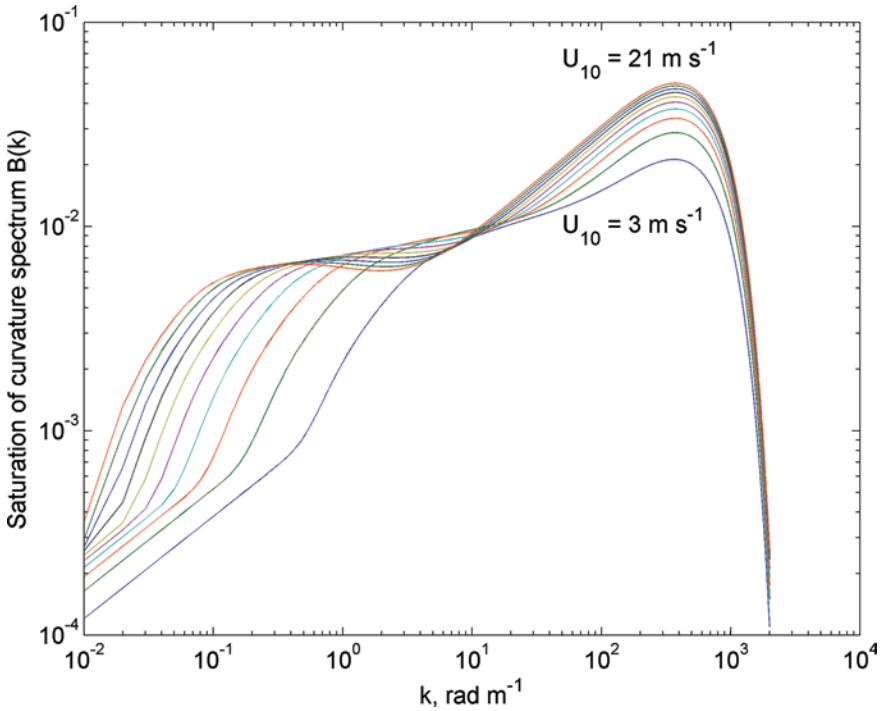

Fig. 1.15 Elfouhaily et al. (1997) wave curvature spectrum $B(k)$ for wind speeds from 3 m s^{-1} up to 21 m s^{-1} with a 2 m s^{-1} step. Note the secondary gravity-capillary peak at ~370 rad m^{-1} corresponding to 0.017 m wavelength. Reprinted with permission by Annual Reviews www.annualreviews.org.

Under very high wind speed conditions, the wind waves are typically relatively young (Donelan et al. 2012). In addition, the two-phase environment is formed by bubbles and spray suppressing short gravity–capillary waves (see Chap. 6), while the regime of the air–sea interaction dramatically changes (Donelan et al. 2004; Powell et al. 2003).

The wave form-induced stress can be calculated from the sea wave spectrum, $\Psi(\vartheta, k)$, in the following way (see, e.g., Plant 1982):

$$\tau_\omega = \rho \int_0^\infty \int_{-\pi}^{\pi} \beta_\omega(\vartheta, k)\, \omega \Psi \cos(\vartheta) k\, d\vartheta\, dk \tag{1.124}$$

where ρ is the water density, (ϑ, k) are polar coordinates in the wave number space ($\vartheta = 0$ corresponds to wind direction, which is also the direction of the wind stress when the wind is steady and no swell is present), ω is the angular frequency, and β_w is the exponential growth rate of the wave energy in response to the wind in the absence of nonlinear interactions and dissipation.

The energy transfer from the wind to the wave field is the driving force for wave growth and breaking, which is the main factor in wave energy dissipation. Direct measurement of the kinetic energy flux from wind to waves is a difficult task. Alternatively, the flux of kinetic energy to waves from wind can be determined as the integral of the growth rate, β_w, over the wave spectrum:

$$F_w = g\rho_w \int_0^\infty \int_{-\pi}^{\pi} \beta_\omega(\vartheta, k)\omega\Upsilon(\vartheta, k)k^{-3} d\vartheta dk. \tag{1.125}$$

Unfortunately, the practical use of formulas (1.124)–(1.125) is complicated due to uncertainty in interpretations of the growth rate, β_w. There are two classical mechanisms of the wave growth in the literature. The Miles (1957, 1959) mechanism results in exponential wave growth in time. However, it uses a linear laminar theory that has no direct role for turbulence in producing the phase lag required for instability. In the Phillips (1957) mechanism, the incoherent stochastic parametric forcing is essentially a result of the turbulence of the boundary layer parameterized as a function of wind speed at some height. The stochastic forcing, entering additively in the Phillips (1957) theory, produces linear-in-time growth versus the exponential growth rate in the Miles theory. Quantitative agreement between these theories and field observations of wave growth appears to be poor. As a result, substantial tuning of parameterization is required in order to account for the fact that theoretical growth rates for long waves appeared to be an order of magnitude smaller than those following from observations (Abdalla and Cavaleri 2002). This suggests that essential physics are missing from the Miles and Phillips wave growth theories. Furthermore, as an indication of the inconsistency in these theories, Donelan et al. (2004) have shown in a laboratory experiment that the aerodynamic drag coefficient has a limiting value in the extreme conditions of very strong winds, which could not be explained in the framework of these theories.

Farrell and Ioannou (2008) proposed a wave growth mechanism by incoherent parametric instability of the Kelvin–Helmholtz type explicitly including instantaneous winds. In contrast to Phillips (1957), the stochastic forcing enters multiplicatively in the Farrell and Ioannou (2008) theory and produces an exponential growth, augmenting the growth from the Miles theory as the turbulence level increases. Soloviev et al. (2013) have extended the Farrell and Ioannou (2008) theory to very high wind speeds by including the effect of the two-phase environment on the ultragravity waves, which results in a more realistic dependence of the air–sea drag coefficient on wind speed. We return to this question in Chap. 6 when considering the regime of the air–sea interaction under hurricane conditions.

1.7 Planetary Boundary Layers

The time and length scales of global oceanic and atmospheric processes are considerably different for reasons related to disparity in the density of the two media. These differences are bridged in the atmospheric and oceanic planetary boundary layers that develop adjacent to the air–sea interface. These boundary layers are subject to strong turbulence, and the turbulent exchange coefficients are much higher within

boundary layers than outside of these regions. Ekman and Monin and Oboukhov developed the 1-D framework for understanding planetary boundary layers.

1.7.1 Ekman Boundary Layer

The theory of the planetary boundary layer formulated by Ekman (1905) provides a convenient framework for the analysis of the Earth's rotation effects. Here, we present this theory in a manner close to that of Stull (1988) and Mellor (1996).

The Ekman theory considers a steady, barotropic flow. Retaining the turbulent stress terms but not the tendency terms, we rewrite equations of motion (1.17) and (1.18) (low Rossby number approximation) as

$$-fv = -\frac{1}{\rho}\frac{\partial p}{\partial x} + \frac{1}{\rho}\frac{\partial \tau_{zx}}{\partial z}, \quad fu = -\frac{1}{\rho}\frac{\partial p}{\partial y} + \frac{1}{\rho}\frac{\partial \tau_{zy}}{\partial z}. \tag{1.126}$$

Since the flow is barotropic, $\partial p/\partial x$ and $\partial p/\partial y$ are constant in the vertical.

It is customary to define geostrophic velocities u_g and v_g from the equations:

$$-fv_g = -\frac{1}{\rho}\frac{\partial p}{\partial x}, \quad fu_g = -\frac{1}{\rho}\frac{\partial p}{\partial y}. \tag{1.127}$$

(The geostrophic velocity is a fictitious velocity, for which the Coriolis acceleration exactly balances the horizontal pressure force.) A combination of (1.126) and (1.127) leads to

$$-fv = -fv_g + \frac{1}{\rho}\frac{\partial \tau_{zx}}{\partial z}, \quad fu = fu_g + \frac{1}{\rho}\frac{\partial \tau_{zy}}{\partial z} \tag{1.128}$$

Above the atmospheric or below the oceanic planetary boundary layer, τ_{zx} and τ_{zy} and their vertical gradients vanish so that $u = u_g$ and $v = v_g$.

Momentum fluxes in (1.128) can be expressed via velocity gradients as follows:

$$\frac{\tau_{zx}}{\rho} = K_M \frac{\partial u}{\partial z}, \quad \frac{\tau_{zy}}{\rho} = K_M \frac{\partial v}{\partial z}, \tag{1.129}$$

where K_M is the turbulent momentum exchange coefficient or eddy viscosity. Thus, (1.128) may be written as

$$\frac{\partial}{\partial z}\left(K_M \frac{\partial u}{\partial z}\right) + fv = fv_g, \quad \frac{\partial}{\partial z}\left(K_M \frac{\partial v}{\partial z}\right) - fu = -fu_g. \tag{1.130}$$

The classical Ekman theory assumes that K_M does not vary with z, which is a very strong constraint, that is discussed in Chap. 3.

The boundary conditions for the atmospheric boundary layer

$$u = v = 0 \text{ at } z = 0, \tag{1.131}$$

and

$$u \approx u_g \text{ and } v = 0 \text{ as } z \to \infty. \tag{1.132}$$

Condition (1.132) means (without loss of generality) that the geostrophic wind vector $\vec{G}$ is directed along the x-axis. In this case, the magnitude of the geostrophic wind

$$G = \left(u_g^2 + v_g^2\right)^{1/2} = u_g. \tag{1.133}$$

When the atmospheric boundary layer is in contact with a moving ocean surface, the atmospheric surface velocity is not exactly zero as stated in (1.131). It is, however, generally small relative to atmospheric geostrophic velocities, so (1.131) can be taken as a fairly good approximation. As stated in equation (1.132), as z increases indefinitely, the velocity will approach the geostrophic velocity, although it is only necessary to state that the velocity is bounded as $z \to \infty$.

Solutions to equations (1.130) with boundary conditions (1.131) and (1.132) are

$$u = G\left[1 - e^{-\gamma_E z} cos\left(\gamma_E z\right)\right], \tag{1.134}$$

$$v = Ge^{-\gamma_E z} \sin(\gamma_E z), \tag{1.135}$$

where $\gamma_E = (2K_m / f)^{1/2}$. The velocity vectors described by solutions (1.134) and (1.135) are shown in Fig. 1.16a as a function of height. The tip of the vectors traces out a spiral, which is known as the *Ekman spiral*.

For constant K_M, the geostrophic wind vector is aligned 45° (counter) clockwise from the surface stress vector in the Northern (Southern) Hemisphere. (Because K_M generally is not constant with respect to z in the turbulent boundary layer, this angle can be different, while the Ekman spiral can in effect be suppressed.) The surface wind stress, which is caused by the drag of the surface wind against the surface, is in the same direction as the surface wind vector. Because, in this model, K_M does not depend on height, (1.129) with (1.134) and (1.135) at $z=0$ result in

$$\tau_0 = (\tau_{0x}^2 + \tau_{0y}^2)^{1/2} = \rho_a G(K_m f)^{1/2}. \tag{1.136}$$

The Ekman layer depth is often defined as $h_E = \pi / \gamma_E$, which is the lowest height at which the wind is parallel to the geostrophic flow (Fig. 1.16). The eddy coefficient in Ekman theory is parameterized as $K_M = c_E \kappa u_{*a} h_E$, where $c_E \approx 0.1$, κ is

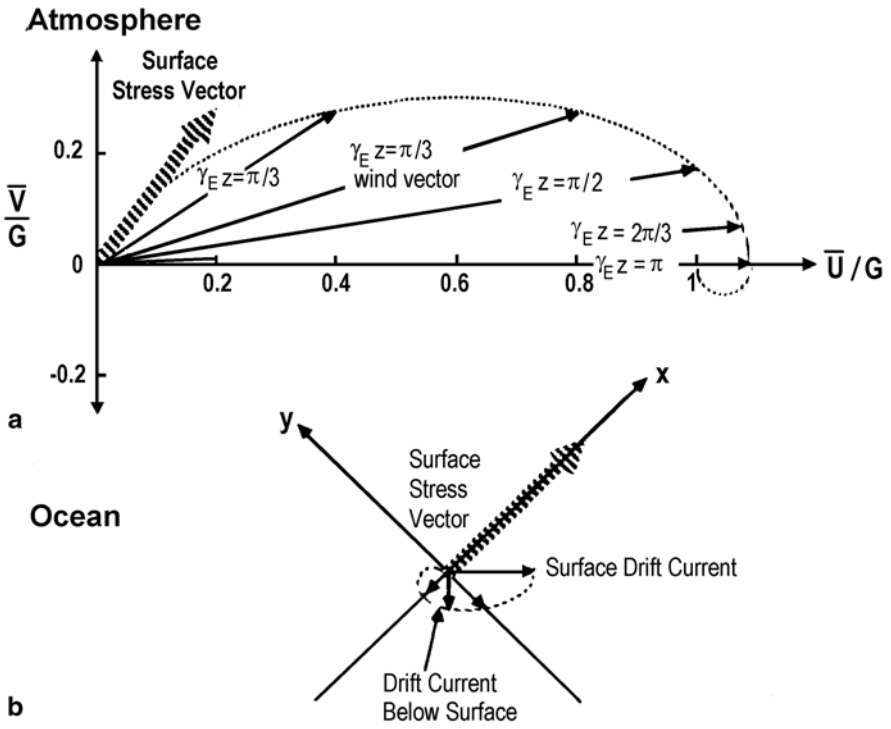

Fig. 1.16 Ekman spiral hodograph for **a** wind and **b** current vectors. After Businger (1982)

the von Karman constant ($\kappa = 0.4$), and u_{*a} is the friction velocity from the airside of the interface defined as $u_{*a} = (\tau_o / \rho_a)^{1/2}$. The Ekman layer depth is then

$$h_E = 2c_E \kappa \pi^2 u_{*a} / f \approx 0.8 u_{*a} / f \,. \tag{1.137}$$

The oceanic boundary layer is different from the atmospheric boundary layer, especially in lower latitudes and due to the difference in stratification and turbulence regimes. We consider details of the upper ocean structure in Chaps. 3 and 4. In this section, the Ekman layer in the upper ocean is assumed to be similar to that in the atmospheric boundary layer (except for the boundary conditions). Equations (1.130) then apply equally well to the ocean mixed layer, and definitions (1.127) are also applicable.

For the analysis of the Ekman layer in the upper ocean, we choose a coordinate system with the x-axis aligned with the surface stress and with z being positive upward. Change of variables, $u - u_g \to u$ and $v - v_g \to v$, transforms (1.130) into

$$\frac{\partial}{\partial z}\left(K_m \frac{\partial u}{\partial z} \right) + fv = 0, \quad \frac{\partial}{\partial z}\left(K_m \frac{\partial v}{\partial z} \right) - fu = 0. \tag{1.138}$$

The boundary conditions for the oceanic side of the interface differ from those for the atmosphere side. First, shear stress is imposed on the sea surface by the wind, so that in the oceanic coordinate system

$$K_m\left(\frac{\partial u}{\partial z}\right)_{z\to -0} = u_*^2 \quad \text{and} \quad K_m\left(\frac{\partial v}{\partial z}\right)_{z\to -0} = 0, \tag{1.139}$$

whereas in deep water the velocity asymptotes to zero:

$$u \to 0 \text{ and } v \to 0 \text{ as } z \to -\infty. \tag{1.140}$$

In equations (1.138) and (1.139), K_m and u_* refer to their ocean values (where the surface stress, τ_0, has been expressed via atmospheric and oceanic friction velocities as follows):

$$\tau_0 = \rho_a u_{*a}^2 = \rho u_*^2 \tag{1.141}$$

Solutions to (1.138) with boundary conditions (1.139)–(1.140) are as follows:

$$u = u_*^2\left(K_m f\right)^{-1/2}\left[e^{\gamma_E z}\cos\left(-\gamma_E z + \pi/4\right)\right], \tag{1.142}$$

$$v = -u_*^2\left(K_m f\right)^{-1/2}\left[e^{\gamma_E z}\sin\left(-\gamma_E z + \pi/4\right)\right]. \tag{1.143}$$

Equations (1.142) and (1.143) describe the Ekman spiral in the upper ocean, which is shown in Fig. 1.16b.

Atmospheric pressure systems drive the atmospheric geostrophic flow that determines the surface wind stress. Across the air–sea interface, the horizontal stress vector is continuous. The sea surface velocity U_0 deviates 45° to the right from the wind stress vector τ_0 (in the Northern Hemisphere) but, remarkably, retains the same direction as the geostrophic wind. It is possible to show (see for instance Kraus and Businger 1994) that

$$\overrightarrow{U_0} = (\nu_a / \nu)^{1.2}\vec{G}\rho_a / \rho \approx 0.005\vec{G}, \tag{1.144}$$

where ν_a and ν are the viscosities of air and water, respectively.

Observations of wind-driven currents in the ocean have shown that the surface current direction does deviate from the surface wind direction. However, the observed deviations are less than the 45° deviation predicted by the Ekman theory. Moreover, the spiral pattern usually is more slab-like than the theoretical Ekman spiral (Price et al. 1987). The main reason is that the vertical mixing coefficient in the ocean changes up to several orders of magnitude depending on depth and stratification, while the Ekman theory treats it as a constant. As a result, compared to a classical Ekman spiral, the speed of the current decreases with depth more rapidly than the current vector rotates (Price and Sundermeyer 1999). These spirals

appear to be flattened or compressed in the downwind direction. This structure may be affected by the temporal variability of a stratification (e.g., due to diurnal cycling) as well.

1.7.2 Monin–Oboukhov Similarity Theory

The Monin–Oboukhov similarity theory is intended to account for the effects of stratification in the planetary boundary layer. This theory is based on the following approximations:

1. horizontal homogeneity,
2. stationary state, and
3. constant stress and heat flux.

In the atmospheric boundary layer, the vertical gradients of horizontal wind velocity u, potential temperature Θ, and the dissipation rate of the TKE ε may then be represented as universal functions of the stability parameter $\zeta = |z| / L_O$ (Monin and Yaglom 1971; Fairall et al. 1980):

$$(\kappa z / u_{*a}) \partial u / \partial z = \phi_M(\zeta), \tag{1.145}$$

$$(\kappa z / T_{*a}) \partial \Theta / \partial z = \phi_T(\zeta), \tag{1.146}$$

$$\kappa |z| \varepsilon / {u_{*a}}^3 = \phi_\varepsilon(\zeta), \tag{1.147}$$

where $T_{*a} = -\overline{w'\Theta'} / (\kappa u_{*a})$, u_{*a} is the friction velocity (in air), ε is the dissipation rate of TKE, stability parameter ζ is defined in (1.41), and u is the horizontal component of wind velocity vector. The stability parameter is negative when the atmosphere is statically unstable and positive when it is statically stable. In order to make this criterion applicable to both atmosphere and ocean, in the definition of the stability parameter we have replaced z with $|z|$.

For intermediate depths, the constant stress and heat flux assumptions (that the Monin–Oboukhov theory is based on) strictly speaking are no longer valid (also because of volume sources). The Monin–Oboukhov theory, however, often holds even in the case of vertically variable fluxes. An approach to modifying the Oboukhov length scale L_O in order to account for the presence of volume sources is considered in Chap. 4.

A commonly used approximation for the universal functions ϕ_m and ϕ_T, based on the Kansas experiment, is as follows (Kraus and Businger 1994):

$$\phi_M \approx \begin{cases} 1 + \beta\zeta & \text{for } 0 \le \zeta \\ (1 - \alpha\zeta)^{-1/4} & \text{for } -0.20 \le \zeta < 0, \\ (1.26 - 8.38\zeta)^{-1/3} & \text{for } \zeta < -0.20 \end{cases} \tag{1.148}$$

$$\phi_T \approx \begin{cases} 1+\beta\zeta & \text{for } 0 \le \zeta \\ (1-\alpha\zeta)^{-1/2} & \text{for } -1.0 \le \zeta < 0 \\ (-28.26-98.96\zeta)^{-1/3} & \text{for } \zeta < -1.0 \end{cases} \tag{1.149}$$

where $\beta = 5$ and $\alpha = 16$. For the dissipation rate of TKE, Wyngaard et al. (1971) proposed:

$$\phi_\varepsilon(\zeta) = \begin{cases} (1+0.5|\zeta|^{2/3})^{3/2}, & \text{for } \zeta < 0 \\ (1+2.5|\zeta|^{2/3})^{3/2}, & \text{for } \zeta \ge 0 \end{cases} \tag{1.150}$$

The mixing coefficients for momentum and temperature are defined as $K_M = -\overline{u'w'} / \partial u / \partial z$ and $K_T = -\overline{w'\Theta'} / \partial\Theta / \partial z$, respectively, and can be defined via the universal functions as follows:

$$\phi_{KM} = \phi_M^{-1}, \phi_{KT} = \phi_T^{-1} \tag{1.151}$$

where

$$\phi_K = K_M / (\kappa u_{*a} z), \phi_{KT} = K_T / (\kappa T_{*a} z). \tag{1.152}$$

Several universal functions from the Monin–Oboukhov theory are shown in Fig. 1.17. There are three asymptotic regimes in this theory:

1. logarithmic layer, where stratification is negligible ($\zeta = 0$),
2. free convection ($\zeta \to -\infty$), and
3. Marginal stability ($\zeta \to \infty$).

Vertical dashed lines in Fig. 1.17 indicate the logarithmic layer regime. The regime of marginal stability is characterized by linear profiles of nondimensional shear ϕ_M and temperature gradient ϕ_T, which is observed starting from sufficiently large positive ζ. A consequence of the marginal stability regime, strong current shear and density gradients can develop in the bottom portion of the diurnal mixed layer (Kudryavtsev and Soloviev 1990) or seasonal mixed layer (Johnston and Rudnick 2009). The asymptotic regimes are discussed in more detail in Sect. 3.5.2

The Monin–Oboukhov similarity theory has provided an important conceptual framework for understanding the dynamics of planetary boundary layers. The constant stress layer assumption, which is the main assumption of this theory, is, however, valid only within approximately 10% of the total thickness of the planetary boundary layer. In addition, the Monin–Oboukhov theory does not account for the Earth's rotation and the nonlocal transport associated with spatially coherent organized motions in planetary boundary layers (see Chap. 5).

The Monin–Oboukhov similarity theory was originally developed for the atmospheric boundary layer. Its application to the upper ocean boundary layer requires some particular modifications, which are discussed in Chap. 3.

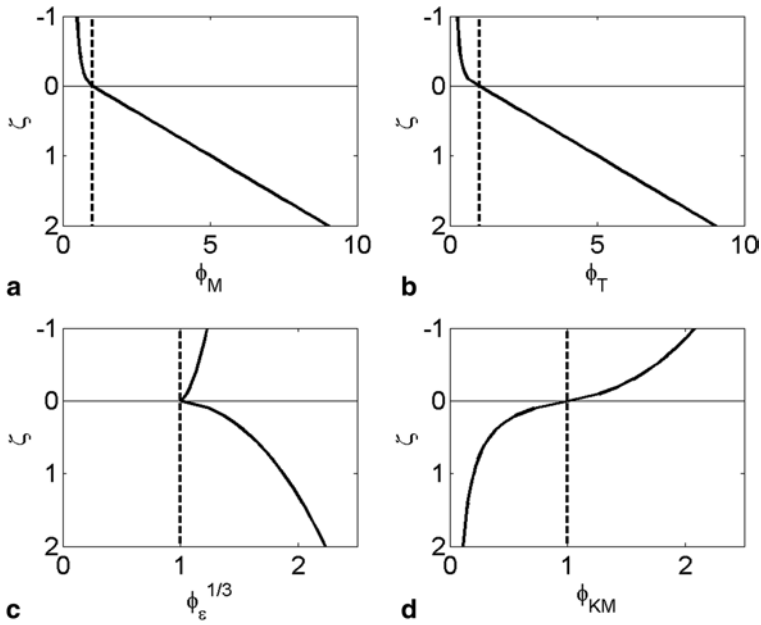

Fig. 1.17 Universal functions for dimensionless **a** shear $\phi_M = (\kappa z / u_{*a})\partial u / \partial z$, **b** potential temperature gradient $\phi_T = (\kappa z / \rho_{*a})\partial \Theta / \partial z$, **c** dissipation rate of the turbulent kinetic energy $\phi_\varepsilon = \kappa |z| \varepsilon / u_{*a}{}^3$, and **d** turbulent eddy coefficient $\phi_{KM} = K_M / (\kappa u_{*a} |z|)$ expressed as a function of stability parameter ζ. The vertical dashed lines represent the logarithmic-layer regime

1.7.3 Surface Mixed Layer

The planetary boundary layers are subject to strong turbulence, and the turbulent exchange coefficients are much higher within boundary layers than outside of these regions. The surface mixed layer is a generic feature of the upper ocean. Vertical profiles of temperature, salinity, and other scalar quantities show nearly constant values adjacent to the surface due to continuous or episodic, but frequent, mixing. Wind-induced shear and waves are important sources of turbulent mixing in the upper ocean. In addition, thermal convection, in the form of loss of heat through longwave radiation flux, and evaporative cooling cause turbulent mixing.

The model of an Ekman layer shows that surface stress is carried away from the boundary layer and toward the interior of the ocean. The Ekman equations assume a dominant balance between the frictional force and the Coriolis force while approximating the equations of motion. The velocity vector then decays in amplitude by spiraling down away from the ocean's surface toward the interior. The Monin–Oboukhov theory assumes that the dominant balance is between the frictional force and buoyancy force. It helps to explain how buoyancy fluxes due to diurnal warming, precipitation, or horizontal advection suppress turbulence in the upper ocean.

Price and Sundermeyer (1999) found that, under fair weather, the temporal variability of stratification due to the diurnal cycle is found to play a major role in the structure of the Ekman layer. McWilliams et al. (2009) have thoroughly explored this problem and have included other complications associated with surface forcing or interior matching. Berger and Grisogono (1998) and Tan (2001) incorporated vertically variable eddy viscosity and boundary-layer baroclinicity (horizontal density gradients) into a generalized Ekman solution.

The Ekman and Monin and Oboukhov theories represent a 1-D framework for understanding planetary boundary layers, which may, however, be a substantial oversimplification in certain cases (see Chap. 5).

The daily averaged depth of the mixed layer changes with season, being relatively shallow during the spring and summer and deeper during the fall and winter. Wind plays a large role in the development of the mixed layer because of the vertical shear resulting from wind-induced surface currents. Seasonal wind variations can account somewhat for seasonal mixed layer depth since winds are stronger in the winter and weaker in the summer. In addition, heating and cooling influence mixed layer depth. Stronger heating during the summer leads to greater stratification, stability, and lower potential energy. On the other hand, cooling destabilizes the water column in the winter, allowing mixing to occur even in the absence of winds. For this reason, winds and surface heat fluxes combine to affect formation and seasonal variation of the mixed layer.

In addition to seasonal differences, latitudinal and hemispheric trends are present in mixed layer depth. Seasonal variation in mixed layer depth generally increases poleward. This is a result of increased winds and cooling toward higher latitudes. Mixed layers are generally deeper in the Southern Hemisphere than in the Northern Hemisphere, especially during the summer (Soloviev and Klinger 2001). This may reflect the fact that winds are generally stronger in the Southern Hemisphere and there is a greater input of heat in the Northern Hemisphere summer.

There are also significant differences in mixed layer depth between oceans. During the winter, the high-latitude North Atlantic develops very deep (>1000 m) mixed layers. The winter deepening is not nearly as intensive in the North Pacific. There is net evaporation and hence higher salinity in the North Atlantic, which may lead to a greater destabilization of the water column, accounting for the difference. In addition, the North Atlantic Ocean extends farther north than the North Pacific Ocean.

The mixed layer of the ocean is an important part of the global climate system. It effectively exchanges momentum, energy, and greenhouse gases with the atmosphere. Spatial–temporal variations of the mixed layer depth are fundamental to the subduction of surface waters and ventilation of the thermocline (Shinoda and Lukas 1995; Williams 2001). Turbulent transport in the mixed layer also controls the supply of nutrients to the upper, sunlit layers, greatly affecting the phytoplankton growth and, consequently, the overall biological productivity of the ocean.

1.7.4 Barrier Layer and Compensated Layer

The depth of the surface mixed layer was traditionally determined as the depth over which the temperature is uniform. However, in the presence of strong freshwater sources (rainfalls, ice melting, and river runoff) there is often a halocline within the isothermal layer, which results in a change in density. Lukas and Lindstrom (1991) refer to the layer between the tops of the halocline and the thermocline as the *barrier layer* because of its impact on the heat budget of the upper ocean. An example of the barrier layer from the Indian Ocean is shown in Fig. 1.18. The temperature within the barrier layer is nearly identical to the mixed layer temperature, while the salinity is larger than in the mixed layer.

The barrier layer is likely to be observed in regions of low winds and high precipitation favoring the development of a thin, fresh surface layer. Such regions are typically in the western equatorial Pacific Ocean, and the eastern Indian Ocean. Freshwater input from rivers is an additional source of freshwater in the Bay of Bengal. The barrier layer can also be important in the dynamics of coastal regions with river runoff (like the Bay of Bengal) and in the marginal polar seas under conditions of ice melting.

In some other situations, an unstable salinity stratification may partially or completely compensate for the stable temperature stratification in the upper layer of the ocean (Kara et al. 2000). Changes in the seasonal thickness of the barrier layer and the compensated layer affect the air–sea interaction regime by altering the effective depth of the mixed layer or the temperature of water at the mixed layer base (Liu et al. 2009)

The existence of the barrier layer plays a key role in the onset of *El Niño* through a complex process that involves ocean vertical mixing, sea surface temperature, wind stress, freshwater flux, and large-scale ocean–atmosphere dynamics (Lukas and Lindstrom 1991; Webster and Lukas 1992; Vialard and Delecluse 1998a, b; Maes et al. 2002; Maes and Belamari 2011). The barrier layer favors the maintenance and displacement of the western Pacific warm pool into the central Pacific by isolating the mixed layer from entrainment cooling at depth and by confining the momentum of westerly wind events to a shallow mixed layer. On average, the tropical cyclones passing over regions with barrier layers intensify by nearly 50 % (Balaguru et al. 2012). Stratification within the barrier layer due to salinity reduces storm-induced vertical mixing and sea surface temperature cooling due to entrainment. As a result, a larger increase in enthalpy flux from the ocean to the atmosphere and, consequently, an intensification of the tropical cyclone may take place.

1.7.5 Modeling Mixing in the Upper Ocean

We conclude this section with a brief overview of numerical methods for modeling mixing in the upper ocean. Analytical solutions are not feasible for the system of governing equations (1.1)–(1.5), except under severe restrictions. However, dis-

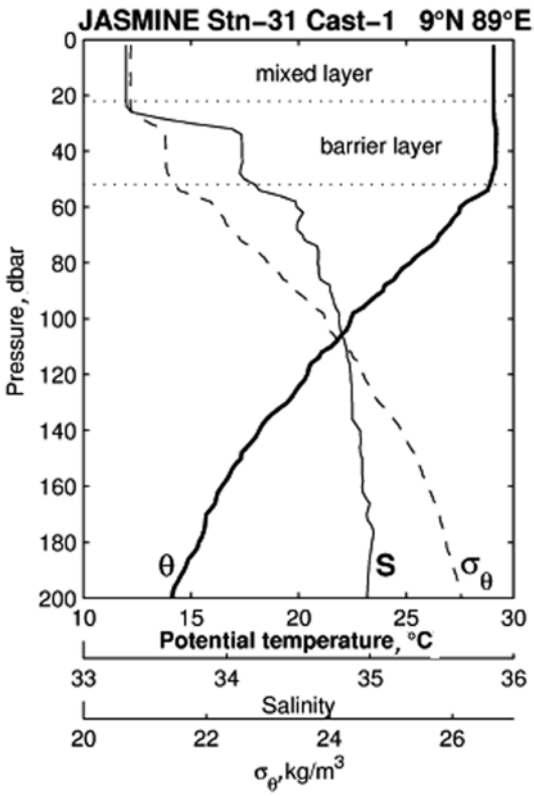

Fig. 1.18 An example of the vertical profiles of potential temperature θ, salinity *S*, and potential density σ_θ in the upper 200 m of the Indian ocean After Lukas et al. (2001)

crete numerical representation of the equations (numerical models) can be integrated forward in time for given initial and boundary conditions. Numerical methods for modeling mixing of the upper ocean range from integral-type 1-D models to 3-D, multiphase CFD models.

1-D integral models reproduce the diurnal cycle of temperature and other properties as a vertical mixing and radiative process driven by the local surface flux of momentum and local surface and volume fluxes of heat (Niiler and Kraus 1977). An advantage of integral type models is their relative simplicity, which is expressed in terms of computational efficiency. Another aspect of integral models is that they are able to implicitly account for the nonlocal vertical transport of properties.

Disadvantages include the uncertainty in parameterizing entrainment fluxes at the bottom of the mixed layer and the inability to reproduce any structure within the mixed layer. The first problem has been addressed by Price et al. (1986) who introduced a Richardson number controlled mixing in the diurnal thermocline below the mixed layer. The second problem has been addressed by Soloviev et al. (2001) who parameterized the turbulent eddy coefficient within the mixed layer as a function of the gradient Richardson number. In particular, the Soloviev et al. (2001) type of parameterization is able to reproduce the strong shear layer developing at the bottom

of the mixed layer and the barrier layer. This type of parameterization is described in Sect. 3.6.2. However, neither the Price et al. (1986) nor Soloviev et al. (2001) parameterization can handle "nonlocal" processes.

Another line of mixed layer model development includes $\kappa - \varepsilon$ turbulence closure schemes (Mellor and Yamada 1982; Peters et al. 1988; Kantha and Clayson 2000; Baumert and Peters 2004). These schemes parameterize the vertical mixing coefficient based on the conservation of TKE and length scale considerations.

The models reviewed above are of diffusive type and do not include nonlocal transport. Turbulence is a fundamentally "nonlocal" process because turbulent transport is performed via a cascade of eddies of different sizes. The nonlocal nature of the turbulent transport is associated with the presence of coherent structures in the upper ocean (Kelvin–Helmholtz billows, Langmuir cells, convective plumes, ramp-like structures, and sharp frontal interfaces—see Chap. 5). An example of the nonlocal transport is given in Sect. 4.4 in relation to rapid deepening of the diurnal thermocline, which is associated with the Kelvin–Helmholtz instability of the diurnal jet and development of billows. Large et al. (1994) attempt to account for the nonlocal transport in previously diffusive 1-D models by including a countergradient term in the expression for the turbulent diffusion coefficient. For the same purpose, Stull and Kraus (1987) previously introduced a 1-D turbulent "transilient" concept for mixing in oceanographic models. The transilient model accounts for the nonlocal transport of properties by a cascade of eddies. Modifications of the transilient model include a total kinetic energy criterion and refinement of a convective term (Kettle 2005).

Kettle (2005) tested the 1-D oceanic boundary-layer models, including those with nonlocal transport features (Price et al. 1986; Large et al. 1994; Stull and Kraus 1987; Zhang and Stull 1992; Burchard et al. 1998; Klein 1980; Klein and Coantic 1981; Gnanadesikan 1996a, b) with the data from an oceanographic cruise near Bermuda. A finding of this study was that all existing 1-D boundary-layer models predicted considerably different mixing intensities and vertical transport rates than those required to close the budget for a passive tracer (carbon monoxide).

Direct numerical simulation (DNS) explicitly resolves the cascade of turbulent eddies in 2-D and 3-D settings. DNS has been applied to reproduce the Kelvin–Helmholtz instability at the air–water interface (Scardovelli and Zaleski 1999) and to model coherent structures in the form of streaks in the near-surface layer of water (Tsai 2001; Tsai and Hung 2007). However, DNS is computationally very expensive at large Reynolds numbers (Pope 2000), which limits its application to modeling of the turbulent oceanic and atmospheric boundary layers. In order to overcome the problem of limited Reynolds numbers, an artificial molecular viscosity has to be introduced in the model. Consequently, DNS may not be able to reproduce viscous sublayers at the air–sea interface.

The large eddy simulation (LES), originally proposed by Smagorinsky (1963), is another approach to 2-D and 3-D modeling. LES separates turbulent motion into large- and small-scale eddies. Large eddies are resolved explicitly, while small eddies are parameterized based on the balance of TKE and length scale considerations.

LES is not limited by Reynolds number, but it implies a spectral gap between large and small eddies, which may not exist in real turbulent flows. LES is also computationally expensive, especially in 3-D versions. In order to improve the computational efficiency, hybrid LES schemes have been under development. An example of such a scheme is the detached eddy simulation (DES), which utilizes LES in the core of the flow and a $\kappa - \varepsilon$ (or similar) diffusive-type scheme near boundaries (Strelets 2001; Matt et al. 2011).

The multiphase volume of fluid (VOF) LES method allows simulation of the air–water interface, including the effect of surface tension (Brackbill et al. 1992). The VOF method can also model the air–sea interface in the presence of air bubbles and sea-spray droplets (Soloviev et al. 2012).

CFD methods are rapidly developing, being driven mostly by industrial applications. Commercial CFD software packages containing multiple modeling options, including LES, do not require significant programming efforts. Furthermore, the introduction of parallel computing, including graphical processing units (GPU) in personal computers, has provided an opportunity to solve many hydrodynamic problems without accessing supercomputers. These two factors dramatically widen access by researchers to the computational tools that are very effective in studying such nonlinear systems as the near-surface layer of the ocean.

At the conclusion of this section, we would like to remind the reader that, despite their amazing capabilities, the numerical models are approximations to the governing laws and still require verification with real data.

References

Abdalla S, Cavaleri L (2002) Effect of wind variability and variable air density on wave modeling. J Geophys Res 107:3080. doi:10.1029/2000JC000639

Apel JR (1994) An improved model of the ocean surface wave vector spectrum and its effects on radar backscatter. J Geophys Res 99:16269–16291

Balaguru K, Chang P, Saravananc R, Leung LR, Xu Z, Mingkui Li, Hsieh J-S (2012) Ocean barrier layers' effect on tropical cyclone intensification. Proceedings of the national academy of sciences of the United States of America. Earth, Atmospheric, and Planetary Sciences 109(36):14343–14347

Baumert H, Peters H (2004) Turbulence closure, steady state, and collapse into waves. J Phys Oceanogr 34:505–512

Beljaars ACM, Holstlag AAM (1991) Flux parameterization over land surfaces for atmospheric models. J Appl Meteorol 30: 327-341

Berger BW, Grisogono B (1998) The baroclinic, variable eddy viscosity Ekman layer. Boundary-Layer Meteorol 87:363–380

Bethoux JP (1968) Adaptation d'une thermipile à la mesure de éclairement sousmarin. Thèse 3ème cycle, Faculté des Sciences de Paris

Bishop JKB, Rossow WB (1991) Spatial and temporal variability of global surface solar irradiance. *J Geophys Res* 96:16839–16858

Bishop JKB, Rossow WB, Dutton EG (1997) Surface solar irradiance from the international satellite cloud climatology project 1983–1991. J Geophys Res 102:6883–6910

Bishop JKB, Potylitsina T, Rossow WB (2000) Documentation and description of surface solar irradiance data sets produced for SeaWiFS. NASA Grant NAG5–6450, Department of Applied Physics, Columbia, University. http://esd.lbl.gov/pub/bishop/seawifs/documentation/seawifs.000217.pdf

Bolin B (1960) On the exchange of carbon dioxide between atmosphere and sea. Tellus 12(3):274–281

Brackbill JU, Kothe DB, Zemach C (1992) A continuum method for modeling surface tension. J Comput Phys 100:335–354. doi:10.1016/0021–9991(92)90240-Y

Budyko MI (1963) Atlas of the heat balance of the earth. Gidrometeorozdat, Moscow, p 255

Burchard H, Petersen O, Rippeth T (1998) Comparing the performance of the Mellor-Yamada and the k-ε two-equation turbulence models. J Geophys Res 103: doi: 10.1029/98JC00261. issn: 0148-0227.

Businger JA (1982) Equations and concepts. Atmospheric turbulence and air pollution modeling. Nieuwstadt FTM, van Dop H (eds) D. Reidel Publishing Co., Dordrecht, pp 1–36

Caldwell DR, Elliott WH (1971) Surface stresses produced by rainfall. J Phys Oceanogr 1:145–148

Charnock H (1955) Wind stress on a water surface. Q J Roy Meteor Soc 81:639–640

Chapman DS, Critchlow PR (1967) Formation of vortex rings from falling drops. J Fluid Mech 29:177–185

Debnath L (1994) Nonlinear waves. Academic Press, London, p 544

de Szoeke SP, Yuter S, Mechen D, Fairall CW, Burleyson CD, Zuidema P (2012) Observations of stratocumulus clouds and their effect on the eastern pacific surface heat budget along 20S. J Climate 25:8542–8567

Dickey T, Banner ML, Bhandari P et al (2012) Introduction to special section on recent advances in the study of optical variability in the near-surface and upper ocean. J Geophys Res 117:C00H20, doi:10.1029/2012JC007964

DOE (1994) Handbook of methods for the analysis of the various parameters of the carbon dioxide system in sea, water;version, 2, Dickson A G, Goyet C (eds) ORNL/CDIAC-74. p 22

Donelan MA, Haus BK, Reul N, Plant W, Stiassnie M, Graber H, Brown O, Saltzman E (2004) On the limiting aerodynamic roughness of the ocean in very strong winds. Geophys Res Lett 31:L18306

Donelan MA, Curcic M, Chen SS, Magnusson AK (2012) Modeling waves and wind stress, J Geophys Res 117:C00J23. doi:10.1029/2011JC007787

Duncan JH (2001) Spilling breakers. Ann Rev Fluid Mech 33:519–547

Ekman VW (1905) On the influence of the earth's rotation on ocean currents. Arkiv Met Astr Fysik 2:1–53

Elfouhaily T, Chapron B, Katsaros K, Vandemark D (1997) A unified directional spectrum for long and short wind-driven waves. J Geophys Res 102:15781–15796

Fairall CW, Markson R, Schacher GE, Davidson KL (1980) An aircraft study of turbulence dissipation rate and temperature structure function in the unstable marine atmospheric boundary layer. Boundary-Layer Meteorol 19:453–469

Fairall CW, Bradley EF, Rogers DP, Edson JB, Young GS (1996) Bulk parameterization of air-sea fluxes in TOGA COARE. J Geophys Res 101:3747–3767

Fairall CW, Bradley EF, Hare JE, Grachev AA, Edson JB (2003) Bulk parameterization of air-sea fluxes: updates and verification for the COARE algorithm. J Climate 16:571–591

Fairall CW, Uttal T, Hazen D, Harre J, Cronin MF, Bond N, Veron DE (2008) Observations of cloud, radiation, and surface forcing in the Equatorial Eastern Pacific. J Climate 21:655–673

Farrell BF, Ioannou PJ (2008) The stochastic parametric mechanism for growth of wind-driven surface water waves. J Phys Oceanogr 38:862–879

Fedorov KN, Ginzburg AI (1988) The near-surface layer of the ocean,. Hydrometeoizdat, Leningrad, p 304 (in Russian)

Foukal P (2003) Can slow variations in solar luminosity provide missing link between the sun and climate? EOS, Trans, Am Geophys Union 84(22):205–208

Fröhlich C (2000) Observations of irradiance variations. Space Sci Rev 94:15–24

Frouin R, Lingner DW, Gautier C, Baker KS, Smith RC (1989) A simple analytical formula to compute clear sky total and photosynthetically available solar irradiance at the ocean surface. *J Geophys Res* 94:9731–9742

Galvin CJ (1972) Wave breaking in shallow water. In: Meyer RE (ed) Waves on beaches and resulting sediment transport. Academic Press, Boston, pp 413–455

Garwood RW Jr (1977) An oceanic mixed layer model capable of simulating cyclic states. J Phys Oceanogr 7:455–468

Garwood RW Jr, Gallacher PC (1985) Wind direction and equilibrium mixed layer depth: general theory. J Phys Oceanogr 15:1325–1331

Gerstner FJ von (1802) Theorie der Wellen. Abhand. Köln Bömischen Gesel. Wiss., Prague

Gnanadesikan A (1996a) Mixing driven by vertically variable forcing: An application to the case of Langmuir circulation. J Fluid Mech 322: 81–107

Gnanadesikan A (1996b) Modeling the diurnal cycle of carbon monoxide: Sensitivity to physics, chemistry, biology, and optics. J Geophys Res 101: 12177–12191

Gosnell R, Fairall CW, Webster PJ (1995) The sensible heat flux of rainfall in the tropical ocean. J Geophys Res 100(9):18437–18442

Grachev AA, Fairall CW (2001) Upward momentum transfer in the marine boundary layer. J Phys Oceanogr 31:1698–1711

Gradshteyn IS, Ryzhik IM (2000) Tables of Integrals, Series, and Products, 6th ed. San Diego, CA: Academic Press.

Green T, Houk DF (1979) The removal of organic surface films by rain. Limnol Oceanog 24:966–970

Hsiao M, Lichter S, Quintero LG (1988) The critical weber number for vortex and jet formation for drops impinging on a liquid pool. Phys Fluids 31:3560–3562

IOC, SCOR IAPSO (2010) The international thermodynamic equation of seawater—2010: calculation and use of thermodynamic properties. Intergovernmental Oceanographic Commission, Manuals and Guides No.56, UNESCO (English), p 196

IOCCG (2000) Remote sensing of ocean color in coastal, and other optically-complex waters. Sathyendranath, S., Ed., Reports of the international ocean-colour coordinating group, no. 3. Published by the International Ocean-Colour Coordinating Group, P.O. Box 1006, Dartmouth, Nova Scotia, B2Y 4A2, Canada, 145 pp.

Ivanoff A (1977) Oceanic absorption of solar energy, In: Kraus EB (ed) Modelling and prediction of the upper layers of the ocean. Pergamon, New York, p 326

Jerlov NG (1976) Marine optics. Elsevier, Amsterdam, p 231

Jin Z, Charlock TP, Rutledge K (2002) Analysis of the broadband solar radiation and albedo over the ocean surface at COVE. J Atmos Ocean Tech 19:1585–1601

Johnston TMS, Rudnick DL (2009) Observation of the transtion layer. J Phys Oceanogr 39:780–797

Kantha LH, Clayson CA (2000) Numerical models of oceans and oceanic processes. Academic Press, International Geophysics Series 66, p 940

Kara AB, Rochford PA, Hulbert HE (2000) Mixed layer variability and barrier layer formation over the North Pacific Ocean. J Geophys Res 105:16783–16801

Katsaros KB (1990) Parameterization schemes and models for estimating the surface radiation budget. In: Geernaert GL, Plant WJ (eds) Surface waves and fluxes, vol 2. Kluwer Academic Publishers, The Netherlands, pp 339–368

Katsaros KB, Buettner KJK (1969) Influence of rainfall on temperature and salinity of the ocean surface. J Appl Meteorol 8:15–18

Katsaros KB, McMurdie LA, Lind RJ, DeVault JE (1985) Albedo of a water surface, spectral variation, effects of atmospheric transmittance, sun angle, and wind speed. J Geophys Res 90:7313–7321

Kettle AJ (2005) Comparison of the nonlocal transport characteristics of a series of one-dimensional oceanic boundary layer models. Ocean Model 8:301–336

Kitaigorodskii SA (1962) Application of the theory of similarity to the analysis of wind generated wave motion as a stochastic process. Bulletin (Izvestya) of the Academy of Sciences of the USSR, Geophysics Series 1:73–80 (English Translation)
Klein P (1980) A simulation of the effects of air-sea transfer variability on the structure of marine upper layers. J Phys Oceanogr 10: 1824–1841
Klein P, Coantic M (1981) A numerical study of turbulent processes in the marine upper layers. J Phys Oceanogr 11: 849–863
Kraus EB, Businger JA (1994) Atmosphere-ocean interaction. Oxford University Press, New York, p 352
Kudryavtsev VN, Soloviev AV (1990) Slippery near-surface layer of the ocean arising due to daytime solar heating. J Phys Oceanogr 20:617–628
Laevastu T (1960) Factors affecting the temperature of the surface layer of the sea: A Study of the Heat Exchange Between the Sea and the Atmosphere, the Factors Affecting Temperature Structure in the Sea and Its Forecasting Societas Scientiarum Fennica, Commentatisnes phisico-mathematicae, Helsinki XXV, 1, p 136
Large WG, McWilliams JC, Doney SC (1994) Oceanic vertical mixing: a review and model with a nonlocal boundary layer parameterization. Rev Geophys 32:363–403
Liu H, Grodsky SA, Carton JA (2009) Observed subseasonal variability of oceanic barrier and compensated layers. J Climate 22:6104–6119
LeBlond PH, Mysak LA (1978) Waves in the Ocean. Elsevier, New York, p 60
LeMéhauté B (1976) An introduction to hydrodynamics and water wave. Springer-Verlag, New York, p 315
Longuet-Higgins MS, Turner JS (1974) An "entraining" plume model of a spilling breaker. J Fluid Mech 63:1–10
Longuet-Higgins MS, Fox MJH (1978) Theory of the almost-highest wave, Part 2, Matching and analytic extension. J Fluid Mech 85:769–435
Lukas R, Hacker P, DeCarlo S, Hummon J, Santiago-Mandujano F, Wright D (2001) Hydrographic observations during the joint air-sea monsoon interaction experimnet (JASMINE) pilot study. SOEST data report 5319, University of Hawaii at Manoa, Honolulu, p 246
Lukas R, Lindstrom E (1991) The mixed layer of the western equatorial Pacific Ocean. J Geophys Res C96 (Supplement):3343–3358
Lumb FE (1964) The influence of cloud on hourly amount of total solar radiation at the sea surface. Q J Roy Meteor Soc 90:43–56
Maes C, Belamari S (2011) On the impact of salinity barrier layer on the pacific ocean mean state and ENSO. Sola 7:97–100
Maes C, Picaut J, Belamari S (2002) Salinity barrier layer and onset of El Niño in a Pacific coupled model. Geophys Res Lett 29(24):2206. doi:10.1029/2002GL016029
Manton MJ (1973) On the attenuation of sea waves by rain. Geophys Fluid Dynam 5:249–260
Marshall JS, Palmer WM (1948) The distribution of raindrops with size. J. Meteorol 5:165–166
Mason MA (1952) Some observations of breaking waves. Gravity Waves. Natl Bur Stand Circ 521:215–20
Matt S, Soloviev A, Rhee S (2011) Modification of turbulence at the air-sea interface due to the presence of surfactants and implications for gas exchange. part ii: numerical simulations. Gas Transfer at Water Surfaces. Kyoto University Press pp 299–312
Maxworthy T. (1972) The structure and stability of vortex rings. J Fluid Mech 51:15–32.
McLean JW, Ma Y-C, Martin DU, Saffman PG, Yuen HC (1981) Three-dimensional instability of finite amplitude gravity waves. Phys Rev Lett 46:817–820
McWilliams JC, Huckle E, Liang J-H (2012) The wavy Ekman layer: Langmuir circulations, breaking waves, and Reynolds Stress. J Phys Oceanogr 42: 1793-1816
McWilliams JC, Huckle E, Shchepetlin AF (2009) Buoyancy effects in a stratified Ekman layer. J Phys Oceanogr 39:2581–2599
Mellor GL (1996) Introduction to physical oceanography. Princeton University, Princeton, p 260
Mellor GL, Yamada T (1982) Development of a turbulence closure model for geophysical fluid problems. Rev Geophys 20:851–875

Melville WK (1996) The role of surface-wave breaking in air-sea interaction. Ann Rev Fluid Mech 28:279–321
Michell JH (1893) On the highest waves in water. Philos Mag, Ser 5 365:430–437
Miles JW (1957) On the generation of surface waves by shear flows. J Fluid Mech 3:185–204
Miles JW (1959) On the generation of surface waves by shear flows. Part 2. J Fluid Mech 6:568–582
Monin AS, Yaglom AM (1971) Statistical fluid mechanics, vol 1 MIT Press, Cambridge p 769
Müller P (2006) The Equations of oceanic motions. Cambridge University Press, p 291
Munk W (2009) An inconvenient sea truth: spread, steepness, and skewness of surface slopes. Annu Rev Mar Sci 1:377–415
Niiler PP, Kraus EB (1977) One-dimensional models. In: Kraus EB (ed) Modeling and prediction of the upper layers of the ocean. Pergamon, New York pp 143–172
Oguz HN, Prosperetti A (1991) Numerical calculation of the underwater noise of rain. J Fluid Mech 228:417–442
Ohlmann JC, Siegel DA, Mobley CD (2000) Ocean radiant heating. part I: optical influences. J Phys Oceanogr 30:1833–1848
Paulson CA, Simpson JJ (1981) The temperature difference across the cool skin of the ocean. J Geophys Res 86:11044–11054
Payne RE (1972) Albedo of the sea surface. J Atmos Sci 29:959–970
Peters H, Gregg MC, Toole JM (1988) On the parameterization of equatorial turbulence J Geophys Res 9 3:1199–1218
Pierson WJ, Moskowitz L (1964) A proposed spectral form for fully-developed wind seas based on the similarity theory of S.A. Kitaigorodsky. J. Geophys. Res. 69:5181–5190
Phillips OM (1957) On the generation of waves by turbulent wind. J. Fluid Mech 2:417–445
Phillips OM (1977) The dynamics of the upper ocean. Cambridge University Press, p 366
Pope SB (2000) Turbulent flows. Cambridge University Press New York, (ISBN 978–0-521–59886–6)
Pope RM, Fry ES (1997) Absorption spectrum (380–700 nm) of pure water. II. Integrating cavity measurements. Appl Opt 36:8710–8723
Powell MD, Vickery PJ, Reinhold TA (2003) Reduced drag coefficient for high wind speeds in tropical cyclones. Nature 422:279–283
Preisendorfer RW (1976) Hydrologic Optics, Vol I: Introduction, U.S. Dept of Commerce, Washington, D.C.
Price JF, Sunermeyer MA (1999) Stratified Ekman layers. J Geophys Res 104(C9):20467–20494
Price JF, Weller RA, Pinkel R (1986) Diurnal cycling: observations and models of the upper ocean response to diurnal heating, cooling, and wind mixing. J Geophys Res 91:8411–8427
Price JF, Weller RA, Schudlich RR (1987) Wind-driven ocean currents and Ekman transport. Science 238: 1534-1538
Pruvost P (1972) Contribution à l'étude des échanges radiatifs Atmospère-Ocèan. Calcul des flux dans la mer. Thèse 3ème cycle. Universite de Lille, n 341
Rascle N, Chapron B, Ardhuin F, Soloviev A (2013) A note on the direct injection of turbulence by breaking waves. Ocean Model 70: 145–151
Rodriguez F, Mesler RJ (1988) The penetration of drop-formed vortex rings into pools of liquid. J Colloid Interface Sci 121:121–129
Scardovelli R, Zaleski S (1999) Direct numerical simulation of free-surface and interfacial flow. Annu Rev Fluid Mech 31:567–603
Schlüssel P, Soloviev AV, Emery WJ (1997) Cool and freshwater skin of the ocean during rainfall. Boundary-Layer Meteorol 95:82437–82472
Schmidt W (1908) Absorption der sonnenstrahlung in wasser. Sitzungsber Acad Wiss Wien 117, p 321
Shinoda T, Lukas R (1995) Lagrangian mixed layer modeling of the western equatorial Pacific. J Geophys Res 100:2523–2541
Smagorinsky J (1963) General circulation experiments with the primitive equations. Mon Weather Rev 91(3):99–164
Smith SD (1988) Coefficients for sea surface wind stress, heat flux, and wind profiles as a function of wind speed and temperature. J Geophys Res 93:15467–15472

Smith SD, Fairall CW, Geernaert GL, Hasse L (1996) Air-sea fluxes: 25 years of progress. Boundary-Layer Meteorol 78(3–4):247–290
Soloviev AV, Schlüssel P (1996) Evolution of cool skin and direct air-sea gas transfer coefficient during daytime. Boundary-Layer Meteorol 77:45–68
Soloviev A, Klinger B (2001) Open ocean convection. Encyclopedia of Ocean Sciences. Academic Press, UK, pp 2015–2022
Soloviev A, Lukas R (1997) Observation of large diurnal warming events in the near-surface layer of the western equatorial Pacific warm pool. Deep-Sea Res. 44: Part I, 1055–1076
Soloviev A, Lukas R, Hacker P (2001) An approach to parameterization of the oceanic turbulent boundary layer in the western Pacific warm pool. J Geophys Res 106:4421–4435
Soloviev A, Fujimura A, Matt S (2012) Air-sea interface in hurricane conditions, J Geophys Res 117:C00J34. doi:10.1029/2011JC007760
Soloviev A, Lukas R, Donelan M, Haus B, Ginis I (2013) The air-sea interface and surface stress under tropical cyclones. Nature Geoscience (manuscript in preparation)
Stokes GG (1880) On the theory of oscillatory waves, math. phys., paper 1, 314. Cambridge University Press, Cambridge, pp 197–229
Strelets M (2001) Detached eddy simulation of massively separated flows. AIAA 2001–0879, 39th AIAA Aerospace Sciences Meeting and Exhibit, Reno, NV
Stull RB (1988) An introduction to boundary layer meteorology, Kluwer Academic Publishers, Dordrecht pp 670
Stull RB, Kraus EB (1987) The transilient model of the upper ocean. J Geophys Res 92:10745–10755
Su M-Y (1982) Three-dimensional deep-water waves, Part I, experimental measurement of skew and symmetric wave patterns. J Fluid Mech 124:73–108
Tan Z-M (2001) An approximate analytical solution for the baroclinic and variable eddy diffusivity semi-geostrophic Ekman boundary layer. Boundary-Layer Meteorol 98:361–385
Tanre D, Herman M, Deschamps PY, De Leffe A (1979) Atmospheric modeling for space measurements of ground reflectances, including bidirectional properties. Appl Optics 18:3587–3594
Tsai W (2001) On the formation of streaks on wind-driven water surfaces. Geophys Res Lett 28(20):3959–3962. doi:10.1029/2001GL013190
Tsai W-T, Hung L-P (2007) Three-dimensional modeling of small-scale processes in the upper boundary layer bounded by a dynamic ocean surface. J Geophys Res 112:C02019. doi:10.1029/2006JC003686
Turner JS (1973) Buoyancy effects in fluids. Cambridge University. Press, NY
Ulbrich CW (1983) Natural variations in the analytical form of the raindrop size distribution. J Clim Appl Meteorol 22:1764–1775
Verevochkin YuG, Startsev SA (2005) Effect of absorption of solar radiation by water of different optical types on convection and heat transfer just under the air-water interface. The case of zero wind speed. J Fluid Mech 523:109–120
Vialard J, Delecluse P (1998a) An OGCM study for the TOGA decade. part I: role of salinity in the physics of the western Pacific fresh pool. J Phys Oceanogr 28:1071–1088
Vialard J, Delecluse P (1998b) An OGCM study for the TOGA decade. part II: barrier-layer formation and variability. J Phys Oceanogr 28:1089–1106
Waliser DE, Weller RA, Cess RD (1999) Comparisons between buoy-observed, satellite-derived, and modeled surface shortwave flux over the subtropical North Atlantic during the Subduction Experiment. J Geophys Res104:31301–31320
Webster PJ, Lukas R (1992) TOGA COARE: the coupled ocean-atmosphere response experiment. Bull Amer Met Soc 73:1377–1416
Williams R (2001) Ocean subduction. Encyclopedia of ocean sciences. Academic Press, UK, pp 1982–1993
Wyngaard JC, Cote OR, Izumi Y (1971) Local free convection similarity, and the budgets of shear stress and heat flux. J Atmos Sci 28:1172–1182
Zaneveld JRV (1989) An asumptotic closure theory for iradiance in the sea and its invsersion to obtain the inherent optical properties. Limnol Oceanogr 34(8):1442–1452

Zhang G, Vivekanandan J, Brandes EA, Meneghini R, Kozu T (2003) The shape–slope relation in observed gamma raindrop size distributions: statistical error or useful information? J Atmos Ocean Tech 20:1106–1119

Zilitinkevich SS (1966) Effect of humidity stratification on hydrostatic stability. Izvestiya: academy of sciences, USSR. Atmos Ocean Phys 2:1089–1094

Chapter 2
Sea Surface Microlayer

Abstract The top few millimeters of the ocean surface, where properties are most altered relative to deeper water, are often referred to as the sea surface microlayer. Physics, chemistry, and biology of the sea surface microlayer are the subject of this chapter. Very close to the air–sea interface, turbulent mixing is suppressed and molecular diffusion appears to dominate the vertical property transport. The viscous, thermal, and diffusive sublayers close to the ocean surface that exist as characteristic features of the air–sea momentum, heat, and mass transport are considered. Their dynamics are quite complex due to the presence of surface waves, capillary effects, penetrating solar radiation, rainfall, and surface films due to the presence of surfactants. The existing theories of the sea surface microlayer, numerical model parameterizations, available observations and new approaches, including computational fluid dynamics modeling and DNA analysis of the bacterial content of the sea surface microlayer, are critically analyzed in this chapter.

Keywords Sea surface microlayer • Viscous sublayer • Thermal sublayer • Diffusion sublayer • Neuston • Surfactant • Surface • Film • Slick • DNA analysis • SAR • Microscale wave breaking • Whitecapping • Coherent structures • Streaks • SST • Dimensional analysis • Renewal model • Renewal time • Cool skin • Solar radiation • Rain • Freshwater skin • Diurnal mixed layer • Diurnal thermocline • Gravity-capillary waves

2.1 Introduction

The microlayer is involved in the heat and momentum transfer between the ocean and atmosphere and plays a vital role in the uptake of greenhouse gases by the ocean. A striking variety of physical, biological, chemical, and photochemical interactions and feedbacks occur in the ocean surface microlayer. There is a widely held presumption that the microlayer is a highly efficient and selective micro-reactor, effectively concentrating and transforming materials brought to the interface from the atmosphere and oceans by physical processes (Liss and Duce 1997). These processes are very intriguing and potentially of great importance for remote sensing of sea surface temperature (SST) and salinity, climate change, and many other practical applications still waiting for their time to come.

A. Soloviev, R. Lukas, *The Near-Surface Layer of the Ocean,* Atmospheric and Oceanographic Sciences Library 48, DOI 10.1007/978-94-007-7621-0_2,

Direct measurement of the sea surface microlayer is still a challenge. As a result, surprisingly little experimental information exists on the structure of the sea surface microlayer. The majority of microlayer results have been obtained from laboratory studies.

The physics of the sea surface microlayer is related to fundamental properties of turbulent boundary layers, such as intermittency (Kline et al. 1967) and quasi-periodic repeating patterns of coherent motion (Robinson 1991). While in the bulk of the water, turbulence largely controls the transport, molecular diffusion takes over the transfer of momentum, heat, and mass from the upper ocean to the sea surface because the vertical component of turbulent velocity is suppressed close to the surface. Surface organic and inorganic films formed as a result of complex interplay between biological, chemical, and physical processes can interfere with air–sea interaction (for instance, by modifying properties of capillary-gravity waves) and affect the properties of molecular sublayers.

Under very high wind-speed conditions, the sea surface can be defined only in the topological sense; as a result, the viscous sublayers is replaced with a two-phase transition layer, which consists of air bubbles, spray droplets, and the overhang of plunging waves (Chap. 6)

As a first approximation, the thickness of the viscous, thermal, and diffusion molecular sublayers at the ocean surface, outside of whitecaps and white outs, can be linked to the Kolmogorov's (1942) internal length scale of turbulence,

$$\eta_\nu = (\nu^3 / \varepsilon)^{1/4}, \tag{2.1}$$

where ν is the molecular kinematic viscosity and ε is the dissipation rate of the turbulent kinetic energy. Similar length scales also exist for thermal and diffusive turbulent processes,

$$\eta_T = \mathrm{Pr}^{-1/2}(\nu^3 / \varepsilon)^{1/4} \tag{2.2}$$

and

$$\eta_D = Sc^{-1/2}(\nu^3 / \varepsilon)^{1/4} \tag{2.3}$$

where $\mathrm{Pr} = \nu / \kappa_T$ is the Prandtl number ($\mathrm{Pr} = 7.1$ for water at 20 °C), $Sc = \nu / \mu$ is the Schmidt number (Sc~10^3), κ_T is the molecular coefficient of kinematic thermal diffusivity, and μ is the molecular coefficient of kinematic molecular diffusivity. The latter equation is applicable to tracer gases, passive contaminants, or sea salts.

An instructive schematic diagram is shown in Fig. 2.1. The logarithmic scale ranges from the diameter of a molecule to the maximum depth of the world ocean emphasizing the top millimeter of the ocean. Molecular sublayers extend from the surface to typical depths of about 1,500 μm (viscous sublayer), 500 μm (thermal sublayer), and 50 μm (diffusion sublayer). There are also organic films on the sea surface, of natural or anthropogenic origin, starting from a few nanometers thickness.

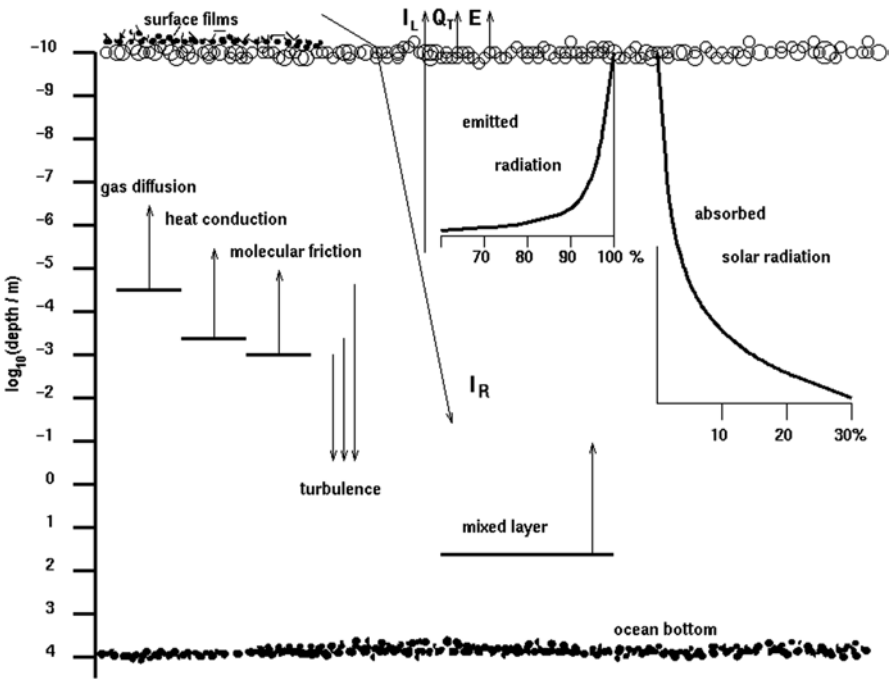

Fig. 2.1 Schematic representation of the vertical structure of physical processes related to the sea surface microlayer. (courtesy of Peter Schlüssel)

These are of course only nominal values. The thickness of molecular sublayers depends substantially on the air–sea interaction regime. In fact, the structure of the molecular sublayers are quite complex. It depends on wind stress acting on the sea surface, on turbulence and coherent motions, on shortwave radiation absorbed in the upper millimeters of the ocean, on heat, salt, freshwater, and gas fluxes crossing these sublayers, and on gravity and capillary waves and surface films. We will consider many of these factors in detail throughout this chapter.

Section 2.2 describes the phenomenology of the viscous, thermal, and diffusion sublayers at the waterside of the air–sea interface. Intimately linked to the physical processes are the complex chemical, photochemical, and biological metamorphoses that take place in the ocean microlayer. The physics of the microlayer, and even the regime of air–sea exchanges, depend on the organics and chemical composition of surface films, and, to some extent, on the sea surface microlayer ecosystem.

The physics of the microlayer are discussed in detail in Sect. 2.3. Renewal and boundary-layer models of the aqueous molecular sublayers are introduced in Sect. 2.4. The renewal model results in a coupled set of parameterizations describing the surface wind-drift current, cool skin, and interfacial gas-transfer velocity. In Sect. 2.5, we discuss the effect of solar radiation absorption on molecular sublayers. Section 2.6 is devoted to the effect of precipitation on the microlayer.

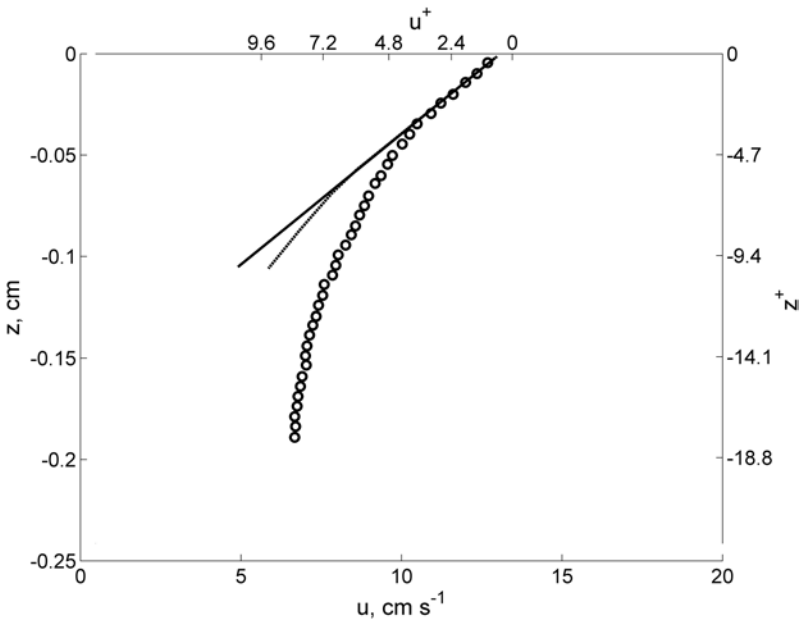

Fig. 2.2 Velocity profile below the free water surface measured in a laboratory tank (circles). The straight line fits the near-surface slope, and the curved line follows the mean profile at a solid boundary. The solid boundary dependence is derived from nondimensional values by Kline et al. (1967). The nondimensional coordinates are as follows: $z^+ = zu_* / \nu$ and $u^+ = (u_0 - u)/u_*$, u_* is the friction velocity in water, ν is the molecular kinematic viscosity of water, u is the downwind water velocity, and u_0 is the downwind water velocity at the surface. (After McLeish and Putland 1975)

2.2 Phenomenology

2.2.1 Viscous Sublayer

Viscous sublayers develop on both sides of the air–sea interface. To our knowledge, direct measurements of the viscous sublayer either from the oceanic or atmospheric side of the air–sea interface have never been made in real oceanic conditions. Information about the aqueous viscous sublayer of the ocean has been mainly obtained from theoretical considerations (for instance, Csanady 1978) or laboratory studies (McLeish and Putland 1975; Wu 1975; and others).

Figure 2.2 shows the velocity profile below the water surface measured at a 0.07 N m^{-2} wind stress in the laboratory experiment of McLeish and Putland (1975). The slope of the near-surface velocity profile is fit with a straight line. The linear vertical profile of velocity is a distinctive feature of the viscous sublayer. The departure of the velocity profile from its linear fit can therefore serve as an indicator of the viscous sublayer depth. It is remarkable that in dimensionless coordinates, the thickness of the viscous sublayer near the free surface is approximately half of

what it would be near a rigid wall. This is explained by the fact that only the vertical component of turbulent fluctuation is effectively suppressed near the free surface; as a result, turbulent eddies can penetrate closer to a free boundary than to a wall. However, this is not the only possible explanation. Another plausible explanation is that microscale wave breaking (see Banner and Phillips 1974; Csanady 1990) increases turbulent mixing near the surface, which reduces the thickness of aqueous viscous sublayer.

2.2.2 Thermal Sublayer

The SST may differ from the temperature of the underlying mixed layer due to the presence of the aqueous thermal molecular sublayer. This sublayer is also referred to as the *cool skin* of the ocean (Saunders 1967b). During daytime, the temperature difference across this aqueous sublayer due to absorption of solar radiation may change sign, turning into the *warm skin* (Soloviev and Schlüssel 1996).

Above the interface, there is a millimeter-thick atmospheric boundary layer, where the vertical transport is also dominated by the molecular diffusion. The largest temperature difference across the air–sea interface is observed in the air rather than water (Volkov and Soloviev 1986).

Figure 2.3 gives an example of the temperature profile in the upper 10 m of the ocean obtained with a *free-rising profiler* (Soloviev 1992). For this measurement, the profiler was equipped with a high-resolution temperature probe (5 μm diameter wire sensing element). The shunting of the micro-wire probe by seawater was small due to the fact that its internal resistance was only 7 Ω, while the surface area of the micro-wire was extremely small (Azizjan et al. 1984).

The vertical temperature profile shown in Fig. 2.3 was taken during night time. The upper part of the profile reveals an abrupt temperature change in the upper few millimeters due to the cool skin. The temperature difference across the cool skin in the example shown in Fig. 2.3 is $\Delta T = T_0 - T_b \approx -0.3°\mathrm{C}$, where T_0 is the SST and T_b is the temperature of the bulk (diurnal mixed layer) water. The temperature gradient below 2 m represents the remnants of the diurnal thermocline formed during the previous daylight hours.

The temperature difference across the cool skin depends on the local regime of air–sea interaction and thus varies in space and time. Historically, much effort has been devoted to the cool-skin parameterization. Saunders (1967b) initially parameterized the average temperature difference across the cool skin $\overline{\Delta T}$ by ascribing a constant value to the nondimensional coefficient, $\lambda_s = c_p \rho u_* \overline{\Delta T} / (\mathrm{Pr} Q_0)$. Grassl (1976) found that λ_s varied with wind speed. The parameter λ_s increased from zero for calm weather conditions to approximately five at moderate wind speeds. Kudryavtsev and Soloviev (1985) explained this dependence of λ_s on wind speed by the transition from convection to a wind–wave regime.

The typical temperature difference across the cool skin is from –0.2 to –0.3 °C increasing approximately two times under calm weather conditions (Horrocks et al.

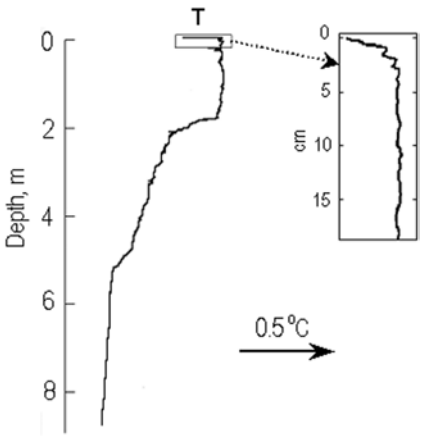

Fig. 2.3 An "instantaneous" vertical profile of temperature in the upper ocean taken under low wind speed conditions. (After Soloviev 1992)

2003). Under strong insolation and/or air temperature exceeding water temperature, the interfacial layer can become slightly warmer than the underlying water.

Collecting high-quality measurements of the cool skin in the open ocean is still a challenge, requiring very specialized techniques. In the oceanographic literature, there are only a few reports of direct profile measurements in the cool skin in the open ocean (Mammen and von Bosse 1990; Soloviev 1992; Ward and Minnett 2001). At the same time, infrared measurement techniques have been under intensive development (Saunders 1967b; McAlister and McLeish 1969; Hasse 1971; Grassl 1976; Paulson and Simpson 1981; Schlüessel et al. 1990; Minnett 2003; and others). As a result, most of the open-ocean data on the cool skin come from infrared SST measurements. A problem of interpretation of the infrared SST measurements is that the longwave radiation reflected from clouds produces strong disturbance of the SST measurement. In order to address this problem, Grassl (1976) constructed an infrared radiometer moving the beam between the sea surface and a seawater bath, which substantially reduced the error due to the signal reflected from clouds. The Tropical Ocean Global-Atmosphere Coupled Ocean-Atmosphere Response Experiment (TOGA COARE) exploited an advanced version of Grassl's method: From 30 January to 24 February 1993, measurements were taken from the R/V *Vickers* in the western equatorial Pacific Ocean (156°E, 2°S). The skin temperature measured with this setup was accurate to 0.05 °C.

Fiedler and Bakan (1997) and Minnett et al. (2001) have developed a multichannel infrared interferometer, which does not require a reference seawater bath. This approach has provided large high-quality data sets of SST of the ocean.

For calculating the temperature difference across the cool skin from the infrared SST measurement, it is also necessary to know the bulk-water temperature below the cool skin. Unfortunately, measurements with sensors towed behind or near the ship are disturbed by the ship's wake, which may introduce substantial errors. The alternative approach is to derive the bulk-water temperature from a ship's thermosalinograph, which takes in water from 3 to 5 m depth, although, a shallow diurnal or rain-formed thermocline may result in a vertical temperature gradient between the

depth of the thermosalinograph intake and the cool-skin layer. An appropriate temperature correction can be calculated with a diurnal mixed layer model forced with the air–sea momentum, heat, and precipitation fluxes, assuming these are available. This correction, however, may introduce outliers by itself due to errors of the model and atmospheric forcing data.

2.2.3 Diffusion Sublayer

The near-surface molecular diffusion sublayer is a crucial element in air–sea gas exchange. The resistance to air–sea gas transfer is mainly due to the diffusion sublayer in water, which is of the order of 50 μm thick (Bolin 1960).

The diffusion sublayer associated with salinity transport has approximately the same thickness as the gas diffusion sublayer (Fedorov et al. 1979). Under evaporative conditions, the sea surface salinity is higher than in the bulk of water, while during rainy conditions, a *freshwater skin* of the ocean is formed (Schluessel et al. 1997).

There are no direct observations of the diffusion molecular sublayer in the open ocean because of the complexity of the microscale measurements near the moving air–sea interface. Some parameters of the aqueous diffusion sublayer can be evaluated from data on the gas-transfer velocity because practically all gas concentration difference is in the ocean rather than the atmospheric diffusion sublayer. In particular, the thickness of the diffusion sublayer is defined as follows:

$$\delta_\mu = \mu \Delta C / G_0 \tag{2.4}$$

where μ is the kinematic molecular diffusion coefficient of gas, G_0 is the flux of property C at the air–sea interface, $\Delta C = C_w - C_0$ is the ensemble averaged air–sea gas concentration difference in property C across the diffusion sublayer, and C_0 and C_b are the averaged concentrations of property C at the water surface and in the bulk (mixed layer) water, respectively. Taking into account (1.50), we obtain the following relationship connecting the gas exchange coefficient and the thickness of the diffusion sublayer:

$$\delta_\mu = \mu / K_\mu. \tag{2.5}$$

2.2.4 Sea Surface Microlayer Ecosystem

The sea surface is a highly productive, metabolically active interface (Hardy et al. 1997). Due to extreme conditions at the air–sea interface, the sea surface is believed to be the place where life on the Planet originated (a competing theory is that of extraterrestrial origin for life on the Earth).

Phytoplankton in the water column produces an abundance of particulate and dissolved organic material, some of which is transported to the surface either passively by buoyancy or actively by upwelling, turbulence, and bubble transport. The natural and anthropogenic compounds deposited from the atmosphere often accumulate on the ocean surface in relatively high concentrations compared to those in the water column. The abundance of organic matter at the sea surface provides a substrate for the growth of the surface-dwelling organisms, the marine *neuston*, which inhabits the sea surface microlayer (Zaitsev 1997).

Neuston realm is a vast habitat. The distinctive physical and chemical characteristics of the sea surface can explain a highly diverse and abundant assemblage of species in the microlayer. Organisms from most major divisions of the plant and animal kingdoms either live or reproduce or feed in the surface layers (Zaitsev 1971). Many of these species are of commercial and ecological importance. The *microneuston*, which may be involved in biogeochemical cycling, and neustonic eggs and larvae of commercially important fish and shellfish, are of particular interest.

Figure 2.4 shows Hardy's (1982) conceptual model of the sea surface microlayer ecosystem. Permanent inhabitants of the surface layer often reach much higher densities than similar organisms found in subsurface waters. The communities of bacteria, phytoplankton, and zooplankton present within this neuston layer are named the bacterioneuston, phytoneuston, and zooneuston, respectively.

There are also numerous temporary inhabitants of the neuston. These are particularly the eggs and larvae of a great number of fish and invertebrate species. The latter utilize the surface during a portion of their embryonic and larval development. Some neuston can remain in the microlayer until turbulence created by breaking waves at winds exceeding 10–15 m s^{-1} disperses them (Zaitsev 1971).

An alternative conceptual model of the sea surface microlayer is schematically shown in Fig. 2.5. In this model, the sea surface microlayer is a gelatinous biofilm, which is formed by transparent exopolymer particles (TEPs). This model is based on the Wurl and Holmes (2008) experimental result suggesting that some TEPs float up to the surface microlayer, forming a gelatinous film. TEPs are a result of the coagulation of biogenic polysaccharides, particularly those produced by phytoplankton. TEPs are critical in the formation of marine aggregates, acting as the binding matrix or "glue" that holds the aggregate together (Verdugo et al. 2004).

TEPs are also readily colonized by microorganisms, including surfactant-producing bacterium. The presence of surfactants may have important impact on dynamics of the sea surface (see Sect. 2.3).

2.2.5 Surfactants and Surface Films

Following Liss and Duce (1997), here we use the following terminology: A film refers to surfactant-influenced surface and a *slick* refers to a visibly surfactant-influenced surface.

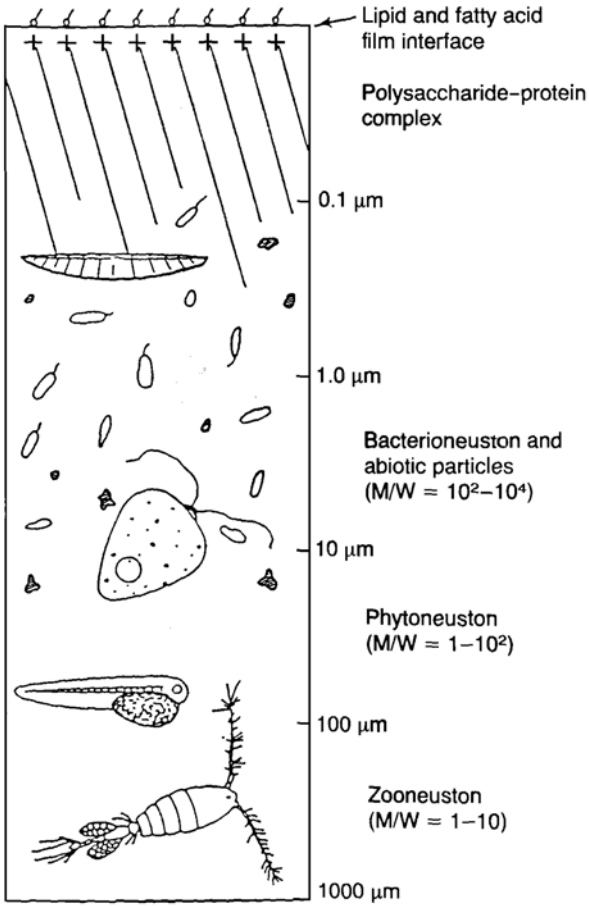

Fig. 2.4 Conceptual model of the sea surface microlayer ecosystem. M/W = typical microlayer to water concentration ratios based on a number of studies. (Reproduced from Hardy (1982) by permission of Elsevier)

Sea surface films are derived from multiple, sea- and land-based sources, including bulk seawater dissolved organic matter, terrestrial sources (natural and anthropogenic), and petroleum seeps and spills (Liss et al. 1997). Surface films dissipate due to loss of material at the surface, including microbial degradation, chemical and photochemical processes, and loss due to absorption and adsorption onto particulates.

Under favorable physical conditions, the concentration of dissolved organic matter is sufficient to produce surface enrichments of organic matter even in oligotrophic waters, where biological productivity is low. Lifecycles of neuston organisms and phytoplankton blooms also lead to the production of the surface-active substances.

The source contribution primarily controls the chemical composition of surface films. A variety of biological, chemical, and physical processes may, nevertheless, change composition, concentration, and spatial structure of the surface films and thus modify physical properties of the air–sea interface. Turbulence and diffusion,

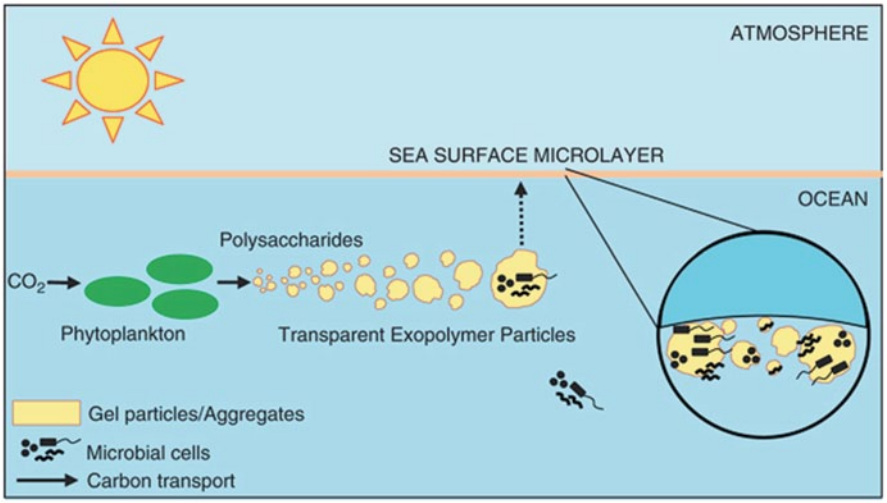

Fig. 2.5 Conceptual model of the sea surface microlayer based on the Wurl and Holmes (2008) study. The formation of transparent exopolymer particles (TEPs) in the near-surface layer of the ocean is a pervasive process, which is also a significant component of the global carbon cycle. Some TEPs float up to the surface microlayer, forming a gelatinous film. TEPs are readily colonized by microbial cells. (Reproduced from Cunliffe et al. (2009) by permission of John Wiley & Sons Ltd)

scavenging, and transport by bubbles and buoyant particles effectively spread surfactants over broad areas of the ocean surface. At the same time, flow convergences associated with organized structures, upwelling events, and internal waves have tendency to localize surface-active materials on various spatial scales, ranging from a few meters to kilometers (Bock and Frew 1993; Liss and Duce 1997).

Sampling of the sea surface microlayer is a challenge. A number of methods have been developed for surface microlayer sampling, including mesh screens (Garrett 1965), glass plates (Harvey and Burzell 1972), and membranes (Kjelleberg et al. 1979). All of these sampling methods, however, result in some degree of contamination, from either the research vessel or underlying water column.

Franklin et al. (2005) implemented DNA analysis of the sea surface microlayer. For this purpose, they used the 47-mm diameter, 2-μm pore polycarbonate membrane. The membrane was placed on the sea surface and attached to the surface by surface tension forces. Water samples were also collected from below the surface. Using this method, Franklin et al. (2005) showed that the bacterioneuston was distinctly different compared with subsurface water 0.4 m below the surface. The weakness of this method is that it is difficult to avoid distortions of the sea surface microlayer from the boat due to proximity of the sampling area to the boat hull.

Kurata (2012) and Kurata et al. (2013) improved this method by attaching the polycarbonate membrane filter to a fishing line and by using the fishing rod to deploy this filter away from the boat wake and then bringing it to the boat. They also used an advanced DNA analysis, which was able to identify surfactant-producing bacteria as well

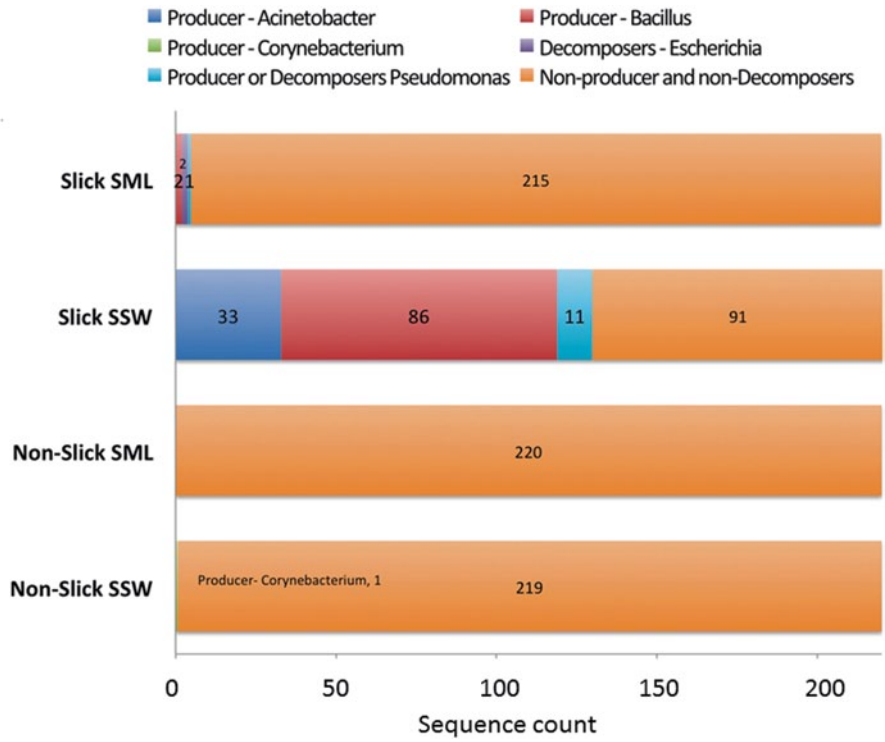

Fig. 2.6 Relative abundance of potential surfactant-associated genera in the sea surface microlayer (SML) and subsurface water (SSW). Sampling in slick and non-slick areas are shown on the synthetic aperture radar (SAR) image in Fig. 2.7. (After Kurata 2012 and Kurata et al. 2013)

as possible bacterial contamination during samples handling and laboratory analysis. The results of a pilot experiment in the Straits of Florida are shown in Fig. 2.6. Note significant diversity of surfactant-associated bacteria in the subsurface layer below the slick, which suggests that surfactants were produced by bacteria in the water column and transported to the surface by diffusion, air bubbles, or organized circulations. This slick was visible on the high-resolution synthetic aperture radar (SAR) satellite image taken during in situ measurements (Fig. 2.7). This case study reported by Kurata (2012) and Kurata et al. (2013) suggests that the DNA analysis of the near-surface organisms opens an opportunity to pinpoint exactly which organisms, and in what environmental conditions, are responsible for generation of surface active materials.

2.3 Physics of Aqueous Molecular Sublayers

The surface microlayer is subject to disturbances from near-surface turbulence (wave breaking, shear, convection, rising bubbles, spray hitting the sea surface, raindrops, etc.). Breaking waves that entrain air and thereby produce whitecaps are

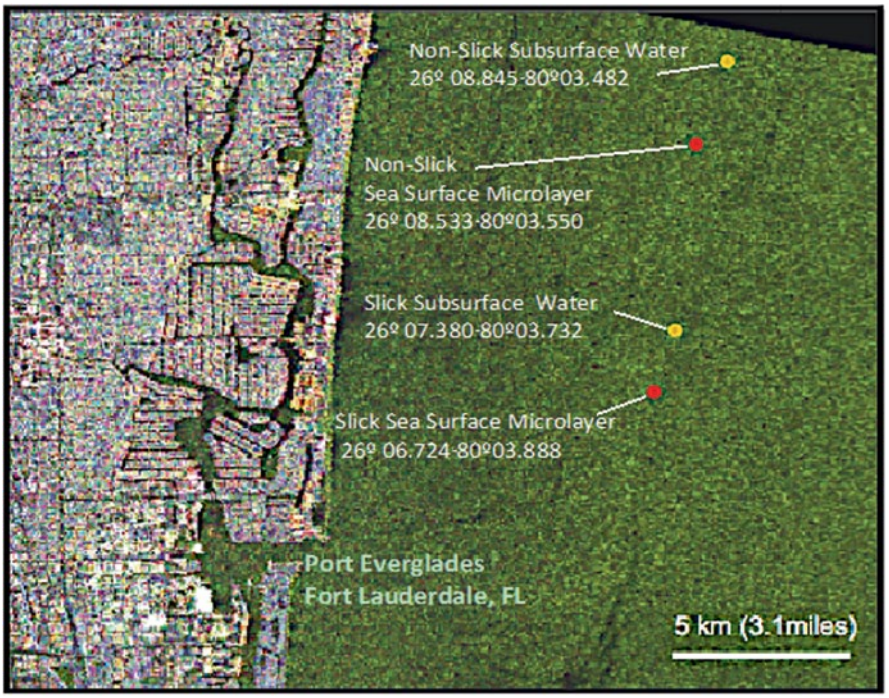

Fig. 2.7 The RADARSAT-2 polarimetric image taken during the pilot experiment in the Straits of Florida on July 10, 2010 to study sea surface microlayer (see Fig. 2.6).Marked are the location of the bacterioneuston in situ sample areas within and out of slicks. (After Kurata et al. 2013)

the most intense and obvious manifestation of the turbulent disturbance. Waves may also break without entraining air and producing whitecapping. This phenomenon is associated with the free-surface boundary condition and is called *microscale wave breaking* (Banner and Phillips 1974) or *rollers* (Csanady 1990). Capillarity effects and the presence of surface-active materials significantly complicate physics of the free surface.

2.3.1 Convective and Shear Instability

Convection and wind-induced shear are important factors in the physics of aqueous molecular sublayers. The molecular sublayers are not stationary and continuous but intermittent in time and space. The boundary-layer processes in the near-surface layer of the ocean are altered by the presence of the free surface (see Chap. 3).

Surface cooling and/or salinity increase due to evaporation initiate convection in the upper layer of the ocean. Convection as a type of hydrodynamic process has a tendency to self-organization and therefore exhibits features of organization (Sect. 5.7). The absorption of solar radiation or rainfall inhibits the convective instability.

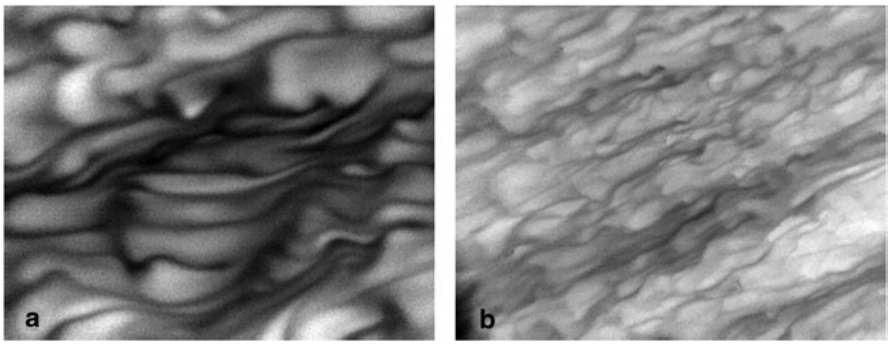

Fig. 2.8 Infrared images of the surface taken in the RSMAS air-sea interaction tank for: **a** light and **b** moderate winds with an imposed air-water temperature difference of 10°C.The water is warmer than the air and light areas are warmer water. (Courtesy of Mark Donelan)

With no solar radiation and precipitation effects, convective instability of a thermal molecular sublayer occurs at low wind speeds. Under moderate and high wind speeds, the molecular sublayers are controlled by the wind stress and surface waves.

Laboratory experimentation involving visualization techniques helps to understand the physics of molecular sublayers. Figure 2.8a shows infrared images of the water surface under convective conditions. The mean temperature is subtracted in the images. White represents temperatures above the mean, and black represents temperatures below the mean. The full range of shades corresponds to 2°C. The spatial and temporal structures observed in the surface temperature field are obviously linked to the near-surface turbulence. The thin cool sheets (black on infrared images) are the convergences, while the wide areas of warm water (white) are divergences. These processes are indicative of surface renewal events. Note a pronounced change in the surface structures from light winds to moderate winds (Fig. 2.8b).

In a laboratory experiment, Syalor et al. (2002) studied the cross-correlation between surface temperature and the vertical component of subsurface velocity in the regime of free convection and found practically zero time lag between the surface and subsurface events. In the Syalor et al. (2002) experiment, the event occurring at the surface would require a delay on the order of 20 s to reach 2 cm depth via turbulent transport. Spangenberg and Rowland (1961), Katsaros et al. (1977), and Volino and Smith (1999) previously reported falling sheet structures during evaporative convection penetrating to several centimeters depth and migrating significant horizontal distances across the surface before disappearing. As structures pass over the measurement location, a sudden change in velocity and temperature resembling bursting event should almost simultaneously be observed at the surface and at 2 cm.

Observations in the open ocean appear to be consistent with the idea of periodic water renewal in near-surface molecular sublayers. Figure 2.9a shows a temperature profile in the upper 10 m obtained with a free-rising profiler under conditions of nighttime convective cooling and low wind speed. The upper part of the tempera-

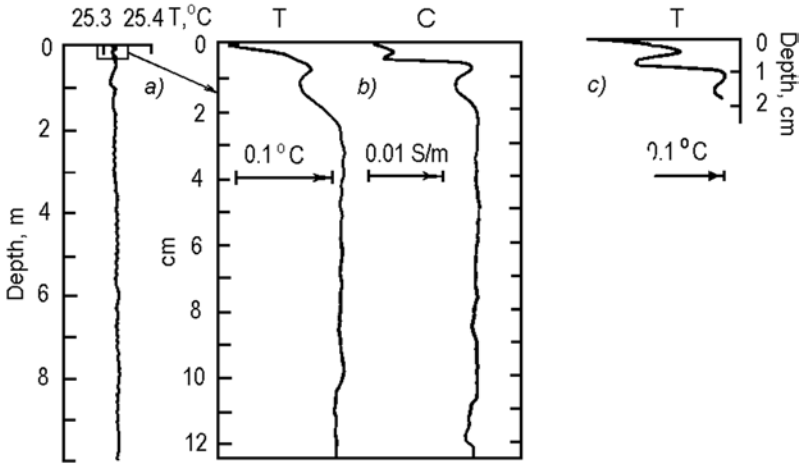

Fig. 2.9 a, b Vertical structure of the near-surface layer of the ocean from measurements with a free-rising profiler in the equatorial Atlantic made at night (02:57 LT) under conditions of low wind speed (U_{10}= 3 m s^{-1}) and intense cooling of the ocean surface (Q_0= 170 W m^{-2}) in comparison **c** with the data from laboratory experiment of Ginzburg et al. (1977). *T* temperature, *C* conductivity of seawater. (Reproduced from Soloviev and Vershinsky (1982) by permission of Elsevier)

ture profile marked by a rectangle in Fig. 2.9a is shown in more detail in Fig. 2.9b. The simultaneous conductivity profile is also shown. The upper 2 mm of the conductivity profile is removed because of the disturbance to the conductivity measurement in the vicinity of the air–water interface.

In the upper few centimeters, the temperature (and conductivity) profile is characterized by inversion, which is presumably caused by convection. According to Katsaros et al. (1977), the temperature inversions in the upper few centimeters can be due to the passage of discrete convective elements (thermals). Figure 2.9c shows a temperature profile obtained near the water surface in a laboratory experiment conducted by Ginzburg et al. (1977) in the free convection regime.

The conductivity sensor in this experiment had a higher spatial resolution (better than 1 mm in vertical direction) than the temperature sensor and therefore revealed more detail (Fig. 2.9b). According to estimates by Soloviev and Vershinsky (1982), in the nighttime convective mixing regime (no precipitation or insolation), the conductivity profiles in the near-surface layer of the ocean mainly depend on the temperature rather than salinity variations. Frictional scales of the turbulent temperature and salinity fluctuations are

$$T_* = \frac{Q_0}{c_p \rho \kappa u_*} \qquad \text{and} \qquad S_* = \frac{Q_E S_0}{\rho \kappa u_* L}, \tag{2.6}$$

respectively, where S_0 is the average surface salinity, L is the latent heat of vaporization, Q_E is the latent heat flux, c_p is the specific heat capacity of water, and κ is the von Karman constant.

For inhomogeneities exceeding the Kolmogorov internal length scale of turbulence (2.1), the ratio of the temperature and salinity scales expressed in terms of the equivalent conductivity changes is as follows:

$$\frac{\Delta C_T}{\Delta C_S} = \frac{\gamma_T T_*}{\gamma_S S_*} = \frac{\gamma_T}{\gamma_S} \frac{LQ_0}{c_p S_0 Q_E} \approx 25, \tag{2.7}$$

where $\gamma_T = (\partial C / \partial T)_{S,p}$ and $\gamma_S = (\partial C / \partial S)_{T,p}$. The estimates of the Kolmogorov length scale for temperature (2.2) and salinity (2.3) are $\eta_T \approx 0.7$ mm and $\eta_D \approx 0.07$ mm, respectively. These estimates are made for the conditions of experiments reported by Soloviev and Vershinsky (1982) under an assumption that the turbulence is driven by convective instability. Since the shear and surface wave instability can only add to the turbulence dissipation level, these are the upper bound estimates of η_T and η_D. According to (2.7), the contribution of temperature to the conductivity changes during nighttime convection well exceeds that of salinity. The high-resolution conductivity profiles can therefore be interpreted in terms of temperature.

Figure 2.10 shows a series of conductivity profiles in the depth range from 2 mm to 20 cm obtained during nighttime. The time interval between successive profiler was from 5 to 9 min; the ship drifted for tens of meters.

For the conditions of this experiment, an estimate for the flux Rayleigh number defined according to Foster (1971) is $Ra_f = \alpha_T g Q_0 h^4 / (\kappa_T{}^2 \nu) \approx 10^{12}$, where h is the mixed layer depth (equal to 50 m in this estimate). Free convection at very large Rayleigh numbers is intermittent in space and time (Turner 1973). Howard (1966) formulated a phenomenological theory of the convection at large Rayleigh numbers that represented turbulent convection as the following cyclic process: The thermal boundary-layer forms by diffusion, grows until it is thick enough to develop convective instability, and is destroyed by convection, which in turn dies down once the boundary layer is destroyed. Then the cycle begins again.

The convective period at the ocean surface is of the order of tens of seconds only; the horizontal length scale of the convective cells is about 1 cm (Foster 1971). The vertical profiles shown in Fig. 2.10 are consistent with Howard's theory in general. Since the profiling time interval greatly exceeded the intermittency period of the convection, in interpreting the results shown in Fig. 2.10 it is necessary to assume that there is no correlation between any two successive temperature profiles in this series of measurements. Following Howard's (1966) phenomenology, the profiles obtained at 02:51, 02:57, 03:18, 03:27, and 00:34 LST can be interpreted as the stage of destruction of the cold surface sublayer by a discrete convective element (thermal). The profiles obtained at 03:04, 03:09, 03:43, and 03:51 LST can be related to the stage of dissipation of the thermal and beginning of the next cycle by the formation of the unstably stratified thermal sublayer due to the molecular heat diffusion.

The observations shown in Figs. 2.9 and 2.10 provide an insight into the renewal process near the surface in convectively unstable conditions. In particular, the data are consistent with the concept of intermittent convection in the near-surface layer, which has found its application for the modeling of the aqueous molecular sublayers.

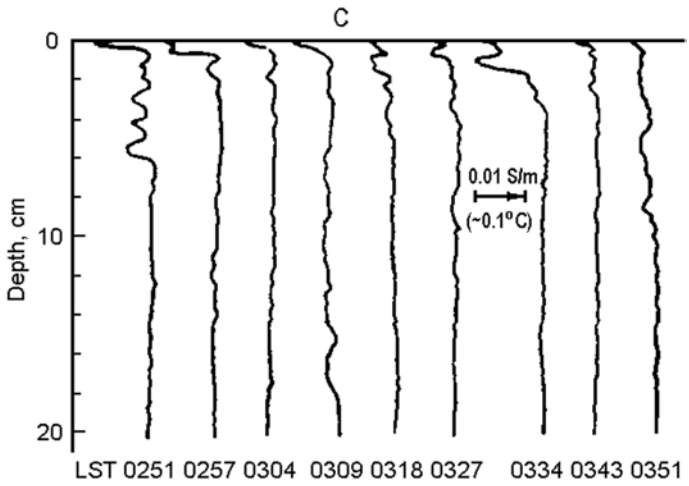

Fig. 2.10 Vertical profiles of conductivity observed during night under convectively unstable conditions near the surface according to measurements in the equatorial Atlantic. The time of observation is marked (LST) under each profile. Wind speed $U_{10} = 3$ m s^{-1}, net surface heat flux $Q_0 = 170$ W m^{2}. The scale of conductivity is shown in the equivalent temperature units under the assumption of constant salinity. (Reproduced from Soloviev and Vershinsky (1982) by permission of Elsevier)

2.3.2 Microscale Wave Breaking

Microscale wave breaking has been the subject of several theoretical, laboratory, and modeling studies. Laboratory wind–wave studies of Okuda (1982) and Ebuchi et al. (1987) revealed a high-vorticity region near the crests of gravity waves with capillary ripples generated ahead of the crests. Longuet-Higgins (1992) identified the origin of vorticity within this surface roller as accompanying parasitic capillaries, which themselves generate fluid rotation (i.e., vorticity) via the surface tension effect (Yeh 1992). Rollers (Longuet-Higgins 1992), breaking wavelets (Csanady 1990), steep wind waves accompanied by a high-vorticity layer near the crest (Okuda 1982), and microscale breaking (Banner and Phillips 1974) appear to be descriptions of the same phenomena.

Microscale breaking waves are typically 0.1–1 m in length and a few centimeters in amplitude. The schematic diagram and the photo from a laboratory experiment shown in Fig. 2.11 illustrate the typical features of microscale wave breaking. Note the bore-like structure at the crest accompanied by parasitic capillary waves distributed along the forward face. Microscale wave breaking is far more widespread than whitecapping. The absence of air entrainment makes the microscale breaking difficult to identify visually. The microscale wave breaking, however, produces the convergence of flow that leads to intense renewal of surface water. The process of surface renewal substantially determines properties of the aqueous molecular sublayers under moderate wind-speed conditions (Csanady 1990).

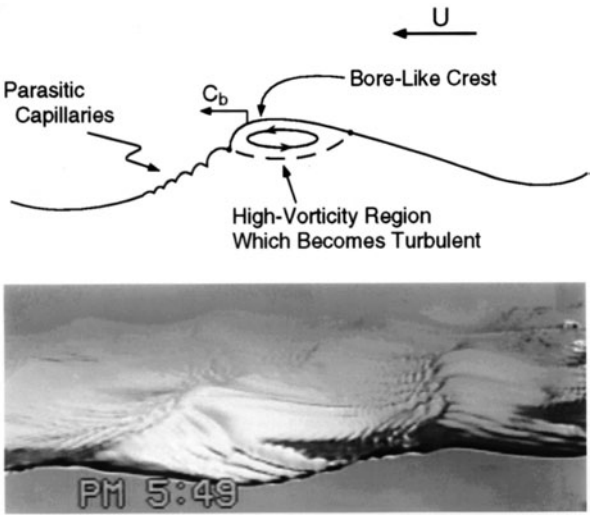

Fig. 2.11 The characteristic feature of a microscale breaking wave is the bore-like crest with parasitic capillary waves riding along the forward face. U wind speed, C_b crest speed of the breaking wavelet (After Longuet-Higgins 1992). Bottom: photograph of a breaking wavelet with a wavelength of roughly 0.1 m (adapted from Jessup et al. 1997). (Reproduced by permission of American Geophysical Union)

2.3.3 *Wave Breaking and Whitecapping*

The widespread occurrence of microscale wave breaking suggests that its cumulative effect on the fluxes of heat and gas across the air–sea interface is significant (Csanady 1990; Banner and Peregrine 1993; Soloviev and Schlüssel 1994; Melville 1996). The aqueous molecular sublayers at the air–sea interface are associated with the action of the tangential wind stress on the sea surface. The tangential component represents only a part of the total wind stress that is transferred from the atmosphere to the ocean. Under high wind speeds, a significant portion of the momentum is transferred to surface waves. Surface waves periodically break destroying the aqueous viscous sublayer as well as the thermal and diffusion sublayers. The molecular sublayers regenerate between wave-breaking events.

The ratio of the tangential wind stress τ_t controlling the aqueous viscous sublayer to the total air–sea momentum flux τ_0 is as follows (Soloviev and Schlüssel 1996):

$$\tau_t = \tau_0 (1 + Ke / Ke_{cr})^{-1}, \tag{2.8}$$

where

$$Ke = u_*^3 / (g\nu) \tag{2.9}$$

is the *Keulegan number*, which is a fundamental parameter in the dynamics of free interfaces (Csanady 1990). At low Keulegan numbers, $Ke << Ke_{cr}$ interfacial instabilities are suppressed by molecular viscosity.

Formula (2.8) reflects the transformation of a substantial part of the surface wind stress to form drag and whitecapping at high wind speeds. Figure 2.12 illus-

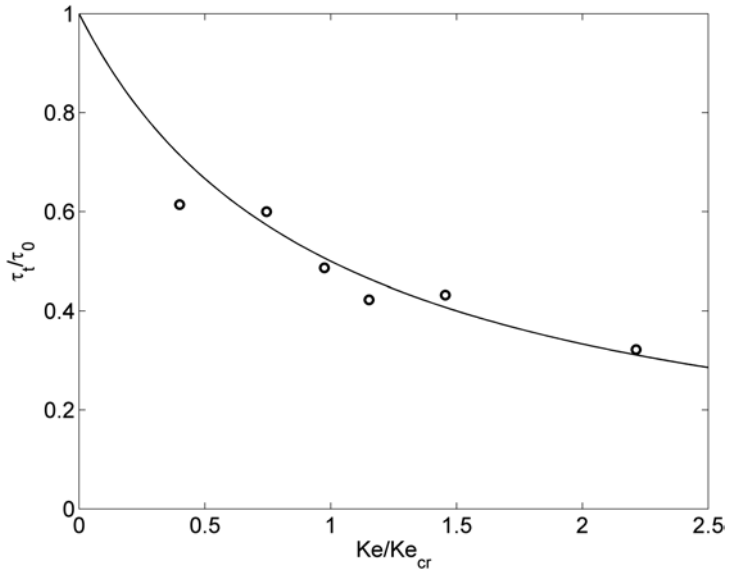

Fig. 2.12 Transformation of the surface wind stress to form drag and whitecapping for high wind speeds. The line is equation (2.8); the circles represent the experiment of Banner and Peirson (1998). (After Soloviev and Schlüssel 1996)

trates this dependence for $Ke_{cr} = 0.18$ in comparison with the data from the Banner and Peirson (1998) laboratory experiment. The theoretical curve is in reasonably good agreement with the experimental data taking into account that the estimate, $Ke_{cr} = 0.18$, had been independently derived by Soloviev and Schlüssel (1994) from the wind-speed conditions for which energy-containing surface waves first start breaking.

2.3.4 Capillary Wave Effects

The presence of capillary waves on the sea surface is a characteristic feature of air–sea interaction. In particular, parasitic capillaries accompany microscale wave breaking, which is one of the principle mechanisms controlling the molecular sublayers, as discussed in the previous section. The overall knowledge about the role of capillary waves in air–sea molecular sublayers and exchanges is still far from satisfactory.

Csanady's (1990) theoretical analysis suggests that the capillary waves by themselves do not contribute substantially to the convergence in the aqueous molecular sublayer. For the molecular sublayers, the surface within capillary waves still appears to be smooth from the waterside, unless there is substantial divergence occur-

ring in parts of the wavelets, for instance, as described by the rollers on top of short gravity waves.

Wu (1996) refers to laboratory measurements reporting a rapid increase in the gas-transfer velocity coinciding with the onset of capillary waves on the water surface (Kanwisher 1963; Broecker et al. 1978). After a critical discussion of the laboratory findings, Wu (1996) proposed the idea of a sudden change of the gas-transfer velocity due to the direct influence of the steep capillary waves on the aqueous molecular sublayer.

Soloviev and Schlüssel (1998) proposed an alternate explanation of the Wu (1996) results: The change of surface roughness due to capillary waves could directly influence the flow on the airside of the interface, thus modifying the wind stress. The sudden change could be merely a reaction to enhanced roughness modifying the wind field rather than a direct impact of the ripples on the aqueous molecular sublayer. The change of roughness could result in a sudden increase in the friction velocity and hence in the intensification of the air–water gas exchange. Another interpretation of the Wu (1996) results points to the connection between microscale wave breaking (rollers) and the parasitic capillaries (Soloviev and Schlüssel 1998). The rollers, if present in the Wu (1996) experiment, would result in a significant effect on the air–sea exchange. In any case, this is a rather indirect influence of capillary waves on the diffusion sublayer.

There is nevertheless evidence of a direct impact of the capillary waves on air–sea exchange. Saylor and Handler (1997) experimented in a small laboratory tank with capillary waves from 2.62 to 3.62 mm wavelength (which corresponds to 400 to 200 Hz frequencies) and found an almost two orders of magnitude increase in the interfacial gas transport rate as the wave slope was increased from 0 to 0.2 mm^{-1}. In this work, small vertical vibration of the tank generated capillary waves via the Faraday instability. The Saylor and Handler (1997) experiment provides remarkable evidence that capillary waves can greatly increase fluxes across the air–water interface. Applicability of these results to the real ocean, however, is not completely clear since the Faraday waves differ from the parasitic capillaries observed in a wind/wave tank or on the open-ocean surface. In natural conditions, the capillary waves of these frequencies (from 200 to 400 Hz) dissipate quickly and may only cover a very small percentage of the sea surface, while in the tank waves excited via the Faraday instability completely covered the water surface.

As seen on the ocean surface, capillary waves indeed appear suddenly when the wind speed exceeds some threshold level. The wind speed has not only a mean but also a variance that makes the sea surface patchy with respect to the coverage with capillary waves (the so-called “cats paws”). As the wind speed increases, the area covered by ripples gradually increases so that the surface averaged over a larger area should demonstrate a smooth transition from no capillary waves to full coverage without an obvious “jump.” This is relevant to the mean gas transfer (i.e., averaged over some space and time intervals). The sudden increase should only be observed on a small scale that might be relevant to fluctuations but not to the mean exchange.

The sudden increase in gas transfer has been observed mainly (if not exclusively) in laboratory studies (see, for instance, Fedorov and Ginzburg 1988). The natural variance of the wind speed, and the implied variance of the surface patches covered with capillaries, does not occur in the laboratory airflow. This is an important difference between the tank airflow and the open-ocean wind pattern; it is basically because timescales of wind velocity fluctuations in the laboratory and in the field conditions are very different (Soloviev and Schlüssel 1998).

Finally, as summarized by Cox (2001), several processes may be at work:

1. Convergence/divergence of orbital motions in waves disturbs the boundary layer at the interface where fluxes are controlled by molecular diffusion.
2. The decay of capillary wave trains accompanying rollers delivers horizontal momentum to the water in patches corresponding to the locations of the wave trains. This patchy driving force can induce turbulent motions of a size corresponding to the length of the wave train.
3. Short gravity waves and capillaries dramatically increase the momentum transferred to the ocean via increased sea surface roughness, thus enhancing near-surface mixing.
4. In addition, the properties of capillary waves depend considerably on the presence of surfactants and surface films.

2.3.5 *Chemical and Photochemical Reactions in the Sea Surface Microlayer*

Complex chemical, photochemical, and biological metamorphoses take place in the ocean microlayer. Photochemical and chemical reactions rapidly developing within the microlayer could produce a variety of feedbacks to the biological and physical processes (Plane et al. 1997). For example, elevated levels of highly reactive intermediate products produced in the microlayer could represent a ‘reaction barrier’ to the transport of gases and some chemicals across the air–sea interface. Certain photochemical reactions destroy or produce surfactants modifying surface films; altered surface waves from the gravity-capillary band then affect gas exchange rates. Many other reactions occur within the microlayer, in particular those increasing or reducing the surface concentrations of certain gases relative to their bulk-water concentrations, as well as those influencing the types and the distributions of microlayer materials ejected to the atmosphere during bubble bursts and delivered to the deep ocean by coalescent particles.

2.3.6 *Natural and Anthropogenic Influences*

In this book, we mainly focus on the physics of aqueous molecular sublayers. The physics, chemistry, and biology of the sea surface, nevertheless, are closely related.

For example, phytoplankton in the water column produces particulate organic matter and a variety of biogenic chemicals and gases, which then rise to the surface where they enter the microlayer (Hardy et al. 1997). This organic matter modifies surface films, which affects the gravity-capillary waves and, thus, the air–sea gas exchange on the global scale.

Increasing pollution of the ocean threatens marine neuston and represents one of the significant factors accelerating global ecological changes. Anthropogenic enrichment of the sea surface impacts natural biochemical processes in the ocean microlayer affecting the air–sea CO_2 exchange with possible consequences for global climate (Hardy et al 1997).

On the other hand, iron (the element which limits primary biological productivity) is supplied to the ocean via the surface microlayer. The increase in productivity due to an increased iron supply stimulates the ocean's "biological pump" increasing the CO_2 uptake by the ocean and potentially reducing the global warming (Wu et al. 2003).

The mechanical influence of disturbances produced by the swimming motion of small zooneuston organisms perhaps may also contribute to the microlayer structure at some level (Gladyshev 1997). Flying fish, birds, and ships disturb the microlayer significantly, though only locally.

2.3.7 Effects of Surface Films

Surface films are an important part of the sea surface microlayer. Air–sea exchanges depend on film properties, especially under low wind-speed conditions. Laboratory and field measurements show that the surface tension can be reduced by up to 60 % due to surface films (Hühnerfuss et al. 1987). The presence of surface films on the ocean is one of the factors leading to uncertainty in the existing air–sea exchange parameterizations.

The effects of surface films are dependent on the type and concentration of surface-active materials (surfactants) and wind–wave regime. Breaking waves and near-surface flow convergences substantially erode the surface films above wind speeds of 5–6 m s^{-1}. Surface films are also fragmented by rain, although there are observations suggesting that even in the case of intense rain the surface films are not completely removed (Baier et al. 1974).

The effect of surfactants on the properties of the sea surface has been studied in relation to air–sea fluxes (Frew 1997; Asher et al. 2005) and SAR imagery of the ocean surface (Chap. 7). The presence of surface films on the ocean is one of the factors leading to uncertainty in the existing air–sea exchange parameterizations under low wind-speed conditions. Surface films can affect air–sea exchanges through static and dynamic mechanisms (Liss 1983). The static mechanism results from the physical barrier provided by the film; it requires the presence of organized (condensed, solid) surfactant films that can easily be reproduced in the laboratory but hardly survive typical oceanic conditions of wind and waves. The films with

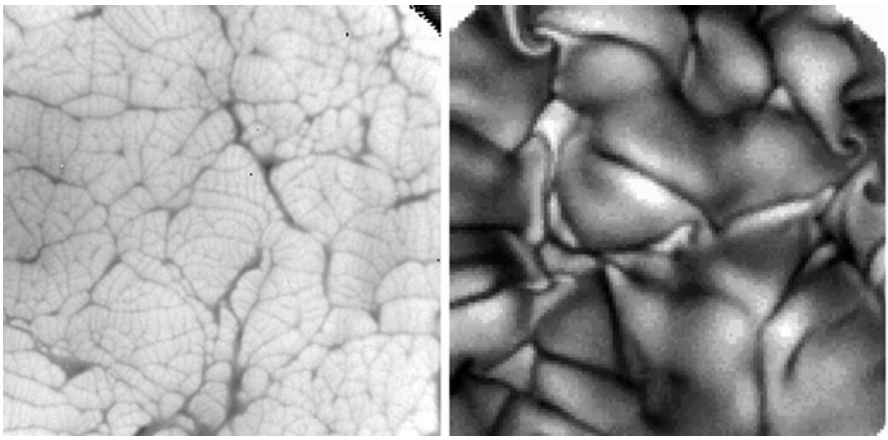

Fig. 2.13 Infrared images of sea temperature under convective conditions for clean (left subplot) and surfactant covered (right subplot) surface for a heat flux of 407 W m^{-2}. The mean temperature is subtracted in the images so that white represents temperatures above the mean and black represents temperatures below the mean. The dynamic range of the image is approximately 1 K. (Reused with permission from Flack et al. 2001 AIP)

high surface concentrations of organic material occupy only a small fraction of the global ocean surface. The dominant point of view among ocean chemists is that the organic matter concentrations are quite low in the open ocean. The static mechanism thereby is not of primary importance for typical open-ocean conditions (Liss and Duce 1997). The dynamic mechanism is more important in the ocean, because it can be effective even with relatively low surfactant concentrations.

The dynamic mechanism relates to the viscoelastic properties of surface films (Frew 1997). Nonzero viscoelasticity modifies the surface boundary conditions, which affects hydrodynamic processes at the air–sea interface. Figure 2.13 shows infrared images of clean and surfactant-covered water surfaces obtained in convectively unstable conditions. The spatial scale of the convective structures dramatically changes when surfactant is present on the water surface compared to a clean surface. The surfactant film inhibits very fine structures and emphasizes larger scale motions, some of which can be vortical. Damping effect of surfactants on the gravity-capillary waves (Fig. 2.14) is the result of the dilatational viscoelasticity of the monomolecular surface film.

The temperature dependence of surface tension leads to circulations driven by horizontal temperature gradients, referred to as the Maragoni effect (Katsaros 1980). Horizontal temperature gradients are produced by adjacent but phase-lagged surface renewals. Calculations of the Maragoni effect for typical temperature gradients produced by the surface renewals show that under low wind-speed conditions the renewal time would be reduced by orders of magnitude in the case of totally film-free water surfaces. This is not observed in the ocean because under natural conditions the sea surface is always covered by surface-active agents that diminish the temperature dependence of the surface tension to negligible values.

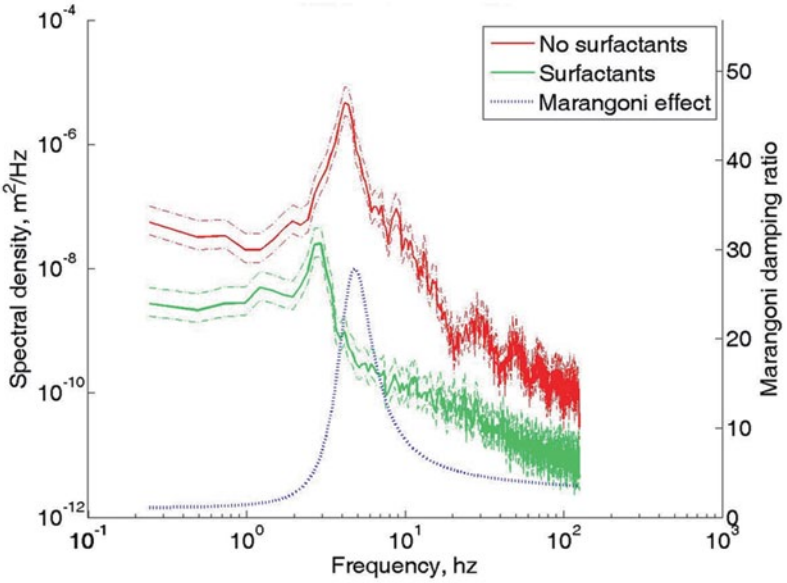

Fig. 2.14 Wind wave spectra of clean water surface (red) and in the presence of oleyl alcohol surface film (green)—measurements in ASIST facility of UM RSMAS. The 95 % confidence interval is shown by the dash-dot lines. The wind speed recalculated to a 10 m height was approximately $U_{10} = 7$ m/s. The dotted line represented the curve (ordinate on the right-hand side) for Marangoni wave theory for oleyl alcohol (eqs. 1–4 in Hühnerfuss 1987). After Soloviev et al. (2011) by permission of Kyoto University Press

Although rain fragments surface films, as already mentioned, there are observations suggesting that even in the case of intense rain the surface films are not completely removed (Baier et al. 1974).

Remarkably, the laboratory result shown in Fig. 2.15 suggests that the presence of surfactant increases the surface drift velocity by approximately 25 %. This is equivalent to the reduction of the drag coefficient from the waterside by 36 %. The reduction is even stronger when taking into account that the momentum transmitted from the air to the water surface is reduced in the presence of surfactant due to reduced surface roughness from the airside of the interface.

In order to understand the nature of the effect of surfactants on the drag coefficient from the waterside and increase in the surface drift velocity, Soloviev et al. (2011) measured the horizontal structure of the velocity field at a 2-cm depth using DIGITAL PARTICLE IMAGE VELOCIMETRY (DPIV). They observed "streak-like" features oriented in the along-tank direction. The streak-like features practically disappeared after the addition of surfactant and the corresponding variance of the horizontal velocity gradient reduced by almost a factor of 2 for both velocity components. Streak-like features have previously been reported from experiments and numerical simulations near the rigid wall (Lesieur 2008) and below the free surface (Dhanak and Si 1999; Tsai 2001). Streaks of low and high longitudinal velocity relative to the local mean velocity profile are a generic feature of the turbulent boundary

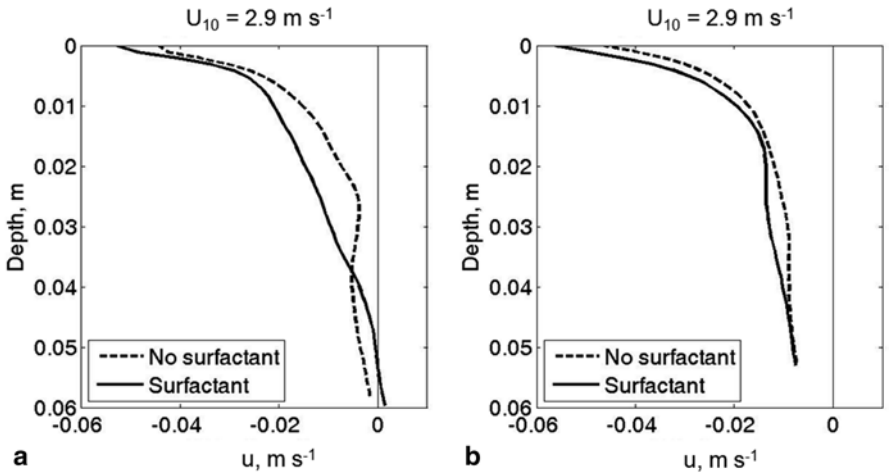

Fig. 2.15 Averaged velocity profiles from DPIV (along tank component) from experiments in ASIST: **a** Experiment 1, and **b** Experiment 2. We used oleic acid in Experiment 1 and oleyl alcohol in Experiment 2. (After Soloviev et al. (2011) by permission of Kyoto University Press)

layer near a ridged wall. These streaks are a type of coherent structures developing in the buffer layer between the viscous sublayer and the area of developed turbulence. Such streaks are observed between approximately $z_+ = 5$ and $z_+ = 40 - 50$, where $z_+ = z/(\nu/u_*), z$ is the distance to the surface, ν is the kinematic viscosity, and u_* is the friction velocity. The streaks near the ridged wall are of spanwise size of about 100 z_+ and of average length of 500 z_+ (Lesieur 2008).

Matt et al. (2011) reproduced the streak-like features reported in the laboratory experiment by Soloviev et al. (2011) using a computational fluid dynamcis (CFD) model. In the numeric model, viscoelastic surface boundary conditions were formulated as follows:

$$\tau_x = \tau_0 + \partial\sigma_w / \partial C \;\; \partial C / \partial x + \partial\sigma_w / \partial T \;\; \partial T / \partial x, \tag{2.8}$$

$$\tau_y = \partial\sigma_w / \partial C \;\; \partial C / \partial y + \partial\sigma_w / \partial T \;\; \partial T / \partial y, \tag{2.9}$$

The last two terms on the right side of (2.8) and (2.9) represent the dependence of surface tension σ_w on the surface concentration of surfactant (C) and on temperature (T). The model results revealed "streak-like" features in the velocity field (Fig. 2.16a). However, noticeable suppression of streaks occurred when the viscoelastic boundary conditions were activated (Fig. 2.16b).

Near rigid walls, the near-surface velocity streaks are subject to the Tollmien–Schlichting (TS) type instability leading to the development of 'hairpin vortices' and ejection of fluid from the viscous sublayer (Kim et al. 1987). A similar instabil-

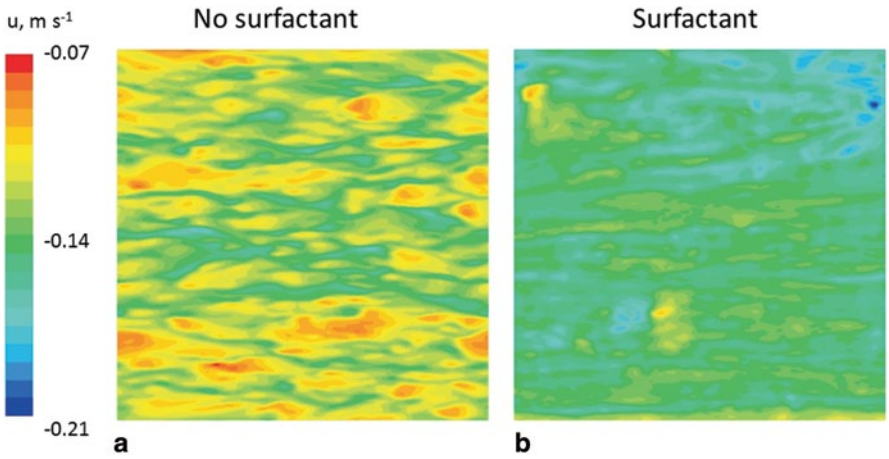

Fig. 2.16 Top view of along tank velocity without **a** and with **b** elastic boundary condition simulating surfactant effect. (After Matt et al. (2011) by permission of Kyoto University Press)

ity, though possibly not exactly of the same type as that near the rigid wall, can also develop near a flexible wall (Benjamin 1960, 1963) or a free surface (Caulleiz et al. 2008). In Chap. 5, we link this type of instability (resulting in fluid ejection from the near-surface layer) to 'ramp-like structures', which are an observable feature in turbulent boundary layers in the atmosphere (Antonia et al. 1979) and ocean (Thorpe 1985; Soloviev 1990). This type of coherent structure is responsible for about 40 % of the momentum transport across the boundary layer (Antonia et al. 1979).

Figure 2.17 shows average current velocity profiles from the numerical simulation of the Soloviev et al. (2011) laboratory experiment. The increase in the surface drift velocity observed in the presence of surfactants in the upper few centimeters of the water layer in the laboratory experiment (Fig. 2.15) is also seen in the numerical results (Fig. 2.17). This is a result of the suppression of turbulent velocity fluctuations and coherent structures due to the dilatational viscoelasticity of the monomolecular surface film, which is schematically illustrated in Fig. 2.18. The concentration of the surfactant in convergence zones reduces surface tension, while the dilution of the surfactant in divergence zones decreases surface tension. As a result, forces opposing fluid motion develop at the water surface and suppress coherent (as well as random) velocity fluctuations in the near-surface layer of water. A consequence of streak and turbulence suppression below the surface is the reduction of the drag coefficient from the waterside of the air–water interface, which explains the effect of surface drift velocity increase observed in the presence of surfactants.

Phongikaroon et al. (2004) demonstrated in a laboratory experiment that surfactants can modify SST by affecting dynamics of the millimeter thick aqueous thermal molecular sublayer (cool skin). The numerical simulations by Soloviev et al. (2012) demonstrate an effect on the temperature difference across the aqueous thermal molecular sublayer in the presence of surfactants during nighttime (Fig. 2.19) and daytime (Fig. 2.20). Note that under strong solar irradiance, "cool skin" turns into a "warm skin."

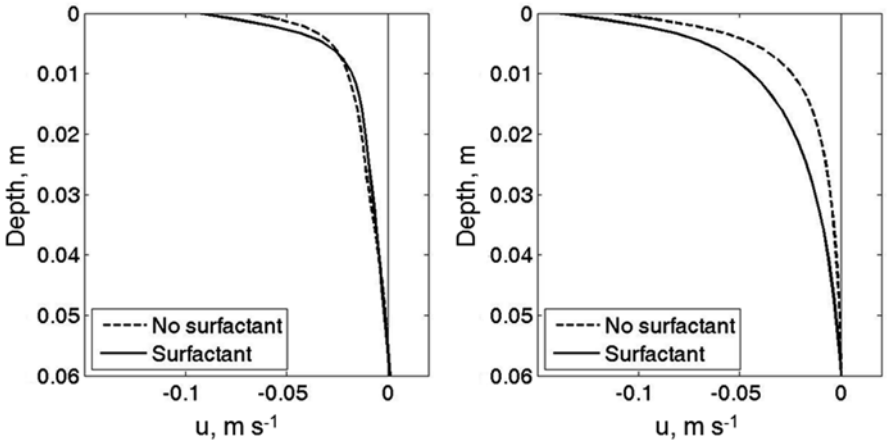

Fig. 2.17 Along tank velocity (u) referenced to $z = -0.06$ m (CFD model). (left) Large eddy simulation wall-adaptive local eddy viscosity model (LES-WALE), (right) detached eddy simulation (DES) model with realizable k-ε. Note increase of the surface drift velocity in the presence of surfactant. (After Soloviev et al. (2011) by permission of Kyoto University Press)

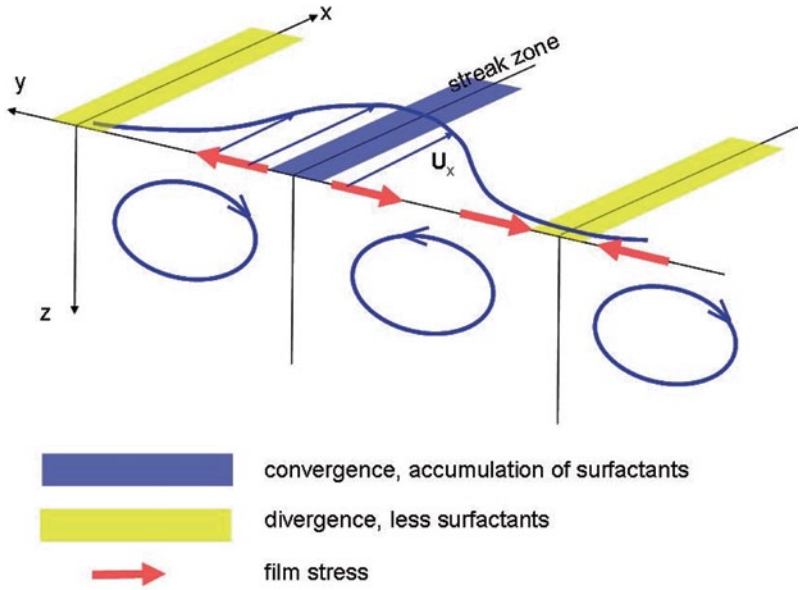

Fig. 2.18 Schematic representation of the effect of surfactants on near-surface circulation. (After Soloviev et al. (2011) by permission of Kyoto University Press)

During nighttime (Fig. 2.19), the temperature difference across the cool skin increased approximately by a factor of 2 in the presence of surfactant. During daytime, under conditions of strong solar radiation and light winds (Fig. 2.18), the presence of surfactants resulted in an increase in the temperature difference across the warm skin by approximately 25 %.

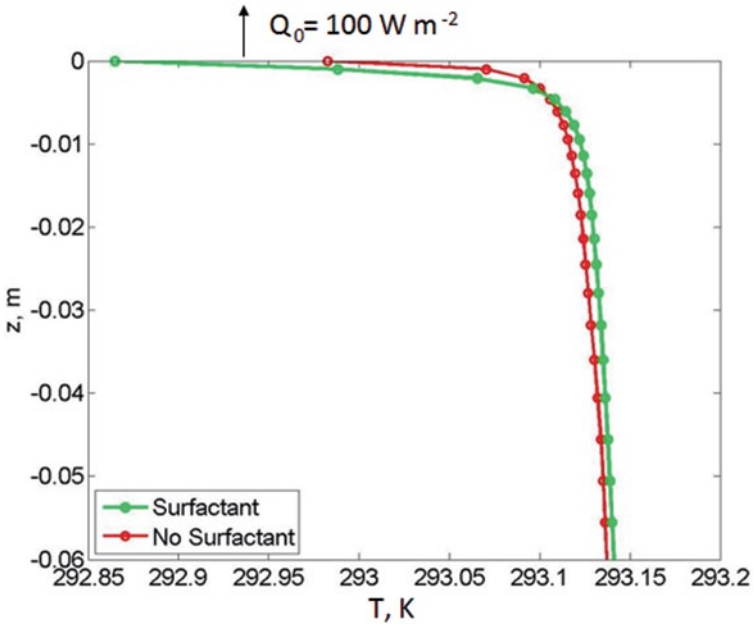

Fig. 2.19 Effect of surfactants on SST during nighttime calculated with CFD model at U_{10} = 4 ms^{-1}. Due to effect of surfactants, temperature difference across the cool skin ΔT changed from −0.15 K to −0.3 K. (After Soloviev et al. 2012)

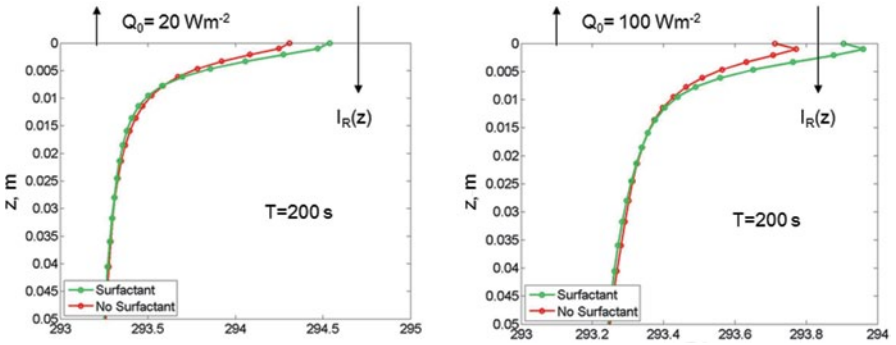

Fig. 2.20 Effect of surfactants on SST during daytime calculated with CFD Model at U_{10}= 1 ms^{-1}, $I_R(0)$ = 1200 Wm^{-2}. Under strong solar irradiance, "cool skin" turns into a "warm skin". (After Soloviev et al. 2012)

The effect of surfactants on SST may be comparable to the global change of SST during the last 30 years, when the satellite technology was introduced in the SST measurement.

The removal of surface films by convection, rain, near-surface shear, and breaking waves affects hydrodynamic processes at the air–sea interface, especially the capillary wave field, which substantially determines the surface roughness and thus air–sea exchanges. This process has a dual effect on the gravity-capillary wave field: It damps waves due to increased turbulence, and it enhances waves due to fragmentation and dissipation of surface films.

The lack of in situ measurements of the viscoelastic properties of films under various ocean regimes and particularly under different forcing conditions, limits the direct estimates of the global surface film effects on air–sea exchange. There are, however, indications that this uncertainty can be largely reduced if the mean square wave slope due to capillary-gravity waves is used rather than wind speed (Frew 1997). Glazman and Greysuku (1993) demonstrated the correlation between the surface wind stress and the sea surface roughness associated with capillary-gravity waves detected by backscattering from altimeters. This means that surface films may have less effect on the air–sea exchange parameterizations that are derived in terms of the mean square wave slope or friction velocity rather than in terms of the wind speed.

2.4 Parameterization of Molecular Sublayers During Nighttime Conditions

Conceptual models of the aqueous molecular sublayers can be divided into two classes: surface renewal models and boundary-layer models. In renewal models, the properties of molecular sublayers depend on the surface *renewal time*. The renewal time is then related to the environmental parameters causing hydrodynamic instabilities that control the properties of molecular sublayers. Boundary-layer models are based on the quasi-stationary representation of boundary-layer processes. We describe these modeling approaches in detail below. The effects of sea surface elasticity, however, have not yet been fully addressed in the parameterization of aqueous molecular sublayers.

2.4.1 Dimensional Analysis

Dimensional considerations can provide initial insight into the dynamics of aqueous molecular sublayers. Here, we ignore the bubble and droplet production in whitecaps and hence account for only interfacial (direct) heat, mass, and momentum transport. For the sake of simplicity, we also ignore here any explicit effects of surfactants (though, surfactant effects can enter the resulting parameterizations implicitly via modified empirical constants). In the case of steady meteorological and wave conditions, the following set of functional dependences can then be formulated:

$$\overline{\Delta u} = function(u_*, q_0, \alpha_T, g, \nu, \kappa_T, \sigma_w, \sigma_f, h) \tag{2.10}$$

$$\overline{\Delta T} = function(u_*, q_0, \alpha_T, g, \nu, \kappa_T, \sigma_w, \sigma_f, h) \tag{2.11}$$

$$K_\mu = function(u_*, q_0, \alpha_T, g, \nu, \mu, \kappa_T, \sigma_w, \sigma_f, h) \tag{2.12}$$

where $\Delta u = u_0 - u_b$ is the velocity difference across the aqueous viscous sublayer, u_b is the magnitude of the bulk (mixed layer) horizontal velocity, and u_0 is the magnitude of the sea surface velocity; $\Delta T = T_0 - T_b$ is the temperature difference across the cool skin, T_0 is the SST, and T_b is the temperature of the bulk (mixed layer); K_μ is the gas-transfer velocity defined by equation (1.50); $q_0 = Q_0 / (c_p \rho) = (Q_T + Q_E + I_L) / (c_p \rho)$ is the scaled net heat flux at the sea surface, Q_T is the sensible heat flux, I_L is the net longwave irradiance, Q_E is the latent heat flux; α_T is the coefficient of thermal expansion of water, g is the acceleration due to gravity, ρ is the water density, ν is the kinematic molecular viscosity, κ_T is the thermal molecular conductivity, σ_w is the surface tension of pure water, σ_s is the surface tension of water covered with film, $\sigma_f = \sigma_w - \sigma_s$ is the film pressure, μ is the coefficient of molecular gas diffusion; and h is the depth of the upper ocean mixed layer.

Since transport across molecular sublayers is intermittent, functional dependences in (2.10)–(2.12) are formulated for ensemble-averaged parameters. These relationships take into account the influence of thermally driven convection, wind-induced turbulence, and surface gravity and gravity-capillary waves on molecular sublayers. The effects of precipitation, solar radiation, and surfactants are ignored here but considered elsewhere in this chapter.

Choosing friction velocity in water (u_*) instead of wind speed reduces the uncertainty caused by surfactants (see discussion at the end of the previous section). The functional connection between the sea surface roughness associated with capillary-gravity waves and the wind stress ($\tau_0 = \rho u_*^2$) also simplifies the application of observational and theoretical results to remote sensing applications. Unfortunately, the replacement of wind speed with friction velocity does not solve the problem of surfactants completely, because the experimental friction velocities are often determined from wind-speed measurements and a bulk flux algorithm, normally ignoring any surfactant effects.

A standard dimensional analysis of functional dependences (2.10)–(2.12) leads to the following dimensionless relations:

$$\Delta \overline{u} / u_* = f_u(Rf_0, Ke, R_w, P_f, \mathrm{Pr}, Ra_h), \tag{2.13}$$

$$\Delta \overline{T} / T_* = f_T(Rf_0, Ke, R_w, P_f, \mathrm{Pr}, Ra_h), \tag{2.14}$$

$$K_\mu / u_* = f_C(Rf_0, Ke, R_w, P_f, \mathrm{Pr}, Sc, Ra_h), \tag{2.15}$$

where $T_* = q_0 / u_*$; f_u, f_T, and f_C are nondimensional functions of their nondimensional arguments; $\mathrm{Pr} = \nu / \kappa_T$ is the Prandtl number, $Sc = \nu / \mu$, $Ra_h = -\alpha_T g q_0 h^4 / (\nu \kappa_T{}^2)$, $Rf_0 = \alpha_T g q_0 \nu / u_*^4$, $Ke = u_*^3 / (g\nu)$, $R_w = u_* / \left(g\sigma_s / \rho\right)^{1/4}$, and $P_f = u_*{}^4 / \left[g(\sigma_w - \sigma_s)/\rho\right]^{1/4}$ (we identify the last four numbers a little bit later in this section).

In the upper ocean the Rayleigh number Ra_h is usually very large. It is well known that in a fully developed turbulent flow, parameters of a molecular boundary layer no longer explicitly depend upon the external scale of the flow. It has been customary in such cases to hypothesize self-similarity for the Ra_h number; this dimensionless number respectively drops out of the number of determining parameters. Dimensionless relationships (2.13)–(2.15) reduce to

$$\Delta\bar{u} / u_* = F_u(Rf_0, Ke, R_w, P_f, \mathrm{Pr}), \tag{2.16}$$

$$\Delta\bar{T} / T_* = F_T(Rf_0, Ke, R_w, P_f, \mathrm{Pr}), \tag{2.17}$$

$$K_\mu / u_* = F_C(Rf_0, Ke, R_w, P_f, \mathrm{Pr}, Sc), \tag{2.18}$$

where F_u, F_T, and F_C are the universal functions of nondimensional arguments Rf_0, Ke, Pr, R_w, P_f, and Sc (in case of the gas-transfer velocity only).

Parameters Sc and Pr entering (2.16)–(2.18) are the Schmidt and Prandtl numbers, respectively, which are well known from the classical boundary-layer theory. Four other dimensionless numbers, Rf_0, Ke, R_s, and P_f are less known but are also important for the physics of aqueous molecular sublayers at the air–sea interface.

The parameter Rf_0 proposed by Kudryavtsev and Soloviev (1985) determines the transition from convective to shear instability of aqueous molecular sublayers. From the definition of the flux Richardson number in the near-surface layer of the ocean $Rf = \alpha_T g q_0 \rho / \left(\tau_{xz}\partial u/\partial z + \tau_{yz}\partial v/\partial z\right)$ and from the expression for the momentum flux within the viscous sublayer $\tau_{xz} = \tau_{x0} = \rho\nu\partial u/\partial z$ and $\tau_{yz} = \tau_{y0} = \rho\nu\partial v/\partial z$ (also using relation $\tau_0 = \rho u_*^2 = \left(\tau_{x0}^2 + \tau_{y0}^2\right)^{1/2}$), the following expression for the flux Richardson number in the viscous sublayer follows:

$$Rf\Big|_{-z<\delta_\nu} = \alpha_T g q_0 \nu / u_*^4 = Rf_0, \tag{2.19}$$

where δ_ν is the thickness of the viscous sublayer. Since Rf_0 appears to be the surface asymptote of Rf, Kudrayvtsev and Soloviev (1985) named this parameter the *surface Richardson number*. For convectively unstable conditions Rf_0 is negative because $\alpha_T q_0 < 0$.

The parameter $Ke = u_* / (g\nu)$ determines the transition to whitecapping at the air–sea interface. Csanady (1990) named this parameter the *Keulegan number*. As emphasized in Sect. 2.3.3, it is a fundamental parameter in the dynamics of free interfaces.

The effect of surface tension on aqueous molecular sublayers is associated with two nondimensional numbers, $R_w = \rho u_*^4 / (g\sigma_w)$ and $P_f = g(\sigma_w - \sigma_s)/(\rho u_*^4)$. The R_w number is assumed to be a determining parameter in direct disruption of the air–sea interface under very strong wind-speed conditions (and possibly in the process of microscale wave breaking under moderate wind-speed conditions). This number is linked to the *Koga number* as follows $R_w = (\rho/\rho_a)^2 Ko^4$. Note that the Koga number, *Ko*, introduced by Soloviev and Lukas (2010) is a characteristic of the Kelvin–Helmholtz (KH) instability at the air–water interface (see Sect. 6.3.4). The dimensionless number P_f is related to the effect of surfactants.

Specification of dependences (2.16)–(2.18) via Rf_0, *Ke*, *Pr*, and *Sc* is now possible within the framework of the physical models considered in the next sections. To our best knowledge, no explicit dependence on R_w and P_f has ever been included in the parameterization of aqueous molecular sublayers. Reasonable assumptions are that P_f is important for low winds only, while R_w is essential for hurricane conditions predominately.

2.4.2 Renewal Model

The renewal concept follows from the idea of intermittent transport of properties across molecular sublayers. Kim et al. (1971) found that the turbulent momentum transport and production in a wall layer take place intermittently in time and space through small-scale bursting motions.

The renewal model developed by Liu and Businger (1975) is based on the Kim et al. (1971) result and considers intermittent transport of properties across molecular sublayers. Liu and Businger (1975) developed a method for calculation of average temperature profiles in molecular sublayers by assuming that the sublayers undergo cyclic growth and subsequent destruction. Kudryavtsev and Soloviev (1985) parameterized the transition from free to forced convection in the cool skin using the surface Richardson number Rf_0 as the determining parameter. Soloviev and Schluessel (1994) incorporated a Keulegan number (*Ke*) dependence for high wind-speed conditions and developed a coupled parameterization for the temperature difference across the cool skin of the ocean and the air–sea gas-transfer velocity.

Further developing the surface renewal model and following Liu and Businger (1975), Soloviev and Schlüssel (1994) and Soloviev (2007), considered a fluid element adjacent to the sea surface. Initially, it had a uniform velocity u_w, temperature T_w, and the concentration of scalar property C_w equal to the corresponding bulk-water value. As the fluid element is exposed to the interface, the appropriate molecular diffusion laws (1.6), (1.10), and (1.12) govern the velocity (Δu) and temperature (ΔT) differences, and the interfacial gas flux (G_o). Under assumption of horizontal homogeneity, no insolation, and no rain, one-dimensional molecular diffusion laws are as follows:

$$\frac{\partial u}{\partial t} = \frac{\partial}{\partial z}\left(\nu \frac{\partial u}{\partial z}\right), \tag{2.20}$$

$$\frac{\partial T}{\partial t} = \frac{\partial}{\partial z}\left(\kappa_T \frac{\partial T}{\partial z}\right), \tag{2.21}$$

$$\frac{\partial C}{\partial t} = \frac{\partial}{\partial z}\left(\mu \frac{\partial C}{\partial z}\right). \tag{2.22}$$

The classic error-function integral solutions of equations (2.20)–(2.22) result in the following dependences:

$$\Delta u(t) = 2\pi^{-1/2}(t/\nu)^{1/2}\tau_t/\rho, \tag{2.23}$$

$$\Delta T(t) = -2\pi^{-1/2}(t/\nu)^{1/2} q_0, \tag{2.24}$$

$$G_0(t) = \pi^{-1/2}(t/\mu)^{-1/2}\Delta C, \tag{2.25}$$

where $\Delta u(t) = u_0(t) - u_w$, $\Delta T(t) = T_0(t) - T_w$, t is the elapsed time, vertical coordinate z is related to the instantaneous position of the sea surface (uncertain during wave-breaking events), and π=3.14. Note that in (2.23)–(2.24) the evolutions of the velocity and temperature differences are considered under conditions of constant tangential stress τ_t and scaled heat flux q_0, respectively, while in (2.25) the gas flux evolution is considered under conditions of constant gas concentration difference across the diffusion sublayer, $\Delta C = C_w - C_0$, which is assumed to be close to effective air–sea concentration difference.

Wind-induced surface current constitutes only a tiny part of the total velocity difference between air and sea (about 2 %). The condition of constant momentum flux rather than constant velocity difference is therefore appropriate in (2.23). Waves are a volume source of momentum in the near-surface layer of the ocean; formally, they do not enter the surface boundary condition for velocity. We nevertheless neglect here the second-order effect relating to the modification of the gravity-capillary waves and, thereby, the surface roughness and momentum fluxes by surface drift current. This secondary effect, however, may become of primary importance under conditions of very high wind speed (see Chap. 6).

The dependence of the net longwave irradiance I_L and latent heat flux Q_E on the temperature difference due to the cool skin is typically within several percent (Paulson and Simpson 1981). Only Q_T may depend appreciably on the cool-skin presence. Usually $|I_L + Q_E| >> |Q_T|$, which means that the net surface flux, q_0, does not depend strongly on the cool-skin presence. As a result, the condition of constant heat flux is justified for deriving dependence (2.24). Solar radiation is a volume

source of heat for the near-surface layer of the ocean and does not enter the surface boundary condition.

The condition of constant concentration difference accepted in (2.25) follows from the fact that the aqueous diffusion sublayer provides the main resistance to the gas transfer (Bolin 1960) and thereby contains the main gas concentration difference across the air–sea interface.

The average velocity and temperature difference across the aqueous viscous and thermal sublayers and the average surface gas flux at the air–sea interface can be defined as follows:

$$\overline{\Delta u} = \int_0^\infty p(t) t^{-1} \left(\int_0^t \Delta u(t') dt' \right) dt \tag{2.26}$$

$$\overline{\Delta T} = \int_0^\infty p(t) t^{-1} \left(\int_0^t \Delta T(t') dt' \right) dt \tag{2.27}$$

$$\overline{G_0} = \int_0^\infty p(t) t^{-1} \left(\int_0^t G_0(t') dt' \right) dt \tag{2.28}$$

where $p(t)$ is the probability density for time periods, t, of bursting motions in the molecular sublayers. This is the probability of local destruction of the molecular sublayers in a time interval $(t, t+dt)$, where t is the elapsed time since the previous destruction.

The experiments of Rao et al. (1971) on the structure of the boundary layer turbulence indicate that the time between bursts is distributed according to a lognormal law. The probability density for such a process is given by

$$p(t) = \pi^{-1/2} (\sigma t)^{-1} \exp\left[-(\ln t - m)^2 / \sigma^2 \right], \; t > 0, \tag{2.29}$$

where m is the mean value and σ^2 is the variance for the logarithm of the random variable t. Garbe et al. (2002) found the lognormal distribution (2.29) as being in good agreement with the histogram of time intervals between two successive renewal events derived from infrared images in a laboratory tank (Fig. 2.21).

Inserting (2.29) into relationships (2.26)–(2.28), we obtain

$$\overline{\Delta u} = (4\pi^{-1/2} / 3) \exp(-\sigma^{2/16}) (t_* / \nu)^{1/2} \tau_t, \tag{2.30}$$

$$\overline{\Delta T} = -(4\pi^{-1/2} / 3) \exp(-\sigma^{2/16}) (t_* / \kappa_T)^{1/2} q_0, \tag{2.31}$$

$$K_\mu = 2\pi^{-1/2} \exp(3\sigma^2 / 16) (t_* / \mu)^{-1/2}, \tag{2.32}$$

where K_μ is the gas-transfer velocity (the piston velocity) defined by equation (1.44), and $t_* = \exp(m + \sigma^2 / 4)$ is the average time between bursts, which has been

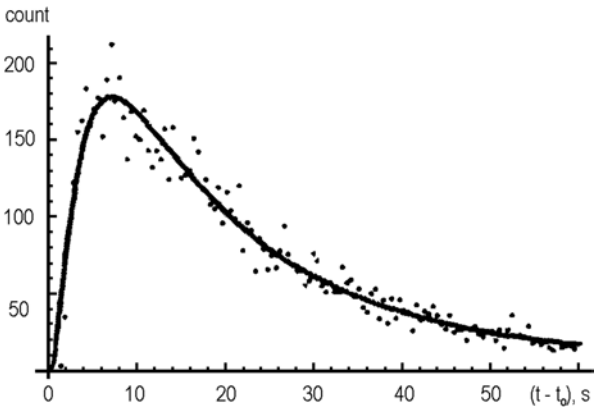

Fig. 2.21 Lognormal distribution (2.29) fitted to the histogram of the time between two consecutive surface renewal events $t - t_0$ for a wind speed of 2 m s^{-1}. (After Garbe et al. 2002. Reproduced by permission of American Geophysical Union)

referred to as the renewal time. Since the bursting events have significant energy, we assume that they affect the viscous, thermal, and diffusion molecular sublayers in the same manner, and the quantity σ^2 in (2.30)–(2.32) is the same.

Soloviev and Schlüssel (1994) considered three wind-speed regimes:

1. Calm and low wind-speed conditions: The cyclic injection of fluid from the molecular sublayers is of convective nature. The time period of the convective bursts is defined by Foster (1971) as follows:

$$t_c = a_c(-\nu / \alpha_T g q_0)^{1/2}, \tag{2.33}$$

where a_c is a dimensionless coefficient.

2. Intermediate wind-speed conditions: According to Csanady (1990), the most intense surface renewal on a wind-blown surface is caused by viscous surface-stress variations associated with rollers on breaking wavelets. The time period of these variations is defined as

$$t_r = a_r \nu / u_*^2, \tag{2.34}$$

where a_r is a dimensionless constant.

3. High wind-speed conditions: Surface waves take most of the wind stress and the development of rollers is less probable. The surface renewal due to waves breaking and whitecapping dominates. For fully developed wind waves, the timescale of the surface renewal depends on the parameters u_* and g. A dimensional analysis leads to the following relation:

$$t_w = a_w u_*^2 / g, \tag{2.35}$$

where a_w is a dimensionless constant.

The surface Richardson number (Rf_0) controls the transition from free convection (regime 1) to rollers (regime 2) at the air–sea interface, while the Keulegan number (Ke) controls the transition from rollers (regime 2) to wave breaking (regime 3). Combining (2.33), (2.34), and (2.35), the renewal (or exposure) time can then be expressed as follows:

$$t_* = \begin{cases} a_c \left[\nu / (-\alpha_T g q_0)^{1/2} \right] \text{ at } 0 \le u_* \le (\alpha_T g q_0 \nu / Rf_{cr})^{1/4} \\ a_r \nu / u_*^2 \quad \text{at } (\alpha_T g q_0 \nu / Rf_{cr})^{1/4} \le u_* \le (Ke_{cr} \nu g)^{1/3} \\ a_w u_* / g \quad \text{at } u_* \ge (Ke_{cr} \nu g)^{1/3} \end{cases} \tag{2.36}$$

where Rf_{cr} and Ke_{cr} are the critical values of the surface Richardson number and the Keulegan number, respectively. In dimensionless form, formula (2.36) is as follows:

$$t_* / (a_r \nu / u_*^2) = \begin{cases} (Rf_0 / Rf_{cr})^{-1/2} \text{ at } Rf_0 / Rf_{cr} \ge 1 \\ 1 \text{ at } Rf_0 / Rf_{cr} \le 1 \text{ and } Ke / Ke_{cr} \le 1 \\ Ke / Ke_{cr} \text{ at } Ke / Ke_{cr} \ge 1 \end{cases} \tag{2.37}$$

where $Rf_{cr} = -(a_c / a_r)^2$ and $Ke_{cr} = a_r / a_w$.

Formula (2.37) can be approximated in the following way:

$$t_* / (a_r \nu / u_*^2) = (1 + Rf_0 / Rf_{cr})^{-1/2} (1 + Ke / Ke_{cr}), \tag{2.38}$$

which is a sufficiently accurate and convenient analytical expression. An interpretation of the Ke-number dependence in (2.38) is that under high wind-speed conditions the tangential stress τ_t relates to the total wind stress τ_0 according to (2.8).

Inserting the renewal time (2.38) into (2.30)–(2.32) and taking into account (2.8) and the definition of the friction velocity $u_* = (\tau_0 / \rho)^{1/2}$ leads to the following coupled set of parametric relationships:

$$\overline{\Delta u} / u_* = \Lambda_0 (1 + Rf_0 / Rf_{cr})^{-1/4}, \tag{2.39}$$

$$\overline{\Delta T} / T_* = -\Lambda_0 \, \mathrm{Pr}^{1/2} (1 + Rf_0 / Rf_{cr})^{-1/4} (1 + Ke / Ke_{cr})^{1/2}, \tag{2.40}$$

$$K_\mu / u_* = A_0 \Lambda_0^{-1} Sc^{-1/2} (1 + Rf_0 / Rf_{cr})^{1/4} (1 + Ke / Ke_{cr})^{-1/2}, \tag{2.41}$$

where $T_* = q_0 / u_*$, $\mathrm{Pr} = \nu / k$, and $Sc = \nu / \mu$. The dimensionless coefficients A_0 and Λ_0 are expressed through the parameter of lognormal distribution (2.29) as follows:

$$A_0 = \left(8\pi^{-1} / 3\right) \exp\left(\sigma^2 / 8\right), \tag{2.42}$$

Table 2.1 Parameter σ in (2.29) from the results of Garbe et al. (2002) and the computation of coefficient A_0 from equation (2.42)

Wind speed, m s^{-1}	2.0	4.2	8.0
σ	1.39	0.8	0.7
A_0	1.08	0.92	0.89

$$\Lambda_0 = \left(4\pi^{-1/2}/3\right)\exp\left(-\sigma^2/16\right)a_r^{1/2}. \tag{2.43}$$

The calculation of A_0 with σ determined from the Garbe et al. (2002) laboratory experiment is presented in Table 2.1.

For low wind-speed conditions, $Rf_0 \to \infty$ and $Ke \to 0$; equations (2.39)–(2.41) have the following asymptotes:

$$\overline{\Delta u} \approx \Lambda_0 u_* \left(\frac{Rf_0}{Rf_{cr}}\right)^{-1/4} = \Lambda_0 u_*^2 \left(\frac{Rf_{cr}}{\alpha_T g q_0 \nu}\right)^{1/4}, \tag{2.44}$$

$$\Delta T \approx -\Lambda_0 \,\mathrm{Pr}^{1/2} \left(\frac{Rf_0}{Rf_{cr}}\right)^{-1/4} \frac{q_0}{u_*} = -\Lambda_0 \,\mathrm{Pr}^{1/2} \left(\frac{Rf_{cr}}{\alpha_T g \nu q_0}\right)^{1/4} q_0, \tag{2.45}$$

$$K_\mu \approx A_0 \Lambda_0^{-1} Sc^{-1/2} u_* \left(\frac{Rf_0}{Rf_{cr}}\right)^{1/4} = A_0 \Lambda_0^{-1} Sc^{-1/2} \left(\frac{\alpha_T g \nu q_0}{Rf_{cr}}\right)^{1/4}. \tag{2.46}$$

Remarkably, formula (2.45) is similar to that of Katsaros et al. (1977),

$$\overline{\Delta T} = a_0^{-3/4} \left(\frac{\nu}{-\alpha_T g \kappa_T^2}\right)^{1/4} q_0^{3/4}, \tag{2.47}$$

obtained for calm weather conditions; the appropriate nondimensional coefficients are interrelated by

$$a_0 = \Lambda_0^{-4/3} \left(-Rf_{cr}\right)^{-1/3}. \tag{2.48}$$

For moderate wind-speed conditions, which is an intermediate asymptotic $|Rf_0| << |Rf_{cr}|$ and $Ke << Ke_{cr}$, parameterizations (2.39)–(2.41) reduce to

$$\overline{\Delta u} = \Lambda_0 u_*, \tag{2.49}$$

$$\overline{\Delta T} \approx -\Lambda_0 \,\mathrm{Pr}^{1/2} T_* = -\Lambda_0 \,\mathrm{Pr}^{1/2} q_0 / u_*, \tag{2.50}$$

$$K_\mu = A_0 \Lambda_0^{-1} Sc^{-1/2} u_*. \tag{2.51}$$

There is presumably no direct analog of (2.49) in the literature. Formula (2.50) has an analog previously derived by Saunders (1967b)

$$\overline{\Delta T} = -\lambda_S \, \mathrm{Pr} \, q_0 / u_*, \tag{2.52}$$

while the formula similar to (2.51),

$$K_\mu = \gamma_0 Sc^{-1/2} u_*, \tag{2.53}$$

can be found in several previous publications on air–sea gas exchange. The dimensionless coefficients entering (2.50) and (2.52) are interrelated by $\lambda_S = \Lambda_0 \, \mathrm{Pr}^{-1/2}$ and $\gamma_0 = A_0 \Lambda_0^{-1}$.

For high wind-speed conditions, equations (2.39)–(2.41) have asymptotes $|Rf_0| << |Rf_{cr}|$ and $Ke >> Ke_{cr}$, which lead to:

$$\overline{\Delta u} = \Lambda_0 u_*, \tag{2.54}$$

$$\overline{\Delta T} \approx -\Lambda_0 \, \mathrm{Pr}^{1/2} T_* (Ke / Ke_{cr})^{1/2} = -\Lambda_0 \, \mathrm{Pr}^{1/2} (\nu g Ke_{cr})^{-1/2} q_0 u_*^{1/2}, \tag{2.55}$$

$$K_\mu \approx A_0 \Lambda_0^{-1} Sc^{-1/2} u_* (Ke / Ke_{cr})^{-1/2} = A_0 \Lambda_0^{-1} Sc^{-1/2} (\nu g Ke_{cr})^{1/2} u_*^{-1/2}, \tag{2.56}$$

Same as for (2.49), no direct analog to (2.54) could be found in literature. Parameterization for the velocity difference across the aqueous viscous sublayer is closely related to the problem of determining the wind-drift coefficient; related issues are considered elsewhere in this section. High wind-speed parameterizations for the temperature difference across the cool skin and the gas-transfer velocity (2.55) and (2.56) were previously derived by Soloviev and Schlüssel (1994). Note that in this chapter we do not consider hurricane conditions and respectively assume any explicit dependence on R_w.

Active breaking events (whitecaps) occupy a relatively small area of the sea surface. In the process of wave breaking, molecular sublayers are destroyed, however they are restored in between wave-breaking events. In accordance with (2.8), a reduced fraction of the momentum flux transfers to tangential stress at higher wind speeds. As a result, the velocity difference is maintained proportional to the friction velocity (2.54). The temperature difference across the cool skin slightly increases with wind speed (2.55), while the interfacial gas-transfer velocity slightly decreases. Equations (2.54)–(2.56), however, do not include two important effects associated with wave breaking: 1) The residual turbulence after wave breaking maintains for several wave periods, affecting the molecular sublayers; 2) bubble production in whitecaps can substantially affect the air–sea gas exchange. The effect of the

residual wave-breaking turbulence on the interfacial gas transport (as well as the inclusion of the bubble-mediated gas transport) is discussed in Chap. 7 of this book.

Bubble-mediated heat transport is apparently negligible in comparison with the direct flux at the ocean–air interface, due to the low heat capacity of air inside the bubbles. In contrast, droplet and spray production by breaking waves is an important mechanism of the air–ocean heat and mass transport at wind speeds greater than about 15–17 m s^{-1} (Chap. 6).

Substituting (2.48) into (2.39)–(2.41), we obtain a coupled set of parameterizations:

$$\Delta\overline{u} / u_* = \Lambda_0 (1 - a_0{}^3 \Lambda_0^4 Rf_0)^{-1/4} \tag{2.57}$$

$$\Delta\overline{T} / T_* = -\Lambda_0 \,\mathrm{Pr}^{1/2} (1 - a_0{}^3 \Lambda_0^4 Rf_0)^{-1/4} (1 + Ke / Ke_{cr})^{1/2} \tag{2.58}$$

$$K_\mu / u_* = A_0 \Lambda_0^{-1} Sc^{-1/2} (1 - a_0{}^3 \Lambda_0^3 Rf_0)^{1/4} (1 + Ke / Ke_{cr})^{-1/2} \tag{2.59}$$

Replacing the surface cooling $Q_0 = Q_E + Q_T + I_L$ with the *virtual cooling*, which includes the buoyancy effects of salinity due to evaporation

$$Q_v = Q_E + Q_T + I_L + \frac{S_0 \beta_S c_p}{\alpha_T L} Q_E, \tag{2.60}$$

the expression for the surface Richardson number transforms in the following way:

$$Rf_0 = \frac{\alpha_T g \nu}{c_p \rho u_*^4} \left(Q_E + Q_T + I_L + \frac{\beta_S S_0 c_p}{\alpha_T L} Q_E \right). \tag{2.61}$$

Coefficients Λ_0, a_0, Ke_{cr}, and A_0 are now to be determined from the comparison with experimental data.

From the comparison with Grassl's (1976) data, which represented a relatively small number of field observations, Kudrayvtsev and Soloviev (1985) derived tentative estimates of the two constants $\Lambda_0 \approx 13.3$ and $Rf_{cr} \approx -1.5 \cdot 10^{-4}$, treating them as independent constants. From relationship (2.48) it then follows that $a_0 \approx 0.6$, which is much bigger than the commonly accepted estimate $a_0 = 0.25$ (Fedorov and Ginzburg 1988).

Since the publication of the Kudryavtsev and Soloviev (1985) work, new laboratory data sets on the surface wind-drift current using particle image velocimetry and infrared imaging have been obtained, which allow us to specify more accurately numerical constant Λ_0. Formulation (2.57)–(2.59) including constants Λ_0 and a_0 is more convenient than formulation (2.39)–(2.41) including constants Λ_0 and Rf_{cr}, because it is believed that, in contrast to Rf_{cr}, the numerical value of a_0 can be determined with an acceptable accuracy from laboratory experiments. A complication

is that a_0 depends on the presence of surfactants, which is characterized by the P_f number. The exact functional dependence, however, is not known.

It is also remarkable that according to (2.57) the dimensionless ratio $\overline{\Delta u}/u_*$ does not depend on the Keulegan number, which means that constant Λ_0 can be estimated from the experimental data on the surface wind-drift current. According to (2.49) and (2.54), for intermediate and high wind-speed conditions $\Lambda_0 = \overline{\Delta u}/u_*$. We assume that there is no explicit dependence of Λ_0 on R_w, since we do not consider in this analysis hurricane force winds.

The ratio, $\overline{\Delta u}/u_*$, is closely related to the *wind-drift coefficient*, u_0/U_{10}, where u_0 is the averaged current velocity at the sea surface (relative to the background ocean current), and U_{10} is the wind speed at 10 m height. The current velocity at the sea surface includes the Stokes drift as well, which provides a relatively small (between 5 and 20 %) contribution to the wind-drift coefficient however. The difference between the current velocity at the sea surface u_0 and the Stokes surface drift u_S is the wind-induced surface drift:

$$u_{wd} = u_0 - u_S. \tag{2.62}$$

The ratio between the wind-induced surface drift u_{wd} and the water friction velocity u_* as measured by Wu (1975) varied between 11 and 20. Wu (1975) concluded that $\langle u_{wd}/u_* \rangle \approx 17.0$ and has no obvious systematic dependence upon friction velocity. Phillips and Banner (1974) laboratory experiment indicated that $\langle u_{wd}/u_* \rangle \approx 16.1$.

Values of u_{wd}/u_* derived from particle image velocimetry and from infrared imaging also demonstrate no obvious dependence on the friction velocity but consistently indicate smaller surface drift currents than those derived from drifter measurements (Zhang and Harrison 2004). The wind-induced velocities derived from the infrared images are shown in Fig. 2.22. Averaging over all friction velocities results in $\langle u_{wd}/u_* \rangle \approx 7.4$. Based on these laboratory results we accept an estimate $\Lambda_0 \approx 7.4$. This is in fact an upper estimate, because it does not take into account the existence of relatively small current velocity difference across the turbulent layer (i.e., below the viscous sublayer).

A fit of parameterization (2.57) to the results of the Zhang and Harrison (2004) is shown in Fig. 2.22. In (2.57) the term $(1 - a_0^3 \Lambda_0^4 R f_0)^{-1/4}$ relating to buoyancy effects is of importance under low wind-speed conditions. Figure 2.22 therefore shows parameterization (2.39) for two values of the net surface heat flux Q_0.

A tentative estimate of $Ke_{cr} \approx 0.18$ was derived by Soloviev and Schlüssel (1994) from indirect data—the critical wind speed, $U_{10} \approx 10$ m s^{-1}, at which, according to the visual Beaufort scale, longwave breaking sets in. Later, Zhao and Toba (2001) proposed a parameter $R_B = u_{*a}^2/(\nu_a \omega_p)$ with a critical value of $R_B = 10^3$ for the onset of wind–wave breaking. Parameter R_B can be rewritten as

$$R_B = A_w u_{*a}^3/(g\nu_a) \tag{2.63}$$

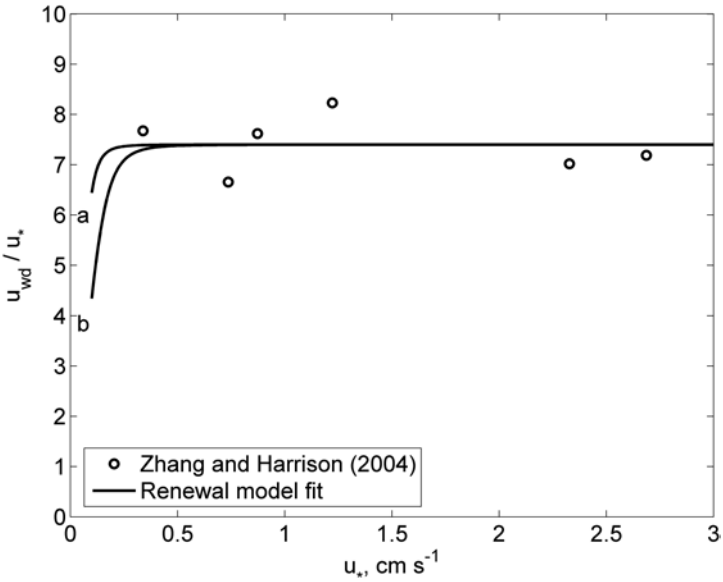

Fig. 2.22 Non-dimensional wind-induced surface current in the laboratory tank for different wind friction velocities and in comparison with the renewal model (2.57) at $a = 0.25$ and $\Lambda_0 = 7.4$, calculated for two surface cooling rates: **a** $Q_0 = 20$ W m^{-2}, and **b** $Q_0 = 200$ W m^{-2}

where A_w is the wave age defined as $A_w = g / \left(\omega_p u_{*a}\right) = c_p / u_{*a}$. The Keulegan number appears to be connected to the Zhao and Toba (2001) nondimensional parameter R_B as follows:

$$Ke = \frac{u_*^3}{g\nu} = \frac{u_{*a}^3}{g\nu_a}\frac{\nu_a}{\nu}\left(\frac{\rho_a}{\rho}\right)^{3/2}\frac{1}{A_w} = R_B\frac{\nu_a}{\nu}\left(\frac{\rho_a}{\rho}\right)^{3/2}\frac{1}{A_w}. \tag{2.64}$$

From (2.64), it follows that critical value $R_B = 10^3$ corresponds to $Ke_{cr} = 0.18$ at $A_w = 3.25$.

During TOGA COARE, Hartmut Grassl collected substantial statistics on the temperature difference across the cool skin in the western equatorial Pacific. Figure 2.23 shows parameterization (2.58) plotted for $a_0 = 0.25$, $\Lambda_0 \approx 7.4$, and wave $A_w = 15$ in comparison with the TOGA COARE data set collected during nighttime. The wave age of $A_w = 15$ corresponds to developed wind waves, which are often observed in the open ocean. There is a reasonable agreement between the COARE data set and the renewal-type model.

Horrocks et al. (2002) collected a large data set on the cool skin in the western tropical and subtropical Pacific using a scanning infrared SST radiometer. Comparison of parameterization (2.56) with the Horrocks et al. (2006) data set has also shown a reasonable correlation (Soloviev et al. 2007).

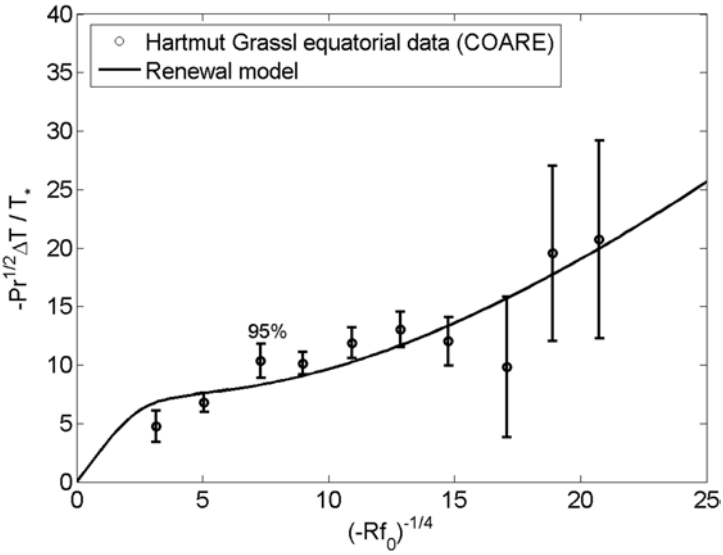

Fig. 2.23 Nighttime cool skin data of Hartmut Grassl obtained in the western equatorial Pacific during TOGA COARE in comparison with renewal model. (After Soloviev 2007 by permission of Elsevier)

Figure 2.24 compares results of direct, eddy-correlation measurements of the CO_2 air–sea flux during *GasEx-01* collected by Hare et al. (2004) with renewal model (2.59). According to Table 2.1, constant A_0 entering the gas-exchange parameterization is close to unity, varying within $\pm 10\%$ as a function of wind speed. For simplicity, we take $A_0 = 1$. The bubble-mediated contribution to the gas-transfer velocity for CO_2 according to the model of Woolf (1997) is shown in Fig. 2.24a. The resultant curve demonstrated in Fig. 2.24b suggests a good agreement between model and observations encouraging further exploration of the applicability of the renewal model for parameterization of the air–sea gas exchange.

Figure 2.25 shows a summary of gas-transfer results over the ocean. The theoretical dependencies correspond to the sum of an interfacial component (renewal model (2.57)) and Woolf's (1997) bubble-mediated component. Both theoretical relationships and field data are color-coded. Blue color indicates low-solubility gases (SF6 and 3He); red color indicates higher solubility gases (Rn and CO_2), and black color is reserved for a well soluble gas (DMS). Under high wind-speed conditions, theoretical curves for different gases diverge but appear to be consistent with the available data.

The renewal model also appears to be useful for parameterizing salinity difference in the aqueous haline diffusion sublayer at the air–sea interface (Fedorov and Ginzburg 1988). Zhang and Zhang (2012) estimated this difference to reach up to 0.3 psu in some regions of the ocean, though being localized in the upper 0.1–0.2 mm layer of the ocean.

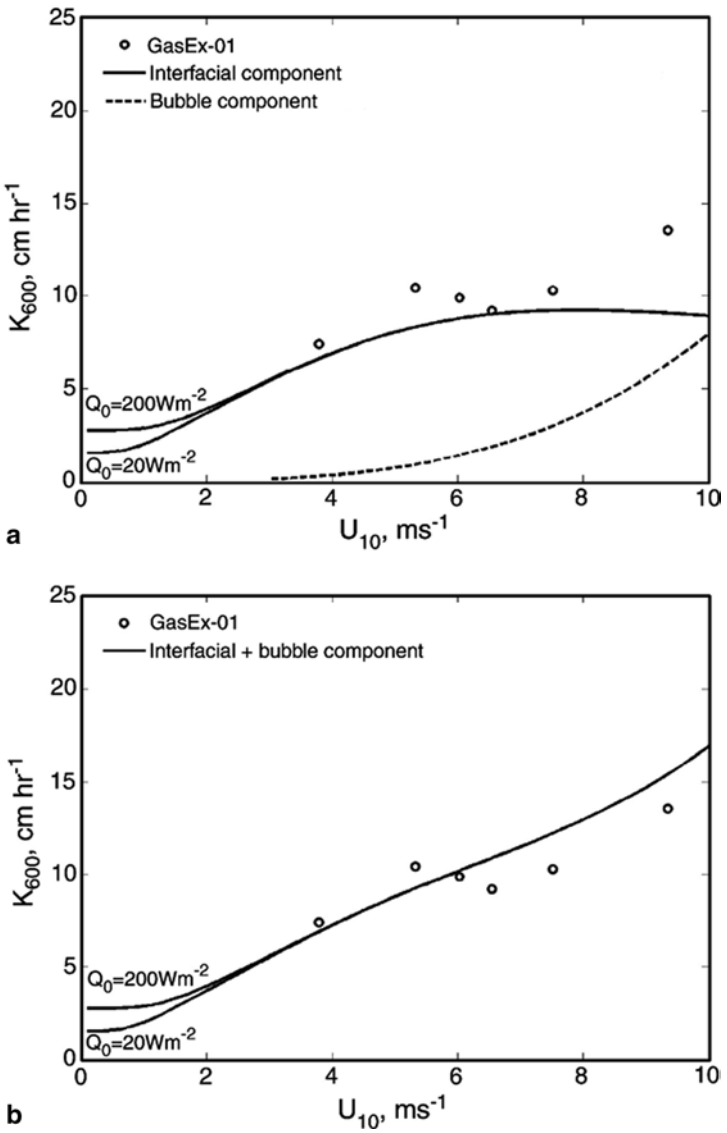

Fig. 2.24 **a** Comparison of the renewal type (interfacial) parameterization (20) for two values of the surface heat flux Q_0 with direct measurements of the CO_2 transfer velocity during GasEx-2001 (Hare et al. 2004). Woolf's (1997) parameterization of the bubble-mediated component is shown with a dashed line. **b** Sum of the interfacial and bubble mediated parameterizations in comparison with the GasEx-2001 data. (After Soloviev 2007 by permission of Elsevier)

2.4.3 Boundary-Layer Model

Though boundary-layer models operate with the averaged turbulent characteristics such as the dissipation rate ε (for instance, defining the viscous sublayer depth as

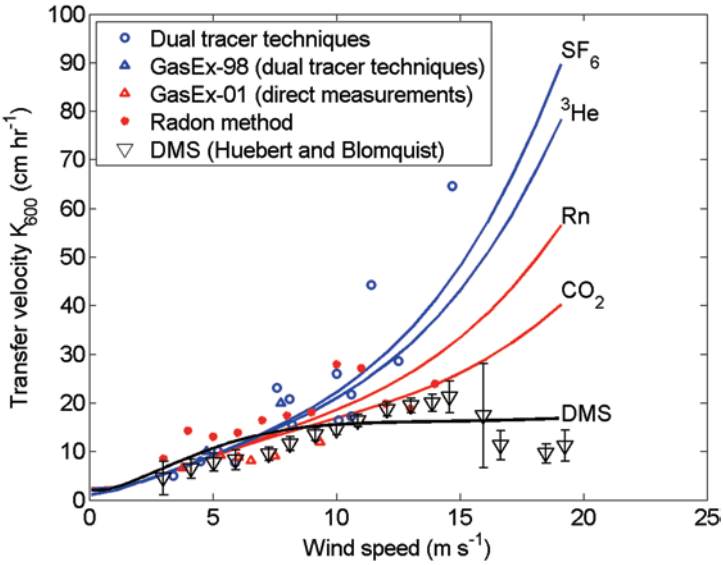

Fig. 2.25 Renewal gas-transfer parameterization in comparison with field data. The dual tracer data are from Wanninkhof et al. (1997), Asher and Wanninkhof (1998), and Nichtingale et al. (2000). The radon data are from Peng et al. (1974), Peng et al. (1979), and Cember (1985). The GasEx-98 data are from Wanninkhof and McGillis (1999), the GasEx-01 data are from Hare et al. (2004), DMS data are from Huebert et al. (2004). To illustrate the effect of surface heat flux and insolation on the air-sea gas exchange at low wind speed the model curves for all gases are calculated for $Q_0 = 130$ W m^{-2}, $Q_E = 60$ W m^{-2} and for two values of $I_R(0) = 0$ W m^{-2} and $I_R(0) = 1000$ W m^{-2}

proportional to Kolmogorov's internal scale of turbulence, $\eta_\nu = \left(\nu / \varepsilon^3\right)^{1/4}$), these models are consistent with the concept of intermittency of molecular sublayers in time and space through small-scale bursting motions (Kim et al. 1971).

Initial development of the boundary-layer model for molecular sublayers is usually attributed to Saunders (1967b) who, based on the wall layer analogy, derived a formula for the temperature difference across the cool skin in the form (2.52). Boundary-layer modeling has also been applied to the free convection problem for a cooling sea surface. A theoretical formula for convective heat transfer over a horizontal plate,

$$Nu = a_0 Ra^{1/3} \tag{2.65}$$

in application to the thermal molecular sublayer below the air–water interface leads to the Katsaros et al. (1977) formula for the temperature difference across the aqueous thermal sublayer (cool skin) (2.47). The Nusselt and Raleigh numbers are defined as follows:

$$Nu = \frac{q_0}{\kappa_T(\overline{\Delta T}/h)}, \; Ra = \frac{\alpha_T g \overline{\Delta T} h^3}{\kappa_T \nu}. \tag{2.66}$$

When the exponent on the Rayleigh number is 1/3, the equality (2.65) becomes independent of depth resulting in the Katsaros et al. (1977) equation (2.47).

Since both shear and convection contribute to the energy dissipation, the boundary-layer model describes the transition from free to forced convection in pretty much the same way as the renewal model. In particular, the same dimensionless number Rf_0 controls this transition. Correspondingly, Fairall et al. (1996) modified the Saunders (1967b) parameterization (2.52) as follows:

$$\overline{\Delta T} = -\lambda_S \,\mathrm{Pr}\, q_0 u_*^{-1}\left[1+\left(a_0^{\,3}\lambda_S^4 Rf_0\,\mathrm{Pr}^2\right)^{3/4}\right]^{-1/3}$$

where $Rf_0 = \alpha_T g Q_v \nu/(c_p \rho u_*^{\,4})$ is the surface Richardson number introduced by Kudryavtsev and Soloviev (1985) from modeling surface renewals, and Q_v is the virtual cooling given by (2.58). The model remains bounded as $u_* \to 0$ (asymptotically approaching Katsaros' formula (2.45) for free convection), which is an improvement over the original Saunders (1967b) formula (2.50).

Taking into account that $\Lambda_0 = \lambda_0 \,\mathrm{Pr}^{1/2}$, boundary-layer parameterization (2.66) practically coincides with parameterization (2.56) for low and moderate wind-speed conditions. Similar to the renewal model, the boundary-layer-type model can be extended to high wind-speed conditions including wave breaking and whitecapping. Such an extension is considered by Soloviev et al. (2007) for the example of air–sea gas-transfer modeling.

Kitaigorodskii and Donelan (1984) and Dickey et al. (1984) proposed a boundary-layer-type model for parameterizing the interfacial gas-transfer velocity:

$$K_{\mathrm{int}} \approx b\left[\varepsilon(0)\,\nu Sc^{-2}\right]^{1/4} \tag{2.67}$$

where b is a dimensionless coefficient, $\varepsilon(0)$ the surface value of the dissipation rate of the turbulent kinetic energy, ν is the kinematic viscosity of water, $Sc = \nu/\mu$ is the Schmidt number, and μ is the kinematic molecular diffusion coefficient of gas in water. Relationship (2.65) can alternatively be derived (as in Fairall et al. 2000) from the hypothesis that the thickness of the diffusive molecular sublayer δ_μ is proportional to the Kolmogorov's internal scale of turbulence for concentration inhomogeneities: $\eta_D = Sc^{-1/2}(\nu^3/\varepsilon)^{1/4}$, where the thickness of the diffusive sublayer is defined as $\delta_\mu = \mu\Delta C/G_{\mathrm{int}} = \mu/K_{\mathrm{int}}$, $\Delta C = C_w - C_0$ is the effective air–sea gas concentration difference (indices "w" and "0" relate to the bulk and surface values, respectively), and G_{int} is the interfacial component of the air–sea gas flux.

Soloviev et al. (2007) have developed the boundary-layer approach in detail by including convection, shear, wave breaking, turbulence patchiness, and wave-age-dependent bubble-mediated component. Figure 2.26 compares Soloviev's et al. (2007) parameterization model with the results of direct, eddy-correlation measurements of the CO_2 air–sea flux during *GasEx-2001* (Hare et al. 2004). The resultant model curves show good agreement between model and available observations. Remarkably, within the wind-speed range of up to 9 m/s, there is practically no dependence of the gas-transfer velocity on wave age.

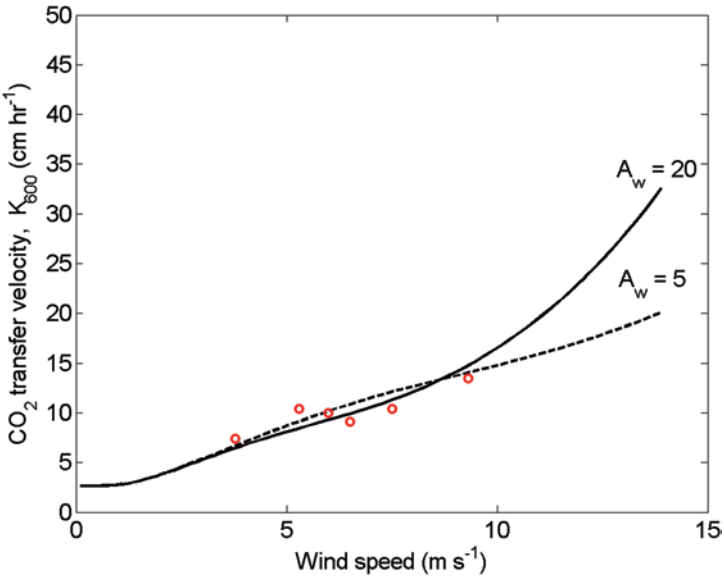

Fig. 2.26 Boundary-layer type gas-transfer parameterization for CO_2 at two wave ages A_w in comparison with the direct air-sea CO_2 flux measurements during GasEx-2001 data by Hare et al. (2004). (After Soloviev et al. 2007)

The boundary layer modeling approach is based on the physics of turbulent boundary layer near near a free interface. In contrast to the renewal model, the boundary-layer model does not explicitly include intermittency of exchange processes near the surface. Instead, it identifies the connection between the interfacial gas-transfer velocity and the dissipation of the turbulent kinetic energy directly, following Kitaigorodskii and Donelan (1984) and Dickey et al. (1984), or indirectly, via the Kolmogorov's internal scale of turbulence (Fairall et al. 2000). Since both the renewal and the boundary-layer model are based on equivalent physical principles of the boundary-layer turbulence, they ultimately lead to quite similar final results.

The effect of surface films of the air–sea exchange processes, which not only is primarily important under low wind-speed conditions but also determines dynamics of gravity-capillary waves under moderate and high wind-speed conditions, is far from complete understanding. At this point, there is no plausible parameterization or sufficient data to address this issue adequately. If future experiments will reveal significant differences in the effect of surface films on the different types of molecular sublayers, then parameterizations (2.57–2.59) will need to be decoupled in their low wind-speed portions via introduction of additional parameters (i.e., P_f) and possibly Sc and Pr number dependences similar to that proposed by Asher et al. (2005).

Consideration of the gas-transfer parameterization in terms of practical applications, including remote sensing and air–sea exchange of CO_2 and DMS gases, is explained in Chap. 7.

2.5 Effect of Penetrating Solar Radiation

2.5.1 Model Equations

The impact of penetrating solar radiation on the dynamics of molecular sublayers can be quantified in a consistent way with a renewal model (Soloviev and Schlüssel 1996). Note that the term "cool skin" might not be completely appropriate during daytime hours since in extreme situations the solar warming may reverse the sign of the temperature gradient in the thermal molecular sublayer.

Following the same approach as in Sect. 2.4.2, consider a fluid element adjacent to the sea surface that participates in the process of cyclic renewal of the surface water in the presence of both surface cooling and the volume absorption of solar radiation. Initially, the fluid element has a uniform temperature equal to the bulk-water value. As it is exposed to the interface, the molecular diffusion law governs the evolution of the temperature difference across the thermal sublayer:

$$\frac{\partial T}{\partial t} = \frac{\partial}{\partial z}\left(\kappa_T \frac{\partial T}{\partial z}\right) + \frac{\partial q_R}{\partial z}, \tag{2.68}$$

where $q_R = I_R / (c_p \rho)$ is the volume source due to absorption of solar radiation in water.

The boundary condition on the waterside of the air–sea interface is

$$-\kappa_T \frac{\partial T}{\partial z}\Big|_{z \to -0} = q_0, \tag{2.69}$$

and the initial condition is formulated as follows:

$$T(z,0) = T_w, \tag{2.70}$$

where $q_0 = Q_0 / (c_p \rho) = (Q_T + Q_E + I_L) / (c_p \rho)$, and T_w is the bulk-water temperature. Q_E and I_L do not depend strongly on the presence of the temperature difference across the cool skin (Paulson and Simpson 1981). The sensible heat flux Q_T can appreciably depend on the temperature difference across the cool skin; the magnitude of Q_T is, however, usually much less than that of Q_E or I_L. The total heat flux Q_0 is thereby assumed to be constant during the time period between successive surface renewals.

Equation (2.68) is a linear equation in partial derivatives with a volume source, and the superposition principle can be applied with initial and boundary conditions (2.69) and (2.70). This is a mixed problem with boundary conditions of the second type. Introducing a new variable $\Delta T(z,t) = T(z,t) - T_w$ the solution can be represented as follows (Vladimirov 1976):

$$\Delta T(z,t) = \Delta T_c(z,t) + \Delta T_R(z,t) \tag{2.71}$$

where

$$\Delta T_c(z,t) = -q_0(\kappa_T \pi)^{-1/2} \int_0^t (t-t')^{-1/2} \exp\left\{-\frac{z^2}{4\kappa_T(t-t')}\right\} dt' \tag{2.72}$$

and

$$\Delta T_R(z,t) = \int_0^t \int_{-\infty}^0 \hat{f}(\eta)\left[4\kappa_T \pi(t-t')\right]^{-1/2} \exp\left\{-\frac{(z-\eta)^2}{4\kappa_T(t-t')}\right\} d\eta dt' \tag{2.73}$$

with $f(z) = \partial q_R / \partial z$. The circumflex denotes an even extension of the function to $z > 0$ so that

$$\hat{f}(z) = \hat{f}(-z). \tag{2.74}$$

The quantities ΔT_c and ΔT_R are interpreted as the near-surface temperature differences due to surface cooling and due to absorption of solar radiation, respectively. Integration of (2.72) results in the following expression for the temperature difference developing due to surface cooling and molecular heat diffusion:

$$\Delta T_c(z,t) = -2q_0(t/\kappa_T)^{1/2}\left[\pi^{-1/2}\exp\left(-\xi^2\right) - \xi erfc(\xi)\right], \tag{2.75}$$

where $\xi = z(4\kappa_T t)^{-1/2}$. Expression (2.73) for the temperature difference due to absorption of solar radiation can be rewritten in the following way:

$$\begin{aligned}\Delta T_R(z,t) = &\int_0^t \int_{-\infty}^0 f(\eta)\left[4\kappa_T \pi(t-t')\right]^{-1/2} \exp\left\{-\frac{(z-\eta)^2}{4\kappa_T(t-t')}\right\} d\eta dt' \\ &+ \int_0^t \int_{-\infty}^0 \hat{f}(-\eta)\left[4\kappa_T \pi(t-t')\right]^{-1/2} \exp\left\{-\frac{(z+\eta)^2}{4\kappa_T(t-t')}\right\} d\eta dt'\end{aligned} \tag{2.76}$$

Since $\hat{f}(\eta) = \hat{f}(-\eta)$ for $\eta < 0$ and $\hat{f}(\eta) \equiv f(\eta)$ for $\eta \geq 0$, (2.76) can be transformed as follows:

$$\begin{aligned}\Delta T_R(z,t) = &\int_0^t \int_{-\infty}^0 f(\eta)\left[4\kappa_T \pi(t-t')\right]^{-1/2} \exp\left\{-\frac{(z-\eta)^2}{4\kappa_T(t-t')}\right\} d\eta dt' \\ &+ \int_0^t \int_{-\infty}^0 f(\eta)\left[4\kappa_T \pi(t-t')\right]^{-1/2} \exp\left\{-\frac{(z+\eta)^2}{4\kappa_T(t-t')}\right\} d\eta dt'\end{aligned} \tag{2.77}$$

Substitution of the expression for the absorption of solar radiation in the form given by equation (1.60):

$$f(\eta) = q_{R0} \sum_1^9 a_i \alpha_i \exp(\alpha_i \eta) \tag{2.78}$$

into (2.77) results in the following formula:

$$\Delta T_R(z,t) = q_{R0}\sum_1^9 a_i\alpha_i\left[I_1(z,t;i)+I_2(z,t;i)\right], \tag{2.79}$$

where

$$\begin{aligned} I_1(z,t;i) &= \int_0^t\int_{-\infty}^0 \exp(-\alpha_i\eta)\exp\left\{-\frac{(z-\eta)^2}{4\kappa_T(t-t')}\right\} \\ &\times\left[4\kappa_T\pi(t-t')\right]^{-1/2} d\eta dt', \end{aligned} \tag{2.80}$$

$$\begin{aligned} I_2(z,t;i) &= \int_0^t\int_{-\infty}^0 \exp(-\alpha_i\eta)\exp\left\{-\frac{(z+\eta)^2}{4\kappa_T(t-t')}\right\} \\ &\times\left[4\kappa_T\pi(t-t')\right]^{-1/2} d\eta dt', \end{aligned} \tag{2.81}$$

and q_{R0} is the scaled solar irradiance just below the sea surface mathematically defined as $q_{R0} = \left(c_p\rho\right)^{-1} I_R(z)\big|_{z\to-0} = \left(c_p\rho\right)^{-1}(1-A)I_\Sigma$.

Change of variables in (2.80) and (2.81) $\theta = t-t'$, $u = (z-\eta)(4\kappa_T\theta)^{-1/2} - \alpha_i(\kappa_T\theta)^{1/2}$, and $u' = (z+\eta)(4\kappa_T\theta)^{-1/2} + \alpha_i(\kappa_T\theta)$ leads to:

$$\begin{aligned} \Delta T_R(z,t) &= q_{R0}\sum_{i=1}^9 a_i\alpha_i\int_0^t\left\{\exp\left(\kappa_T\alpha_i^2\theta-\alpha_i z\right)\left[1+erf\left(\frac{z}{\left(4\kappa_T\theta\right)^{1/2}}\right.\right.\right. \\ &\left.\left.\left.-\alpha_i\left(\kappa_T\theta\right)^{1/2}\right)\right]+\exp\left(\kappa_T\alpha_i^2\theta+\alpha_i z\right)\left[1-erf\left(\frac{z}{\left(4\kappa_T\theta\right)^{1/2}}+\alpha_i\left(\kappa_T\theta\right)^{1/2}\right)\right]\right\}d\theta. \end{aligned} \tag{2.82}$$

Equation (2.82) is integrated to obtain

$$\begin{aligned} \Delta T_R(z,t) &= \frac{1}{2}q_{R0}\kappa_T{}^{-1}\sum_{i=1}^9 a_i\alpha_i\left\{\exp(-\alpha_i z+\delta_i^2)\left[1+erf(\xi-\delta_i)\right]\right. \\ &+\exp(\alpha_i z+\delta_i^2)\left[1-erf(\xi+\delta_i)\right]-2\exp(-\alpha_i z)+ \\ &\left.4\delta_i\left[\pi^{-1/2}\exp(-\xi^2)-\xi+\xi erf(\xi)\right]\right\} \end{aligned} \tag{2.83}$$

where $\xi = z(4\kappa_T t)^{-1/2}$ and $\delta_i = \alpha_i(\kappa_T t)^{1/2}$ are nondimensional depth and time, respectively.

According to (2.75) and (2.83), the near-surface temperature difference between the renewal events evolves in the following way:

$$\Delta T(0,t) = \Delta T_c(0,t) + \Delta T_R(0,t) = -2q_{R0}\left(\frac{t}{\kappa_T \pi}\right)^{1/2} + q_{R0}\kappa_T{}^{-1}\sum_{i=1}^{9} a_i \alpha_i^{-1}\left\{\exp(\delta_i^2)\left[1 - erf(\delta_i^2)\right] - 1\right\} + 2q_R(0)\left(\frac{t}{\kappa_T \pi}\right)^{1/2} \tag{2.84}$$

The average temperature difference across the thermal molecular sublayer of the ocean is defined as follows:

$$\Delta \overline{T} = \int_0^{\infty} p(t)\Delta T_w(0,t)dt \tag{2.85}$$

where

$$\Delta T_m(0,t) = \frac{1}{t}\int_0^t \Delta T(0,t')dt', \tag{2.86}$$

and $p(t)$ is the probability density. From (2.84) and (2.86), the following expression can be obtained:

$$\Delta T_m(0,t) = -\frac{4}{3}q_0\left(\frac{t}{\kappa_T \pi}\right)^{1/2} + \frac{q_{R0}}{\kappa_T}\sum_{i=1}^{9} a_i \alpha_i^{-1}\left(\delta_l^{-2}\left\{\exp(\delta_l^2)\left[1 - erf(\delta_l^2)\right] - 1\right\} + 2\pi^{-1/2}\delta_l - 1\right) + \frac{4}{3}q_{R0}\left(\frac{t}{\kappa_T \pi}\right)^{1/2} \tag{2.87}$$

With the Rao et al. (1971) probability density function (2.29), expression (2.85) can be rewritten in the following way:

$$\Delta \overline{T} = \pi^{-1/2}\sigma^{-1}\int_{-\infty}^{+\infty} \exp\left[-\frac{\left(t_{\ln} - m\right)^2}{\sigma^2}\right]\Delta T_m\left(0, \exp\left(t_{\ln}\right)\right)dt_{\ln}, \tag{2.88}$$

where $t_{\ln} = \ln t$, $m = \ln t_* - \sigma^2/4$, t_* is the mean time between bursting events (renewal time); m and σ^2 are the mean value and the variance of the logarithm of the random variable t, respectively. Transformation to the logarithmic variable $t_{\ln}$ is required to estimate integral (2.88) numerically.

2.5.2 Renewal Time

It follows from (2.38) that the renewal time can be expressed in the following way:

$$t_* = \frac{9\pi\nu}{16u_*^2}\exp(\sigma^2/8)\Lambda_0^2\left(1-a_0{}^3\Lambda_0^4 Rf_0\right)^{-1/2}(1+Ke/Ke_{cr}). \tag{2.89}$$

The introduction of a coefficient $A_0 = \frac{8}{3}\pi^{-1}\exp\left(\sigma^2/8\right)$, which appears in the parameterization of the air–sea gas-transfer velocity, leads to the following expression for the renewal time:

$$t_* = \frac{27A_0\nu\pi^2}{128u_*^2}\Lambda_0^2(1-a_0{}^3\Lambda_0^4 Rf_0)^{-1/2}(1+Ke/Ke_{cr}). \tag{2.90}$$

The expression for renewal time (2.90) is applicable only for nighttime conditions, when the surface flux is negative and, therefore $Rf_0 < 0$. During daytime, solar heating can affect the renewal time by inhibiting convective instability of the near-surface layer of the ocean. Moreover, in some regions of the ocean evaporation may be replaced by condensation of vapor at the ocean surface; the latent heat flux reverses its sign, and Rf_0 may become positive. In the next section, the definition of the surface Richardson number is extended for conditions of solar heating and condensation of vapor at the ocean surface.

2.5.3 Convective Instability of the Cool Skin During Daytime

Under calm weather $Rf << -a_0{}^{-3}\Lambda_0^{-4}$, and the renewal time is determined by convective instability. The positive buoyancy flux due to absorption of solar radiation may modify dynamics of the near-surface layer of the ocean. Woods (1980) proposed the following Rayleigh-number criterion characterizing the influence of solar radiation absorption on thermally driven convection in the upper ocean:

$$Ra(z) = \frac{z^4\alpha_T g q_{R0}\left[f_R(D)-f_R(z)\right]}{\nu\kappa_T{}^2}, \tag{2.91}$$

where $f_R(z)$ is the solar radiation absorption function (defined in Sect. 1.4.6), q_{R0} is the solar irradiance just below the sea surface, and D is the *compensation depth* defined from the following relationship:

$$q_0 = q_{R0}\left[1-f_R(D)\right]. \tag{2.92}$$

The maximum of $Ra(z)$ is determined by

$$dRa(z)/dz = 0 \tag{2.93}$$

With (2.91) and (2.92), condition (2.93) reduces to

$$4\left[f_R(z)-1+q_0/q_{R0}\right]+zdf_R(z)/dz=0, \tag{2.94}$$

which is used to determine the value, $z=z_{\max}$ (being somewhere between 0.7 D and 0.9 D) so that $Ra_{\max}=Ra(z_{\max})$. The absorption of solar radiation in water inhibits the thermally driven convection in the near-surface layer of the ocean when

$$Ra_{\max}=-\frac{z_{\max}^4\alpha_T g\left[-q_0+q_{R0}-q_{R0}f_R\left(z_{\max}\right)\right]}{\nu\kappa_T{}^2}<Ra_{cr}=1700 \tag{2.95}$$

Under low and calm wind-speed conditions, the absorption of solar radiation may therefore dramatically increase the renewal time especially near midday. Such an extreme effect supposedly takes place in lakes and rivers under low wind-speed conditions and a strong insolation. In the open ocean, however, additional convective instability is caused by the increase in sea surface salinity due to evaporation. The effect of absorption of solar radiation and of the additional buoyancy flux due to evaporation from the ocean surface can be included into the renewal time parameterization (2.90) by extending the definition of the surface Richardson number (2.61) in the following way:

$$Rf_0=\frac{\alpha_T g\nu}{c_p\rho u_*^4}\begin{cases}(Q_E+Q_T+I_L+(\beta_S S_0 c_p Q_E)/\alpha_T L) & \text{for } Ra_{\max}\geq Ra_{cr}\\ (\beta_S S_0 c_p Q_E)/\alpha_T L & \text{for } Ra_{\max}<Ra_{cr}\end{cases} \tag{2.96}$$

In order to extend the parameterization to cases with positive latent heat flux (condensation), Rf_0 should be reset equal to zero if it becomes positive according to expression (2.96).

2.5.4 Model Calculations

Penetrating solar radiation is specified according to (1.59)–(1.60). There are also material coefficients to be set in the model as functions of temperature and salinity; they are $\nu,\kappa_T,\alpha_T,L,c_p$, and ρ. As a first approximation, the influence of SST and salinity variability on the material coefficients is ignored, while the dimensionless product $\beta_S S_0$ is fixed at 0.026.

In Fig. 2.27, vertical profiles of ΔT_R, ΔT_c, and ΔT within the upper 43 cm of the ocean have been calculated for three wind-speed and two heat-flux regimes from equations (2.75), (2.83), and (2.71), respectively. Shown in Fig. 2.27 are the instantaneous profiles developed after a surface renewal event at the end of the renewal time period (i.e., at $t=t_*$). The renewal time is determined from formula (2.89) with the surface Richardson number defined by equation (2.96).

As expected the low wind-speed regime shows the greatest temperature deviations extending to depths of several centimeters (Fig. 2.27a, b). The model calcula-

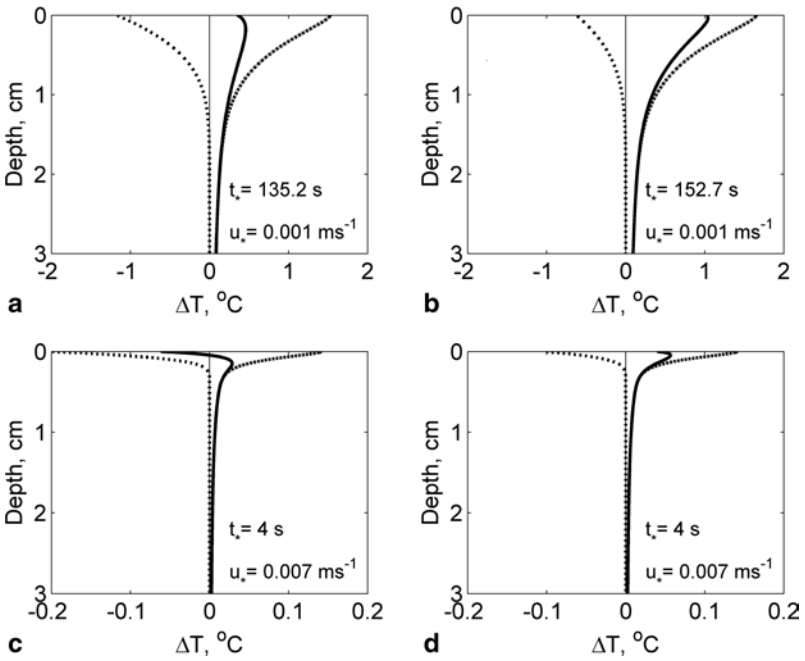

Fig. 2.27 Instantaneous vertical temperature profiles in the upper 3 cm of the ocean at the end of the time period between renewal events. The contribution of the solar heating (dash-dotted), surface cooling (dashed), and the combined effect (contiguous) are calculated from a renewal model for **a, c** $Q_0 = 140$ W m^{-2}, $Q_E = 70$ W m^{-2} and **b**, **d** $Q_0 = 70$ W m^{-2}, $Q_E = 35$ W m^{-2}. The top row (**a, b**) corresponds to free and the bottom row (**c, d**) to forced convection regimes. Solar irradiance just below the sea surface $I_R(0) = 1000$ W m^{-2}, water temperature $T_0 = 29$ °C, and salinity $S_0 = 36$ psu are the same in all cases. Note the different temperature scale between the top and bottom pairs of diagrams

tions are consistent with the instantaneous temperature profiles in the open ocean that have been observed with the free-rising profiler (see Fig. 2.3).

In contrast, the profiles generated by the model for higher friction velocities (Fig. 2.27c, d) are affected by surface cooling and heating only very close to the interface. The combined effect, $\Delta T(z)$, shows a maximum in a small range of depths between 50 and 150 μm. Above this maximum, surface cooling prevails at high wind speeds, while for the values of energy fluxes chosen here, the net effect at low wind speed is a surface warming.

Calculations with different water types from Table 2.1 do not show the temperature differences larger than 0.02 °C. The absorption and scattering of light in near-infrared band mainly determine the transmission of solar radiation within the upper few millimeters of the ocean. Dependence on the water type is small for this wavelength range.

Observation of SST by infrared radiometer averages over relatively large areas and shows an integrated contribution of the surface renewal process at different stages. Figure 2.28 shows the average temperature difference across the aqueous

Table 2.2 Comparison of different parameterizations and models for the temperature difference, ΔT, between the sea surface and 4 m depth (ship's thermosalinograph intake), with measurements made by Hartmut Grassl during TOGA COARE

Cool-skin model	Diurnal mixed layer and thermocline model	Night		Day		Day and night	
		Bias	Std. dev.	Bias	Std. dev.	Bias	Std. dev.
H	Included	0.32	0.27	0.28	0.23	0.30	0.25
S	Included	0.14	0.10	−0.02	0.19	0.05	0.15
PS	PWP	0.06	0.13	0.14	0.20	0.10	0.17
SS	PWP	0.01	0.13	0.06	0.20	0.03	0.17
SS_m	PWP	0.02	0.12	0.05	0.20	0.02	0.17
SS	SK	0.06	0.11	0.10	0.18	0.08	0.15

The cool-skin models are labeled as follows: H (Hasse 1971), S (Schluessel et al. 1990), PS (Paulson and Simpson 1981), SS (Soloviev and Schlüssel 1996), and SS_m (Soloviev and Schlüssel 1996 with updated empirical constants); the diurnal thermocline models, PWP (Price et al. 1986) and SK (Stull and Kraus 1987). All temperature differences are in °C.

thermal molecular sublayer ΔT, as well as its components ΔT_c and ΔT_R, as a function of u_*. The main effect of solar radiation on the cool skin is observed at low wind speeds. Figure 2.29 shows the diurnal evolution of the temperature difference across the aqueous thermal molecular sublayer and the direct (interfacial) air–sea gas-transfer velocity under idealized insolation conditions. For low wind speeds, suppression of free convection due to the absorption of solar radiation has a strong effect on the gas transfer at the ocean–air interface. This is because the surface renewal time "jumps" at some threshold level of insolation. For the temperature difference across the aqueous thermal molecular sublayer, this effect is not as big as for the gas exchange because of the partial compensation of surface cooling by solar heating.

2.5.5 Comparison with Daytime and Nighttime Cool-Skin Field Data

SST measurements in the western equatorial Pacific made by Hartmut Grassl from the R/V *Vickers* during TOGA COARE from 30 January to 26 February 1993 near 156°E, 2°S have provided the data set that is particularly useful in validating parameterizations for the temperature difference across the cool skin. The SST data were taken with infrared radiometer. The bulk-water temperature was measured with a standard shipboard thermosalinograph pumping water from 3 m depth. At night, the temperature differences in the upper 3 m were usually very small (a few hundredths of a degree at most). During daytime the difference between SST and water temperature taken at 3 m depth could be affected by the presence of shallow diurnal thermocline as schematically shown in Fig. 2.30. In addition, precipitation effects result in a stable salinity stratification (the near-surface rain-formed halocline), which is usually accompanied by temperature gradients. The likely presence

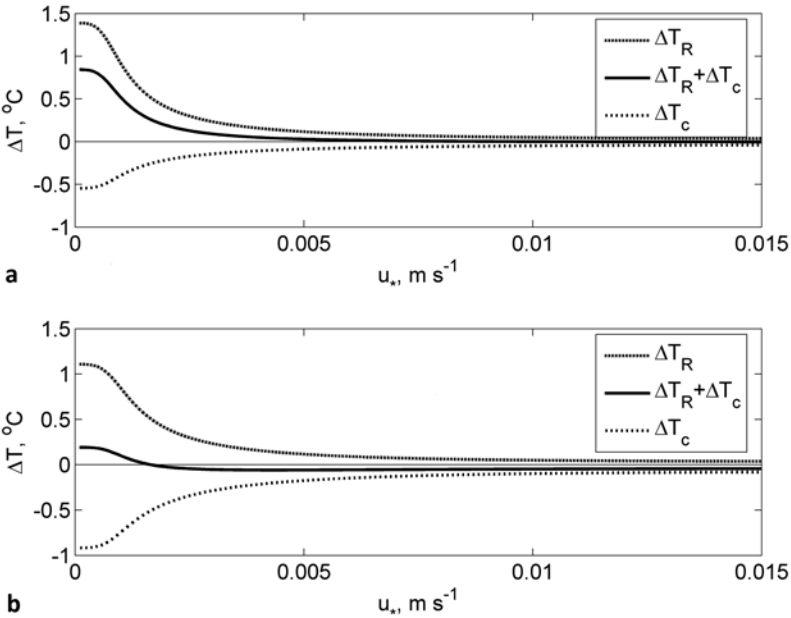

Fig. 2.28 Temperature difference across the cool skin due to solar heating ΔT_R, surface cooling ΔT_c, and the combined effect, $\Delta T_R + \Delta T_c$, as a function of friction velocity u_* calculated from parameterization (2.88) for **a** $Q_0 = 70$ W m^{-2}, $Q_E = 35$ W m^{-2}, and **b** $Q_0 = 140$ W m^{-2}, $Q_E = 70$ W m^{-2}. The solar irradiance just below the ocean surface is $I_{R0} = -1000$ W m^{-2}, water temperature $T_0 = 29$ °C, and salinity $S_0 = 36$ psu are the same for both cases

of fine thermohaline structure in the upper few meters of the ocean under low wind-speed conditions is one of the limitations of the cool-skin model validation. (More details about the fine thermohaline structure of the near-surface layer of the ocean can be found in Chap. 4)

As a first approximation, the temperature difference across the diurnal thermocline (ΔT_d) can be accounted for with a model of the diurnal mixed layer and thermocline. We make use of two types of models for the diurnal mixed layer and thermocline. The first model is that of Price et al. (1986), hereafter referred to as PWP. The second model is that of Stull and Kraus (1987), hereafter referred to as SK. The SK model is the so-called transilient (nonlocal) model, which represents the turbulent transport by a cascade of eddies. The absorption of solar radiation is simulated with nine spectral components for water type IB according to Jerlov (1976) classification (see Chap. 1, Table 1.2), because this type of water is typical for in the TOGA COARE domain.

Figure 2.31 compares parameterization (2.88), hereafter referred to as SS_m, with the TOGA COARE data. Since the field measurements include both the thermal molecular sublayer and diurnal thermocline, a diurnal mixed layer model has been included, either PWP or SK (only the PWP model results are shown in Fig. 2.31c). Both mixed layer model calculations include the surface heat and radiation fluxes,

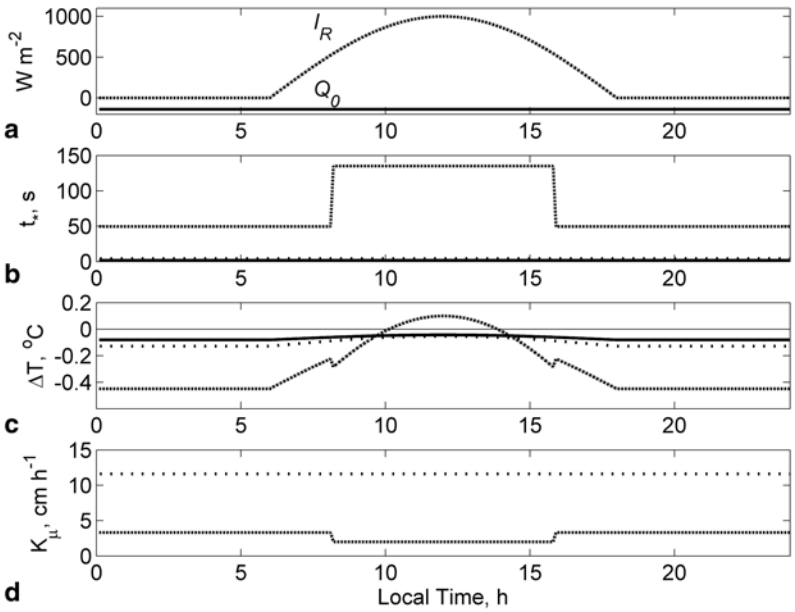

Fig. 2.29 Evolution of temperature difference across the cool skin and of the direct air-sea gas transfer coefficient during 24 h at three different friction velocities: **a** idealized diurnal cycle of the surface solar irradiance and the net surface heat flux, **b** renewal time, **c** temperature difference across the cool skin, **d** direct air-sea gas transfer coefficient for a Schmidt number Sc = 430 (CO_2 at 29 °C and 35 psu). In (b), (c), and (d) the dash-dotted, dotted and contiguous lines correspond to the condition of free convection ($u_* = 0.001$ m s^{-1}), forced convection ($u_* = 0.007$ m s^{-1}), and intensive surface waves breaking ($u_* = 0.015$ m s^{-1}), respectively

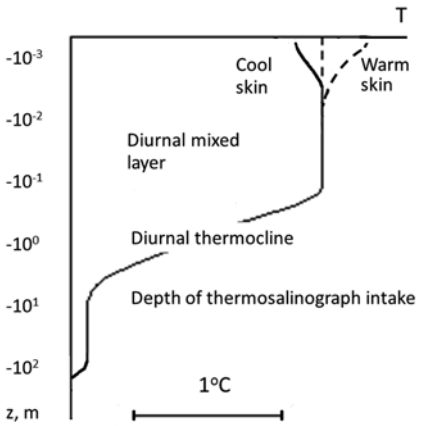

Fig. 2.30 Schematic representation of the vertical temperature profile during a large diurnal warming event. Typical depth and temperature scales are shown (but may vary greatly)

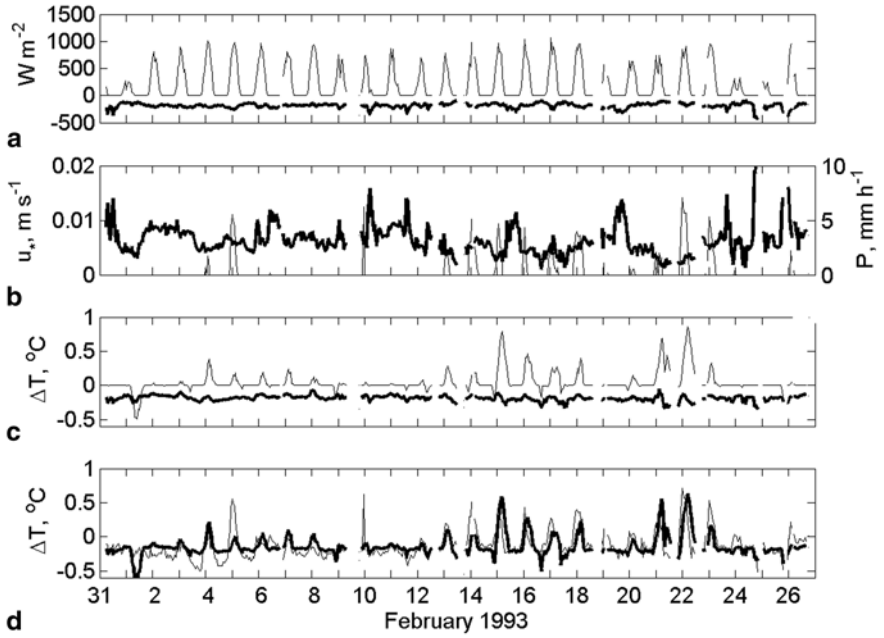

Fig. 2.31 Comparison of parameterization SS_m with measurements during TOGA COARE. **a** hourly means of the surface solar irradiance I_R0 (thin line) and net surface heat flux Q_0 (bold line), **b** hourly means of friction velocity u_* (bold line) and rain rate P (thin line), **c** calculated temperature difference across the cool skin (parameterization SS_m, bold line) and across the diurnal thermocline with the PWP model, thin line), **d** hourly means of the difference between bulk and skin temperature as observed during COARE (thin line), parameterized by SS_m plus PWP model (bold line). (After Soloviev and Schlüssel 1996)

wind stress, and rainfall rates as measured from the R/V *Vickers*. (Technical details relating to mixed layer modeling in this case can be found in Soloviev and Schlüssel 1996.) Figure 2.31d suggests that there is a phase shift between the PWP model prediction and field data under conditions of evening deepening. This is related to the slow, diffusive response of the PWP model during deepening of the diurnal thermocline. The SK model reproduces the SST evolution with no phase delay; it, however, results in a larger bias than the PWP model.

Table 2.2 compares several parameterizations and models of the cool skin with the TOGA COARE data set. The Paulson and Simpson (1981) parameterization (labeled PS), the Soloviev and Schlüssel (1996) parameterization (labeled SS), as well as the Hasse (1971) model (labeled H) are designed to calculate $\Delta\overline{T}$ during day and night. The parameterization specified by Schlüssel et al. (1990) is labeled S; it has the night- and daytime components. Models H and S implicitly include the effect of the diurnal thermocline (ΔT_d); PS, SS, and SS_m are designed to parameterize the temperature difference $\Delta\overline{T}$ across the thermal molecular sublayer (cool skin) only.

The SS cool-skin parameterization combined with the PWP model produces a bias of –0.03 °C and a standard deviation of 0.17 °C. The SS parameterization

combined with a nonlocal model of the diurnal thermocline SK gives a slightly better standard deviation (0.15 °C) but larger bias (–0.08 °C). The SS_m cool-skin parameterization, which represents the SS parameterization with updated constants ($a_0 = 0.23$, $\Lambda_0 \approx 10$, and $Ke_{cr} \approx 0.18$), produces a bias of –0.02 °C and a standard deviation of 0.17 °C.

Model S (including both cool-skin and diurnal thermocline parameterizations) and the PS+PWP model produced comparable results. Traditional parameterization H exhibits a larger bias and standard deviation. The H parameterization is, however, based entirely on data from a field experiment in the Northeast Atlantic Ocean and is not necessarily valid in other parts of the world ocean.

Though parameterization SS_m, combined with the PWP model follows the main features of the field data (Fig. 2.31) and on average outperforms the other models brought to the analysis, in some situations, especially under low wind-speed conditions, the "instantaneous" difference between the model and data exceeds 0.5 °C. As mentioned above, numerical models of the diurnal mixed layer and thermocline are not yet perfect, in particular under low wind-speed conditions. Improvement of the mixing parameterization is one of the closely related issues (see Sect. 1.7.5).

Note that the SS cool-skin model uses the Soloviev and Schlüssel (1996) version of the renewal model. New field data instigated a modification of the empirical coefficients entering this model, as described in Sect. 2.4.2. Qualitative comparison of the revised model with the COARE data set presented in has not been done.

Both mixed layer models, SK and PWP, account for the rain-formed stratification in the near-surface layer. None of the cool-skin models mentioned in this section, however, accounts for the rain-related effects that are the subject of the next sections.

2.6 Cool and Freshwater Skin of the Ocean during Rainfall

Rain falling into the sea modifies the aqueous molecular sublayers through a variety of different effects. These effects include additional momentum flux and stabilizing buoyancy flux from air to sea, additional sensible heat flux of the rain, modification of physical water constants because of temperature and salinity changes, increase in the surface roughness, damping of short gravity waves, excitation of capillary waves at higher wave frequencies, and the surface mixing by droplets.

During rainfall the raindrops penetrate to tens of centimeters directly affecting the near-surface salinity. Rain falling on the sea surface also establishes a haline diffusive molecular sublayer with a salinity gradient. Schlüssel et al. (1997) refer to this layer as the *freshwater skin* of the ocean. The freshwater skin is only about 50 μm thick. The salinity difference developing in the haline diffusive molecular sublayer can to some extent affect the interpretation of the radar and radiometric observations of the sea surface at low microwave frequencies. The dielectric constant of water depends on the sea surface salinity at centimeter wavelengths (Lager-

loef et al. 1995). The dielectric constant change may cause interpretation problems when remotely measuring wind speed or SSTs at these frequencies. The dielectric constant dependence on salinity may also be used for remote sensing of the sea surface salinity. Though the depth of the haline molecular sublayer is much less than the penetration depth of the electromagnetic radiation at these wavelengths, the exponential decay of the radiation energy entering the ocean can, however, make it sensitive to salinity changes in the skin layer.

An important effect is the dependence of gas solubility on salinity. For instance, a 1 % decrease in the seawater salinity results in a 0.5 % increase in the CO_2 solubility and 0.1 % increase in the O_2 solubility (Stephen and Stephen 1964; Riley and Skirrow 1965).

In view of the different effects that can be expected from rainfall on the surface molecular sublayer, Schlüssel et al. (1997) provide a comprehensive description of the modifications of this layer of the ocean due to precipitation. According to these authors, the impact of precipitation on the thermal and diffusive molecular sublayers of the ocean includes the following processes:

1. The freshwater flux due to rain produces a buoyancy flux in the near-surface layer of the ocean, which tends to suppress convection (Ostapoff et al. 1973).
2. Raindrop temperatures are usually lower than the SST (Katsaros 1976). The precipitation falling into the ocean results in an interfacial sensible heat flux Q_{rs} caused by small drops that do not penetrate into the ocean and in a volume heat flux Q_{rV} due to drops submerging into the ocean and gradually mixing with depth.
3. Changes in the temperature and salinity due to rain mentioned in the previous two points modify physical constants of sea surface water (Katsaros and Buettner 1969). In particular, the kinematic viscosity increases with decreasing temperature and decreases with decreasing salinity.
4. Rainfall can enhance the surface roughness as much as two orders of magnitude by generation of impact craters, Rayleigh jets, splash drops, and small waves (Houk and Green 1976).
5. Raindrops falling into the ocean fragment and partly remove surface films (Green and Houk 1979).
6. Raindrops penetrating through the surface disturb wave motions and damp the short gravity waves by reducing the amplitudes at which they break (Yakimov 1959; Manton 1973; Tsimplis and Thorpe 1989; Le Méhauté and Khangaonkar 1990; Poon et al. 1992). As a result, small-scale wave breaking intensifies and the surface renewal time period decreases.
7. Raindrops impact the sea surface and submerge into the ocean, generating additional surface renewals.
8. Raindrops obtain horizontal momentum from the airflow at cloud levels. These raindrops subsequently pass this momentum to the atmospheric boundary layer and to the sea surface, adding to the wind stress that acts on the surface (Caldwell and Elliot 1971). All the momentum of the drop is transferred to the ocean, as opposed to only a small fraction the air.

9. The freshwater skin coexisting with the cool skin is subject to irreversible thermodynamic processes due to significant local temperature and salinity gradients (Doney 1995).

Schlüssel et al. (1997) made an attempt to quantify the various effects of rain on the aqueous molecular sublayers. The irreversible thermodynamic processes in the presence of the cool skin and freshwater skin, however, have not yet been quantified.

2.6.1 Effects of Rain on the Cool Skin

Following again the same approach as in Sect. 2.4.2, consider a fluid element adjacent to the sea surface that participates in the process of cyclic renewal of the surface water in the presence of rain. Initially, the fluid element has a uniform temperature equal to the bulk-water value T_w. As it is exposed to the interface, the molecular diffusion law governs the evolution of the temperature difference across the thermal sublayer.

In the framework of the surface renewal theory described in Sect. 2.4.2 the temperature change between subsequent renewal events in the thermal molecular sublayer of the ocean including a volume source is described by the molecular diffusion equation similar to (2.68) but, instead of solar radiation term, including the volume source of heat due to rain:

$$\frac{\partial T}{\partial t} = \frac{\partial}{\partial z}\left(\kappa_T \frac{\partial T}{\partial z}\right) - P(T_0 - T_r)\frac{\partial f_V}{\partial z}, \tag{2.97}$$

where f_V is the volume source function defined according to (1.78) and T_r the raindrop temperature. We ignore here the difference between specific heats and densities of seawater and rainwater.

The surface boundary condition is defined by rain-induced surface heat flux (1.80):

$$-\kappa_T \frac{\partial T}{\partial z} = \frac{Q_{rs}}{c_p \rho} = P\left(T_0 - T_r\right)\left[1 - f_V\left(0\right)\right]. \tag{2.98}$$

Instead of the volume heat source due to the absorption of solar radiation, equation (2.97) includes the volume source of heat due to raindrops mixing with their environment. In order to reduce the problem of the rain effect to the already considered problem of the solar radiation effect on the cool skin, Schlüssel et al. (1997) approximated the volume source function in (2.97) by a sum of exponentials (similar to the solar radiation absorption function):

$$\partial f_V(z)/\partial z \simeq \sum_{i=1}^{N_r} \varsigma_l \exp(\psi_l \Lambda z / a_r), \tag{2.99}$$

where ς_l and ψ_l are coefficients obtained by a nonlinear least-squares fit. The requirements, $\varsigma_l > 0$ and $\psi_l > 0$, resulted in $N_r = 14$ terms for a good fit. The numerical values of these coefficients for $r_c = 0.40$ mm and $r_c = 0.75$ mm can be found in the original publication of Schlüssel et al. (1997).

The solution to a linear problem (2.97)–(2.98) with a homogeneous vertical temperature profile as the initial condition is obtained in the same way as for equation (2.97) (for details, see Sect. 2.5.1). The temperature difference between the SST $\Delta T_r(0,t)$ and the bulk-water temperature is then as follows:

$$\Delta T_r(0,t) = \Delta T_{rs}(0,t) + \Delta T_{rv}(0,t) \tag{2.100}$$

where

$$\Delta T_{rs}(0,t) = P(T_r - T_w)2\sqrt{\frac{t}{\kappa_T \pi}}\left(1 + 2\Lambda r_c + \frac{4\Lambda^2 r_c^2}{2} + \frac{8\Lambda^3 r_c^3}{6}\right)\exp(-2\Lambda r_c),$$

$$\Delta T_{rV}(0,t) = P\left(T_r - T_w\right)\frac{1}{\kappa_T}\sum_{l=1}^{L}\frac{\varsigma_l a_r}{\Lambda \psi_l}\left[\exp\left(\delta_l^2\right)\left[erf\left(\delta_l\right) - 1\right] + 1 - \pi^{-1/2}\delta_l\right],$$

$\xi = z/\sqrt{4\kappa_T t}$, and $\delta_l = \psi_l \Lambda\sqrt{kt}/a_r$. The first term on the right side of (2.100) is related to the surface flux of rainwater, while the second term is related to the volume source of rainwater.

In accordance with the renewal concept, this temperature difference should be averaged over time by weighting with probability density $p(t)$ of the surface renewals:

$$\overline{\Delta T} = \int_0^\infty p(t)\Delta T_{wr}(0,t)\,dt \tag{2.101}$$

where

$$\Delta T_{wr}(0,t) = \frac{1}{t}\int_0^t \Delta T_r(0,t')dt' \tag{2.102}$$

With (2.100), the solution to (2.102) is

$$\begin{aligned}
&\Delta T_{wr}(0,t) = P(T_r - T_w)\times \\
&\left\{\frac{4}{3}\sqrt{\frac{t}{\kappa_T \pi}}\left(1 + 2\Lambda r_c + \frac{4\Lambda^2 r_c^2}{2} + \frac{8\Lambda^3 r_c^3}{6}\right)\exp(-2\Lambda r_0) - \right. \\
&\frac{1}{\kappa_T}\sum_{l=1}^{L}\frac{\varsigma_l a_r}{\Lambda \psi_l}(\delta_l^{-2}\left\{\exp(\delta_l^2)\left[1 - erf(\delta_l^2)\right] - 1\right\} + 2\pi^{-1/2}\delta_l - 1) - \\
&\left.\sum_{l=1}^{L}\frac{4}{3}\varsigma_l\sqrt{\frac{t}{\pi\kappa_T}}\right\},
\end{aligned} \tag{2.103}$$

which is used together with (2.101) and the lognormal probability density function of the surface renewals similar to (2.87)–(2.88); this allows the numerical integration that gives the modification of the cool skin caused by the sensible heat flux related to the rain.

2.6.2 Freshwater Skin of the Ocean

Besides the modification of the cool skin, rainfall creates a freshwater skin on the top of the ocean where a salinity flux takes place via molecular diffusion (Schlüssel et al. 1997). Under no-rain conditions, evaporation at the sea surface increases salinity, which tends to destabilize the near-surface water enhancing the renewal process at the surface. However, when rain starts, the part of the rain that does not submerge into the ocean can compensate for the evaporation effect and create a stably stratified freshwater skin. This is analogous to the conversion of the cool skin into its antipode, the warm skin, which sometimes occurs under conditions of strong insolation. Consequently, this freshwater effect on diffusion can be described by the diffusion equation in analogy to equation (2.97) that was derived for the thermal sublayer:

$$\frac{\partial S}{\partial t} = \frac{\partial}{\partial z}\left(\mu \frac{\partial S}{\partial z}\right) - PS\frac{\partial f_V}{\partial z}, \tag{2.104}$$

where μ is the coefficient of molecular salinity diffusion and f_V is the volume source function due to rain submerging into the ocean.

The surface boundary condition for salinity flux due to rain that is to be included in the boundary condition for the diffusion equation (2.104) is as follows:

$$-\mu \frac{\partial S}{\partial z} = J_{rs} = S_0 P\left[1 - f_V(0)\right]. \tag{2.105}$$

Assuming that

$$\Delta S << S_w, \tag{2.106}$$

the salinity S and its surface value $S_{0,}$ entering equations (2.104) and (2.105), respectively, are both replaced with the bulk-water salinity S_b. The solution to the linear problem (2.104)–(2.106) is then obtained in the same way as in Sect. 2.5.1 (as well as in the previous section, Sect. 2.6.1):

$$\Delta S_r(0,t) = \Delta S_{rs}(0,t) + \Delta S_{rv}(0,t), \tag{2.107}$$

where

$$\Delta S_{rs}(0,t) = -PS_0 2\sqrt{\frac{t}{\kappa_T \pi}}\left(1 + 2\Lambda r_c + \frac{4\Lambda^2 r_c^2}{2} + \frac{8\Lambda^3 r_c^3}{6}\right)\exp(-2\Lambda r_c)$$

and

$$\Delta S_{rV}(0,t) = -PS_0 \frac{1}{\kappa_T}\sum_{l=1}^{L}\frac{\varsigma_l a_r}{\Lambda \psi_l}\left[\exp(\delta_l^2)\left[erf(\delta_l) - 1\right] + 1 - \pi^{-1/2}\delta_l\right].$$

The first term on the right side of (2.107) is related to the surface flux of rainwater, while the second term is related to the volume source of rainwater.

The first term on the right side of (2.100) is related to the surface flux of rainwater, while the second term is related to the volume source of rainwater.

The salinity difference should be averaged over time by weighting with probability density $p(t)$ of the surface renewals:

$$\overline{\Delta S} = \int_0^\infty p(t)\Delta S_{mr}(0,t)\,dt \tag{2.108}$$

where

$$\begin{aligned}
&\Delta S_{mr}(0,t) = -PS_0 \times \\
&\left\{\frac{4}{3}\sqrt{\frac{t}{\kappa_T \pi}}\left(1 + 2\Lambda r_c + \frac{4\Lambda^2 r_c^2}{2} + \frac{8\Lambda^3 r_c^3}{6}\right)\exp(-2\Lambda r_0)\right. \\
&- \frac{1}{\kappa_T}\sum_{l=1}^{L}\frac{\varsigma_l a_r}{\Lambda \psi_l}(\delta_l^{-2}\left\{\exp(\delta_l^2)\left[1 - erf(\delta_l^2)\right] - 1\right\} + 2\pi^{-1/2}\delta_l - 1) \\
&\left. - \sum_{l=1}^{L}\frac{4}{3}\varsigma_l\sqrt{\frac{t}{\pi\kappa_T}}\right\}.
\end{aligned} \tag{2.109}$$

Solutions (2.109) hold for the linear case only under an assumption that $S \approx S_w$ (i.e., $\Delta S << S_w$) and physical properties of seawater do not change substantially because of the salinity dependence. The properties that could be affected by the rain-caused changes in sea surface salinity are the thermal expansion coefficient, kinematic viscosity, density, specific heat, and latent heat of vaporization. The large salinity differences arising from substantial freshwater influx and relatively long renewal times would require a nonlinear solution to (2.104)–(2.105). However, as shown in the next section, under moderate and heavy rain conditions the renewal time is restricted to very small values, while in light rain the drop of surface salinity remains relatively small so that the solution for the nonlinear case may not be required in most cases.

2.6.3 Surface Renewals Due to Rain Mixing

Small raindrops do not produce an impact crater on the sea surface, while large drops do, disturbing the aqueous molecular sublayer. The area covered by each impact crater is subject to a surface renewal event since the impact crater is deeper than the conductive layer and represents a "catastrophic" event for the molecular sublayer (Engel 1966). (Note that spray droplets from breaking waves also have to be considered in this regard.)

Rodriguez and Mesler (1988) studied drops falling from low heights into pools of liquid; they found that the impact crater radius r_k exceeds about two to three times the corresponding drop radius r_0. Drops falling from higher altitudes generate even bigger craters, with radii up to $r_k \approx 4r_0$ (Prosperetti and Oguz 1993). Dimensional analysis conducted by these authors suggests that the radius of the impact crater can be represented by a formula

$$r_k = r_0 \left(\frac{8}{3} Fr \right)^{1/4} \approx \varphi_c r_0 Fr^{1/4}, \tag{2.110}$$

where $Fr = w_t^2 / gr_0$ is the Froude number, g is the acceleration of gravity, w_t is the terminal velocity of raindrops, and $\varphi_c = (8/3)^{1/4} \approx 1.278$ is a dimensionless constant. Relationship (2.110) has been supported by observations of Pumphrey and Elmore (1990). Comparison with data from Engel (1966) suggests a somewhat smaller constant of about $\varphi_c = 1.05$. This discrepancy is nevertheless relatively small compared to other uncertainties relating to rain-induced mixing (e.g., the size distribution of droplets).

The terminal velocity of raindrops falling on the ocean surface can be estimated from an empirical formula given by Best (1950):

$$w_t = w_\upsilon \left[1 - \exp\left(-\left(r_0 / r_\upsilon \right)^\upsilon \right) \right], \tag{2.111}$$

where $w_\upsilon = 9.43$ m s^{-1}, $r_\upsilon = 1.77 \times 10^{-3}$ m, and $\upsilon = 1.147$. For radii 0.3×10^{-3} m $< r_0 < 6 \times 10^{-3}$ m, representing the majority of the raindrops, (2.111) is approximated within 0.1 m s^{-1} accuracy by

$$w_t = w_\upsilon \left[b_1 - b_2 \exp\left(-r_0 / r_\upsilon \right) \right] \tag{2.112}$$

where $b_1 = 1.0528$ and $b_2 = 1.07733$. Substituting w_t from (2.112) into (2.110) transforms formula (2.110) into a functional dependence of the impact crater radius solely on the raindrop radius:

$$r_k = \varphi_c r_0 \left(\frac{w_u^2 \left[b_1 - b_2 \exp\left(-r_0 / r_\upsilon \right) \right]^2}{gr_0} \right)^{1/4}. \tag{2.113}$$

The area that is subject to renewal due to the raindrop impact is equal to the impact crater area. The number of drops of size $r_0 \pm dr_0$ that reach the surface per unit time and unit area is $n(r_0)w_t(r_0)dr_0$, where $n(r_0)$ is the drop size distribution in the atmosphere near the water surface. Respectively, Craeye and Schlüssel (1998) represented the crater flux density (i.e., the production rate of crater area per unit area and unit time) as follows:

$$F_k = \int_{r_c}^{\infty} \pi r_k(r_0)^2 n(r_0) w_t(r_0) dr_0. \tag{2.114}$$

Representing the distribution of the rain above the sea surface by the Marshall–Palmer drop size spectrum (1.64) and substituting relationships (2.112) into equation (2.114), and (2.113) into (2.114) results in the following formula:

$$\begin{aligned} F_k = & \int_{r_c}^{\infty} \pi r_0^2 \varphi_c^{\,2} \left(\frac{w_v^2 \left[b_1 - b_2 \exp\left(-r_0 / r_v\right) \right]^2}{g r_0} \right)^{1/2} \\ & \times n\left(r_0\right) w_v \left[b_1 - b_2 \exp\left(-r_0 / r_v\right) \right] dr_0. \end{aligned} \tag{2.115}$$

The renewal time is then defined as the inverse of the impact-flux density F_k,

$$t_{*r} = 1 / F_k \tag{2.116}$$

The calculation of the integral on the right side of (2.115) and substituting the result into (2.116) leads to

$$\begin{aligned} t_{*r} = & \frac{g^{1/2}}{\pi n_0 \varphi_c^{\,2} w_v^2} \left[b_1^2 \left(2\Lambda\right)^{-5/2} \Gamma\left(5/2, 2\Lambda r_c\right) \right. \\ & - 2 b_1 b_2 \left(2\Lambda + r_v^{-1}\right)^{-5/2} \Gamma\left(5/2, 2\Lambda r_c + r_c r_v^{-1}\right) \\ & \left. + b_2^2 \left(2\Lambda + 2 r_v^{-1}\right)^{-5/3} \Gamma\left(5/2, 2\Lambda r_c + r_c r_v^{-1}\right) \right], \end{aligned} \tag{2.117}$$

where Γ is the incomplete gamma function.

Figure 2.32 shows the surface renewal time t_{*r} as a function of rain rate P. The rainfall strongly influences the renewal time even for low rain rates. For $P > 2$ mm h^{-1}, the rain-induced surface disruptions dominate the renewal process including the surface renewals caused by breaking wavelets or long breaking waves. In calm situations, even light rainfall easily surpasses the effect of free convection on the renewal time.

Figure 2.33a shows the skin cooling due to rainfall for renewal times determined by the rain as a function of rain rate. The variation of the volume flux of heat with rain rate is compensated by the rain-induced mixing, leaving an almost constant,

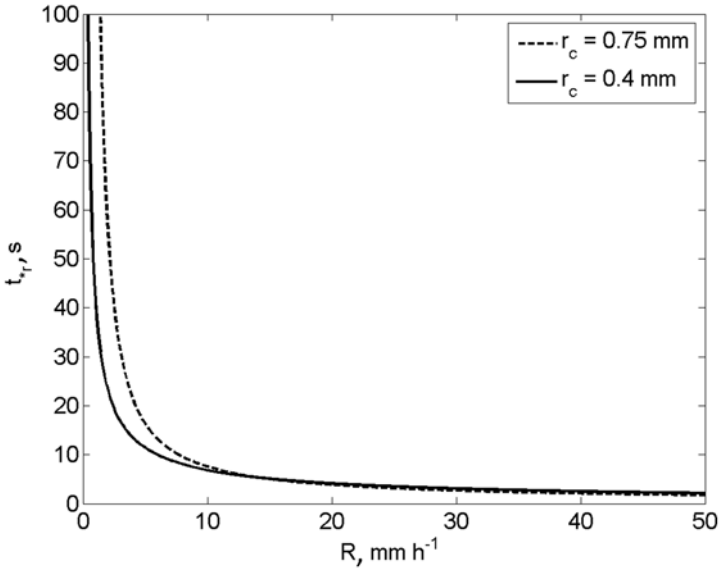

Fig. 2.32 Surface renewal time due to rain calculated from (2.117) as a function of rain rate for two critical radii r_c . (After Schlüssel et al. 1997)

but small temperature difference that depends on the difference between surface and rain temperatures only (the latter is here held constant at 5 °C). The effect of surface heat flux, however, does increase with rain rate. Nevertheless, at rain rates below 50 mm h^{-1} the temperature difference across the cool skin does not exceed $\Delta T = -0.08$ °C for the given surface versus rain temperature difference.

Figure 2.33b shows the freshwater skin due to rainfall for renewal times determined by the rain. The maximum salinity difference across the diffusion sublayer does not exceed $\Delta S = 5$ psu for rain rates up to 50 mm h^{-1}. It is, nevertheless, a dramatic salinity change compared to the range of typical salinity variations in the ocean. The drop in the surface salinity due to rain is mainly due to the surface component of the freshwater flux; the contribution of submerging raindrops appears to be small.

The combined renewal time can be derived by considering renewal events caused by skin friction and kinetic energy fluxes and rain-induced renewals as independent processes. Hence, within a given time period, the number of total renewals equals the sum of renewals due to rain t_{*r} and renewals due to momentum and energy fluxes t_{*f}. The combined renewal time is then given by formula suggested in Schlüessel et al. (1997):

$$1/t_* = 1/t_{*f} + 1/t_{*r} \tag{2.118}$$

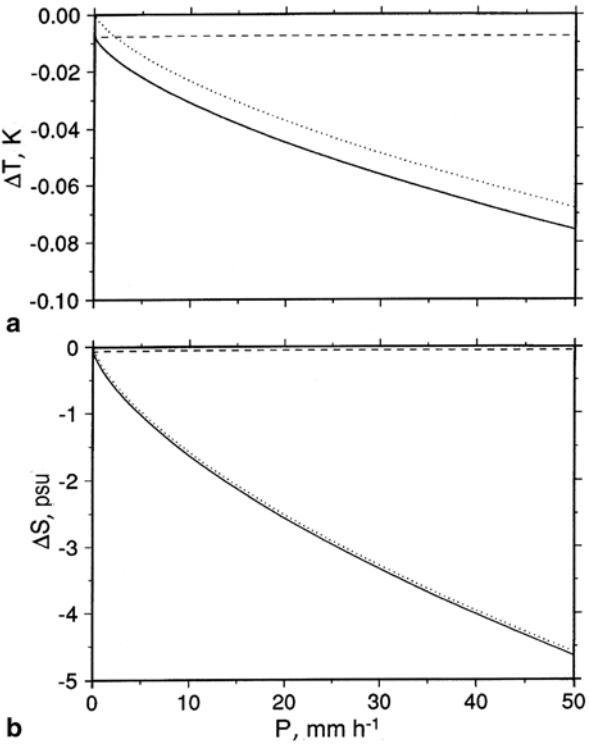

Fig. 2.33 Skin cooling by rainfall with a typical rain drop temperature of 5 °C below the sea surface temperature **(a)** and freshwater skin due to rainfall at bulk salinity of $S_w = 35$ psu **(b)**, both as a function of rain rate with respect to renewal times determined by the rainfall; the total effects are shown by the solid line, the effects due to drops penetrating into the ocean by the dashed lines and that due to surface heat flux by the dotted lines. (After Schlüessel et al. (1997). Reproduced with permission from Springer Science and Business Media)

2.6.4 Buoyancy Effects in Molecular Sublayer Due to Rain

At the sea surface from the waterside ($z \to -0$) the vertical flux of buoyancy is as follows:

$$B_0 = -\frac{g}{\rho}\overline{(w'\rho')}\Big|_{z\to -0} = -\frac{\alpha_T g}{c_p \rho}\left(Q_E + Q_T + Q_L + Q_{rs}\right) - \beta_S S_0 g \frac{Q_E}{\rho L} - \beta_S g Q_{rs}. \quad (2.119)$$

The buoyancy flux due to rain stabilizes the upper ocean, which affects the dynamics of molecular sublayers. The description of this effect is included through a modification of the surface Richardson number Rf_0

$$Rf_0 = -\nu B_0 / u_*^4, \quad (2.120)$$

where B_0 is defined in (2.119).

Expression (2.120) accounts for surface fluxes only; volume absorption of solar radiation or raindrops submerging into the ocean complicates the analysis. In the general case, the approach described in Sect. 2.5.3 can be applied: B_0 is set to zero when the maximum Rayleigh number is less than the critical value for negative val-

ues of Rf_0; positive values of Rf_0 are always set to zero. Estimates, however, show that even for very low rain rates the buoyancy flux due to freshwater input is stronger than the counterparts due to the thermal convection and evaporative surface salinity increase. Under low wind-speed and rainy conditions Rf_0 easily becomes zero, leading to very high values of t_{*f}. Below a certain rain rate (~ 0.1 mm h^{-1}) the buoyancy effect inhibits the additional mixing due to rain, while, the additional mixing due to rain prevails at larger rain rates.

The analysis of Fig. 2.33 also suggests that the contribution of the volume freshwater flux into the diffusion molecular sublayer (freshwater skin) is relatively small compared to that of the surface freshwater flux. The contribution of the volume source into the freshwater skin is negligible in most cases.

2.6.5 Rain Effects on Sea Surface Roughness

Disruptions of the sea surface produced by rain increase the sea surface roughness. The Rayleigh-jet columns, together with the raindrops on their tops and the wavelets radiated from the drop impact zones, are roughness elements that can increase the surface roughness beyond the wind-induced roughness. The roughness elements produced by the rain do not propagate as the wind-induced waves do and therefore resemble fixed obstacles such as roughness elements on land surfaces.

The molecular sublayers of the surface ocean are mainly controlled by the tangential shear stress. The flow above the surface is aerodynamically smooth as long as the height of the roughness elements is smaller than $5\nu/u_*$, where ν is the kinematic viscosity and u_* is the friction velocity of the air (Schlichting 1979). In the aerodynamically smooth flow, the momentum is passed to the ocean by skin friction only. If the roughness elements are greater than $70\nu/u_*$, the flow is aerodynamically rough, and the momentum transfer is affected by the form drag. Figure 2.34a shows the smooth and rough regimes as a function of friction velocity. There is a transition zone between these regimes, where both skin and form drag are important. The Rayleigh-jet that extends a centimeter or more into the air (Siscoe and Levin 1971) therefore affects form drag, except for situations with very low friction velocities when the thickness of the viscous sublayer increases without bound.

Engel (1966) proposed a formula for the maximum height of the waves directly adjacent to the impact craters generated by drop impacts:

$$h_{w,\max} = \alpha_0 \left(\left[\alpha_1 \frac{r_0^3 \rho_r w_t^2}{g\rho} + \alpha_2 \frac{\sigma_s^{\,2}}{g^2 \rho^2} \right]^{1/2} - \alpha_3 \frac{\sigma_s}{g\rho} \right)^{1/2} \tag{2.121}$$

where σ_s is the surface tension of the sea surface, $\alpha_0 = 33.33$, $\alpha_1 = 1.2 \times 10^8$, $\alpha_2 = 3.1149 \times 10^{10}$, and $\alpha_3 = 1.7649 \times 10^5$. Figure 2.34a shows dependence of $h_{w,\max}$ on the drop radius (2.121) with the terminal velocity parameterized according to (2.111); the flow is smooth no matter what the drop size is for very small fric-

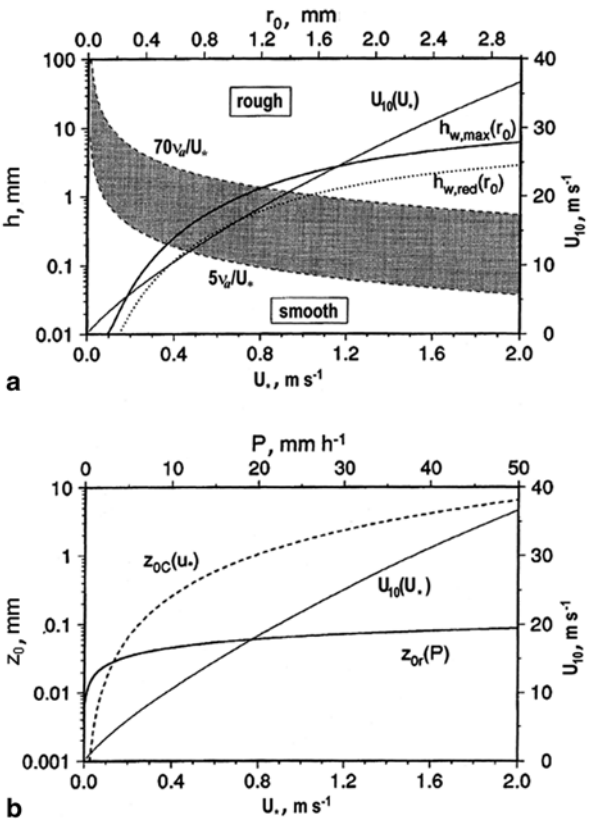

Fig. 2.34 **a** Separation of aerodynamically smooth and rough domains (dashed curves) with the transition region indicated by the hashed area, maximum ($h_{w,max}(r_0)$, solid) and reduced ($h_{w,red}(r_0)$, dotted) heights of the rain-induced wavelets depending on drop radius r_0 and the relation between wind speed u_{10} and friction velocity of the air u_* (thin solid); **b** roughness length z_0 of wind-roughed surface (dashed) and rain-induced wavelets (solid) as a function of friction velocity of air u_* and rain rate R, respectively, as well as the relation between wind speed and friction velocity (thin solid). Note: axes on opposite sides are not independent. (After Schlüessel et al. (1997). Reproduced with permission from Springer Science and Business Media)

tion velocities owing to the unbounded increase in the viscous sublayer thickness. With increasing friction velocities, drops with radii greater than about 1 mm lead to waves that cause a rather rough flow, while waves produced by smaller drops do not disturb the flow smoothness.

Smooth surface waves contribute to the surface roughness in a different way compared to random roughness elements. According to Motzfeld's (1937) experiment in a wind tunnel, the drag coefficient at a height of 0.2 m over surface waves is about seven times smaller than that over a surface with rough elements of the same size. Schlüessel et al. (1997) estimated that under the assumption of a logarithmic wind profile this implies a reduction of the roughness length of the rain-induced wavelets by a factor of 0.4 when compared to the roughness length of random rough elements of the same height. This effect leads to some increase in the wave height above which the flow becomes rough shown by the curve labeled $h_{w,red}(r_0)$ in Fig. 2.34a. Taking into account the Marshall–Palmer drop-size distribution (1.64) an upper limit of the mean height of the wavelets is estimated from the formula

$$\bar{h}_{w,red}(P) = \int_{r_c}^{\infty} h_{w,red} n_0 \exp(2\Lambda r_0)\, dr_0 \Big/ \left(\int_{r_c}^{\infty} n_0 \exp(2\Lambda r_0)\, dr_0 \right) \qquad (2.122)$$

Formula (2.122) implies that the rain-induced waves do not decay and uniformly cover the sea surface. Equation (2.122) has been resolved substituting (2.112) into (2.121) and subsequently approximating

$$h_{w,red} = \beta_0 + \beta_1 r_0^{3/4}(1 - \beta_2 \exp(-r_0 / r_\upsilon)), \tag{2.123}$$

where $\beta_0 = 0.0129$ mm, $\beta_1 = 1.60686\ \text{mm}^{1/4}$, and $\beta_2 = 1.0978$. The resulting relationship is

$$\begin{aligned}\overline{h}_{w,red}(R) = \beta_0 + \Big\{&\beta_1 (2\upsilon)^{-7/4}\Gamma(7/4, 2\Lambda r_c) \\ &+ \beta_2 (r_\upsilon^{-1} + 2\Lambda)^{-7/4}\Gamma(7/4, (r_\upsilon^{-1} + 2\Lambda) r_c)\Big\} 2\Lambda \exp(2\Lambda r_c).\end{aligned} \tag{2.124}$$

Figure 2.34b shows the roughness length calculated for the rain-induced wavelets using a coarse estimate given by Lettau (1969) as $z_{0r} \approx 0.058\overline{h}_{w,red}^{1.19}$. For comparison purposes, the roughness length z_{0C} of the wind-induced surface roughness under neutral conditions according to Charnock's (1955) formula is also given on this composite plot. The above estimate for the rain-induced roughness length is the maximum possible value, requiring an optimal drop impact and a surface uniformly covered with rain-induced wavelets. Wave interactions, which have been neglected here, likely result in greater wave heights.

The rain-induced roughness increases strongly with rain rates up to about 2 mm h^{-1}, while at higher rain rates z_{0r} increases only slightly (Fig. 2.34b). Only for air friction velocity less than approximately 0.15 m s^{-1} can the rain-induced waves appreciably contribute to the surface roughness. Charnock's (1955) formula employed for the calculation of z_{0C} in Fig. 2.34b, however, does not work under low wind-speed conditions. In fact, due to viscous effects, the surface roughness under low wind stresses increases with decreasing wind.

Figure 2.34b exhibits considerable differences in the rain-induced roughness lengths compared to those from laboratory studies by Houk and Green (1976). This is because of a more realistic raindrop spectrum employed by Schlüessel et al. (1997), which also covers many small, submillimeter drops, while in the laboratory the effect of large drops (several millimeters in diameter) had been mainly investigated. The large drops in fact cover a very small portion of the natural spectrum of raindrops (Pruppacher and Klett 1978).

The rain-induced stress leads, together with the wind stress, to increased surface wind-drift currents. This effect coexists with the attenuation of short gravity waves by enhanced turbulence in the upper ocean during rainfall (Tsimplis and Thorpe 1989). The rain-induced wind-drift currents also reduce the amplitude threshold at which short gravity waves break (Philips and Banner 1974).

From investigations in a wind–wave tank, Poon et al. (1992) found that gravity waves in the frequency range between 2 and 5 Hz decay during rainfall. At the same time, the spectral density of wave slopes in the frequency domain between 10 and 100 Hz drastically increases. The latter effect is due to rain-induced waves; however, it is pronounced only under low wind-speed conditions. The results of experi-

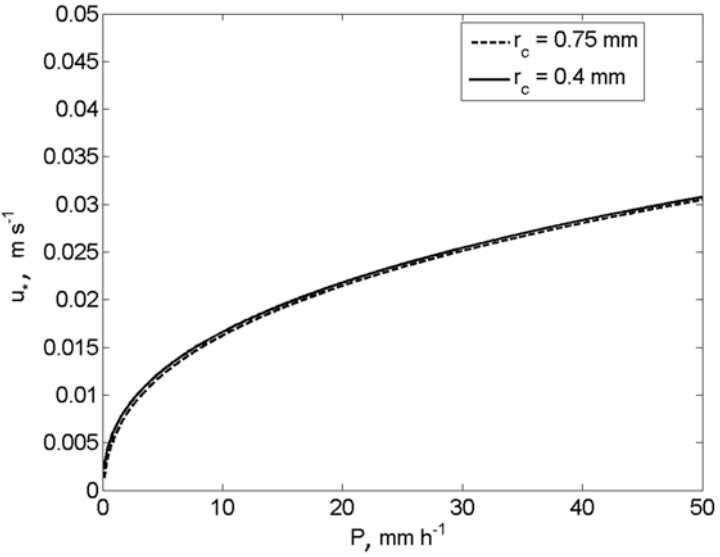

Fig. 2.35 Friction velocity in the upper ocean attributed to the flux of kinetic energy carried by rain as function of rain rate for two values of critical radii r_c calculated from (2.130). (After Schlüssel et al. 1997)

ments in a wind–wave tank by Yang et al. (1997) are consistent with the Poon et al. (1992) findings but provided some more details to the rain effects on fine structure of wind waves.

Due to damping of short gravity waves, a substantial part of the momentum transferred to the ocean by form drag under non-precipitating situations is instead transferred by skin friction during rainfall. This results in decrease of the surface renewal time, which is concurrent with the damping of short gravity waves.

2.6.6 Flux of Kinetic Energy Carried by Rain

According to Tsimplis (1992), the flux of kinetic energy carried by rain with a uniform drop size distribution is

$$F_k = \frac{1}{2}\rho P w_t^2. \tag{2.125}$$

In order to include the effect of natural drop size distributions, Craeye and Schlüssel (1998) introduced the spectral rain rate falling on the sea surface

$$\frac{dP}{dr_0} = \frac{4}{3}\pi r_0^3 n(r_0) w_t \tag{2.126}$$

which leads to a kinetic energy flux of

$$F_k = \frac{2}{3}\pi\rho\int_{r_c}^{\infty} r_0^3 n(r_0) w_t^3 dr_0. \tag{2.127}$$

For rain with a drop size distribution (1.64) and terminal velocities described by (2.112) the kinetic energy flux is then determined by

$$\begin{aligned} F_k = {} & \frac{2}{3}\pi\rho n_0 \int_{r_c}^{\infty} r_0^3 \left[b_1^3 \exp(-2\Lambda r_0) - 3b_1^2 b_2 \exp\left(-\left(2\Lambda + r_\upsilon^{-1}\right) r_0\right) \right. \\ & \left. + 3b_1 b_2^2 \exp\left(-\left(2\Lambda + 2v r_\upsilon^{-1}\right) r_0\right) - b_2^3 \exp\left(-\left(2\Lambda + 3r_\upsilon^{-1}\right) r_0\right)\right], \end{aligned} \tag{2.128}$$

where only drops entering the ocean ($r_0 > r_c$) are considered. The solution is

$$\begin{aligned} F_k = {} & \frac{2}{3}\pi\rho n_0 w_\upsilon{}^3 \left[\frac{b_1^3}{(2\Lambda)^4}\Gamma(4, 2\Lambda r_c) - \frac{3b_1^2 b_2}{\left(2\Lambda + r_\upsilon^{-1}\right)^4}\Gamma\left(4, 2\Lambda + \frac{r_c}{r_\upsilon}\right) \right. \\ & \left. + \frac{3b_1 b_2^2}{\left(2\Lambda + 2r_\upsilon^{-1}\right)^4}\Gamma\left(4, 2\Lambda r_c + \frac{2r}{r_\upsilon}\right) - \frac{b_2^3}{\left(2\Lambda + 3r_\upsilon^{-1}\right)^4}\Gamma\left(4, 2\Lambda r_c + \frac{3r_c}{r_\upsilon}\right)\right] \end{aligned} \tag{2.129}$$

The equivalent friction velocity scale in the upper ocean is

$$u_{*r} = \left(F_k / \rho\right)^{1/3} \tag{2.130}$$

Figure 2.35 shows the friction velocities corresponding to the flux of kinetic energy carried by the rain as a function of rain rate for two critical radii r_c. The friction velocity in water u_* reaches 3 cm s^{-1} at $P = 50$ mm h^{-1}.

2.6.7 Combined Effect

The enhancement of the near-surface mixing by rain is estimated by accounting for the area impacted by the raindrops of given rain rate and size distribution. It turns out that the interval between rain-induced surface renewal events can be far shorter than for wind-generated renewal events, which strongly reduces the temperature difference across the cool skin. However, for small rain rates this can be counteracted by the density stratification caused by the freshwater input. Subsequently, the extra momentum carried by the rain to the surface is accounted for, and the creation of additional surface roughness by rain-induced waves is estimated. The enhanced surface stress causes increased wind-drift currents, which, according to laboratory observations, can reduce the amplitude threshold for short gravity waves to break. This effect is parameterized as a function of rain rate. The rain-induced changes of

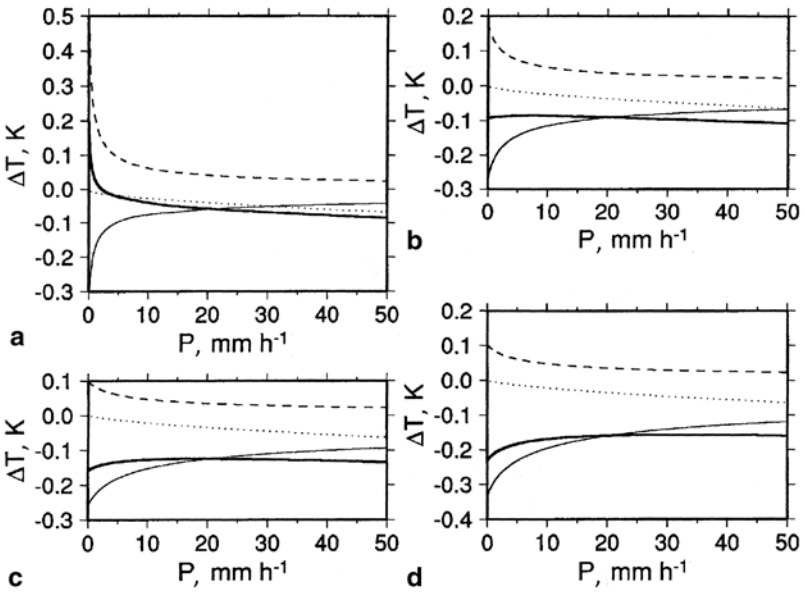

Fig. 2.36 Temperature differences across the thermal molecular sublayer as a function of rain rate for **a** $U_{10} = 1$ m s^{-1}, **b** $U_{10} = 5$ m s^{-1}, **c** $U_{10} = 10$ m s^{-1}, and **d** $U_{10} = 15$ m s^{-1}. The curves correspond to differences due to cooling by turbulent and long wave fluxes (thin solid line), warming due to the absorption of solar radiation (dashed line), rain-induced cooling (dotted line) and the combined effect (thick solid line). (After Schlüessel et al. 1997. Reproduced with permission from Springer Science and Business Media)

physical properties of seawater become important at low wind speeds, while the effect of surface film fragmentation and removal by rain is believed to be negligible in affecting the molecular sublayer (Schlüessel et al. 1997).

Schlüessel et al. (1997) incorporated all of the effects described above in a surface renewal model in order to study the combined effect of the processes involved in the physics of the aqueous molecular sublayers at the ocean surface. Figure 2.36 shows temperature differences for wind speeds of $U_{10} = 1, 5, 10, 15$ m s^{-1} for an air–sea temperature difference of 1 °C, a dew point difference of 6 K, a net longwave radiative flux of 70 W m^{-2}, and a solar irradiance of 1,000 W m^{-2}. (Note that fixing the radiative fluxes as done here is unrealistic, but is done to illustrate the physics. As wind and rain rate increase, clouds will change, certainly affecting both shortwave and longwave components.) The turbulent heat fluxes are calculated from the TOGA COARE bulk flux algorithm version 2.5b (Fairall et al. 1996). For the situations simulated, the corresponding latent and sensible heat fluxes are $Q_E = 33, 107, 186, 252$ W m^{-2} and $Q_T = 2, 7, 11, 14$ W m^{-2}. The rain temperature is assumed equal to the wet-bulb temperature calculated from the psychometric equation; its value is $T_r = 20.6$ °C when compared to the surface temperature of $T_0 = 25$ °C.

Figure 2.36 suggests that the most pronounced effect is due to additional mixing caused by the rain. This is observed at low rain rates where the rather high tempera-

ture differences prevailing in the non-precipitating situations quickly drop to low values when the rain rate increases to a few mm h^{-1}. However, with further rain rate increase the temperature difference weakens. It is remarkable that the temperature differences do not vanish even for precipitation rates of 50 mm h^{-1}. The additional skin cooling by the rain increases with rain rate though it does not exceed –0.1 K. At low wind speeds and very low rain rates the combined effect of solar warming and cooling by the turbulent and longwave fluxes results in a warm skin. At higher wind speeds, the combined effect shows a minimum skin cooling at a distinct rain rate, which depends on the actual friction velocity. Further increasing rain rates lead to a slightly enhanced cooling due to the rain-induced heat flux (Fig. 2.36b–d).

2.6.8 Comparison with Data

The surface renewal model including the precipitation component described above has been tested by Schlüessel et al. (1997) with the COARE data taken from the R/V *Vickers* in January–February 1993 near 156 °E, 2 °S and from the R/V *Wecoma* near 156 °E, between 2 °S and 5 °N (Fig. 2.37). The frequent convective rain in the western equatorial Pacific shows strong variability with rain rates ranging from less than 0.1 to more than 100 mm h^{-1}; this tests the parameterization under a great variety of situations.

The R/V *Vickers* surface fluxes in the Schlüessel et al. (1997) comparison were identical to those shown in Fig. 2.31. The calculated temperature differences across the cool skin that were caused by surface and volume cooling due to the rain showed values generally below 0.05 °C; only one case with heavy precipitation exceeding 100 mm h^{-1} gave a cooling by more than 0.1 °C. There were just a few cases with strong daytime precipitation; during these rare periods the solar warming of the skin was about halved, according to the model. During nighttime the net effect of rain on the cool skin was rather small. Apart from several cases with strong rain when the cool skin was reduced by rain-induced mixing to values below 0.1 °C, the effects of mixing and additional cooling partly canceled each other during this observation in the western equatorial Pacific Ocean.

Similar to the analysis shown in Fig. 2.31a, quantitative comparison of the parameterization with measurements of the skin versus bulk temperature difference from the R/V *Vickers* required that the temperature difference between the bulk sampling depth (i.e., the depth of the thermosalinograph intake) and the surface microlayer was accounted for. This temperature difference was calculated with the mixed-layer model of Price et al. (1986) (PWP).

The overall agreement of the cool-skin parameterization including rain is slightly better when compared to the results presented in Fig. 2.31. While the RMS error remains unchanged (0.17 °C), the small bias of 0.03–0.02 °C found earlier (Table 2.2) has now vanished completely. This is also true for the night and daytime data considered separately. In view of the skin measurement errors and the relatively small amount of data (total sample size of hourly means is 578) the result of this com-

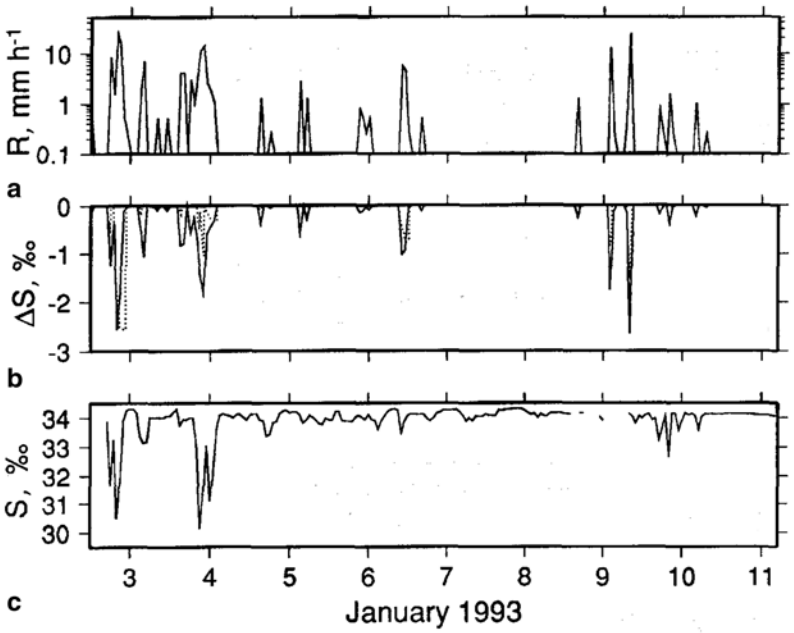

Fig. 2.37 Parameterization of the freshwater skin during raining episodes of COARE; **a** hourly mean rain rates, **b** calculated hourly mean salinity difference across the haline molecular layer (solid) and across the upper part of the mixed layer (dotted), **c** hourly mean salinity of water collected from the upper 2–3 cm of the ocean; the labels of the time axis identify the end of the days in UT. (After Schlüessel et al. 1997. Reproduced with permission from Springer Science and Business Media)

parison is rather an indication that the inclusion of the rain parameterization in the surface renewal model is useful.

Paulson and Lagerloef (1993) performed a pilot study of the near-surface salinity under rainy conditions in the tropical Pacific Ocean near 156 °E and between 2 °S and 5 °N. From the R/V *Wecoma* during COARE leg 2, they collected surface water from the upper 2–3 cm of the ocean with a scoop and hose. The temperature and salinity of the water were measured with a thermosalinograph. The salinity measurements were accompanied by detailed measurements of surface meteorological parameters including rain rates and downwelling shortwave and longwave radiation. Schlüessel et al. (1997) averaged these data sets over hourly intervals and used them with the surface renewal model to estimate the parameters of the freshwater skin of the ocean.

Figure 2.37 shows time series of the rain rate, the salinity difference across the freshwater skin, and the salinity measured at the surface for a rainy time period in January 1993. The direct comparison of the model and field data is not feasible because the model calculation is for the freshwater skin (the upper few tens of micrometers of the ocean only), while the measured salinities include surface water from the upper few centimeters.

Schlüssel et al. (1997) assumed that the freshwater skin layer must account for the greater part of the observed salinity changes because even heavy rainfall (≈ 60 mm h^{-1}) alters the salinity in the upper mixed layer by less than 1 psu (Kantha and Clayson 1994). Because the wind speeds during this experiment were rather low, the salinity changes in the mixed layer can be expected to be slightly higher. Calculations with the model of Price et al. (1986) show maximum differences exceeding 2 psu over the top half meter on 3 January that are of the same magnitude as the difference across the freshwater skin. The observed salinity changes on this day are up to 4 psu (some of this signal may, however, be associated with nonlocal rain).

For other rainfall events during this time series, the observed salinity differences in the mixed layer are generally smaller than those across the skin. A full explanation of the salinity deficits measured can only be given by considering the combined differences across the skin and mixed layers, which has not yet been done.

2.6.9 Discussion

Of the various processes that can modify the molecular layers during rainfall, the most important appears to be the rain-induced mixing that leads to enhanced surface renewals and the additional surface and volume cooling by raindrops with temperatures below the SST. Simulations with the renewal model have shown that the additional surface cooling by rain could exceed 1 °C, if the rain did not affect the surface renewal time. Nevertheless, the additional mixing and the implied increase in renewal frequencies limit the effect to less than 0.1 °C when the rainwater is 5 K cooler than the sea surface. The more impressive effect is the creation of a haline molecular diffusion layer during rainfall—a freshwater skin of the ocean—that exhibits salinity differences greater than 4 psu during strong rains.

Since laboratory studies overemphasized large drops that are a small fraction of the natural raindrop spectrum, the calculations of the rain-induced surface roughness for a realistic drop size spectrum show that this effect has been overestimated in the past (Houk and Green 1976). The wind-induced surface roughness is more important than that caused by rain except during low wind-speed conditions.

The application of the cool-skin parameterization, including the rain component, to the field measurements taken during COARE, shows some additional surface cooling that is still generally less than 0.1 °C. The cooling and mixing effects of the rainfall on the molecular sublayer partly compensate each other so that the net effect on the temperature difference almost vanishes. Nevertheless, the measured bulk versus skin temperature difference across the cool skin shows a reduction of systematic deviations of parameterized from measured differences when the rain effects are included. The errors in the measured parameters and parameterization of the turbulent surface fluxes that enter the surface renewal and mixed layer models, however, prevent a statistically significant improvement between the measured and parameterized cool skin. The salinity changes during rainfall observed in the upper

2–3 cm of the ocean can only be explained when the salinity difference across the haline molecular diffusion layer is included.

Studies of rain impacts on the sea surface have been limited to a single rain drop-size distribution, namely the Marshall–Palmer distribution. While this limitation is due to the fact that it is a distribution based on the rain rate as the only available rain parameter (which is really not a justification), the effects induced by a more precise drop-size distribution should be assessed. Further work is necessary to analyze the effect of high-latitude types of precipitation on the molecular boundary layers. For example, snowfall certainly leads to enhanced surface cooling without much volume flux, while hail falling on the sea surface penetrates deeper into the ocean than rain but subsequently returns to the surface. Precipitation in the form of hail results in more complicated surface and volume fluxes, because of a prolonged decay time compared to rain or snow.

References

Antonia RA, Chambers AJ, Friehe CA, Van Atta CW (1979) Temperature ramps in the atmospheric surface layer. J Atmos Sci 36:99–108

Asher WE, Atmane MA, Jessup AT (2005) An application of a surface penetration model to air-water gas transfer. 37th International Liège Colloquium on Ocean Dynamics (2–6 May 2005) gas transfer at water surfaces (abstract only)

Azizjan GV, Volkov YA, Soloviev AV (1984) Experimental investigation of vertical thermal structure of thin boundary layers of the sea and atmosphere. Atmos Ocean Phys 20(6):511–519

Baier RE, Goupil DW, Perlmutter S, King R (1974) Dominant chemical composition of sea surface films, natural slicks and foams. J de Rech Atmos 8:571–600

Banner ML, Peregrine DH (1993) Wave breaking in deep water. Annu Rev Fluid Mech 25:373–397

Banner ML, Peirson WL (1998) Tangential stress beneath wind-driven air-water interface. J Fluid Mech 364: 107–137

Banner ML, Phillips OM (1974) On the incipient breaking of small scale waves. J Fluid Mech 65:647–656

Benjamin TB (1960) Effects of a flexible boundary on hydrodynamic stability. J Fluid Mech 9:513

Benjamin TB (1963) The threefold classification of unstable disturbances in flexible surfaces bounding in viscid flows. J Fluid Mech 16:436–450

Best A (1950) The size distribution of raindrops. Q J Roy Meteor Soc 76:16–36

Bock EJ, Frew NM (1993) Static and dynamic response of natural multicomponent oceanic surface films to compression and dilation: laboratory and field observations. J Geophys Res 98:14599–14617

Bolin B (1960) On the exchange of carbon dioxide between atmosphere and sea. Tellus 12(3):274–281

Broecker WS, Peng TH, Stuiver M (1978) An estimate of the upwelling rate in the equatorial Atlantic based on the distribution of bond radiocarbon. J Geophys Res 83(C12):6179–6186

Caldwell DR, Elliott WH (1971) Surface stresses produced by rainfall. J Phys Oceanogr 1:145–148

Caulliez G, Makin V, Kudryavtsev V (2008) Drag of the water surface at very short fetches: observations and modeling. J Phys Oceanogr 38:2038–2055

Cember R (1989) Bomb radiocarbon in the Red Sea: A medium scale gas exchange experiment. J. Geophys Res 94: 2111-2123

Charnock H (1955) Wind stress on a water surface. Q J Roy Meteor Soc 81:639–640

Cox C (2001) Sea surface micro-structure: relation to air-sea fluxes, bubble transport and electromagnetic wave radiation. SIO Report A969093, La Jolla, CA
Craeye C, Schlüssel P (1998) Rainfall on the sea: surface renewal and wave damping. Bound-Lay Meteorol 89:349–355
Csanady GT (1978) Turbulent interface layers. J Geophys Res 83:2329–2342
Csanady GT (1990) The role of breaking wavelets in air-sea gas transfer. J Geophys Res 95:749–759
Cunliffe M, Murrell JC (2009) The sea surface microlayer is a gelatinous biofilm. ISME J 3: 1001–1003
Cunliffe M, Upstill-Goddard RC, Murrell JC (2011) Microbiology of aquatic surfacemicrolayers. FEMS Microbiol Rev 35:233–246
Dhanak MR, Si C (1999) On reduction of turbulent wall friction through spanwise wall oscillations. J Fluid Mech 383:175–195
Dickey TD, Hartman B, Hammond D, Hurst E. (1984) A laboratory technique for investigating the relationship between gas transfer and fluid turbulence. In: Gas Transfer at Water Surfaces, W. Brutsaert and G.H. Girka, Eds.: 93-100
Doney SC (1995) Irreversible thermodynamics and air-sea exchange. J Geophys Res 100:8541–8553
Ebuchi N, Kawamura H, Toba Y (1987) Fine structure of laboratory wind-wave surfaces using an optical method. Bound-Lay Meterol 39:133–151
Engel OG (1966) Carter depth in fluid mechanics. J Appl Phys 37:1798–1808
Fairall CW, Bradley EF, Rogers DP, Edson JB, Young GS (1996) Bulk parameterization of air-sea fluxes in TOGA COARE. J Geophys Res 101: 3747–3767
Fairall CW, Hare JE, Edson JB, McGillis W (2000) Parameterization and micrometeorological measurements of air-sea gas transfer. Bound Layer Meteorol 96: 63-105.
Fedorov KN, Ginzburg AI (1988) The near-surface layer of the ocean, Hydrometeoizdat, Leningrad. Translated into English in 1992 by VSP, P.O. Box 346, 3700 AH Zeist, The Netherlands
Fedorov KN, Vlasov VL, Ambrosimov AK, Ginzburg AI (1979) Investigating the surface layer of evaporating sea water by optical interferometry. Izvestya, Academy of Sciences, USSR, Atmospheric and Oceanic Physics 15:742–747
Fiedler L, Bakan S (1997) Interferometric measurements of sea surface temperature and emissivity. German J Hydrogr 49(2/3):357–365
Flack KA, Saylor JR, Smith GB (2001) Near-surface turbulence for evaporative convection at an air-water interface. Phys Fluids 13:3338
Foster TD (1971) Intermittent convection. Geophys Fluid Dyn 2:201–217
Franklin MP, McDonald IR, Bourne DG, Owens NJ, Upstill-Goddard RC, Murrell JC (2005) Bacterial diversity in the bacterioneuston (sea surface microlayer): the bacterioneuston through the looking glass. Environ Microbiol 7:723–736
Frew NM (1997) The role of organic films in air–sea exchange. In: Liss PS, Duce RA (eds) The sea surface and global change. Cambridge Univ. Press, New York, pp 121–172
Garrett WD (1965) Collection of slick-forming materials from the sea surface. Limnol Oceanogr 10:602–605
Caulliez G, Makin V, Kudryavtsev V (2008) Drag of the Water Surface at Very Short Fetches: Observations and Modeling. J Phys Oceanogr 38: 2038–2055
Ginzburg AI, Zatsepin AG, Fedorov KN (1977) Fine structure of the thermal boundary layer in the water near the air-water interface. Izvestya, Academy of Sciences, USSR, Atmospheric and Oceanic Physics 13:869–875
Gladyshev MI (1997) Biophysics of the sea surface film of aquatic ecosystems. In: Liss PS, Duce RA (eds) The sea surface and global change. Cambridge University Press, UK, pp 321–338
Glazman RE, Greysukh A (1993) Satellite altimeter measurements of surface wind. J Geophys Res 98:2475–2483
Grassl H (1976) The dependence of measured cool skin of the ocean on wind stress and total heat flux. Bound Lay Meteorol 10:465–474

Green T, Houk DF (1979) The removal of organic surface films by rain. Limnol Oceanogr 24:966–970
Hardy JT (1982) The sea-surface microlayer: biology, chemistry and anthropogenic enrichment. Prog Oceanogr 11:307–328
Hardy JT, Hunter KA, Calmet D, Cleary JJ, Duce RA, Forbes TL, Gladyshev ML, Harding G, Shenker JM, Tratnyek P, Zaitsev Y (1997) Report group 2–biological effects of chemical and radiative change in the sea surface. In: The Sea Surface and Global
Hare JE, Fairall CW, McGillis WR, Edson JB, Ward B, Wanninkhof R (2004) Evaluation of the National Oceanic and Atmospheric Administration/Coupled-Ocean Atmospheric Response Experiment (NOAA/COARE) air-sea gas transfer parameterization using GasEx data. J Geophys Res 109:C08S11
Harvey GW, Burzell LA (1972) A simple microlayer method for small samples. Limnol Oceanogr 11:156–157
Hasse L (1971) The sea surface temperature deviation and the heat flow at the air-sea interface, Bound. Layer Meteor 1: 368-379
Horrocks LA, Candy B, Nightingale T, Saunders RW, O'Carroll AG, Harris AR (2003) Parameterisations of the skin effect and implications for satellite-based measurement of sea-surface temperature. J Geophys Res 108:3096
Houk DF, Green T (1976) A note on surface waves due to rain. J Geophys Res 81:4482–4484
Howard LN (1961) Note on a paper of John Miles. J Fluid Mech 10:509–512
Howard LN (1966) Convection at high Rayleigh number. Proc of the Eleventh Intern. Congress of Applied Mechanics, Munich, pp 1109–1115
Hühnerfuss H, Walter W, Lange PA, Alpers W (1987) Attenuation of wind waves by monomolecular sea slicks and the Marangoni effect. J Geophys Res 92(4):3961–3963
Jessup AT, Zappa CJ, Yeh HH (1997) Defining and quantifying microscale wave breaking with infrared imagery. J Geophys Res 102(C10):23,145–23,154
Kantha LH, Clayson CA (1994) An improved mixed layer model for geophysical applications. J Geophys Res 99:25,235–25,266
Kanwisher J (1963) Effect of wind on CO2 exchange across the sea surface. J Geophys Res 68(13):3921–3927
Katsaros KB (1976) Effect of precipitation on the eddy exchange in a wind-driven sea. Dynam Atmos Oceans 1:99–126
Katsaros KB (1980) The aqueous thermal boundary layer. Bound Layer Meteorol 18:107–127
Katsaros KB, Buettner KJK (1969) Influence of rainfall on temperature and salinity of the ocean surface. J Appl Meteorol 8:15–18
Katsaros KB, Liu WT, Businger JA, Tillman JE (1977) Heat transport and thermal structure in the interfacial boundary layer measured in an open tank of water in turbulent free convection. J Fluid Mech 83:311–335
Kim HT, Kline SJ, Reynolds WC (1971) The production of turbulence near a smooth wall in a turbulent boundary layer. J Fluid Mech 50:133–160
Kim J, Moin P, Moser R (1987) Turbulence statistics in fully developed channel flow at low Reynolds number. J Fluid Mech 177:133–166
Kitaigorodskii SA, Donelan MA (1984) Wind-wave effects on gas transfer, In: Gas Transfer at the Water Surfaces, W. Brutseart and G.H. Jirka, Eds., Reidel: 147-170
Kjelleberg S, Stenstrom TA, Odham G (1979) Comparative study of different hydrophobic devices for sampling liquid surface films and adherent microorganisms. Mar Biol 53:21–25
Kline SJ, Reynolds WC, Schraub FA, Runstadler PW (1967) The structure of turbulent boundary layers. J. Fluid Mech 30: 741–773
Kolmogorov AN (1942) Equations of turbulent motion of an incompressible fluid. Izvestia, Academy of Sciences, USSR; Physics 6(1) & (2): 56-58
Kudryavtsev VN, Soloviev AV (1985) On parameterization of cool skin of the ocean. Izvestia, Atmos Ocean Phys 21(2):177–183
Kurata N (2012) Sea Surface Microlayer Microbial Observation System. MS Degree Thesis. Nova Southeastern University Oceanographic Center, Dania Beach, Florida, pp 45

Kurata N, Vella K, Soloviev A, Matt S, Tartar A, Shivji M, Perrie W. (2013)Surfactant-Associated Bacteria in the Near Surface Layer of the Ocean. Geophysical Research Abstracts 15, EGU2013-13199, EGU General Assembly, pp. 1

Lagerloef GSE, Swift CT, Le Vine DM (1995) Sea surface salinity: the next remote sensing challenge. Oceanography 8:44–50

Lesieur M (2008) Turbulence in fluids, Fourth Revised and Enlarged Edition. Springer pp 148

Lettau H (1969) Note on aerodynamic roughness-parameter estimation on the basis of roughness-element description. J Appl Meteorol 8:828–832

Liss PS (1983) Gas transfer, experiments, and geochemical implications. In: Liss PS, Slinn GN (eds) Air-sea exchange of gases and particles. D. Reidel, Dordrecht, pp 241–298

Liss PS, Duce RA (1997) Preface. In: Liss PS, Duce RA (eds) The sea surface and global change. Cambridge University Press, UK, pp XIII-XV

Liss PS, Watson AJ, Bock EJ, Jaene B, Asher WE, Frew NM, Hasse L, Korenowski GM, Merlivat L, Phillips LF, Schlüssel P, Woolf DK (1997) Report group 1—physical processes in the microlayer and the air-sea exchange of trace gases. In: Liss PS, Duce RA (eds) The sea surface and global change. Cambridge University Press, UK, pp 1–34

Liu WT, Businger JA (1975) Temperature profile in the molecular sublayer near the interface of fluid in turbulent motion. Geophys Res Lett 2:403–404

Longuet-Higgins MS (1992) Capillary rollers and bores. J Fluid Mech 240:659–679

Mammen TC, Bosse N von (1990) STEP – a temperature profiler for measuring the oceanic thermal boundary layer at the ocean-air interface. J Atmos Ocean Tech 7:312–322

Manton MJ (1973) On the attenuation of sea waves by rain. Geophys Fluid Dynam 5:249–260

Matt S, Soloviev A, Rhee S (2011) Modification of turbulence air-sea interface due to the presence of surfactants and implications for gas exchange. Part II: numerical simulations. In: Gas Transfer at Water Surfaces, Kyoto University Press, pp 299–312

McAlister ED, McLeish W (1969) Heat transfer in the top millimeter of the ocean. J Geophys Res 74:3408–3414

McLeish W, Putland GE (1975) Measurements of wind-driven flow profiles in the top millimeter of water. J Phys Oceanogr 5:516–518

Melville WK (1996) The role of surface-wave breaking in air-sea interaction. Ann Rev Fluid Mech 28:279–321

Le Méhauté Bernard, Tarang Khangaonkar (1990) Dynamic interaction of intense rain with water waves. J Phys Oceanogr 20:1805–1812

Minnett PJ (2003) Radiometric measurements of the sea-surface skin temperature – the competing roles of the diurnal thermocline and the cool skin. Int J Remote Sens 24(24):5033–5047

Minnett PJ, Knuteson RO, Best FA, Osborne BJ, Hanafin JA, Brown OB (2001) The Marine-Atmosphere Emitted Radiance Interferometer (M-AERI), a high-accuracy, sea-going infrared spectroradiometer. J Atmos Ocean Tech 18:994–1013

Motzfeld H (1937) Die turbulente Stromung an welligen Wanden. Z Angew Math Mech 17:193–212

Nightingale PD, Malin G, Law CS, Watson AJ, Liss PS, Liddicoat MI, Boutin J, Upstill-Goddard RC (2000) In situ evaluation of air-sea gas exchange parameterizations using novel conservative and volatile tracers. Glob Biogeochem Cy 14: 373-387

Okuda K (1982) Internal flow structure of short wind waves, Part I. The vorticity structure. J Oceanogr Soc Japan 38:28–42

Ostapoff F, Tarbeyev Y, Worthem S (1973) Heat flux and precipitation estimates from oceanographic observations. Science 180:960–962

Paulson CA, Lagerloef GSE (1993) Fresh surface lenses caused by heavy rain over the western Pacific warm pool during TOGA COARE. EOS Trans AGU 74(Suppl. to No. 43):125

Paulson CA, Simpson JJ (1981) The temperature difference across the cool skin of the ocean. J Geophys Res 86:11,044–11,054

Peng TH, Takahashi T, Broecker WS (1974) Surface radon measurements in the North Pacific Ocean station PAPA. J Geophys Res 79:1772–1780

Peng TH, Breocker WS, Mathieu GG, Li YH, Bainbrige EA (1979) Radon evasion rates in the Atlantic and Pacific Ocean as determined during the GEOSECS program. J Geophys Res 84:2471–2486

Phillips OM, Banner ML (1974) Wave breaking in the presence of wind drift and swell. J Fluid Mech 66:625–640
Phongikaroon S, Judd KP, Smith GB, Handler RA (2004) Thermal structure of clean and contaminated free-surfaces subject to an impinging gas jet. Exp Fluids 37(2):153–158
Plane JMC, Blough NV, Ehrhardt MG, Waters K, Zepp RG, Zika RG (1997) Report Group 3—Photochemistry in the sea-surface microlayer. In: Liss PS, Duce RA (eds) The sea surface and global change. Cambridge University Press, UK, pp 71–92
Poon Y-K, Tang S, Wu J (1992) Interactions between wind and waves. J Phys Oceanogr 22:977–987
Price JF, Weller RA, Pinkel R (1986) Diurnal cycling: observations and models of the upper ocean response to diurnal heating, cooling, and wind mixing. J Geophys Res 91:8411–8427
Prosperetti A, Oguz HN (1993) The impact of drops on liquid surfaces and the underwater noise of rain. Ann Rev Fluid Mech 25:577–602
Pruppacher HR, Klett JD (1978) Microphysics of clouds and precipitation. D. Reidel Publishing Company, Dordrecht, 714pp
Pumphrey HC, Elmore PA (1990) The entrainment of bubbles by drop impacts. J Fluid Mech 220:539–567
Robinson SK (1991) Coherent motions in the turbulent boundary layer. Ann Rev Fluid Mech 23:601–639. doi:10.1146/annurev.fl.23.010191.003125
Rodriguez F, Mesler RJ (1988) The penetration of drop-formed vortex rings into pools of liquid. J Colloid Interface Sci 121:121–129
Rao KN, Narasima R, Badri Narayanan M (1971) The "bursting" phenomenon in a turbulent boundary layer. J Fluid Mech 48:339–352
Riley JP, Skirrow G (1965) Chemical oceanography, Bd I. Academic Press, London, pp 712pp
Saunders PM (1967a) Shadowing on the ocean and the existence of the horizon. J. Geophys. Res. 72: 4643-4649
Saunders PM (1967b) The temperature at the ocean-air interface. J Atmos Sci 24:269–273
Saylor JR, Handler RA (1997) Gas transport across an air/water interface populated with capillary waves. Phys Fluids 9:2529–2541
Saylor JR, Flack KA, Schultz MP, Smith GB (2002) The correlation between surface temperature and subsurface velocity during evaporative convection. Exp Fluids 32: 570-579
Schlichting H (1979) Boundary-layer theory. McGraw-Hill, New York, pp 817pp
Schlüssel P, Emery WJ, Grassl H, Mammen TC (1990) On the bulk-skin temperature difference and its impact on satellite remote sensing of the sea surface temperature. J Geophys Res 95:13,341–13,356
Schlüssel P, Soloviev AV, Emery WJ (1997) Cool and freshwater skin of the ocean during rainfall. Bound.-Layer Meteor 95:82,437–82,472
Siscoe GL, Levin Z (1971) Interaction of water drops with surface waves. J Geophys Res 76:5112
Soloviev AV (1990) Coherent structure at the ocean surface in the convectively unstable conditions. Nature 346:157–160
Soloviev AV (2007) Coupled renewal model of ocean viscous sublayer, thermal skin effect and interfacial gas transfer velocity. J Marine Syst (Elsevier) 66:19–27
Soloviev AV (1992) Small-scale structure of the open ocean boundary layers. Dissertation for doctor of physical-mathematical sciences degree, Russian Academy of Sciences, Moscow (in Russian)
Soloviev A, Donelan M, Graber H, and Haus B (2007) An approach to estimation of near-surface turbulence and CO2 transfer velocity from remote sensing data. Journal of Marine Systems (Elsevier) 66: 182-194
Soloviev A, Donelan M, Graber HC, Haus B, Schlussel P (2007) An approach to estimation of near-surface turbulence and CO2 transfer velocity from remote sensing data. J. Marine Syst 66: 182–194
Soloviev A, Kurata N, Vella K, Tartar A, Matt S, Shivji M, Fujimura A, Perrie W (2012) Effect of surfactants on sea surface temperature and salinity. IEEE Geoscience and Remote Sensing Society Symposium (IGARSS 2012) July 22–27, 2012, Munich, Germany. Abstract only

Soloviev A, Lukas R (2010) Effects of bubbles and spray on air-sea exchange in hurricane conditions. Bound -Lay Meteorol 136:365–376
Soloviev A, Matt S, Gilman M, Hühnerfuss H, Haus B, Jeong D, Savelyev I, Donelan M (2011) Modification of turbulence at the air-sea interface due to the presence of surfactants and implications for gas exchange. Part I: laboratory experiment. In: Gas transfer at water surfaces. Kyoto University Press, pp 245–258
Soloviev A, Schlüssel P (1998) Comments on "air-sea gas transfer: mechanisms and parameterizations." J Phys Oceanogr 28:1643–1645
Soloviev AV, Schlüssel P (1996) Evolution of cool skin and direct air-sea gas transfer coefficient during daytime. Bound Layer Meteor 77:45–68
Soloviev AV, Schlüssel P (1994) Parameterization of the temperature difference across the cool skin of the ocean and of the air-ocean gas transfer on the basis of modelling surface renewal. J Phys Oceanogr 24:1339–1346
Soloviev AV, Vershinsky NV (1982) The vertical structure of the thin surface layer of the ocean under conditions of low wind speed. Deep-Sea Res 29(12A):1437–1449
Spangenberg WG, Rowland WR (1961) Convective circulation in water induced by evaporative cooling. Phys Fluids 4:743–750
Stephen H, Stephen T (eds) (1964) Solubilities of inorganic and organic compounds; 2: Ternary Systems, Part I. Pergamon Press, McMillian Company, NY, pp 944p
Stull RB, Kraus EB (1987) A transilient model of the upper ocean. J Geophys Res-Oceans 92:10,745–10,755
Thorpe SA (1985) Small-scale processes in the upper ocean boundary layer. Nature 318:519–522
Tsai W (2001) On the formation of the streaks on wind-driven water surfaces. Geophys Res Lett 28(20):3959–3962
Tsimplis M (1992) The effect of rain in calming the sea. J Phys Oceanogr 22:404–412
Tsimplis M, Thorpe SA (1989) Wave damping by rain. Nature 342:893–895
Turner JS (1973) Buoyancy effects in fluids. Cambridge Univ. Press, NY
Verdugo P, Alldredge AL, Azam F, Kirchman DL, Passow U, Santschi PH (2004) The oceanic gel phase: a bridge in the DOM-POM continuum. Mar Chem 92:67–85
Vladimirov VS (1976) Equations of mathematical physics. Nauka, Moscow (In Russian) 527 pp
Volkov YA, Soloviev AV (1986) On vertical thermal structure of near-surface layer of atmosphere above the ocean. Izvestiya: Atmos Ocean Phys 22(9):899–903
Volino RJ, Smith GB (1999) Use of simultaneous IR temperature measurements and DPIV to investigate thermal plumes in a thick layer cooled from above. Exp Fluids 27:70–78
Wanninkhof R, McGillis WR (1999) A cubic relationship between air-sea CO2 exchange and wind speed. Geophys Res Lett 26(134):1889–1892 (Check on pg 48)
Wanninkhof R, Hitchcock G, Wiseman W, Vargo G, Ortner P, Asher W, Ho D, Schlosser P, Dickson M-L, Anderson M, Masserini R, Fanning K, Zhang J-Z (1997) Gas exchange, dispersion, and biological productivity on the west Florida shelf: Results from a lagrangian tracer study. Geophys Res Lett 24: 1767-1770
Ward B, Minnett PJ (2001) An autonomous profiler for near surface temperature measurements. Gas transfer at water surfaces. In: Donelan MA, Drennan WM, Saltzmann ES, and Wanninkhof R (eds) American Geophys Union Monogr 127:167–172
Wu J (1975) Wind-induced drift current. J. Fluid Mech 68: 49-70
Woods JD (1980) Diurnal and seasonal variation of convection in the wind-mixed layer of the ocean. Q J Roy Meteor Soc 106:379–394
Woolf DK (1997) Bubbles and their role in air-sea gas exchange. In: The Sea Surface and Global Change. P.S. Liss and R.A. Duce, Eds., Cambridge University Press, UK: 173-205
Wurl O, Holmes M (2008) The gelatinous nature of the sea-surface microlayer. Marine Chem 110:89–97
Yakimov YL (1959) Why waves are extinguished by rain. Izvestiya: Sib. Akad. Nauk SSR 5: 125-126 (in Russian)
Yang Z, Tang S, Wu J (1997) An experimental study of rain effects on fine structures of wind waves, J Phys Oceanogr 27: 419–430

Yeh (1992) Vorticity generation at a fluid interface. In Breaking Waves, edited by M. Banner and R.H.J. Grimshaw, Springer-Verlag, New York: 257-265

Zaitsev YP (1971) Marine neustonology (translated from Russian). National Marine Fisheries Service, NOAA and National Science Foundation, National Technical Information Service, Springfield, Virginia, 207 pp

Zaitsev Y (1997) Neuston of seas and oceans. In: The Sea Surface and Global Change. P.S. Liss and R.A. Duce, Eds., Cambridge University Press, UK: 371-382

Zhang X, Harrison S (2004) A laboratory observation of the surface temperature and velocity distributions on a wavy and windy air-water interface. Physics of Fluids 16: L5-L8

Zhang Y, Zhang X (2012) Ocean haline skin layer and turbulent surface convections. J Geophys Res-Oceans 117, 10.1029/2011jc00746

Zhao D. and Toba Y (2001) Dependence of whitecap coverage on wind and wind-wave properties. J Oceanography 57: 603-616

Chapter 3
Near-Surface Turbulence

Abstract Physical processes that determine the character and magnitude of turbulence in the upper ocean are surveyed and the challenges of studying near-surface turbulence are revealed. The free-surface boundary layer has some specifics, which distinguish it from the classic wall layer. The wall layer analogy is, however, still useful for understanding the near-surface turbulence. The major problem in studying the near-surface turbulence is obtaining reliable data in the wave-disturbed layer. A substantial part of the kinetic energy is dissipated by the breaking waves that are saturated with air bubbles, while most of the available ocean sensor technologies do not provide useful data in this environment. Methodological requirements are followed by examples of turbulence data obtained with a free-rising profiler and bow-mounted sensors in comparison with other results. The field data provide context for discussion of models of wave-enhanced turbulence. As a transition to Chap. 4, the effects of thermohaline stratification on the near-surface turbulence regime and the parameterization of these effects are considered.

Keywords Wave-enhanced turbulence • Free-surface layer • Wall-layer turbulence • Turbulence measurements • Thermohaline stratification • Turbulence models • Turbulence parameterizations

3.1 Introduction

The main sources of turbulence in the near-surface layer of the ocean are breaking surface waves, shear, and convection. Upper ocean turbulence resulting from shear and convective instabilities may be substantially influenced by the diurnal cycle of solar radiation and by precipitation events. The shear that develops at the bottom of a shallow diurnal or rain-formed mixed layer can greatly increase the turbulence generation (though on relatively small scales) and thus the dissipation rate of turbulence. Below the mixed layer (i.e., in the pycnocline), turbulence decays due to the stabilizing effect of buoyancy forces. The dramatic effect of stratification is observed under low wind speed conditions when the turbulence regime depends strongly on near-surface stratification, while the strong stratification is also the result of reduced turbulent mixing.

The near-surface thermohaline stratification is eliminated quickly when wave breaking starts. It is therefore reasonable to analyze the thermohaline stratification

A. Soloviev, R. Lukas, *The Near-Surface Layer of the Ocean,* Atmospheric and Oceanographic Sciences Library 48, DOI 10.1007/978-94-007-7621-0_3,

effects separately, but we cannot do this for bubble-related stratification. Bubbles from breaking waves alter density and thus stratification. The bubble volume fraction (void fraction) is high in spilling breakers; the resulting increased stability affects near-surface dynamics. Conversely, the bubble size distribution appears to depend on turbulence parameters. Beyond the near-surface zone stirred by breaking waves, the average void fraction is too small to influence the flow dynamics but may serve as a tracer for detection of turbulence and coherent structures.

The analysis of turbulence observations reveals different, often contradictory, aspects of the role of surface waves. Since methodological issues of turbulence measurements in the near-surface layer of the ocean still greatly affect the study of wave-enhanced turbulence, one of the sections in this chapter (Sect. 3.3) is devoted to the analysis of the challenges of observing the near-surface turbulence.

In this chapter, we consider only local and essentially one-dimensional models of near-surface turbulence; this is the so-called "small eddy" theory. We consider the role of large eddies (Langmuir circulations, billows, and ramp-like structures) in Chap. 5 when discussing coherent structures in the near-surface layer.

3.2 Free-Surface Turbulent Boundary Layer

An important feature of the upper ocean turbulent boundary layer is that it develops near a free, elastic surface. In the near-surface layer affected by waves and wave-breaking turbulence, the properties of the boundary layer may differ substantially from the classic wall layer. In contrast to a rigid wall, the tangential component of the velocity field at the free surface may not be zero. Velocity components in all directions disappear at the wall due to no-slip conditions, while the free surface restricts motion in the normal direction only.

3.2.1 Wave-Following Coordinate System

An important factor for interpreting near-surface data is the choice of coordinate system. In a fixed coordinate system, it is practically impossible to study near-surface layers with thickness less than the maximum surface wave height. In fact, any observational point between the wave trough and crest will be alternately in water and in air.

The influence of surface waves on the near-surface flow can be provisionally divided into reversible (kinematic) and irreversible deformations. The former are due to linear (irrotational) components of surface waves, while the latter are caused by nonlinear (rotational) components of surface waves and by turbulence. Examples of irrotational waves are swell and long wind waves. Nonlinearity increases as wavelength decreases. An extreme effect of wave nonlinearity is wave breaking.

A reasonable approach is to interpret the near-surface layer of the ocean in a coordinate system linked to the ocean surface. Csanady (1984) suggested that "… depth should be expressed in the coordinate system connected with the surface produced by the nearly irrotational component of the wave field." This allows one to analyze the near-surface processes between wave troughs and crests.

The amplitude of wave oscillations in the water decreases as e^{kz} with depth, where k is the wavenumber and z is the vertical coordinate (conventionally directed upward). Csanady's (1984) coordinate system can, therefore, only be used close to the air–sea interface (i.e., for $|z| << k^{-1}$). Soloviev (1992) proposed an extension of the Csanady (1984) approach by introducing a Lagrangian coordinate system that accounts for the depth attenuation of the surface wave-induced perturbation. This coordinate system is described by the following transformation:

$$x' = x; y' = y; z' = z + \eta(z,t), \tag{3.1}$$

where x and y are the horizontal axes and z is the vertical coordinate fixed to the still water level of the ocean. Wave displacement, η, is given as a Fourier–Stieltjes integral (Iyanaga and Kawada 1980),

$$\eta(x,y,z,t) = \iint \exp(-k|z|)\exp i(\vec{k}\cdot\vec{l} - \omega t)dZ(\vec{k},\omega), \tag{3.2}$$

where $dZ(\vec{k},\omega)$ is the Fourier– Stieltjes amplitude introduced in such a way that $\left\langle dZ(\vec{k},\omega)dZ(\vec{k},\omega)^* \right\rangle = \Phi_\eta(\vec{k},\omega)d\vec{k}d\omega$, $\Phi_\eta(\vec{k},\omega)$ is the surface wave spectrum, $\vec{k}$ is the wavenumber vector with components (k_x, k_y), and $\vec{l}$ is the vector with components (x, y). In order to filter out rotational components of the wave field, the upper limits on frequency and wave number can be set at $\omega = \omega_u = 2\pi f_u$ and $(k_x, k_y) = k_u = \omega_u^2 / g$. In the light of the Munk (2009) work, the transition from the irrotational to rotational component can be linked to the transition from the gravity to ultra-gravity portion of the wave spectrum, which takes place at frequency $f_u \sim 1$ Hz, though it may depend on wind speed.

An important property of transformation (3.1)–(3.2) is that kinematic effects of waves on the near-surface flow in this Lagrangian coordinate system are largely eliminated. Transformation (3.1)–(3.2) projects the surface layer disturbed by the linear potential waves into a flat near-wall layer. Turbulence properties of this near-wall layer may differ from the classical wall layer because of slip boundary conditions. Nevertheless, it is sometimes convenient to compare the near-surface turbulence to well-known properties of the turbulent boundary layer near a wall.

3.2.2 Wall-Layer Analogy

A classical horizontally homogeneous and steady wall layer consists of an inner and outer part. Following Nowell (1983), the inner part of the wall layer is defined as $0 < |z| \le 0.2h$; the outer part, as $0.2h \le |z| \le h$ (where z is the distance to wall and h is the depth of the mixed layer or the thickness of the turbulent boundary layer). Some authors define the inner part of the wall layer as $0 < |z| \le 0.1h$; the outer part is then defined as $0.1h \le |z| \le h$, respectively.

In the inner boundary layer, the velocity profile, $u(z)$, depends on boundary conditions (surface stress and hydrodynamic surface roughness) and distance $|z|$.

The properties of the inner boundary layer near a rigid wall are well known from classical works in hydrodynamics (Hinze 1955; Monin and Yaglom 1971; and others). In particular, a logarithmic layer may develop in the inner boundary layer. The velocity and dissipation rate profiles in the log layer are as follows:

$$u(z) = \frac{u_*}{\kappa} \ln \frac{|z| + z_0}{z_0}, \tag{3.3}$$

$$\varepsilon = \frac{u_*^3}{\kappa(|z| + z_0)}, \tag{3.4}$$

where $u_* = (\tau_0 / \rho)^{1/2}$, τ_0 is the surface stress (which is measured only in specialized air–sea interaction experiments, but can roughly be estimated from a bulk-flux algorithm; see Sect. 1.3.2), ρ the density, κ the von Karman constant, and z_0 is the surface roughness length scale.

In the outer boundary layer, $0.2h \le |z| \le h$, buoyancy and/or rotation effects are important. These factors limit the depth of the turbulent boundary layer. The lower boundary of the surface mixed layer is usually identified by a sharp change of temperature, salinity, and density with depth.

When buoyancy forces are weak, the Earth's rotation controls the depth of the upper ocean turbulent boundary layer and, thus, the depth of the surface mixed layer. The Ekman boundary layer is scaled with the length scale,

$$L_E = u_* / f, \tag{3.5}$$

where $f = 2\Omega \sin\varphi$ is the Coriolis parameter, Ω is the angular velocity of Earth's rotation, and φ is the latitude.

The heat flux at the air–sea interface affects near-surface turbulence via buoyancy forces. This process is scaled with the buoyancy (Oboukhov) length scale, which, in the absence of salinity fluxes, is as follows:

$$L_O = \frac{c_p \rho u_*^3}{\alpha_T g Q_0 \kappa}, \tag{3.6}$$

where Q_0 is the net heat flux at the ocean surface, α_T is the thermal expansion coefficient for water ($\alpha_T < 0$), g is the acceleration of gravity, c_p and ρ are the specific heat and density of sea water, respectively, and κ is the von Karman constant. Note that the definition of the Oboukhov length scale for the upper ocean can be extended to include the buoyancy effect of salinity, which is at no rain conditions typically of the order of 10 % of the thermal buoyancy effect (though it depends on the mean water temperature and salinity and on the latent to total heat flux ratio). The depth at which buoyancy forces become important is proportional to the Oboukhov length scale. With a positive L_O, the near-surface turbulent boundary layer is stably strati-

fied. Stable stratification inhibits turbulence, which leads to the restriction of the turbulent boundary-layer thickness and thus of the surface mixed-layer depth.

The turbulent near-surface flow is dominated by buoyancy forces when:

$$L_O / L_E = c_p \rho u_*^2 f / \left(\alpha_T g Q_0\right) << 1. \tag{3.7}$$

Hence, as the friction velocity decreases, the influence of buoyancy forces increases. In this limiting case, the surface mixed-layer depth, h, is determined by buoyancy rather than rotational forces and $h \sim L_O$. A similar effect is observed when approaching the Equator, where the Coriolis parameter f becomes zero.

Note that the quadratic dependence of the ratio L_O/L_E on friction velocity in (3.7) means that the buoyancy influence rapidly increases with decreasing friction velocity. Stratification effects in the near-surface layer of the ocean, which become prominent under low wind speed conditions, are considered in more detail in Sect. 3.5.

Lombardo and Gregg (1989) found the wall-layer analogy to be useful for the analysis of dissipation rate profiles in the upper ocean under convectively unstable conditions. These observations were essentially below the layer affected by breaking waves. Thorpe (1985) was able to explain his observation of ramp-like structures in the upper ocean turbulent boundary layer based on the wall-layer analogy. The wall-layer analogy can also provide a reference level for the analysis of the turbulence dissipation in the wave-turbulent layer (see Sect. 3.4).

3.2.3 Deviations from the Wall-Layer Analogy in a Free-Surface Layer

Important deviations from the wall-layer analogy are associated with the slip condition at the air–sea interface (from the waterside) and with the surface waves developing at the free ocean surface. The vortices with horizontal axes weaken when approaching the free surface, while vertically aligned vortices tend to attach to the free surface and are long-lived (Shen et al. 1999). In near-surface flows with significant vorticity, there is a thin transitional layer inside which the values of the two horizontal vorticity components and the vertical derivative of the vertical vorticity component change from their bulk (isotropic) values to the much smaller values imposed by the zero-stress conditions at the free surface.

In the absence of surface stress but in the presence of internal sources of turbulence (for instance, in the post wave-breaking interval or in a ship's wake), the surface layer developing near a free surface is a region of decreased kinetic energy dissipation and increased enstrophy dissipation (enstrophy is the total squared vorticity). When surface stress is imposed, the properties of the near-surface turbulent eddies are still determined by the slip conditions at the free surface; as a result, the mean shear flow near a free surface is different from that near a rigid wall.

According to the direct numeric simulation (DNS) by Shen et al. (1999), a vertically aligned vortex can attach to the ocean surface and experience significantly

slower decay. The vertical shear of the second-order Stokes drift of the waves tilts and stretches such vortices in the horizontal direction presumably leading to the generation of Langmuir circulations (see Chap. 5). At low wind speeds, when wind waves cease, the wind-induced shear current could carry out the same function as the Stokes drift tilting and stretching the turbulent vortices.Remarkably, there are numerous reports of wind streaks on the ocean surface even before waves develop, which resemble miniature Langmuir circulations (see, e.g., Fig. 2.16).

The Shen et al. (1999) concept of a free-surface turbulent boundary layer has practical applications for surface sensing to deduce characteristics of the underlying flow (Swean et al. 1991; Handler et al. 1993). This concept has not yet been applied to situations with finite-amplitude surface waves.

The presence of surface waves alters the hydrodynamics of near-surface flows. Borue et al. (1995) found that the interaction of surface waves and free-surface turbulence is weak. Their numerical simulation (DNS) model, however, was confined to infinitesimally small waves. Ardhuin and Jenkins (2006) showed that the mean wave-induced shear, despite zero vorticity, results in production of turbulence as if Stokes drift shear were a mean flow shear. This value is about an order of magnitude smaller than the production of turbulence due to wave breaking. Furthermore, mostly high-frequency waves, which effectively decay within half wavelength depth, contribute to the mean Stokes drift (Kudryavtsev et al. 1999). According to observations by Snodgrass et al. (1966), long waves with periods above 15 s were hardly attenuated between New Zealand and the Equator. More recently, Benilov (2012) discussed the possibility of generating turbulence due to the vortex instability of the potential surface waves. His analytical model was not restricted to small waves and showed a more significant turbulence production than that of Ardhuin and Jenkins (2006).

High-resolution numerical simulations for the realistic spectrum of ocean surface waves interacting with turbulence have not yet been done due to high computational costs. New specially designed experiments are therefore required in order to verify the aforementioned parametric models of the turbulence induced by non-breaking waves. One potential complication is that strong current shears tend to develop near the bottom of the mixed layer, producing elevated levels of turbulence dissipation (see Sect. 3.5.1); as a result, it could be difficult to distinguish them from the mechanisms described in Ardhuin and Jenkins (2006) and Benilov (2012).

There are also other deviations of the free-surface boundary layer from the wall-layer analogy associated with surface waves. In particular, breaking waves distinguish the free-surface boundary layer from the wall layer. This is a very powerful source of turbulent energy. The process of wave breaking is associated with the entrainment of air and the production of bubbles. Conversely, bubbles have a significant effect on the turbulence dynamics in wave breakers.

In the case of near-surface stratification (low wind speed conditions), resonant interaction between two surface waves and an internal wave developing on a near-surface pycnocline may result in the energy transfer from surface to internal modes. Such interaction is obviously impossible near a rigid wall. Surface waves also modulate strain and shear (thus the gradient Richardson number), which may result in

flow instability, turbulence, and microstructure when the Richardson number drops below its critical value.

3.2.4 *Structure of the Upper Ocean Turbulent Boundary Layer Below Breaking Surface Waves*

Surface waves produce turbulence due to wave breaking and vortex instability. Wave breaking is a powerful mechanism producing significant energy flux to small-scale turbulence and momentum flux to the mean surface current. The local vorticity production due to vortex instability of the surface waves should also be taken into account in the balance of momentum and turbulent kinetic energy (TKE) below breaking waves.

Mean shear flow is a principal source of small-scale turbulence in the ocean. In this respect, upper ocean turbulence should be similar to the classical shear turbulence when the mean shear energy production dominates. The effect of stratification on the near-surface mean shear flow can be substantial, especially for low winds. In contrast, under high wind speed conditions when waves break, the influence of stratification on the wave-turbulent layer is negligible (except when wind squalls are accompanied by strong rainfalls). This means that when waves start breaking there is a near-surface layer where the effect of the Coriolis and buoyancy forces can be neglected.

With no stratification effects, energy from the mean shear flow, wave motion, and wave breaking all contribute to the turbulent energy balance. The dominant source will control the TKE and dissipation rate creating sublayers where the energy takes different forms. Accordingly, Benilov and Ly (2002) suggested that the upper ocean turbulent boundary layer where stratification and rotation effects are negligible could be conveniently divided into three sublayers.These are

1. The wave-stirred layer: the TKE production by wave breaking significantly exceeds the mean shear effect, and the turbulent diffusion of the wave kinetic energy dominates in the range of depths where the wave motion continues to be vigorous.
2. The turbulent diffusion layer: here the turbulent diffusion of TKE from the wave-stirred layer exceeds the wave (as well as the mean shear) effect in the TKE budget.
3. The wall layer: the mean shear production of turbulent energy dominates. In terms of the classic horizontally homogeneous and steady turbulent boundary-layer problem, this layer obeys wall-layer laws. As discussed in Sect. 3.2.2, a classic wall layer consists of an inner and outer part. In the inner part, a logarithmic velocity profile can develop; stratification and rotation effects are important in the outer part.

Figure 3.1 illustrates the concept described above. In order to complete the Benilov and Ly (2002) dynamical scheme, we have included an additional characteristic feature of the upper ocean turbulent boundary layer:

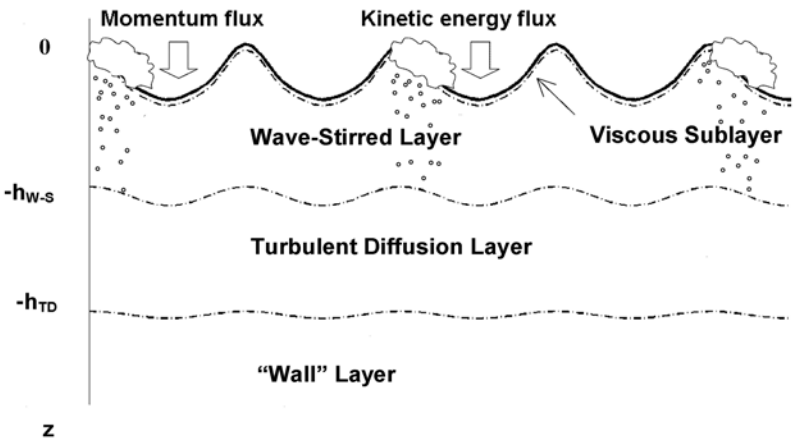

Fig. 3.1 Diagram of the upper ocean turbulent boundary-layer dynamic structures. Here, $h_{W\text{-}S}$ is the wave-stirred layer depth, and h_{TD} is the turbulent diffusion layer depth

4. The aqueous viscous sublayer: viscous sublayers develop at both the waterside and airside of the air–sea interface due to the suppression of the normal component of turbulent velocity fluctuations near the density interface. This sublayer is controlled by the tangential wind stress τ_t and is an important component of the sea surface microlayer (Sect. 2.2). Under low wind speed conditions, the aqueous viscous sublayer is also controlled by the buoyancy flux. Under high wind speed conditions, τ_t represents only a small fraction of the total momentum flux, τ_0, from the atmosphere to the ocean. Breakers disrupt the viscous sublayer; however, it recovers rapidly and is believed to exist between the wave-breaking events even in high seas. The viscous sublayer is found within the upper few millimeters of the ocean; its thickness is proportional to the Kolmogorov internal scale of turbulence, η_v, defined in (2.1). Note that the viscous sublayer should be considered in the wave-following coordinate system (3.1)–(3.2), because the sublayer thickness is much less than the wave height.

A comprehensive theoretical model of upper ocean turbulence has yet to be developed. It should include the momentum and kinetic energy equations for the mean and fluctuating components of the turbulent flow, interactions between turbulence and surface waves, wave breaking and turbulent mixing length, quasi-organized (coherent) motions, viscous sublayers, and bubble dynamics. The boundary conditions should describe the fluxes of momentum and energy produced by wave breaking as well as from direct atmospheric action on the ocean surface. Several approaches to one-dimensional modeling of the turbulent processes in the near-surface layer of the ocean are presented in Sects. 3.4–3.6.

3.3 Observation of Near-Surface Turbulence

3.3.1 Observational Challenges

Breaking surface waves generate strong turbulence in the near-surface layer of the ocean. These same waves present serious challenges to turbulence measurements. Bubble clouds and random, sometimes huge, vertical motions of the ocean surface due to surface waves complicate collecting, analyzing, and understanding turbulence data close to the ocean surface.

The velocity scale of near-surface turbulent fluctuations is about 1 cm s^{-1}, while typical surfacewave orbital velocities are 1 m s^{-1}. The energy of wave orbital velocities is four orders of magnitude higher than that of the turbulence signal. In terms of the dissipation rate of TKE, ε, the wave disturbance is six orders of magnitude greater than the useful signal. Such exceptionally strong disturbance from surface waves imposes special requirements on the measurement techniques and sensors for observations of near-surface turbulence. Buoy devices (Jones and Kenney 1977), ship- or submarine-mounted instruments (Stewart and Grant 1962; Volkov et al. 1989; Osborn et al. 1992; Soloviev and Lukas 2003), free ascending profilers (Soloviev et al. 1988), tower-based instruments (Terray et al. 1996), and autonomous underwater vehicles (AUVs; Thorpe et al. 2003a) have been utilized to obtain measurements in the upper few meters of the ocean.

Each approach offers different insights into near-surface physics and suffers from different limitations. For example, tower-based measurements yield temporal measurements. However, there is no clear separation in frequency space of the surface wave velocity field and turbulence. The lack of a dependable mean speed prevents conversion to the spatial domain, which complicates correct estimation of the kinetic energy dissipation rate. Vertical profiling methods can provide such estimates if the vertical speed of the profiler is much greater than the surface wave orbital velocities. However, vertical profiling is inefficient for obtaining large sample sets of turbulence statistics in the near-surface region due to the change of the turbulent statistics as a function of depth. It might also be difficult to detect and adequately measure regions of large horizontal gradients by vertical profiling.

Among the key factors that can affect the quality and interpretation of measurements in the near-surface layer from a vessel are surface wave perturbations, influence of the ship wake, variation of the sensor motion, impact of bubbles on conductivity (and hence salinity and density) measurements, and strong electrical currents coupled to the water near the vessel due to the ship's electrical field. Sharp vertical gradients in the near-surface physics can also be a factor depending on the measurement approach.

Towed methods can efficiently generate large sample sets of dissipation estimates, but they are typically degraded by broadband motion contamination due to the nonstationary push/pull motion of these devices. The large area of influence of the ship's wake can also affect near-surface measurements. Ship's bow-, submarine-, or AUV-mounted devices can efficiently produce large sample sets, but offer

unique challenges, such as the need to assess and minimize ship motion-induced effects and flow perturbations in the vicinity of the sensors due to interaction of the vehicle with the wave field.

Three principal questions associated with collecting turbulence data near the ocean surface are as follows:

1. What reference system should be used?
2. How can the flow disturbance from the vehicle carrying the sensor be reduced?
3. How can surface wave disturbances be eliminated from the signal?

3.3.2 Wave-Following Versus Fixed Coordinate System

Since the wave-breaking energy substantially dissipates in the thin near-surface layer of the ocean (less than one significant wave height), and the dissipation rate profile is a nonlinear function of depth, the difference between fixed and wave-following measurements can be significant. For instance, in a fixed coordinate system it is practically impossible to study near-surface layers with a thickness less than the surface wave height. Any observational point between the lowest wave trough and highest wave crest will alternate between water and air. Therefore, in order to study turbulence close to the ocean surface, a wave-following coordinate system should be used. Csanady (1984) suggested analyzing near-surface data in a coordinate system connected to the ocean surface; this system is, however, efficient only close to the ocean surface (within a few significant wave heights). It is easy to see that for depths where the surface wave motion diminishes, this coordinate system is irrelevant. The coordinate system proposed in Sect. 3.2.1 (equations (3.1)–(3.2)) resolves this difficulty.

The Craig and Banner (1994) and Benilov (2002) models of wave-enhanced turbulence that are discussed throughout this chapter are consistent with the coordinate system (3.1)–(3.2). The Terray et al. (1996) model, which was originally fitted to the data collected in a fixed coordinate system, would produce a different dissipation profile in the wave-following coordinate system.

The coordinate system (3.1)–(3.2) at a first glance seems to be infeasible. However, it can be easily implemented with a free-ascending instrument by a proper choice of its hydrodynamic characteristics (Sect. 3.3.4).

3.3.3 Disturbances from Surface Waves

The orbital velocities of surface waves influence turbulence measurements by

a. Generating an additive fluctuation velocity signal and
b. Modulating the relative speed (and direction) of the flow.

We should mention here that (a) is an additive (that is a linear) process, while (b) is a nonlinear process, which resembles the process of frequency modulation in radio techniques (Dozenko 1974). An additional complication is that the timescales of surface waves and near-surface boundary-layer turbulence substantially overlap.

Linear filtering has been widely used to separate waves from turbulence in mooring or tower-based velocity records (e.g., Benilov and Filyushkin 1970; Kitaigorodskii et al. 1983). This filtering procedure is capable of distinguishing turbulence from linear waves, which effectively addresses problem (a). Problem (b), however, is essentially nonlinear.

In the case of mooring and tower-based measurements, the orbital velocity fluctuation of surface waves usually exceeds the mean drift current. Taylor's frozen field approximation (3.8), which requires that the fluctuation of the flow is less than 10% of its mean speed, cannot be satisfied for these types of measurements; the standard techniques of turbulence analysis, therefore, are not applicable. To address problem (b) for tower-based observations, Kitaigorodskii et al. (1983) used the root mean square (RMS) fluctuation velocity in Taylor's hypothesis of frozen turbulence instead of the mean drift velocity. The error in calculations of the turbulence dissipation rates using these alternative techniques is unknown.

Linear filtering cannot remove nonlinear components of surface waves from the measured signal, however. This may have resulted in an overestimation of the turbulence dissipation rate calculated from tower measurements. Not yet mentioned are the flow reversals due to orbital velocities of surface waves that are typical for tower-based measurements. A turbulent patch produced by the sensor package or mounting structure can occasionally get into the sensing area and disturb measurements.All these circumstances sometimes make tower-based turbulence measurements difficult to interpret.

It is remarkable that energy-containing spatial scales of turbulence and surface waves may differ greatly, and this can be exploited. Stewart and Grant (1962) and Soloviev et al. (1988) demonstrated that a fast-moving sensor provides an effective separation between the turbulence and surface waves. As a result, no statistical filtering is required to solve problem (a). Moreover, if the sensor moves fast enough when compared to the velocity scale of wave orbital motions, problem (b)—modulation of the relative speed (and direction) of the flow due to surface wave disturbances—can be solved as well (Drennan et al. 1996; Soloviev et al. 1999). The frequency spectrum $S_u(f)$ can then be transformed into the wavenumber domain using Taylor's (1938) frozen field hypothesis:

$$k_x = 2\pi f / U_0, \quad E_u(k_x) = S_u(f) U_0 / (2\pi) \tag{3.8}$$

where f is the frequency in Hz, U_0 is the relative flow speed (towed or mean flow advection speed), and k is the wavenumber in m^{-1} (all through this chapter we use the radian wavenumber). Taylor's hypothesis is acceptable if the RMS variation of the flow does not exceed 10% of the mean flow speed.

3.3.4 Dynamics of a Free-Rising Instrument in the Near-Surface Layer of the Ocean

The equation for the vertical motion of a freely ascending device (e.g., free-rising profiler) in the coordinate system referenced to the mean sea level and in the presence of long surface waves has the following form (Soloviev et al. 1988):

$$(m_d + m_a)\frac{dw}{dt} = (\rho V_d - m_d)g - C_d S_d \rho (w - w_w)^2. \tag{3.9}$$

where m_d is the mass of the instrument, m_a is the added (virtual) mass due to unsteady motion in fluid, w is the vertical velocity of the instrument center of mass, V_d is the volume of the profiler, ρ is the water density, C_d is the drag coefficient of the profiler, g is the acceleration of gravity, S_d is the cross-sectional area of the profiler as seen from above, and w_w is the vertical component of the velocity field induced by surface waves. The virtual mass has to be added to the momentum equation due to unsteady motion of the profiler (Stokes 1851). Equation (3.9) is true for wavelengths $\lambda >> L_d$, where L_d is the vertical size of the instrument.

The velocity sensor mounted on the device measures the relative vertical velocity $w_r = w - w_w$. Substituting new variable w_r into equation (3.9) and expressing it in nondimensional form results in the following equation:

$$\frac{d}{dt}(w_r / w_0) = A_d\left[1 - (w_r / w_0)^2\right] - \frac{d}{dt}(w_w / w_0), \tag{3.10}$$

where $A_d = g(\rho V_d - m_d)(m_d + m_a)^{-1} w_0^{-1}$, and w_0 is the nominal ascending speed of the profiler in still water obtained from the equation

$$\left(\rho V_d - m_d\right) g = C_d S_d \rho w_0^2. \tag{3.11}$$

Solution to equation (3.10) in still water ($w_w = 0$) with initial condition $w = 0$ at $t = 0$ is as follows:

$$w(t) / w_0 = \tanh(A_d t). \tag{3.12}$$

The instrument achieves 99% of the nominal ascending speed within the time interval,

$$t_0 = a \tanh(0.99) / A_d. \tag{3.13}$$

During this time interval, the profiler passes the vertical distance,

Table 3.1 Dynamical parameters for two versions of the free-rising profiler described in (a) Soloviev et al. (1988) and (b) Soloviev et al. (1995)

Instrument version	m_d kg	$10^3 V_d$ m^3	w_0 m s^{-1}	A_d s^{-1}	t_0 s	d_0 m
a	5	6.75	2.2	1.6	1.65	0.4
b	10.5	10.4	2.8	2.8	0.95	0.3

$$d_0 = \int_0^{t_0} w(t)\,dt = w_0 \int_0^{t_0} \tanh\left(A_d t\right) dt = w_0 A_d^{-1} \ln\left|\cosh\left(A_d t_0\right)\right|. \tag{3.14}$$

Substituting (3.12) and (3.13) into (3.14) gives

$$d_0 \approx 0.28 w_0 A_d^{-1}. \tag{3.15}$$

According to Table 3.1, the free-rising profiler described in Soloviev et al. (1988, 1995) achieved 99% of the nominal velocity after rising only 0.4 m and 0.3 m, respectively.

For small velocity disturbances $\left|w_r^{'}\right| << w_0$, equation (3.10) in the presence of surface waves takes the following form:

$$\frac{dw_r^{'}}{dt} + 2A_d w_r^{'} = -\frac{dw_w}{dt}, \tag{3.16}$$

where $w_r^{'} = w_r - w_0$.

A random surface elevation $\eta(\vec{x},t)$ can be represented in terms of a Fourier–Stieltjes integral (3.2). The vertical component of the orbital velocity field is then expressed as follows:

$$w_w(z,t) = \frac{\partial}{\partial t}\eta(z,t) = \int_{-\infty}^{\infty} (-i\omega)\exp(-i\omega t)\exp\left(-\omega^2 \mid z \mid / g\right) dZ_\eta(\omega), \tag{3.17}$$

where $dZ_\eta(\omega)$ is the Fourier– Stieltjes amplitude introduced in such a way that $\left\langle dZ(\omega) dZ(\omega)^* \right\rangle = S_\eta(\omega) d\omega$, and $S_\eta(\omega)$ is the surface wave spectrum. For wavelength λ much exceeding the characteristic size of the instrument L, wavenumber dependence in the Fourier–Stieltjes integral (3.2) can be ignored.

The solution of linear equation (3.16) can be expressed in terms of the transfer function, $H(i\omega)$, and the frequency spectrum of surface waves, $S_\eta(\omega)$. Substituting the vertical component of orbital velocities in the form (3.17) into equation (3.16) results in the following formula:

$$\left|H(i\omega)\right|^2 = \frac{\omega^2 + w_0^2\omega^4 / g^2}{\omega^2 + \left(2A_d - w_0\omega^2 / g\right)^2}, \tag{3.18}$$

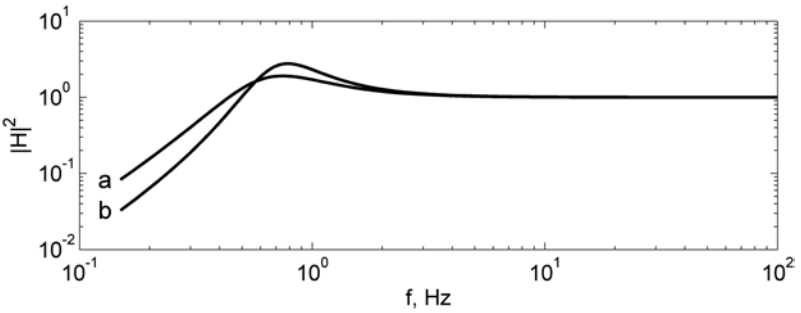

Fig. 3.2 Squared modulus of the transfer function calculated from equation (3.18) for two versions of the freely ascending profiler, (**a**) and (**b**), explained in Table 3.1

where $\omega = 2\pi f = 2\pi / T$, and T is the wave period. The transfer function for two versions of the free-rising profiler is illustrated in Fig. 3.2.

The interpretation of the results shown in Fig. 3.2 is that long surface waves entrain the profiler if its excess buoyancy-to-weight ratio is sufficiently large. For wave frequencies $f < f_c \approx 0.4$ Hz, the transfer function drops sharply, which means that the free-ascending profiler is coupled with surface waves. The profiler does not follow waves with higher frequencies. The wavelength corresponding to $f_c = 0.4$ Hz calculated from the dispersion relationship for surface gravity waves is $\lambda_c = g / (2\pi f_c^2) = 9.5$ m. The length of the profiler $L_d \approx 1$ m appears to be much smaller than λ_c and has therefore been ignored in this simple model. Note also a small peak of the transfer function for $f = 0.7$ Hz, which results from the exponential depth dependence of the orbital wave motion.

The RMS velocity disturbance in the coordinate system moving with the freely ascending instrument can be written in the following way:

$$\sigma_p{}^2(z) = \int_{-\infty}^{+\infty} |H(i\omega)|^2 \, S_\eta(\omega) \exp(-2\omega^2 |z| / g) d\omega \tag{3.19}$$

Substituting $|H(i\omega)|^2$ in the form (3.18) and using a dispersion relation for linear surface gravity waves $k = \omega^2/g$ (3.19) is written as follows:

$$\sigma_p(z) = \left[\int_{-\infty}^{+\infty} \frac{\left(\omega^2 + w_0^2 \omega^4 / g^2\right) \omega^2 \, \exp\left(-2\omega^2 |z| / g\right) S_\eta(\omega)}{\left(2A_d - w_0 \omega^2 / g\right)^2 + \omega^2} d\omega \right]^{1/2}. \tag{3.20}$$

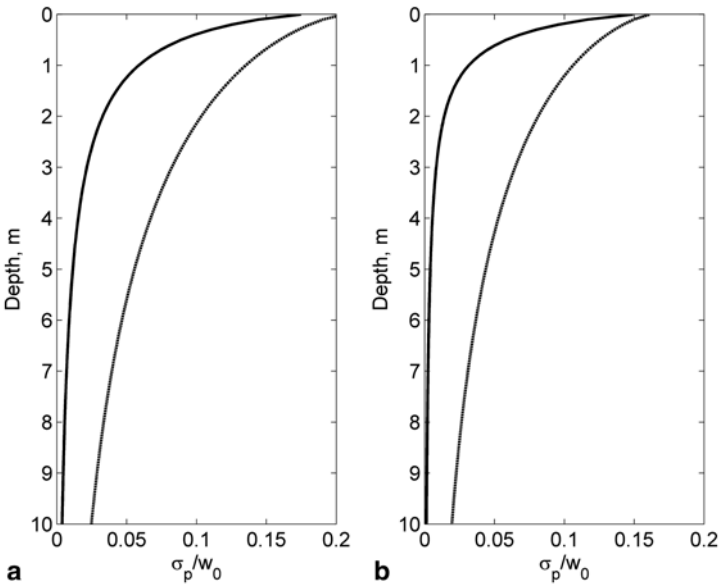

Fig. 3.3 RMS velocity disturbance from waves in the coordinate system moving with a freely ascending instrument (*bold lines*), for two versions of the profiler (explained in Table 3.1) for 7 m s^{-1} wind speed. For comparison, the RMS velocity disturbance from waves for an instrument moving with a steady vertical velocity in a fixed coordinate system is shown by *thin lines*

Figure 3.3 shows the relative velocity disturbance in the coordinate system of the moving profiler for two different weight-to-buoyancy ratios calculated with the Pierson and Moskowitz (1964) spectrum of surface waves (1.118) for a 7 m s^{-1} wind speed at 19.5 m height above the sea surface. The reduction of the RMS velocity disturbance due to the profiler's coupling with surface waves is significant; the depth range where Taylor's hypothesis of frozen turbulence is applicable ($\sigma_p/w_0 < 0.1$) substantially increases. For stronger winds, the profiler is even more coupled with waves, since the surface wave spectral peak shifts to lower frequencies.

The coefficient A_d entering (3.20) is determined by the ratio of profiler's excess buoyancy to its weight and profiler's terminal velocity. Due to energy constraints, A_d is relatively small for Argo floats and sea gliders. As a result, these instruments do not effectively follow wave motion when approaching the sea surface and are not ideal for microstructure and turbulence measurements in the near-surface layer of the ocean.

3.3.5 *A Near-Surface Turbulence and Microstructure Sensor System*

Original instrumentation and techniques were developed for near-surface turbulence and microstructure studies during Tropical Ocean-Global Atmosphere Coupled

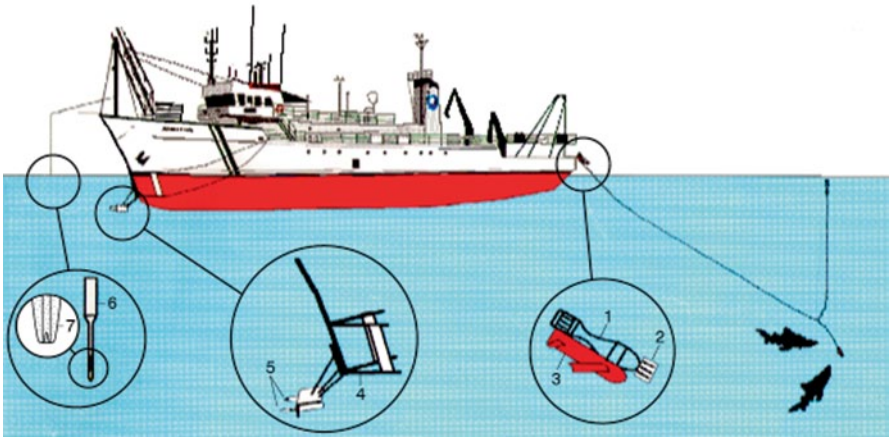

Fig. 3.4 Schematic illustration of devices deployed for small-scale measurements near the ocean–air interface on the R/V *Moana Wave*. Here, *1* free-rising profiler coupled with carrier; *2* temperature, conductivity and fluctuation-velocity probes on free-rising profiler; *3* carrier; *4* bow frame; *5* bow units (temperature, conductivity, pressure sensor; fluctuation-velocity, tilt sensor); *6* dropsonde; *7* temperature probe of micro-wire type

Ocean-Atmosphere Response Experiment (TOGA COARE) and *GasEx-98* (Soloviev et al. 1998, 1999). They were based on the following experimental approach:

1. Turbulence measurements are acquired with a fast-moving sensor;
2. Sensors with linear output are used; and
3. The analysis is made in a wave-following coordinate system.

The system consisted of a free-rising profiler, the bow-mounted sensors, and the dropsonde. Figure 3.4 schematically shows deployment of the devices on board the R/V *Moana Wave*. Figure 3.5 includes a photograph of the free-rising profiler and the bow sensors. They are also described briefly below and details are found in Soloviev et al. (1995, 1998, 1999). Azizjan et al. (1984) and Volkov and Soloviev (1986) described the dropsonde.

a) Free-Rising Profiler

An advantage of this method proposed by Vershinsky and Soloviev (1977) is the absence of a rigid mechanical connection with the ship's body. The measurement is done from below the surface, which assures minimal disturbance of natural conditions at the air–sea interface. This approach appears to be effective in measuring parameters of near-surface turbulence (Soloviev et al. 1988, 1998). The increased excess buoyancy-to-weight ratio of this free-ascending device reduces the influence of surface waves on turbulence measurements (see Sect. 3.3.4).

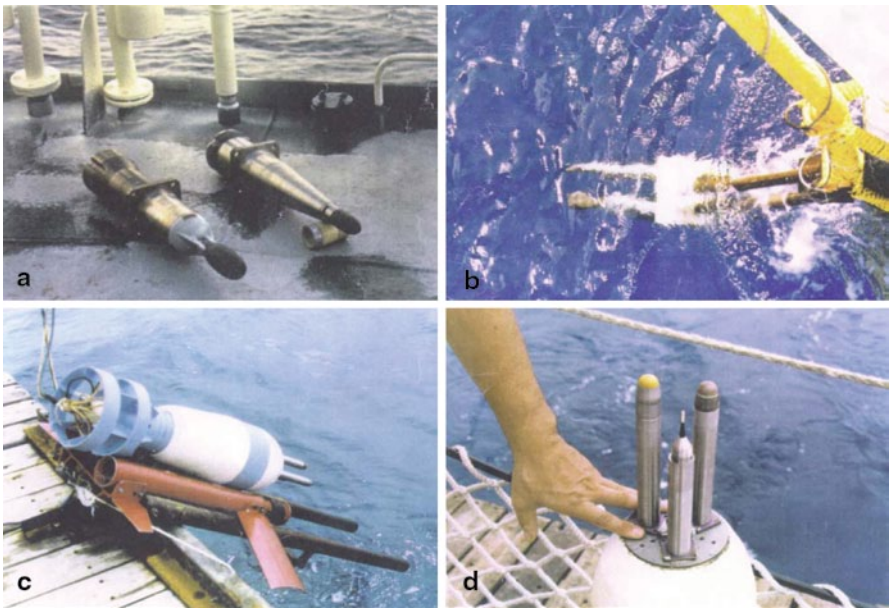

Fig. 3.5 Photos of bow sensors (**a**, **b**) and free-rising profiler (**c**, **d**)

The profiler's body is a hydrodynamic cylinder with a semi-spherical front constructed from dense foam that is positively buoyant (Fig. 3.5c). The tail section uses a weighted ring with stabilizers to assure vertical orientation during ascent and to increase the efficiency of water flow around the instrument. The electrical communication cable attaches at the tail section so as not to disturb the water being measured. The sensors protrude 15 cm out of the front of the instrument, which assures that undisturbed water is sampled by the sensors (Fig. 3.5d). A weighted delivery device is used to shuttle the profiler to its desired depth, 15–25 m, where a pressure-sensitive mechanism releases the profiler for ascent to the surface.

During TOGA COARE, a free-rising profiler connected with the "shuttle" (winged frame) was deployed from the stern of the R/V *Moana Wave* with the help of a metal frame, which allowed the device to slide from the ship into the water (Fig. 3.5c). After leaving the metal frame, the profiler fell into the water and slid outside the ship's wake to a distance of about 15–35 m as it sank (Fig. 3.4). This distance depended on the drift of the ship and the intensity of near-surface currents. Normally at 20-m depth, the pressure release mechanism released the profiler from the shuttle and the profiler turned to a vertical orientation. The profiler then ascended to the surface with a vertical velocity of 2–3 m s^{-1}, depending on the net buoyancy of the profiler. The rather large net buoyancy-to-weight ratio of the profiler provided nearly constant vertical speed with respect to the surrounding water mass (see Sect. 3.3.4). Studies of the temperature, salinity, and density profiles in the near-surface layer of the ocean with the free-rising profiler are described in Chap. 4.

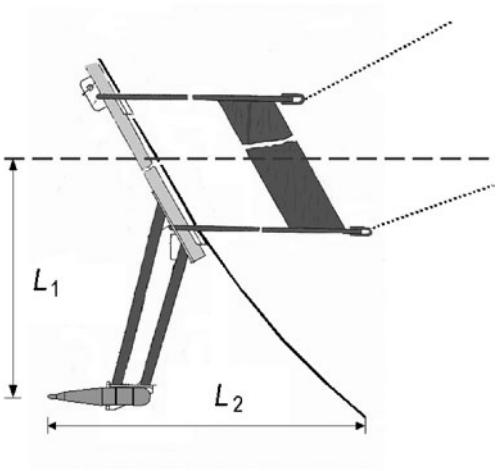

Fig. 3.6 Schematic diagram showing the probe mounting on the bow of the R/V *Moana Wave*. Mean depth of the probe $L_1 \approx 1.7$ m, spacing from the ship's hull $L_2 \approx 2$ m

b) Bow Probes

Bow probes included the electrical conductivity, temperature, and pressure (ECTP) probe and the electromagnetic velocity and acceleration (EMVA) probe (Fig. 3.5a). The EMVA sensor, originally developed for use on submarines, had a hydrodynamic form and a low hydrodynamic noise level. This probe is a linear device for a wide flow-speed range (0–12.5 m/s); the spatial resolution is about 1 cm. According to laboratory tests, the electronic noise level of the velocity sensor in the frequency range 2–400 Hz was equivalent to 0.8 mm s^{-1}. More details about the EMVA probe and the ECTP probe can be found in Soloviev et al. (1998, 1999).

A special metal frame was designed to install these probes on the bow of the vessel (Figs. 3.5b and 3.6). The mean depth of the sensors was about 1.7 m, which varied slightly during the cruise, depending on the levels of the ship's fuel and water tanks, and the ship speed.

The pressure wave in front of a moving ship can result in a rapid flow distortion (Fornwalt et al. 2002). From classical hydrodynamics, it is known that the flow in front of a moving sphere is significantly disturbed within approximately 3 radii of the sphere (Van Dyke 1982). To reduce disturbances by ship's hydrodynamics, a vessel with a sharp-angled hull should be used. At the level of the sensors, the angle of the hull of the R/V *Moana Wave* was ±15° and the curvature radius of the bow tip was about 0.2 m. The pressure wave therefore concentrated within a distance of approximately 0.6 m ahead of the hull. The bow frame (Fig. 3.6) positioned the sensor system at a distance of 2 m from the ship's hull, therefore, placing it outside the zone of most intense pressure disturbance.

Ship pitching and surface waves (including those reflected from the ship's hull) induce fluctuations in the mean flow at the sensor location. A strong velocity fluctuation may result in flow reversal, which affects the turbulence measurements. Although the problem of flow reversals during measurements with bow-mounted sensors is not that severe as in the case of mooring or tower-based systems, it may increase the noise level of measurements under low ship speeds and/or large waves.

To identify such cases, Soloviev et al. (1999) analyzed the sum $U_0 + V_x$, where U_0 is the ship speed and V_x is the longitudinal component of the bow velocity signal. (For the analysis of small-scale processes in this chapter, we assume that the sensor moves in the x-direction.) Negative values of $U_0 + V_x$ are flow reversals; these recorded segments are removed from further analysis. Flow reversals were found mainly at low ship speeds ($U_0 < 2$ m s^{-1}). Most of the data were taken at $U_0 \approx 5$ m s^{-1}; the cases with $U_0 < 2$ m s^{-1} have been removed from the analysis.

Due to surface waves and the ship pitching, the instantaneous depth of the sensors (defined here as the distance to the ocean surface) was continuously changing. The pressure signal was used to estimate the distance of the sensor to the ocean surface. To reduce dynamic pressure effects, the pressure sensor was positioned in the tail part of the bow probe. An RMS uncertainty of < 0.1 dbar (equivalent to less than 0.1 m) in pressure-to-depth conversion at a ship speed of 10–11 knots was estimated by Soloviev and Lukas (1996) using the pressure readings at the intersections of the water–air interface as detected by the conductivity sensor. The sensor depth variation profiled the vertical structure of the near-surface layer of the ocean.

The data were collected at a sampling rate of either 400 or 40 Hz. Due to pitching of the vessel, at times the sensors broke through the surface. The segments of signal corresponding to the probe surfacing or entering bubble clouds were removed from the analysis using the algorithm described in Soloviev et al. (1995). (A significant part of the TKE in the near-surface layer dissipates within the actively breaking waves that produce bubble clouds. Removing the segments affected by bubbles may unfortunately introduce a bias in the turbulence statistics close to the ocean surface.)

Figure 3.7 provides an example of the V_x-velocity spectrum calculated from a 10-min segment obtained at 5.5 m s^{-1} ship speed and 4 m s^{-1} wind speed. For spectral calculations, the measured velocity is "pre-whitened" by numerical differentiation in the time domain and then integrated in the frequency domain. The pre-whitening is a procedure aimed at reducing the "spectral leakage" (Jenkins and Watts 1998).

For comparison, the spectrum of integrated acceleration is also shown in Fig. 3.7a. The acceleration spectrum suggests that the vibration contamination occurs in narrow frequency bands. Further evidence of the nature and degree of the vibration contamination can be seen in the plot of the coherence between the velocity and integrated acceleration, as shown in Fig. 3.7c. The velocity contamination at frequencies less than 1 Hz is associated with the ship's motion and is outside of the band used for turbulence estimates. Above 8 Hz, there are varying degrees of vibration, with high coherence at 18, 25, 50, and 110 Hz.The removal of this vibration contamination by extrapolating the spectrum through known motion peaks or using a notch filter turns out to be relatively ineffective here because the resonant properties of the bow frame and ship depend on the position of the air–water interface with respect to the frame, which changes during the pitching period. Instead, we use the coherent noise cancellation technique, based on the Wiener filter, developed by Schoeberlein and Baker (1996) and tested with the TOGA COARE bow data in Soloviev et al. (1999).

One important aspect of implementing the Wiener filter is to insure that the reference correlation matrix is not singular and thus can be inverted. This can be a

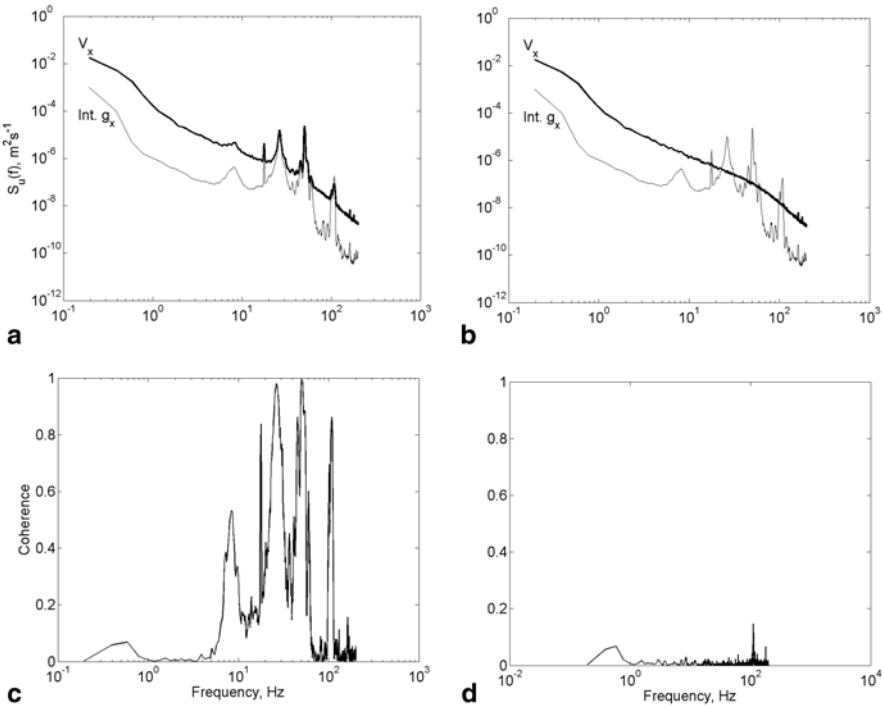

Fig. 3.7 Spectra of longitudinal velocity V_x and integrated longitudinal acceleration g_x **a** before and **b** after the coherent noise reduction using the Wiener filter. The coherence function between these two signals **c** before and **d** after filtering reveals practically complete cancellation of the ship vibrations in the velocity signal. (After Soloviev and Lukas 2003, with permission from Elsevier)

problem when using data that contain a strong low-frequency component, such as the ship's motion and the surface wave velocities at frequencies less than 1 Hz. To avoid this problem, the data are pre-whitened by numerical differentiation. To restore the velocity spectrum after the coherent noise cancellation, the signal is integrated.

Figure 3.7b shows the velocity spectrum after applying the coherent noise cancellation techniques using the Wiener filter with 60 weights; Fig. 3.7d presents the residual coherence. The 95% confidence intervals of the coherence (not shown here) enclose zero. This means that no statistically significant coherent contamination is left in the filtered signal. The effectiveness of the Wiener filter in the time domain is demonstrated in Fig. 3.8.

In Fig. 3.9, the spectrum of the velocity signal processed with the Wiener filter as described above is compared to the sensor electronics noise spectrum. The corresponding 95% confidence intervals are shown with thin lines. The confidence intervals for the spectral estimates calculated from 10-min velocity segments are very small because the number of degrees of freedom is large (234). The noise spectrum shown in Fig. 3.9a was measured in a laboratory tank with motionless

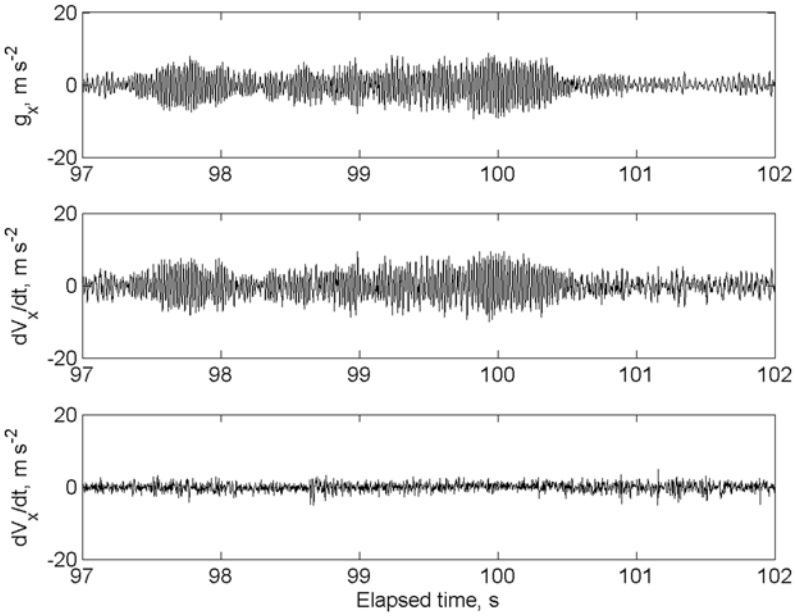

Fig. 3.8 Illustration of the coherent noise cancellation techniques in the time domain. This is a 5-s segment from the 10-min record used for spectral calculations in the example shown in Fig. 3.7. **a** Longitudinal component of acceleration, **b** time derivative of the original longitudinal velocity signal, and **c** time derivative of the longitudinal velocity signal after the coherent noise cancellation using a Wiener filter. The acceleration signal is shown in the same scale as that of the velocity derivative. (After Soloviev and Lukas 2003, with permission from Elsevier)

seawater during the post-cruise calibration.The RMS noise for the u channel over the frequency range 2–200 Hz was 0.8 mm s^{-1}.

Since the electronic noise and the measured velocity signal are not correlated, the noise spectrum can be subtracted from the u velocity spectrum. However, if the experimental spectrum is close to its noise level, this procedure may result in unrealistic negative spectral components at some frequencies. (Note that in Fig. 3.10,we subtract the noise spectrum from the velocity spectrum only for demonstration purposes.)

According to Kolmogorov's hypothesis, at sufficiently high wave numbers, the statistical structure of turbulence has a universal form; the scaling parameters depend only upon ε, the dissipation rate of TKE, and upon ν, the kinematic viscosity. This hypothesis implies that at high wave numbers the turbulence is locally isotropic. The one-dimensional velocity spectrum in the *inertia-viscous subrange* that is taken by a sensor moving in the x-direction is as follows (Stewart and Grant 1962):

$$E_u(k_x) = (\varepsilon\nu^{-5})^{1/4} F_u(k_x\eta_\nu) \tag{3.21}$$

where E_u is the longitudinal (in the x-direction) velocity spectrum, k_x is the wavenumber in the x-direction ($k_x = 2\pi f/U_0$ by Taylor's hypothesis (3.8)), F_u is a univer-

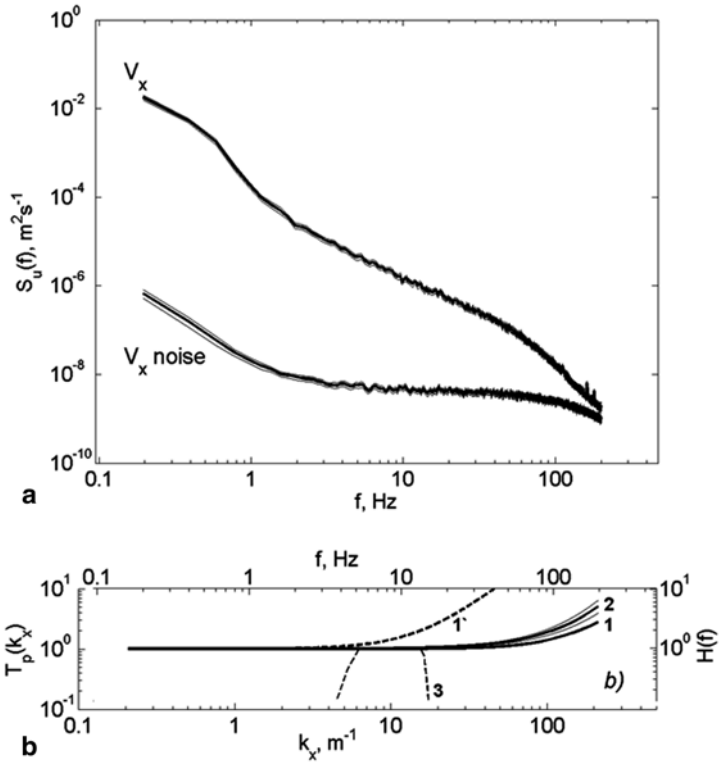

Fig. 3.9 **a** Spectrum of the velocity signal *u* after processing with the Wiener filter in comparison with the spectrum of electronic noise measured in the laboratory tank. *Thin lines* represent 95 % confidence intervals. **b** Transfer functions and corresponding corrections: *line 1* is the correction for antialias filter for 400 Hz sampling rate, while *line 1*‘ is the correction for 40 Hz sampling rate; *curve 2* is the correction for the spatial averaging of the sensor (the *thin lines* indicate the error interval in determining the sensor’s transfer function in laboratory); *curve 3* (*dashes*) shows the frequency range that is being used for calculation of dissipation rates from short velocity segments. Both frequency and wavenumber axes are displayed. The wavenumber axis is calculated using the frozen field hypothesis (3.8) for $U_{0=}5.94$ m s^{-1}. (After Soloviev and Lukas 2003, with permission from Elsevier)

sal function of its non-dimensional argument $k_x\eta_v$, and $\eta_v = \nu^{3/4}\varepsilon^{-1/4}$ is the Kolmogorov internal scale of turbulence. In the inertial subrange ($k_x\eta_v << 1$), equation (3.21) reduces to $E_u(k_x) = \alpha_1\varepsilon^{2/3}k_x^{-5/3}$, where dimensionless constant $\alpha_1 \approx 0.5$.

Several interpolation formulas of the universal function F_u can be found in the literature on turbulence (Novikov 1961; Hinze 1975; Oakey 1982; Moum et al. 1995). Here we will use the form of function F_u as empirically determined by Nasmyth (1970; c.f. Oakey 1982), which has been used in many studies of oceanic turbulence.

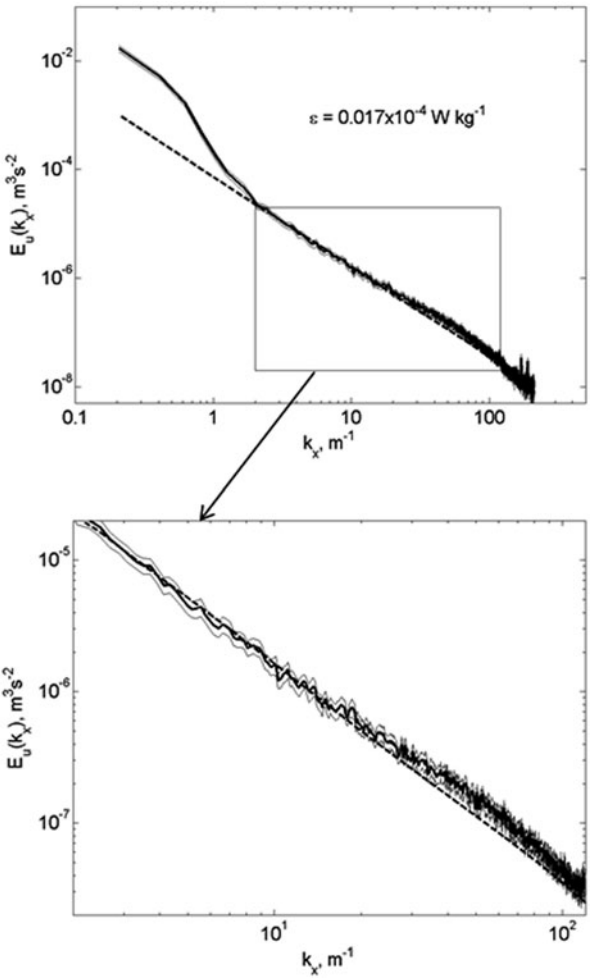

Fig. 3.10 Theoretical spectrum of turbulence and its fit to the experimental spectrum using the Stewart and Grant (1962) techniques. The *dashed line* is the Nasmyth turbulence spectrum, the *bold line* is the experimental velocity spectrum, and the *thin lines* indicate 95 % confidence limits. The segment marked by a *rectangle* is shown in more detail. (After Soloviev and Lukas 2003, with permission from Elsevier)

The theoretical spectrum of turbulence and its fit to a measured velocity spectrum using the Stewart and Grant (1962) techniques are shown in Fig. 3.10. The measured timeseries are transformed into a frequency spectrum, which is then converted into the wavenumber spectrum using Taylor's hypothesis and transfer functions for the antialias filter and spatial averaging (Fig. 3.9b). The theoretical spectrum in Fig. 3.10 corresponds to $\varepsilon = 1.7 \times 10^{-6}$ W kg^{-1}.

The large deviation from the theoretical turbulence spectrum on the left (Fig. 3.10, upper subplot) is due to the surface wave and ship pitching disturbances, consistent with the results of Stewart and Grant (1962). There is also a slight difference between the experimental and theoretical spectra in the wavenumber range from 20 to 120 m^{-1}. This is presumably an effect of the rapid flow distortion produced by the pressure wave in front of the moving ship. Recently, Fornwalt et al. (2002) modeled this effect numerically and found that the rapid flow distortion results in the

net production of TKE concentrated at relatively small scale, which thus affects the velocity spectrum primarily at high wave numbers. Note that the observed deviation might also be introduced by the correction factor for the probe spatial resolution that is known with only 20 % accuracy (Fig. 3.9b). Similar to the disturbance from surface waves, this deviation is not expected to affect the dissipation rate estimate made with the spectrum fitting techniques of Stewart and Grant (1962).

The uncertainty of the ε estimation due to spectral scatter is small in this example because confidence intervals are small. The spectral scatter, however, is not the only source of error in the dissipation rate estimation. Other errors are introduced by the uncertainty of the instrument towing speed and probe calibration. As we analyze only the data that satisfy Taylor's hypothesis of frozen turbulence, the fluctuation of the towing speed does not exceed 10 %. The calibration coefficient for the velocity probe is known with 5 % accuracy.

Both the ship's pitching and surface waves induce fluctuations of angle between the flow direction and the probe's longitudinal axis. At sufficiently large angles, the 40-mm diameter tip of the electromagnetic velocity probe may start shedding vortices, which are the source of additional hydrodynamic noise. In the example shown in Fig. 3.9a, the ship speed $U_0 = 5.9$ m s^{-1}; disturbances with 40-mm wavelength translate into a frequency $f = 140$ Hz. There are several relatively small, but persistent, spectral peaks observed in the velocity spectrum for $f > 140$ Hz (Fig. 3.9a). These peaks are not observed in the noise spectrum taken in the laboratory (motionless water) and are supposedly due to the hydrodynamic noise of the sensor. The signal in the frequency range from 4 to 16 Hz that we use here for dissipation rate estimates, however, is not affected by this type of hydrodynamic noise.

Not included are the errors associated with the assumption of isotropy that are implicit in (3.21), which alone may introduce a 50 % error (Oakey and Elliott 1982). The individual estimates of ε are therefore known within a factor of 2.

The dissipation rates calculated from the records longer than the ship's pitching period are in fact averages over the probe depth range. In the near-surface layer of the ocean (where the vertical profile of dissipation rate can be a nonlinear function of depth), this may result in additional errors in the calculation of ε. To address this problem, Soloviev and Lukas (2003) have developed an alternative technique: Dissipation rates are estimated from short segments and are sorted by depth. Confidence intervals are reduced by subsequent averaging within depth bins.

Calculation of the dissipation rate from short segments consists of the following steps:

a) Each 10-min u record is edited with the processing algorithm described in Soloviev et al. (1995) to remove the segments when the probes surface or enter bubble clouds. Continuous segments of 5 s or longer are identified and processed with a 60-weight Wiener filter to remove the vibration contamination.

b) Variance $\sigma_u^2 = \mathrm{var}(u')$ is calculated for 0.1 s long, 50 % overlapping segments, where u' is the velocity signal processed with the Wiener filter and band-passed with a finite impulse response (FIR) filter. The transfer function of the band-pass filter is shown in Fig. 3.9b. The 4–16 Hz frequency band is selected to

minimize the influence of surface waves and ship's pitching from one side and possible rapid flow distortion and the uncertainty in the probe's spatial resolution from the other side.

c) The theoretical variance, σ_{ut}^2, is defined as a function of the dissipation rate ε as follows:

$$\sigma_{ut}^2(\varepsilon) = \int_0^\infty H_{hp}(f) H_{lp}(f) S(f;\varepsilon) df, \tag{3.22}$$

where $H_{hp}(f)$ is the transfer function of the band-pass FIR filter and $H_{lp}(f)$ is the transfer function of the antialias filter; $S(f;\varepsilon) = 2\pi U_0^{-1} E_u(k_x;\varepsilon)'$, $E_u'(k_x;\varepsilon) = T_p(k_x) E_u(k_x;\varepsilon)$, $T_p(k_x)$ is the transfer function characterizing probe's spatial averaging, $E_u(k_x;\varepsilon)$ is calculated from (3.21) using the Nasmyth spectrum, and wavenumber $k_x = 2\pi U_0^{-1}$. The transfer functions, $H_{bp}(f)$, $H_{lp}(f)$, and $T_p(k_x)$ are shown in Fig. 3.9b.

d) In order to estimate ε, the equation

$$\sigma_u^{\,2} = \sigma_{ut}^{\,2}(\varepsilon) \tag{3.23}$$

is solved by an iteration method, where $\sigma_{ut}^{\,2}(\varepsilon)$ is determined using the discrete version of integral (3.22). The iteration process starts from a very small initial dissipation rate $\varepsilon = 1.2 \times 10^{-12}$ W kg^{-1} and finishes at the value of ε that satisfies Eq. (3.23) with 1 % accuracy.

e) The dissipation rate estimates obtained from 0.1-s segments are then averaged within overlapping 10 cm depth bins over the 10-min record segments. In order to account for the intermittent nature of turbulence, the mean dissipation rate and the confidence intervals are calculated using formulas of Baker and Gibson (1987). These formulas assume a lognormal distribution of the turbulence dissipation rate.

Note that the fluctuation of the mean flow speed during a 0.1-s interval is much smaller than for a segment including the full pitching period. The reduction of the mean flow fluctuation facilitates the use of Taylor's hypothesis of frozen turbulence under conditions of high seas and strong pitching of the ship. Figure 3.11a, b demonstrates two examples of the averaged vertical profile of dissipation rate ε obtained with this algorithm. The example shown in Fig. 3.11b was taken under high wind and wave conditions. The confidence intervals in Fig. 3.11b are bigger than in Fig. 3.11a in part because a larger percentage of points were removed due to the probe surfacing or entering bubble clouds.

For further analysis, we use the dissipation rates calculated from short segments according to the method described above. The dissipation rates calculated for a month-long COARE cruise are plotted in Fig. 3.12 as a function of wind speed. The cases when the ship speed was less than 2 m s^{-1} or the ship course or speed varied

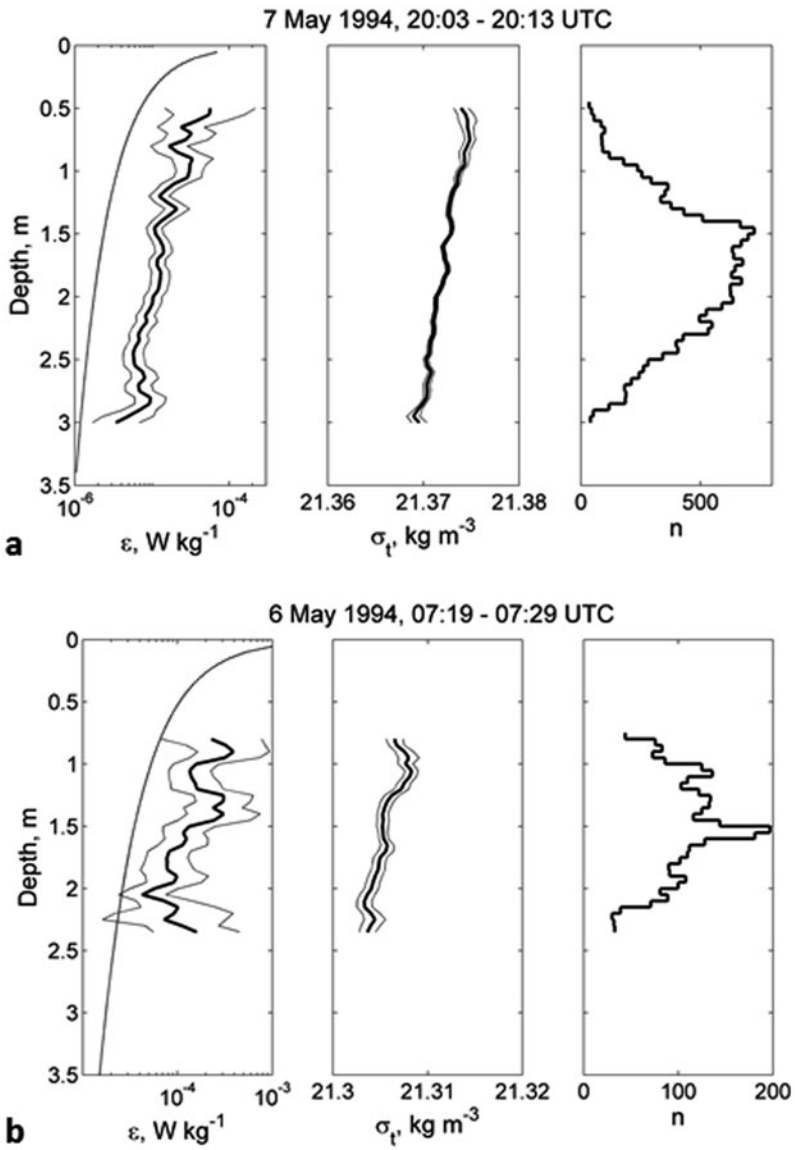

Fig. 3.11 Vertical profiles of dissipation rate ε and σ_t density averaged within 5 cm depth bins over a 10-min bow record segment. *Thin lines* are 95% confidence intervals calculated using the method of Baker and Gibson (1987). *Dashed line* is the logarithmic layer prediction. Number of points N in each depth bin is also shown. **a** Wind speed $U_{15} = 9.4$ m s^{-1}, significant wave height $H_s = 1.8$ m; **b** $U_{15} = 19$ m s^{-1} and $H_s = 3.3$ m. (After Soloviev and Lukas 2003, with permission from Elsevier)

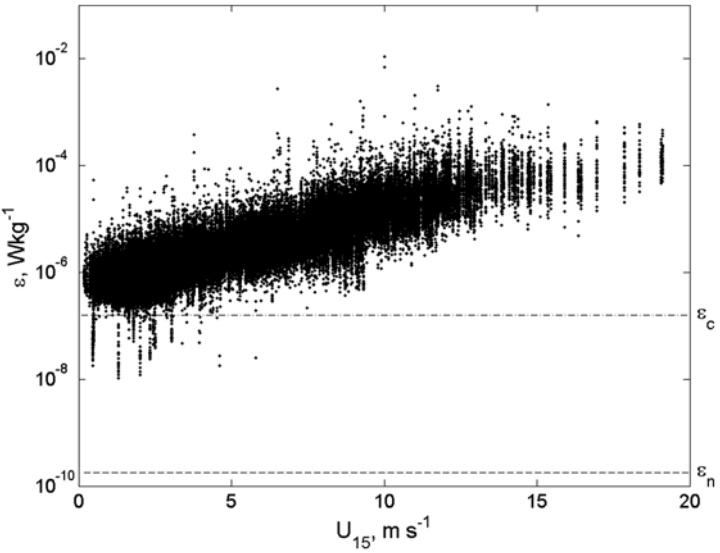

Fig. 3.12 Estimated ε from the bow sensors versus wind speed, U_{15}, at 15 m height during the month-long COARE EQ-3 cruise of the R/V *Moana Wave*. Each point represents a 10-min average (no sorting by depth in this graph). The electronic noise of the sensor is indicated as a *horizontal dashed line* $\varepsilon_n = 1.8 \times 10^{-10}$ W kg^{-1}. (After Soloviev and Lukas 2003, with permission from Elsevier)

more than 10 % are excluded from these statistics. Note that the data in Fig. 3.12 are not sorted by depth.

The equivalent electronics noise level of the velocity sensor, $\varepsilon_n = 1.8 \times 10^{-10}$ W kg^{-1}, shown in Fig. 3.12 by a horizontal line is obtained by processing the laboratory noise record via steps (a) through (d). According to Fig. 3.12, this noise level is much less than the dissipation rate that is typically observed in the near-surface layer of the ocean. No noise correction is therefore required for moderate and high wind speed conditions.

To elucidate possible influence by surface waves on the dissipation rate estimation, we have calculated the wave kinetic energy in the wavenumber band that is used here for dissipation rate estimates. The theoretical variance is calculated using the Pierson and Moskowitz (1964) spectrum (multiplied by ω^2, where $\omega = 2\pi f$), surface wave dispersion relationship $k = \omega^2 / g$, the transfer function of the band-pass filter (shown in Fig. 3.9b, curve 3), and the depth attenuation factor, e^{2kz}. The theoretical variance is then processed via steps a) through d) to obtain an error estimate, ε_r. The relative error, $\varepsilon_r/\varepsilon$ exceeded 10 % only in 0.2 % of all cases collected during the EQ-3 cruise. These points are removed from the analysis, but this does not affect the dissipation rate profile averaged over the EQ-3 cruise in any significant way (Soloviev and Lukas 2003). The above error estimate may however be slightly higher if to use the Elfouhaily et al. (1997) instead of Pierson and Moskowitz (1964) spectrum.

3.4 Wave-Enhanced Turbulence

3.4.1 Dimensional analysis

One of the important parameters of turbulence is the dissipation rate of TKE, ε. Some conclusions about the vertical profile of ε in the near-surface layer of the ocean can be made from dimensional analysis. This is irreversible loss of kinetic energy to molecular motion. In contrast to TKE, the dissipation rate of TKE does not explicitly depend on the length scale of turbulence, which is not a well-defined parameter due to broad wavenumber spectrum of the turbulent motion.

For an equilibrium surface wave spectrum, ignoring buoyancy, Earth's rotation, molecular viscosity (for length scales above Kolmogorov's internal length scale of turbulence), and capillary wave effects, the following functional dependence can be hypothesized (Soloviev et al. 1988):

$$\varepsilon = function(u_*, |z|, g), \tag{3.24}$$

where u_* is the friction velocity in the near-surface layer of the ocean, g is the acceleration of gravity, and z is the depth (expressed in a wave-following coordinate system (3.1), for instance). Standard dimensional analysis leads to the following dependence:

$$\varepsilon\kappa|z|/u_*^3 = \psi(g|z|/u_*^2), \tag{3.25}$$

where ψ is a universal function of its nondimensional parameter $g|z|/u_*^2$. The asymptote of (3.25) for $z \to -\infty$ should be the logarithmic layer law (3.4), which corresponds to $\psi \equiv 1$.

Figure 3.13a shows the data obtained by Soloviev et al. (1988) and Thorpe (2003a) under conditions of developed seas (wave age $A_w = c_p / u_{*a} > 13$). For turbulence measurements, Soloviev et al. (1988) used a free-rising profiler, while Thorpe et al. (2003a) employed an AUV. In order to minimize the influence of thermohaline stratification on the near-surface turbulence, only the data obtained under conditions of surface wave breaking ($U_{10} \geq 6$ m s^{-1}) are analyzed in Fig. 3.13a.

Though the nondimensional variables $g|z|/u_*^2$ and $\varepsilon\kappa|z|/u_*^3$ provide a convenient reference system for the analysis of near-surface turbulence data for developed seas, this scaling may not work well under conditions of developing seas. The latter conditions are typical for lakes and coastal regions with short fetch but are also often observed in the open ocean due to changing wind patterns. Note that the wave-breaking process and, hence, parameters of near-surface turbulence depend on the stage of surface wave development (which includes wind stress history) rather than on the instantaneous wind stress.

A simple way to account for the effect of surface wave age on the near-surface turbulence dissipation has been proposed by Terray et al. (1996). These authors hy-

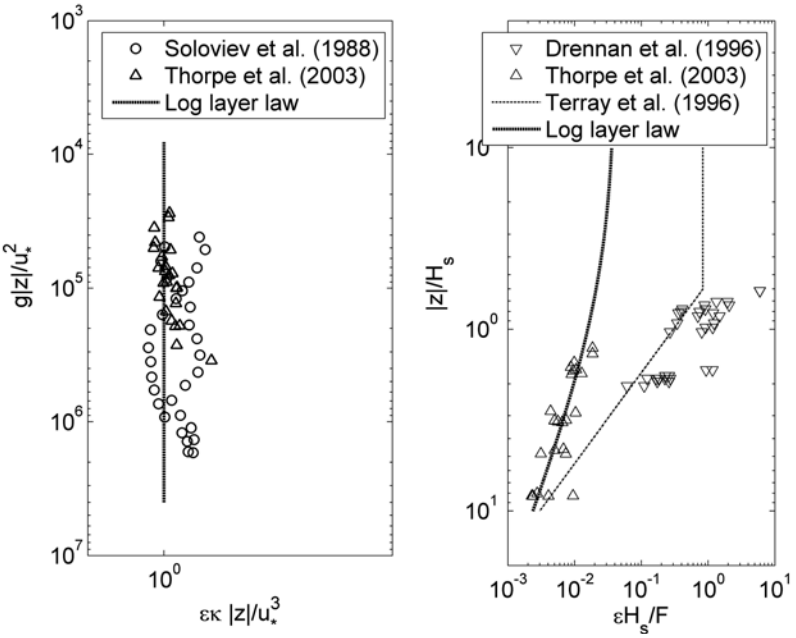

Fig. 3.13 The vertical distribution of **a** nondimensional dissipation $\varepsilon\kappa|z|/u_*^3$ as a function of nondimensional depth $g|z|/u_*^2$ according to measurements of Soloviev et al. (1988) and Thorpe et al. (2003a); **b** data of Drennan et al. (1996) and Thorpe et al. (2003a) in dimensionless coordinates $\varepsilon H_S/F_0$ and $|z|/H_S$. The field data shown here are for developed seas. In order to reduce possible effects of thermohaline stratification (as well as contributions from sensor noise), only data obtained under wave-breaking conditions ($U_{10}\geq 6$ m s^{-1}) are shown

pothesized that the proper nondimensional variables for the analysis of near-surface turbulence at different stages of surface wave development are $|z|/H_S$ and $\varepsilon\kappa z/F_0$, where H_s is the significant wave height and F_0 is the surface flux of TKE. Standard dimensional analysis then leads to the following formula:

$$\varepsilon H_S/F_0 = \psi_D\left(|z|/H_S\right), \tag{3.26}$$

where Ψ_D is a universal function of dimensionless depth z/H_S. A drawback of using functional dependence (3.26) is that the surface flux of TKE (F_0) is practically impossible to measure (since it is a third moment) and difficult to parameterize because of uncertainty in the wave generation models (see Sect. 1.6.6 and Chap. 6).

Furthermore, the surface flux of TKE from waves to the upper ocean, F_0, is an assumption. In fact, breaking waves are a volume source of TKE rather than surface flux. This assumption is relaxed in Sect. 3.4.3.

From the tower-based data collected in Lake Ontario under conditions of developing seas, Terray et al. (1996) proposed the following parameterization for the wave dissipation rate ε_{wv} based on scaling (3.26):

$$\varepsilon_{wv} H_S / F_0 = \begin{cases} 0.3(|z|/H_S)^{-2} & \text{for } |z| > 0.6H_S \\ 0.83 & \text{for } |z| < 0.6H_S \end{cases}. \tag{3.27}$$

Parameterization (3.27) represents only the wave-breaking turbulence; the shear-generated turbulence must be treated separately.

Figure 3.13b demonstrates the dissipation data sets of Thorpe et al. (2003a) and Drennan et al. (1996), which were obtained under conditions of developed seas. The flux of the TKE from wind to waves was determined from the parameterization formula for a fully developed wave spectrum (1.118). (The measurements of Soloviev et al. (1988) could not be scaled according to (3.26), because only visual estimates of surface wave heights were available.) One group of data (Thorpe et al., 2003a) is consistent with the log layer model (3.4), while the other (Drennan et al. 1996) appears to follow the Terray et al. (1996) parameterization (3.27). Since both datasets are for developed seas, the wave age is not expected to be a major factor in this difference. However, these data sets are reconciled in Sect. 3.4.3 with theoretical models of wave-enhanced turbulence of Craig and Banner (1994) and Benilov and Ly (2002).

3.4.2 *Craig and Banner (1994) Model of Wave-Enhanced Turbulence*

Craig and Banner (1994; hereafter CB94) proposed a one-dimensional model of wave-enhanced turbulence based on the level 2.5 Mellor and Yamada (1982) turbulence closure scheme. All statistical characteristics of turbulence and surface waves are functions of z and t only. Thus, three-dimensional (3D) processes are not explicitly included in CB94 though they may be of importance (see Chap. 5). Surface wave-breaking effects are incorporated into this model via the TKE flux from waves to upper ocean. Basic assumptions of the CB94 model are that the TKE flux is a surface flux, which is applied at the air–sea interface, and the random hydrodynamic fields of the upper layer are horizontally homogeneous.

The momentum equations (1.17) and (1.18) for the mean flow driven by the wind represent a balance between the flow acceleration, Coriolis force, and the change of the vertical momentum flux with depth under low Rossby number approximation. These equations under the additional assumption of horizontal homogeneity and no mean horizontal pressure gradients are as follows:

$$\frac{\partial u}{\partial t} = -\frac{1}{\rho_0}\frac{\partial \tau_{zx}}{\partial z} + fv, \tag{3.28}$$

$$\frac{\partial v}{\partial t} = -\frac{1}{\rho_0}\frac{\partial \tau_{zy}}{\partial z} - fu, \tag{3.29}$$

in which t is the time, z is the vertical coordinate measured positive upward, f is the Coriolis parameter; $\tau_{zx} = -\rho K_M \partial_z u$, $\tau_{zy} = -\rho K_M \partial_z v$, and K_M is the eddy viscosity for momentum transfer. In (3.38)-(3.29), $u(z,t)$ is the mean velocity component in the x direction and $v(z,t)$ is the mean velocity component in the y-direction, normal to the mean wind stress. The vertical coordinate z in CB94 is specified relative to the still water surface. The model, however, is compatible with the wave-following coordinate system described by transformation (3.1)−(3.2).

The eddy viscosity K_M is expressed in CB94 according to the Prandtl and Kolmogorov-type hypothesis (Mellor and Yamada 1982):

$$K_M = lqS_M, \tag{3.30}$$

where l is the turbulent length scale; and q, the turbulent velocity scale, is formally introduced as $q=(2b)^{1/2}$, where b is the TKE. The dimensionless parameter S_M in (3.30) is an empirical constant; for stratified conditions, however, it will depend on the Richardson number.

The equation for TKE is as follows:

$$\frac{\partial b}{\partial t} = \frac{\partial}{\partial z}\left(lqS_q \frac{\partial b}{\partial z} \right) + lqS_M \left[\left(\frac{\partial u}{\partial z} \right)^2 + \left(\frac{\partial v}{\partial z} \right)^2 \right] - \varepsilon, \tag{3.31}$$

where S_q and S_M are empirical constants (S_M=0.39 and S_q=0.2). Equation (3.31) follows from Eq. (1.24) given in Chap. 1 and the parameterization for eddy viscosity (3.30). Buoyancy forces are ignored in CB94. The term on the left-hand side of (3.31) is the rate of change of the TKE, the first term on the right-hand side describes the diffusion of the TKE, and the second term on the right-hand side represents energy generation by shear. The final term is the dissipation due to turbulent motion, which is parameterized via another hypothesis by Kolmogorov,

$$\varepsilon = q^3 / (Bl), \tag{3.32}$$

where B=16.6 is a dimensionless constant. The length scale in the CB94 model is approximated as a linear function of depth (distance from the surface):

$$l = \kappa(|z| + z_0). \tag{3.33}$$

where κ=0.4 is von Karman's constant, $|z|$ is the depth (expressed in coordinate system (3.1), for instance), and z_0 is the surface roughness parameter (from the water side).

Boundary conditions for the momentum equations (3.28) and (3.29) are respectively:

$$K_M \frac{\partial u}{\partial z} = u_*^2 \quad \text{and} \quad K_M \frac{\partial v}{\partial z} = 0. \tag{3.34}$$

Boundary conditions (3.34) orient the wind stress along the $\dot{x}$-axis.

The TKE input due to waves is set as a surface boundary condition (see also (1.124)):

$$F_0 = lqS_q \frac{\partial b}{\partial z} = \alpha_w u_*^3, \tag{3.35}$$

where $a_w \approx 100$. This parameterization is relatively insensitive to the sea state for wave ages encompassing wind seas from wave age $A_w = c_{pw}/u_{*a} > 13$ to fully developed situations, where u_* is the friction velocity in the atmospheric boundary layer. For $A_w < 13$, a_w is no longer constant and depends on the wave age.

Boundary condition (3.35) is based on an assumption that wavebreaking is a surface source of turbulence. In fact, wave stirring penetrates to some finite depth and is a nonlocal source of turbulence (due to shear fluctuations in plunging or spilling wave breakers). Equation (3.31) does not include the corresponding volume source. An approach that treats breaking surface waves as a volume source of TKE is described in Sect. 3.4.

Boundary conditions for the momentum components and TKE at $z \to -\infty$ are set in the following way:

$$K_M \frac{\partial u}{\partial z} = 0, K_M \frac{\partial v}{\partial z} = 0, \text{ and } lqS_q \frac{\partial b}{\partial z} = 0. \tag{3.36}$$

The interpretation of the CB94 model presented here is slightly simplified, because it involves an infinite-depth layer (i.e., open ocean conditions).

Now consider the situation where the shear production of TKE balances dissipation, which leads to the classic logarithmic boundary layer. The steady-state solution for this asymptotic regime is obtained by neglecting terms with time derivative in (3.28), (3.29), and (3.31). The balance of two terms on the right-hand side of (3.31), representing the shear turbulence production and the dissipation, the assumption of a constant stress layer, and the surface boundary conditions, produce the relationship

$$q = u_*(B/S_M)^{1/4}. \tag{3.37}$$

Substituting q and l in (3.32) with (3.33) and (3.37), respectively, gives the classic formula (3.4) for the dissipation rate in the logarithmic layer:

$$\varepsilon_{sh} = \frac{u_*^3 (B/S_m)^{3/4}}{B\kappa(|z| + z_0)} = \frac{u_*^3}{\kappa(|z| + z_0)}. \tag{3.38}$$

Note that constants in the Mellor and Yamada (1982) closure scheme are chosen so that $S_M{}^3 B \equiv 1$ to ensure that for $|z| >> z_0$ the logarithmic layer asymptote (3.4) is achieved; the logarithmic layer (or constant stress layer) asymptote requires that the Coriolis terms in (3.28) and (3.29) are neglected. According to the CB94 estimate, the Coriolis terms are unimportant for $|z| << \kappa u_* / f$. This condition is typically satisfied within the wave-stirred layer, which is relatively thin (less than one significant wave height thick), according to observations. Below the wave-stirred layer, the Coriolis as well as buoyancy force (ignored in CB94) gradually take over dynamics of the upper ocean boundary layer as depth increases. (See discussion on the Coriolis and buoyancy effects in Sect. 3.6.)

For the asymptotic steady-state regime, when TKE is produced at the surface according to (3.35) and the shear production term is eliminated from (3.31), the TKE equation represents a balance between the downward diffusion of energy injected at the surface and dissipation ε_{wv}. Thus, (3.31) reduces to

$$S_q \kappa^2 B \frac{\partial}{\partial z}\left[\left(|z| + z_0 \right) \frac{\partial q^3}{\partial z} \right] = 3 \frac{q^3}{\left(|z| + z_0 \right)}. \tag{3.39}$$

The solution to (3.39) is as follows:

$$q^3 = c_+ \left(|z| + z_0 \right)^n + c_- \left(|z| + z_0 \right)^{-n}, \tag{3.40}$$

where $n = [3 / (S_q \kappa^2 B)]^{1/2} = 2.4$, and constants c_+ and c_- are to be determined from (3.36) and the condition of turbulence decay at large depth: $b = 0$ for $z \to -\infty$. The c_- term in (3.40) represents decay away from the surface, while the c_+ term should be equal to zero to satisfy the boundary condition for $z \to -\infty$. The turbulence velocity scale is then described as follows:

$$q = c_-{}^{1/3} (|z| + z_0)^{-n/3}, \tag{3.41}$$

and the asymptotic formula for dissipation rate due to wave breaking reads

$$\varepsilon_{wv} = c_- (|z| + z_0)^{n-1} / (\kappa B) \tag{3.42}$$

The constant c_- can be determined from boundary condition (3.35) to give

$$\varepsilon_{wv} = \alpha_w u_*{}^3 \sqrt{\frac{3B}{S_q}} \left(\frac{z_0}{|z| + z_0} \right)^n \tag{3.43}$$

When both shear production and diffusion are present, the dissipation rate can be approximated as a sum of the two asymptotic terms, (3.38) and (3.43):

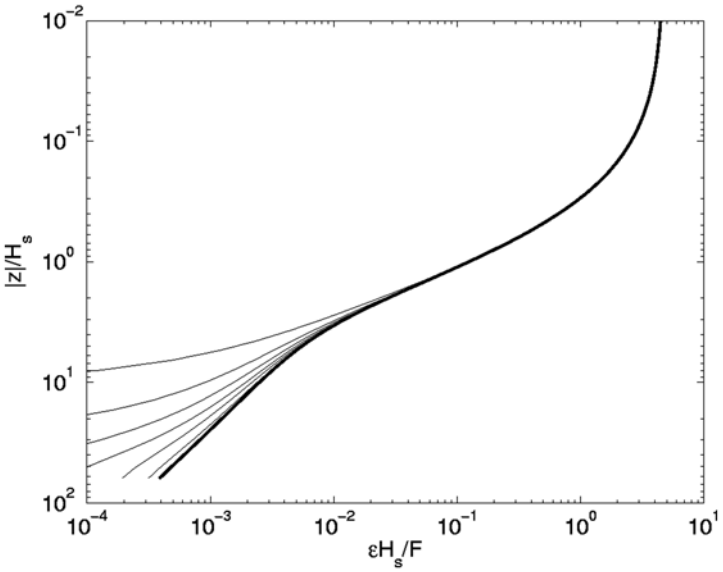

Fig. 3.14 Numerical solution of the Craig and Banner (1994) model for a finite-depth layer $H=100$ m. First *thin line* is the solution for $t=0.5$ h and the *bold line* is the solution for $t=10$ h. Time interval between lines is 95 min. (After Soloviev and Lukas 2003, with permission from Elsevier)

$$\varepsilon \approx \varepsilon_{sh} + \varepsilon_{wv} = \frac{u_*^3}{\kappa\left(|z| + z_0\right)}\left[1 + \alpha_w \sqrt{\frac{3}{BS_q}}\left(\frac{z_0}{|z| + z_0}\right)^n\right]. \tag{3.44}$$

where $\sqrt{3/(BS_q)} \approx 0.95$.

Adjustment of the turbulence regime to local conditions is relatively fast (Fig. 3.14); in many cases, it is possible to use the steady-state solution for the upper few meters of the ocean. Figure 3.15 demonstrates the numerical steady-state solution of the CB94 model, its asymptotes, and analytical approximation (3.44). According to Fig. 3.15, formula (3.44) approximates the numerical solution very well (they are almost indistinguishable on the plot).

In nondimensional coordinates $\tilde{\varepsilon} = \varepsilon\kappa(|z| + z_0)/u_*$ and $\tilde{z} = (|z| + z_0)/z_0$, formula (3.44) reduces to a compact form:

$$\tilde{\varepsilon} = 1 + \alpha_w \sqrt{\frac{3}{BS_q}}\tilde{z}^{-n} \approx 1 + 0.95\,\alpha_w \tilde{z}^{-n}. \tag{3.45}$$

According to CB94, for developed waves ($A_w > 13$): $\alpha_w \approx 95$. For developing waves ($A_w < 13$), α_w is no longer a constant and depends on wave age $A_w = c_p / u_{*a}$, where $u_{*a} = \tau_0 / \rho_a$ and τ_0 is the surface momentum flux.

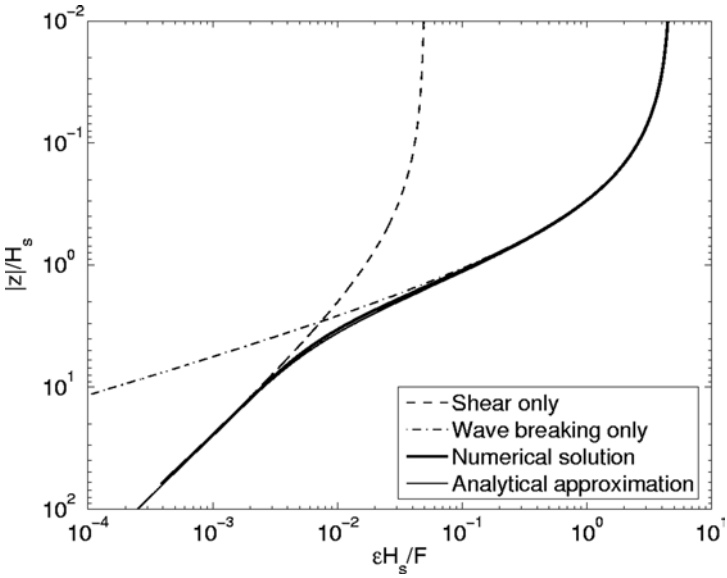

Fig. 3.15 Steady-state numerical solution of the Craig and Banner (1994) model and its analytical approximations (3.38), (3.43), and (3.44). Note that approximation (3.44) is difficult to distinguish in this figure because it is very close to the numerical solution. (After Soloviev and Lukas 2003, with permission from Elsevier)

The surface roughness from the waterside, z_0, is a critical but still poorly known parameter. It depends both on the physics of the turbulent boundary layer and on the properties of the free sea surface. Bye (1988) proposed a Charnock's (1955) type formula for z_0:

$$z_0 = a_C u_*^2 / g \tag{3.46}$$

with a_C=1,400. Terray et al. (1996) concluded that for wave-breaking conditions, dimensionless coefficient a_C is much larger (a_C~150,000). A magnitude of a_C higher than in Bye (1988) also follows from the modeling study of the near-surface circulation in Knight Inlet by Stacey (1999) who noted that it also depends on wave age.

Alternatively, Terray et al. (1996) parameterized surface roughness via significant wave height:

$$z_0 = c_T H_S, \tag{3.47}$$

where c_T~1. According to Pierson and Moskowitz (1964), for a fully developed (equilibrium) surface wave spectrum,

$$H_S = 4\sigma_\eta \approx 1.576 \times 10^5 u_*^2 / g. \tag{3.48}$$

Assuming that parameterizations (3.46) and (3.47) should converge for conditions of fully developed waves, that is,

$$z_0 = c_T H_S = a_C u_*^2 / g, \tag{3.49}$$

one can find that $c_T = 1$ corresponds to $a_C = 157{,}600$. The two orders of magnitude difference in a_C between authors is an indication of the extent of the problem of parameterizing and modeling near-surface turbulence.

Integration of the dissipation profile given by equation (3.43) from $z = 0$ to depth h_{50} (above which 50 % of the wave energy dissipates) results in the following equation for h_{50},

$$\int_{-h_{50}}^{0} \varepsilon dz = \alpha_w u_*^{\,3} \left(3B / S_q\right)^{1/2} \int_{-h_{50}}^{0} \left[z_0 / \left(z + z_0\right)\right]^n dz = 0.5\, \alpha_w u_*^{\,3} \tag{3.50}$$

The solution of this equation is

$$h_{50} = z_0 \left(2^{1/n} - 1\right) \approx z_0 / 3. \tag{3.51}$$

This means that in the CB94 model, 50 % of the wave-breaking energy dissipates within the layer $h_{50} = c_T H_S / 3 \approx 0.2 H_S$ (if parameterization (3.47) holds). Solution (3.51) is invariant with respect to constant α_w. However, the vertical distribution of dissipation rate (3.44) does depend on α_w (in general α_w is a function of wave age).

In Fig. 3.16, the COARE turbulence dissipation rates and the CB94 model (3.45) are plotted together in dimensionless coordinates $\varepsilon\kappa(|z| + z_0)/u_*^3$ and $(|z| + z_0)/z_0$, where z_0 is parameterized with formula (3.46) or (3.47). Dissipation rates ε are 10-min averages of the dissipation rate calculated from 0.1 s segments with techniques described in Sect. 3.3.5. The wall-layer prediction is shown by dashed vertical line $\tilde{\varepsilon} \equiv 1$.

According to the time-averaged experimental results presented here, a dissipation rate 3–20 times larger than the logarithmic layer prediction is observed in the upper few meters of the ocean under moderate and high wind speed conditions. We interpret these increased turbulence levels as the effect of surface wave breaking.

The main cause of the scatter of dissipation rate estimates shown in Fig. 3.16 is believed to be turbulence intermittency, which is a fundamental property of turbulence (though complicated here by the intermittency of the wave-breaking events). Gurvich and Yaglom (1967) presented theoretical considerations based on Kolmogorov's idea of intermittent turbulence leading to the conclusion that the dissipation rate of TKE should have a lognormal distribution.

Figure 3.17 illustrates the average COARE profiles of the dissipation rate from Fig. 3.16. Averaging is done according to Baker and Gibson (1987); confidence intervals are shown with thin lines. The fit between the field data and model profiles

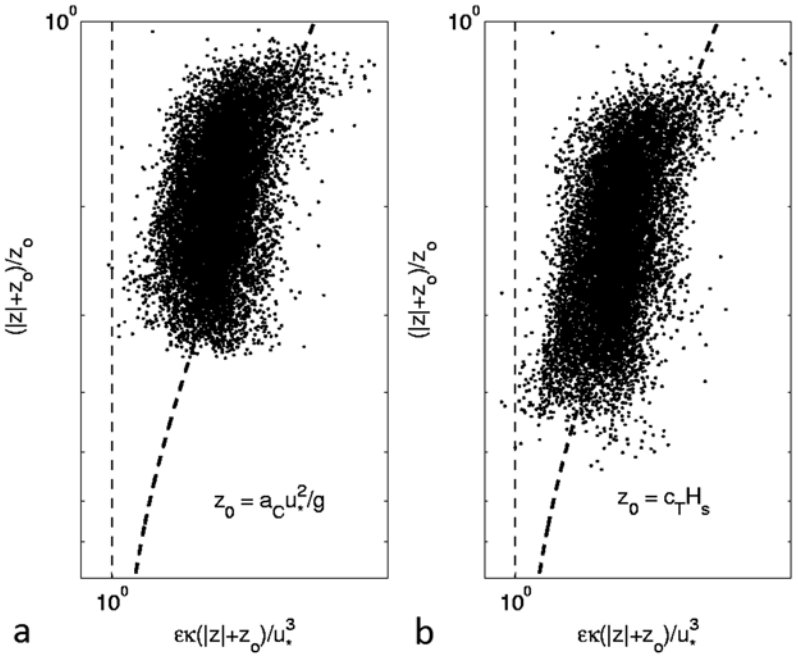

Fig. 3.16 **a** Dissipation rates scaled according to (3.45) and the waterside surface roughness z_0 parameterized with (a) Eq. (3.46) and (b) Eq. (3.47). *Points* are the COARE EQ-3 bow data (10-min averages) taken under moderate wind speed conditions (U_{15}>9.5 ms^{-1}). The *vertical dashed line* is the logarithmic layer model. The *bold dashed curves* are the Craig and Banner (1994) model of wave-enhanced turbulence (3.45) at (a) $a_C=9\times10^4$ and (b) $c_T=0.6$. (After Soloviev and Lukas 2003, with permission from Elsevier)

shown in Fig. 3.17a is obtained with z_0 parameterized according to (3.46) with $a_C=9\times10^4$. Further tuning of constant a_C does not improve the agreement between the experimental data and theory. The same experimental data and the same model are shown in Fig. 3.17b for z_0 parameterized according to (3.47) with $c_T=0.6$, close to that of Terray et al. (1996).

From equation (3.48) and equality (3.49), $c_T=0.6$ corresponds to $a_C=94{,}560$. This is consistent with $a_C=90{,}000$ obtained from the fit of the CB94 model to the field data shown in Fig. 3.17b.

Very close to the ocean surface, a substantial part of the data was removed from the analysis because of bubbles disturbing the measurements. The editing procedure thus might bias average dissipation rate estimates close to the ocean surface because bubble areas are associated with the most energetic wave-breaking events. To determine the constant c_T, we therefore used the deeper part of the experimental profile. (This constant would be smaller if we used the near-surface part of the profile.)

Figure 3.18 shows the COARE data scaled according to the Terray et al. (1996) variables z/H_s and $\varepsilon H_s/F_0$. The CB94 model (3.44) with z_0 parameterized according

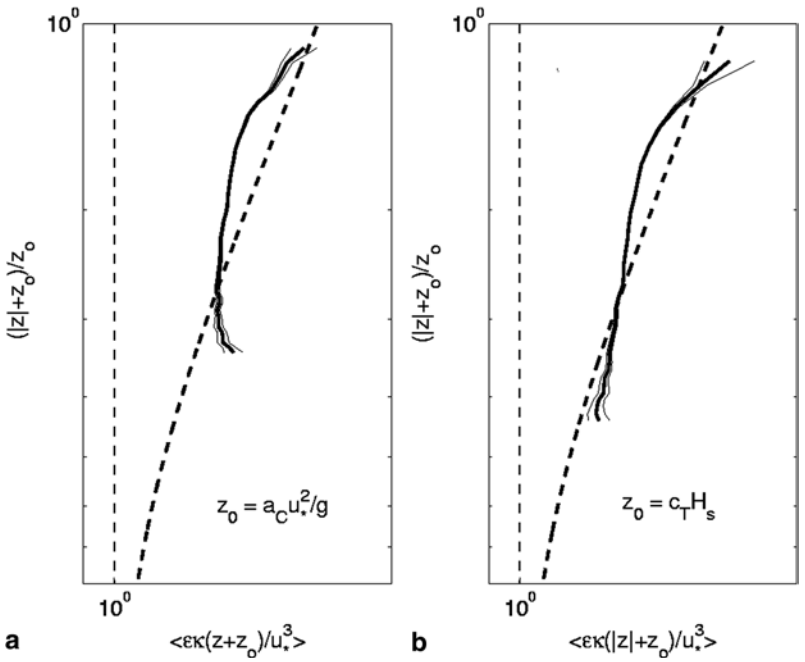

Fig. 3.17 Average dimensionless dissipation rate profiles for the COARE EQ-3 cruise versus dimensionless depth at $U_{15}>7$ m s^{-1}, for different parameterizations ofthe waterside surface roughness length: (a) formula (3.46) for $a_C=90{,}000$, (b) formula (3.47) with $c_T=0.6$. *Thin lines* represent the 95% confidence intervals. The *vertical dashed line* is the logarithmic layer model. The *bold dashed curves* are the Craig and Banner (1994) model (3.45). (After Soloviev and Lukas 2003, with permission from Elsevier)

to (3.47) and with the turbulence flux of the kinetic energy expressed with (3.35) reads in dimensionless coordinates $\varepsilon H_S/F_0$ and z/H_S as follows:

$$\varepsilon H_S/F_0 = \frac{1+\alpha_w\sqrt{3/(BS_q)}(1+c_T^{-1}z/H_S)^{-2.4}}{\kappa(c_T+z/H_S)}. \tag{3.52}$$

The original Terray et al. (1996) model (3.27), the Craig and Banner (1994) model (3.44) with $c_0=0.6$, and the logarithmic layer model (3.4) are also shown.

The horizontal point-dashed line in Fig. 3.18 represents the depth of the layer, $H_{50}=0.6H_s$, within which 50% of the wave energy dissipates according to the model of Terray et al. (1996) given by (3.27). Depth h_{50}, where 50% of the wave-induced turbulence energy dissipates, is determined for the Craig and Banner (1994) model by $h_{50}=z_0/3$ (see (3.51)). With parameterization (3.47) for $c_T=0.6$, this corresponds to

$$h_{50} \approx 0.2H_S, \tag{3.53}$$

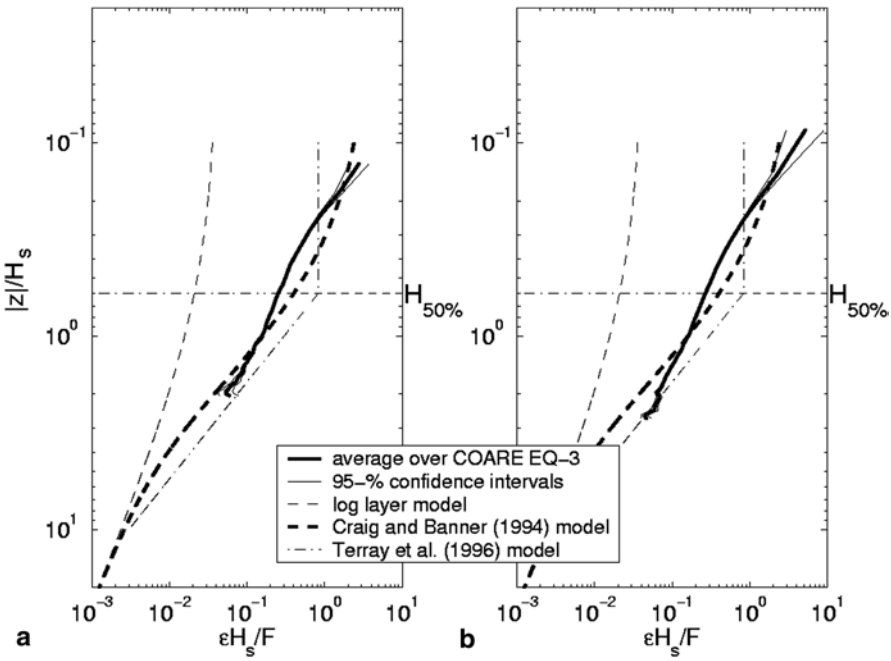

Fig. 3.18 The normalized dissipation rate, $\varepsilon H_s/F_0$, versus dimensionless depth, z/H_s, for **a** wind speed range from 9.5 to 19.1 m s^{-1} and **b** wind speed range from 7 to 19.1 m s^{-1}. The CB94 dependence is calculated with surface roughness from waterside parameterized as $z_0 = 0.6\ H_s$. (After Soloviev and Lukas 2003, with permission from Elsevier)

which is 3 times smaller than H_{50} from Terray et al. (1996). Equation (3.53) means that 50 % of the wave breaking turbulence dissipates very close to the surface, within only 20 % of significant wave height.

According to Fig. 3.18a, the near-surface dissipation rates are in a better agreement with the Craig and Banner model (3.52) using the Terray et al. (1996) parameterization (3.47) than with the original Terray et al. (1996) model (3.27). Note that no tuning coefficients are available in the original Terray et al. (1996) model. Model (3.52) predicts lower values of dissipation than model (3.27) in the layer, $z > 0.4\ H_s$; above this layer, model (3.52) has larger dissipation rates than (3.27).

A possible reason for this difference is the use of the wave following versus fixed co-ordinate system. If the wave breaking energy substantially dissipates above the trough line, and the vertical dissipation rate profile is a nonlinear function of depth, then the difference between fixed and wave-following measurements can be significant. For instance, in a fixed coordinate system it is practically impossible to study near-surface layers with a thickness less than the surface wave height. In fact, any observational point between the wave trough and crest will alternate between water and air. Therefore, in order to study turbulence above the trough line, a wave-following coordinate system is required. We follow here Csanady's (1984) suggestion to analyze the near-surface data in the coordinate system connected to the ocean

surface. The Craig and Banner (1994) model is consistent with the Csanady (1984) concept. The Terray et al. (1996) model, which is originally fit to tower-based data, would produce a different dissipation profile in the wave-following coordinate system.

Two other possible reasons for unresolved differences between (3.27) and (3.52) can be related to the fact that model (3.27) is substantially based on the fit to a tower-based data set. The standard Taylor hypothesis of a frozen field of turbulent eddies cannot be directly applied for the turbulence analysis of the tower-based measurements because the velocity fluctuation is not small relative to the mean flow. In addition, nonlinear components of surface waves, which are not removed from the tower-based velocity records, might result in an overestimation of ε.

It should be noted that there is no reliable estimate of the average dissipation rate within the wave-turbulent layer $|z|<0.6H_s$ in the literature. The constant dissipation rate that is set in (3.27) for $|z|<0.6\ H_s$ is not based on any experimental data; it results from energy constraints. In Soloviev and Lukas (2003), the dissipation data were averaged in a wave-following coordinate system and were available starting from a depth $|z|=0.1H_s$. These estimates of the dissipation rate in the layer stirred by breaking surface waves could, however, be biased because of extensive editing of the bubble-disturbed segments. This editing procedure might exclude the most energetic turbulence events associated with breaking waves from the statistics. The experimental dissipation profile systematically deviates from model (3.52) for $|z|<0.6\ H_s$ (Fig. 3.18a). In the layer $0.1\ H_s<|z|<0.6\ H_s$, the integral dissipation rate, $\int \varepsilon(z)\,dz$, is about 5 times less than that predicted by model (3.52). This suggests that during these measurements about 80 % of the wave energy dissipating in the layer stirred by breaking waves might be unaccounted for because of bubble disturbances. Although the averaging technique of Baker and Gibson (1987) accounts for the turbulence intermittency, it nevertheless may not completely compensate for editing bubble-disturbed segments. For the same reason, the confidence intervals might also be underestimated close to the ocean surface.

Figure 3.18b shows the same graphs but for the average dissipation rate profile for moderate and high wind speed conditions ($U_{15}=7$–19.2 m s^{-1}). The experimental profile in Fig. 3.18b extends to deeper layers than in Fig. 3.18a. The interpretation of Fig. 3.18b is, however, hindered because of larger uncertainty in the significant wave height data than in Fig. 3.18a. In the experiment of Soloviev and Lukas (2003), this uncertainty rapidly increases with the decrease in the wind speed.

The main features of the CB94 model can be summarized as follows:

1. Prandtl-type mixing length specification;
2. A TKE equation representing a balance between parameterized versions of diffusion, dissipation, and shear generation;
3. The Kolmogorov-type eddy viscosity proportional to the mixing length and the square root of TKE;
4. Dimensionless constants (κ, B, Sq, andS_M) are determined from fluid dynamics problems that are not related directly to wave-enhanced turbulence; and

5. A surface TKE input, due to the waves, set proportional to the cube of the friction velocity.

We should make one final remark here about the CB94 model, which is based on the turbulence closure scheme of Mellor and Yamada (1982). There have been reports that this closure scheme does not work well in flows with negligible shear-production (Umlauf and Burchard 2003). Though the flow in spilling wave breakers is not shearfree because of intense air entrainment leading to the formation of a bore-like structure (Sect. 1.6.4), the length scale hypothesis (3.33) may not necessarily hold in this case. In the next section, we consider the model of Benilov and Ly (2002), which addresses this problem.

3.4.3 *Benilov and Ly (2002) Wave-Turbulent Model*

The CB94 model treats breaking waves as a surface source for the TKE. Benilov and Ly (2002; hereafter BL02) considered breaking waves as a volume source of energy. They incorporated wave kinetic energy b_w into the TKE budget equation (1.24) following ideas of Kitaigorodskii et al. (1983):

$$\frac{\partial b}{\partial t} = \mathrm{Pr}_b^{-1} \frac{\partial}{\partial z}\left[\nu_T \left(\frac{\partial b}{\partial z} + \sigma_w \frac{\partial b_w}{\partial z} \right) \right] + \nu_T \left[\left(\frac{\partial u}{\partial z} \right)^2 + \left(\frac{\partial v}{\partial z} \right)^2 \right] - \varepsilon \qquad (3.54)$$

where Pr_b is the Prandtl number for the TKE diffusion, $\sigma_w = \mathrm{Pr}_b/\mathrm{Pr}_\varepsilon$, Pr_ε is the turbulent Prandtl number for dissipation rate, $b_w = \frac{1}{2}\left(u_w^2 + v_w^2 + w_w^2\right)$, u_w, v_w, w_w are the velocity components of the potential velocity wave field, and the eddy viscosity in terms of k-ε turbulence theory is as follows:

$$\nu_T = c_\nu b^2 / \varepsilon = l b^{1/2}. \qquad (3.55)$$

Parameterization (3.55) for eddy viscosity ν_T is derived from the same (Kolmogorov-type) hypothesis as that for K_M in the CB94 model. The numerical values of the corresponding empirical constants in BL02 are however somewhat different from CB94. We therefore reserved a separate symbol for eddy viscosity in this section.

A common estimate of the turbulent Prandtl number is $\mathrm{P}_b\mathrm{r} = 1$, and constant c_ν is the dimensionless empirical constant with typical numerical value $c_\nu = 0.09$ (Hoffmann 1989). Equation (3.54) is similar to the regular form of the kinetic energy budget equation (3.31). There is, however, an important difference—the kinetic energy of potential waves b_w appears to enter the TKE budget in the form of the turbulent diffusion of the wave kinetic energy. Parameter σ_w shows the relative wave kinetic energy that can be transferred by turbulence. According to Longuet-Higgins (1969),

$\sigma_w << 1$. In the formulation of BL02, parameter σ_w is an eigenvalue of the boundary-layer problem.

In the BL02 model, the equation for length scale (3.33) is replaced with the equation for dissipation rate in the form of $k-\varepsilon$ turbulent theory with an extra term Π_v, which is the wave source of dissipation increase:

$$\frac{\partial \varepsilon}{\partial t} = \mathrm{Pr}_\varepsilon^{-1} \frac{\partial}{\partial z}\left(\nu_T \frac{\partial \varepsilon}{\partial z}\right) + c_1 c_v b\left[\left(\frac{\partial u}{\partial z}\right)^2 + \left(\frac{\partial v}{\partial z}\right)^2\right] + \Pi_v - c_2 \frac{\varepsilon^2}{b} \tag{3.56}$$

where c_1, c_v, and c_2 are the dimensionless constants.

As $b_w \to 0$, equation (3.54) reduces to the corresponding equation (3.31) in the CB94 model. As we mentioned above, the numerical constants in CB94 and BL02 appear to be somewhat different.The variability of all constants for the k-ε group models is discussed in Patel et al. (1984). In order to preserve the integrity of the BL02 model we accept the same typical numerical values, $\mathrm{Pr}_\varepsilon = 1.3$, $c_1 = 1.44$, $c_v = 0.09$, and $c_2 = 1.92$, as in the original BL02 model. The impact of the variability of constants on the BL02 model output has not yet been studied.

The term Π_v in the equation for ε describing the "production of dissipation" due to the wave kinetic energy b_w is not known. From general considerations, it should vanish as $z \to -\infty$ because the wave motion degrades far enough from the ocean surface. The system of equations (3.54)–(3.56) has hence two unknown functions: the kinetic energy of potential waves, b_w, and the production of the dissipation rate by waves, Π_v.

An analytical expression for the vertical distribution of the wave kinetic energy, $b_w(z)$, can be obtained from the linear theory of waves. The wave kinetic energy via the spectrum of surface waves $S_\eta(w)$ is described by the formula

$$b_w(z) = \tfrac{1}{2}\int_0^\infty S_\eta(\omega)\,\omega^2 \exp\left(-2\omega^2 |z|/g\right) d\omega, \tag{3.57}$$

which follows from the formulation of the surface wave spectra via the Fourier–Stieltjes integral (see Chap. 1, Sect. 1.6.5).

For the spectrum of surface waves in the form (1.118), which is the Pierson–Moskowitz spectrum, Benilov and Ly (2002) derived the following formula:

$$b_w(z) = b_w(0)(1 + \sqrt{|z|/L_*}) \exp(-\sqrt{|z|/L_*}) \tag{3.58}$$

where $b_w(0) = 0.5\beta_0 (g/\omega_p)^2$, $L_* = g/(24\omega_p^{\,2}) = \sigma_\eta/(12\beta_0^{1/2})$, $\beta_0 \approx 10^{-2}$, σ_η^2 is the variance of surface wave elevation, and ω_p is the frequency of the surface wave spectral peak.

Boundary conditions for the momentum balance equations, (3.28) and (3.29), remain the same as for the CB94 model (3.34). The boundary condition for the kinetic energy balance equation (3.54) is specified as the kinetic energy flux at $z = 0$:

$$F_0 = \mathrm{Pr}_b^{-1}\, \nu_T \frac{\partial}{\partial z}(b + \sigma_w b_w), \tag{3.59}$$

where the energy flux F_0 can be expressed either via the wave phase speed,

$$F_0 = \tfrac{1}{3}\, \gamma_1 \beta_0 \rho c_{pw}{}^3, \tag{3.60}$$

or via the friction velocity as in (3.35). Here $c_{pw} = g / \omega_p$ is the phase velocity of the wind waves spectral peak ω_p.

The boundary condition for the dissipation rate ε in equation (3.56) is specified as follows:

$$\varepsilon(0,t) = \varepsilon_0. \tag{3.61}$$

As $z \to -\infty$,

$$\frac{\partial b}{\partial z} = 0,\ \varepsilon = 0,\ \nu_T \frac{\partial u}{\partial z} = 0, \text{ and } \nu_T \frac{\partial v}{\partial z} = 0. \tag{3.62}$$

Following the vertical structure of the upper ocean turbulent boundary layer outlined in Sect. 3.2.4 (Fig. 3.1), there are three intermediate asymptotic solutions:

(1) *The wave-stirred layer*. This is a layer where the surface wave effect dominates and defines the dynamics of the turbulence. Hence, in the equation for the TKE (3.54), the energy production by the mean shear can be neglected (perhaps, except the upper few millimeters where the viscous effects between wave-breaking events are of importance). The vertical diffusion of the TKE is relatively small in this layer due to anticipated nearly uniform vertical distribution of TKE. Thus in the wave-stirred layer, $0 \le |z| \le H_{w-s}$:

$$\left|\frac{\partial b}{\partial z}\right| << \sigma_w \left|\frac{\partial b_w}{\partial z}\right| \text{ and } \nu_T \left[\left(\frac{\partial u}{\partial z}\right)^2 + \left(\frac{\partial v}{\partial z}\right)^2\right] << \varepsilon \tag{3.63}$$

The equation of TKE budget (3.54) in the steady case reduces as follows:

$$\sigma_w\, \mathrm{Pr}_b^{-1} \frac{d}{dz}\left[\nu_T \left(\frac{db_w}{dz}\right)\right] = \varepsilon \tag{3.64}$$

Rather than dealing with basically unknown function Π_v in (3.56), the BL02 model defines the turbulence length scale for the wave-stirred layer from relationship,

$$\mathrm{Pr}_v^{-1}\, \nu_T \frac{db_w}{dz} = r_c b^{1/2} b_w, \tag{3.65}$$

and from accepting the hypothesis that the correlation coefficient $r_c = \text{const}$. Substituting the Kolmogorov-type relationship(3.55) into (3.65) results in the following equation:

$$l = \chi b_w / \frac{db_w}{dz} = 2\sigma_w^{-1} \mathrm{Pr}_b \, rL_* \left(1 + \sqrt{\frac{|z|}{L_*}}\right), \tag{3.66}$$

where χ is the dimensionless proportionality constant.

Equation (3.64) with relationships (3.55) and (3.66) has an exact solution in the form

$$\varepsilon(z)/\varepsilon_0 = \left[\frac{\frac{3}{2}\left(1+\sqrt{|z|/L_*}\right)^{1/3}\exp\left(-\sqrt{|z|/L_*}\right)}{1+\frac{1}{2}\left[\left(1+\sqrt{|z|/L_*}\right)\exp\left(-\sqrt{|z|/L_*}\right)\right]^3}\right]^{3/2}, \tag{3.67}$$

where $L_* = H_s/(48\beta_0^{1/2}) \approx 0.21 H_S$ and

$$\varepsilon_0 = a_\varepsilon F_0 / H_S, \tag{3.68}$$

and a_ε is a dimensionless coefficient.

(2) *The turbulence diffusion layer*. This layer is a transition zone between the wave-stirred layer and the layer where the mean shear controls the turbulent regime,

$$H_{w-s} \le |z| \le H_{TD} \tag{3.69}$$

In this layer, the wave-stirring effect becomes insignificant compared to the turbulent diffusion of TKE, that is,

$$\left|\frac{db}{dz}\right| >> \sigma_w \left|\frac{db_w}{dz}\right| \tag{3.70}$$

The turbulent diffusion still significantly exceeds the mean shear contribution to the TKE budget, which can be expressed by the following inequality:

$$\nu_T\left[\left(\frac{\partial u}{\partial z}\right)^2 + \left(\frac{\partial v}{\partial z}\right)^2\right] << \varepsilon. \tag{3.71}$$

The BL02 model finds the solution in this layer as an intermediate asymptotic, where the TKE flux is balanced by the dissipation, and the dissipation production

term Π_v is assumed to be insignificant. Equations (3.54) and (3.56) then reduce to a set of two nonlinear ordinary equations:

$$\mathrm{Pr}_b^{-1}\frac{d}{dz}\left(\nu_T\frac{db}{dz}\right)=\varepsilon,\quad \nu_T=c_v\frac{b^2}{\varepsilon}=lb^{1/2}, \tag{3.72}$$

$$\mathrm{Pr}_\varepsilon^{-1}\frac{d}{dz}\left(\nu_T\frac{d\varepsilon}{dz}\right)=c_2\frac{\varepsilon^2}{b}. \tag{3.73}$$

The boundary condition for (3.72) and (3.73) is set at $z=-H_{w\text{-}s}$ in the following way:

$$c_v\,\mathrm{Pr}_b\left(\frac{b^2}{\varepsilon}\frac{db}{dz}\right)\Bigg|_{z=-H_{w-s}}=q_{w-s},\quad \varepsilon\Big|_{z=-H_{w-s}}=\varepsilon_1. \tag{3.74}$$

where q_{w-s} is the TKE flux from the wave-stirred layer and ε_1 is the dissipation rate at the lower boundary of the wave-stirred layer. As $|z|-H_{w-s}\to\infty$, the solutions for b and ε tend to zero since the asymptotic analysis assumes that the boundary conditions at the lower boundary of this layer does not influence the solution. This implies that the turbulence diffusion layer is sufficiently thick for the existence of the asymptotic behavior of the solution.

There is an ambiguity in the BL02 model in identifying the boundary between the wave-stirred and turbulence diffusion layers, $z=-H_{w-s}$, which is in fact the boundary between two asymptotic solutions. This ambiguity extends to the formulation of the TKE flux q_{w-s} at $z=-H_{w-s}$.

We will use here continuity of the dissipation rate ε at $z=-H_{w-s}$ and the value of coefficient α_ε in the formula for the surface dissipation rate of wave energy (3.68) preserving the total energy flux from wind to waves in the following way:

$$\int_{-\infty}^{-H_{w-s}}\varepsilon dz+\int_{-H_{w-s}}^{0}\varepsilon dz=F_0. \tag{3.75}$$

Boundary conditions (3.74) are correspondingly specified as follows:

$$c_v\,\mathrm{Pr}_b\left(\frac{b^2}{\varepsilon}\frac{d_z b}{dz}\right)\Bigg|_{z=-H_{w-s}}=F_0-\int_{-H_{w-s}}^{0}\varepsilon dz,\quad \varepsilon\Big|_{z=-H_{w-s}}=\varepsilon_1 \tag{3.76}$$

The exact solution of (3.72)–(3.73) for the dissipation rate in the turbulence diffusion layer is found in the form

$$\varepsilon=\varepsilon_1\left[1+(|z|-H_{w-s})/L_{*1}\right]^{-\nu_2}, \tag{3.77}$$

where ε_1 and L_{*1} are linked by boundary conditions (3.76) as follows:

$$L_{*_1} = 3q_{w-s} / \varepsilon_1, \tag{3.78}$$

and parameter v_2 is set as $v_2 = 4$ based on the laboratory measurements of the turbulence decay behind an oscillating grid (Thompson and Turner 1975).

(3) *The logarithmic layer.* In this layer, the equation for the dissipation rate of TKE is as follows:

$$\varepsilon_{sh} = u_*^3 / (\kappa |z|). \tag{3.79}$$

This solution is simply added to the wave solution to obtain the following parameterization formula for the dissipation rate:

$$\varepsilon = \varepsilon_{sh} + \varepsilon_{wv} \tag{3.80}$$

where ε_{sh} is the shear-generated dissipation and ε_{wv} is the wave-induced dissipation. The latter is described for developed waves by equations (3.67)–(3.77), which are combined below into a single expression:

$$\varepsilon_{wv} = 3.78 \frac{F_0}{H_S} \begin{cases} \left[\dfrac{3\left(1+\sqrt{\gamma\dfrac{|z|}{H_S}}\right)^{1/3} \exp\left(-\sqrt{\gamma\dfrac{|z|}{H_S}}\right)}{2+\left[\left(1+\sqrt{\gamma\dfrac{|z|}{H_S}}\right)\exp\left(-\sqrt{\gamma\dfrac{|z|}{H_S}}\right)\right]^3} \right]^{3/2} & \text{for } \dfrac{|z|}{H_S} \le 0.6 \\ 0.22\left[1+0.66\left(\dfrac{|z|}{H_S}-0.6\right)\right]^{-4} & \text{for } \dfrac{|z|}{H_S} > 0.6 \end{cases} \tag{3.81}$$

where $\gamma = 48\beta_0^{1/2}$.

The BL02 model accounts for the transfer of kinetic energy from breaking waves to turbulence and the length scale is not constrained by formula (3.33). This model is therefore expected to perform well in the wave-stirred layer. Note that the diffusive and logarithmic sublayers in this model are practically identical to CB94.

An important feature of the BL02 model is that it does not require z_0 to be specified (as in the CB94 model). The surface roughness from the waterside is no longer a model parameter in BL02. In the wave-stirred layer, the BL02 model, nevertheless, employs a simplified version of the dissipation rate budget equation, which unfortunately introduces a new adjustable parameter, which is the effective depth of the wave-stirred layer, $H_{w\text{-}s}/H_s$.

Figure 3.19 summarizes the results of recent field and theoretical studies of wave-enhanced turbulence. In order to minimize the influence of thermohaline

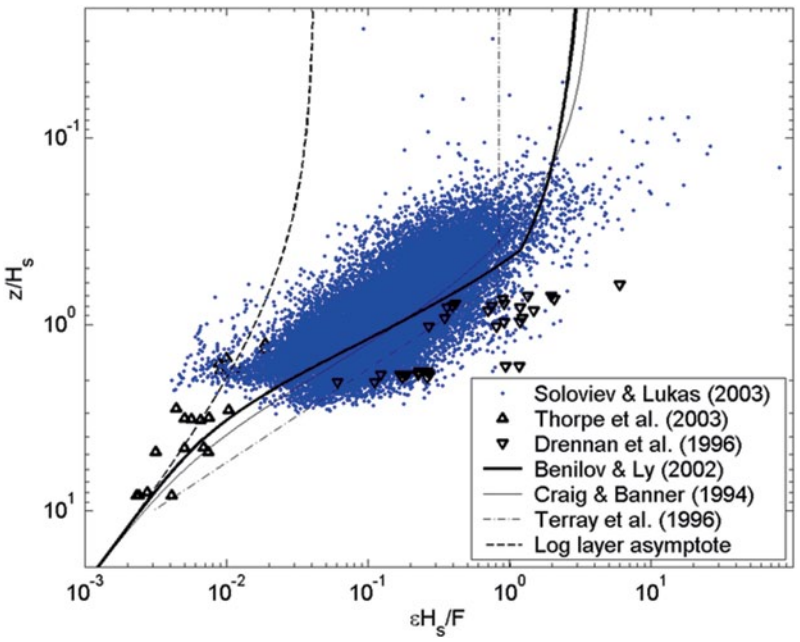

Fig. 3.19 Normalized dissipation rate $\varepsilon H_s/F_0$ versus dimensionless depth $|z|/H_s$ according to field (open ocean) and theoretical results. Here ε is the dissipation rate of the turbulent kinetic energy, F_0 the flux of the kinetic energy from wind to waves, and H_s is the significant wave height. Wind speed range is from 7 to 19 m s^{-1}. The Craig and Banner (1994) model is calculated with surface roughness from waterside parameterized as $z_0 = 0.6\ H_s$; the Benilov and Ly (2002) model is for $H_{w\text{-}s}/H_s = 0.4$, where $H_{w\text{-}s}$ is the effective depth of the wave-stirred layer. (After Soloviev and Lukas 2006),

stratification effects on near-surface turbulence characteristics, only the data obtained during high wind speeds are analyzed. The 1-month long data set of Soloviev and Lukas (2003) was collected under various wind–wave conditions. The contribution of remotely forced swell to the significant wave height, H_s, could contribute some scatter in the nondimensional dissipation rate, $\varepsilon H_s/F_0$, and the nondimensional depth, $|z|/H_s$.

Solution (3.80) is shown in Fig. 3.19 in comparison with the field data. At $H_{w\text{-}s}/H_s = 0.4$, parameterization formula (3.80) approximates reasonably well both the Thorpe et al. (2003a) and Drennan et al. (1996) data sets (in contrast to the analysis shown in Fig. 3.13b); it is also as consistent with the Soloviev and Lukas (2003) data.

Somewhat different from BL02, turbulence injection profiles have been implemented in Sullivan et al. (2007) and Kudryavtsev et al. (2008) models. Rascle et al. (2013), however, concluded that the injection depth in Sullivan et al. (2007) was too shallow, while in Kudryavtsev et al. (2008) too deep.

3.4.4 Concluding Remarks on Wave-Enhanced Turbulence

One of the first observations of near-surface turbulence dissipation was made by Stewart and Grant (1962) with a velocity sensor (thermo-anemometer) mounted on the bow of a vessel. Their data indicated that wave-generated turbulence essentially dissipates above the trough line.

A similar conclusion was reached by Soloviev et al. (1988) based on the analysis of dissipation rate profiles obtained with a free-rising profiler and of the observations made by Arsenyev et al. (1975), Jones and Kenney (1977), Dillon et al. (1981), and Oakey and Elliott (1982). In nondimensional coordinates $g|z|/u_*^2$ and $\varepsilon\kappa|z|/u_*^3$, the dissipation rates were near or slightly exceeding (within a factor of 2–3) the logarithmic layer prediction (Soloviev et al. 1988). Apparently, all of these data came mainly from below the layer of wave-enhanced turbulence. Furthermore, these analyzed data were confined to low and moderate wind speed conditions. Later, Greenan et al. (2001), Thorpe et al. (2003a), and Soloviev and Lukas (2003) obtained dissipation rate data sets under higher wind speed conditions(Fig. 3.19) that appeared to confirm the conclusion of Stewart and Grant (1962) and Soloviev et al. (1988) that the main part of the wave-generated turbulence dissipates within a near-surface layer whose depth is less than one significant wave height.

Tower-based turbulence measurements made in lakes by Kitaigorodskii et al. (1983) and Agrawal et al. (1992) under a wide range of wind speed conditions produced evidence in favor of a thicker layer of wave-enhanced turbulence and higher turbulence levels. Terray et al. (1996) proposed a new scaling that accounted for the limited fetch in the lake observations and dramatically reduced the differences between the two groups of data. Some differences, however, could not be explained solely by fetch and wave age and might be related to methodical issues. The interpretation of the above tower-based turbulence measurements is somewhat uncertain because the transfer from frequency to wavenumber domain is not well defined for oscillating flows and flow reversals may result in contamination by the structure.

Gerbi et al. (2008, 2009) advanced tower-based techniques by monitoring the current and wave direction relative to platform legs and the instrument, which largely eliminated the disturbances to turbulence measurements inflicted by the platform and the instrument housing. In addition, Gerbi et al. (2008, 2009) modified the Lumley and Terray (1983) method for dissipation rate estimates in oscillating flows by replacing the RMS velocity (σ_U) with the magnitude of the mean velocity (U). The data were analyzed only for $\sigma_U / U < 200\%$. Gerbi et al. (2008) provided theoretical justification for this 200% threshold, which was nevertheless 20 times higher than that formally allowed by Taylor's hypothesis of frozen turbulence.

For turbulence measurements, Soloviev et al. (1988) used a free-rising profiler, Greenan et al. (2001) employed a free-gliding instrument, and Thorpe et al. (2003a) utilized an AUV. All of these were moving instruments: It is apparently easier to satisfy Taylor's hypothesis of frozen turbulence with a moving instrument. All of these three instruments to some extent follow surface waves and, hence, have a tendency to provide the data in the Lagrangian wave-following coordinate system

(see Sect. 3.2.1). At the same time, the parameterization of Terray et al. (1996) is based on tower data that are collected and interpreted in a fixed coordinate system.

Energy budget considerations provide an estimate of the wavelength λ_{dis} where the transition toward the dissipation regime occurs (Kitaigorodskii 1991):

$$\lambda_{dis} = 2\pi E_0^{2/3} / (a_1 g) \tag{3.82}$$

where E_0 is the energy flux from the region of energy input through the non-dissipative region of the wave spectrum toward the dissipation subrange, and $a_1 \approx 1\times10^{-4}$ according to the most recent estimates of Gemmrich and Farmer (1999). Following Gemmrich et al. (1994), we equate this energy flux to the integral dissipation of surface wave energy due to wave breaking in the upper ocean, which in stationary conditions is equal to the flux of the TKE at the air–sea interface, $E_0 = F_0$. According to Pierson and Moskowitz (1964), for the saturated surface wave spectrum, the dominant wavelength $\lambda_p \approx 2\pi a_2 u_*^2 / g$, where $a_2 = 8.3\times10^{-5}$. From equations (3.35) and (3.82), it follows that $\lambda_{dis} / \lambda_p = \alpha_w^{2/3} / (a_1 a_2) \approx 0.26$. This means that breaking waves are much shorter than the dominant wave. Moreover, in the open ocean, about 98 % of breaking waves are of spilling type, which do not penetrate deeply (Gemmrich and Farmer 1999). About 2 % of breaking events show deeper penetration. The deeper penetrating events, which are typical for plunging wave breakers, however, play a minor role in upper ocean dynamics (even under the condition of swell opposing wind waves, when the occurrence of deep penetrating events increases to 10 % of the total number of breaking waves). The TKE produced by spilling breakers is localized in a shallow layer (also due to intensive bubble entrainment—see Melville 1994) and decays quickly with depth (Ly and Garwood 2000; Benilov and Ly 2002). This is consistent with results shown in Fig. 3.19, indicating that the wave-breaking energy mostly dissipates within less than one significant wave height from the ocean surface.

Gemmrich and Farmer (2004) and Farrar (2011) made direct spatial measurements of the velocity field with a pulse-to-pulse coherent acoustic Doppler sonar (DopBeam). This approach provides turbulent velocity spectra directly in the wavenumber domain, thus eliminating the need to use Taylor's hypothesis of frozen turbulence. It has been tested in a few field experiments (Gemmrich 2010; Gemmrich 2012). The measurement using DopBeam resulted in the thickness of the wave-stirred layer of about $0.2H_s$, which is consistent with our estimates.

The flux of TKE at the air–sea interface F_0 is a key component of the upper ocean parameterization schemes considered above. Although the direct (eddy correlation) measurement of F_0 is still a challenge, it can be estimated as the integral of the growth rate over the surface wave spectrum. Unfortunately, the commonly accepted wave generation theory based on the Miles (1957, 1959) mechanism still has significant uncertainty; as a result, it is not completely clear how accurate the estimates of F_o are using this theory (see discussion in Sect. 1.6.6 and Chap. 6).

Another complication of near-surface turbulence measurements under breaking waves is that substantial turbulence dissipation takes place in the active, bubble-saturated wave breakers that are practically not accessible by any of the existing measurement techniques. In fact, up to 80% of turbulent dissipation may occur in these active wave breakers (Soloviev and Lukas 2003).

Estimates of the thickness of the wave-stirred layer from observations of the turbulence dissipation rate to some extent depend on the flux of the kinetic energy from waves to turbulence (F_0) and on the unaccounted fraction of the turbulent dissipation in active wave breakers. The wave generation theory may be improved in the future by adding to the existing (Miles) theory the Farrell and Ioannou (2008) wave growth mechanism due to stochastic parametric instability of the Kelvin–Helmholtz type. Furthermore, Soloviev et al. (2012) have proposed a new approach, utilizing recent achievements in 3D sonar technology to study turbulence characteristics of ship wakes with high concentrations of air bubbles. The 3D sonar operating in the edge detection mode contours the shape of the turbulent wake by detecting the boundary of the bubble cloud (see an example in Chap. 7). Geometrical properties of boundaries, such as fractal dimensions, provide clues to the distribution of physical scales in turbulent flows (Sreenivasan et al. 1989; Catrakis 2000). The power spectral density of turbulence can be related to the image fractal dimension (Voss 1988; Meneveau and Sreenivasan 1991). An effective method for evaluating the fractal dimension from images of turbulent clouds has been developed by Zubair and Catrakis (2009). This method is applicable to the analysis of sonar images due the capability of this 3D sonar to produce quantitative measurements of length scales.

The models of CB94, Terray et al. (1996), and BL02 do not consider bubbles. A model of wave-enhanced turbulence incorporating the buoyancy effect of bubbles provides a better insight into the problem of turbulence closure (Liang et al. 2012). The role of bubbles will be considered in Sect. 6.2.

3.5 Effects of Thermohaline Stratification

In our analysis of wave-enhanced turbulence in the previous section, we have ignored convection as a source of TKE in the near-surface layer of the ocean. According to Lombardo and Gregg (1989), the dissipation rate of TKE due to gravitational convection in the upper ocean

$$\varepsilon_c \approx -\alpha_T g Q_0 / (c_p \rho), \tag{3.83}$$

where α_T is the thermal expansion coefficient of seawater, g is the acceleration of gravity, and Q_0 is the net surface heat flux. For $Q_0 = 200$ W m^{-2}, we obtain $\varepsilon_c \approx 2 \times 10^{-7}$ W kg^{-1}, which is much less than dissipation rates in the upper few meters of the ocean observed under high wind speed conditions in the western equatorial Pacific (see Fig. 3.12). Typically, gravitational convection is not a primary source of turbulence in the wave-stirred layer of the tropical ocean. Addition of the

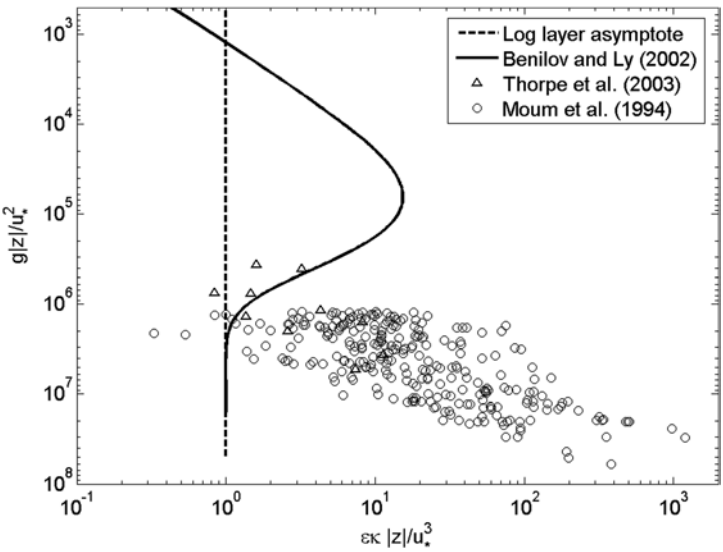

Fig. 3.20 The effect of stratification on near-surface turbulence. Note significant deviation of the observed dissipation rates below the layer of wave-enhanced turbulence from both the wall layer (*vertical dashed line*) and wave-enhanced turbulence (*continuous line*) parameterizations. The nondimensional scaling used here is discussed in Sect. 3.4.1

salinity effect due to evaporation (see (3.96)) does not change the above estimate substantially. Nevertheless, in polar regions (e.g., in polynyas), the contribution of the gravitational (haline) convection to the near-surface turbulence dissipation can be appreciable due to strong evaporation and brine formation.

Figure 3.20 shows the turbulence dissipation data obtained in stratified conditions, below the layer of wave-enhanced turbulence. The dissipation rate exhibits a three order-of-magnitude enhancement compared to the log layer prediction. This is a much stronger relative increase in the dissipation rate compared to what can be caused by surface wave breaking. This shows that the effect of stratification on the dissipation of turbulent energy can be significant below the layer of wave-enhanced turbulence.

3.5.1 Formulation of the Monin–Oboukhov Theory for the Upper Ocean

The effect of thermohaline stratification on the turbulent boundary layer can be characterized via the stability parameter, $\zeta = |z| / L_O$, where $|z|$ is the depth and L_O is the Oboukhov length scale. The stability parameter is related to the Monin–Oboukhov similarity theory, which has been found useful in many studies of the atmospheric boundary layer (see Chap. 1).

Application of the Monin–Oboukhov theory to the upper ocean boundary layer, however, is not straightforward. The main problem is that the velocity scale in water is $\sqrt{\rho/\rho_a} \approx 30$ times smaller than that in air. For the identical length scale, the kinematic mixing coefficient in water is about 30 times smaller than in the air. It therefore takes much more time for heat and momentum fluxes from the ocean surface to propagate to the same distance in the oceanic boundary layer compared to the atmospheric boundary layer. During this time interval, surface heat fluxes may change significantly, especially due to the diurnal cycle of solar radiation. This can make the Oboukhov scale, which includes the surface fluxes, irrelevant.

Soloviev et al. (2001) suggested using an earlier version of the Monin–Oboukhov theory for upper ocean conditions, which was formulated in terms of the gradient Richardson number:

$$Ri = \frac{g\rho^{-1}\partial\rho/\partial z}{(\partial u/\partial z)^2 + (\partial v/\partial z)^2}, \tag{3.84}$$

where ρ is the density, z is the depth, u and v are the horizontal velocity components, and g is the acceleration of gravity.

Although ζ and Ri are both related to the stratified turbulent boundary layer, ζ is a function of the surface boundary conditions and Ri is a function of the local density and velocity gradients. For a statistically steady and homogeneous turbulent boundary layer, parameters ζ and Ri are related:

$$Ri(\zeta) = \zeta\phi_\rho(\zeta)\phi_m(\zeta)^{-2} = \begin{cases} \zeta & \text{for } 0 \geq \zeta \geq \zeta_m \\ \zeta/(1+\beta\zeta) & \text{for } \zeta > 0 \end{cases}, \tag{3.85}$$

where β is a dimensionless constant, and ϕ_ρ and ϕ_m are the universal functions for density and velocity, respectively (see Chap. 1). According to (3.85), Ri monotonically increases with ζ, achieving an extreme as $\zeta \to \infty$:

$$Ri(\zeta)|_{\zeta\to\infty} = \beta^{-1} = Ri_{cr} \approx 0.25 \tag{3.86}$$

The Richardson number within the steady turbulent boundary layer is restricted from above to its critical value Ri_{cr}. If the Richardson number exceeds the critical value, this is an indication that this is an area outside of the surface turbulent boundary layer (though intermittent turbulence may still exist there). Note that the Monin–Oboukhov theory is based on the assumption of a statistically stationary and horizontally homogeneous turbulent boundary layer. Effects of turbulence hysteresis can be addressed in mixed-layer models.

From (3.85), ζ can be expressed as a function of Ri:

$$\zeta = \begin{cases} Ri \text{ at } -0.20 \leq Ri < 0 \\ Ri/(1 - Ri/Ri_{cr}) \text{ at } 0 \leq Ri < Ri_{cr} \end{cases} \tag{3.87}$$

(The analytical relationship between Ri and z is bulky for $\varsigma < -0.20$; therefore, it is not shown in (3.85) and (3.87).)

The universal functions for velocity $\phi_m(\zeta)$, density $\phi_s(\zeta)$, and dissipation rate $\phi_\varepsilon(\zeta)$ can then be expressed through Ri using formula (3.87). We do not give here the corresponding analytical expressions, $\phi_m(Ri)$, $\phi_\rho(Ri)$, and $\phi_\varepsilon(Ri)$, because of their bulkiness. They can be easily derived from (1.148), (1.149), and (1.150) by substituting ζ with Ri according to relationship (3.87).

The coefficients of turbulent exchange for momentum and scalar properties in the boundary layer are defined as $K_M = \overline{w'u'} / \partial u / \partial z$ and $K_s = \overline{w'\rho'} / \partial\rho / \partial z$, respectively. Using the definition of the universal functions in the Monin–Oboukhov theory (see formulas (1.145)–(1.147) in Chap. 1), the mixing coefficients can be expressed as follows:

$$K_M = \kappa u_* |z| / \phi_m \tag{3.88}$$

$$K_\rho = \kappa \rho_* |z| / \phi_\rho \tag{3.89}$$

where $u_*^2 = (\overline{w'u'})|_{z=0}$ and $\rho_* = (\overline{w'\rho'})\big|_{z=0} / (\kappa u_*)$.

Figure 3.21 shows boundary-layer functions $\phi_m = (\kappa|z| / u_*)\partial u / \partial z$, $\phi_\rho = (\kappa|z| / \rho_*)\partial\rho / \partial z$, $\phi_\varepsilon = \varepsilon\kappa|z| / (\overline{w'u'})^{3/2}$, and $\phi_{Km} = K_M / (\kappa u_* |z|)$ plotted versus Ri. It is remarkable that the vertical shear and density gradients as well as the dissipation rate increases sharply when Ri approaches its critical value, Ri (corresponding to the mixed-layer bottom), while the turbulent exchange coefficient vanishes as $Ri \to Ri_{cr}$.

The stratified turbulent boundary layer has the following three asymptotic regimes: 1) logarithmic layer (no stratification effects, i.e., $Ri = 0$), 2) free convection (unstable stratification and $u_* = 0$, i.e., $Ri = -\infty$, and 3) marginal stability ($Ri = Ri_{cr}$).

3.5.2 *Asymptotic regimes*

3.5.2.1 Logarithmic Layer

With neutral stratification (i.e., $Ri = 0$) the buoyancy forces are not important, and Ri falls out from the set of defining parameters in the Monin–Oboukhov similarity theory. As a result, functions ϕ_m, ϕ_ρ, ϕ_ε, and ϕ_{Km} become constants. According to conventional normalization, $\phi_m(0) = \phi_\rho(0) = \phi_e(0) = \phi_{Km}(0) \equiv 1$. The shear and vertical gradient of a scalar property in this layer for $|z| >> z_0$ are determined by well-known formulas:

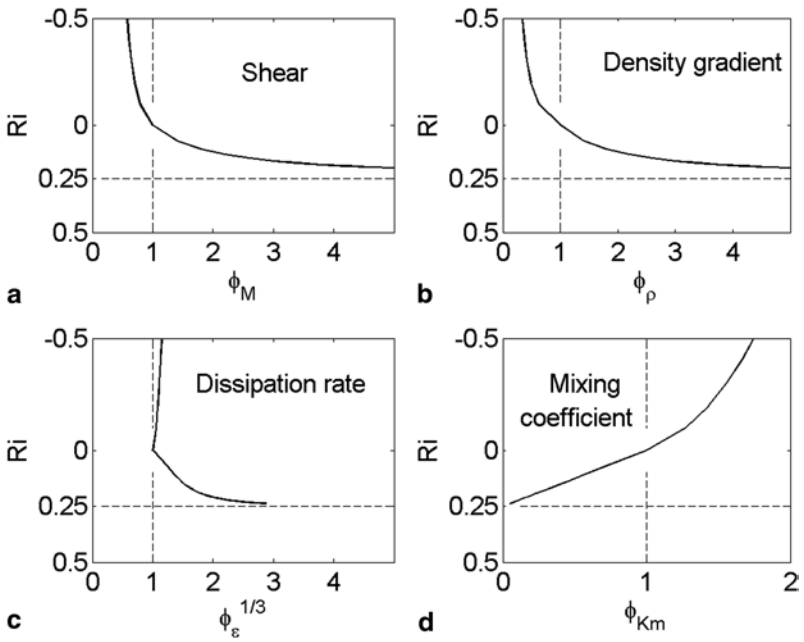

Fig. 3.21 Universal functions for dimensionless **a** shear ϕ_m, **b** density gradient ϕ_ρ, **c** dissipation rate of the turbulent kinetic energy ϕ_ε, and **d** turbulent eddy coefficient ϕ_{Km} expressed as a function of *Ri*. (After Soloviev et al. 2001. Reproduced with permission from American Geophysical Union)

$$\partial u / \partial z = u_* / (\kappa |z|), \tag{3.90}$$

$$\partial \rho / \partial z = \rho_* / (\kappa |z|). \tag{3.91}$$

The dissipation rate of TKE in the logarithmic layer

$$\varepsilon = u_*^{\,3} / (\kappa |z|), \tag{3.92}$$

while the mixing coefficient is

$$K_0 = \kappa u_* |z|. \tag{3.93}$$

The very near-surface part of the oceanic turbulent boundary layer is subject to strong wave influence. The wave dissipation is essentially concentrated within a relatively thin near-surface layer of the ocean, equal to only about 20% of the significant wave height (Sect. 3.4.4). Csanady (1984) and Cheung and Street (1988) showed that the surface waves influence only the surface roughness parameter z_0 rather than the logarithmic velocity law.

3.5.2.2 Free Convection

According to Beljaars (1994), the mixing coefficients for unstable stratification and zero wind stress can be expressed as follows:

$$K_M = \kappa w_* |z|, \tag{3.94}$$

where

$$w_* = a_p \left(hB_0\right)^{1/3} \tag{3.95}$$

is the Priestly (1959) convective velocity scale, a_p is an empirical constant close to unity, h is the mixed-layer depth, and B_0 is the vertical buoyancy flux. A similar expression can be derived for $K\rho$.

The dissipation rate of the TKE under free-convection conditions is

$$\varepsilon = -\alpha_T g Q_0 / (c_p \rho) + \beta_S S_0 g Q_E / (L\rho), \tag{3.96}$$

which differs from (3.83) by an additional term due to evaporation from the sea surface and the respective salinity increase. Here S_0 is the surface salinity and L is the latent heat of vaporization.

3.5.2.3 Marginal Stability

The situation when Ri is near its critical value is of special interest. In this case, the flow is in the so-called regime of marginal stability (Turner 1973). This is a self-regulated state where the flow adjusts to the existing gross shear and stratification. It is characterized by essentially linear profiles of horizontal velocity and density (note that the linear profiles of density and velocity are the asymptotic limit of relations (1.148) and (1.149) as $\zeta \to \infty$. The regime of marginal stability has been observed in the atmospheric boundary layer over the ice in Antarctica, in the nocturnal atmospheric boundary layer, in the outer boundary layer of the gravity current (Turner 1973), during dust storms in the atmosphere (Barenblatt and Golitsyn 1974), and in the equatorial diurnal thermocline (Kudryavtsev and Soloviev 1990).

The self-regulated layer effectively isolates the near-surface turbulent boundary layer from the water below. From (1.148), (3.87), and (3.88), follows that for $0 < Ri < Ri_{cr}$,

$$K_M = K_0 (1 - Ri / Ri_{cr}), \tag{3.97}$$

where $K_0 = \kappa u_* |z|$ is the coefficient of turbulent mixing in the logarithmic boundary layer. According to (3.97), the turbulent boundary-layer exchange vanishes

when $Ri \to Ri_{cr}$. Actually, $K_M|_{Ri=Ri_{cr}} \neq 0$ because there is always some background turbulence below the mixed layer (i.e., for $Ri \geq Ri_{cr}$) caused by intermittent mixing events. However, $K_M|_{Ri=Ri_{cr}} << K_0$.

3.5.3 Boundary-Layer Scaling of the Velocity and Dissipation Rate Profiles

Though the gradient Richardson number *Ri* appears to be a convenient parameter for study of the upper ocean turbulent boundary layer, its measurement *in situ* is complicated by velocity measurement errors and resolution of shear. Within the turbulent boundary layer the observed shear is usually small (on the order of the measurement accuracy or even less), which results in an enormous relative error for *Ri*. (Note that in definition (3.84) the shear enters into the denominator.) Velocity measurements involve both systematic and random errors. However, it is notable that acoustic Doppler current profiler (ADCP) techniques provide almost unbiased shear measurements (limited only by the effects described by Lien et al. (1996)), thus substantially reducing the systematic error. Ensemble averaging can significantly reduce the random error.

Shipboard ADCP instruments typically obtain measurements from the depth range 16–300 m. The boundary-layer laws can be tested with this technique only for relatively high wind speed conditions when the mixed-layer depth exceeds 20 m.

In Fig. 3.22, observations of shear within the depth range of 20–80 m are plotted as a function of the Richardson number. The data were taken from the repeated ship track observations of the R/V *Wecoma* during TOGA COARE. The Richardson number was calculated from the towed undulating Conductivity, Temperature, Depth (CTD) sensors (SEASOAR) and ADCP gridded data (10 m in depth and ~3 km in horizontal distance) and the formula

$$Ri = N^2 / S_h^{\,2}, \tag{3.98}$$

where $N^2 = g\overline{\Delta\rho/\Delta z}/\rho$ and $S_h^{\,2} = \overline{(\Delta u/\Delta z)^2} + \overline{(\Delta v/\Delta z)^2}$. The averaging is performed on the corresponding depth surfaces along the individual R/V *Wecoma* sections. Note that the terms in the numerator and denominator of the expression for the Richardson number are averaged separately.

The shear magnitude in Fig. 3.22 is normalized with the friction velocity calculated from the meteorological measurements with the COARE 2.5 bulk-flux algorithm. There are 17 points within the Richardson number range $-0.1 < Ri < 0.05$ that correspond to the logarithmic layer regime. Most of the shipboard ADCP measurements during the R/V *Wecoma* surveys are, however, taken at higher magnitudes of the Richardson number, when the influence of stratification cannot be neglected. Within the turbulent boundary layer ($Ri < 0.25$), the boundary-layer dependence is consistent with the experimental data; however, the scatter of the individual points

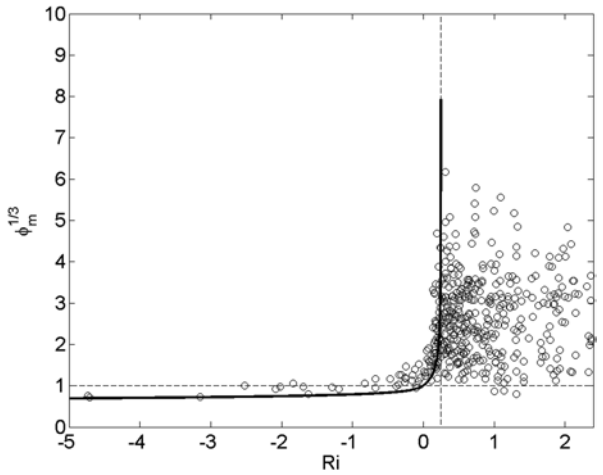

Fig. 3.22 Dimensionless shear $\phi_m = (\kappa|z|/u_*)\partial u/\partial z$ as a function of Richardson number *Ri*. The *bold line* represents the turbulent boundary-layer law from atmospheric measurements. *Points* are the observations from the depth range of 20–80 m for three R/V *Wecoma* surveys during TOGA COARE. Measurements taken under light winds ($u_* < 0.3$ cm s^{-1}) are excluded. The *vertical dashed line* represents the critical value of the Richardson number, $Ri_{cr} = 1/4$, while the horizontal dashed line corresponds to the logarithmic layer dependence. (After Soloviev et al. 2001. Reproduced with permission from American Geophysical Union)

is relatively large. For $Ri > 0.25$, the data are more scattered. Note that the universal boundary-layer dependences are not defined for $Ri > Ri_{cr}$. (This implies criteria $Ri = Ri_{cr}$ as a definition of the surface mixed-layer depth.)

In Fig. 3.23, the shear data for $Ri < Ri_{cr}$ are averaged for overlapping Richardson number intervals, $\Delta Ri = 0.1$. The averaged shear is shown as a function of the averaged Richardson number. For consistency, the theoretical boundary-layer dependence is also averaged over the same *Ri* number intervals on this plot. Within the turbulent boundary layer the averaged dissipation rates are consistent with the theoretical boundary-layer dependence, demonstrating the striking effect of increased shear at $Ri \sim Ri_{cr} = 0.25$. Some points, however, deviate from the theoretical dependence by more than the 95 % confidence interval.

Dimensionless dissipation rates are plotted as a function of the Richardson number in Fig. 3.24. Measurements made under light winds ($u_* < 0.3$ cm s^{-1}) are excluded. The boundary-layer dependence for dissipation rate (bold line) is consistent with data from within the mixed layer (i.e., $Ri < Ri_{cr}$). Outside the mixed layer ($Ri > Ri_{cr}$), the dimensionless dissipation rate data are almost randomly scattered; this can be explained by the fact that the boundary-layer scaling is no longer valid outside the turbulent boundary layer. The rate of turbulence dissipation below the surface mixed layer relates to the statistics of internal wave shear rather than to the surface forcing (Peters et al. 1988). To some extent, internal wave-breaking events

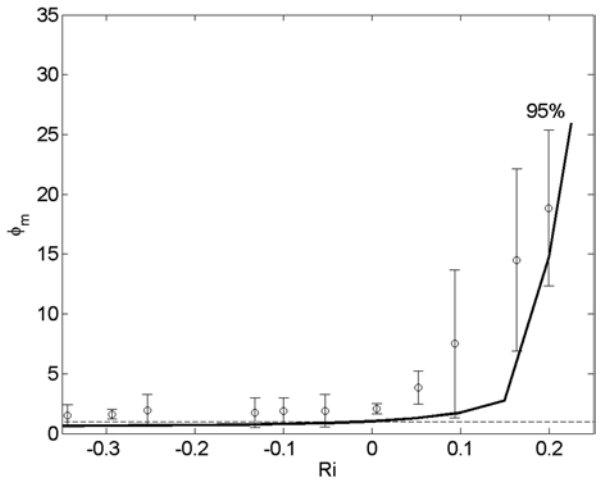

Fig. 3.23 Dimensionless shear (from Fig. 3.22) averaged within the mixed layer (i.e., $Ri<0.25$). *Circles* represent the mean for overlapping intervals of $\Delta Ri=0.1$. The 95% confidence limits are constructed on the basis of Student's distribution (Rabinovich 1995). The *bold line* represents the theoretical turbulent boundary-layer law averaged over the same *Ri* intervals. The *horizontal dashed line* is the logarithmic layer dependence. (After Soloviev et al. 2001. Reproduced with permission from American Geophysical Union)

may depend on surface wind stress as well (Thorpe 1975), which is, however, beyond the scope of this book.

In Fig. 3.25, the averaged dissipation rate data for $Ri<Ri_{cr}$ are presented as in Fig. 3.23. The averaged data are consistent with the boundary-layer dependence (three points, however, deviate from the theoretical dependence by more than the 95% confidence interval). The maximum dimensionless dissipation rate of TKE near the bottom of the mixed layer $\varepsilon\sim 5\times10^2 u_*^3/(\kappa|z|)$, which substantially exceeds the log layer prediction, $\varepsilon=u_*^3/(\kappa|z|)$. The strong increase in the dissipation rate as $Ri\to Ri_{cr}$, which corresponds to $\zeta\to\infty$, is in accordance with the Wyngaard et al. (1971) formula (1.150). Note that the increase of ε at $Ri\sim Ri_{cr}$ is not in contradiction to the decrease of dimensionless mixing coefficient $K_m/(\kappa u_* z)$ predicted by (3.97); this is because K_M also depends on the turbulent mixing scale that rapidly decreases at $Ri\to Ri_{cr}$.

3.6 Parameterization of Turbulent Mixing

3.6.1 Parameterization of Wave-Enhanced Mixing Coefficient

In the framework of the CB94 model (see Sect. 3.4.2), the vertical mixing coefficient due to wave breaking can be calculated from the following relationship:

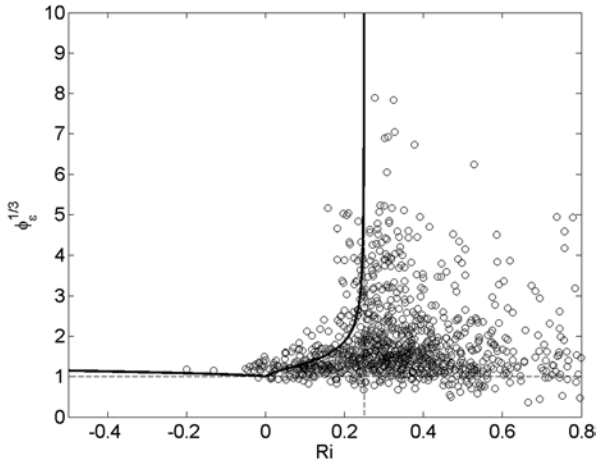

Fig. 3.24 Dimensionless dissipation rate $\phi_\varepsilon = \varepsilon\kappa|z|/u_*^3$ as a function of *Ri* during TOGA COARE. The *bold line* corresponds to the turbulent boundary-layer law. *Points* are the dissipation rate of turbulent kinetic energy ε from Moum and Caldwell's (1994) and Smyth et al.'s (1996) turbulence measurements. Friction velocity u_* is calculated from the WHOI mooring meteorology data using the COARE 2.5 bulk-flux algorithm (Fairall et al. 1996). The *horizontal dashed line* corresponds to logarithmic layer dependence. (After Soloviev et al. 2001. Reproduced with permission from American Geophysical Union)

$$K_M = S_M B^{1/3} \varepsilon^{1/3} l^{4/3} \approx \varepsilon^{1/3} l^{4/3}. \tag{3.99}$$

With the expression for the dissipation of TKE in the form (3.44), and for the length scale defined by equation (3.33), formula (3.99) is as follows:

$$K_M = \kappa u_* (|z| + z_0)\left[1 + \sqrt{3}\alpha_w (BS_q)^{-0.5} z_0{}^n / (|z| + z_0)^n\right]^{1/3}. \tag{3.100}$$

Formula (3.100) is shown in Fig. 3.26 for surface roughness z_0 parameterized via significant wave height H_s according to (3.47) with $c_0 = 0.6$.

As expected, the main enhancement of the vertical mixing is observed within the layer of approximately one significant wave height depth. Bubbles from breaking waves produce density stratification that may affect the turbulence close to the ocean surface. At this point, however, it is not yet clear how to include this effect into a mixing parameterization.

Asymptotically, as $z \to -\infty$, (3.100) tends to the log layer mixing parameterization (3.93). Parameterization (3.100), however, does not account for the Langmuir circulations. One possible approach to the parameterization of the Langmuir circulations contribution into vertical mixing is proposed in Chap. 5, Sect. 5.6.2.

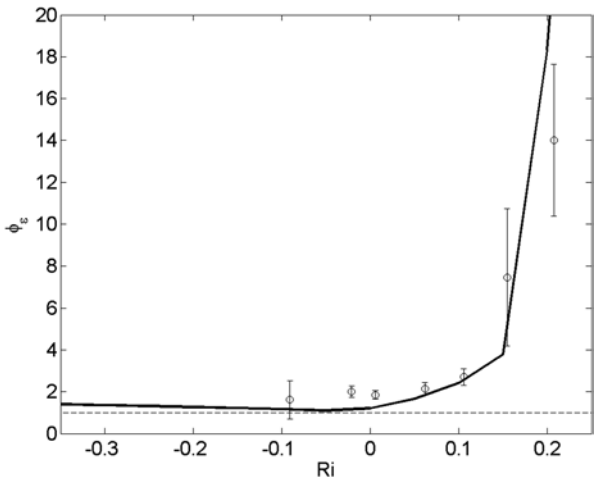

Fig. 3.25 Dimensionless dissipation rate from Fig. 3.24 averaged within the mixed layer $Ri<0.25$. (After Soloviev et al. 2001. Reproduced with permission from American Geophysical Union)

3.6.2 Richardson-Number Type Mixing Parameterization

The vertical variation of the wind-induced momentum flux is a common problem for the nonstationary oceanic (Large et al. 1994) and atmospheric (Tennekes 1973) boundary layers. To test the constant stress layer hypothesis for the mixed layer in the western Pacific warm pool, Soloviev et al. (2001) examined profiles of the local friction velocity, $u_{*l}=sqrt(\tau_l)$, where τ_l is the vertical momentum flux magnitude calculated from measurements. The corresponding surface value u_* was calculated from the meteorological observations using the COARE 2.5 bulk-flux algorithm (Fairall et al. 1996).

The upper ocean is neither stationary nor horizontally homogeneous. Moreover, the heat and momentum fluxes within the surface turbulent boundary layer may change with depth. The Ri-type scheme, however, adjusts to the environmental conditions on the relatively short turbulence timescale, which substantially reduces effects of nonstationarity.

Figure 3.27 shows the mean profile of u_{*l}/u_* as a function of Ri. The number of points within the mixed layer ($Ri<0.25$) and especially within the logarithmic layer ($-0.1<Ri<0.05$) is relatively small. Nevertheless, it is sufficient to provide acceptable confidence intervals because of the substantial volume of the data collected during TOGA COARE. According to Fig. 3.27, within the stably stratified mixed layer ($0<Ri<Ri_{cr}$) the maximum deviation of u_{*l} from its surface value u_* is about 30 % and can be approximated as follows:

$$u_{*l} \approx u_*(1-0.7Ri/Ri_{cr}). \tag{3.101}$$

A possible approach to account for the vertical momentum flux change with depth is to parameterize K_M using the profile of local friction velocity rather than its sur-

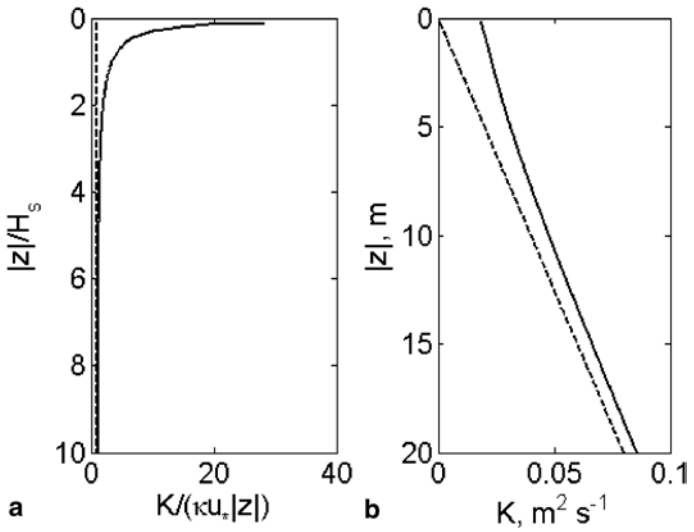

Fig. 3.26 Vertical mixing coefficient in the wave-enhanced turbulent boundary layer (*continuous line*) in comparison with the logarithmic layer prediction (*dashed line*) in **a** nondimensional and **b** dimensional coordinates. In (**b**), the mixing coefficients are given for $u_* = 0.01$ m s^{-1} and $H_s = 1.6$ m

face value u_*. This does not follow directly from the boundary-layer theory but was previously employed by several investigators (e.g., Large et al. 1994) including non-equatorial (in fact, polar) conditions (McPhee et al. 1987).

The mixing parameterization should match to a small but finite turbulence level below the boundary layer because the background mixing levels are nonzero due to internal wave breaking. Comprehensive discussions of the eddy momentum exchange coefficient parameterization below the surface turbulent boundary layer are given in McComas and Muller (1981), Peters et al. (1988), Gregg et al. (1993), Polzin (1996), and Gregg et al. 2003). Peters et al. (1988) approximated the momentum eddy coefficient in the upper shear zone, 23–81 m depth, as follows:

$$K_{Mb} = 5.6 \times 10^{-8} Ri^{-8.2} m^2 s^{-1} \tag{3.102}$$

For the higher *Ri* range, Peters et al. (1988) obtained the semiempirical formula

$$K_{Mt} = 5 \times 10^{-4} (1 + 5Ri)^{-1.5} + 2 \times 10^{-5} m^2 s^{-1} \tag{3.103}$$

The final parameterization of the eddy viscosity coefficient K_M by Peters et al. (1988) is obtained by adding (3.102) and (3.103):

$$K_M = K_{Mb} + K_{Mt} \tag{3.104}$$

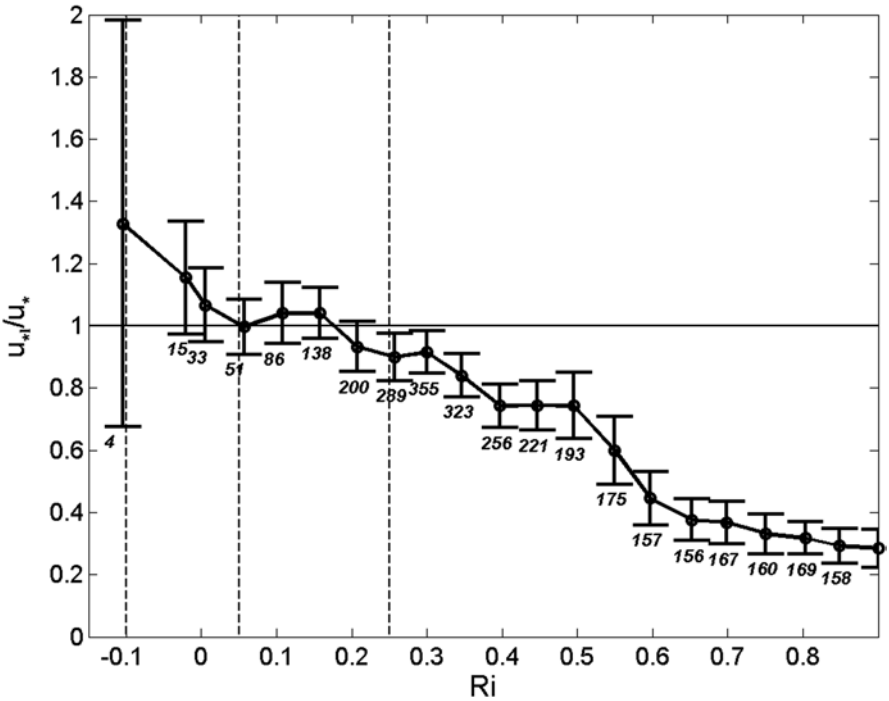

Fig. 3.27 Test of the constant stress assumption. Friction velocities calculated from the turbulence data (Moum and Caldwell 1994; Smyth et al. 1996), normalized by surface values u_*, are shown as a function of gradient Richardson number *Ri*. Each *circle* represents the mean for overlapping intervals of $\Delta Ri = 0.1$; the *vertical bars* cover the 95 % confidence intervals, and the numbers below each bar are the number of points averaged. Averaging is done over all profiles (taken every 1 h) during the R/V *Moana Wave* COARE cruise. *Ri* and τ_l are calculated using the data from the depth range of 16–100 m. Averages over intervals with $Ri < -0.1$ are not shown because there are less than five points falling into these intervals. (After Soloviev et al. 2001. Reproduced with permission from American Geophysical Union)

The strong power dependence and unboundedness of (3.102) as $Ri \to 0$ eliminates its practical use within the mixed layer.

In this situation, we replace (3.102) with the parameterization of the boundary-layer type defined by (3.88). From (1.148), (1.149), (1.151), (1.152), and (3.87), the mixing coefficients for the momentum and a scalar property in the boundary layer can be expressed as follows (Soloviev et al. 2001):

$$K_{Mb} = \begin{cases} \kappa u_* z (a_m - c_m Ri)^{1/3}, \text{for } Ri < Ri_m \\ \kappa u_* z (1 - \alpha Ri)^{1/4}, \text{ for } Ri_m < Ri < 0 \\ \kappa u_* z (1 - Ri / Ri_{cr}) + K_{m2}, \text{for } 0 \le Ri < Ri_{cr} \end{cases} \tag{3.105}$$

$$K_{sb} = \begin{cases} \kappa u_* z(a_s - c_s Ri)^{1/3}, \text{for} Ri < Ri_s \\ \kappa u_* z(1 - \alpha Ri)^{1/4}, \text{for} 0 > Ri \geq Ri_s \\ \kappa u_* z(1 - Ri / Ri_{cr}), \text{for} 0 \leq Ri < Ri_{cr} \end{cases} \tag{3.106}$$

where dimensionless constants $Ri_m = -0.20$, $R_{is} = -1.0$, $Ri_{cr} = 0.25$, $\alpha = 16$, $a_m = 1.26$, $a_s = -28.86$, $c_m = 8.38$, and $c_s = 98.96$ are derived from atmospheric measurements (see Chap. 1, Sect. 1.7.2).

The first two lines in (3.105) and (3.106) are the boundary-layer parameterization for the unstably stratified mixed layer; the third line is the boundary-layer parameterization for the stably stratified mixed layer (which is similar to (3.97)).

In order to ensure a smooth transition from the mixed layer to the thermocline, the eddy mixing coefficient for momentum is finally defined as

$$K_M = \max(K_{Mb}, K_{Mt}) \tag{3.107}$$

where K_{Mb} and K_{Mt} are the mixing coefficients for momentum in the mixed layer and thermocline, respectively. The mixing coefficient for scalar property s is defined in the similar way:

$$K_s = \max(K_{sb}, K_{st}), \tag{3.108}$$

where K_{sb} and K_{st} are the mixing coefficients for scalar properties in the mixed layer and thermocline, respectively. Furthermore, under the assumption that the turbulent Prandtl number is equal to unity in thermocline,

$$K_{st} = K_{Mt}. \tag{3.109}$$

To take into account the free convection above a stratified layer, u_* in (3.105) and (3.106) can be replaced by $(u_*^2 + w_*^2)^{1/2}$, where w_* is the Priestly (1959) convective velocity scale (3.95).

Figure 3.28 compares parameterization (3.107) with the mixing coefficient for momentum that is derived from the R/V *Moana Wave* COARE IOP leg 2 turbulence data of Moum and Caldwell (1994) and Smyth et al. (1996). The mixing coefficient in the thermocline K_{Mt} entering (3.107)is parameterized with equation (3.103). The vertical mixing coefficient for momentum is calculated using the "dissipation method" as in Peters et al. (1988):

$$K_M = \overline{\varepsilon} / \left[\left(\Delta \overline{u} / \Delta z \right)^2 + \left(\Delta \overline{v} / \Delta z \right)^2 \right] \tag{3.110}$$

where $\Delta z = 4$ m. The Richardson number is calculated from the formula,

$$Ri = g(\Delta \overline{\rho} / \Delta z) / [(\Delta \overline{u} / \Delta z)^2 + (\Delta \overline{v} / \Delta z)^2] \tag{3.111}$$

The hourly 4 m gridded vertical profiles of dissipation rate and velocity were averaged at each depth for 12 h (with a 6-h overlap). The original data set contained 550 hourly sampled vertical profiles of dissipation rate and velocity. After the averaging, it turned out that a very few points with the magnitude of the velocity difference, $\left[(\Delta\overline{u})^2+(\Delta\overline{v})^2\right]^{1/2}\le 1.2\times10^{-3}$ m s^{-1}, produced an enormous scatter in the calculated vertical eddy coefficient and Richardson number compared with the rest of points. These low-shear points (0.99 % of the whole data set) were removed. Finally, the experimental points were averaged over overlapping Richardson number intervals, $\Delta Ri=0.1$; confidence intervals are calculated using Student's probability distribution. The average at $Ri=-0.2$ is calculated from four points only; it is not shown here because the confidence interval is quite large.

In the mixed layer ($Ri<Ri_{cr}$), parameterization (3.107) is in a good agreement with observational data shown in Fig. 3.28. (Remember that the mixed-layer portion of the parameterization is mainly represented by equation (3.105).)

In the thermocline ($Ri\ge Ri_{cr}$), the parameterization (3.107) underestimates mixing. For $Ri\ge Ri_{cr}$, coefficient K_{Mt} is of primary importance (although K_{Mt} can also be relevant for Ri slightly below Ri_{cr}). Nonlocal transport in the form of internal waves is one possible explanation for the discrepancy. Soloviev and Lukas (1996) reported observations of large-amplitude internal waves in the diurnal thermocline and rain-formed halocline (see Chap. 5). Zilitinkevich and Calanca (2000) parameterized the effect of internal waves on the mixing coefficient in the atmospheric boundary layer; a comparable theory could be developed for the ocean (Vladimir Kamenkovich, private communication).

Two other mixing parameterizations, from Peters et al. (1988) and Monin and Yaglom (1971), are also shown in Fig. 3.28. The parameterization of Peters et al. (1988) is based on data taken from below the mixed layer, and its comparison with the mixed-layer dependence, in particular with the logarithmic layer law, is not appropriate. The parameterization taken from Monin and Yaglom (1971) has the correct neutral (logarithmic) layer asymptote, but it is not valid for unstable stratification and apparently overestimates the mixing coefficient for $Ri>0.05$.

The important feature of the parameterizations (3.105) and (3.106) is that they have the correct boundary-layer asymptotes for stable, unstable, and neutral stratification. As a result, these new parameterizations are capable of resolving such details of the actively mixed layer as the shear and stratification. Within the mixing layer, these are relatively small but dynamically important factors; they are associated with the vertical transfer of buoyancy and momentum.

Note that if the mixing coefficient K_M is scaled using the local friction velocity u_{*l} determined from equation (3.101) rather than its surface value u_*, parameterization (3.105) is in better agreement with the data. The difference is, however, relatively small (Soloviev et al. 2001).

The scaling used in parameterizations (3.105) and (3.106) is consistent with the idea by Stommel (1960) that the shear within the mixed layer is proportional to the friction velocity. For the vertical eddy viscosity, Ekman (1905, cf. Santiago-Mandujano and Firing 1990) proposed a parameterization $K_M\sim u_*^2$, which is not consistent with the logarithmic layer asymptote observed for neutral stratification

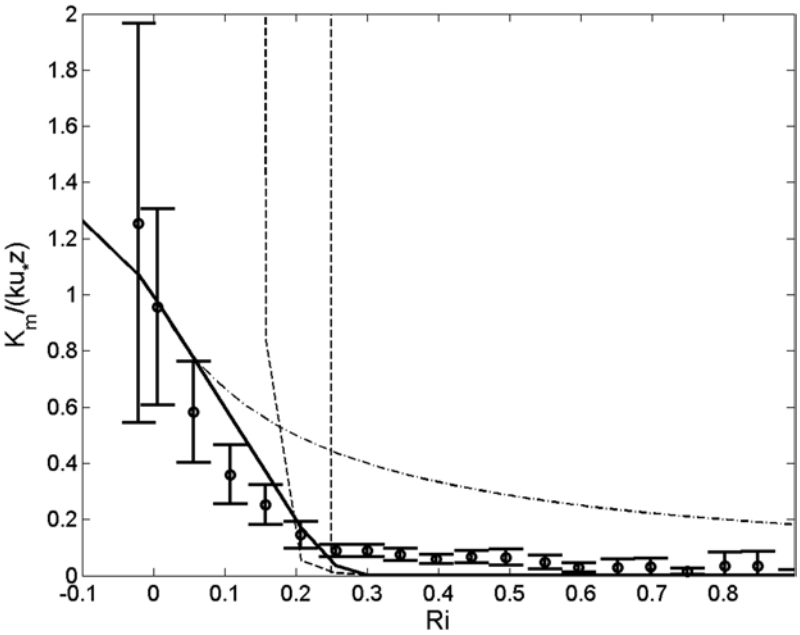

Fig. 3.28 The vertical eddy coefficient for momentum K_M (normalized by logarithmic layer eddy coefficient $\kappa u_*|z|$) as a function of *Ri*. *Open circles* are COARE data from the R/*V Moana Wave* (Moum and Caldwell 1994; Smyth et al. 1996). Each circle represents the mean over *Ri* intervals as in Fig. 3.27. The *solid bold line* is parameterization (3.107). The *vertical dashed line* corresponds to $Ri = Ri_{cr} = 0.25$. The *bold dashed line* is the parameterization of Peters et al. (1988) calculated for the heat and momentum flux conditions during the R/V *Moana Wave* COARE cruise. The *dash-dotted line* is the parameterization of Monin and Yaglom (1971). (After Soloviev et al. 2001. Reproduced with permission from American Geophysical Union)

conditions in the mixed layer. The analysis of Santiago-Mandujano and Firing (1990) shows that Ekman's parameterization $K_M \sim u_*^2$ appears as a result of assuming that the mixed-layer depth is proportional to the Ekman scale, $L_E = u_* / f$. Ekman's parameterization ignores any dependence of K_M on depth z.

The boundary-layer parameterizations (3.105) and (3.106) results in $K_M \sim u_*$, which is consistent with the logarithmic layer asymptote $K_M = \kappa u_* |z|$. The parameterization of Large et al. (1994) based on boundary-layer scaling also implies that $K_M \sim u_*$.

An important feature of turbulence that has to be taken into account in mixing parameterization schemes is that it is a fundamentally *nonlocal* process (Stull and Kraus 1987; Large et al. 1994). This is because the turbulent transport is performed via a cascade of eddies. The nonlocal behavior of turbulence is associated with the presence of spatially coherent organized motions. There are numerous observations of coherent structures in the surface layer of the ocean, including Kelvin–Helmholtz billows (Thorpe 1969), Langmuir cells (Weller and Price 1988; Thorpe et al. 2003b), convective plumes and ramp-like structures (Thorpe 1988; Soloviev 1990),

and sharp frontal interfaces (Soloviev and Lukas 1997). These structures are considered in detail in Chap. 5.

The Monin–Oboukhov theory, which parameterization (3.106) is based on, does not account for the nonlocal transport. The *transilient* (Stull and Kraus 1987) and *large eddy simulation* (LES; Skyllingstad et al. 1999) models involve nonlocal features. Diffusive models, which are based on the parameterization of turbulent transports by eddy coefficients, are essential local. Systematic incorporation of the coherent structures into subgrid parameterizations is one of the important tasks to be performed for improving mixed-layer models.

3.6.3 Rotation Effects

On a rotating sphere with no stratification effects, the boundary layer depends on the two components of rotation: $f = f_z = 2\Omega \sin \varphi$ and $f_y = 2\Omega \cos \varphi$, where Ω is the magnitude of the Earth's rotation vector and φ is the latitude. The Coriolis parameter f determines the Ekman length scale, $L_E = u_* / f$. An interesting situation is observed at the equator because f vanishes. The shallow equatorial stratification makes the deep classical Ekman layer there irrelevant (Table 3.2). However, the Reynolds stress may interact with the horizontal component of Earth's rotation f_y to exchange TKE between horizontal and vertical components (Garwood and Gallacher 1985; Garwood et al. 1985), resulting in the length scale $L_G = u_* / (f_y \sin \theta)$, where θ is the wind direction. The effect of horizontal Coriolis acceleration on the turbulent eddies in the equatorial turbulent boundary layer, however, appears to be relatively small (Wang et al. 1996; Soloviev et al. 2001).

3.6.4 Boundary-Layer Horizontal Pressure Gradients

In the tropical ocean, the surface turbulent boundary layer has some unique features because of its proximity to the equator. As mentioned above, in Ekman's solution for the drift of water in a rotating homogeneous ocean when acted upon by a steady stress applied to the surface, the depth of the spiral and the amplitude of the surface current increase without limit as the latitude and vertical component of rotation approach zero. Stommel (1960) was first to show that there is actually no singularity at the equator. However, to remove the singularity, a zonal pressure gradient is required. At the equator, such a pressure gradient cannot be balanced by the horizontal Coriolis component but must be balanced by friction or inertial forces (Charney 1960). The wind stress penetrates into the ocean through the surface mixed layer, and the vertical turbulent viscosity provides the principle balance for the zonal pressure gradient driving the Equatorial Undercurrent (McCreary 1981).

Later, Lukas and Firing (1984) found evidence of geostrophic balance of the Equatorial Undercurrent, which provides an alternative perspective compared to the result of Charney (1960). The zonal pressure gradient and the vertical turbulent

Table 3.2 Order of magnitude estimate of buoyancy (D_B), rotation (D_E and L_G), and pressure-gradient (L_P) length scales for different surface stress values[a]

u_*, cm s^{-1}	D_B, m	L_P, m	D_E, m	L_G, m
0.1	0.1[D]	20	50	14
0.5	12.5[D]	100	250	69
1.0	100[D]	200	500	137
2.0	800	800	1,000	274[D]

According to Kraus and Businger (1994), the depth of the mixed layer is $D_E \approx 0.25 L_E$ in the case of no stratification. Buoyancy forces apparently dominate over Coriolis forces when $D_B << D_E$

[D] Minimum values of the length scale

viscosity were nevertheless still principal components of the momentum balance at the equator. Joyce et al. (1988) showed that the vertical Coriolis force is not negligible in the EUC as well.

It is known from hydraulics engineering that the longitudinal pressure gradient can influence the structure of the turbulent boundary layer (White 1986). Following Yaglom (1979), one can construct the so-called pressure gradient length scale, $L_p = \rho u_*^2 / \partial p / \partial x$. L_p may be derived from the momentum equations under the assumption that the horizontal pressure gradient is approximately balanced by vertical mixing. Veronis (1960) related a similar scale to the depth of the Equatorial Undercurrent.

Typical estimates of L_p are given in Table 3.2. This horizontal pressure gradient length scale exceeds all of the other mixed-layer length scales. This estimate suggests that the horizontal pressure gradient is not a major factor in determining the vertical structure of the ocean mixed layer. It may nevertheless play an important role in the dynamics of sharp frontal interfaces to be considered in Chap. 5.

References

Agrawal YC, Terray EA, Donelan MA, Hwang PA, Williams AJ, III, Drennan WM, Kahma KK, Kitaigorodskii SA (1992) Enhanced dissipation of kinetic energy beneath surface waves. Nature 359:219–220

Ardhuin F, Jenkins AD (2006) On the interaction of surface waves and upper ocean turbulence. J Phys Oceanogr 36:551–557

Arsenyev SA, Dobroklonsky SV, Mamedov RM, Shelkovnikov NK (1975) Direct measurements of some characteristics of fine structure from a stationary platform in the open sea. Izvestiya, Fizika Atmosphery i Okeana 11:845–850 (English translation)

Azizjan GV, Volkov YA, Soloviev AV (1984) Experimental investigation of vertical thermal structure of thin boundary layers of the sea and atmosphere. Atmos Oceanic Phys 20(6):511–519

Baker MA, Gibson CH (1987) Sampling turbulence in the stratified ocean: Statistical consequences of strong intermittency. J Phys Oceanogr 17:1817–1837

Barenblatt GI, Golitsyn GS (1974) Local structure of mature dust storms. J Atmos Sci 31:1917–1933

Beljaars ACM (1994) The parameterization of surface fluxes in large-scale models under free convection. Q J Roy Meteor Soc 121:255–270

Benilov AY (2012) On the turbulence generated by the potential surface waves. J Geophys Res 11 C00J30, doi:10.1029/2012JC007948
Benilov AY, Filyushkin BN (1970) Application of the linear filtration methods to the fluctuation analysis in the sea upper layer. Izvestiya, Fizika Atmosphery i Okeana 6:477–482
Benilov AY, Ly LN (2002) Modeling of surface waves breaking effects in the ocean upper layer. Math Comput Model 35:191–213
Borue V, Orszag SA, Staroselsky I (1995) Interaction of surface waves with turbulence: Direct numerical simulations of turbulent open-channel flow. J Fluid Mech 286:1–23
Bye JAT (1988) The coupling of wave drift and wind velocity profiles. J Mar Res 46:457–472
Catrakis HJ (2000) Distribution of scales in turbulence. Phys Rev E 62:564–578
Charney JG (1960) Non-linear theory of a wind-driven homogeneous layer near the equator. Deep-Sea Res 6:303–310
Charnock H (1955) Wind stress on a water surface. Q J Roy Meteor Soc 81:639–640
Cheung TK, Street RL (1988) The turbulent layer in the water at an air-water interface. J Fluid Mech 194:133–151
Craig PD, Banner ML (1994) Modeling wave-enhanced turbulence in the ocean surface layer. J Phys Oceanogr 24:2546–2559
Csanady GT (1984) The free surface turbulent shear layer. J Phys Oceanogr 14:402–411
Dillon TM, Richmann JG, Hansen CG, Pearson MD (1981) Near-surface turbulence measurements in a lake. Nature 290:390–392
Dozenko SV (1974) Theoretical basis of measuring physical fields in the ocean. Hydrometeoizdat, Leningrad, p. 152 (in Russian only).
Drennan W, Donelan MA, Terray EA, Katsaros KB (1996) Oceanic turbulence dissipation measurements in SWADE. J Phys Oceanogr 26:808–815
Ekman VW (1905) On the influence of the earth's rotation on ocean currents. Arkiv Met Astr Fysik 2:1–53
Elfouhaily T, Chapron B, Katsaros K, Vandemark D (1997) A unified directional spectrum for long and short wind-driven waves. J Geophys Res 102:15781–15796
Fairall CW, Bradley EF, Rogers DP, Edson JB, Young GS (1996) Bulk parameterization of air-sea fluxes in TOGA COARE. J Geophys Res 101:3747–3767
Farrell BF, Ioannou PJ (2008) The stochastic parametric mechanism for growth of wind-driven surface water waves. J Phys Oceanogr 38:862–879
Farrar JT (2011) Moored turbulence measurements in the open ocean using pulse-coherent Doppler sonar. J Ocean Techn 6(2):66–67
Fornwalt B, Terray G, Voulgaris G, Trowbridge J (2002) Flow modeling around an autonomous underwater vehicle with applications to turbulence measurements. Abstract to 2002 Ocean Sciences Meeting, 11–15 February 2002, Honolulu, Hawaii. Published in supplement to EOS, transactions, American Geophysical Union 83(4):143.
Garwood Jr RW, Gallacher PC (1985) Wind direction and equilibrium mixed layer depth: General theory. J Phys Oceanogr 15:1325–1331
Garwood Jr. RW, Muller P, Gallacher PC (1985) Wind direction and equilibrium mixed layer depth in the tropical Pacific Ocean. J Phys Oceanogr 15:1332–1338
Gemmrich J (2010) Strong turbulence in the wave crest region, J Phys Oceanogr, 40(3):583–595
Gemmrich J (2012) Bubble-induced turbulence suppression in Langmuir circulation. Geophys Res Lett 39, L10604, doi:10.1029/2012GL051691
Gemmrich JR, Farmer DM (1999) Observations of the scale and occurrence of breaking surface waves. J Phys Oceanogr 29:2595–2606
Gemmrich JR, Farmer DM (2004) Near-surface turbulence in the presence of breaking waves, J Phys Oceanogr 34(5):1067–1086
Gemmrich JR, Mudge TD, Polonchicko VD (1994) On the energy input from wind to surface waves. J Phys Oceanogr 24:2413–2417
Gerbi GP, Trowbridge JH, Edson JB, Plueddemann AJ, Terray EA, Fredericks JJ (2008) Measurements of momentum and heat transfer across the air–sea interface. J Phys Oceanogr 38:1054–1072

Gerbi GP, Trowbridge JH, Terray EA., Plueddemann AJ, Kukulka T (2009) Observations of turbulence in the ocean surface boundary layer: energetics and transport. J Phys Oceanogr 39:1077–1096

Greenan BJW, Oakey NS, Dobson FW (2001) Estimates of dissipation in the ocean mixed layer using a Quasi-horizontal microstructure profiler. J Phys Oceanogr 31:992–1004

Gregg MC, Sanford TB, Winkel DP (2003) Reduced mixing from the breaking of internal waves in the equatorial waters. Nature 422:513–516

Gregg MC, Seim HE, Percival DB (1993) Statistics of shear and turbulent dissipation profiles in random internal wave fields. J Phys Oceanogr 23:1777–1979

Gurvich AS, Yaglom AM (1967) Breakdown of eddies and probability distributions for small-scale turbulence. Phys Fluids 10 (Suppl., Part II):559–565

Handler RA, Swean TF, Leghton Jr RI, Swearingen JD (1993) Length scales and the energy balance of turbulence near a free surface. AIAA J 31 1998–2007

Hinze JO (1955) Fundamentals of the hydrodynamic mechanism of splitting in dispersion process. AICHE J 1:289–295

Hinze J (1975) Turbulence. McGraw-Hill, New York, p. 790

Hoffmann KA (1989) Computational fluid dynamics for engineers. Engineering education system, Austin, Tex, p. 567

Iyanaga S, Kawada Y (eds) (1980) Encyclopedic dictionary of mathematics. MIT Press, Cambridge, p. 618

Jenkins GM Watts D (1998) Spectral analysis and its applications. Emerson Adams Pr Inc, p. 525

Jones ISF, Kenney BC (1977) The scaling of velocity fluctuations in the surface mixed layer. J Geophys Res 82:1392–1396

Joyce TM, Lukas R, Firing E (1988) On the hydrostatic balance and equatorial geostrophy. Deep-Sea Res Part A 35(8):1255–1257

Kitaigorodskii SA (1991) The dissipation subrange of wind wave spectra. In: Banner ML, Grimshaw RHJ (eds), Breaking waves, UTAM Symposium, Sydney, Australia, 1991:199–206

Kitaigorodskii SA, Donelan MA, Lumley JL, Terray EA (1983) Wave-turbulence interactions in the upper ocean: Part II. J Phys Oceanogr 13:1988–1999

Kraus EB, Businger JA (1994) Atmosphere-ocean interaction. Oxford University Press, p. 352

Kudryavtsev VN, Makin VK, Chapron B (1999) Coupled sea surface–atmosphere model. 2. Spectrum of short wind waves. J Geophys Res 104:7625–7639

Kudryavtsev V, Dulov V, Shira V, Malinovsky V (2008) On vertical structure of wind-driven sea surface currents. J Phys Oceanogr 38(10):2121–2144

Kudryavtsev VN, Soloviev AV (1990) Slippery near-surface layer of the ocean arising due to daytime solar heating. J Phys Oceanogr 20:617–628

Large WG, McWilliams JC, Doney SC (1994) Oceanic vertical mixing: a review and a model with a nonlocal boundary layer parameterization, Rev Geophys 32:363–403

Liang J-H, McWilliams JC, Sullivan PP, Baschek B (2012) Large eddy simulation of the bubbly ocean: new insights on subsurface bubble distribution and bubble-mediated gas transfer, J Geophys Res 117:C04002

Lien R-C, McPhaden MJ, Gregg MC (1996) High-frequency internal waves at 0°, 140°W and their possible relationship to deep-cycle turbulence. J Phys Oceanogr 26:581–600

Lombardo CP, Gregg MC (1989) Similarity scaling of viscous and thermal dissipation in a convecting surface boundary layer. J Geophys Res 94:6273–6284

Longuet-Higgins MS (1969) On wave breaking and the equilibrium spectrum of wind-generated waves. Proc Roy Soc A310(1501):151–159

Lukas R, Firing E (1984) The geostrophic balance of the pacific equatorial undercurrent. Deep-sea Res 31:61–66

Lumley J, Terray E (1983) Kinematics of turbulence convected by a random wave field. J Phys Oceanogr 13:2000–2007

Ly LN, Garwood RW Jr. (2000) Numerical modeling of wave-enhanced turbulence in the oceanic upper layer. J Oceanogr 56:473–483

McComas CH, Muller P (1981) The dynamic balance of internal waves. J Phys Oceanogr 11:970–986
McCreary JP (1981) A linear, stratified ocean model of the equatorial undercurrent. Phil Trans Roy Soc London Ser. A 298:603–635
McPhee MG, Maykut GA, Morison JH (1987) Dynamics and thermodynamics of the ice/upper ocean system in the marginal ice zone of the Greenland Sea. J Geophys Res 92:7017–7031
Mellor GL, Yamada T (1982) Development of a turbulence closure model for geophysical fluid problems. Rev Geophys 20:851–875
Melville WK (1994) Energy dissipation by breaking waves. J Phys Oceanogr 24:2041–2049
Meneveau C, Sreenivasan KR (1991) The multifractal nature of turbulent energy dissipation. J Fluid Mech 224:429–484
Miles JW (1957) On the generation of surface waves by shear flows. J Fluid Mech 3:185–204
Miles JW (1959) On the generation of surface waves by shear flows. Part 2. J Fluid Mech 6:568–582
Monin S, Yaglom AM (1971) Statistical fluid mechanics, Vol. 1. MIT Press, Cambridge, p. 769
Moum JN, Caldwell DR (1994) Experiment explores the dynamics of the ocean mixing. EOS, T Am Geophys Un 75:489, 494–495
Moum JN, Gregg MC, Lien RC, Carr ME (1995) Comparison of turbulence kinetic energy dissipation rates estimates from two ocean microstructure profilers. J Atmos Ocean Tech 12:346–366
Munk W (2009) An inconvenient sea truth: Spread, steepness, and skewness of surface slopes. Annu Rev Mar Sci 1:377–415
Nasmyth PW (1970) Oceanic turbulence. Ph.D. dissertation, University of British Columbia, Vancouver.
Novikov EA (1961) The energy spectrum of the turbulent flow in an incompressible fluid. Dokl Akad Nauk SSSR 139(2).
Nowell ARM (1983) The benthic boundary layer and sediment transport. Revs Geophys 21(5):1181–1192
Oakey NH (1982) Determination of the rate of dissipation of turbulent energy from simultaneous temperature and velocity shear microstructure measurements. J Phys Oceanogr 12:256–271
Oakey NS Elliott JA (1982) Dissipation within surface mixed layer. J Phys Oceanogr 12:175–195
Osborn T, Farmer DM, Vagle S, Thorpe S, Cure M (1992) Measurements of bubble plumes and turbulence from a submarine. Atmos–Ocean 30:419–440
Patel VC, Rodi W, Scheurer G (1984) Turbulence models for near-wall and low Reynolds number flows. A review. AIAA J 23(9):1306–1319
Peters H, Gregg MC, Toole JM (1988) On the parameterization of equatorial turbulence. J Geophys Res 93:1199–1218
Pierson WJ, Moskowitz L (1964) A proposed spectral form for fully-developed wind seas based on the similarity theory of S.A. Kitaigorodsky. J Geophys Res 69:5181–5190
Polzin K (1996) Statistics of the Richardson number mixing models and finestructure. J Phys Oceanogr 26:1409–1425
Priestly CHB (1959) Turbulent transfer in the lower atmosphere, 3rd edn. University of Chicago Press, Chicago, p 130
Rabinovich SG (1995) Measurement errors: theory and practice. American Institute of Physics, Woodbury, p 279
Rascle N, Chapron B, Ardhuin F, Soloviev A (2012) A note on the direct injection of turbulence by breaking waves. Ocean Model 70: 145–151
Santiago-Mandujano F, Firing E (1990) Mixed-layer shear generated by wind stress in the central equatorial Pacific, J Phys Oceanogr 20:1576–1582
Schoeberlein HC, Baker MA (1996) Status report: Reduction of motion contamination in TOGA COARE velocity measurements. Technical report, 13 December 1996, The Johns Hopkins University, Applied Physics Laboratory, Laurel, MD 20723, p 46
Shen L, Zhang X, Yue DKP, Triantafyllou GS (1999) The surface layer for free-surface turbulent flows. J Fluid Mech 386:167–212

Skyllingstad ED, Smyth WD, Moum JN, Wijesekera H (1999) Upper ocean turbulence during a westerly wind burst: a comparison of large-eddy simulation results and microstructure measurements. J Phys Oceanogr 29:5–28

Smyth WD, Hebert D, Moum JN (1996) Local ocean response to a multiphase westerly wind burst, 1, Dynamic response. J Geophys Res 101:22,495–22,512

Snodgrass FE, Groves GW, Hasselmann K, Miller GR, Munk WH, Powers WH (1966) Propagation of ocean swell across the Pacific. Philos Trans Roy Soc Lond A 249:431–497

Sreenivasan KR, Ramshankar R, Meneveau C (1989) Mixing, entrainment and fractal dimensions of surfaces in turbulent flows. Proc Roy Soc Lond A 421:79–108

Soloviev AV (1990) Coherent structure at the ocean surface in the convectively unstable conditions. Nature 346:157–160

Soloviev AV (1992) Small-Scale Structure of the Open Ocean Boundary Layers. Dissertation for Doctor of Physical-Mathematical Sciences Degree, Russian Academy of Sciences, Moscow (in Russian)

Soloviev A, Lukas R (1996) Observation of spatial variability of diurnal thermocline and rain-formed halocline in the western Pacific warm pool. J Phys Oceanogr 26(11):2529–2538

Soloviev AV, Lukas R (2003) Observation of wave-enhanced turbulence in the near-surface layer of the ocean during TOGA COARE. Deep-Sea Res Part I 50:371–395

Soloviev A, Lukas R (1997) Sharp frontal interfaces in the near-surface layer of the ocean in the western equatorial Pacific warm pool. J Phys Oceanogr 27(6):999–1017 Soloviev A, Lukas R (2006) The Near-Surface Layer of the Ocean: Structure, Dynamics and Applications. Springer, NY, 572 p.

Soloviev AV, Lukas R, DeCarlo S, Snyder J, Arjannikov A, Baker M, Khlebnikov D (1995) Small-scale measurements near the ocean-air interface during TOGA-COARE. Data Report. SOEST-95–05. University of Hawaii, Honolulu, HI, p 257.

Soloviev A, Lukas R, DeCarlo S, Snyder J, Arjannikov A, Turenko V, Baker M, Khlebnikov D (1998) A near-surface microstructure sensor system used during TOGA-COARE. Part I: Bow measurements. J Atmos Ocean Tech 15:563–578

Soloviev A, Lukas R, Hacker P (2001) An approach to parameterization of the oceanic turbulent boundary layer in the western pacific warm pool. J Geophys Res 106:4421–4435

Soloviev A, Lukas R, Hacker P, Baker M, Schoeberlein H, Arjannikov A (1999) A near-surface microstructure sensor system used during TOGA COARE. Part II: Turbulence Measurements. J Atmos Oceanic Tech 16:1598–1618

Soloviev AV, Vershinsky NV, Bezverchnii VA (1988) Small-scale turbulence measurements in the thin surface layer of the ocean. Deep-Sea Res 35:1859–1874

Soloviev A, Maingot C, Agor M, Nash L, Dixon K (2012) 3D Sonar measurements in wakes of ships of opportunity. J Atmos Oceanic Techn 29:880–886

Stacey MW (1999) Simulation of the wind-forced near-surface circulation in knight inlet: A parameterization of the roughness length. J Phys Oceanogr 29:1363–1367

Stewart RW, Grant HL (1962) Determination of the rate of dissipation of turbulent energy near the sea surface in the presence of waves. J Geophys Res 67:3177–3180

Stokes GG (1851) On the effect of the internal friction of fluids on the motion of pendulums. Trans Camb Phil Soc 9:8–106

Stommel H (1960) Wind-drift near the equator. Deep-Sea Res 6:298–302

Stull RB, Kraus EB (1987) A transilient model of the upper ocean. J Geophys Res-Oceans 92:10,745–10,755

Sullivan PP, McWilliams JC, Melville WK (2007) Surface gravity wave effects in the oceanic boundary layer: Large-eddy simulation with vortex force and stochastic breakers. J Fluid Mech 593:405–452

Swean Jr. TF, Leighton RI, Handler R, Swearingen JD (1991) Turbulence modeling near the free surface in open channel flow. AIAA Paper 91–0613

Taylor GI (1938) The spectrum of turbulence. Proc Roy Soc Lond 164:476–490

Tennekes H (1973) The logarithmic wind profile. J Atmos Sci 30:558–567

Terray EA, Donelan MA, Agrawal YC, Drennan WM, Kahma KK, Williams AJ III, Hwang PA, Kitaigorodskii SA (1996) Estimates of kinetic energy dissipation under breaking waves. J Phys Oceanogr 26:792–807

Thompson SM, Turner JS (1975) Mixing across an interface due to turbulence generated by an oscillating grid.J Fluid Mech 67:349–368

Thorpe SA (1969) Experiments on the stability of stratified shear flows. Radio Sci 4:1327–1331

Thorpe SA (1988) The dynamics of the boundary layers of the deep ocean. Sci Prog Oxf 72:189–206

Thorpe SA (1975) The excitation, dissipation, and interaction of internal waves in the deep ocean. J Geophys Res 80:328–338

Thorpe SA (1985) Small-scale processes in the upper ocean boundary layer. Nature 318:519–522

Thorpe SA, Jackson JFE, Hall AJ, Lueck RG (2003a) Measurements of turbulence in the upper ocean mixing layer using Autosub. J Phys Oceanogr 33:122–145

Thorpe SA, Osborn TR, Farmer DM, Vagel S (2003b): Bubble clouds and Langmuir circulation: observations and models. J Phys Oceanogr 33:2013–2031

Turner JS (1973) Buoyancy effects in fluids. Cambridge University Press, NY

Umlauf L, Burchard H (2003) A generic length-scale equation for geophysical turbulence models. J Mar Res 61:235–265

Van Dyke M (1982) An album of fluid motion. Parabolic Press, Stanford, CA, p. 176

Veronis G (1960) An approximate theoretical analysis of the equatorial undercurrent. Deep-Sea Res 6:318–327

Vershinsky NV, Soloviev AV (1977) A profiler for the studies of the ocean surface layer. Oceanology 17:358–363 (in Russian)

Volkov YA, Soloviev AV (1986) On vertical thermal structure of near-surface layer of atmosphere above the ocean. Izvestiya: Atmospheric and oceanic physics 22(9):899–903

Volkov YA, Soloviev AV, Turenko VV, Bezverchnii VA, Vershinsky NV, Ermolaev FMA (1989) Investigation of hydrophysical fields structure of the thin surface layer of the ocean from a moving vessel. Izvestiya: Atmospheric and oceanic physics 25(7):695–701

Voss R (1988) Fractals in nature: from characterization to simulation. In Peitgen H, Saupe D (eds), The science of fractal images, chapter 1, pp 21–70. New York, Springer-Verlag

Wang D, Large WG, McWilliams JC (1996) Large-eddy simulation of the equatorial ocean boundary layer: diurnal cycling, eddy viscosity, and horizontal rotation. J Geophys Res 101:3649–3662

Weller RA, Price JF (1988) Langmuir circulation within the oceanic mixed layer. Deep-Sea Res 35:711–747

White FM (1986) Fluid mechanics. McGraw-Hill, NY, pp 732

Wyngaard JC, Coté OR, Izumi Y (1971) Local free convection, similarity and the budgets of shear stress. J Atmos Sci 28:1171–1182

Yaglom AM (1979) Similarity laws for constant-pressure and pressure-gradient turbulent flows. Ann Rev Fluid Mech 11:505–540

Zilitinkevich SS, Calanca P (2000) An extended similarity-theory for the stably stratified atmospheric surface layer. Q J Roy Meteorol Soc 126:1913–1923

Zubair FR, Catrakis HJ (2009) On separated shear layers and the fractal geometry of turbulent scalar interfaces at large Reynolds numbers. J Fluid Mech 624:389–411

Chapter 4
Fine Structure and Microstructure

Abstract Under light winds or heavy rainfall, upper ocean turbulence is strongly suppressed by stratification and large vertical gradients of any properties can develop in the upper few meters of the ocean. We consider the penetrative solar radiation and the impacts of the distribution of radiant heating on the near-surface layer dynamics. Stable stratification in the near-surface ocean due to diurnal warming or rainfall can reduce the turbulence friction, which results in the intensification of near-surface currents. Unstable stratification leads to convective overturning, which increases turbulent friction locally. In addition, discrete convective elements—analogs of thermals in the atmosphere—penetrate into the stably stratified layer below and initiate nonlocal transport. Experimental studies at the equator have produced striking examples of local and nonlocal effects on the dynamics of the diurnal mixed layer and thermocline. A discussion of new approaches to modeling the diurnal cycle of sea surface temperature (SST) using computational fluid dynamics (CFD) capabilities is included. Fine thermohaline structure of the near-surface layer of the ocean in polar seas influences the sea ice coverage, which has important climate consequences.

Keywords Fine structure • Microstructure • Diurnal warming • Diurnal mixed layer • Diurnal thermocline • Sea ice • Rain • River runoff • Turbulence

4.1 Introduction

In the oceanographic literature, the term *fine structure* is traditionally reserved for inhomogeneities relating to stratification, while the term *microstructure* has often been applied to inhomogeneities associated with small-scale turbulence (Gregg 1975).

Air–sea momentum, heat, and freshwater fluxes are crucial factors determining the thermohaline structure of the near-surface layer of the ocean. Under moderate-to-high wind speed conditions, the upper ocean is usually well mixed due to strong turbulence. When the wind drops below about 5 m s^{-1}, and with solar warming, the turbulent regime dramatically changes. The stabilizing buoyancy flux suppresses turbulent mixing and the air–sea exchange is effectively trapped within a thin near-

A. Soloviev, R. Lukas, *The Near-Surface Layer of the Ocean*, Atmospheric and Oceanographic Sciences Library 48, DOI 10.1007/978-94-007-7621-0_4,

surface layer. Under these conditions, the diurnal thermocline can be found close to the ocean surface contributing to the fine structure and microstructure of the near-surface layer.

In addition to solar heating, the freshwater cycle may substantially modify the structure, dynamics, and thermodynamics of the near-surface layer of the ocean. The main components of the hydrologic cycle in the ocean are precipitation, evaporation, river discharge, and sea ice melting/formation.

Precipitation effects are pronounced in low latitudes, especially within intertropical convergence zones (ITCZ), warm pools, and monsoon regions. Lateral advection of freshwater may contribute to the fine structure of the near-surface layer of the ocean in the coastal areas with river runoff, in the marginal ice zones, and in regions of strong mesoscale convection.

4.2 Near-Surface Thermohaline Structures

4.2.1 Diurnal Mixed Layer and Diurnal Thermocline

A fundamental mode of upper ocean variability is the diurnal cycle, which is forced by the diurnal cycle of solar irradiance. As a result of this forcing, a diurnal mixed layer and diurnal thermocline can develop near the ocean surface. Following Fedorov and Ginzburg (1988), three main types of vertical temperature structures are associated with this process as schematically illustrated in Fig. 4.1.

Wind–wave mixing and/or nighttime convection produce a well-mixed layer (Fig. 4.1a). This is the surface mixed layer of the ocean, which is also referred to as the seasonal mixed layer wherever the climate has seasons.

During daytime, a warmer diurnal mixed layer and a diurnal thermocline form on the background of the mixed layer (Fig. 4.1b), due to the absorption of solar radiation in the upper ocean. From Chap. 1 the reader knows that solar forcing $I_R(z)$ is a volume source of heat and strictly speaking should not be considered as a surface flux. The surface flux consists of latent (Q_E) and sensible (Q_T) heat fluxes and the net longwave radiation (I_L). Wind–wave mixing and convection produce a diurnal mixed layer. The diurnal mixed layer is clearly pronounced (as in the sketch shown in Fig. 4.1b) when Q_0, the sum of Q_E, Q_T, and I_L, is positive (i.e., net surface cooling takes place) and its magnitude is not too small compared to the solar heating.

For $Q_0 < 0$ (for example, in cases when air is warmer than water and relative humidity is close to 100 %), the diurnal mixed layer can hardly be seen in temperature profiles (Fig. 4.1c) but may still be resolved from turbulence or gradient Richardson number profiles. Similar temperature profiles can be observed under calm weather conditions during peak insolation. In this case, the sea surface can lose heat to the atmosphere $Q_0 > 0$ but the volume source of heat (absorption of solar radiation) is so

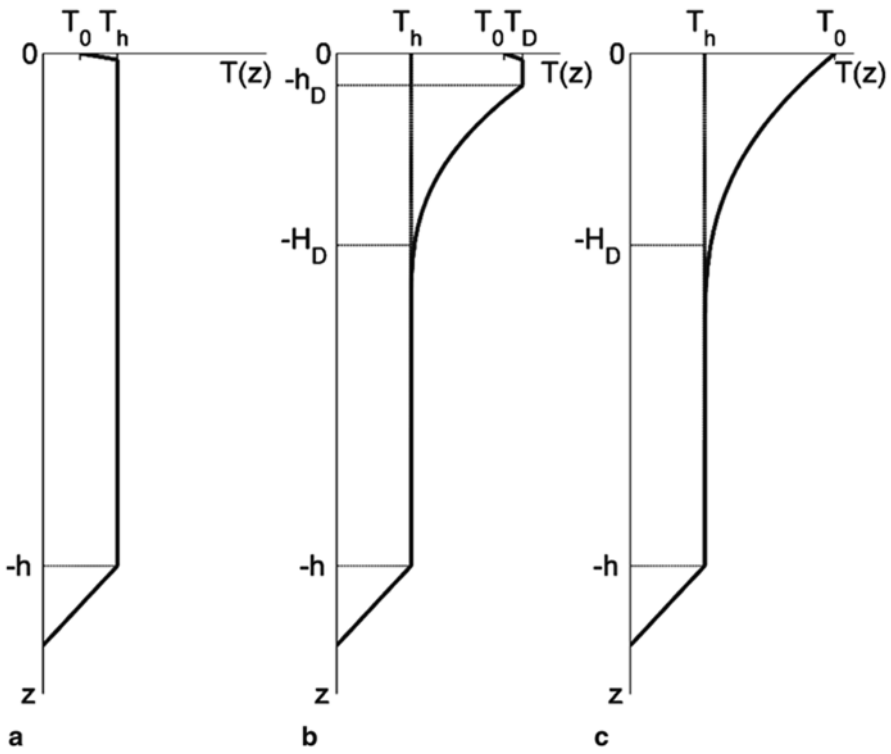

Fig. 4.1 Typical vertical thermal structures of the upper ocean associated with the diurnal cycle: **a** nighttime well-mixed layer, **b** diurnal mixed layer and diurnal thermocline develop in the top of the mixed layer, **c** diurnal mixed layer is stratified or does not exist. Here, h is the depth of the upper ocean mixed layer, H_D is the depth of the bottom boundary of diurnal thermocline (which can often, but not always, be considered as the lower boundary of the near-surface layer of the ocean), h_D is the diurnal mixed-layer depth; T_h is the bulk temperature of the upper ocean mixed layer, T_D is the bulk temperature of the diurnal mixed layer, and T_0 is the sea surface temperature

strong that convective mixing ceases, and there is no surface mixed layer (Soloviev and Lukas 1997).

Freshwater cycling may affect the ocean diurnal cycle in two ways: (1) evaporation from the sea surface or ice formation results in increased surface salinity that adds to the convection due to surface cooling; (2) precipitation, river discharge, or sea ice melting inhibits convection. These effects are considered elsewhere in this chapter (as well as in Chap. 2 in relation to the sea surface microlayer).

The structure of the diurnal mixed layer and diurnal thermocline depends on atmospheric forcing (wind speed, solar radiation, rain, and heat fluxes), which is generally spatially inhomogeneous. The internal processes associated with pressure gradient equilibration and mass redistribution in the upper ocean are often

quasi-two-dimensional and may exhibit features of organization. As a result, the diurnal thermocline can reveal spatial patterns in the form of nonlinear internal waves, billows, fronts, etc. Examples of the vertical and horizontal structure of the diurnal thermocline are given in the next section. Spatially coherent organized structures in the near-surface layer of the ocean are considered in Chap. 5.

4.2.2 *Examples of Near-Surface Structures Associated with Diurnal Cycle*

Figure 4.2 illustrates the vertical structure of the turbulent boundary layer in the near-surface North Atlantic Ocean under strong, moderate, and low wind speed conditions during afternoon hours when it was not raining. Pertinent information about these measurements is given in Table 4.1.

The example shown in Fig. 4.2a corresponds to 8.3 m s^{-1} wind speed. As observed from the turbulent fluctuation velocity and temperature profiles, the upper 20-m layer of the ocean is well mixed, and there is no significant vertical stratification due to *diurnal warming* in this layer.

In the second example (Fig. 4.2b), obtained at a moderate wind speed (6.2 m s^{-1}), there is a diurnal mixed layer and diurnal thermocline in the upper 8 m of the ocean. The turbulent velocity fluctuations are intense within the upper 5 m. The turbulent area near 8 m presumably represents a sporadic mixing event possibly driven by shear. Below 8 m, turbulence levels are close to the noise level of the sensor.

The third example (Fig. 4.2c) represents low wind speed conditions. There is a diurnal thermocline near the surface. While the diurnal mixed layer is not clearly seen in the temperature profile, intense velocity fluctuations in the upper 0.5-m indicate the presence of mixing.

Figure 4.3 shows three series of vertical temperature profiles obtained under different wind speeds in the equatorial Pacific on different days but during approximately the same afternoon time period. The series of nine profiles shown in Fig. 4.3a was obtained under relatively strong winds (~7 m s^{-1}) and clouds of medium altitude (cloud fraction 6/8). The depth of the diurnal mixed layer varied from 12 to 17 m and the maximum temperature increase in the upper 18 m was about 0.2°C.

The series of ten temperature profiles shown in Fig. 4.3b was obtained under light winds (~2 m s^{-1}) with midlevel clouds (cloud fraction 2/8), revealing a more substantial diurnal warming of the near-surface layer. The temperature difference across the diurnal thermocline was between 0.6°C and 0.8°C. The diurnal mixed-layer depth varied from 1 to 7 m. The strong variations of the mixed-layer depth as well as the depth and thickness of the diurnal thermocline were presumably caused by internal waves in the diurnal thermocline. The diurnal thermocline appears to be of almost constant thickness but of variable depth, changing from one cast to another.

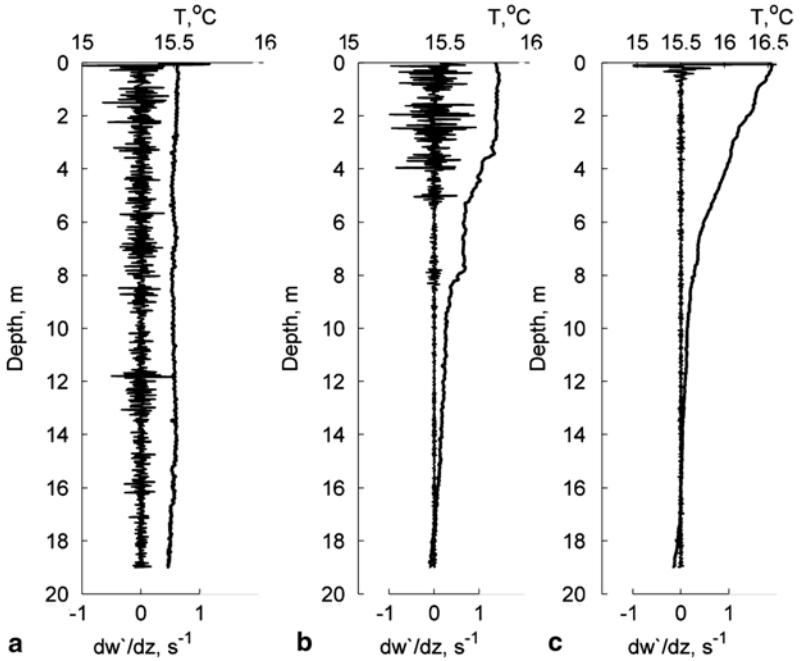

Fig. 4.2 Examples of temperature T and strain fluctuation dw'/dz profiles under different wind conditions: **a** strong wind $(U_{18} = 8.3\text{ms}^{-1})$, **b** moderate wind $(U_{18} = 6.2\text{ms}^{-1})$, and **c** low wind $(U_{18} = 3.3\text{ms}^{-1})$ as observed in the North Atlantic during *GasEx-1998* with a free-rising profiler by Soloviev et al. (2001b). U_{18} is the wind speed at 18 m height (shipboard observations). The vertical profile of dw'/dz is an indicator of the turbulent mixing processes. Reproduced with permission from American Geophysical Union

Table 4.1 Pertinent information for the example profiles shown in Fig. 4.2

Fig. 4.2	Coordinates lat, lon	Date, 1998	Time LT	U_{18} m s^{-1}	u_* m s^{-1}	I_Σ W m^{-2}	Q_0 W m^{-2}
a)	46°07'N, 20°25'W	13 Jun	14:41	8.3	0.0093	472	42
b)	46°03'N, 20°44'W	5 Jun	14:26	6.2	0.0068	645	103
c)	46°02'N, 20°54'W	6 Jun	15:51	3.3	0.0036	582	100

U_{18} wind speed at 18 m above the sea surface, u_* friction velocity in the upper ocean, I_Σ insolation (surface solar irradiance), Q_0 sum of latent Q_E and sensible Q_T heat fluxes and net longwave irradiance I_L.

The series of five temperature profiles (Fig. 4.3c) obtained under calm weather conditions and high clouds (cloud fraction 2/8) shows that the diurnal heating is mainly localized in the upper meter. The temperature difference across the diurnal

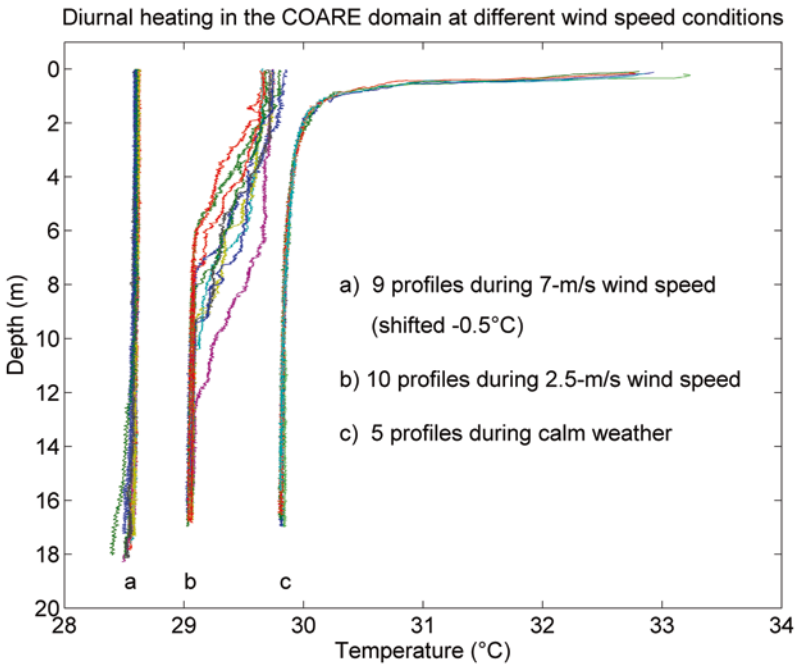

Fig. 4.3 Vertical temperature profiles in the western equatorial Pacific obtained by a free-rising profiler during different wind speed conditions taken at approximately the same afternoon time on different days. After Soloviev and Lukas (1997) with permission from Elsevier

thermocline is larger than 3°C, with the sea surface temperature (SST) reaching 33.25°C. Based on cloud information, we can conclude that for the example shown in Fig. 4.3c the shortwave solar forcing was larger than for examples *a* and *b,* which contributed to the large diurnal warming of the near-surface layer.

Examples from diverse climatic zones presented in this section and elsewhere in this chapter, from the equatorial Pacific (0°N) to the North Atlantic (59°N), demonstrate that a common feature of the upper ocean diurnal cycle is its strong dependence on the local wind speed. As we also know from Chap. 3, under light winds and strong insolation the turbulent regime in the upper ocean dramatically changes. Consequently, the diurnal thermocline is found very close to the ocean surface; the amplitude of the diurnal warming sometimes reaches a few degrees Celsius.

4.2.3 Wave-Like Disturbances in the Diurnal Thermocline

Under certain conditions, the diurnal thermocline can exhibit structures resembling large-amplitude internal waves. The contour plot of temperature (Fig. 4.4a) from

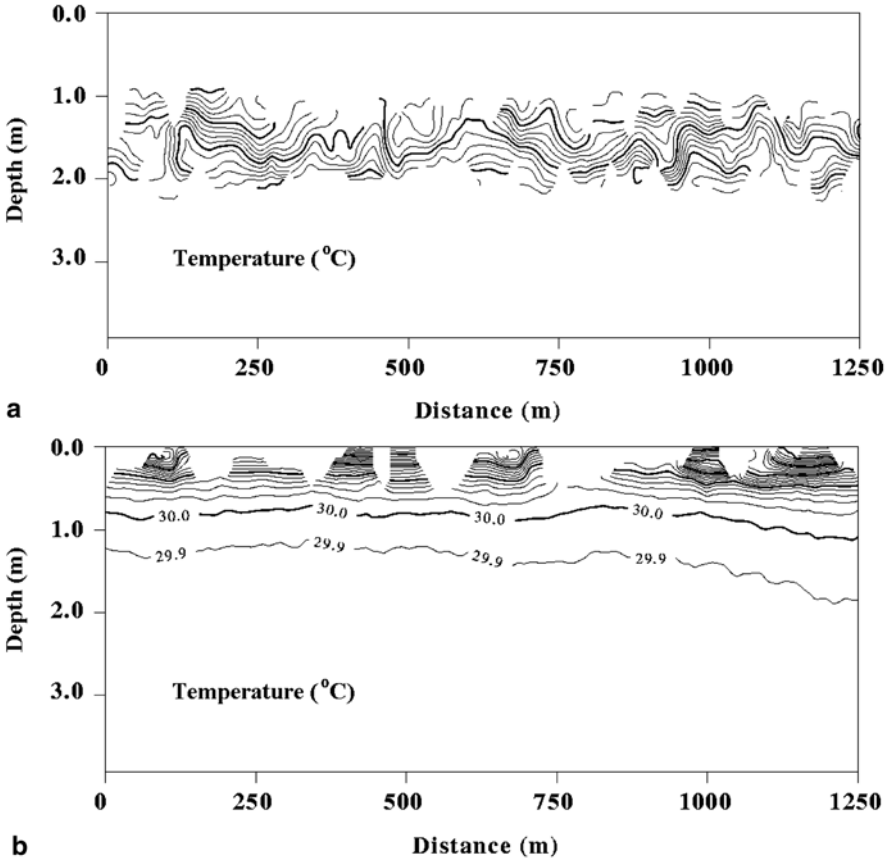

Fig. 4.4 Contour plots of temperature in the coordinate system connected to the instantaneous position of the ocean surface. Measurements by bow sensors on **a** 26 April 1994, 15:16-15:22 LST and on **b** 1 May 1994, 15:20-15:29 LST. After Soloviev and Lukas (1997) with permission from Elsevier

measurements by bow sensors made on 26 April 1994, just before profiling shown in Fig. 4.3b, reveals wave-like disturbances of the diurnal thermocline of ~200 m wavelength with an amplitude > 1 m. Because of surface waves and pitching of the vessel, the bow probes profiled portions of the upper 4 m. This method, described in more detail in Chap. 3, provides an opportunity to study both vertical and horizontal structures of the near-surface layer of the ocean.

The contour plot of temperature from the bow record on 1 May 1994, just after the measurements of Fig. 4.3c, is shown in Fig. 4.4b. It is much more "quiet" than that in Fig. 4.4a.

Other sources of the horizontal variability in the diurnal thermocline include spatially coherent organized motions, which are considered in Chap. 5.

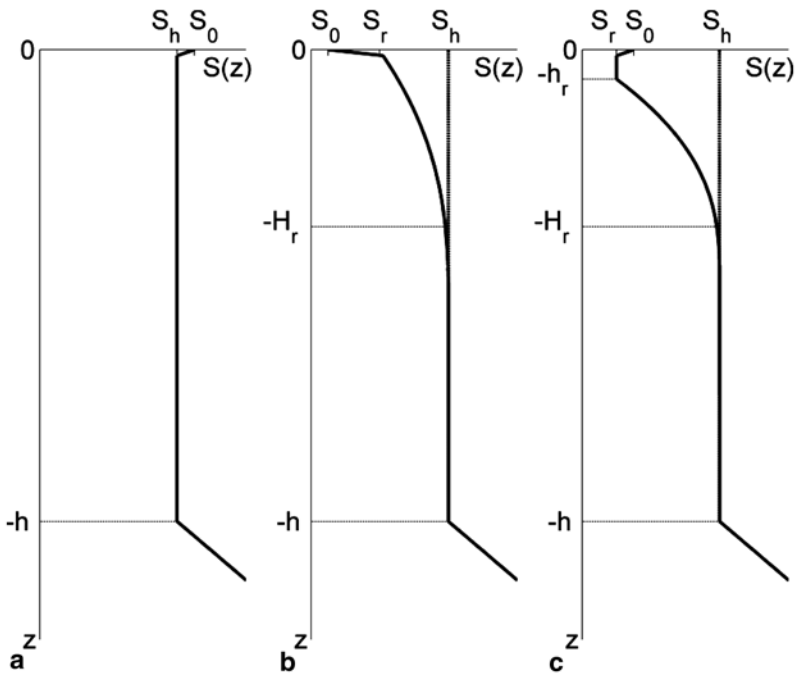

Fig. 4.5 Typical vertical haline structures of the upper ocean layer associated with rainfall events compared with a well-mixed layer (**a**) under no rain conditions. Under rainy conditions (**b**) a halocline develops at the top of the mixed layer; the rain-formed mixed layer may not be clearly seen in the vertical salinity profile. A rain-formed mixed layer and halocline after the end of rain are schematically shown in (**c**). Here, h is the depth of the mixed layer, H_r is the depth of the bottom boundary of rain-formed halocline (which can often, but not always, be considered as the lower boundary of the near-surface layer of the ocean), h_r is the rain-formed mixed-layer depth; S_h is the bulk salinity of the mixed layer, S_r is the bulk salinity of the rain-formed mixed layer, and S_0 is the sea surface salinity

4.2.4 Rain-Formed Mixed Layer and Halocline

In addition to the diurnal cycle, near-surface freshening due to rain is another fundamental mode of upper ocean variability. A rain-formed mixed layer and halocline can be formed in the upper ocean mixed layer. Three main types of vertical salinity structures associated with this process are schematically illustrated in Fig. 4.5. This sketch implies conditions of no thermal stratification in the upper ocean.

Wind–wave mixing and/or nighttime convection produce a well-mixed layer (Fig. 4.5a). With no rain, salinity in the molecular diffusion sublayer just below the sea surface is slightly increased due to evaporation.

The rain forcing consists of a volume flux and a surface flux of freshwater (Sect. 1.5). When rain starts, the kinetic energy of raindrops, as well as the associated buoyancy flux, contributes to the turbulent kinetic energy (TKE) balance in the near-surface layer. The rain-formed mixed layer may not be clearly seen in the verti-

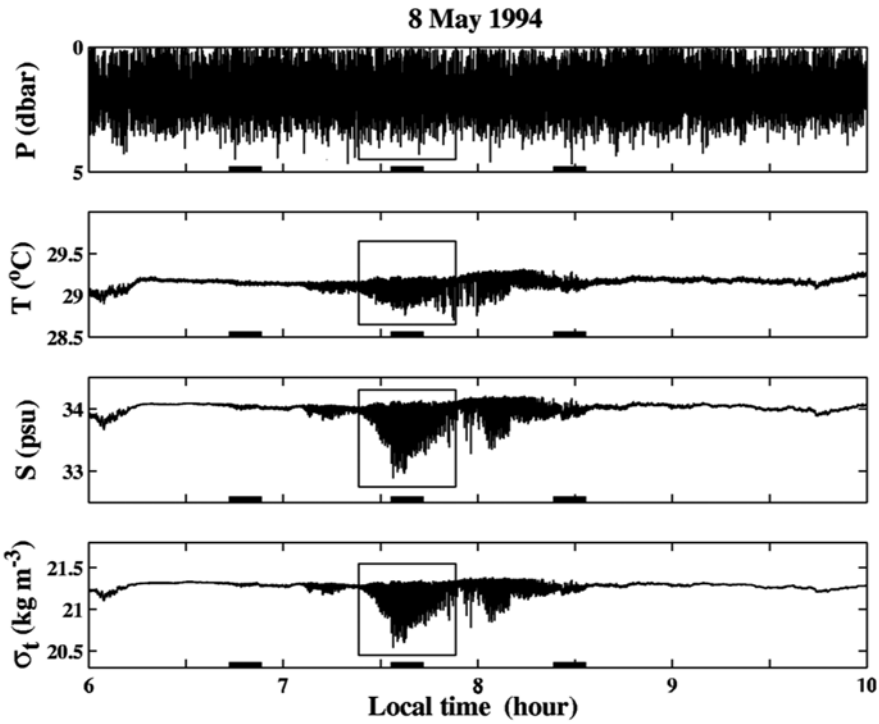

Fig. 4.6 Example of records made by bow sensors in the western Pacific warm pool during a strong rain event while steaming at 10–11 knots. (Note that 1 dbar = 0.98 m.) Segments marked by rectangles are shown in more detail in Fig. 4.8. Solid segments on the time axis correspond to 10-min averaging intervals for calculation of vertical profiles of T, S, and σ_t shown in Fig. 4.7. After Soloviev and Lukas (1996). Copyright © 1996 American Meteorological Society. Used with permission

cal salinity profile (as in the sketch shown in Fig. 4.5b) during strong rain. However, when the rain ceases, the rain-formed mixed layer is usually well defined from the vertical salinity profile (as schematically shown in Fig. 4.5c).

Rain droplet size is exponentially distributed (Bell 1987), intermittent in time and space. As a result, the rain-formed halocline usually varies spatially. Examples of the vertical and horizontal structures of the rain-formed halocline are given in the next section.

4.2.5 Low-Salinity Patches Due to Convective Rains

Convective rains produce low-salinity patches in the upper ocean. Measurements with bow sensors across such a patch (associated with strong rain event) are shown in Fig. 4.6. Averaged vertical profiles of temperature (T), salinity (S), and density

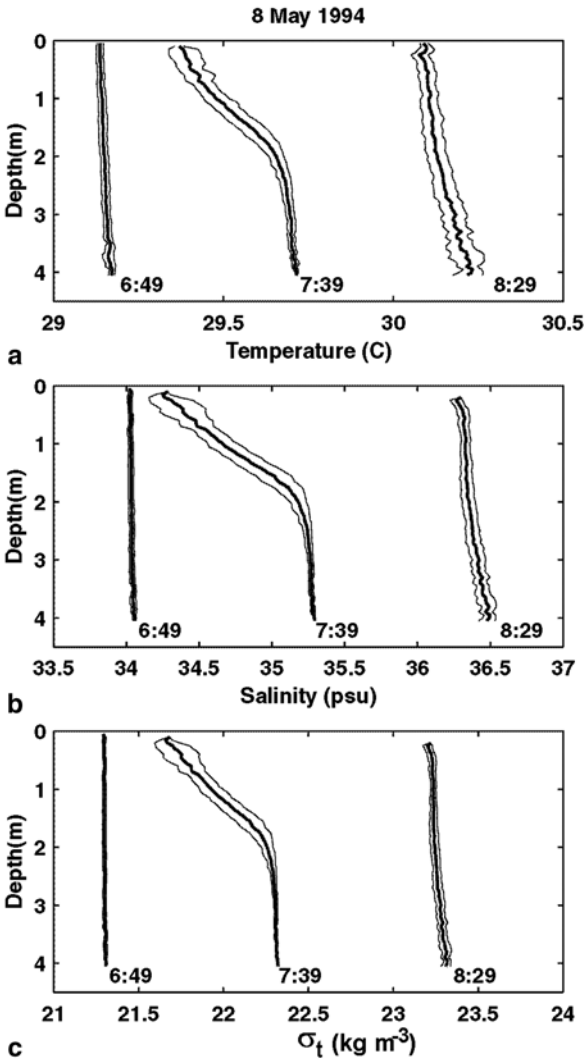

Fig. 4.7 Vertical profiles of **a** temperature, **b** salinity, and **c** density obtained by averaging 10-min intervals of bow sensor data within 0.1 dbar pressure bins. Each successive profile is shifted by 0.5°C in temperature, by 1.2 psu in salinity and by 1.0 kg m^{-3} in σ_t density in subplots (**a**), (**b**), and (**c**), respectively. The local time below each profile corresponds to the middle of the 10-min segment. Thin lines represent one standard deviation. After Soloviev and Lukas (1996). Copyright © 1996 American Meteorological Society. Used with permission

(σ_t) are shown in Fig. 4.7. They are calculated by sorting the data in pressure (P) and averaging over the 10-min intervals, indicated on the time axis of Fig. 4.6 by heavy line segments. Segments marked by rectangles in Fig. 4.6 are shown in Fig. 4.8 in more detail.

This low-salinity patch is also traced in the temperature record because the temperature of the raindrops is lower than the SST (Gosnell et al. 1995). High-frequency fluctuations of T, S, and σ_t primarily result from depth variations of the probes.

Figure 4.8 gives a more detailed picture of the core of the rain patch (the T, S, and σ_t records for the corresponding segment in Fig. 4.6 are marked by rectangles). The contour plot of σ_t versus depth (Fig. 4.8d) reveals disturbances that look like internal waves with apparent wavelengths of ~200 m or more. The true wavelengths cannot be estimated from these measurements because the ship's motion relative to the internal wave propagation is unknown.

Averaged vertical profiles of T, S, and σ_t at 6:49LT (Fig. 4.7) just before entering the rain zone show a well-mixed layer within the depth range of the bow probes. The wind speed was 7.8 m s^{-1} and there were no signatures of diurnal heating or previous rain events in the upper 4 m of the ocean.

The vertical profiles at 7:39LT corresponding to the core of the freshwater patch showed a near-surface halocline with salinity difference $\Delta S \sim 1$ psu localized in the upper ~2 m and accompanied by a temperature inversion of $\Delta T \sim 0.3$°C. The σ_t vertical profile at 7:39LT revealed a stably stratified layer of ~2 m depth; the turbulent mixing in the near-surface layer of the ocean was not sufficient to mix this near-surface stratified layer. (The wind speed fluctuated strongly both in magnitude (3.2–6.9 m s^{-1}) and in direction (230–360°) because of squalls accompanying the rain event.)

The vertical profiles at 8:29LT (Fig. 4.7) correspond to the end of the rain zone (Fig. 4.6). Stratification in the upper 4 m of the ocean is much reduced in comparison with the core of the patch. Wind speed increased up to 10–12 m s^{-1} and its direction became more stable (250–280°).

The dashed line S in the σ_t-depth contour plot (Fig. 4.8d) corresponds to the root mean square (RMS) uncertainty of pressure-to-depth conversion (the hydrostatic pressure bias has already been removed) at occasional intersections of the water–air interface as detected by the conductivity cell. It illustrates the uncertainty of pressure-to-depth conversion due to the dynamic pressure component and the ~0.6-m horizontal spacing between the C, T, and P sensors. The RMS uncertainty in the pressure-to-depth conversion is estimated as being between 0.02 and 0.1 dbar (Soloviev and Lukas 1996).

The contour plot of salinity in density coordinates (Fig. 4.8e) shows practically no anomalies. This supports the wavelike nature of the disturbances observed on the σ_t-depth contour plot on the horizontal scales resolved by this contour plot ($l > 100$ m).

4.2.6 *Combined Effect of Diurnal and Freshwater Cycles on the Upper Ocean Structure*

The schematics of the diurnal thermocline in Fig. 4.1 do not include cases with precipitation effects. Rainfalls produce near-surface salinity stratification, which helps to trap the net solar heating during daytime and cooling during nighttime in the near-surface layer of the ocean, thus enhancing the diurnal SST amplitude.

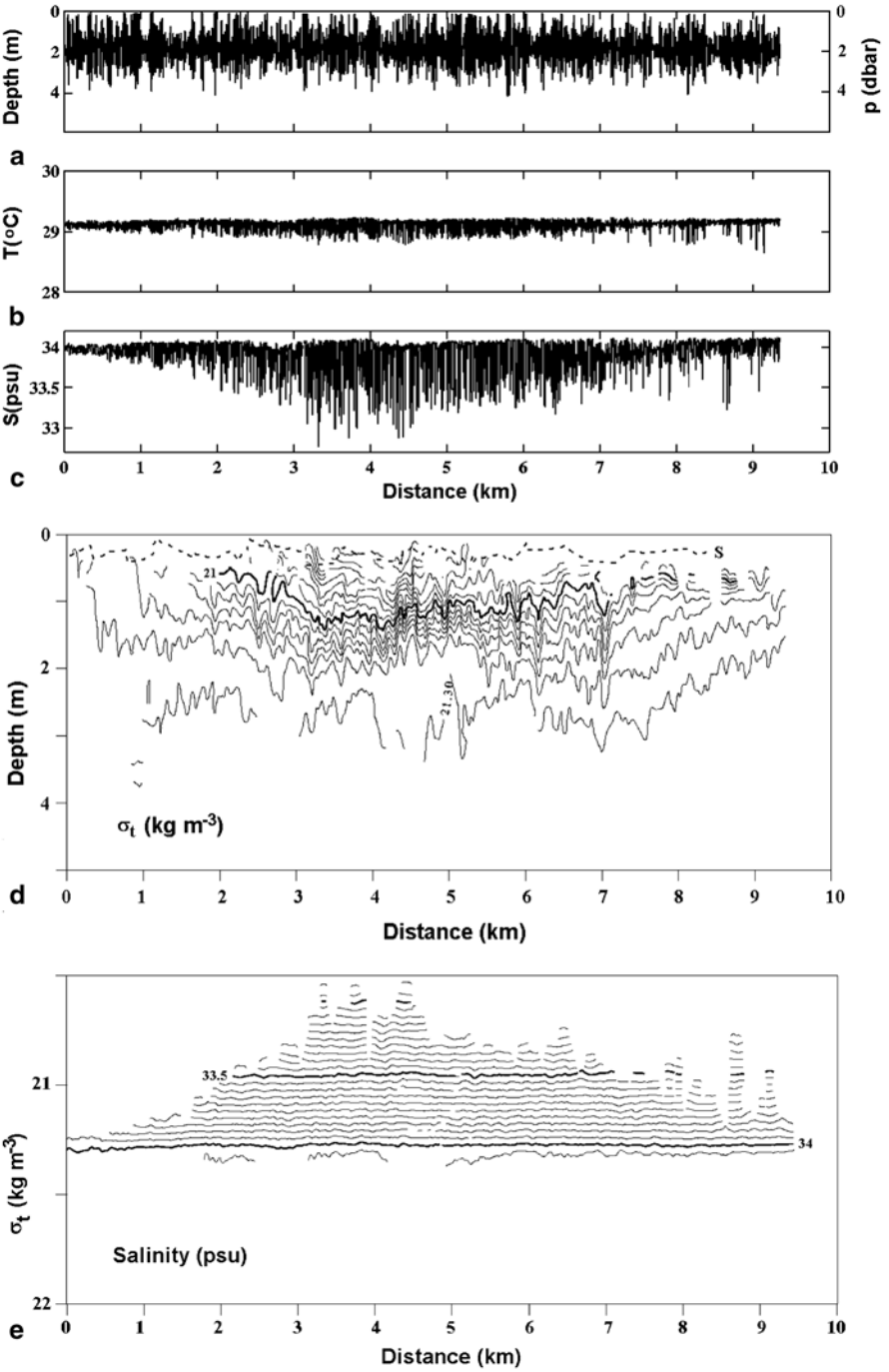

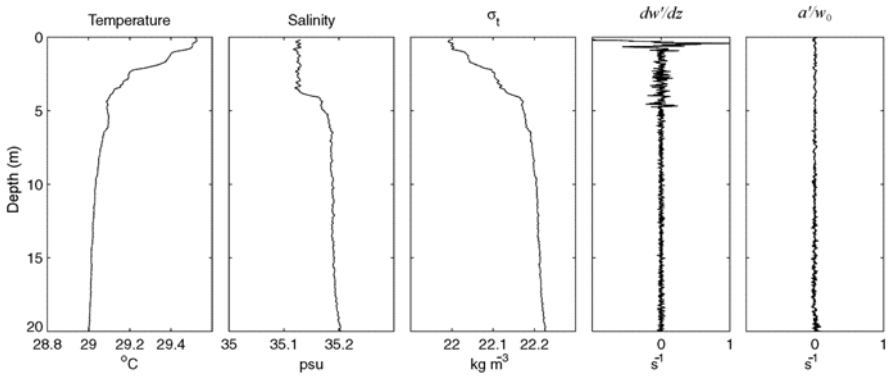

Fig. 4.9 Temperature, salinity, sigma-t density, and turbulent velocity (strain) fluctuation profiles in the upper 20 m of the ocean as measured with a free-rising profiler within a shallow freshwater lens in the western equatorial Pacific (15 April 1994, 04:29 GMT, 1°58'N, 165°E) under light winds (2.1–3.7 m s^{-1}). Note the larger velocity strain fluctuations (dw'/dz) within the upper 4.5 m. Acceleration fluctuations of the profiler a' are scaled in such a way (a'/w_0) that they are comparable with and are in fact much less than dw'/dz, where w_0 is the nominal vertical velocity of the profiler. Vertical velocity w' and acceleration a' signals are high-passed with a 4-Hz cutoff frequency and low-passed with a 40-Hz cutoff frequency. After Soloviev et al. (1999). Copyright © 1999 American Meteorological Society. Used with permission

The freshwater cycle may thus modify diurnal heating of the near-surface layer of the ocean. Buoyancy fluxes due to precipitation increase the static stability of the upper ocean, suppressing turbulent exchange with deeper waters. The rainfall influences the diurnal cycle by trapping heat near the surface (Anderson et al. 1996). An example is given in Fig. 4.9. The salinity profile shows a salinity depression within the upper 5 m due to a previous rain. Turbulent mixing is mainly localized within this stably stratified near-surface layer (note larger velocity strain fluctuations dw'/dz in the upper 5 m). Subsequent diurnal warming develops within this freshwater lens.

Figure 4.10 gives additional experimental evidence of a strong modification of the near-surface layer due to rain. It helps to understand how the combined effect of daytime solar heating and previous freshwater influx due to rain results in the strong density stratification of the upper ocean. In the case shown in Fig. 4.10,

Fig. 4.8 Intersection of a shallow fresh water patch near 4.43°N, 137.01°E during COARE cruise EQ-3. The upper part of the figure shows records of **a** depth (pressure), **b** temperature, and **c** salinity. The lower part shows **d** the corresponding contour plots of σ_t versus depth and **e** S versus σ_t. The dashed line (S) in the contour plot σ_t –T corresponds to the air–sea interface as indicated by the conductivity sensor using criteria C=4.6 S/m, where C is the water conductivity. Wind speed is 3.3–6.9 m s^{-1} (rain squalls), direction 338–353°; ship speed is 5.2 m s^{-1}, direction 1°; height of swell waves observed from the bridge ~2.5 m, direction ~30°. After Soloviev and Lukas (1996). Copyright © 1996 American Meteorological Society. Used with permission

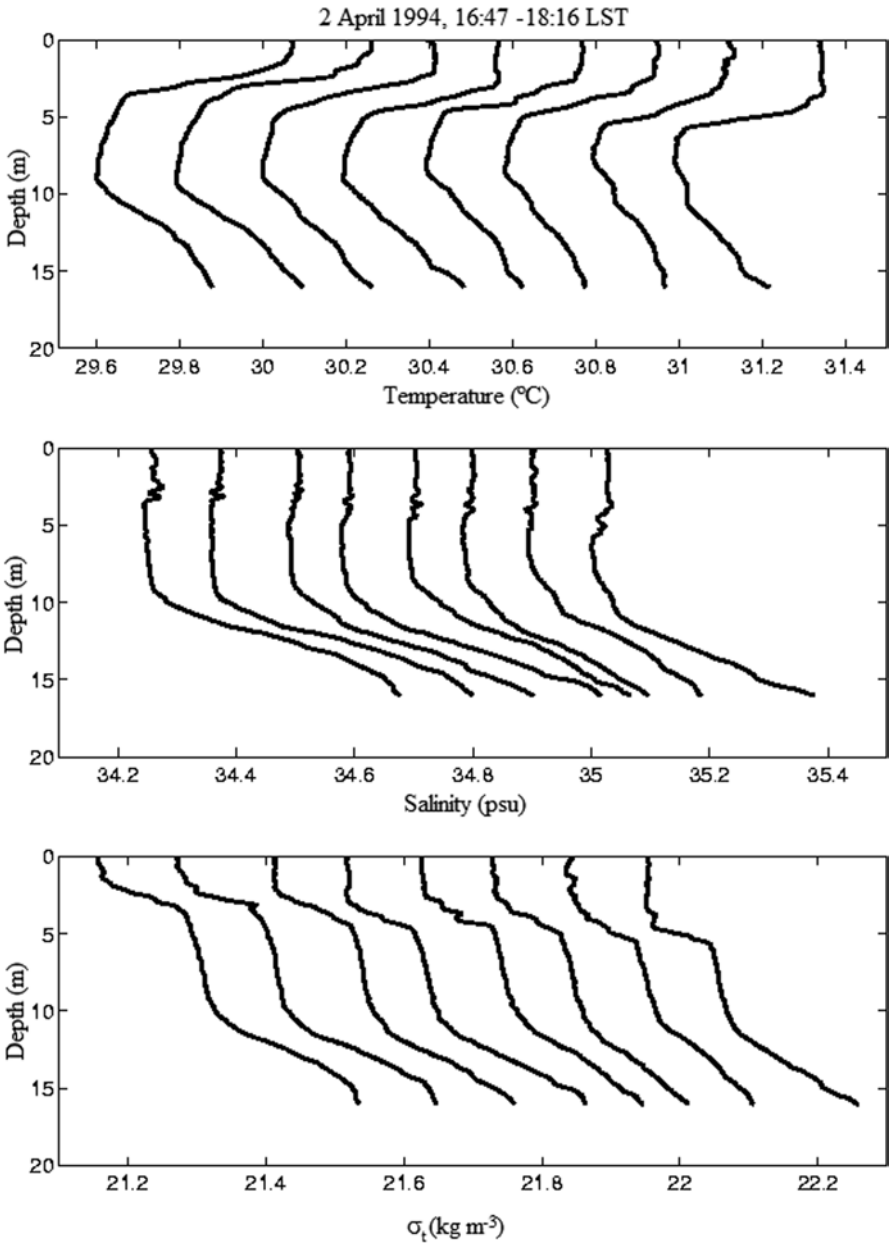

Fig. 4.10 Vertical temperature, salinity, and density profiles obtained by a free-rising profiler. Each successive profile is shifted by 0.2°C for temperature, by 0.1 psu for salinity, and by 0.1 kg m^{-3} for density. After Soloviev and Lukas (1997) with permission from Elsevier

the diurnal mixed layer and diurnal thermocline evolve on the background of the temperature structure within the rain-formed mixed layer. According to Fig. 4.10, the temperature of the rain-formed mixed layer is lower than that of the underlying water mass. This is typical for a rain-formed mixed layer after previous nighttime surface cooling (Fedorov and Ginzburg 1988; Lukas 1990b). The profiles shown in Fig. 4.10 are taken during the early evening and show a gradual deepening of the diurnal mixed layer.

Double-diffusion effects may also contribute to mixing in the stably stratified near-surface layer. (See the description of the phenomena of salt fingers and layering convection, for instance, in Turner 1973.)

Conditions leading to salt fingers can occur in the diurnal thermocline because excess salinity due to evaporation accumulates within the diurnal mixed layer. There is a slight but systematic increase in salinity within the diurnal mixed layer and diurnal thermocline in the profiles of Fig. 4.10. The increase in salinity of about 0.01–0.02 psu within the layer of diurnal heating is also clearly seen in Fig. 4.23 (except at 19:00 local solar time (LST) because of rain). The corresponding density profiles are stable, excluding the diurnal mixed layer where some inversions are associated with convective cooling and excess salinity. Remember that due to volume absorption of solar radiation in the upper ocean, convective cooling may exist even during the daytime. Evaporation usually increases the destabilizing buoyancy flux on the order of 10 %. The step-like structure after strong rain, presumably connected to layering convection, is shown in Fig. 4.11.

Figure 4.11 shows the temperature and salinity microstructure of the upper ocean after rainfall. These observations were made in the ITCZ where the hydrologic cycle is a crucial factor in upper ocean dynamics. Near-surface layers with distinctly lower salinity are formed, which suppress the turbulent exchange with the deeper water. Intense solar heating often alternates with heavy rains. A fraction of the solar energy is effectively trapped in the near-surface layer of the ocean, which in combination with the rain forcing results in complicated vertical stratification.

These measurements shown in Fig. 4.11 were made during morning hours after a heavy nighttime rainfall. A salinity depression of about 0.3 psu is observed in the upper 9 m of the ocean. Judging from the salinity profile the amount of precipitation was approximately 60 mm.

There is a 3.3-m deep quasi-homogeneous layer in the salinity profile. It presumably results from the nighttime convective mixing that worked against stable salinity stratification (Fig. 4.9). The temperature inversion observed between 3.3 and 4.2 m is consistent with this interpretation.

In the upper right corner of Fig. 4.11, the near-surface temperature and salinity profiles are shown with higher resolution. There is a 0.4-m thick diurnal mixed layer and the diurnal thermocline is found in the depth range from 0.4 to 0.8 m. The diurnal mixed layer and diurnal thermocline are found close to the ocean surface due to low wind speed conditions.

The layer between 3.3 and 4.2 m depth, with unstable temperature stratification, is expanded in the upper right corner of Fig. 4.11. This temperature inversion is

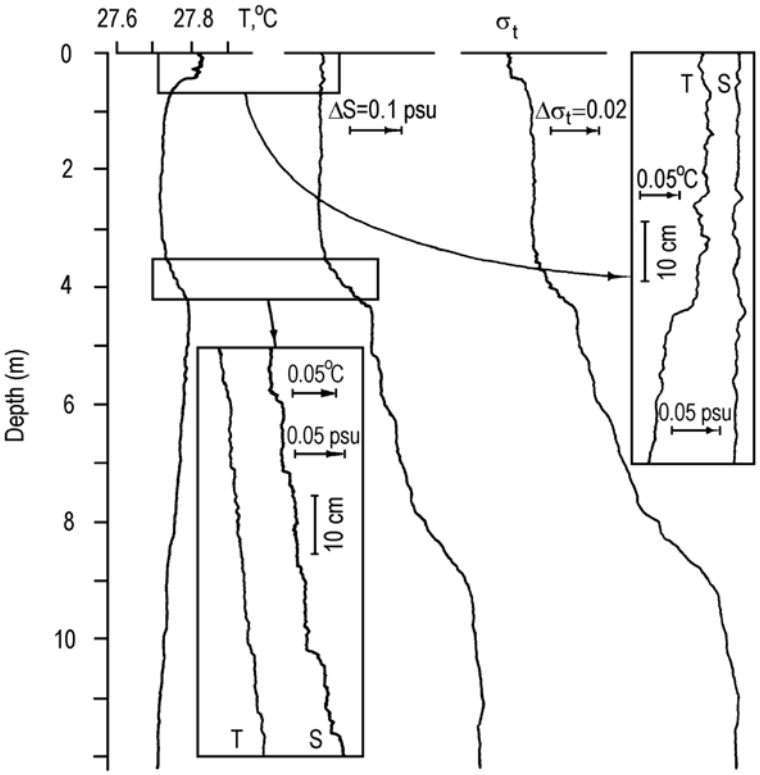

Fig. 4.11 Vertical temperature *T*, salinity S, and σ_t density profiles several hours after a rainfall. σ_t scale is in kg m^{-3}. The measurements are taken with a free-rising profiler by Soloviev and Vershinsky (1982). Reproduced with permission from Elsevier

overcompensated by the stable salinity stratification; thus, the density profile is stable. The combination of unstable temperature stratification and stable salinity stratification provides favorable conditions for the development of layering convection due to double diffusion of heat and salt. It is remarkable that a step-like structure, typical for layering convection, is evident within the depth range from 3.3 to 4.2 m.

Freshwater input often results in forming a barrier layer in the upper ocean mixed layer (see Sects. 1.7.4 and 7.8.2). The barrier layer has been recognized as a crucial element of tropical warm pool dynamics (Lukas and Lindstrom 1991). The barrier layer isolates the warm water of the upper ocean layer by reducing the entrainment cooling from below the mixed layer. The existence of the barrier layer plays a key role in the onset of El Niño, through a complex process that involves ocean vertical mixing, SST, wind stress, freshwater flux, and large-scale ocean-atmosphere dynamics.

4.3 Surface-Intensified Jets

4.3.1 Slippery Near-Surface Layer of the Ocean Arising Due to Diurnal Warming

Woods (1968) hypothesized that the water above a strong thermocline can slide over the underlying water with a minimum of friction. Houghton (1969) called this phenomenon the *slippery seas*. He observed the slippery seas in the coastal region of Acapulco; the stratification was associated with lateral advection of warm water.

Montgomery and Stroup (1962) reported that near-surface currents in the equatorial ocean intensify during daytime but obtained only fragmentary data. Woods and Strass (1986) and Price et al. (1986) described the diurnal jet developing as a result of diurnal warming. Their studies, however, did not include conditions of low wind speed when the diurnal thermocline is localized very near the surface.

Kudryavtsev and Soloviev (1988; 1990) undertook simultaneous measurements of the vertical stratification and the current velocity difference in the upper layer of the ocean in the equatorial Atlantic using a combination of a free-rising profiler deployed from a research vessel and pairs of drifters simultaneously deployed from a small boat. They found that during low wind speeds the jet is often localized in the upper few meters of the ocean.

Kudryavtsev and Soloviev (1990) concluded that the stabilizing buoyancy flux due to absorption of solar radiation reduces the turbulent friction. As a result, the near-surface warm layer slips over the underlying water mass with practically no turbulent friction. A similar slippery layer may result from positive buoyancy flux due to precipitation or due to the lateral advection (as in the aforementioned observation by Houghton 1969).

Kudryavtsev and Soloviev (1990) also noted the somewhat surprising fact that the speed of the diurnal jet did not drop with decreasing wind speed. This is nevertheless easy to understand, at least qualitatively. It is due to the diurnal mixed-layer thinning at nearly the same rate as the wind stress decreases, thus concentrating the smaller momentum flux in a thinner layer.

Figure 4.12 shows the solar radiation and wind speed during the experiment of Kudryavtsev and Soloviev (1990) in the equatorial Atlantic alongside with the temperature and velocity differences across the upper 5-m layer of the ocean. When the wind speed U_{20} measured at 20 m height drops below approximately 6 m s^{-1}, the temperature difference, ΔT_5, measured between depths of 0.35 and 5 m dramatically increases (Fig. 4.12c), as does the corresponding velocity difference Δu_5 (Fig. 4.12d). These observations suggest that the temperature and velocity differences in the diurnal jet are interrelated.

Figure 4.12e shows the variability of the wind drift coefficient, $\Delta u_5 / U_{20}$. This coefficient is calculated from the velocity difference Δu_5 measured by a pair of drifters with drogue depths of 0.35 and 5 m and from the wind speed 20 m above the sea surface, U_{20} (Fig. 4.12e). Solid lines in diagrams (d) and (e) indicate the current

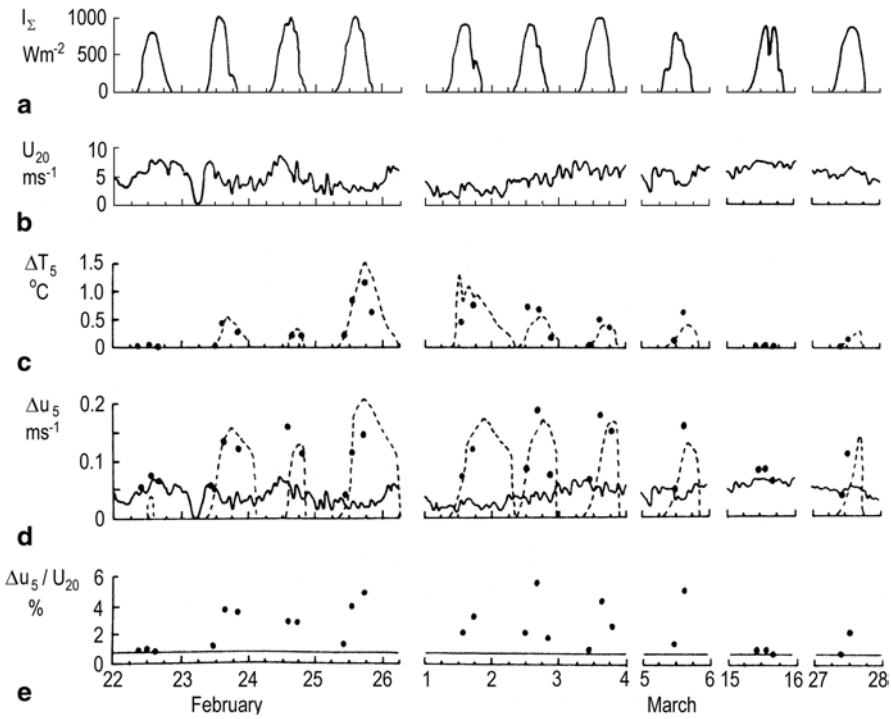

Fig. 4.12 Observations of the slippery near-surface layer of the ocean arising due to daytime solar heating. Measurements in the equatorial Atlantic and model-computed data encompass the period from 22 February to 28 March 1987. Time is UTC. **a** Insolation I_Σ, **b** wind speed 20 m above the ocean $U_{20,}$ **c** temperature difference ΔT_5 between the drogue depths (0.35 and 5 m) observed from a small boat (*points*) and model-computed time series of the temperature difference between the surface and 10 m depth (*dashed line*). **d** Current velocity difference Δu_5 between the drogue depths (0.35 and 5 m) registered by the drifters (*points*) and the model-computed time series of the current velocity difference between the surface and 10 m depth (*dashed line*). Solid line corresponds to the current velocity difference calculated between 0.35 and 5 m depth for an unstratified (*constant stress*) layer using formula (4.1), **e** coefficient of wind drift $\Delta u_5/U_{20}$: measured (*points*) and calculated from Eq. (4.1) (*solid line*). After Kudryavtsev and Soloviev (1990). Copyright © 1990 American Meteorological Society. Used with permission

velocity difference, Δu_5, calculated between 0.35 and 5 m depth from the logarithmic layer model as follows:

$$\Delta u_5 = C_{20}^{1/2} (\rho_a / \rho)^{1/2} \kappa^{-1} \ln(z_2 / z_1) \approx 0.85 \times 10^{-3} U_{20} \tag{4.1}$$

where $C_{20} \approx 1.3 \times 10^{-3}$ is the bulk flux coefficient (for 20 m height), $\kappa = 0.4$ (the von Karman constant), $z_2 = 5$ m, and $z_1 = 0.35$ m.

The data from 22 February and 15 March (Fig. 4.12) obtained during wind speeds $U_{20} \geq 7 \text{ms}^{-1}$ show that the measured velocity difference, Δu_5, and the wind drift coefficient, $\Delta u_5 / U_{20}$, were close to the logarithmic layer prediction. When the

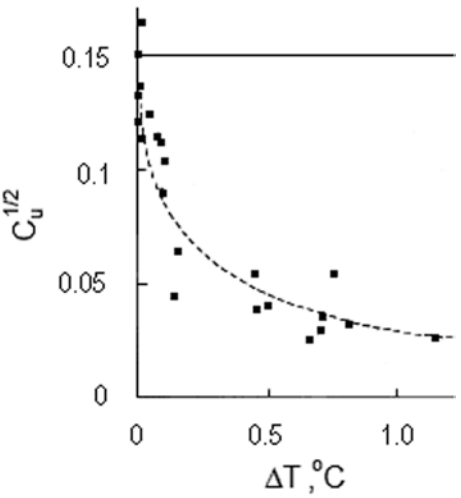

Fig. 4.13 Dependence of the drag coefficient in the near-surface layer of the ocean on the temperature difference across the diurnal thermocline during a period of intense warming (morning and noon hours). *Horizontal line* corresponds to the drag law in the logarithmic boundary layer. After Kudryavtsev and Soloviev (1990). Copyright © 1990 American Meteorological Society. Used with permission

wind speed drops below approximately 6 m s^{-1}, the temperature and velocity differences in the upper 5-m layer of the ocean caused by the diurnal warming rapidly increase, and the wind drift coefficient exceeds the logarithmic layer prediction by up to a factor of 5.

In order to illustrate the near-surface slippery layer phenomenon, Fig. 4.13 shows the dependence of the drag coefficient defined as

$$C_u = (u_* / \Delta u_5)^2 \tag{4.2}$$

on the temperature difference ΔT_5 in the upper 5-m layer of the ocean. These data indicate a systematic decrease in the drag coefficient as the temperature difference across the diurnal thermocline increases. For $\Delta T_5 = 1^\circ\mathrm{C}$, the drag coefficient C_u is reduced by a factor of 25–30 compared to the case of neutral stratification. This result suggests that during periods of intense diurnal warming, the near-surface layer of the ocean can slip over the underlying water mass practically without friction.

4.3.2 Self-Regulating State of the Diurnal Thermocline

From the theory of stratified turbulent boundary layers (cf., Turner 1973), the mixed-layer depth depends on the balance between positive buoyancy flux and the TKE available for mixing. In the stationary case with rotation effects, the depth of the mixed layer is proportional to the Oboukhov length scale L_O (Niiler and Kraus 1977):

$$h \sim L_O = u_*^3 / \left[\kappa \alpha_T g Q_n / (c_p \rho) \right] = L_* / \kappa \tag{4.3}$$

where u_* is the friction velocity in water, and

$$Q_n = Q_0 - (1 - A)I_\Sigma \tag{4.4}$$

is the net heat flux into the ocean. (Note that for typical oceanic salinity S ~ 35 psu, the sign of thermal expansion coefficient of water α_T is negative.) In this analysis, we ignore the effect of volume absorption of solar radiation in the near-surface layer of the ocean (though it is incorporated at a later stage).

Under high wind speed conditions, the depth of the diurnal mixed layer is relatively large; the rate of diurnal warming, which is inversely proportional to the mixed-layer depth, is small. When wind speed U_{10} drops, the friction velocity u_* also drops approximately as U_{10}, and according to Eq. (4.3) the mixed-layer depth rapidly reduces.

From a simple model with isolating boundary conditions at the bottom of the diurnal mixed layer, the temperature of the diurnal mixed layer with respect to the underlying water mass increases with time as

$$\Delta T = \frac{-Q_n t}{c_p \rho h_D} \sim \frac{-Q_n t}{c_p \rho L_O} = \frac{-\alpha_T g \kappa}{u_*^3}\left(\frac{Q_n}{c_p \rho}\right)^2 t = \frac{-\alpha_T g \kappa}{C_{10}^{3/2}}\left(\frac{Q_n}{c_p \rho}\right)^2 U_{10}^{-3} t. \tag{4.5}$$

The water within the mixed layer also accelerates horizontally under the action of the tangential wind stress $\tau_0 = \rho u_*^2$ according to the equation

$$\Delta u = \frac{\tau_0 t}{\rho h_D} \sim \frac{\tau_0 t}{\rho L_O} = \frac{\kappa \alpha_T g Q_n}{c_p \rho u_*} t = \frac{\kappa \alpha_T g Q_n}{c_p \rho C_D^{1/2}} U_{10}^{-1} t. \tag{4.6}$$

Under very low wind speed conditions, the effect of volume absorption of solar radiation (which is ignored here but discussed in later in this section) limits the minimum depth of the diurnal mixed layer and thus the maximum values of ΔT and Δu.

According to Eq. (4.6), under the assumption of isolating boundary conditions, a discontinuity of the temperature and velocity should occur at the bottom of the diurnal mixed layer. A discontinuity of the tangential velocity profile in incompressible fluid is always unstable (see, for instance, Landau and Lifshits 1986). As a result, a transitional layer of finite thickness ΔH (which can be interpreted as the diurnal thermocline thickness ΔH_D) is formed below the mixed layer. The dynamic state of the diurnal thermocline depends on the bulk Richardson number,

$$Ri = -\alpha_T g \Delta T \Delta H / \Delta u^2 \tag{4.7}$$

where ΔT and Δu are bulk temperature and velocity differences in the diurnal thermocline, respectively.

Substituting ΔT and Δu in Eq. (4.7) from Eqs. (4.5) and (4.6) gives

$$Ri \sim \frac{\Delta H}{\kappa u_* t}. \tag{4.8}$$

According to Eq. (4.8) the Richardson number decreases inversely proportionally to the elapsed time, t. At a fixed ΔH, Ri unavoidably drops below its critical value $Ri_{cr} \approx 0.25$, at some point. The diurnal thermocline becomes dynamically unstable and an overturning event occurs, increasing ΔH and, thus, returning Ri to a stable (overcritical) value. Since the diurnal warming continues and the temperature and velocity differences across the diurnal thermocline continue increasing, after a certain time of period the Richardson number should again drop below its critical value. This cyclic process will repeat itself while the diurnal warming continues. This is the regime of marginal stability, which maintains the diurnal thermocline in a quasi-equilibrium state:

$$Ri \approx Ri_{cr}. \tag{4.9}$$

This self-regulating regime of the diurnal thermocline is similar to the regime of marginal stability on the external boundary of turbidity currents described by Turner (1973). For the diurnal jet, the concept of the critical Richardson number was proposed by Price et al. (1986).

According to Turner's (1973) similarity theory for stratified turbulent boundary layers, in the self-regulating regime the local gradients of temperature ($\partial_z T$) and velocity ($\partial_z u$) can be expressed through the buoyancy ($-\alpha_T g \Delta T$) and velocity (Δu) differences across the diurnal thermocline as follows:

$$-\alpha_T g \partial_z T = K_2 (-\alpha_T g \Delta T / \Delta u)^2 \tag{4.10}$$

$$\partial_z u = K_1 (-\alpha_T g \Delta T / \Delta u) \tag{4.11}$$

where K_1 and K_2 are nondimensional constants.

Relations (4.10) and (4.11) describe linear temperature and velocity profiles. This is because the set of determining parameters no longer includes vertical coordinate z, and no length scale can be produced combining parameters $-\alpha_T g \Delta T$ and Δu. The interpretation is that in a stable boundary layer the vertical size of turbulence eddies is restricted; the turbulence is not directly affected by the presence of a boundary (the ocean surface). As a result, the boundary layer structure no longer explicitly depends on z (Neuwstadt 1984).

The vertical temperature and current profiles in the diurnal mixed layer and diurnal thermocline for the regime of marginal stability are schematically shown in Fig. 4.14a. They include the diurnal mixed layer ($0 < z < h_D$) with constant T and u and the diurnal thermocline ($h_D < z < H_D$) with linear profiles of T and u. In this notation, the thickness of the thermocline is $\Delta H_D = H_D - h_D$.

The diurnal thermocline under conditions of low wind speed in fact often exhibits a linear temperature profile, which is prominent even in individual temperature profiles (Fig. 4.14b). The temperature profiles in the diurnal thermocline may contain fluctuations (microstructure). Averaging over several casts produces smoother vertical profiles. Figure 4.15 shows mean temperature profiles averaged over two or three successive individual profiles from Kudrayvtsev and Soloviev (1990). Only

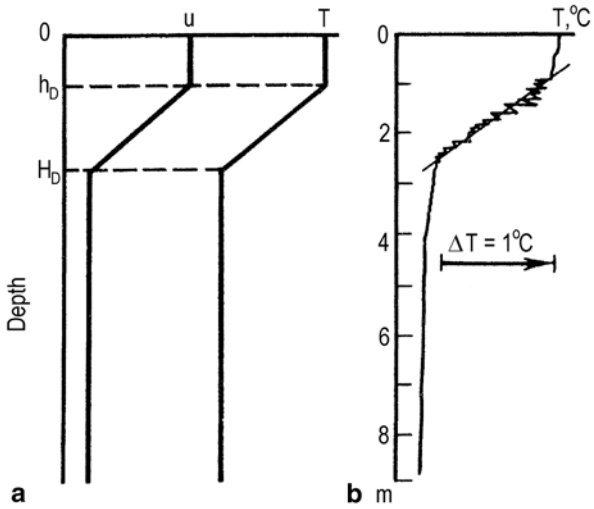

Fig. 4.14 Vertical profiles of temperature and horizontal velocity in the diurnal jet: **a** schematic representation; **b** temperature profile obtained with a free-rising profiler. (After Kudryavtsev and Soloviev 1990). Copyright © 1990 American Meteorological Society. Used with permission

those profiles obtained under conditions of daytime solar heating and when the lower boundary of the diurnal thermocline did not exceed 5 meters (i.e., the maximum drogue depth of the drifter pair) are shown.

According to Fig. 4.15, during daytime the averaged vertical temperature profiles have linear segments in the diurnal thermocline. An appreciable deviation from linearity is observed only at the lower boundary of the diurnal thermocline. This deviation is likely due to the volume absorption of solar radiation below the diurnal thermocline or just the remains of a relic diurnal thermocline formed at a previous stage of the diurnal cycle.

In order to estimate the thickness of the diurnal thermocline, ΔH_D, the temperature profiles in the diurnal thermocline were linearly extrapolated (Fig. 4.15). The bulk Richardson number, Ri, is then estimated from Eq. (4.7) under an assumption that $H=\Delta H_D$, $\Delta T=\Delta T_5$, and $\Delta u=\Delta u_5$, where ΔT_5 and Δu_5 are the temperature and current velocity difference between the drogue depths of the drifters, 0.35 and 5 m, respectively, and Δ_D is the thickness of the diurnal thermocline obtained from the linear extrapolation as shown in Fig. 4.15. The estimates of the Richardson number are given in Table 4.2. The average Richardson number, $\overline{Ri} = 0.3 \pm 0.1$, is close to the theoretical critical gradient Richardson number, $Ri_{cr} = 1/4$. This fact and the existence of linear temperature profiles in the diurnal thermocline are evidence in favor of a self-regulating state of the diurnal thermocline during the observations summarized in Fig. 4.15 and Table 4.2.

Thus, for the self-regulating state of the diurnal thermocline, the vertical temperature and current velocity profiles can be approximated in the simple way shown in Fig. 4.14a. For the model temperature and velocity profiles of this type, the integrated heat and momentum balance equations (1.10) and (1.6) under the assumption of horizontal homogeneity and no rotation effects take the following shape:

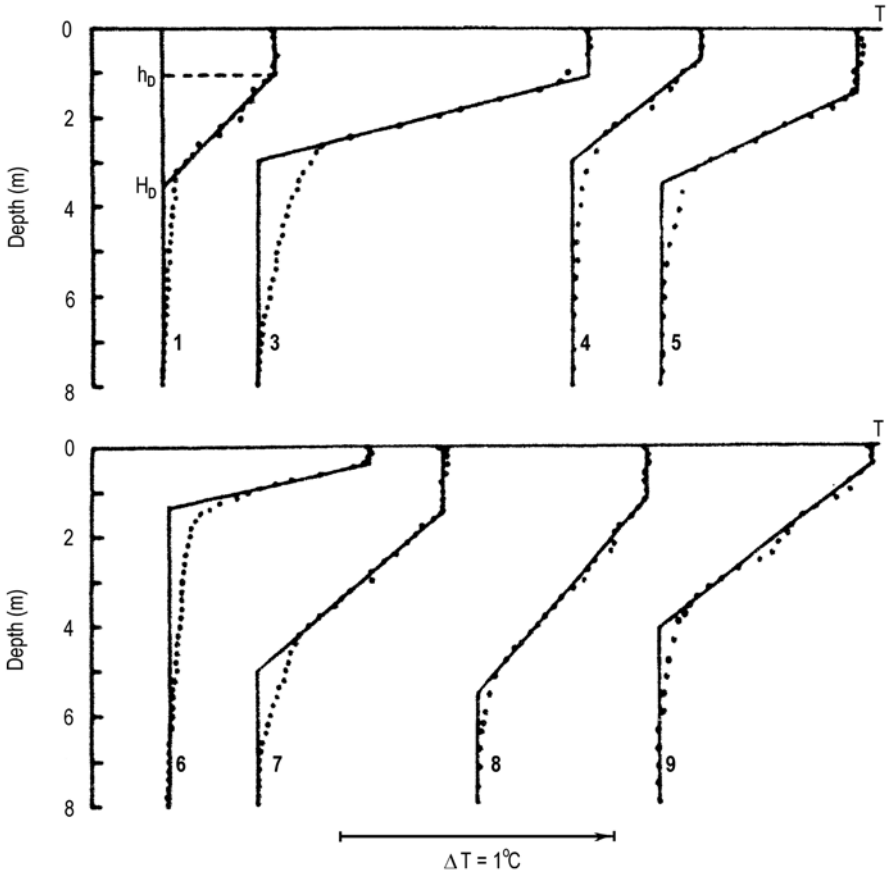

Fig. 4.15 Average temperature profiles from measurements with a free-rising profiler during daytime solar heating. Pertinent information can be found in Table 4.2. After Kudryavtsev and Soloviev (1990). Copyright © 1990 American Meteorological Society. Used with permission

$$\Delta T\left(h_D + 0.5\Delta H_D\right) = -\int_0^t \frac{Q_D}{c_p \rho}\, dt', \tag{4.12}$$

$$\Delta u\left(h_D + 0.5\Delta H_D\right) = \int_0^t \frac{\tau_0}{\rho}\, dt', \tag{4.13}$$

where h_D is the depth of the diurnal mixed layer, ΔH_D is the thickness of the diurnal thermocline, T and u are the temperature and current velocity differences across the diurnal thermocline; τ_0 is the momentum flux at the air–sea interface,

$$Q_D = Q_0 - (1 - A) I_\Sigma \left[1 - f_R\left(H_D\right)\right] \tag{4.14}$$

Table 4.2 Pertinent information for the Kudryavtsev and Soloviev (1990) observations

#	Date 1987	Time LST	Coordinates		U_{20} m s^{-1}	ΔH_D m	ΔT_5 °C	Δu_5 m s^{-1}	Ri
			Lat N	Lon W					
1	23 Feb	13:51–13:55	01°30’	22°01’	3.9	2.5	0.45	0.131	0.19
2	25 Feb	11:59	02°29’	23°29’	2.7	1.8	0.8	0.113	0.33
3	25 Feb	14:51–15:08	03°00’	23°30’	2.9	1.8	1.15	0.143	0.30
4	1 Mar	11:29–11:42	06°30’	24°59’	3.2	2.4	0.45	0.073	0.60
5	1 Mar	14:56–15:10	06°01’	25°00’	3.3	2.0	0.7	0.118	0.30
6	2 Mar	11:28–11:41	03°03’	24°59’	4.0	1.2	0.75	0.091	0.32
7	2 Mar	15:10–15:33	02°28’	24°59’	4.4	3.8	0.7	0.19	0.22
8	3 Mar	12:58–13:13	00°28’	25°00’	5.6	4.2	0.5	0.177	0.20
9	5 Mar	13:16–13:36	06°00’	26°30’	3.0	3.7	0.65	0.156	0.29

The first column is the profile number in Fig. 4.15. Profile #2 is a single one and is not shown in Fig. 4.15. This profile can, however, be found in Fig. 2 of the original publication by Kudryavtsev and Soloviev (1990)
LST local solar time

is the net heat flux into the upper ocean layer of depth H_D (taking into account the volume absorption of solar radiation), and t is the elapsed time from the beginning of the diurnal warming.

An important feature of the model (4.12)–(4.13) is that it operates with integral rather than instantaneous fluxes, so the diurnal amplitudes depend on the “history” of fluxes Q_D and τ_0 (at least from sunrise). It is convenient to introduce time-averaged parameters:

$$\overline{Q_D} = \frac{1}{t}\int_0^t Q_D dt', \tag{4.15}$$

$$\overline{\tau_0} = \frac{1}{t}\int_0^t \tau_0 dt'. \tag{4.16}$$

From Eqs. (4.7), (4.9), (4.12), and (4.13), it follows that

$$\Delta T / \Delta H_D = Ri_{cr}^{-1}\overline{T_*} / \overline{L_*}, \tag{4.17}$$

$$\Delta u / \Delta H_D = Ri_{cr}^{-1}\overline{u_*} / \overline{L_*}, \tag{4.18}$$

$$\Delta H_D / h_D = (1 + 2Ri_{cr}\overline{L_*}\,\overline{u_*}t / h_D^{\,2})^{1/2} - 1, \tag{4.19}$$

where $\overline{u_*} = (\overline{\tau_0} / \rho)^{1/2}$, $\overline{T_*} = \overline{Q_D} / (c_p \rho \overline{u_*})$, and $\overline{L_*} = c_p \rho \overline{u_*}^3 / (\alpha_T g \overline{Q_D})$.

Equations (4.17) and (4.18) connect the mean temperature and velocity gradients in the diurnal thermocline with the accumulated heat and momentum fluxes at the air–sea interface. These equations yield a simple relationship

$$\Delta u / \overline{u_*} = -\Delta T / \overline{T_*}\,, \tag{4.20}$$

which can be used to estimate the velocity difference Δu (here interpreted as the speed of the diurnal jet) from the temperature difference ΔT across the diurnal thermocline and the history of heat and momentum fluxes are known.

Equation (4.19) describes the evolution of the diurnal thermocline thickness ΔH_D as a function of time. At the initial stage of the diurnal warming, when $t \ll \frac{1}{2} h_D^{\,2} / (Ri_{cr}\,\overline{u_*}\,\overline{L_*})$, Eq. (4.19) is approximated with

$$\Delta H_D \approx Ri_{cr}\,\overline{u}_*\,\overline{L}_*\,t / h_D\,. \tag{4.21}$$

At the stage when $t \gg \frac{1}{2} h_D^{\,2} / (Ri_{cr}\,\overline{u}_*\,\overline{L}_*)$, Eq. (4.19) can be approximated as follows:

$$\Delta H_D \approx \left(2Ri_{cr}\,\overline{u}_*\,\overline{L}_*\,t\right)^{1/2} \tag{4.22}$$

Thus, initially the thermocline thickness ΔH_D grows proportional to time t, while at late stages ΔH_D grows as $t^{1/2}$.

4.3.3 Upper Velocity Limit for the Diurnal Jet

The model of the self-regulating diurnal thermocline allows a simple estimate of the upper velocity limit for the diurnal jet. In this model, the heat content of the warm layer is

$$\Upsilon_D = c_p\,\rho\,\Delta T\left(h_D + 0.5H_D\right). \tag{4.23}$$

Since only a fraction of the solar radiation is absorbed in the diurnal mixed layer and diurnal thermocline,

$$\Upsilon_D < \int_0^t \left[(1-A)I_\Sigma - Q_0\right] dt, \tag{4.24}$$

where t is the elapsed time from the beginning of the diurnal warming. From Eqs. (4.7), (4.9), and (4.24), and an obvious inequality $(h_D + 0.5H_D) > 0.5H_D$, it follows that $(\Delta u)^2 < 2Ri_{cr}^{\,-1}\,\alpha_T\,g J_D / (c_p\,\rho)$. Hence, the upper limit of the diurnal jet velocity is

$$\Delta u_{\max} = \left[-2Ri_{cr}^{\,-1}\,\alpha_T\,g\,\Upsilon_D / (c_p\,\rho)\right]^{1/2}. \tag{4.25}$$

The heat accumulated in the upper ocean due to diurnal warming is mainly determined by solar radiation. The maximum quantity of the solar radiation absorbed by the ocean during daytime is roughly equal to 2×10^7 J m^{-2}. Substituting this value into Eq. (4.25) gives an estimate $\Delta u_{\max} \approx 0.3 \mathrm{m s}^{-1}$, which represents the upper velocity limit for the diurnal jet.

4.3.4 Upper Velocity Limit for the Rain-Formed Jet

Slippery layers can also develop due to freshwater input from rain. An equation similar to Eq. (4.25) can be derived for estimating the upper velocity limit in the case of rain-formed jet:

$$\Delta u_{\max} = \left[2 Ri_{cr}^{-1} \beta_S g S_0 M_r \right]^{1/2}, \tag{4.26}$$

where M_r is the cumulative precipitation, defined from equation

$$M_r = \int_0^t P dt', \tag{4.27}$$

where P is the precipitation rate and t is the elapsed time from the beginning of the rain event. For a strong tropical rainfall with $M_r = 100$ mm, the upper estimate of the velocity following from Eq. (4.26) is $\Delta u_{\max} \approx 0.5$ m s^{-1}.

4.4 Evolution of the Diurnal Mixed Layer and Diurnal Thermocline Under Low Wind Speed Conditions

Figure 4.16 offers the following classification of the diurnal mixed-layer and diurnal thermocline evolution under low wind speed conditions. During Phase I nighttime, convection typically penetrates to the bottom of the mixed layer. After sunrise, increasing solar radiation gradually suppresses convective mixing and forms a diurnal mixed layer, which rapidly thins (Phase II). The diurnal mixed-layer depth stabilizes at a depth of the order of 1 m or less (depending on the wind speed and surface heat fluxes); a diurnal thermocline develops with gradually increasing temperature difference and thickness (Phase III). The maximum temperature difference across the diurnal thermocline occurs around 2–3 pm local time. During Phase III, the warm near-surface layer typically slips over the underlying water mass, with little turbulent friction; as a result, the diurnal jet develops.

When the surface solar irradiance drops below a certain level that depends on wind speed and surface heat fluxes, the diurnal mixed layer starts its evening deepening (Phase IV). The positive buoyancy flux can no longer stabilize the diurnal mixed layer and cannot maintain slippery conditions on its lower boundary. The diurnal jet releases its kinetic energy, which results in the K–H-type instability fol-

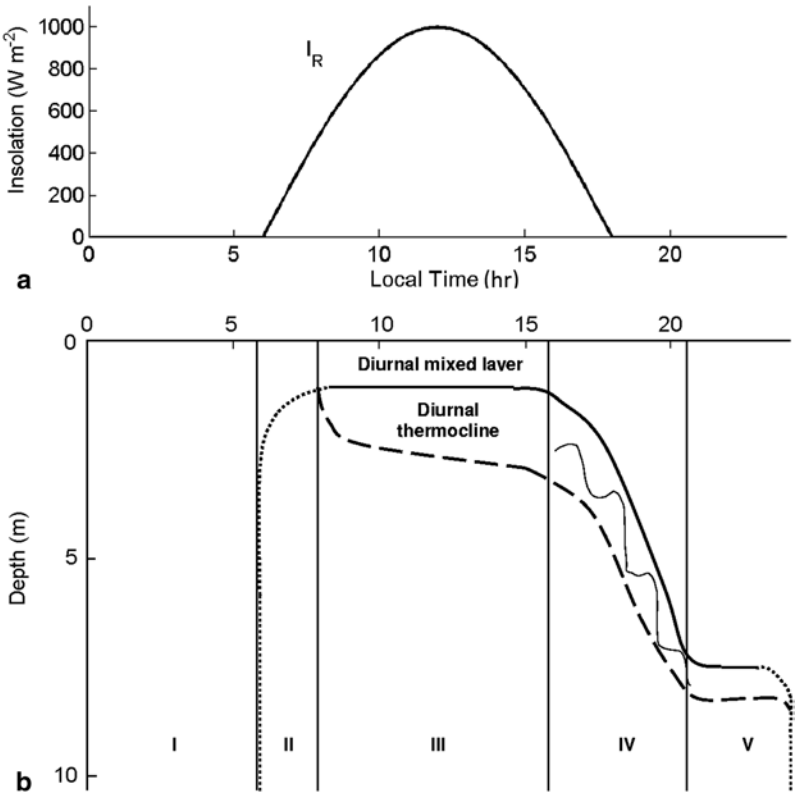

Fig. 4.16 Schematic representation of the diurnal mixed-layer and diurnal thermocline depth under low wind speed conditions. Here **a** surface solar irradiance cycle, **b** diurnal mixed-layer and diurnal thermocline evolution: Phase I is the nighttime convection; Phase II is the detrainment phase when the diurnal mixed layer is formed; Phase III is the daytime warming phase; Phase IV is the evening deepening of the diurnal mixed layer and diurnal thermocline; and Phase V is the erosion of the diurnal thermocline by convection. *Light, wavy line* in Phase IV signifies the Kelvin–Helmholtz (K–H) instability

lowed by overturning events (billows). The diurnal mixed layer and diurnal thermocline rapidly deepen. The intensive deepening of the diurnal thermocline is often associated with jumps of temperature between the diurnal mixed layer and diurnal thermocline. These jumps result from the K–H instability accompanied by overturning events.

After reaching a depth of several meters, the excess kinetic energy of the diurnal jet is pretty much spent on entrainment of colder water from below the thermocline; the deepening of the diurnal mixed layer and thermocline slows down. At this stage, the diurnal thermocline mainly erodes from its top due to convective cooling from the ocean surface (Phase V). Turbulent entrainment is relatively small in this phase.

In order to illustrate the above classification, Fig. 4.17 shows a series of temperature profiles characterizing the diurnal warming of the subtropical ocean under conditions of low wind speed and strong insolation. This series of measurements

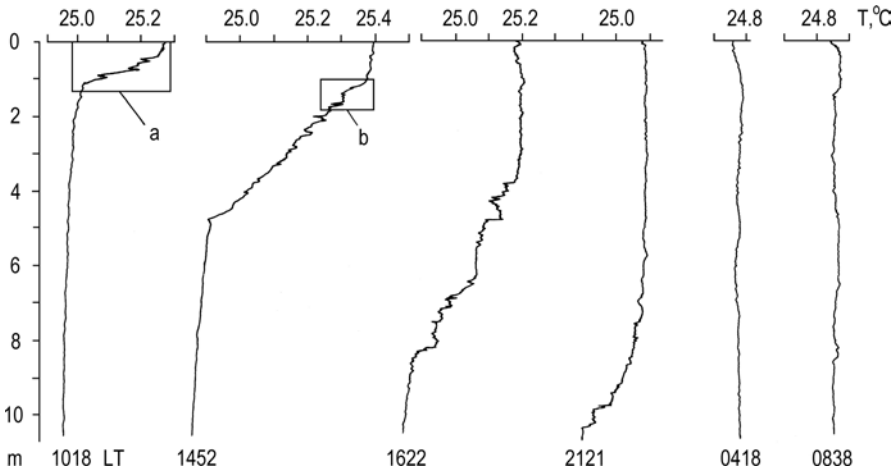

Fig. 4.17 Vertical profiles of temperature in the upper 10 m of the Atlantic Ocean at 28°N, 21°W. After Soloviev and Vershinsky (1982). Local times are indicated at the bottom of each profile. Reproduced with permission from Elsevier

was made with a free-rising profiler equipped with high-resolution temperature and conductivity sensors. The cold film temperature sensor (DISA) had a response time in water of ~3 milliseconds. For the profiler speed of 1 m s^{-1}, this corresponds to a resolution of ~3 mm in the vertical. Vertical resolution of the conductivity sensor was better than 1 mm with practically zero response time.

The first profile shown in Fig. 4.17 reveals a 0.4-m thick diurnal mixed layer and a diurnal thermocline in the depth range from 0.4 to 1.2 m. Below 1.2 m, the vertical temperature change is relatively small. According to the classification given in Fig. 4.16, this profile corresponds to Phase III.

The subsequent temperature profiles demonstrate development (1452 LST) and evening deepening (1622 and 2121 LST) of the diurnal mixed layer and diurnal thermocline. These are Phase IV (1622 LST) and Phase V (2121 LST). At 0418 LST next morning, the diurnal thermocline could not be seen within the upper 10 m. A slight temperature inversion near the surface was related to the convective cooling of the ocean surface. This is Phase I. The temperature profile taken after sunrise (0838 LST) indicated that a new warm layer had begun to form (Phase II).

The section of temperature profile marked by rectangle *a* in Fig. 4.17 is shown in Fig. 4.18 in more detail (including conductivity, salinity, and density). There are numerous small-scale temperature inhomogeneities within the diurnal thermocline, associated with intermittent turbulent mixing, which can be classified as microstructure. Local vertical gradients of temperature reach 6°C m^{-1}. Above and below the diurnal thermocline, the temperature gradients are considerably smaller.

The conductivity profile in Fig. 4.18 almost repeats the corresponding temperature profile. The conductivity profile reveals finer structure than the temperature profile, mainly because of a better spatial resolution of the conductivity sensor.

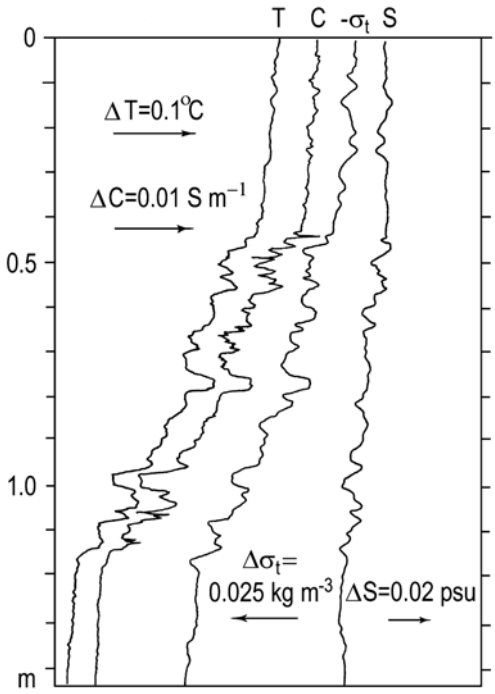

Fig. 4.18 Microstructure of the diurnal thermocline at 10:18 LT (from Fig. 4.17, box a). *C* stands for conductivity; other symbols are standard. After Soloviev and Vershinsky (1982). Reproduced with permission from Elsevier

These small-scale features partially disappear in the salinity profiles because, in order to avoid spikes, salinity was calculated from smoothed (over 1 cm) temperature and conductivity signals.

The salinity profile in Fig. 4.18 shows a small (~0.02 psu) increase in salinity toward the surface, associated with evaporation from the ocean surface. The salinity stratification is unstable and contributes to convective mixing within the diurnal mixed layer. Within the diurnal thermocline, the unstable salinity stratification is compensated by the stable stratification of temperature; the density profile is dominated by the temperature contribution and is therefore stable. Strong stratification in the diurnal thermocline makes it more difficult for the excess near-surface salinity to penetrate into deeper layers. This results in a slightly elevated level of salinity within the diurnal mixed layer and, in part, within the diurnal thermocline. In this situation (stable temperature and unstable salinity stratification), double diffusion convection may develop in the form of salt fingers.

The section of the temperature profile marked by rectangle *b* (Fig. 4.17) is shown in Fig. 4.19 in more detail. In this example, the diurnal thermocline reveals a remarkable step-like structure. This profile was taken at the beginning of the evening deepening of the diurnal thermocline (Phase IV). Step-like structures often appear in the diurnal thermocline in this phase of the diurnal cycle. The next temperature profile taken at 16:22 also reveals step-like structures but with larger vertical scale

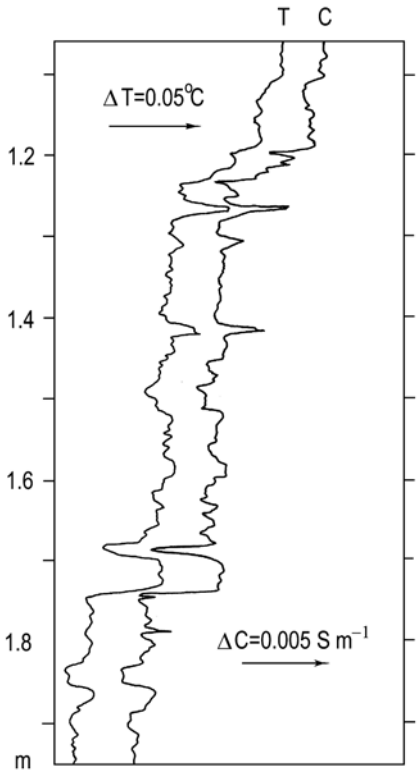

Fig. 4.19 Microstructure of the diurnal thermocline at 14:52 LT (from Fig. 4.17, box b). After Soloviev and Vershinsky (1982) with permission from Elsevier

(Fig. 4.17). In Sect. 5.5, we consider two possible mechanisms leading to overturning and step-like structure in the diurnal thermocline, which are the K–H instability and the resonant interaction between surface and internal waves.

Billowing due to the K–H instability is probably the most frequent cause of the observed step-like structures. As already mentioned at the beginning of this section, the diurnal jet can slip over the underlying water mass with little turbulent friction due to the stabilizing positive buoyancy flux from the absorbed solar radiation. When the solar radiation decreases in the evening (or due to clouds) the balance between turbulence and positive buoyancy flux is disturbed. As a result, the shear stress at the bottom of the mixed layer intensifies, which creates favorable conditions for the K–H instability followed by the overturning events.

The K–H instability is also a plausible explanation of step-like structures observed in the near-surface ocean in the example shown in Fig. 4.20. This series of measurements was made in the North Atlantic during a period of relatively calm weather (see Table 4.3). The appearance of step-like structures in the profiles correlates well with the deepening phase of the diurnal thermocline (which occurred either due to changing atmospheric conditions like for the profile at 12:58 LT or due to reduction of insolation in the evening time as in the profile taken at 15:18 LT) and can also be associated with the K–H instability.

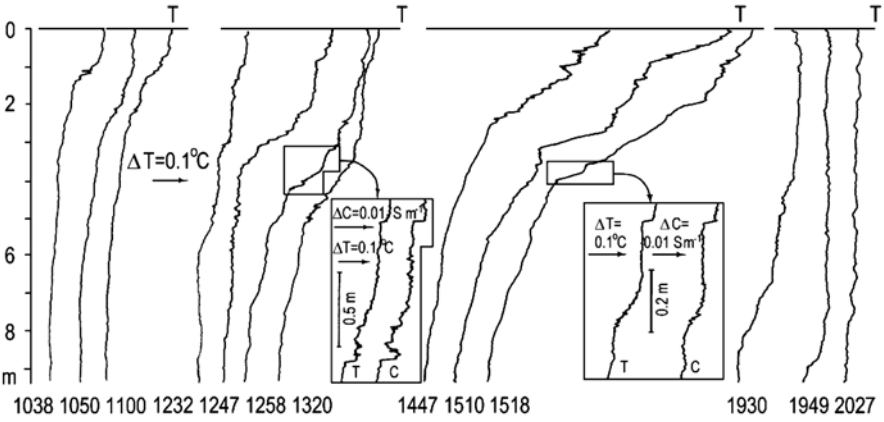

Fig. 4.20 Vertical profiles of temperature in the upper 9 m obtained with a free-rising profiler at 59°N, 13°W during the Joint Air–Sea Interaction (*JASIN*) experiment. After Soloviev and Vershinsky (1982) with permission from Elsevier

Table 4.3 Pertinent information for the field observations of near-surface microstructure

Fig. #	Date	Time LST	Position	U_{10} m s^{-1}	(1-A) $I_{\sum}$ W m^{-2}	Q_0 W m^{-2}
4.11	27 Aug 1979	09:00	09°N, 23°W	0.5–2	630	70–120
4.17, 4.18	6 Oct 1978	10:18	28°N, 21°W	2	840	150
4.17, 4.19	6 Oct 1978	14:52	28°N, 21°W	3	620	190
4.17	6 Oct 1978	16:22	28°N, 21°W	3	210	170
4.17	6 Oct 1978	21:21	28°N, 21°W	4	0	190
4.17	7 Oct 1978	04:18	28°N, 21°W	5	0	240
4.20	3 Sep 1978	08:38	59°N, 13°W	4.5	510	220
4.20	3 Sep 1978	10:38–11:00	59°N, 13°W	2	270–380	30
4.20	3 Sep 1978	12:32	59°N, 13°W	2.5	260	40
4.20	3 Sep 1978	12:47	59°N, 13°W	2.5	270	40
4.20	3 Sep 1978	12:58	59°N, 13°W	2.5	260	40
4.20	3 Sep 1978	13:20	59°N, 13°W	2.5	250	40
4.20	3 Sep 1978	14:47	59°N, 13°W	1.0	400	20
4.20	3 Sep 1978	15:10	59°N, 13°W	1.0	280	20
4.20	3 Sep 1978	15:18	59°N, 13°W	1.0	240	20
4.20	3 Sep 1978	19:30–20:27	59°N, 13°W	4	0	50

Figure 4.21 shows a series of near-surface measurements in the Atlantic Ocean during evening deepening of the diurnal thermocline and diurnal mixed layer. During these measurements, the 10-m wind speed was about 2–2.5 m s^{-1} and the surface waves were small. The temperature profiles shown in Fig. 4.21 are calculated from conductivity profiles under the assumption of constant salinity. No rain was observed on the day of these measurements. No signs of previous rains were found in the upper 10 m of the ocean from a salinity profile measured 3 h in advance of the data set shown in Fig. 4.21.

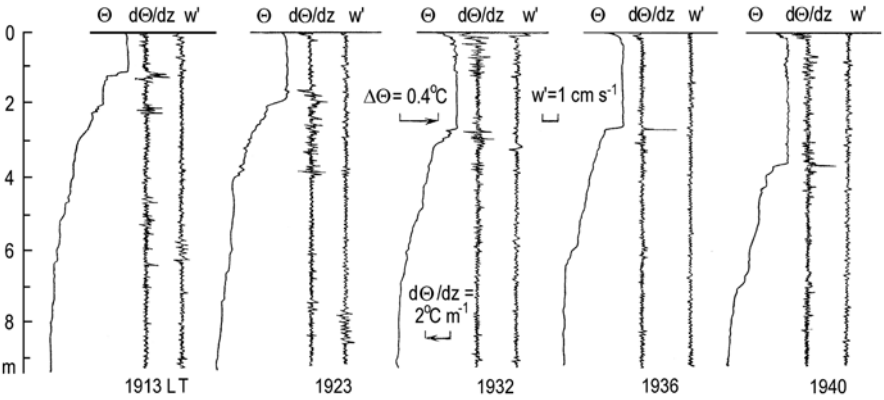

Fig. 4.21 Series of vertical profiles of temperature (Θ), temperature gradient (Θ_z'), and longitudinal (vertical) velocity fluctuation (W') during the evening deepening of the diurnal mixed layer and diurnal thermocline. The local time for each measurement is given below the profiles. After Bezverkhny and Soloviev (1986)

In addition to the temperature profiles calculated from conductivity profiles, there are profiles of the vertical temperature gradient and velocity fluctuation. Fluctuation velocity profiles are high-pass filtered with a 12-Hz cutoff frequency. Because free-rising profiler motions and surface wave orbital velocities are insignificant for frequencies above 12 Hz, velocity fluctuations shown in Fig. 4.21 are ascribed to small-scale turbulence.

The diurnal mixed layer and diurnal thermocline can be clearly seen in the temperature profiles (Fig. 4.21). The mean velocity of the diurnal mixed-layer deepening calculated from the least squares method is $\bar{w}_e \approx 0.1$ cm s^{-1}. Due to large-amplitude internal waves developing in the deepening diurnal thermocline (presumably because of the K–H instability), the depth of the diurnal mixed layer and diurnal thermocline oscillates. This depth may also vary due to horizontal variability of the studied phenomenon, since the ship drifted between the individual casts.

A characteristic feature of the temperature profiles in Fig. 4.21 is the sharp temperature jump separating the bottom of the mixed layer and the top of the diurnal thermocline. In some cases, the local magnitude of the vertical temperature gradient exceeded 1°C m^{-1}. The conductivity sensor installed on the free-rising profiler had the spatial resolution of about 1 cm, thus smoothing temperature jumps and underestimating vertical gradients. In reality, jumps with local temperature gradients up to 30°C m^{-1} have been observed in the deepening diurnal thermocline when measured with higher resolution sensors (Soloviev and Vershinsky 1982).

According to Barenblatt (1982), for $w_e \sim (K_T / \tau)^{1/2}$ (here K_T and τ are the turbulent diffusion coefficient and the relaxation time for temperature inhomogeneities in the diurnal thermocline, respectively), the turbulent exchange is principally nonstationary (and nonlocal), and ordinary, diffusion-type models of turbulent transport are no longer relevant. One of the consequences of the nonstationary nature of turbulence in a rapidly deepening thermocline is the appearance of a temperature jump or a discontinuity separating the mixed layer and the thermocline.

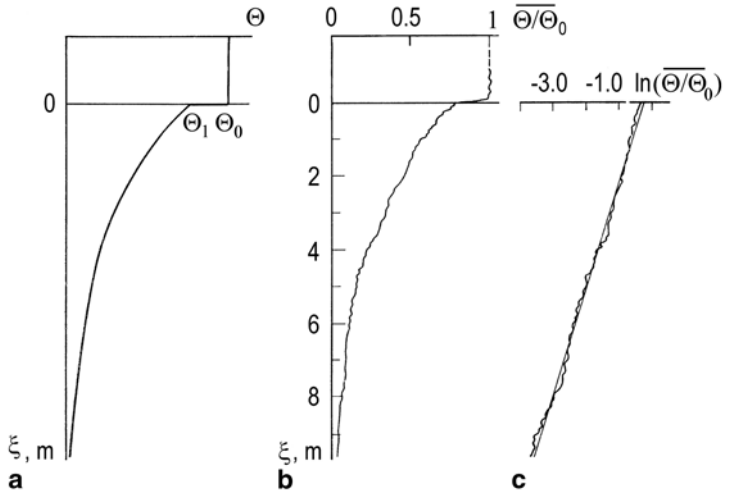

Fig. 4.22 **a** Schematic representation of vertical temperature profiles for rapid evening deepening of the diurnal thermocline. **b** Average temperature profiles calculated from five individual temperature profiles shown in Fig. 4.21 in the depth coordinate system referenced to the bottom boundary of the diurnal mixed layer. **c** The average temperature profile in the diurnal thermocline plotted in semilogarithmic coordinates approximated with a straight line. After Bezverkhny and Soloviev (1986)

A schematic temperature profile from Barenblatt's (1982) model is shown in Fig. 4.22a. The temperature profile below the point of discontinuity has the exponential form

$$\Theta = \Theta_1 \exp(-\alpha_B \xi) \tag{4.28}$$

where $\alpha_B = \left[\left(K_T^2 + 4w_e^{\,2}\eta\right)^{1/2} - K_T\right] \Big/ 2w_e\eta,\ \eta = \tau K_T,$

$$\xi = z - w_e t - h_0, \tag{4.29}$$

z is the depth referenced to the ocean surface, t is the time, and h_0 is the depth of the upper boundary of the thermocline at the initial moment $t=0$. The temperature profile at the point of discontinuity is determined from relation

$$\Theta_1 = 2\Theta_0 \Big/ \left[1 + \left(1 + \beta_B\right)^{1/2}\right], \tag{4.30}$$

where $\beta_B = 4w_e^{\,2}\tau / K_T$. Order-of-magnitude estimates suggest that the nonstationary effect becomes important in the dynamics of the deepening thermocline for $w_e > 0.001$–0.1 cm s^{-1} (Barenblatt 1982).

Average temperature profiles calculated from five individual temperature profiles are shown in Fig. 4.21 in the depth coordinate ξ according to Eq. (4.29). Note that ξ is referenced to the top of the diurnal mixed layer rather than to the ocean

surface, and that before averaging, the individual profiles were normalized by the corresponding total temperature difference across the diurnal thermocline.

A comparison of the model (Fig. 4.22a) and experimental (Fig. 4.22b) profiles shows good qualitative agreement between them. There is a sharp temperature jump at the top of the diurnal thermocline, and the temperature profile below the "discontinuity" point in general follows an exponential law (Fig. 4.22c). The temperature jump constitutes about 16% of the overall temperature difference across the diurnal thermocline. The estimate of α_τ derived from Fig. 4.22c and Eq. (4.28) is $\alpha_B \approx 4.16\times10^{-1}$ m^{-1}. From Eqs. (4.28) and (4.30), parameters K_T and τ can be expressed via Θ_1/Θ_0 and α_B as follows:

$$K_T = \frac{w_e\Theta_1}{\alpha_B\Theta_0}, \tag{4.31}$$

$$\tau = \frac{\Theta_0 - \Theta_1}{\alpha_B w_e \Theta_1}. \tag{4.32}$$

For $w_e = 0.1$ cms^{-1} and $\Theta_1/\Theta_0 = 0.84$, Eqs. (4.31) and (4.32) result in the estimates, $K_T \approx 20$ ms^{-1} and $\tau \approx 460$ s.

Bezverkhny and Soloviev (1986) provide independent estimates of the turbulent mixing coefficient K_T obtained from fluctuation characteristics of the velocity and temperature profiles shown in Fig. 4.21. From the fluctuation velocity signal, they obtained estimates of $b^{1/2}$ ranging from 0.2 to 0.3 cm s^{-1} in the diurnal thermocline (where b is the TKE). The turbulence length scale, l, estimated from the temperature profiles (Fig. 4.21) within the diurnal thermocline was in the range of 20–100 cm. Estimates of the mixing coefficient obtained with the Kolmogorov's (1942) formula

$$K_T = lb^{1/2} \tag{4.33}$$

are within the range from 4 to 30 cm^2 s^{-1}, consistent with the estimate $K_T \approx 20$ cms^{-1} following from the comparison of the average temperature profiles with Barenblatt's (1982) model.

An alternate estimate of the turbulent mixing coefficient can be obtained from the Osborn and Cox (1972) equation:

$$K_T \approx (2\pm1)C_\kappa\kappa_T \tag{4.34}$$

where $C_\kappa = \overline{(\partial_z\Theta')^2}/(\partial_z\bar{\Theta})^2$ is the Cox number and κ_T is the coefficient of thermal molecular diffusion. The '+' sign pertains to the case for isotropic turbulence, while the '−' sign is intended for the case of anisotropic (layered) structure. The estimate of the Cox number within the diurnal thermocline following from the data shown in Fig. 4.21 is $C_\kappa \approx 40$. The mixing coefficient estimate from Eq. (4.34) is $K_T \approx 0.06 - 0.17$ cm^2 s^{-1}, which is much less than the estimate from Eq. (4.33). One possible explanation is that, strictly speaking, the Osborn and Cox (1972) for-

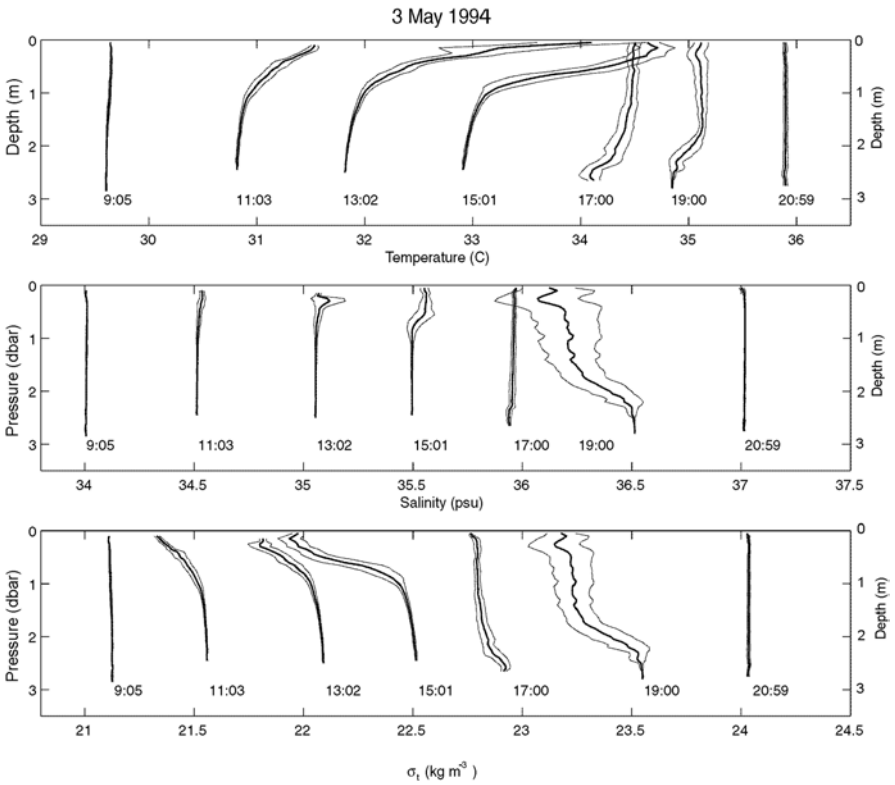

Fig. 4.23 Vertical profiles of temperature, salinity, and density obtained by averaging the bow sensor data within 0.1 dbar pressure intervals in 10-minute segments. Successive temperature, salinity, and density profiles are shifted by 1°C, 0.5 psu, and 0.5 kg m^3, correspondingly. Under each profile the corresponding LST is given. The thin lines represent one standard deviation from the mean profiles. After Soloviev and Lukas (1997) with permission from Elsevier

mula is derived under the assumptions that may not be valid for nonstationary turbulence. Another possible explanation is that the temperature (conductivity) sensor did not fully resolve the convective-viscous subrange of turbulence, possibly leading to underestimation of the Cox number.

4.5 Large Diurnal Warming Events

4.5.1 In Situ Data

Another example of a large diurnal warming event from the western equatorial Pacific warm pool is given in Fig. 4.23. These are measurements by bow sensors "scanning" the near-surface layer of the ocean as described in Sect. 4.2.3. In this

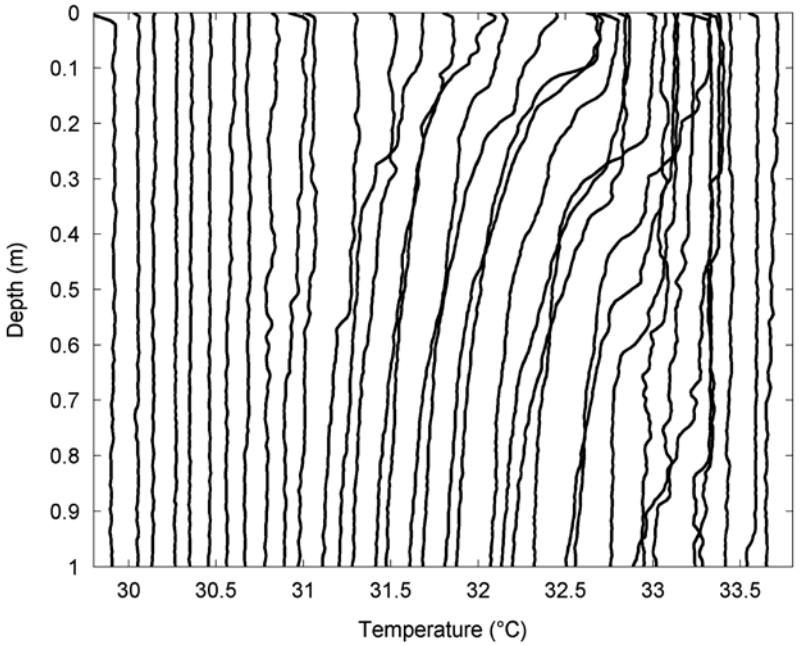

Fig. 4.24 Temperature profiles in the upper meter of the ocean obtained by a free-rising profiler equipped with a 3-ms response time temperature sensor. These 35 profiles were obtained between 10:55 and 16:10 LST. Each successive temperature profile is shifted by 0.1°C. Note the cool skin effect in many of the profiles. After Soloviev and Lukas (1997) with permission from Elsevier

experiment, the vessel was steaming at 4–5 knots perpendicular to the dominant surface waves to increase the ship pitching for ~15 min every 2 h.

These observations illustrate the evolution of the vertical temperature profile in the near-surface layer of the ocean due to diurnal warming under conditions of very low wind speed. In this example, the temperature difference across the diurnal thermocline is localized in the upper ~1 m and at 13:02 reaches as much as 3°C.

A slight salinity increase within the diurnal mixed layer and diurnal thermocline at 11:03, 13:02, 15:01, and 17:00 is related to evaporation and trapping excessive salinity within the diurnal mixed layer due to the underlying diurnal thermocline (see Sect. 4.2.6). Substantial salinity and density variability noticeable in the profile at 19:00 is because of convective rainfall.

A series of individual vertical temperature profiles shown in Fig. 4.24 provides evidence that the depth of the diurnal mixed layer can decrease to ~10 cm or even disappear completely for some time under weak winds and strong insolation. The part of the vertical temperature profiles most near the surface sometimes has a slightly unstable stratification. Negative temperature gradients arise during daytime due to a combination of the volume absorption of solar radiation in the upper centimeter of the ocean and the surface cooling (Kraus and Rooth 1961; Turner 1973; Soloviev 1979; and Chap. 2).

The examples shown in Figs. 4.3c, 4.23, and 4.24 demonstrate that the diurnal cycle under low wind speed conditions is dramatically different from the high and moderate wind speed regime. Intensive insolation in low wind areas leads to large diurnal variations of SST. There, the diurnal thermocline is found close to the ocean surface, where standard shipboard oceanographic measurements may be disturbed by the ship's hull. As a result, large diurnal warming events are often undetected during shipboard surveys and unaccounted for when quantifying SST.

4.5.2 Global Distribution of Large Diurnal Warming Events

Satellites using infrared or microwave imagery provide a broad overview of SST and its spatial and temporal variability. Recent studies (Kawai and Kawamura 2002; Gentemann et al. 2003; Stuart-Menteth et al. 2003) indicate that extended regions of the World Ocean including the tropics, subtropics, mid- and, perhaps, a part of high latitudes are subject to large diurnal warming events (Fig. 4.25). These regions are correlated with low wind speed zones. The largest diurnal signal is observed in the tropics and the northern Indian Ocean. Freshening of the near-surface layer of the ocean by rainfalls and river discharges can also increase diurnal SST amplitudes. It is therefore not surprising that the regions highly susceptible to diurnal warming include the ITCZ, the northern Indian Ocean during the monsoon transitions, the western Pacific warm pool, and the waters off the west coast of Mexico. The regions experiencing larger diurnal warming are also the Mediterranean Sea and mid-North Atlantic in boreal summer and the southern midlatitudes in austral winter.

Diurnal SST amplitude variability depends on the time of year (Fig. 4.26), following the seasonal cycle of solar radiation. Satellite data also reveal remarkable interannual variability of diurnal SST amplitudes (Fig. 4.27).

Accounting for diurnal SST variability is important for formulation of accurate boundary conditions for modeling the atmospheric general circulation and weather prediction (Shinoda et al. 1998) and biophysical processes (McCreary et al. 2001). Diurnal cycling also has important implications for air–sea gas exchange (McNeil and Merlivat 1996; Soloviev et al. 2001b). Relatively strong dependence of the CO_2 solubility on temperature suggests that diurnal warming shifts the partial pressure difference between atmosphere and the ocean surface toward lower CO_2 uptake by the ocean.

These studies also emphasize the necessity for improving theoretical methods of quantifying the SST variations due to diurnal cycling. The main reason is that clouds affect the space-based infrared imagery of the sea surface. The microwave measurement does not depend on clouds, but its RMS accuracy is not better than 0.5 K (Gentemann et al. 2004), which may not always be sufficient to resolve the diurnal cycle of SST. Rains also affect the microwave signal.

An effective approach to resolve this situation is to enhance the remote-sensing results with the diurnal mixed-layer model forced with remotely sensed heat and momentum fluxes (the latter may not depend so critically on cloudiness as infrared

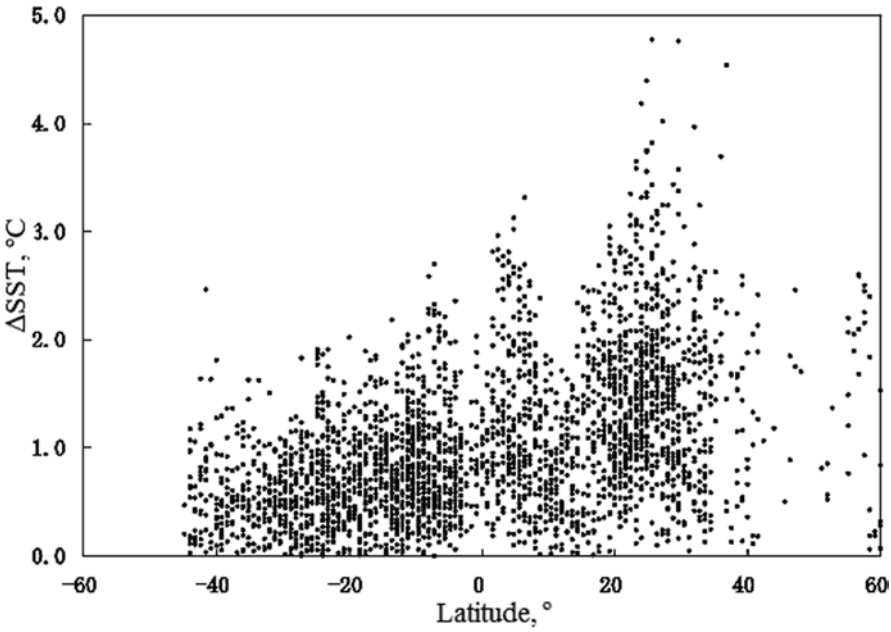

Fig. 4.25 The latitudinal distribution of diurnal amplitudes (day minus night SST) on 15 June 1997 obtained from a geostationary satellite. After Tanahashi et al. (2003) with permission from American Geophysical Union

SST methods). Under low wind speed conditions the diurnal warming, however, is a nonlinear function of heat and momentum fluxes. Simple regression-type parameterizations of the diurnal SST amplitudes may not be effective in conjunction with remote-sensing methods because, strictly speaking, they require tuning empirical coefficients for each region and event. An accurate model of the diurnal cycle combined with remotely sensed data may improve the accuracy of estimating the temperature difference across the diurnal thermocline globally (including regions with cloud cover) compared to the use of regression-type parameterizations.

Adequate sampling is another critical factor for realistic simulation of large diurnal warming episodes because they depend not only on instantaneous fluxes but also on their history (at least from sunrise). The fundamental problem is that for polar-orbiting satellites, track-repeat times are too long to resolve the diurnal cycle of SST. A multi-satellite approach including geostationary satellites can help in solving this problem. In particular, the International Satellite Cloud Climatology Project (see Sect. 1.4.4) has demonstrated the possibility of providing shortwave radiation data globally every 3 h.

A variety of retrieval schemes to derive boundary layer parameters from polar-orbiting satellites of the National Oceanic and Atmospheric Administration (NOAA) and Defense Meteorological Satellite Program (DMSP) series have been developed (Gautier and Katsaros 1984; Schlüssel and Luthardt 1991; Wick et al. 1992; Bauer and Schlüssel 1993; Emery et al. 1994; Chou et al. 1995). These retrieval methods

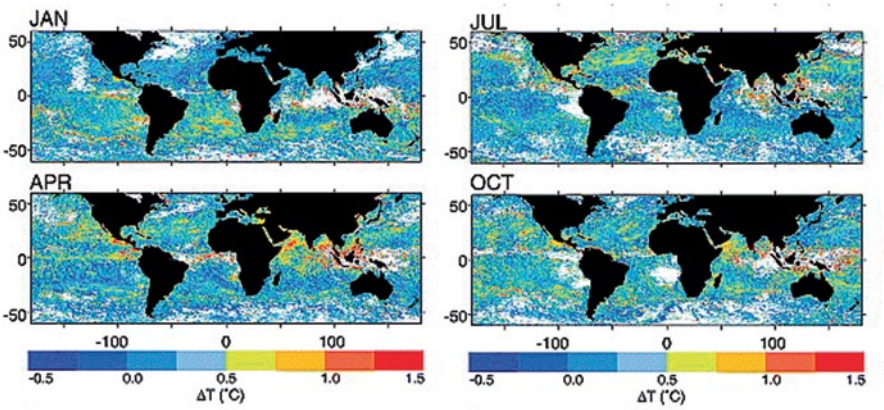

Fig. 4.26 Seasonal distribution of diurnal warming for 1989: monthly mean ΔT computed from daily day–night SST differences for January, April, July, and October. After Stuart-Menteth et al. (2003) with permission from American Geophysical Union

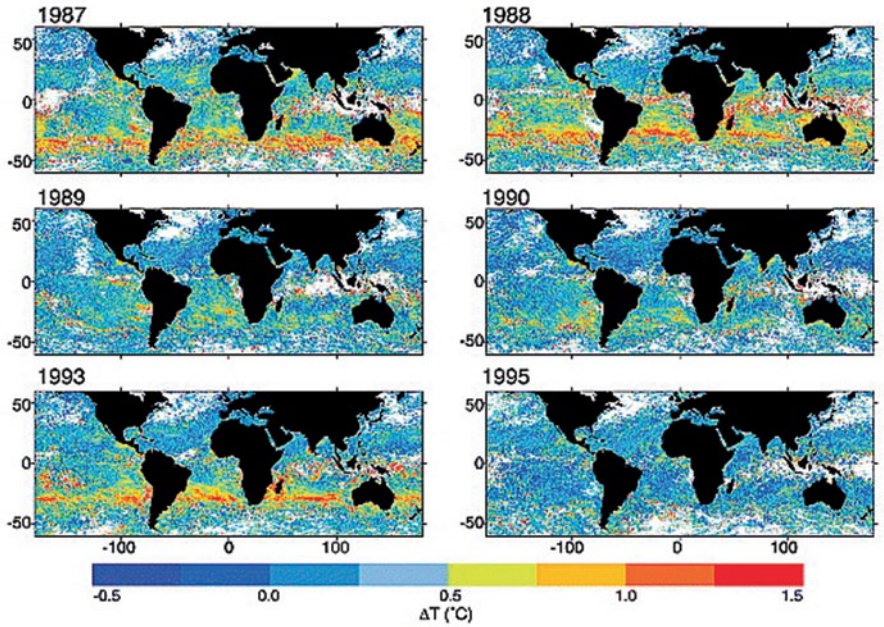

Fig. 4.27 Interannual distribution of monthly mean ΔT computed from daily day–night SST differences. Monthly mean ΔT for January for 6 years (1987, 1988, 1990, 1993, and 1995). After Stuart-Menteth et al. (2003) with permission from American Geophysical Union

can be used to estimate surface heat and momentum fluxes (Schlüssel et al. 1995; Schlüssel 1996; Quilfen et al. 2001).

Applying these data to mixed-layer modeling faces some problems. In particular, the relative error of wind speed measurement with microwave methods approaches 100 % in low wind speed zones. Fortunately, the sensitivities of the diurnal mixed-layer depth and warming rate to wind diminish with decreasing wind speed, because of increased contributions from convection (Soloviev 1982).

The convective mixing is driven by the net surface heat flux Q_0, which is the sum of sensible, latent, and net longwave radiation fluxes. The accuracy of the retrieval of these fluxes depends on averaging period. Achieving a time resolution of a few hours necessary for accurately modeling the diurnal cycle is still a challenge but one, which can be addressed with a multi-satellite approach.

4.5.3 Physics of Large Diurnal Warming Events

The Oboukhov buoyancy length scale,

$$L_O = u_*^3 \Big/ \left[\kappa \alpha_T g Q_n / (c_p \rho) \right], \tag{4.35}$$

has a cubic dependence on friction velocity, while the Ekman length scale,

$$L_E = u_* / f, \tag{4.36}$$

has a linear dependence. (Here Q_n is defined according to Eq. (4.4).) When wind speed U_{10} drops, the friction velocity u_* also drops approximately as U_{10}, and according to Eq. (4.35), the Oboukhov length scale strongly reduces. The smaller of the two length scales, L_O and L_E, determines the mixed-layer depth (provided that L_O is not negative), and the transition between "rotational" and "buoyant" regimes depends on the ratio between the Oboukhov and Ekman length scales. The buoyancy forces thus dominate Coriolis forces when

$$\frac{L_O}{L_E} = \frac{c_p \rho u_*^2 f}{\kappa \alpha_T g Q_n} << 1 \tag{4.37}$$

Qualitative analysis of Eq. (4.37) suggests that the buoyancy forces should dominate over rotational forces under low wind speed conditions. The range of wind speeds where buoyancy dominates over rotation increases toward the equator where $f \to 0$.

For the rotational regime, the equilibrium diurnal mixed-layer depth is proportional to the Ekman length scale, ($h_D \sim L_E$). In the model with isolating boundary conditions at the bottom of the diurnal mixed layer the rate of diurnal warming is accordingly as follows:

$$\Delta T / \Delta t = \frac{-Q_n}{c_p \rho h_D} \sim \frac{-Q_n}{c_p \rho L_E} = \frac{-Q_n}{c_p \rho} \frac{f}{u_*} = \frac{-Q_n}{c_p \rho} \frac{f}{C_{10}^{1/2}} U_{10}^{-1} \sim U_{10}^{-1}. \tag{4.38}$$

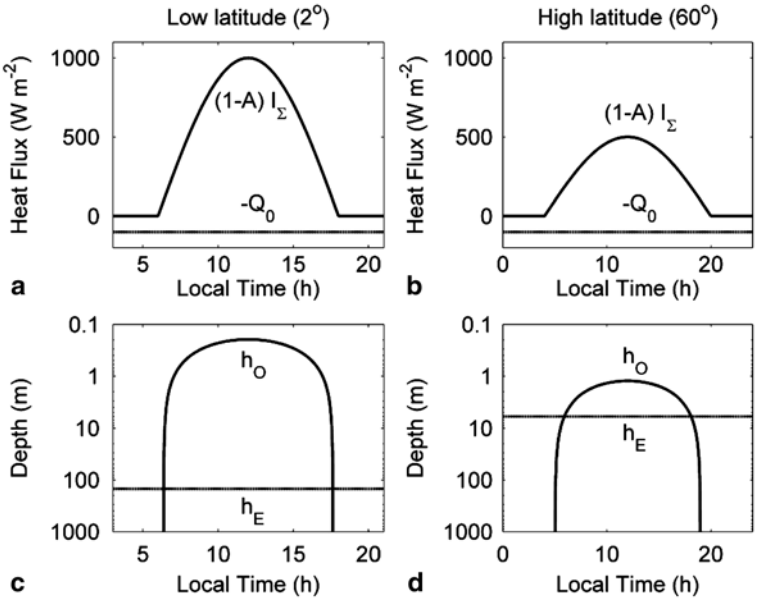

Fig. 4.28 Idealized heat fluxes for low (**a**) and high (**b**) latitudes. Corresponding diurnal mixed-layer depth estimates from relationships $h_O = c_O L_O$ and $h_E = c_E L_E$, where c_0=2, c_E=0.25, and L_0 and L_E are determined from Eqs. (4.35) and (4.36), respectively (**b**, **c**). In both examples, wind speed is $U_{10} = 2.5\text{ms}^{-1}$, surface salinity $S_0 = 35\text{psu}$, and net heat flux $Q_0 = 100\text{Wm}^{-2}$. Surface temperature T_0 is 28°C for the low-latitude example and 5°C for the high-latitude example

For the buoyant regime, which is associated with low wind speed conditions, the rate of the diurnal warming from Eq. (4.5) is $\Delta T / \Delta t \sim U_{10}{}^{-3}$. The cubic dependence of the diurnal warming rate on wind speed leads to substantial distinction between the high and low wind speed regimes, which are separated by a critical wind speed of about 4–5 m s^{-1}.

The above estimates imply that the entrainment at the lower boundary of the diurnal mixed layer is negligible. The entrainment conditions are incorporated into the analysis in Sect. 4.6.5, in the framework of parameterizations and numerical models. In particular, this leads to a u_*^{-2} rather than u_*^{-3} dependence for the diurnal temperature amplitude (as well as a u_*^{0} rather than u_*^{-1} dependence for the diurnal jet amplitude).

From the above analysis, it is also obvious that large diurnal warming events are exclusively associated with the buoyant regime in the near-surface layer of the ocean. Inequality (4.37) is thus a necessary condition for the development of large diurnal warming events. Figure 4.28 shows results of calculations of the equilibrium mixed-layer depths for low and high latitudes at a low wind speed. Interestingly, during intense diurnal warming, inequality (4.37) can be satisfied for both low and high latitudes. This suggests that large diurnal events can be observed not only in mid- and low latitudes but also at relatively high latitudes (during the boreal and

austral summer, respectively), which is consistent with the satellite-derived diurnal amplitudes shown in Fig. 4.25.

Rotation effects nevertheless can indirectly influence the diurnal cycle even under low wind speed conditions by affecting dynamics of the diurnal jet (see Sect. 4.3). The Coriolis force deflects the diurnal jet to the right (left) of the wind in the Northern (Southern) Hemisphere. Under the same environmental conditions, the magnitude of the diurnal jet is maximal in equatorial regions, where the direction of diurnal jet coincides with the wind stress direction.

It should be noted that similar relationships hold for the rain-induced mixed layer. The buoyancy flux due to rain can play a similar, stabilizing role as the buoyancy flux due to solar heating. This can explain substantial drops of salinity observed in the rain patches in low wind speed zones.

In the polar seas where SST can drop to 0°C (or even below it), the thermal expansion coefficient is small. The buoyancy contribution due to the absorption of solar radiation diminishes, and the buoyancy effects can no longer dominate over rotation effects. An exception is the marginal ice zone with melting ice where the freshwater supply leads to restratification of the upper ocean mixed layer. Fine structure of the near-surface layer of the polar seas is considered in Sect. 4.7.

4.6 Modeling Large Diurnal Warming Events

4.6.1 Radiative–Convective Mixed Layer

Raschke (1975) calculated vertical profiles of temperature in the upper ocean during equinoxes under the assumption of no turbulent mixing and no surface cooling. These vertical profiles showed that the heating depends strongly on latitude and could amount to as much as 10–30°C per day in the uppermost centimeters of tropical and subtropical oceans. It is interesting that during midsummer the subpolar ocean in the summer can be exposed to even more radiative energy than near the equator because of the longer days. These high heating rates do not result in a big change in the water temperature because internal turbulent processes immediately transport the absorbed thermal energy into deeper layers, and because some energy is lost to the atmosphere above.

In the presence of both volume and surface sources of heat, the vertical flux of heat near the surface is

$$Q(z) = Q_0 - (1 - A) I_\Sigma \left(1 - f_R(z)\right), \tag{4.39}$$

where I_Σ is the insolation, A is the sea surface albedo, function $f_R(z)$ characterizes the absorption of solar radiation with depth (see Sect. 1.4.6), and Q_0 is the surface heat flux, which is a sum of latent, sensible, and effective longwave radiation flux

($Q_0 = Q_E + Q_T + I_L$). Q changes sign at some depth z_c. This is the *compensation depth* determined from the equation

$$0 = Q_0 - (1-A)I_\Sigma\left(1 - f_R(z)\right). \tag{4.40}$$

During daytime, z_c often amounts to only a few millimeters (Soloviev 1979).

The layer $0 < |z| < z_c$ can become convectively unstable since $Q > 0$. Discrete convective elements from this layer overshoot the compensation depth and penetrate into the stably stratified layer below (Kraus and Rooth 1961). The kinetic energy generated in the convectively unstable layer $0 < |z| < z_c$ works against the buoyancy forces in the stable layer $z_c < |z| < h_c$, where h_c is the penetration depth of convection. When z_c is very small, the convection is close to a laminar regime, and, as a first guess, we will ignore the viscous dissipation of the kinetic energy balance.

Remarkably, z_c does not depend on the ocean turbulence regime. Equations (4.39–4.40), however, imply an unlimited depth of the surface mixed layer. In fact, this depth is limited and equal to h_c.

The depth of penetration of convection into the stably stratified layer, h_c, can be determined from an integral model including the differential equations for temperature, salinity, and kinetic energy balance (Soloviev 1979):

$$c_p \rho \frac{\partial T}{\partial t} = -\frac{\partial Q}{\partial z} + \frac{\partial I_R}{\partial z}, \tag{4.41}$$

$$\rho \frac{\partial S}{\partial t} = -\frac{\partial J}{\partial z}, \tag{4.42}$$

$$0 = -\frac{\alpha_T g Q}{c_p \rho} - \frac{\beta_S g J}{\rho} - \frac{1}{\rho}\frac{\partial E}{\partial z}, \tag{4.43}$$

where S is the salinity, J is the salinity flux, $\alpha_T g Q/(c_p\rho) + \beta_S g J/\rho$ is the net buoyancy flux, which can be related to the buoyant energy source/sink, and E is the vertical flux of the kinetic energy. These equations can be derived from equations (1.10), (1.11), and (1.24) under the following assumptions: potential temperature is equal to the thermodynamic temperature; there is no wind, rain, or upwelling; penetrating convection works mainly against stable stratification, therefore the dissipation term is negligible compared to other terms in the equation for the TKE. Equation (4.43) for the TKE is given in the stationary form because the equilibration time for turbulence is much smaller than for thermal and salinity inhomogeneities. The processes that shape the vertical temperature profile under calm conditions and strong insolation are schematically shown in Fig. 4.29.

Soloviev (1979) suggested that under conditions of strong insolation (and calm weather) convection might become nonturbulent (laminar), which has recently been confirmed in the numerical experiment by Verevochkin and Startsev (2000). Fortunately, the system of equations in Eqs. (4.41)–(4.43) is valid for laminar convection as well.

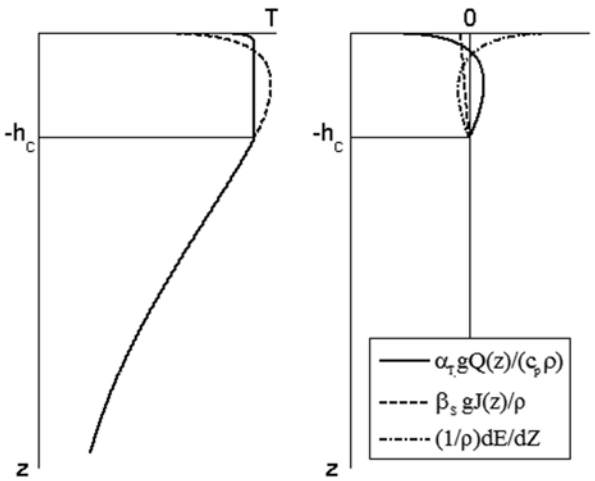

Fig. 4.29 Formation of a convective mixed layer due to volume absorption of solar radiation and surface cooling under calm weather conditions. The penetration depth of convection for this example, $h_c = 0.073$ m, is calculated from Eq. (4.48) for $Q_0 = 140$ W m^{-2}, $Q_E = 70$ W m^{-2}, and $(1 - A)$ $I_\Sigma = 560$ W m^{-2}. **a** Schematic representation of the temperature profile with penetrative convection (*continuous line*) and no convection (*dashed line*). **b** Terms of the turbulent kinetic energy (TKE) balance Eq. (4.43) within the convective mixed layer

In theory, under extremely strong solar radiation, the thermal convection may be completely suppressed (see Sect. 2.4). In that case, the problem is reduced to that of molecular heat diffusion with volume sources, and Eq. (4.43) becomes irrelevant.

Boundary conditions for the sea surface are formulated as follows:

$$Q(0,t) = Q_0,\ \mathrm{J}(0,t) = -(S_0 / L)Q_E,\ E(0,t) = 0. \tag{4.44}$$

Boundary conditions at the bottom of the mixed layer formed by penetrative convection are (Kraus and Rooth 1961):

$$Q(h_c,t) = 0,\ \mathrm{J}(h_c,t) = 0,\ E(h_c,t) = 0. \tag{4.45}$$

These are isolating boundary conditions; entrainment fluxes at the bottom of the mixed layer are ignored. This assumption should not lead to significant errors when h_c does not change substantially.

A small amount of heat and salt can penetrate through the bottom of the convective mixed layer because of double diffusion. A warmer and slightly saltier layer is formed near surface, which may result in convecting layers (Stern and Turner 1969). This effect is not accounted for here, but is discussed in Sect. 4.2.6.

A customary constraint for integral models is that temperature and salinity profiles are constant with depth within the mixed layer (Kraus and Turner 1967). The diurnal mixed layer, however, sometimes exhibits nonzero vertical temperature and

salinity gradients (see examples in Figs. 4.2c and 4.7). Soloviev (1979) therefore relaxed the Kraus and Turner (1967) condition by requiring that $\partial T/\partial t$ and $\partial S/\partial t$ (rather than T and S) do not depend on depth z. The latter condition does not prohibit dependence of T and S on z within the radiative–convective layer.

By integrating Eqs. (4.41) and (4.42) over z with boundary conditions (4.44)–(4.45) and excluding terms $\partial T/\partial t$ and $\partial S/\partial t$, fluxes Q and J can be expressed as follows:

$$Q(z) = Q_0\left(1+\frac{z}{h_c}\right) - (1-A)I_\Sigma\left[1+\frac{z}{h_c} - f_R(z) - f_R(h_c)\frac{z}{h_c}\right], \tag{4.46}$$

$$J(z) = -\frac{S_0}{L}\left(1+\frac{z}{h_c}\right)Q_E, \tag{4.47}$$

and function $f_R(z)$ characterizes the absorption of solar radiation with depth.

Absorption of solar radiation in the upper meters of the ocean is then parameterized with nine exponentials according to formula (1.60). The vertical profiles, $Q(z)$ and $J(z)$, expressed in terms of corresponding buoyancy fluxes are shown in Fig. 4.29. Substituting Q and J in the energy balance equation (4.43) with their expressions (4.46) and (4.47), and integrating Eq. (4.43) over depth, a transcendental equation for the convective diurnal mixed-layer depth h_c is obtained:

$$1 - \frac{Q_0}{(1-A)I_\Sigma} + \frac{\beta_S Sc_p Q_E}{\alpha_T L(1-A)I_\Sigma} = \sum_{i=1}^{9}\left[\frac{2a_i}{\beta_i h_c} - \left(1+\frac{2}{\beta_i h_c}\right)a_i \exp(-\beta_i h_c)\right]. \tag{4.48}$$

Verevochkin and Startsev (2000) performed direct numeric simulation (DNS) of free convection taking into account the volume absorption of solar radiation. The results of their calculations are shown in Fig. 4.30. Profile (a) corresponds to the ratio, $(1-A)I_\Sigma/Q_0 = 4$, showing a distinct convective–radiative mixed layer. Convective mixing confined within the quasi-homogeneous layer appears to be of laminar nature. The convection is completely suppressed for the ratio $(1-A)I_\Sigma/Q_0 = 4.75$ (profile b in Fig. 4.30).

A convective diurnal mixed layer observed in the Sargasso Sea is shown in Fig. 4.31. The vertical temperature profiles obtained with a free-rising profiler in the upper 5 m during afternoon hours under calm weather conditions and 1.2 m swell revealed a shallow diurnal mixed layer and strong diurnal thermocline that developed at the top of the seasonal mixed layer of 20–25 m depth. Low relative humidity (~70%) and clear skies resulted in appreciable surface cooling ($Q_0 \approx 140$ W m^{-2}) even under calm weather conditions.

The solar irradiance during the first measurement (14:47 LT) was $(1-A)I_\Sigma = 594$ W m^{-2}. There is a diurnal (convective) mixed layer in the upper 7–12 cm of the ocean and a thermocline in the upper 1 m with a temperature difference of 1.3–1.4°C (Fig. 4.31a). The vertical temperature profile obtained 17 min later (Fig. 4.31b) has a similar diurnal mixed layer. The intermediate thermocline that is seen in Fig. 4.31b near 3 m is presumably of advective nature.

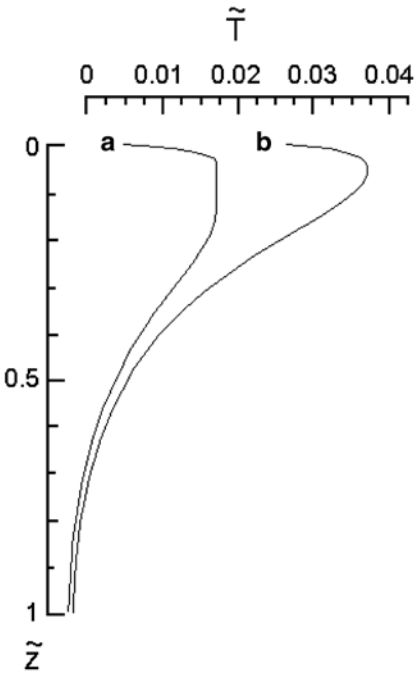

Fig. 4.30 Numerical simulation of the radiative–convective equilibrium temperature profiles in the near-surface ocean by Verevochkin and Startsev (2000) for **a** $(1-A)I_\Sigma / Q_0 = 4$ and **b** $(1-A)I_\Sigma / Q_0 = 34.8$. Here $\tilde{T} = c_p \rho \kappa_T (T - T_h) / (Q_0 h)$ is the nondimensional temperature, T_h is the bulk temperature of the upper ocean mixed layer, κ_T is the molecular coefficient of kinematic thermal diffusivity; $\tilde{z} = z / h$ is the nondimensional depth, and h is the layer depth determining the model domain. Note the similarity of the model profiles to the observations under calm weather conditions and strong solar insolation shown in Fig. 4.31. Copyright © 2000 Cambridge University Press

The temperature profile taken on the same day but in the evening time (17:31 LT) is shown in Fig. 4.31c. The diurnal mixed-layer depth increased to approximately 1 m. The diurnal thermocline became sharper; the temperature difference across the diurnal thermocline dropped to approximately 0.8°C. There are also inversions and other microstructure features in the diurnal thermocline. They are presumably associated with overturning events, which are often observed in the diurnal thermocline during the deepening stage.

Note that these measurements were made with a temperature sensor (DISA) having a response time of only 3 ms in water. At the 1 m s^{-1} ascent speed of the profiler, this sensor partially resolved the cool skin of the ocean, which resulted in a remarkably sharp drop of temperature in the upper few millimeters of the ocean (Fig. 4.31).

For estimated irradiance $(1-A)I_\Sigma = 560$ W m^{-2} and heat flux $Q_0 = 140$ W m^{-2} for 14:47 LT, 1 October 1977 the compensation depth calculated from Eqs. (4.40) is $z_c = 0.02$ m. The discrete convective elements developing in this layer then penetrate to approximately 0.1 m depth according to the radiative–convective model (4.48), which is consistent with the vertical temperature profile taken at 14:47 LT

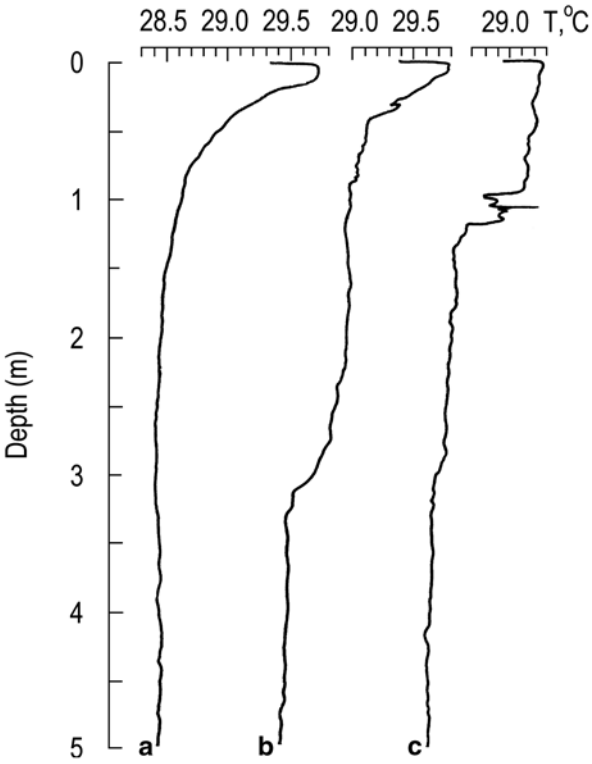

Fig. 4.31 Vertical temperature profiles in the upper 5 m according to measurements with a free-rising profiler in the Sargasso Sea during POLYMODE on 1 October 1977 at **a** 14:47, **b** 15:04, and **c** 17:31. After Soloviev (1979)

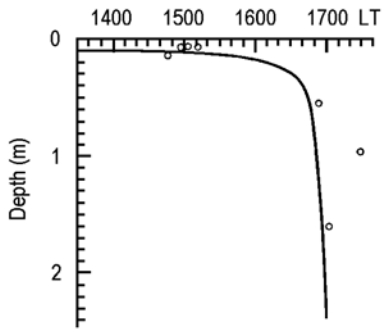

Fig. 4.32 Diurnal mixed-layer depth under calm weather conditions as a function of local time. Open circles are experimental data; continuous line is the depth of convective mixed layer calculated from Eq. (4.48)

The DNS result for $(1-A)I_\Sigma / Q_0 = 4$ (Fig. 4.30a) exhibits a temperature profile that is qualitatively consistent with the observations shown in Fig. 4.31a, b. The temperature profiles taken around 1700–1800 LT showed that by 1700 LT the diurnal mixed layer had substantially deepened (Fig. 4.31c). After 1700 LT, the evening deepening of the mixed layer slowed down significantly.

Figure 4.32 shows the evolution of the diurnal mixed-layer depth during afternoon and early evening hours estimated from the measurements with a free-rising

profiler on 1 October 1977. Three of seven total profiles taken during this day are shown in Fig. 4.31. In cases when a second quasi-homogeneous layer was observed, only the upper one is taken into account.

Figure 4.32 also shows the radiative–convective mixed-layer depth calculated from Eq. (4.48) for the case of no cloud conditions during POLYMODE (Soloviev 1979). During daytime, the model curve $h_c(t)$ is in good agreement with field data. It is remarkable that h_c practically does not change during daytime hours although the solar radiation flux does change. At about 1600 LT, when the insolation drops below some level, h_c, starts a rapid increase. The model demonstrates an unbounded increase in the diurnal mixed-layer depth around 1700 LT. The experimental mixed-layer depth, however, does not follow the model prediction after 1700 LT. This is related to the fact that the model ignores entrainment fluxes at the bottom of the mixed layer, which become important when the diurnal mixed-layer depth increases. The water densification due to evaporation only slightly increases h_c (by about 5–10% during daytime).

4.6.2 *Transition from Radiative-Convective to Wind Mixing Regime*

The wind-induced mixing can be accounted for by adding the momentum balance equations (1.17) and (1.18) and by including the shear production term according to the equation for TKE balance (1.24). Under an assumption of horizontal homogeneity and with no rotation effects, the equations for momentum balance are

$$\frac{\partial u}{\partial t} = \frac{1}{\rho}\frac{\partial \tau_{zx}}{\partial z}, \tag{4.49}$$

$$\frac{\partial v}{\partial t} = \frac{1}{\rho}\frac{\partial \tau_{zy}}{\partial z}. \tag{4.50}$$

Equation (1.24) for the TKE balance in stationary form then reads

$$0 = \tau_{xz}\frac{\partial u}{\partial z} + \tau_{yz}\frac{\partial v}{\partial z} - \frac{\alpha_T g Q}{c_p \rho} - \frac{\beta_S g J}{\rho} - \frac{1}{\rho}\frac{\partial E}{\partial z} - \varepsilon, \tag{4.51}$$

where $E = \overline{w'(b' + p'/\rho)}$ is the vertical flux of TKE. Dissipation term ε is retained in Eq. (4.51). In contrast to the purely convective case described by Eq. (4.43), the dissipation term can no longer be ignored when turbulence production due to shear is included (Soloviev 1982). Equation (4.51) is given in a stationary form because the turbulence regime equilibrates much faster than the diurnal mixed layer evolves.

Boundary conditions at the sea surface are formulated as follows:

$$Q(0,t) = Q_0,\ J(0,t) = -\left(S_0 / L\right)Q_E,\ E(0,t) = E_0. \tag{4.52}$$

Boundary conditions at the bottom of the diurnal mixed layer, $z = -h_D$, are similar to Eq. (4.45):

$$Q(-h_D,t) = 0,\ J(-h_D,t) = 0, E(-h_D,t) = 0. \tag{4.53}$$

The boundary condition in the form (4.53) limits the model application only to conditions of no entrainment (decreasing or quasi-stationary mixed-layer depth).

The Kraus and Turner (1967) hypothesis is used to close the system of Eqs. (4.41), (4.42), and (4.51)s:

$$-E_0 - \int_{-h_D}^{0} \left(-\tau_{xz}\partial u/\partial z - \tau_{yz}\partial v/\partial z\right) dz - \int_{-h_D}^{0} \varepsilon dz = m_1 u_*^3, \tag{4.54}$$

where m_1 is the nondimensional empirical constant.

Assuming again that $\partial_t T$ and $\partial_t S$ are not depth dependent within the mixed layer and integrating Eqs. (4.41), (4.42), and (4.51) with boundary conditions (4.52) and (4.53) and closure hypothesis (4.54), we obtain a transcendental equation with respect to the diurnal mixed-layer depth, h_D, in the following form:

$$1 - \frac{Q_0}{(1-A)I_\Sigma} + \frac{\beta_S Sc_p}{\alpha_T L}\frac{Q_E}{(1-A)I_\Sigma} + \frac{2m_1 c_p \rho}{\alpha_T g}\frac{u_*^3}{h_D(1-A)I_\Sigma} = \sum_{i=1}^{9}\left[\frac{2a_i}{\beta_i h_D} - \left(1 + \frac{2}{\beta_i h_D}\right) a_i \exp(-\beta_i h_D)\right], \tag{4.55}$$

Following Soloviev (1982), we select $m_1 = 0.9$.

Figure 4.33a shows the variation of the diurnal mixed-layer depth obtained from free-rising profiler measurements in the Atlantic Ocean. The insolation and wind speed are also shown (Fig. 4.33b, c). The first profile was made at 5:57 LST (before sunrise). There is a diurnal thermocline left from the previous diurnal cycle. The depth of this "relic" diurnal mixed layer is ~ 6 m (see Fig. 4.33a). At the time of the temperature profile taken at 7:49 LST (immediately after sunrise), the relic thermocline had disappeared, though the new diurnal mixed layer and diurnal thermocline had not yet formed.

The temperature profile at 7:49 LST was practically homogeneous within the upper 10 m. This measurement is indicated in Fig. 4.33a by a vertical dashed line. The temperature profiles taken later this day show the formation of a shallow diurnal mixed layer and diurnal thermocline and their subsequent evening deepening. By 19:06 LST, the diurnal thermocline disappeared from the depth range of the free-rising profiler. This measurement is indicated in Fig. 4.33a by a second vertical dashed line.

The depth of the diurnal mixed layer calculated from Eq. (4.55) is in remarkable agreement with the experimental data even in the presence of substantial variability

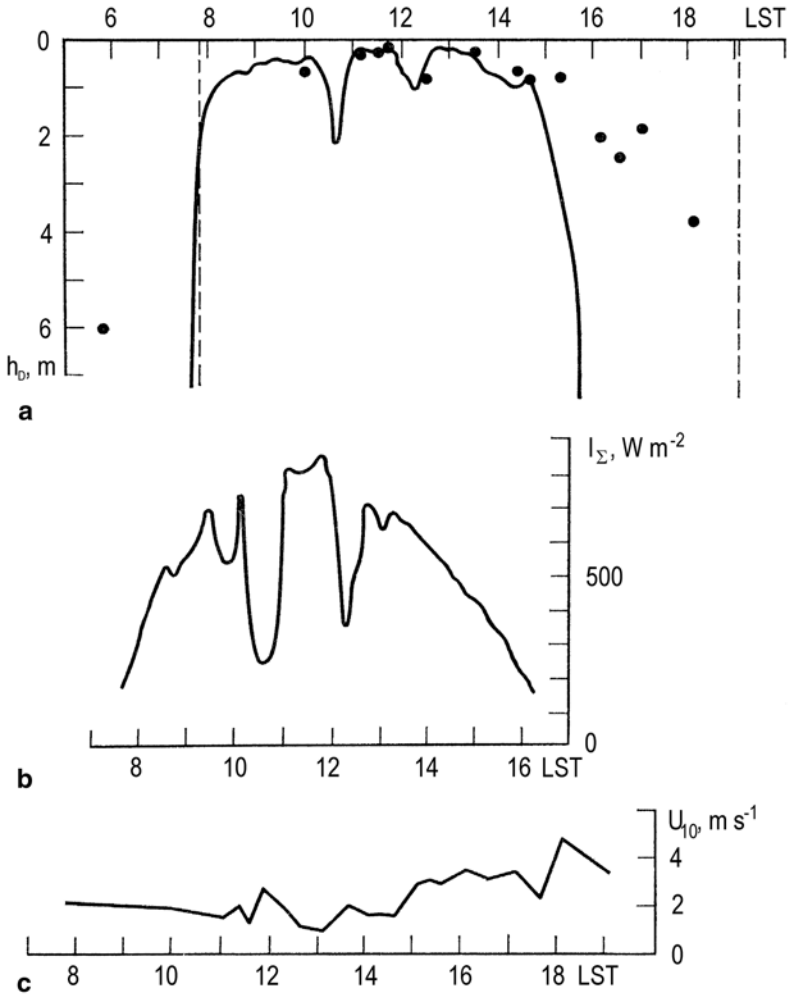

Fig. 4.33 **a** Variation of the diurnal mixed-layer depth at 35°03'N, 12°52'W derived from free-rising profiler measurements on 16 October 1978 (*dots* are experimental data, *continuous line* is the results of calculations from Eq. (4.55), *vertical dashed lines* indicate the measurements when no diurnal thermocline was found), **b** insolation (10-min averages), **c** wind speed measured in discrete time intervals (linearly interpolated in between the measurements). After Soloviev (1982)

of the solar radiation due to clouds (Fig. 4.33b). The situation, however, radically changes during the evening hours when the model depth tends to infinity and is no longer able to predict the actual depth of the diurnal mixed layer. This is because entrainment fluxes at the bottom of the diurnal mixed layer are not taken into account in Eq. (4.53).

Soloviev (1982) demonstrated that the effect of volume absorption of solar radiation leads to a reduced sensitivity of the model diurnal mixed-layer depth to changes

of external parameters. (This is true only at relatively small depths of the mixed layer, $h_D < 2$ m.) For larger mixed-layer depths, the effect works in the opposite direction, increasing the sensitivity of the mixed-layer depth to changes in the air–sea heat fluxes and the wind speed. This, in particular, explains the characteristic Π-shape of the diurnal mixed-layer dependence on the time of the day clearly seen in Fig. 4.33c.

In order to predict the diurnal mixed-layer dynamics during the evening hours as well as the temperature difference across the diurnal thermocline, a numerical model is required that accounts for entrainment fluxes (see Sect. 4.6.5). Rotation effects can also be included.

4.6.3 A Rapid Increase in the SST When the Air is Warmer Than the Water and Low Wind Speed Conditions Persist

Kara et al. (2002, 2005) interpolated the exchange coefficients of wind stress (C_D), latent heat flux (C_L), and sensible heat flux (C_S) used in the COARE bulk formulas with polynomial functions. The C_D and C_L coefficients are shown in Fig. 4.34 as a function of the air–sea temperature difference for wind speeds, 1 m s^{-1} and 6 m s^{-1}.

A striking feature of these dependences (Fig. 4.34) is a dramatic drop of exchange coefficients on the air–water temperature difference under low wind speed conditions. Furthermore, when the air temperature is higher than the water temperature, the C_D and C_L bulk coefficients dramatically reduce. This suggests that wind stress and the latent heat flux drop practically to zero when the air temperature is higher than the water temperature and low wind speed conditions persist. As a result, the SST will rapidly warm due to absorption of the solar radiation (Soloviev et al. 2013). The warming will significantly slow down when the SST will equilibrate with the air temperature. As a result, the diurnal warming will be strong in upwelling regions and localized in the near-surface layer of the ocean. A similar effect is responsible for vanishing horizontal temperature gradients of SST under low wind speed conditions on averaged satellite imagery in such places like the Gulf of Mexico during summer months (Katsaros and Soloviev 2003; Katsaros et al. 2005). In addition, the SST in the cold wake of hurricanes may equilibrate quickly with the surrounding water due to this effect, though the water below a thin near-surface layer will still be relatively cold.

4.6.4 Parameterizations for the Diurnal SST Range

Early empirical parameterizations for diurnal SST amplitudes (for instance, Hasse 1971; Deschamps and Frouin 1984) operated with instantaneous wind velocities and instantaneous or peak solar radiation fluxes. Since the diurnal warming is a cumulative process, which depends on the "history" of the heat and momentum fluxes during the hours after sunrise, Lukas (1991) proposed connecting the SST

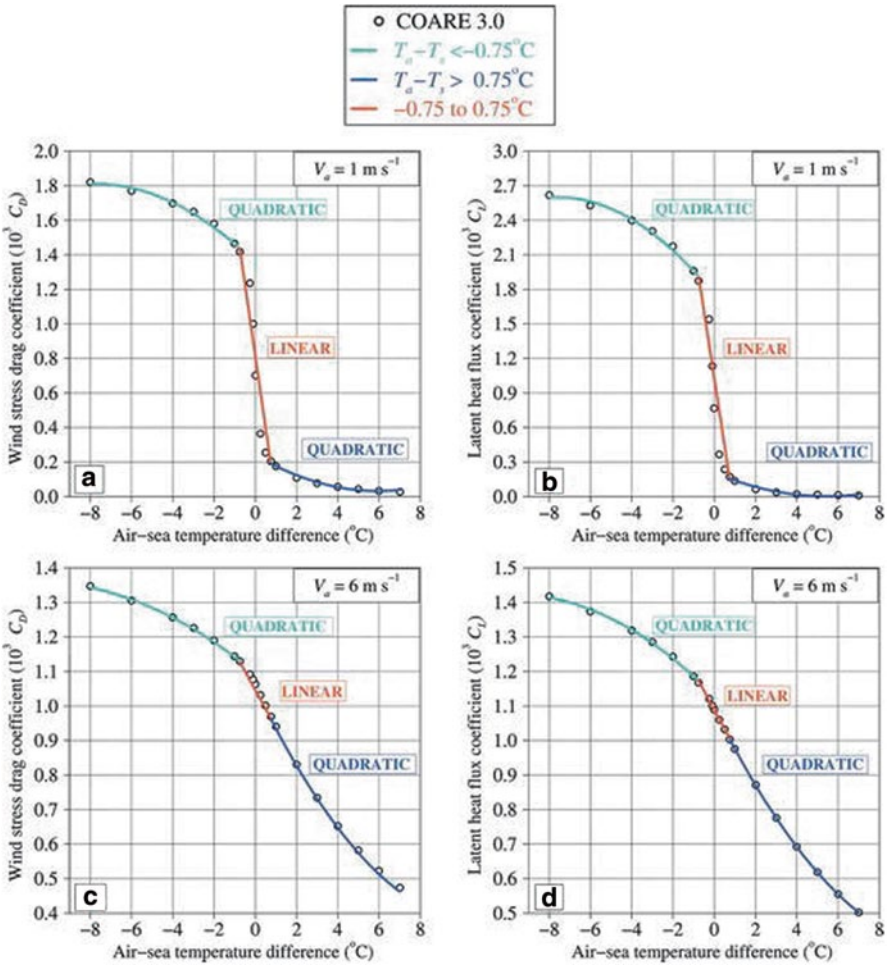

Fig. 4.34 The exchange coefficients: **a** C_D for $V_a = 1$ m s^{-1}, **b** C_L for $V_a = 1$ m s^{-1}, **c** C_D for $V_a = 6$ m s^{-1}, and **d** C_L for $V_a = 6$ m s^{-1}. Note that the exchange coefficients shown with open circles are obtained from the COARE algorithm. After Kara et al. (2005). Copyright © 2005 American Meteorological Society. Used with permission

range (ΔT_{max}) with daily average cloud fraction ($\bar{C}$) and daily average wind speed ($\bar{U}$) by a regression formula:

$$\Delta T_{max} = 0.75 + 14.67 \frac{(1 - \bar{C})}{\bar{U}^2}. \tag{4.56}$$

This parameterization was intended for the equatorial ocean, where the daily average cloud fraction is a good proxy for the cumulative daily insolation.

The presence of $\bar{U}^2$ in the right side of the regression implies that below some critical value of the wind speed the diurnal warming of the ocean surface layer

Table 4.4 Empirical coefficients for the Clayson and Curry (1996) parameterization (Eq. (4.57))

$\bar{U}$ <2 m s^{-1}		$\bar{U}$ >2 m s^{-1}	
Coefficient	Magnitude	Coefficient	Magnitude
a_0	0.328	a_0	0.262
b_0	0.002	b_0	0.00265
c_0	0.041	c_0	0.028
d_0	0.212	d_0	−0.838
e_0	−0.000185	e_0	−0.00105
f_0	−0.329	f_0	0.158

rapidly increases. Equation (4.56) is derived using data only for wind speed exceeding 2.7 m s^{-1}, because the scatter of points strongly increases under very low wind speed conditions. This equation should not therefore be applied for very low and calm winds. It was not intended for use outside the western Pacific warm pool but it should be applicable to other regions with possible change of coefficients.

Clayson and Curry (1996) extended the Lukas (1991) approach to low wind speeds by modifying the set of determining parameters and separating wind speed conditions below and above a 2 m s^{-1} threshold. Their regression parameterization of the diurnal SST range has the following form:

$$\Delta T_{\max} = a_0 + b_0(I_S) + c_0(\bar{P}) + d_0 \ln(\bar{U}) + c_0(I_S)\ln(\bar{U}) + f_0(\bar{U}), \qquad (4.57)$$

where I_S is the peak insolation, $\bar{P}$ is the daily average precipitation, and $\bar{U}$ is the daily average wind speed. The empirical coefficients for Eq. (4.57) as determined by Webster et al. (1996) from observations in the western Pacific warm pool are given in Table 4.4. Comparison of ship-measured ΔT_{max} variability with parameterization (4.57) shows a bias of 0.13°C (derived SST range lower than observed) with a standard deviation of 0.31°C and a correlation coefficient of 0.85 (Clayson and Curry 1996). Inclusion of the nighttime rainfall into the parameterization is, however, problematic. In some cases, it may improve the fit, while in other case, it can make prediction of the diurnal SST range even worse.

The advantage of the regression-type parameterizations is that they are simple and are easy for practical applications, especially when only limited information on the environmental conditions is available. A fundamental problem of such parameterizations is that, strictly speaking, they require adjustment of empirical coefficients to each geographical region, season, and, perhaps, even to synoptic conditions. Their application for the global coverage of large diurnal warming events is therefore very limited.

4.6.5 One-Dimensional Numerical Simulation of Diurnal Cycle

Early numerical models of the diurnal cycle employed the turbulent heat diffusion equation with constant mixing coefficient. Foster (1971) undertook direct numerical simulation of an idealized diurnal cycle in the upper ocean by solving the equations of

motion, heat, and continuity. Wind mixing was introduced by setting a constant turbulent mixing coefficient; the solar radiation was treated as a time-dependent volume source. The surface cooling was represented by a constant heat flux from the ocean surface. The model in general reproduced some qualitative features of the diurnal cycle. Convection developed during nighttime but was suppressed by solar radiation during daytime. The initial wind-induced turbulence was unimportant in the vertical transport after development of the nighttime gravitational convection. Yet for strong initial (wind-induced) mixing, the convection could not start during nighttime.

The main problem of Foster's (1971) model was that the mixing coefficient did not depend on depth or on time. Thus, it could not be correct under light winds. Remember that an important feature of turbulent mixing in the upper ocean under light winds is that it both influences, and is influenced by, stratification arising due to diurnal heating. This results in a nonlinear response of the diurnal cycle to external forcing, which could not be captured by Foster's (1971) model.

More realistic models of the diurnal mixed layer include the Kraus and Turner (1967) integral-type model, a second-moment turbulence closure mixed-layer model (Wick 1995), the K-profile parameterization (KPP) model (Large et al. 1994; Soloviev et al. 2001a), the Price–Weller–Pinkel (PWP) model (Price et al. 1986), and the transilient model (Stull and Kraus 1987; Soloviev and Lukas 1997). No perfect model of the diurnal cycle, however, has been developed: They all have advantages and disadvantages. Application of the integral model for the diurnal mixed-layer and thermocline modeling is complicated by some limitations in parameterizing entrainment fluxes at the bottom of the diurnal mixed layer. The KPP model requires specifying the nonlocal transport term that has not been well defined. The PWP model does not have the correct asymptotic convective regime under conditions of very low wind speed when the effect of volume absorption of solar radiation is of importance.

Below we consider modeling of the diurnal cycle for the example of the transilient model (though it also has a disadvantage in that it does not allow unstable stratification to develop). The transilient model deals with the parameterization of turbulent transports by a spectrum of eddies that transport fluid properties over a range of distances (Stull and Kraus 1987). The transilient model specifies a velocity scale $u_l = u_*$ and a vertical length scale $l = \kappa|z|$, where u_* is the frictional velocity in water, κ is the von Karman constant, and z is the vertical coordinate. For the unstably stratified near-surface layer (nighttime), Soloviev and Lukas (1997) proposed to use a different scaling: $u_l = w_*$ and $l = L_c$, where according to Priestly (1959) $w_* = (L_c B_0)^{1/3}$, L_c is the depth of the unstably stratified near-surface layer, and B_0 is the surface buoyancy flux. The absorption of solar radiation with depth was parameterized with a 9 exponential dependence (1.60).

Figure 4.35 shows the results of a simulation of the diurnal cycle in the western Pacific warm pool area with the transilient model. The vertical resolution and the time step were 0.25 m and 15 s, respectively. The vertical profiles of temperature and salinity were initialized to be a constant in the upper 20 m of the ocean, while the velocity profile was initialized with a 0.0004 s^{-1} shear to ensure finite values of the Richardson number for the first step of the simulation. The model was forced with the wind stress and sensible and latent heat fluxes calculated with the Tropical

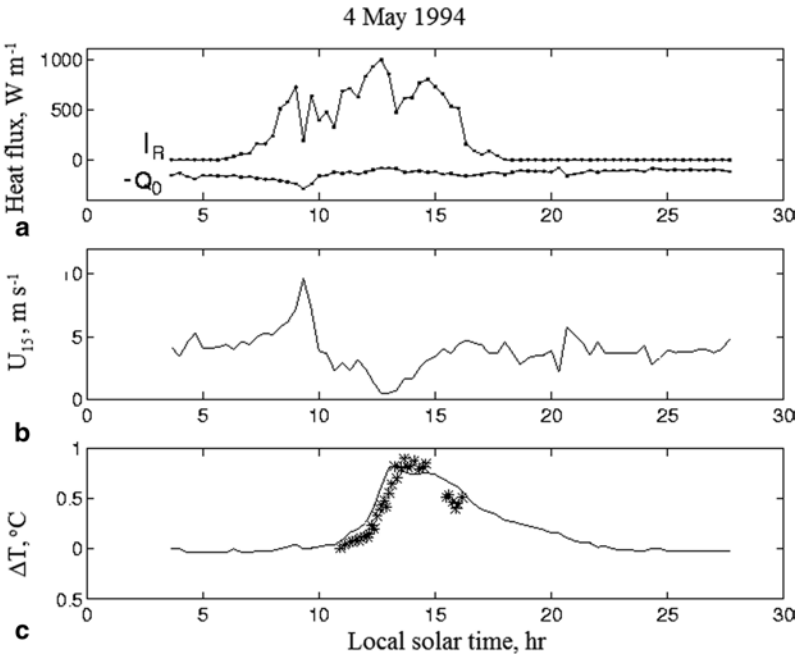

Fig. 4.35 Evolution of the diurnal temperature increase averaged over 0–0.25 m. **a** Insolation (I_Σ) and surface cooling heat fluxes ($Q_0 = I_L + Q_T + Q_E$), **b** wind speed at 15 m height U_{15}, **c** temperature difference $\Delta T = T_0 - T_8$ in the near-surface layer of the ocean as measured by a free-rising profiler (*asterisk*) and simulated by the transilient model (*contiguous line*); here T_0 and T_8 are the temperatures averaged over depth range 0–0.25 m and 8–8.25 m, correspondingly. The free-rising profiler measurements are the same as shown in Fig. 4.24. After Soloviev and Lukas (1997) with permission from Elsevier

Ocean-Global Atmosphere Coupled Ocean–Atmosphere Response Experiment (TOGA COARE) version 2.5a bulk-flux algorithm. The net long-wave radiation flux was calculated using the parameterization of Simpson and Paulson (1979).

Figure 4.35 shows the heat fluxes and wind speeds for the vertical temperature profiles shown in Fig. 4.24. Corresponding evolution of the temperature difference in the upper 8 m of the ocean according to the measurements with a free-rising profiler is compared to calculations of the same temperature difference with the transilient model. The model and field data are in good agreement. The dependence of the diurnal heating on the wind speed is clearly seen in this figure. During the morning wind forcing, there is practically no rise in SST. Although diurnal warming is suppressed during morning hours, it increases strongly at 10 am when the wind speed drops below 5 m s^{-1}.

According to Fig. 4.36a, the daily variation in atmospheric temperature is even larger than it is in the ocean. Hoeber (1970) previously observed a similar effect in the equatorial region. This effect is supposedly because the moist equatorial atmosphere absorbs solar radiation directly during the daytime and is cooled again during the nighttime (see discussion in Kraus and Businger 1994, p. 170).

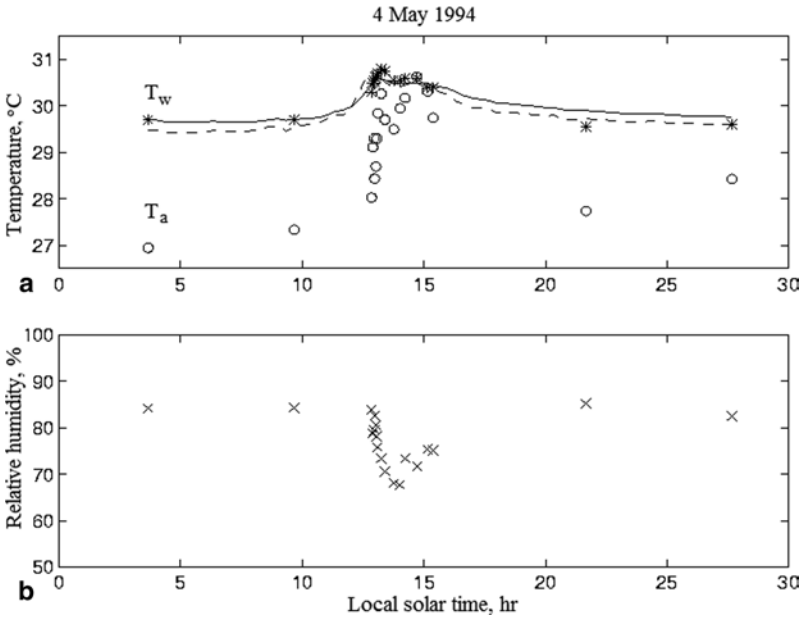

Fig. 4.36 **a** Air and water temperatures on 4 May 1996. Here, *asterisks* are the bucket thermometer bulk temperatures, open circles are the dry air temperature (corrected to 10 m height), the contiguous line is the surface temperature (0–0.25 m average) calculated using the transilient model, and the dashed line is the SST calculated using the transilient model and the cool skin model. **b** Relative humidity on 4 May 1996. After Soloviev and Lukas (1997) with permission from Elsevier

Note the diurnal cycle of relative humidity (Fig. 4.36b). The relative humidity decreases with the daytime SST increase, thus enhancing the latent heat flux. This is a manifestation of the negative feedback mechanism stabilizing the SST (Greenhut 1978; Gautier 1978; Lukas 1990a; Katsaros and DeCosmo 1990; Kraus and Businger 1994).

Direct numerical simulation represents another possible approach to modeling the diurnal cycle of SST under low wind speed conditions. The model of Verevochkin and Startsev (2000) mentioned in Sect. 4.6.1 is one of the first attempts in this direction. The present version of this model, unfortunately, does not include wind mixing.

4.6.6 Three-Dimensional Numerical Simulation of Diurnal Cycle

For the numerical simulation of the near-surface layer of the ocean, Soloviev et al. (2012) used a three-dimensional (3D) large eddy simulation (LES) model implemented with the computational fluid dynamics (CFD) software ANSYS Fluent (Fig. 4.37). The solar radiation was included as a volume source of heat, while the sensible and latent heat and longwave radiation were included as surface fluxes.

In contrast to local (diffusion-type) models, the LES model accounts for nonlocal transport and has a better performance in nonstationary conditions of the deep-

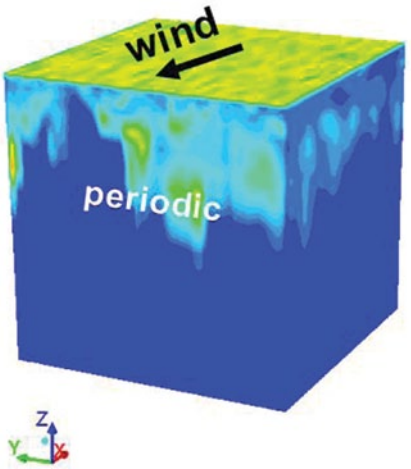

Fig. 4.37 Computational fluid dynamics model of diurnal warming. The numerical domain is 30 m x 30 m x 30 m. Hexahedral mesh is as follows: top cell = 20 cm (depth) x 20 cm x 20 cm, and vertical size increased with 1.3 growth rate to the bottom. A hybrid LES model (detached eddy simulation) was implemented. Wind speed = 4 m s^{-1}, surface heat flux = 100 W m^{-2}, peak solar insolation = 1,200 W m^{-2}. (Courtesy of Silvia Matt)

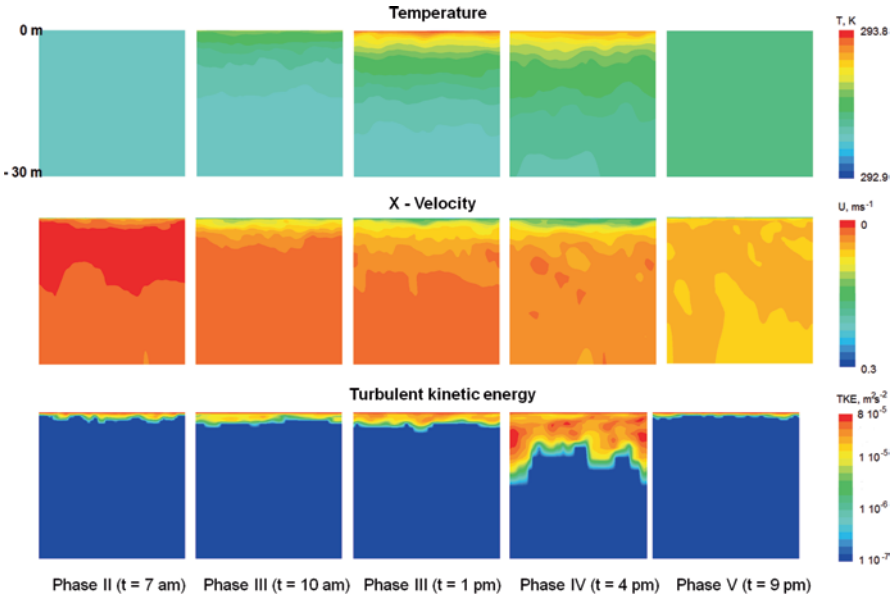

Fig. 4.38 CFD simulation of the diurnal cycle (*side view*). Phases correspond to the schematic representation of the diurnal mixed-layer and diurnal thermocline depth under low wind speed conditions shown in Fig. 4.16. After Soloviev et al. (2011)

ening diurnal mixed layer. As an example, Fig. 4.38 shows the simulation of the temperature, current velocity, and TKE for the idealized diurnal solar insolation cycle similar to that shown in Fig. 4.16. During Phase II, and III, the diurnal thermocline and diurnal jet were localized in the upper few meters of the ocean and a diurnal jet was developing in the upper few meters of the ocean due to the slippery

effect of the near-surface layer of the ocean (see Sect. 4.3.1). On the stage of evening deepening, Phase IV, K–H instability developed across the diurnal thermocline, which produced large eddies and significant increase in the TKE. A result was the rapid deepening of the diurnal thermocline, which was powered by the kinetic energy of the diurnal jet accumulated during daytime. As soon as the kinetic energy exhausted, the deepening of the thermocline stopped and the thermocline slowly eroded due to convective cooling (Phase V). This modeling result is consistent with the conceptual representation of the diurnal cycle given in Fig. 4.16.

The 3D CFD model, however, is computationally expensive. For global modeling application, only a computationally more effective, one-dimensional (1D) model of the diurnal cycle can be used. One approach is to approximate the vertical temperature profile in the diurnal thermocline with a piecewise linear profile (Fig. 4.15) during Phases I–III and with an exponential vertical temperature profile in nonstationary conditions during the evening deepening of the thermocline (Fig. 4.22) during Phase IV. In Phase IV, the vertical profile of temperature may contain a jump at the bottom of the mixed layer following the Barenblatt (1982) model for unsteady heat and mass exchange in a fluid with a strong stratification. This 1D model can then be fine-tuned using the 3D CFD model results and finally verified with field data.

4.7 Fine Structure of the Near-Surface Layer in the Polar Seas

Structure and dynamics of the upper ocean in the Arctic and Antarctic seas influence the sea ice coverage, which has important climate consequences. Few details are, however, known about the near-surface layer of the polar seas. The upper ocean layer in polar regions is often characterized by the strong halocline stratification, which controls vertical fluxes of deep ocean heat to the surface and sea ice (e.g., Toole et al. 2010). As a result, barrier layers similar to those observed in the Indo-Pacific warm pool (Lukas and Lindstrom 1991) are an important factor in the dynamics of the polar seas.

Figure 4.39 demonstrates typical vertical profiles of temperature, salinity, and potential density in the ice-covered, central Canada Basin of the Arctic Ocean during late winter and late summer seasons. The late winter profiles (Fig. 4.39a) show a well-mixed surface layer extending down to a 40-m depth where it is bounded by the barrier layer due to salinity. Water temperature in this relatively fresh mixed layer (27.7 psu) was only slightly above the freezing point. The temperature profile below the mixed layer in this part of the Arctic Ocean was formed by intrusions of water from the Pacific Ocean (forming a local maximum at a 50-m depth) and from the Atlantic Ocean (forming a local maximum at 400 m depth) (Shimada et al. 2001; Toole et al. 2010; Steele et al. 2004). Strong salinity stratification in the halocline maintained stable density stratification, which effectively isolated the mixed-layer water from the warmer water below the mixed layer, preventing the ice from melting.

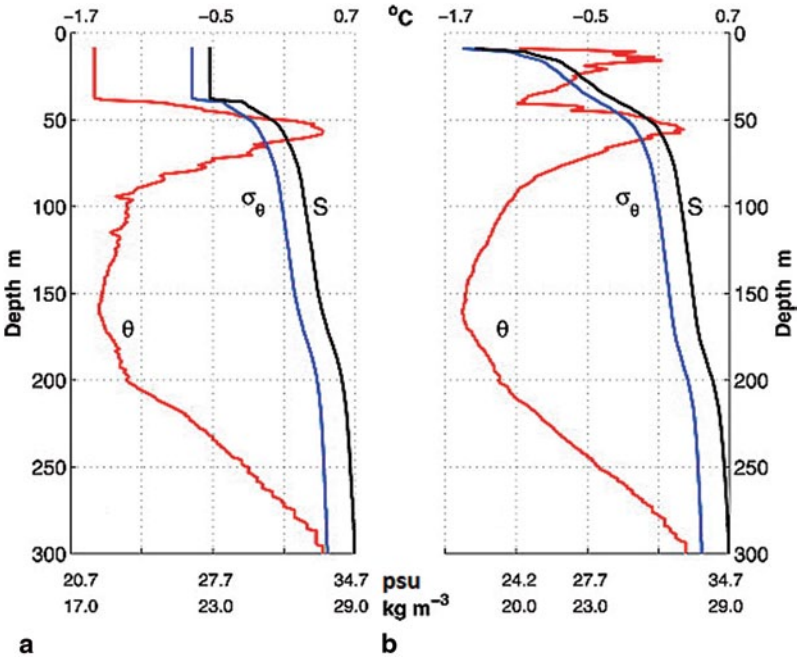

Fig. 4.39 Typical vertical profiles of temperature (*red*), salinity (*black*), and potential density anomaly (*blue*) observed under Arctic ice on **a** 30 April 2007 and **b** 13 September 2007 in the Canada Basin(within 25 km of 76°24′N, 140°45′W). After Toole et al. (2010) by permission of American Geophysical Union

The late summer profiles (Fig. 4.39b) revealed significant restratification of the previously mixed layer in the upper 40 m of the ocean. An additional temperature maximum emerged at a 10-m depth, due to solar heating through leads and horizontal advection (Perovich and Maykut 1990; Toole et al. 2010). The near-surface salinity dropped by 5 psu compared to the winter near-surface salinity, developing extremely strong density stratification in this layer.

In the cold surface water of the polar seas, the coefficient of thermal expansion α_T is substantially smaller than in mid- and low-latitude surface waters. The thermal component of the buoyancy flux, $-\alpha_T g Q_n / (c_p \rho)$, is therefore small. As a result, the suppression of turbulence due to absorption of solar radiation is less probable than in warmer environments. Substantial contribution to the buoyancy flux, nevertheless, comes from fresh water released by melting ice. (The salinity contraction coefficient β_S does not depend as much on water temperature as α^T does.)

When the Arctic or Antarctic pack ice melts in spring, it releases fresher water, which leads to the formation of near-surface plumes. These plumes tend to spread horizontally in the near-surface layer, forming low-salinity, stably stratified layers. Timmermans et al. (2012) observed the near-surface stratification under the Arctic ice, which was attributable to lateral processes. The lateral advection driven by the horizontal buoyancy gradients due to salinity differences results in restratification

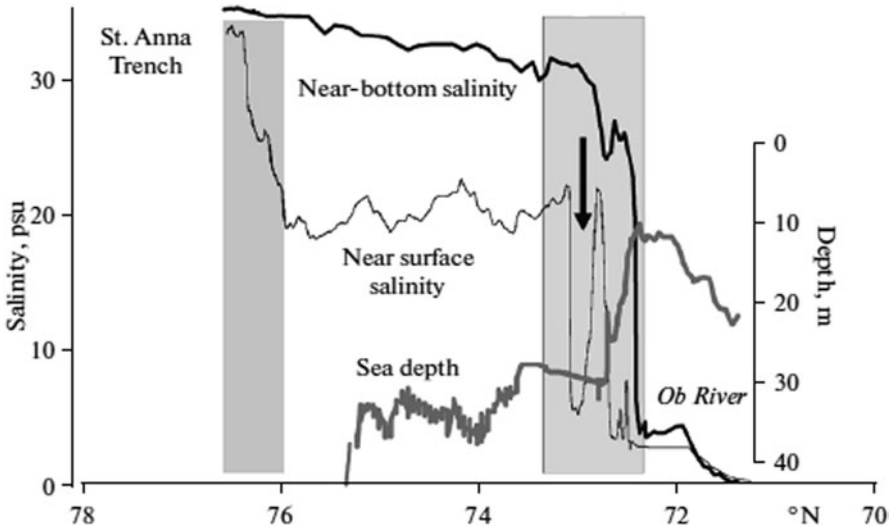

Fig. 4.40 Horizontal salinity profiles near the bottom and in the near-surface layer in the Ob River section of the Kara Sea. The ocean frontal zones are marked by *gray color*, and *the arrow* points to a meander of low-salinity water. After Zatsepin et al. (2010) with permission from Springer

of the near-surface layer. The stable salinity stratification inhibits turbulent mixing, which effectively isolates the ice from warmer deep water during winter time (as in the example shown in Fig. 4.39a) or traps the air–sea heat and mass exchange near the surface during summer time (as an example shown in Fig. 4.39b). The latter effect increases melting of the ice in spring and summer.

The source of fresh water (melting ice) is often localized within the relatively thin near-surface layer of the ocean. In the Antarctic, for example, the typical thickness of the pack ice is less than 1 m.

In coastal areas of the Arctic Ocean, the river runoff is a major source of fresh water. Figure 4.40 demonstrates a cross section in the Kara Sea, which shows significant desalination of the near-surface layer of the ocean due to the offshore propagation of fresh water, taking place predominately near the sea surface.

Sea ice adds dramatic variation to all atmosphere–ocean interactions (McPhee 1983; Muench 1990; Gow and Tucker III 1990). The classic problem of air–sea interaction obtains a new dimension when air–sea–ice interaction is considered, especially in the marginal ice zone. While the previous studies in polar seas (see Muench 1990 and McPhee 2008 for reviews) have revealed fundamental principles regarding the coupling of the ice cover, ocean, and atmosphere, applying these principles to conditions at the pack ice edge is not simple. The processes in the marginal ice zone are complicated by large spatial gradients and by strong temporal variability. For example, field data from the Greenland Sea (Buckley et al. 1979; Johannessen et al. 1983) show that the marginal ice zone is an area of extreme upper ocean variability with numerous fronts, upwelling or downwelling features, and eddies. In the marginal ice zone, the ice concentration varies from 100% in the interior to 0% at the edge, with large fluctua-

tions occurring over distances of a few kilometers in both across edge and along edge directions. Also, because of the effect of incoming surface waves, average floe size in the marginal ice zone changes from a few meters at the edge to thousands of meters at a distance of 100–200 km into the interior (Wadhams 1973).

Though the marginal ice zone represents a small percentage of the total ice cover in the polar region, its dynamical description is crucially important in many processes associated with the pack ice variation. These include (Brown 1990): "…the growth, extent, and break up of the pack ice; the regional ocean circulations and associated problems of the ocean mixed-layer dynamics, biology, and thermal structure; the dynamics of bottom-water formation in the marginal ice zone; the enhanced biological activity with high phytoplankton concentration and large standing stock near the marginal ice zone; and the mechanics of the long-time influence of the pack ice and marginal ice zone on climatic and oceanic circulation."

The upper ocean processes and ice mass changes that control the vertical transfer of momentum, heat, and salt between the ice and water are of fundamental importance in controlling ice extent and motion in the marginal ice zone. When the ice is blown over warm water, the underside melts; how fast it melts depends on the rate of heat exchange in the ocean–ice boundary layer (McPhee 2008). At the same time, the transfer of heat, salt, and momentum modifies the upper ocean and changes the physics of subsequent ice and ocean interaction. When the upper surface ice is melted by radiative and sensible heat input, the resultant mass flux also has an impact on upper ocean processes. The ice and upper ocean thus represent a strongly coupled system which description should rely on a detailed understanding of these heat-, salt-, and momentum-transfer processes.

Antarctic pack ice is relatively thin. The ice drift patterns prevent most Antarctic sea ice from reaching ages greater than 1–2 years. Wadhams et al. (1987) found the mean thickness of ice floes formed during 1 year to be about 50–60 cm only.

In the Antarctic, melt occurs mainly from the bottom and the sides of the ice, which are in contact with the ocean. Divergence of the pack creates more open water, allowing more solar radiation to be absorbed by the ocean with a subsequent warming of the surface water. As austral summer approaches the surface layer of the ocean warms up and the rate of melting of the ice increases. Ice edge retreat begins in November, accelerates in December, and continues throughout February along the entire East Antarctic coastline. By November, areas of open water within the pack are no longer exclusively sites of enhanced ice production; rather they become a focus for the uptake of solar radiation and contribute to the rapid decay of the ice. By this process, the pack ice decays "from within" as well as by the retreat of the ice edge from north to south. Particularly, rapid retreat occurs in regions where the ice edge extended furthest north at maximum extent.

Figure 4.41 shows an example when a weak salinity-controlled upper layer frontal structure was generated by melt-water input in the summer marginal ice zone in the Antarctic. This front migrated as the ice edge retreated in spring, releasing melt-water to the upper ocean.

McPhee (1983) and Mellor et al. (1986) demonstrated that the stabilizing effect of the surface flux of freshwater reduces the interfacial drag coefficient and this

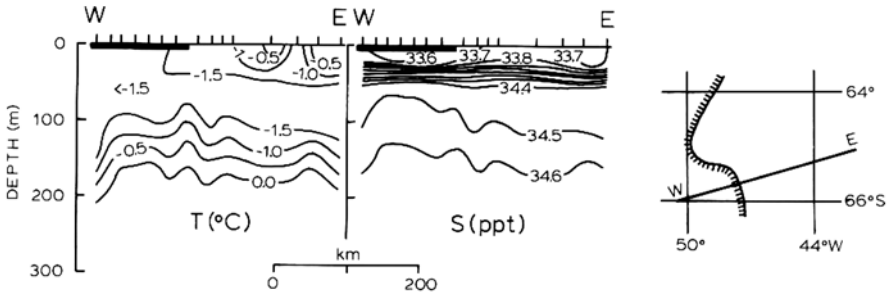

Fig. 4.41 Vertical distributions of temperature (C; *left*) and salinity (psu; *middle*) along a transect normal to the late summer ice edge in the northwestern Weddell Sea. Approximate location of the transect is shown to the right, with ice edge indicated by the heavy hachured line (ice cover to the left of the line). After Muench (1990)

appears to account for observed divergence of ice packs in the marginal ice zone. Strong stable salinity stratification in the marginal ice zone can, however, lead to the coupling of the drifting ice with the internal wave field thus increasing the drag coefficient. This effect has been observed during Marginal Ice Zone Experiment (MIZEX) (Morrison et al. 1987; McPhee and Kantha 1989).

At times when winds are blowing off the ice, the ice edges of the ocean are generally the site of regularly spaced (~20 km) surface bands of ice floes. McPhee et al. (1987) suggested that this is a result of the coupling between the internal wave field and ice floes; this coupling is possible due to stable salinity stratification in the near-surface layer of the ocean maintained by melting along the ice edges.

Smith and Nelson (1985) observed a dense phytoplankton bloom near a receding ice edge off the coast of Victoria Land in the Antarctic. The bloom area extended 250 km from the ice edge and was confined to waters where melting ice had reduced salinity. Presumably, stable salinity stratification (barrier layer) in this area favored phytoplankton growth and accumulation.

An extensive phytoplankton bloom in the northern Gerlache Strait was studied during the Research on Antarctic Coastal Ecosystem Rates (RACER; see Karl 1991). The bloom abruptly declined when the mixing-layer depth changed. It was concluded that the phytoplankton bloom was controlled largely by the physical processes in the water column. Massive summer algae blooms under the Arctic sea ice observed by Arrigo et al. (2012) was presumably stimulated by the near-surface physical processes as well.

References

Anderson SP, Weller RA, Lukas RB (1996) Surface buoyancy forcing and mixed layer of the western Pacific warm pool: observations and 1D model results. J Climate 9:3056–3085

Arrigo KR, Perovich DK, Pickart RS et al (2012) Massive phytoplankton blooms under arctic sea ice. Science 336(6087):1408

Barenblatt GI (1982) A model of unsteady heat- and mass exchange in a fluid with a strong stratification. Izvestiya, (Bulletin), USSR Academy of Sciences, Atmospheric and Oceanic Physics 18(3):201–205 (English Translation)
Bauer P, Schlüssel P (1993) Rainfall, total water, ice water and water vapour over sea from polarized microwave simulations and SSM/I data. J Geophys Res 98:20, 737–20, 760
Bell TL (1987) A space-time stochastic model of rainfall for satellite remote-sensing studies. J Geophys Res 92(D8):9631–9643. doi:10.1029/JD092iD08p09631
Bezverkhny VA, Soloviev AV (1986) Experimental data on the vertical structure of the non-stationary near-surface thermocline. Izvestiya, (Bulletin), USSR Academy of Sciences, Atmospheric and Oceanic Physics 22, No. 1, pp. 71–77 (In Russian)
Brown PA (1990) Meteorology. In: Smith WO Jr (Ed) Polar Oceanography. Academic Press, San Diego, pp 1–46
Buckley JR, Gammelsrod T, Johannessen JA, Johannessen OM, Roed IP (1979) Upwelling: Oceanic structure at the edge of the Arctic ice pack in winter. Science 203:165–167
Chou S-H, Atlas RM, Shie C-L, Ardizzone J (1995) Estimates of surface humidity and latent heat fluxes over oceans from SSM/I data. Mon Weather Rev 123:2405–2425
Clayson CA, Curry JA (1996) Determination of surface turbulent fluxes for TOGA COARE: comparison of satellite retrievals and in situ measurements. J Geophys Res 101:28, 503–28, 513
Deschamps PY, Frouin R (1984) Large diurnal heating of the sea surface observed by the HCMR experiment. J Phys Oceanogr 14:177–184
Emery WJ, Yu Y, Wick GA, Schlüssel P, Reynolds R (1994) Improving satellite infrared sea surface temperature estimates by including independent water-vapor observations. J Geophys Res 99: 5219–5236
Fedorov KN, Ginzburg AI (1988) The near-surface layer of the ocean, Hydrometeoizdat, Leningrad. Translated into English in 1992 by VSP, P.O. Box 346, 3700 AH Zeist, The Netherlands
Foster TD (1971) A convective model for a diurnal cycle in the upper ocean. J Geophys Res 76(3):666–675
Gautier C (1978) Cold anomaly in sea surface temperature associated with a GATE tropical depression. J Phys Oceanogr 8:162–166
Gautier C, Katsaros K (1984) Insolation during STREX. Prt I: comparisons between suface measurements and satellite estimates. J Geophys Res 89:11, 779–11, 788
Gentemann CL, Donlon CJ, Stuart-Menteth A, Wentz FJ (2003) Diurnal signals in satellite sea surface temperature measurements. Geophys Res Lett 30. doi:10.1029/2002GL016291
Gentemann CL, Wentz FJ, Mears CA, Smith DK (2004) In situ validation of Tropical Rainfall Measuring Mission microwave sea surface temperatures. J Geophy Res 109:C04021, 1–9
Gosnell R, Fairall CW, Webster PJ (1995) The sensible heat of rainfall in the tropical ocean. J Geophys Res 100:18, 437–18, 442.
Gow AJ, Tucker WB III (1990) Sea ice. In: Polar Oceanography, Academic Press, San Diego et al. pp 47–122
Gregg MC (1975) Oceanic fine and microstructure. Rev Geophys Space Ge 13:586–591 and 635–636
Greenhut GK (1978) Correlations between rainfall and sea surface temperature during GATE. J Phys Oceanogr 8:1135–1138
Hasse L (1971) The sea surface temperature deviation and the heat flow at the air–sea interface. Bound-Lay Meteorol 1:368–379
Hoeber H (1970) Measurements in the atmospheric surface layer above the tropical atlantic. Weather 25:419–424
Houghton D (1969) Acapulco'68. Weather 24:2–18
Johannessen OM, Johannessen JA, Morison JH, Farrelly BA, Svendsen EAS (1983) Oceanographic conditions in the marginal ice zone north of Svilbard in early fall 1979 with an emphasis on mesoscale processes. J Geophys Res 88:2755–2769
Kara AB, Rochford PA, Hurlburt HE (2002) Air–Sea Flux Estimates and the 1997–1998 ENSO Event. Bound-Layer Meterol 103:439–458

Kara AB, Hurlburt HE, Wallcraft AJ (2005) Stability-Dependent exchange coefficients for Air–Sea fluxes. J Atmos Oceanic Technol 22:1080–1094

Karl DM (1991) RACER: Research on antarctic coastal ecosystem rates. Preface Deep-Sea Res 38:v–vii

Katsaros KB, DeCosmo J (1990) Evaporation at high wind speeds, sea surface temperature at low wind speeds: examples of atmospheric regulation. Proceedings, Workshop on Modeling the Fate and Influence of Marine Spray, Marseille, France, June 5–7, 1990, 1–11

Katsaros KB, Soloviev AV (2003) Vanishing horizontal sea surface temperature gradients at low wind speeds. Bound-Layer Meterol 112:381–396

Katsaros KB, Soloviev AV, Weisberg RH, Luther ME (2005) Reduced horizontal sea surface temperature gradients under conditions of clear sky and weak winds. Bound-Layer Meteorol 116:175–185

Kawai Y, Kawamura H (2002) Evaluation of the diurnal warming of sea surface temperature using satellite-derived marine meteorological data. J Oceanography 58:805–814

Kolmogorov AN (1942) Equations of turbulent motion of an incompressible fluid. Izvestia, Academy of Sciences, USSR; Physics, 6(1 & 2):56–58

Kraus EB, Businger JA (1994) Atmosphere-Ocean Interaction. University Press Oxford, 352 pp

Kraus EB, Rooth C (1961) Temperature and steady state vertical heat flux in the ocean surface layer. Tellus 13:231–238

Kraus EB, Turner JS (1967) A one-dimensional model of the seasonal thermocline. Pt. II The general theory and its consequences. Tellus 19:98–105

Kudryavtsev VN, Soloviev AV (1988) Daytime near-surface current, Doklady Akademii Nauk SSSR 303(1):59–62

Kudryavtsev VN, Soloviev AV (1990) Slippery near-surface layer of the ocean arising due to daytime solar heating. J Phys Oceanogr 20:617–628

Landau LD, Lifshits EM (1986) Theoretical physics, hydrodynamics vol. 6, Nauka Moscow, S 736

Large WG, McWilliams JC, Doney SC (1994) Oceanic vertical mixing: a review and a model with a nonlocal boundary layer parameterization. Rev Geophys 32:363–403

Lukas R (1990a) Freshwater input to the western equatorial Pacific Ocean and air–sea interaction. In: proceedings of the symposium on Western Tropical Pacific Air–Sea interactions, 15–17 November 1988. China Ocean Press, Beijing, pp 305–327

Lukas R (1990b) The role of salinity in the dynamics and thermodynamics of the western Pacific warm pool, in preprint, Proceedings, International TOGA Scientific Conference, WCRP-43, WMO/TD 379, pp 73–81

Lukas R (1991) The diurnal cycle of sea surface temperature in the western equatorial Pacific. TOGA Notes, January 1991, No. 2: 1–5

Lukas R, Lindstrom E (1991) The mixed layer of the western equatorial Pacific Ocean. J Geophys Res 96(S01): 3343–3357

McCreary JP Jr, Kohler KE, Hood RR, Smith S, Kindle J, Fischer AS, Weller RA (2001) Influences of diurnal and intraseasonal forcing on mixed-layer and biological variability in the Central Arabian Sea. J Geophys Res 106:7139–7155

McNeil CL, Merlivat L (1996) The warm oceanic surface layer: implications for CO_2 fluxes and surface gas measurements. Geophys Res Lett 23:3575–3578

McPhee MG (1983) Turbulent heat and momentum transfer in the oceanic boundary layer under melting pack ice. J Geophys Res 88:2827–2835

McPhee MG (2008) Air-ice-ocean interaction: turbulent ocean boundary layer exchange, Springer, New York

McPhee MG, Kantha LH (1989) Generation of internal waves by sea ice. J Geophys Res 94:3287–3302

McPhee MG, Maykut GA, Morison JH (1987) Dynamics and thermodynamics of the ice/upper ocean system in the marginal ice zone of the Greenland Sea. J Geophys Res 92:7017–7031

Mellor GL, McPhee MG, Steele M (1986) Ice-seawater turbulent boundary layer interaction with melting or freezing. J Phys Oceanogr 16:1829–1846

Montgomery RB, Stroup ED (1962) Equatorial waters and currents at 150 W in July-August 1952. The Johns Hopkins Oceanographic Studies, vol 1. The Johns Hopkins Press, Baltimore, pp 68
Morrison JH, McPhee MG, Maykut GA (1987) Boundary layer, upper ocean, and ice observations in the Greenland Sea marginal ice zone. J Geophys Res 92:6987–7011
Muench RD (1990) Mesoscale phenomena in the Polar Oceans. In: Polar Oceanography, Smith WO Jr (Eds). Academic Press, San Diego, pp 223–286
Neuwstadt FTM (1984) The turbulent structure of the stable, nocturnal boundary layer. J Atmos Sci 41:2202–2216
Niiler PP, Kraus EB (1977) One-dimensional models. In: Modeling and Prediction of the Upper Layers of the Ocean, Kraus EB, (Ed). Pergamon, New York, pp 143–172
Osborn TR, Cox CS (1972) Oceanic fine structure. Geophys Fluid Dyn 3:321–345
Perovich D, Maykut G (1990) Solar heating of a stratified ocean in the presence of a static ice cover.J Geophysic Res 95(C10): doi:10.1029/90JC01117. ISSN: 0148–0227
Price JF, Weller RA, Pinkel R (1986) Diurnal cycling: observations and models of the upper ocean response to diurnal heating, cooling, and wind mixing. J Geophys Res 91:8411–8427
Priestly CHB (1959) Turbulent transfer in the lower atmosphere. University of Chicago Press, Chicago Ill, p 130
Quilfen Y, Chapron B, Vandemark D (2001) The ERS scatterometer wind measurement accuracy: evidence of seasonal and regional biases. J Atmos.Ocean Tech 18(10):1684–1697
Raschke E (1975) Numerical studies of solar heating of an ocean model. Deep-Sea Res 22:659–666
Schlüssel P (1996) Satellite remote sensing of evaporation over sea. In: Raschke E (Ed). In: radiation and water in the climate system: remote measurements, NATO ASI Series, I 45. Springer Verlag, Berlin, pp 431–461
Schlüssel P, Luthardt H (1991) Surface wind speeds over the North Sea from SSM/I observations. J Geophys Res 96:4845–4854
Schlüssel P, Schanz L, Englisch G (1995) Retrieval of latent heat flux and longwave irradiance at the sea surface from SSM/I and AVHRR measurements, Adv. Space Res 16:107–115
Shimada K, Carmack EC, Hatakeyama K, Talizawa T (2001) Varieties of temperature maximum waters in the western Canada Basin of the Arctic Ocean, J Geophys Res 28(18):3441–3444. doi:10.1029/2001GL013168
Shinoda T, Hendon HH, Glick JD (1998) Mixed layer modeling of intraseasonal sea surface temperature variability in the tropical western Pacific and Indian Ocean. J Climate 11:2668–2685
Simpson JJ, Paulson CA (1979) Mid-ocean observations of atmospheric radiation. Q J Roy Meteor Soc 105:487–502
Smith OW, Nelson DM (1985) Phytoplankton bloom produced by a receding ice edge in the Ross Sea: spatial coherence with density field. Science 227:163–166
Soloviev AV (1979) Thin thermal structure of the ocean surface layer in the POLYMODE-77 region. Izvestiya, Atmospheric and Oceanic Physics 15:750–754 (in Russian)
Soloviev AV (1982) On vertical structure of a thin surface layer of the ocean under conditions of low wind speed. Izvestiya. Atmospheric and Oceanic Physics 18(7):751–760 (in Russian)
Soloviev AV (1990) Coherent structure at the ocean surface in the convectively unstable conditions. Nature 346:157–160
Soloviev A, Lukas R (1996) Observation of spatial variability of diurnal thermocline and rain-formed halocline in the western Pacific warm pool. J Phys Oceanogr 26(11):2529–2538
Soloviev A, Lukas R (1997) Observation of large diurnal warming events in the near-surface layer of the western equatorial Pacific warm pool. Deep-Sea Res. 44:Part I, 1055–1076
Soloviev A, Lukas R, Hacker P (2001a) An approach to parameterization of the oceanic turbulent boundary layer in the western pacific warm pool. J Geophys Res 106:4421–4435
Soloviev A, Edson J, McGillis W, Schlüssel P, Wanninkhof R (2001b) Fine thermohaline structure and gas-exchange in the near-surface layer of the ocean during GasEx-98. In AGU Monograph Gas Transfer at Water Surfaces, Saltzman ES, Donealn M, Drennan W, Wanninkhof R (Eds) 181–185

Soloviev A, Lukas R, Hacker P, Baker M, Schoeberlein H, Arjannikov A (1999) A near-surface microstructure sensor system used during TOGA COARE. Part II: Turbulence Measurements. J Atmos Oceanic Tech 16:1598–1618

Soloviev A, Matt S, Fujimura A (2011) Sea surface temperature: modeling of the diurnal cycle of the sea surface temperature and air–sea exchange of carbon dioxide in application to remote sensing techniques. WCRP open science confernce: Climate Research in Service to Society. 24–28 October 2011, Denver, CO, USA

Soloviev A, Matt S, Fujimura A (2012) Sea surface temperature: modeling of the diurnal cycle of the sea surface temperature and air–sea exchange of carbon dioxide in application to remote sensing techniques. WCRP Open Science Conference, Session C14, Poster T44A. 24–28 October 2011, Denver, CO, USA

Soloviev AV, Vershinsky NV (1982) The vertical structure of the thin surface layer of the ocean under conditions of low wind speed, Deep-Sea Research 29, N 12A, 1437–1449

Steele M, Morison J, Ermold W, Rigor I, Ortmeyer M, Shimada K (2004) Circulation of summer Pacific Halocline water in the Arctic Ocean. J Geophys Res 109, C02027. doi:10.1029/2003JC002009

Stern ME, Turner JS (1969) Salt fingers and convecting layers. Deep-Sea Res 16:497–511

Stuart-Menteth AC, Robinson IS, Challenor PG (2003) A global study of diurnal warming using satellite-derived sea surface temperature. J Geophys Res 108(C5):3155. doi:10.1029/2002JC001534

Stull RB, Kraus EB (1987) A transilient model of the upper ocean. J Geophys Res-Oceans 92:10, 745–10, 755

Tanahashi S, Kawamura H, Takahashi T, Yusa H (2003) Diurnal variations of sea surface temperature over the wide-ranging ocean using VISSR on board GMS. J Geophys Res 108:3216. doi:10.1029/2002JC001313

Timmermans M-L, Cole S, Toole J (2012) Horizontal density structure and restratification of the arctic ocean surface layer.J Phys Oceanogr 42:659–668. doi:http://dx.doi.org/10.1175/JPO-D-11–0125.1

Toole JM, Timmermans M.-L, Perovich DK, Krishfield RA, Proshutinsky A, Richter-Menge JA (2010) Influences of the ocean surface mixed layer and thermohaline stratification on Arctic sea ice in the central Canada Basin. J Geophys Res 115, C10018. doi:10.1029/2009JC005660

Turner JS (1973) Buoyancy effects in fluids. Cambridge University Press, New York

Verevochkin YuG, Startsev SA (2000) Numerical simulation of convection and heat transfer in water absorbing solar radiation. J Fluid Mech 421:293–305

Wadhams P (1973) Attenuation of swell by sea ice. J Geophys Res 78:3525–3563

Wadhams P, Lange MA, Ackley SF (1987) The ice thickness distribution across the Atlantic sector of the Antarctic Ocean in midwinter. J Geophys Res 92:14,535–14,552

Webster PJ, Clayson CA, and Curry JA (1996) Clouds, radiation and the diurnal cycle of sea surface temperature in the tropical western Pacific Ocean. J Clim 9: 1712-1730

Wick GA (1995) Evaluation of the variability and predictability of the bulk-skin sea surface temperature difference with application to satellite-measured sea surface temperature. Thesis (Ph.D.), University of Colorado at Boulder. Dissertation Abstracts International, Volume: 56–09, Section: B, p 4798

Wick GA, Emery WJ, Schlüssel P (1992) A comprehensive comparison between satellite-measured skin and multichannel sea surface temperature, J Geophys Res 97:5569–5595

Woods JD (1968) An investigation of some physical processes associated with the vertical flow of heat through upper ocean. Meteorology Magazine 97(1148):65–72

Woods JD, Strass V (1986) The response of the upper ocean to solar heating. 2. The wind-driven current. Q J Roy Meteor Soc 112(471):29–42

Zatsepin AG, Zavialov PO, Kremenetskiy VV, Poyarkov SG, Soloviev DM (2010) The upper desalinated layer in the Kara Sea. Oceanology 50(5):657–667 (translated from Russian)

Chapter 5
Spatially-Varying and Coherent Structures

Abstract This chapter is devoted to the theory and observation of coherent structures in the near-surface layer of the ocean. The upper ocean boundary layer is turbulent but not completely random. The phenomenon of self-organization occurs in a variety of nonlinear dissipative systems. Spatially coherent, organized motions have been recognized as an important part of turbulent boundary-layer processes. These motions provide nonlocal transport of properties across the boundary layer. Spirals on the sea surface and sharp frontal interfaces are intriguing examples of self-organization. Other types of quasiperiodic structures in the near-surface ocean, such as freshwater lenses produced by rainfalls, may have distinct signatures in the sea surface temperature field. Due to the presence of surface gravity waves, the Ekman boundary layer is unstaented perpendicular to the wind direction, while Langmuir cells are roughly aligned with the wind. Internal waves, resonant interactions between surface and internal modes, billows in the diurnal thermocline, and convection also produce organized motions in the upper ocean under certain conditions.

Keywords Coherent structure • Ramp-like structure • Langmuir circulation • Self-organization • Two-dimensional turbulence • Sharp frontal interfaces • Stommel's overturning gate • Resonant interaction • Internal wave • Convection

5.1 Introduction

The upper ocean is turbulent, in other words chaotic, because the Reynolds number is large. This chaos may include organized, so-called *coherent structures*.

In the presence of stochastic fluctuations and nonlinear interactions, quasi-stationary and stable states having an ordered structure can be formed naturally (Nicolas and Prigogine 1977). Self-organization occurs in a variety of nonlinear dissipative systems; the formation of life may be regarded as one example of such a process.

Kraichnan (1967); Rhines (1975); Hasegawa (1985), and others developed the self-organization conjecture for hydrodynamic systems. Important common features of these systems are as follows: The system should contain more than one quadratic or higher order conserved quantity in the absence of dissipation; when the dissipation is introduced, there exists a selective dissipation process among the

A. Soloviev, R. Lukas, *The Near-Surface Layer of the Ocean,* Atmospheric and Oceanographic Sciences Library 48, DOI 10.1007/978-94-007-7621-0_5,

conserved quantities, that is, one conserved quantity decays faster than the other(s); and finally, the nature of the mode coupling through the nonlinear term(s) in the equation is such that the modal cascade in one of the quadratic quantities is toward small wavenumbers.

An example of such a hydrodynamic system is the two-dimensional incompressible fluid. It conserves the total energy, $b(t) = \frac{1}{2}\rho\int_D |\vec{u}|^2\, dV$, as well as a second quadratic quantity, the total squared vorticity (enstrophy), $W(t) = \frac{1}{2}\int_D \left|(\nabla \times \vec{u})\right|^2 dV$, where $\vec{u}(\vec{x},t)$ is the Eulerian velocity field defined in a three-dimensional domain D (bounded or unbounded). The enstrophy is a measure for the total vorticity of the flow.

When finite viscous dissipation is introduced, the energy spectrum for two-dimensional hydrodynamic turbulence cascades to smaller wavenumbers. On the other hand, the enstrophy spectrum cascades to higher wavenumbers (normal cascade) and dissipates due to viscosity. Consequently, energy accumulates at the longest wavenumber permitted in the system. From an energy point of view, such a state is considered organized.

The process of self-organization in two-dimensional turbulence is discussed in detail in Sect. 5.2. On a horizontal scale l exceeding the boundary-layer thickness h, the vertical component of motion in the upper ocean boundary layer is effectively suppressed due to stratification, and the boundary-layer processes are effectively two-dimensional. Mesoscale eddies and spirals, which are often seen in satellite images of the ocean surface, have been linked to two-dimensional turbulence. The baroclinic Rossby radius, L_R, determines the maximum horizontal scale of these coherent structures.

Another example of a nonlinear dissipative system with a tendency to self-organization is the helical structure (Moffatt and Tsinober 1992; Branover et al. 1999). The *helicity* of a fluid flow is defined as the integrated scalar product of the velocity field and the vorticity field in the following way: $\mathrm{H}(t) = \int_D \vec{u}\cdot(\nabla\times\vec{u})dV$. On an intuitive level, the vortex that has a nonzero axial component of velocity is characterized by nonzero helicity. Langmuir circulations in the ocean and tornadoes and tropical cyclones in the atmosphere are examples of the helical structure.

Organized structures are a characteristic feature of the atmospheric boundary layer as well. For instance, atmospheric convection produces clouds. The clouds modulate radiative fluxes and are a source of freshwater flux at the air–sea interface and thus induce spatial patterns in the sea surface temperature and salinity. This effect is especially strong in the tropical warm pools, because of deep atmospheric convection accompanied by heavy rainfalls. The "images" of the atmospheric processes in the upper ocean turbulent boundary layer evolve according to the laws of two-dimensional turbulence, producing organized structures in the upper layer of the ocean (possibly on scales different from the initial atmospheric scales). In Sect. 5.3, this process is described in the framework of a nonlinear diffusion model. This process is also interesting because the energy accumulation on large scales is accompanied by the development of narrow frontal zones between large-scale

structures. If a front becomes sharp enough, it may interact with the wind stress via the mechanism of *Stommel's overturning gate* (Sect. 5.4.4).

Since the diurnal thermocline and rain-formed halocline are stably stratified, they can develop internal wave motions. Under low wind speed conditions, the mixed layer depth reduces dramatically; as a result, the diurnal thermocline or rain-formed halocline is found in the upper few meters of the ocean. In this case, internal waves can be observed close to the ocean surface (Sect. 5.5). In some situations, perhaps due to interaction with shear or to resonant wave interactions, internal waves developing on the shallow diurnal thermocline become strongly nonlinear and exhibit billowing.

On horizontal scales $l \sim h$, the transition from two- to three-dimensional boundary-layer regimes occurs. Various types of organized structures like penetrative convection, ramps, billows, and Langmuir cells are interpreted as modes of the turbulent boundary-layer instability. These spatially coherent organized motions are discussed in Sects. 5.6–5.8.

Ramp-like structures appear in near-surface horizontal temperature records. The ramp-like structures have been found under both stable and unstable stratification conditions. Their phenomenology and the theory of this type of organized motion are discussed in Sect. 5.6.

In Sect. 5.7, we try to distinguish between the myths and realities regarding Langmuir circulations, one of the most controversial phenomena in the history of oceanography. Convection is discussed in Sect. 5.8. The importance of penetrative convection in the dynamics of the surface mixed layer has been addressed with a nonlocal parameterization scheme. How other types of organized structures contribute to nonlocal transport, however, is not yet completely clear.

5.2 Self-Organization in Two-Dimensional Turbulence

On horizontal scales exceeding the thickness of the upper ocean boundary layer, motions are quasi-two-dimensional due to stratification and/or rotation effects. Three-dimensional flow at large Reynolds numbers is chaotic and obeys statistical laws of isotropic turbulence, while a two-dimensional flow is governed by the anisotropic turbulence law and has the tendency to self-organization.

The upper ocean boundary layer is turbulent, yet it reveals features of organization. From this point of view, coherent structures in the ocean can be interpreted as a form of self-organization. Self-organization is a fundamentally nonlinear process; the mathematical description of the organized structures is hence complicated.

A distinction between three-dimensional and two-dimensional hydrodynamic processes is related to the effect of *vortex stretching*. Vortex stretching pulls matter toward the rotation axis of the vortex; owing to the conservation of angular momentum, it will rotate faster. Van Heijst (1993) compares this effect with the pirouette of a figure skater, who can increase her rotation rate by bringing both arms against her body. The absence of vortex stretching in two-dimensional flow leads to a spectral

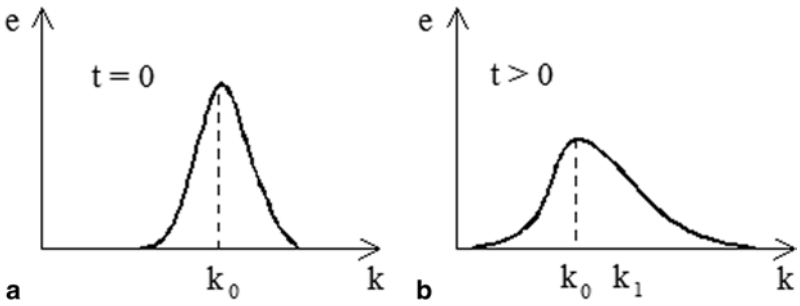

Fig. 5.1 The kinetic energy peak that initially is at the wave number k_0 **a** shifts to smaller values of k **b** in a two-dimensional flow due to nonlinear evolution of the system governed by conservation laws (5.2) and (5.3). (After Van Heijst 1993.)

flux of the kinetic energy from small to large spatial scales. This property directly follows from the equation for the vorticity $\vec{\omega} = (\nabla \times \vec{u})$ of the flow, where $\vec{u}$ is the velocity vector in the Eulerian coordinate system.

In a two-dimensional flow field $\vec{u} = (u, v, 0)$, as a result, the vorticity vector $\vec{\omega} = (0, 0, \omega)$ is always directed perpendicular to the flow direction. For inviscid flows, the vorticity vector $\vec{\omega}$ is a conserved quantity. Two other conservation laws that follow from the inviscid vorticity equation are

$$b = const \text{ and } W = const \tag{5.1}$$

where b is the kinetic energy and W is the *enstrophy* (defined in Sect. 5.1).

The *inverse energy cascade* in the wavenumber domain, a fundamental property of two-dimensional flows, is illustrated below by considering the conserved quantities b and V in spectral form (Van Heijst 1993). The kinetic energy and enstrophy are represented as follows:

$$b \sim \int_0^\infty e(k,t)dk = const. \tag{5.2}$$

$$W \sim \int_0^\infty k^2 e(k,t)\,dk = const. \tag{5.3}$$

where $e(k,t)$ is the wavenumber spectrum of kinetic energy at time t.

Suppose that the energy spectrum at some initial moment $t=0$ has a peak around a wavenumber k_0 (see schematic diagram in Fig. 5.1). Due to nonlinear interactions in the flow, the kinetic energy peak will broaden with time. According to (5.2), the total kinetic energy (*i.e.*, the area underneath the curve of e) should remain constant. In order to satisfy (5.2), the spectrum broadening has to be associated with a decrease in the spectral peak value. At the same time, according to (5.3), the spectral distribution of enstrophy, $k^2 e(k;t)$, must be conserved as well. In order to

satisfy both (5.2) and (5.3) in the process of the peak broadening the energy has to be redistributed from larger k to smaller k. As a result, the energy peak shifts to smaller k, and the energy spectrum becomes asymmetric (as schematically shown in Fig. 5.1). This effect is called the inverse energy cascade, because the kinetic energy of the two-dimensional flow exhibits a spectral flux from smaller to larger length scales, which is opposite to the normal energy cascade that is observed in three-dimensional flows.

In two-dimensional flows, an initial chaotic state where the various characteristics are distributed over the whole wavenumber spectrum ("white noise" is an example) evolves into a spatially coherent vortex structure. The kinetic energy of the flow thus concentrates or, adopting the terminology from similar nonlinear processes in quantum mechanics, "*condenses"* in the large-scale vortices. These vortices are often very stable and weakly dissipative.

The energy b and the enstrophy W are no longer conserved in two-dimensional turbulence in the presence of viscosity. If, however, the viscosity is not too large, the energy still shows a cascade to larger scales leading to organization. Two-dimensional flows are weakly dissipative, because molecular dissipation effects depend on velocity gradients and are relatively small on larger scales. In contrast to two-dimensional flows, energy in three-dimensional flows cascades to smaller length scales and efficiently dissipates due to molecular viscosity.

An important insight into the process of self-organization in two-dimensional flows comes from numerical simulations. Figure 5.2 shows the direct numerical simulation by McWilliams (1984). The striking result of this simulation is that initially randomly distributed vortices evolve into isolated vortex structures concentrating much of the kinetic energy.

Many times, almost circular vortices develop, although the formation of other types of vortices is observed under certain conditions. Van Heijst and Kloosterziel (1989) proposed the following classification for stable vortices: (1) a *monopolar vortex*, approximately axisymmetric (or slightly elliptic), possessing a net angular momentum; (2) a *dipolar vortex*, which consists of two counter-rotating vortices and has net linear momentum; and (3) a *tripole vortex*, which consists of an elliptic central vortex, flanked by two weaker satellite vortices of opposite circulation. Even higher order vortex structures form but seem to be unstable.

In addition to numerical simulations, the dynamics of coherent vortices has been studied in laboratory experiments. The flow in the laboratory setting can effectively be made two-dimensional by the presence of rotation and/or stratification, magnetic fields, or geometry (Van Heijst 1993). Likely, as a result of the variety of mechanisms used to make a flow two-dimensional, there is increasing interest not only within the field of geophysical fluid dynamics but also in disciplines such as plasma physics and even astrophysics. In particular, the Great Red Spot on Jupiter is believed to be an organized structure—the eddy. Coherent structures are also likely present on the Sun and in the accretion disks of neutron stars.

In the laboratory experiments of Van Heijst and Flor (1989) and Voropayev et al. (1991), a dipole was generated by horizontal, turbulent injection of a small amount of fluid in a tank filled with a continuously stratified fluid (Fig. 5.3). Although the

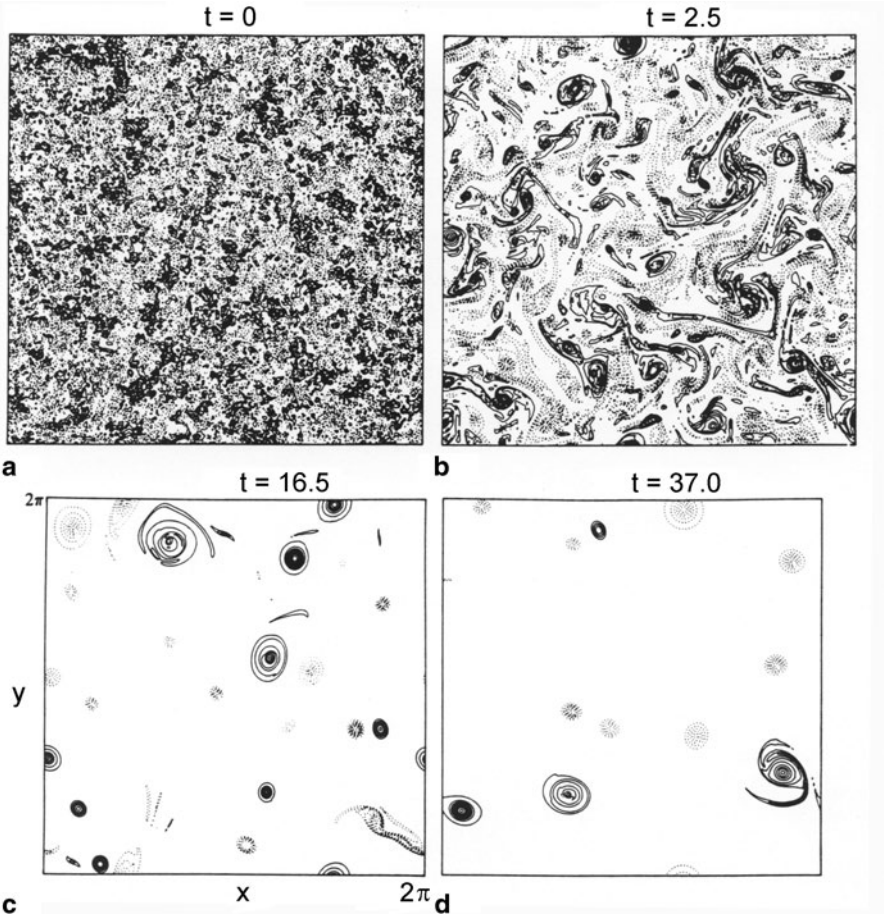

Fig. 5.2 In a two-dimensional flow, initially randomly distributed vorticity. **a** Evolves into isolated vortex structures (**b**, **c**, and **d**). Results of direct numerical simulation by McWilliams (1984). Reproduced with permission from Cambridge University Press

generated motion was initially three-dimensional, vertical motions of the injected turbulent cloud are rapidly suppressed by the surrounding stratification. As a result, the turbulence rather quickly assumes a two-dimensional character. Next, the effect of the inverse energy cascade increases the vortex scales, for instance, by merging vortices (as demonstrated in Fig. 5.4), ultimately resulting in the appearance of an organized dipolar structure.

The interaction between separate vortices is an important part of the process of self-organization in two-dimensional flows. A basic interaction occurs between two monopolar vortices, of either equal or different size, strength, and polarity. Figure 5.4 illustrates the merging of two identical monopolar vortices. At a specific distance from each other, the vortices merge to form a new vortex. At first the vortex

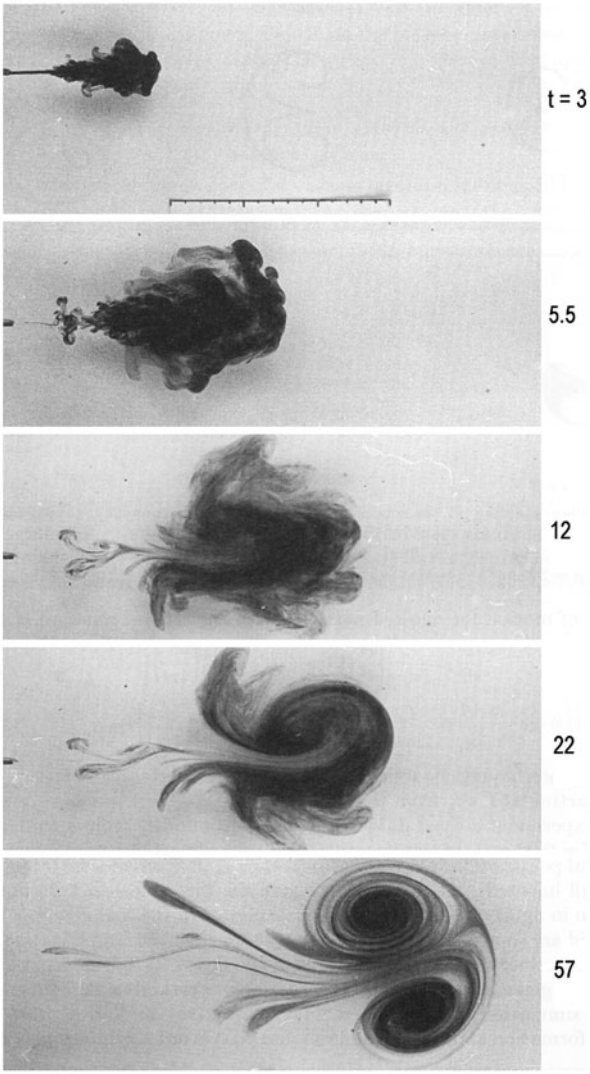

Fig. 5.3 Top-view photographs made during the laboratory experiment of Voropayev et al. (1991) in a stratified fluid: An organized dipolar vortex appears from a turbulent cloud.Scale is in cm, time (t) in s. Reproduced with permission from Cambridge University Press

is elliptic, but later it becomes axisymmetric. The 'strain' caused by the neighboring vortex causes the development of two characteristic spiral arms in both initial vortices, consisting of thin vorticity filaments. Formation of spiral arms is also observed in a single vortex placed in a nonuniform background flow, which may be caused by the presence of remote vortices.

The spiral eddies observed in the laboratory experiments can be seen in images of the ocean surface from manned space flights. Dr. Robert Stevenson was the first to discover such spiral eddies on the ocean surface. The spirals appear to be globally distributed, 10–25 km in size and overwhelmingly cyclonic in the North-

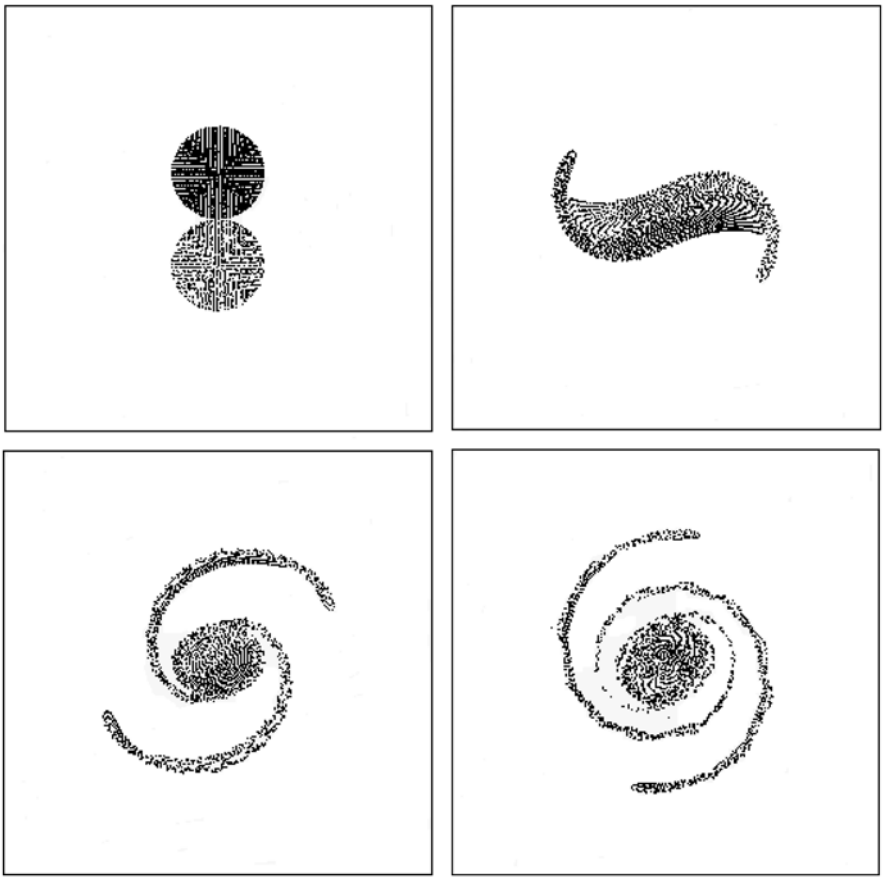

Fig. 5.4 Merging of two identical monopolar vortices from the numerical simulation by Van Heijst (1993)

ern Hemisphere and anticyclonic in the Southern Hemisphere. Figure 5.5 shows a visual image of spiral structures taken during a Space Shuttle mission. During this mission, the crew had excellent viewing conditions in the Southern Hemisphere:

> …During the first two days of the mission, the crew commander reported that the southern oceans were 'essentially featureless'. By the third day, the ocean had changed. The commander reported to Mission Control that the entire southern Indian Ocean, Tasman Sea, and southwestern Pacific Ocean were covered with spiral eddies and remained so for the rest of the mission. The crew took overlapping pairs of photographs showing the spiral eddy field in great detail. Streamlines of the flow into and between eddies formed slicks on the sea surface. At first, the features were supposed to be the result of local wind action over the sea, but other data indicated that eddies extended to depths of several tens of meters and thus were an integral part of the dynamics of the upper ocean. Other data showed that the streamline slicks did indeed flow into eddies at speeds greater than the surrounding water. (Stevenson 1998, 1999.)

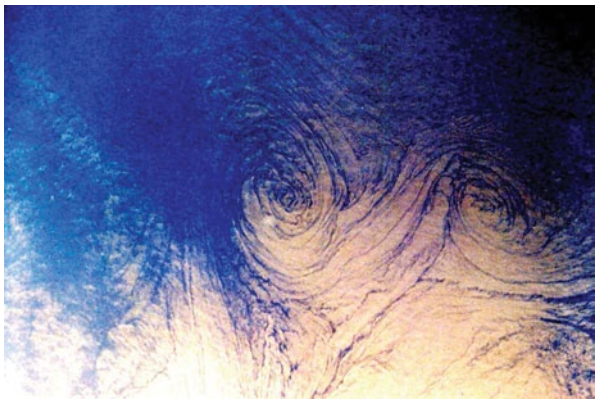

Fig. 5.5 Spirals on the ocean surface from the collection of Stevenson (1985)

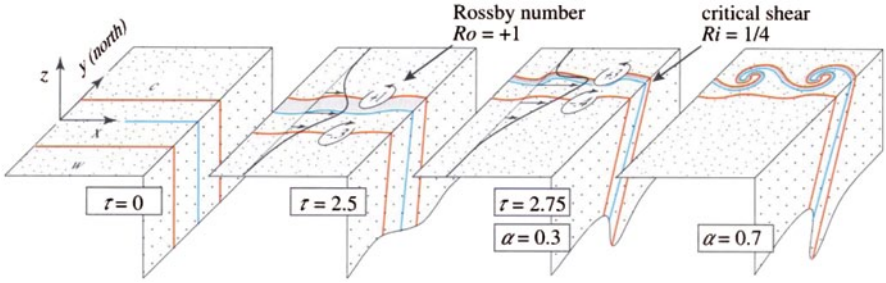

Fig. 5.6 Cartoon of ocean spiral generation. An initial horizontal density gradient (cold to the north) in a mixed upper layer is portrayed by the central isopycnal (*blue*) and the two frontal isopycnals (*red*). With increasing time t, the isopycnals move together, tilt toward the north, translate northward, and eventually converge at the surface on the positive frontal isopycnal. A developing eastward jet turns increasingly asymmetric, with strong cyclonic shear (large positive Rossby numbers) to the north and weak anticyclonic shear to the south. A downward tongue under the "north wall" and upwelling to the south modify the depth of the mixed layer. The Rossby number along the north wall increases rapidly from +1 to +3 between the times t=2.5 and 2.75, when critical vertical shear develops near the surface. Horizontal shear instability develops along the north wall for $Ro > 1$, with an intensifying cat's-eye flow pattern characterized by nondimensional parameter a (see Stuart (1967) for details). Ambient surfactants are compressed and aligned along the north wall, and wound into cyclonic spirals. (After Munk and Armi 2001.)

Munk and Armi (2001) proposed the explanation for spiral structures illustrated in Fig. 5.6. The local frontogenesis process enhances the geostrophically balanced ambient ocean vorticity (which is of order $\pm 10^{-1} f$) and concentrates surfactants along a converging line. When the frontal shear becomes comparable to f, instabilities lead to cross-frontal flow accompanied by a twisting, *cat's-eye* circulation pattern. The cat's-eye circulation twists the convergence line and neighboring linear features into a cyclonic spiral, while stretching and further thinning the lines of surfactant concentration.

The mathematical basis of the spiral structures in the ocean can be linked to the theory of singular solutions of two-dimensional quasi-linear hyperbolic equations (Golitsyn 2012). In a general form, these singular solutions are described as follows (Maslov 1980; Dobrokhotov et al. 2003):

$$\omega = f(x,t) + g(x,t)F(S(x,t)) \tag{5.4}$$

where ω is a vector (or scalar) function, $x \in R^n$, $F(\tau)$ is a scalar function with a singularity at the point $\tau = 0$ and smooth outside $\tau = 0$; the phase $S(x,t)$, as well as the vector (or scalar) background $f(x,t)$ and the amplitude $g(x,t)$, are smooth functions.

Equation (5.4) represents three types of singular solutions (Maslov 1980): delta function, a piecewise constant function (the Heaviside function), and a solution, which is characterized by root singularities. The oceanic analogs of these solutions are narrow solitons (e.g., linked to the Korteweg–de Vries soliton), sharp fronts, and solitary eddies. For the third-type solution, the shallow water equation of a rotating fluid produces a vortex solution of an arbitrary type, which can be related to spiral structures in the upper ocean.

According to Golitsyn (2012), the Munk and Armi (2001) shear instability mechanism, as well as the Eldevik and Dysthe (2002) baroclinic instability mechanism, take from 5 to 15 days to generate spiral type eddies. Golitsyn (2012) considered an additional mechanism, which can lead to a rapid formation of spiral structures. This mechanism is related to convective mixing of the upper ocean due to surface cooling interacting with the Earth's rotation. The scale estimates following from the Boubnov and Golitsyn (1990) laboratory experiment in a rotating layer of fluid with convective motions are consistent with observations of spiral structures in the ocean. Interestingly, this mechanism is also applicable to dynamics of tropical cyclones and polar lows in the atmosphere (Golitsyn 2008).

Near the equator, thin lines on the sea surface rather than spirals are observed (Fig. 5.16), due to diminished planetary vorticity. The next two sections, Sects. 5.3 and 5.4, elucidate the role of nonlinear interactions in the formation of organized structures in the near-surface ocean for the example of equatorial warm pools.

5.3 Horizontal Mixing as a Nonlinear Diffusion Process

Atmospheric convective complexes dominate the planetary boundary layer in the warm pool area and are responsible for the 3–5 m yr^{-1} of precipitation. Convective rains produce surface *puddles* of the order of 10 km diameter containing appreciable salinity, temperature, and density anomalies. These puddles store significant potential energy, which when released in the form of gravity currents substantially contributes to mixing. This process is associated with vertical shearing, which involves nonlinear dynamics. Since it is a two-dimensional system, the initial disturbances have a tendency to self-organization.

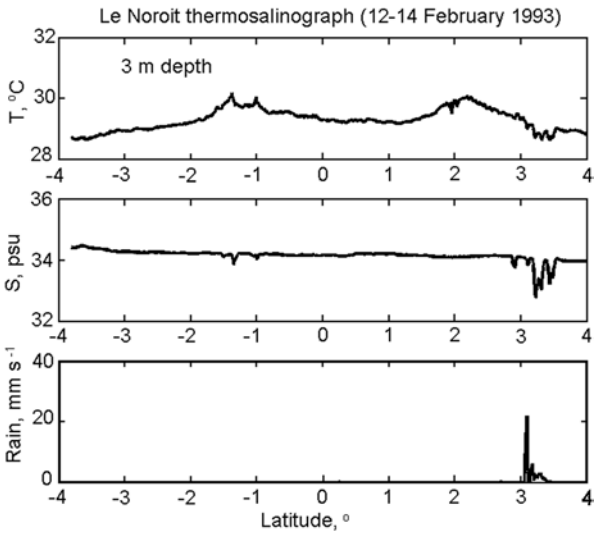

Fig. 5.7 Patchy rainfall from convective clouds produces localized freshwater puddles in the near-surface layer of the ocean

5.3.1 Horizontal Wave Number Statistics

We start our discussion from the analysis of some observable features of the horizontal wavenumber statistics in the warm pool area. Figure 5.7 shows a record from a shipboard thermosalinograph (TSG) in the western Pacific warm pool obtained during the Tropical Ocean-Global Atmosphere Coupled Ocean–Atmosphere Response Experiment (TOGA COARE) from a depth of 3 m (Delcroix et al. 1993). Rainfall was observed between 3°N and 3.5°N. This rainfall produced a localized salinity anomaly. In the temperature record, the freshwater puddle did not produce any prominent feature.

Figure 5.7 represents one of 16 sections of the R/V *Le Noroit* made from 5°S to 5° N along 156° E during TOGA COARE from December 1992 through March 1993. The average density spectrum calculated from all 16 sections of the TSG data is shown in Fig. 5.8. In the wavenumber range $k < 4 \cdot 10^{-4}$ m^{-1}, the experimental spectrum is approximated by a k^{-1} dependence, which is consistent with the k^{-1} law that follows from the theory of quasi-geostrophic two-dimensional turbulence for a passive tracer (Batchelor 1969; Kraichnan 1975). According to the same theory, at even lower wavenumbers the k^{-1} law transforms into a $k^{-5/3}$ spectral law. The statistics presented in Fig. 5.8, however, are not sufficient to resolve the spectral dependence at low wavenumbers with sufficient confidence.

For $k > 4 \cdot 10^{-4}$ m^{-1}, which corresponds to wavelengths $\lambda < 16$ km, the experimental spectrum switches to a k^{-3} dependence. In this subrange, the experimental spectrum is not consistent with the theory of Batchelor (1969) and Kraichnan (1975). An explanation is that for submesoscales, density can no longer be treated as a passive tracer.

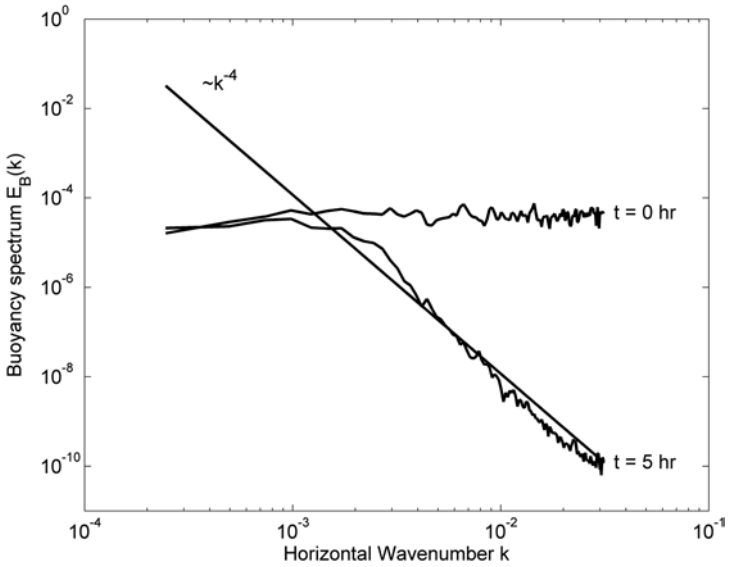

Fig. 5.8 Scaled density wave number spectra from the *Le Noroit* thermosalinograph observations (averaged over 16 meridional sections)

The equatorial baroclinic Rossby radius for the density anomalies within the mixed layer of the warm pool area, L_β, is of the order of 10–20 km. Rotation effects therefore are not expected to be of primary importance on scales smaller than 10 km.

5.3.2 Nonlinear Advection–Diffusion Model

The process of puddle evolution is associated with vertical shearing, which involves Taylor's shear dispersion mechanism and nonlinear dynamics. Ferrari and Young (1997; hereafter FY97) and Ferrari et al. (2001) considered a nonrotating stratified fluid and developed a model for nonlinear horizontal diffusion. They used the Boussinesq approximation and a linear equation of state for seawater to derive the following system of equations:

$$D\vec{u} / Dt = -\nabla p + g(\rho - \rho_0) / \rho_0 \vec{z} + mix \tag{5.5}$$

$$\nabla \cdot \vec{u} = 0, \tag{5.6}$$

$$DS / Dt = mix \tag{5.7}$$

$$DT / Dt = mix \tag{5.8}$$

where $\vec{u} = (u, v, w)$, g is the acceleration of gravity, ρ is density, ρ_0 is a constant reference density, D is the full (material) derivative operator, ∇ is the gradient operator, and "*mix*" indicates that an instantaneous homogenization is applied to momentum and the stratifying components.

Based on Taylor's shear dispersion mechanism, Young (1994) introduced a nonlinear dependence of the mixing coefficient on the buoyancy gradient, which, in the formulation of FY97, is as follows:

$$K_h = \gamma f(|\nabla_h B|)(\nabla_h B \cdot \nabla_h B), \tag{5.9}$$

where $\gamma = h^2\tau^3 / 96$, h is the depth of the mixed layer, τ is the vertical homogenization timescale, $B = -g(\overline{\rho} - \rho_0)/\rho_0)$ is the buoyancy, $\overline{\rho}$ is the fluid's density (averaged over the mixed layer depth and some time interval), ρ_0 is a constant reference density, g is the acceleration of gravity, ∇_h is the horizontal gradient operator, and $f\left(\left|\nabla_h B\right|\right)$ is a nondimensional function whose form depends on details of the hydrodynamic instabilities that dominate the flow.

Applying (5.9) to the equations for buoyancy (averaged over the depth of the upper ocean mixed layer), FY97 obtained the following nonlinear advection–diffusion equation:

$$\partial_t B + \vec{u} \cdot \nabla B = \gamma \nabla \cdot \left[f(|\nabla B|)(\nabla B \cdot \nabla B)\nabla B \right] + \Phi_B, \tag{5.10}$$

where $\vec{u}$ is the horizontal velocity field and the term Φ_B relates to the thermohaline fluxes from the top and bottom of the mixed layer.

5.3.3 *Buoyancy Flux Through the Bottom of the Mixed Layer*

Turbulent entrainment, upwelling events, and internal wave effects can cause the horizontal modulation of the buoyancy flux through the bottom of the mixed layer. Horizontal wavenumber statistics below the mixed layer can help to understand this process.

Figure 5.9 gives an example of the horizontal wavenumber spectrum averaged over a 60–110 m depth range. These data are also from the western equatorial Pacific for approximately the same time period as the spectrum in the mixed layer shown in Fig. 5.8. Comparison of the experimental spectra with the theoretical model of internal waves that accounts for the isotropic internal wave field and the lower modes of the M_2 baroclinic tide suggests that the internal wave processes could substantially determine the wavenumber statistics in this depth range and in the wavenumber range under consideration.

Internal waves modulate the vertical shear and the density gradient and, ultimately, the gradient Richardson number, *Ri*. The spectrum of the Richardson number associated with the Garrett and Munk model of internal waves is "white" (*i.e.*, it does not depend on frequency), except for the lowest few modes that are close to the

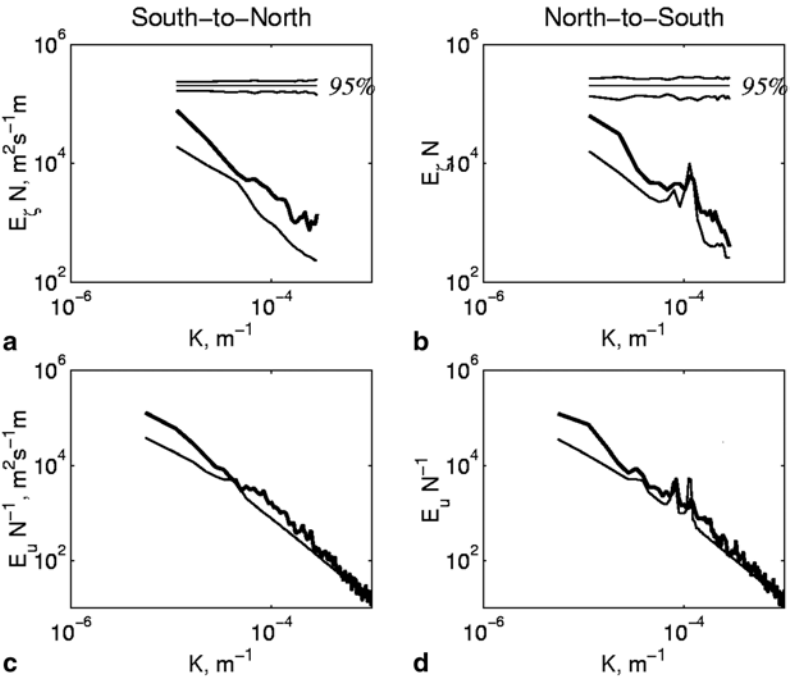

Fig. 5.9 Comparison of the WKB-scaled (**a**, **b**) density displacement and (**c**, **d**) horizontal velocity spectra from the R/V *Le Noroit* South-to-North and North-to-South meridional sections (5° S to 5° N) with the internal wave towed spectral model. The experimental spectra (bold lines) are averaged within the depth range from 60 to 110 m. The model spectra (thin lines) represent the sum of the Feng et al. (1998) tidal model and the Garrett–Munk wave number spectrum. Confidence intervals are also shown. The ADCP and SEASOAR data were collected by Eric Firing and Kelvin Richards. Reproduced with permission from John Wiley and Sons

inertial frequency. Near-inertial waves are associated with a drop in *Ri*. Overturning and turbulent entrainment occurs when *Ri* drops below its critical magnitude (about 0.25). The buoyancy influx from the thermocline to the mixed layer caused by the isotropic internal wave field is therefore more probable on horizontal scales of inertia-gravity waves.

Cabanes (1999) analyzed the modulation of the mixed layer thermodynamics by a long ($\lambda_{IG} \sim 1000$ km), equatorial inertia-gravity wave using a quasi-two-dimensional model of the Price-Weller-Pinkel (PWP) type (Price et al. 1994). He concluded that these waves could produce mixed layer temperature and salinity anomalies with the same horizontal length scale and a cascade of smaller scale anomalies due to the differential entrainment depending on the internal wave shear and atmospheric forcing.

Tidal motions constitute a significant fraction of the background velocity field in the COARE domain (note tidal peaks on the spectra from north-to-south sections in Fig. 5.9). Having low vertical mode structure away from their generation region, the internal tidal waves have relatively small shear (Pinkel 2000). The M_2 baroclinic

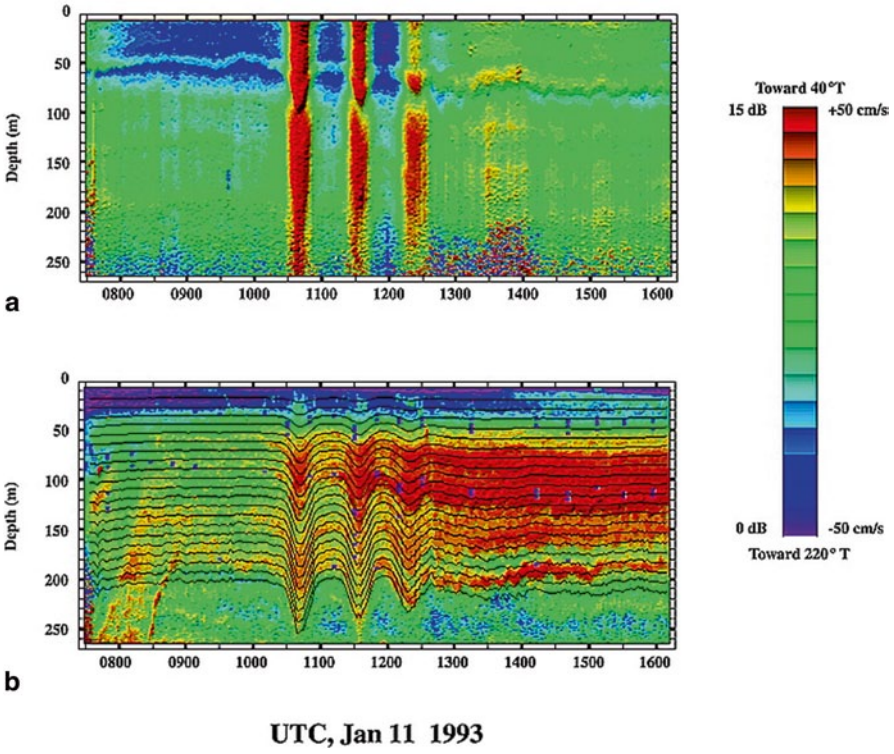

Fig. 5.10 A solibore observed on 11 January 1993 in the COARE domain at 2° S, 156° E. **a** The along-path (40°–220°) component of absolute ocean velocity. Note that sonar precision degrades below 200 m, a consequence of low signal level at great range. **b** The acoustic scattering strength field at 161 KHz, following adjustment for inverse square spreading and attenuation. Colors represent variation on a logarithmic scale over a factor of 30. Calculated flow streamlines are superscribed in black. Regions of the thermocline with unstable density gradient, as determined by the CTD, are indicated by purple rectangles. After Pinkel (2000). Copyright © 2000 American Meteorological Society. Used with permission

tidal wave in the western equatorial Pacific warm pool is, however, often accompanied by solitary internal wave packets (*solitons*), which, during spring tides, take the form of undular bores (*solibores*) (Fig. 5.10).

The COARE solitons are phase-locked with the internal tides. The wavelength of the first M_2 baroclinic mode in the COARE domain is $L_{BT} \sim 100$ km (Feng et al. 1998). However, the wavelength of the soliton is only about 6 km.

In the example shown in Fig. 5.10, three wave crests appear ordered in amplitude. The first crest is the largest one and has a horizontal velocity that exceeds 0.8 m s^{-1} relative to the Earth and 1.0 m s^{-1} relative to the background mixed layer. The crests are spaced ~40 min apart (when interpolated to a fixed position of the ship).

The packet passage occurred several hours after the internal tide elevation of the thermocline reached maximum around 0800 UTC. The currents in the upper ocean (0–80 m) continued to be directed toward the southwest for several hours following the first soliton, reversing to a northwest flow only after passage of the third soliton.

According to Pinkel (2000), the intrinsic shear associated with solibores is not sufficient to trigger Kelvin–Helmholtz instability in a quiescent background. The minimum Richardson number remained relatively large (above 15). Solibores, however, may trigger instability of the background shear in an environment with gradient Richardson number not much larger than ¼ and can result in the thermohaline fluxes through the bottom of the mixed layer.

The rapid development of high-frequency internal waves on the equatorial shear has also been observed in association with the nocturnal convection in the eastern equatorial Pacific (Mack and Hebert 1997). Nocturnal convection can also trigger packets of strongly nonlinear internal waves on the shear associated with the diurnal jet (see Sect. 5.5).

Mathematical modeling of the response of the mixed layer to the soliton forcing is complicated by the difficulty in solving the resulting nonlinear equations in the presence of vertical shear, which is ubiquitous in the upper ocean environment. As a result, the induced dynamic instability in a nearly critical background flow is still largely unexplored (Sandstrom and Oakey 1995).

5.3.4 Atmospheric Buoyancy Forcing

In general, the buoyancy flux into the mixed layer through the air–sea interface is as follows:

$$\Phi_{Ba} = -\frac{\alpha_T g}{c_p \rho}\left\{Q_E + Q_T + I_L - (1-A)I_\Sigma[1 - f_R(h)]\right\} + \beta_S g S_0 \left(\frac{Q_E}{\rho L} - P\right) + \alpha_T g P \frac{c_p \rho}{c_{pr}\rho_r}(T_r - T_0), \tag{5.11}$$

where P is the rain rate, c_p is the specific heat, ρ is the density of sea water; c_{pr} is the specific heat, ρ_r is the density of rain water; L is the latent heat of evaporation, S_0 is the surface salinity, β_S is the coefficient of salinity expansion, T_r is the raindrop temperature, and T_0 is the sea surface temperature. The term in brackets on the right side of eq. (5.11) is the buoyancy flux due to air–sea heat fluxes (I_R is the insolation, I_L is the effective longwave radiation, and Q_E and Q_T are the latent and sensible heat fluxes, respectively). The second term is the buoyancy flux due to the surface salinity change because of evaporation and rain. The third term is the buoyancy flux due to the heat flux because of the difference between the raindrops and seawater temperature. Here, we ignore the volume nature of the rain-induced buoyancy flux.

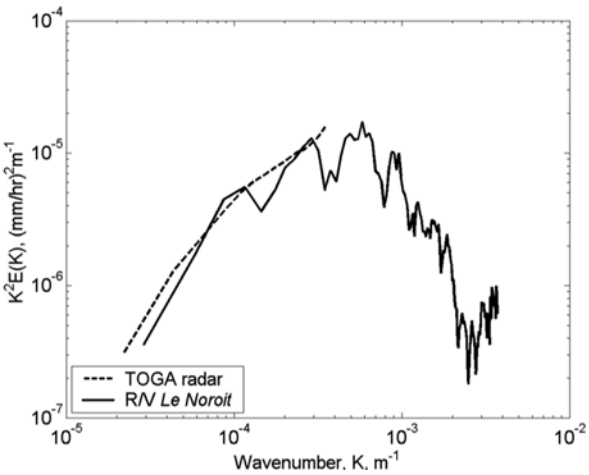

Fig. 5.11 Comparison of the TOGA rain radar and the R/V *Le Noroit* rain gauge spectra averaged over the time period from 14 December 1992 through 2 January 1993 and over approximately the same latitude range as in Fig. 5.8 (the longitudinal coverage is different, but overlapping). Here, $E(k)$ is the rain rate wave number spectrum. Rain radar data after Short et al. (1997); shipboard data are after Delcroix et al. (1993).

Substantial spatial and temporal variability of the buoyancy flux into the mixed layer is observed in the tropics due to convective rainfalls. Rain rate spectra from the TOGA radar and the R/V *Le Noroit* rain gauge shown in Fig. 5.11 reveal a maximum in the spectrum of horizontal precipitation rate gradients, $k^2E(k)$, at approximately 20 km wavelength.

5.3.5 Equilibrium Subrange

The analysis in the rest of Sect. 5.3 considers the effects of buoyancy flux into the top of the mixed layer. However, it is applicable to the anomalies produced by internal forcing as well. In the latter case, parcels of heavier water would spread along the bottom of the mixed layer (in contrast to the parcels of lighter water spreading along the ocean surface).

During heavy rainfalls, low-salinity lenses of the order of $L_c \sim 10$ km diameter form at the surface (see Sect. 4.2.5). The initial buoyancy anomalies produced by convective rains tend to spread due to pressure gradient forces and produce frontal structures due to nonlinear interactions. On horizontal scales comparable to the thickness of the upper ocean boundary layer, the density inhomogeneities are three-dimensional and dissipate due to turbulent mixing. On these spatial scales, the boundary-layer mechanisms that eliminate horizontal density anomalies can be enhanced or suppressed due to the effects of wind stress crossing sharp frontal interfaces (see Sect. 5.4). Rotation effects are important on the horizontal scales comparable to the baroclinic Rossby radius L_f (or to its equatorial version L_β).

Since there is frequent influx of buoyancy from convective rainfalls, there is a continuous creation, evolution, and dissipation of the density anomalies in the warm pool area. Here, we hypothesize that there is a wavelength range, $h << \lambda << \min$

$\{L_c, \lambda_{IG}, L_\beta, L_f\}$, in which the spectrum of horizontal buoyancy inhomogeneities in the warm pool area, $E_B(k)$, can be saturated. The analysis of Eq. (5.10) suggests that the equilibrium buoyancy spectrum in this subrange will depend on horizontal wavenumber vector $\vec{k}$, mixed layer depth h, vertical homogenization time τ, and a parameter characterizing the horizontal variability of the density field, $\langle \nabla B \cdot \nabla B \rangle$.

A standard dimensional analysis then leads to the following formulation for the horizontal wavenumber spectrum of buoyancy:

$$\Psi_B(\vec{k}) / \langle \nabla B \cdot \nabla B \rangle = k^{-4} f_B(\alpha, kh, \mu), \tag{5.12}$$

where α denotes the direction of the wavenumber vector $\vec{k}$ (the polar angle relative to wind direction, for instance), f_B is a function, and parameter kh is associated with the turbulent boundary-layer processes. For horizontal scales exceeding 1 km, parameter kh is very small and formally can be dropped from the number of determining parameters in (5.12). Parameter μ is given by

$$\mu = \tau^4 \cdot \langle \nabla B \cdot \nabla B \rangle. \tag{5.13}$$

Under the assumption of directional isotropy, the one-dimensional wavenumber buoyancy spectrum is obtained by integration over angle α:

$$E_B(k_x) / \langle \nabla B \cdot \nabla B \rangle = \int_0^{2\pi} \Psi_B(\vec{k})\, k\, d\alpha \approx k_x^{-3} F(k_x h, \mu) \approx c(\mu) k_x^{-3}, \tag{5.14}$$

where F is a universal function of its nondimensional arguments kh and μ. For $kh << 1$, we assume that $F(kh, \mu) \approx c_B(\mu)$, since kh can formally be dropped out of the number of determining parameters. The explicit form of F as a function of kh can in principle be obtained by merging turbulent boundary-layer spectra (Kamal et al. 1972; Wijesekera et al. 2001) with the spectrum of two-dimensional turbulence.

After replacing buoyancy B in (5.14) with its expression via density ρ, the one-dimensional horizontal wavenumber spectrum of density is as follows:

$$E_\rho(k_x) / \mathrm{var}(\partial_x \rho) \approx c_B(\mu) k_x^{-3} \tag{5.15}$$

where c_B is another universal function of its nondimensional argument μ.

As we can see from Fig. 5.8, in the wavenumber range, $k_x > 4 \cdot 10^{-4}\ \mathrm{m}^{-1}$, which corresponds to the wavelength range $\lambda < 16$ km, the experimental spectrum follows the k_x^{-3} law predicted by Eq. (5.15). Function $c_B(\mu)$ used to show the k^{-3} spectral law in Fig. 5.8 depends on parameter μ, which is related to the vertical mixing process and horizontal buoyancy gradients via Eq. (5.13).

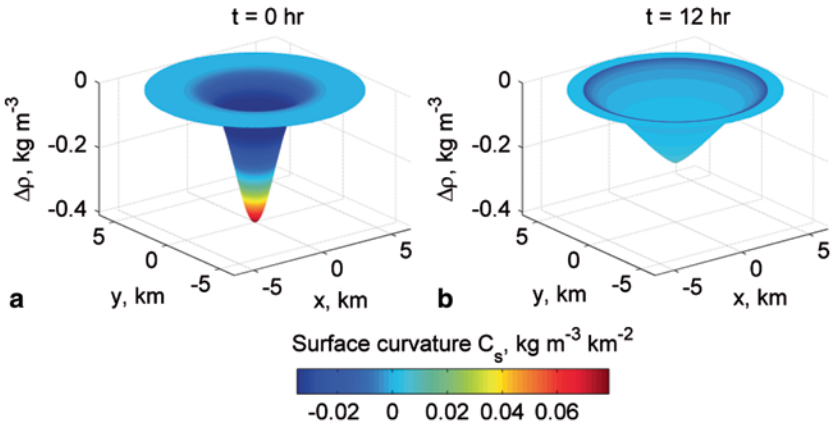

Fig. 5.12 Evolution of a freshwater lens: **a** initial condition ($t=0$), and **b** solution of the advective–diffusion equation for $t=12$ hrs. Here, $\Delta\rho = \rho - \rho_0$. The surface curvature, which is defined here as a Laplacian $C_s = (\partial^2_{xx}\rho + \partial^2_{yy}\rho)/4$, is indicated by color (scale given by color bar). In subplot (**b**) the surface curvature at the cone apex is so localized that it cannot be effectively displayed in color

5.3.6 *Numerical Diagnostics of Nonlinear Diffusion Equation*

Numerical diagnostics of the nonlinear diffusion equation (5.10) can help to understand the essential physics beyond the universal spectrum (5.13). We consider the following simplified form of Eq. (5.10):

$$\partial_t B = \gamma \partial_x \left[(\partial_x B)^3 \right] + \Phi_B, \tag{5.16}$$

where $B = -g\Delta\rho(x,t)/\rho_0$, $\gamma = h^2\tau^3/96\,h$ is the mixed layerdepth, and τ is the vertical mixing timescale. Boundary conditions are set as follows: $\partial_x B = 0$ at $x=-\Delta L/2$ and $x=\Delta L/2$, where ΔL is the domain size.

For an axisymmetric case, Eq. (5.10) can be written in polar coordinates (r, α), where r is the radial distance and α is the polar angle. Being extended evenly for $r<0$, the axisymmetric version of equation has the same form and the same boundary conditions as Eq. (5.16) but with x replaced by r.

The preliminary numerical diagnosis of Eq. (5.16) was performed in *Matlab* with a partial differential equation (PDE) solver. This solver had been tested with an analytical solution of Eq. (5.16) given in Landau and Lifshitz (1993); the test showed a perfect agreement between the analytical and numerical solution.

The numerical solution for an axisymmetric smooth initial shape (Gaussian type profile) and at $\Phi_B = 0$ (*decay problem*) is shown in Fig. 5.12. The initial shape of the density anomaly has a tendency to evolve into a *conic* structure (Fig. 5.12b). Zones with increased curvature are localized at the top and the base of the conic structure,

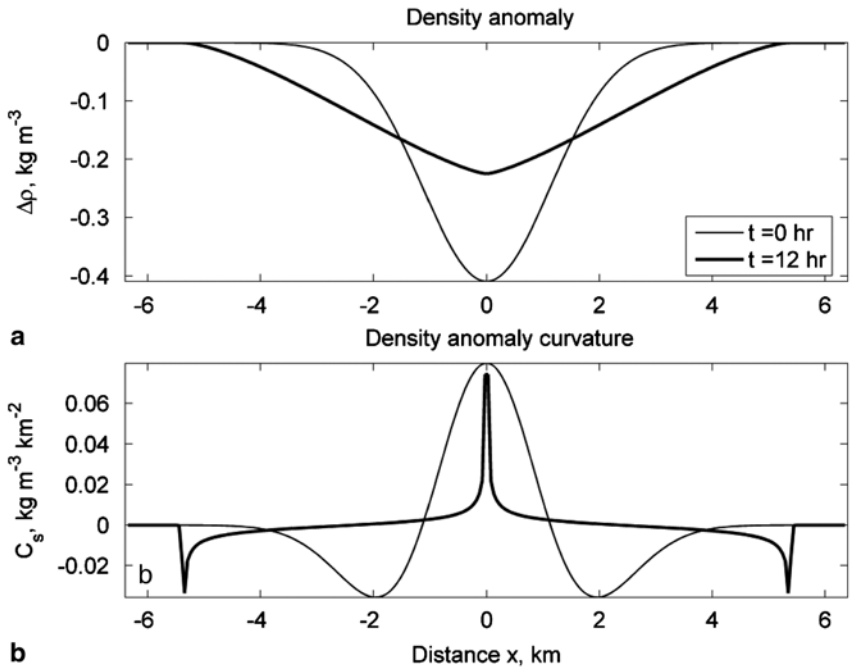

Fig. 5.13 **a** A projection of the axisymmetric solution shown in Fig. 5.12 onto the x-axis. Note the tendency to form "spikes" of the horizontal buoyancy curvature (**b**), which leads to certain spectral laws

which appears to have important implications for the wavenumber statistics to be considered later. Between the top and the base of this cone, the solution asymptotically tends to a linear dependence on the radial distance r, which means that $\partial_r \rho(r) \to const$ and no length scale dependence is involved.

A projection of this axisymmetric solution onto the x-axis is shown in Fig. 5.13. In this projection, the initial Gaussian profile evolves into a *triangular structure*. The triangular structure has curvature spikes at the top and base points. The wavenumber spectrum of such spikes is white noise. Double-integrating the density anomaly curvature back to the buoyancy in the wavenumber domain spectrum is equivalent to multiplication by k^{-4}. Integrating the density anomaly spectrum over all directions, as in (5.14), results in a k_x^{-3} spectral law, which is consistent with experimental data shown in Fig. 5.8.

The second numerical experiment used a random initial condition in the form of white noise. Results of this experiment are shown in Fig. 5.14. In this case, the initial white spectrum also evolves into a k^{-4} dependence (which corresponds to a k_x^{-3} spectrum after integrating over all directions).

The above tests indicate that the nonlinear system described by Eq. (5.16) tends to produce spikes in buoyancy curvature. According to Simpson and Linden (1989), an increased curvature of buoyancy drives frontogenesis.

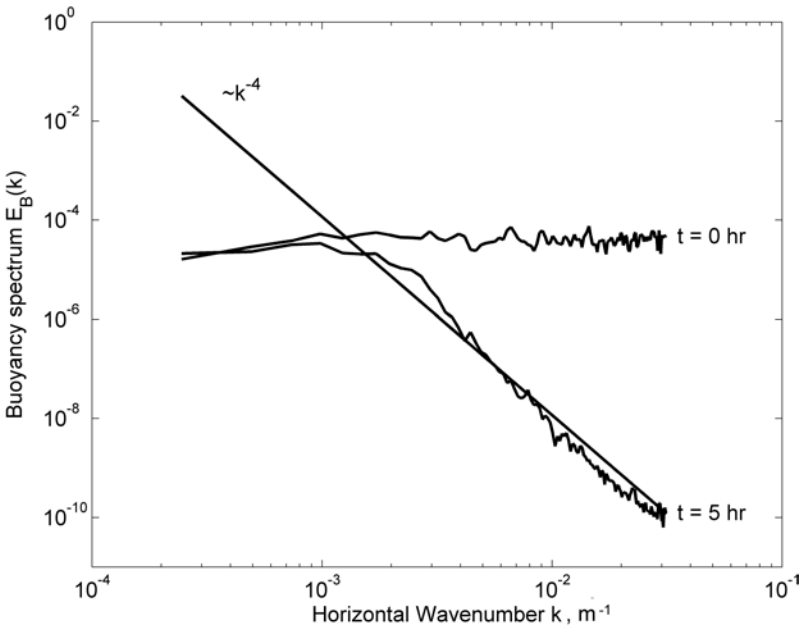

Fig. 5.14 Spectral saturation due to nonlinear diffusion

The model considered above is a vertically integrated, slab model of the mixed layer. It is not able to describe the vertical structure of fronts, which are characterized by the presence of an inclined pycnocline. In this type of model, the signature of a front is the increased curvature of the horizontal buoyancy (temperature, salinity) distribution.

The approach undertaken here to derive the theoretical spectrum (5.15) has some analogy with that used by Phillips (1977) to derive the wavenumber spectrum of surface waves in the saturation subrange. According to Belcher and Vassilicos (1997), the surface wave field is a superposition of sinusoids plus sharp-crested breaking waves. The sharp-crested waves have a spike-like curvature, which leads to Phillip's spatial $F(\vec{k}) \sim k^{-4}$ and, thus, one-dimensional $f(k_x) \sim k_x^{-3}$ wavenumber spectra. In particular, this analogy may be useful in specifying function $c_B(\mu)$ entering spectrum (5.15).

In this preliminary analysis, we have ignored the advection term $\vec{u} \cdot \nabla B$. Feng et al. (2000) showed the importance of advection on the salinity budget within the western Pacific warm pool. Comparative analysis of advection and atmospheric forcing may elucidate the difference between the warm pool and mid-latitude processes. In fact, when the advection forcing with no atmospheric forcing is considered, the wavenumber spectrum appears to be steeper than k_x^{-3} (Ferrari and Paparella 2003).

Table 5.1 Estimates of horizontal mixing coefficient in the warm pool area from Eq. (5.17) (h is the mixed layer dept hand τ is the vertical homogenization time)

Environmental conditions	h m	τ s	$g^2\overline{\nabla\rho\cdot\nabla\rho}/\rho_0^2$ s^{-4}	K_h m^2 s^{-1}	K_h/K_V
Westerly wind burst	75	3600	1.6×10^{-13}	0.44	1.1
Low wind and heavy rain	10[a]	12×3600	5×10^{-12}	420	726,000

[a] A barrier layer is assumed to be located below 10 m depth

5.3.7 Relationship Between Vertical and Horizontal Mixing and Atmospheric Forcing Conditions

Within the range of horizontal length scales exceeding the thickness of the mixed layer but not yet affected by the Coriolis force, the horizontal mixing coefficient is as follows:

$$K_h = \gamma\overline{\nabla B\cdot\nabla B} = \frac{h^2\tau^3}{96}\frac{g^2\overline{\nabla\rho\cdot\nabla\rho}}{\rho_0^2} \tag{5.17}$$

which has been inspired by theoretical formula (5.9) and an assumption that $f\equiv 1$ (as in FY97). In the framework of this model, the vertical mixing coefficient is defined as

$$K_V = \frac{h^2}{4\tau}. \tag{5.18}$$

From (5.17, 5.18), and (5.13), the ratio between horizontal and vertical mixing coefficients is as follows:

$$\frac{K_h}{K_V} = \frac{\tau^4}{24}\frac{g^2\overline{\nabla\rho\cdot\nabla\rho}}{\rho_0^2} = \frac{\mu}{24}. \tag{5.19}$$

The parameter $\mu = \tau^4\langle\nabla B\cdot\nabla B\rangle$ that emerged from dimensional analysis in Sect. 5.3.5 thus characterizes the relative importance of the vertical and horizontal mixing processes in the equatorial region. A strong dependence of parameter μ on the somewhat uncertain relaxation time τ makes it difficult to make quantitative estimates of the horizontal to vertical mixing coefficient ratio. The estimates for typical conditions in the warm pool area given in Table 5.1 should at this point be treated only as qualitative.

The first row in Table 5.1 is an estimate for westerly wind burst conditions; the horizontal mixing coefficient K_h is relatively small, on the order of the vertical mixing coefficient. Under low wind speed conditions and strong rainfalls (the second row in Table 5.1), K_h equals 420 m^2 s^{-1}. (For comparison, Large et al. (2001) used

a constant horizontal mixing coefficient of order 1000 $m^2\ s^{-1}$ in order to reproduce the equatorial zonal currents.) The ratio between the horizontal and vertical mixing is highly dependent on the regime of air–sea interaction; it dramatically increases under low wind speed conditions when the vertical mixing is suppressed by stratification.

Due to rotation effects, the relationship between vertical and horizontal mixing may depend on latitude even relatively close to the equator, but it is essentially different from mid-latitude regions. In mid-latitudes, the sheared flow within the mixed layer that arises due to horizontal density inhomogeneities can be partitioned between a geostrophic response and an ageostrophic response (Young 1994; Tandon and Garrett 1995; Roemmich et al. 1994). A relevant limitation on the horizontal length scale is the baroclinic Rossby radius (L_f), and the respective limitation on the timescale is the inertial timescale (f^{-1}). The analysis develope din this section relates to the ageostrophic response of the sheared flow within the mixed layer. For the geostrophic response, the theory of quasi-geostrophic two-dimensional turbulence of Batchelor (1969) and Kraichnan (1975) must be used.

5.3.8 *Implications for Horizontal Mixing Parameterization*

The numerical diagnostics performed in Sect. 5.3.6 with axisymmetric initial conditions indicate that the asymptotic (equilibrium) solution of Eq. (5.10) is a conic structure. Between the top and the base of the "cone," $\partial_r \rho(r)$ tends to a limiting (equilibrium) value and, hence, does not depend on the radial distance r. An important consequence of this fact is that the mixing coefficient is no longer an explicit function of the horizontal length scale. If the initial disturbance is represented by an ensemble of random disturbances, as in the example illustrated in Fig. 5.14, in the process of nonlinear evolution only the disturbances that have maximal length scale possible in the system survive. A relevant limitation on the horizontal length scale in the ocean is the baroclinic Rossby radius (L_f) or the equatorial baroclinic Rossby radius (L_β). For the equilibrium subrange, we can therefore use a tentative approximation, $\overline{\nabla\rho\cdot\nabla\rho} \approx \overline{\left(\rho'/L_R\right)^2} = \overline{\rho'^2}/L_R^2$, where L_R is the appropriate baroclinic Rossby radius (either L_f or L_β), and $\overline{\rho'^2}$ is the variance of the submesoscale density fluctuations. Equation (5.17) then reads

$$K_h \approx \frac{h^2\tau^3}{96}\frac{g^2\overline{\rho'^2}}{L_R^2\rho_0^2} \tag{5.20}$$

On the time and space scales where the determining parameters h, τ, and $\overline{\rho'^2}$ can be treated as stationary, formula (5.20) results in a constant horizontal mixing coefficient. Parameterization of the horizontal mixing thus reduces to the classical problem described by a linear diffusion equation. An example is Brownian motion. According to Einstein's (1905) formula for Brownian motion:

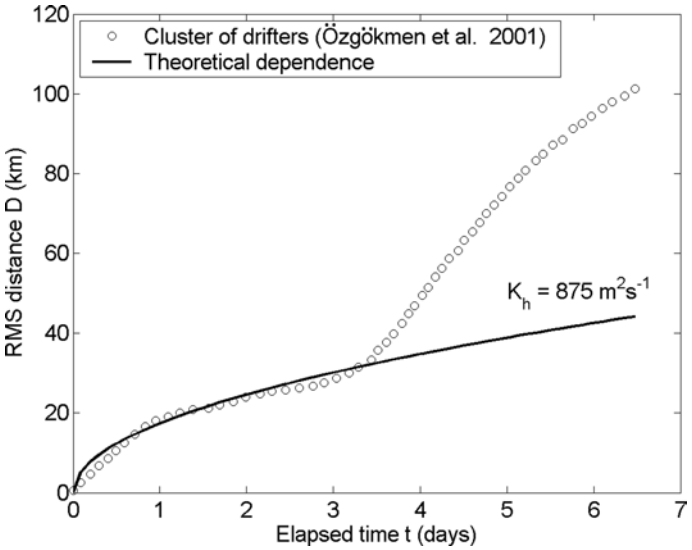

Fig. 5.15 RMS distance D in the cluster of 5 drifters released on 25 October 1993 (−5° S, 90° W) as a function of time t elapsed from the drifter release

$$D = 2(K_h t)^{1/2}, \tag{5.21}$$

where D is the RMS distance.

Evidence in favor of (5.21) can be found from drifter cluster release experiments (Özgökmen et al. 2001). Figure 5.15 shows the RMS distance D in the cluster of five drifters released on 25 October 1993 (5°S, 90°W) as a function of elapsed time t since the drifter release. Mean flow advection has been subtracted. Theoretical dependence (5.21) that follows from the nonlinear diffusion model is shown for a constant $K_h = 875$ m^{2}s^{-1}. According to Fig. 5.15, the constant coefficient diffusion law (5.21) appears to be valid for about 3.5 days. During this time, the RMS distance between drifters increased to $D_{0=}35$ km, which is close to the values of the baroclinic Rossby radius estimated for typical stratification disturbances within the mixed layer of the tropical sea. On larger horizontal scales, (5.21) is apparently no longer valid.

The inhomogeneity of the buoyancy (or density) field in the upper ocean induced by atmospheric forcing can be estimated from a simple budget relationship as follows:

$$\nabla B = g\frac{\nabla\rho}{\rho_0} = \int_0^\tau \nabla\left(\frac{\Pi_{Ba}}{h}\right)dt, \tag{5.22}$$

where Φ_{Ba} is then et buoyancy flux at the air–sea interface defined by Eq. (5.11) and h is the depth of the mixed layer. Respectively, the variation of the mixed layer density ρ' due to precipitation only can be estimated as follows:

$$\rho' = \rho_0 \int_0^\tau P / h \cdot dt \tag{5.23}$$

Formulas (5.20) and (5.23) then link the horizontal mixing coefficient with the atmospheric forcing (precipitation):

$$K_h \approx \frac{g^2 \tau^3}{96 L_R^2} \overline{M_r^2}, \tag{5.24}$$

where $M_r = \int_0^\tau P dt$ is the cumulative precipitation during rain event.

Rainfalls are in fact the major contributor to the temporal and spatial intermittency of the buoyancy flux between the atmosphere and ocean in the warm pool area. During TOGA COARE, the spatial and temporal structure of the rain rate was known from radar measurements (Fig. 5.11) and from NCAR's cloud resolving models (Moncrieff et al. 1997; Redelsperger et al. 2000). For the implementation of the horizontal mixing parameterization in an ocean general circulation model (GCM), subgrid precipitation statistics with 1 km resolution can, in principle, be provided by the new generation of atmospheric cloud resolving models (Grabowski and Smolarkiewicz 1999; Randall et al. 2003).

Brief conclusions for Sect. 5.3 are as follows:

1. The TSG data from the western Pacific warm pool reveal the k_x^{-3} spectral subrange.
2. The hypothesis of an equilibrium spectrum leads to wavenumber dependence $E(k) \sim k_x^{-3}$, which is consistent with the field data.
3. Numerical experiments illustrate how nonlinear diffusion transforms initial horizontal density anomalies into conic structures with spike-type buoyancy curvature at their corners, which leads to a k_x^{-3} wavenumber spectrum.
4. For the equilibrium state, the nonlinear diffusion problem then reduces to a linear problem with the constant horizontal diffusion coefficient.
5. The increased horizontal curvature of buoyancy drives frontogenesis.

The last conclusion thus links the process of nonlinear diffusion to the problem of oceanic fronts.As we have seen from previous sections of this chapter, the process of self-organization involves a cascade of energy from smaller to larger scales. At the same time, horizontal gradients must simultaneously increase to satisfy the conservation law (5.3). One interpretation is that, in the process of self-organization, boundaries of the spatially coherent organized structures become sharper. The data presented in the next section indeed show that sharp frontal interfaces are an observable feature of the near-surface layer of the ocean. The FY97 model is, however, hydrostatic and is not capable of simulating fronts.

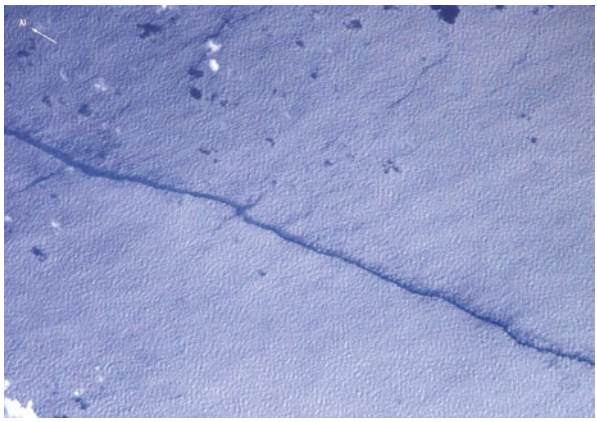

Fig. 5.16 An image taken from International Space Station on May 24, 2001 in the equatorial Pacific (2.3° N 159.1° E) by Increment 2 crew, Jim Voss and Susan Helms (courtesy of Susan Runko, NASA)

5.4 Sharp Frontal Interfaces

Recent global surveys using the Pathfinder sea surface temperature (SST) dataset reveal persistent fronts in many parts of the World Ocean (Belkin et al. 2001). Oceanic fronts have been linked to the process of subduction, where one watermass sinks below another without substantial mixing (see for instance Rudnick and Luyten 1996). Subduction appears to be an important process in maintaining the salt-stratified barrier layer often found below the warm, fresh mixed layer of the western Pacific warm pool (Lukas and Lindstrom 1991; Shinoda and Lukas 1995; Tomczak 1995; You 1995; Ando and McPhaden 1997; Vialard and Delecluse 1998).

Woods (1980) and Fedorov (1986) linked ocean fronts to dissipation of large-scale and mesoscale horizontal inhomogeneities of the physical fields in the upper ocean. Fronts sometimes are so narrow that in images from space they may look like "cracks" on the sea surface (Fig. 5.16).

The front sometimes splits into a group of frontal interfaces. In mid-latitudes and high latitudes, the Coriolis effect winds these lines up into spirals (Fig. 5.5), but they may still be very narrow.

Although oceanic fronts are observed over a wide range of horizontal scales, turbulent mixing events in the ocean tend to occur on relatively small scales. The small-scale structure of oceanic fronts therefore potentially contains information about horizontal and vertical exchange processes in the upper ocean.

In situ measurements sometimes reveal sharp frontal interfaces in the upper ocean (Zenk and Katz 1975; Soloviev and Zatsepin 1992; Yoder et al. 1994; Soloviev and Lukas 1997). Many sharp frontal interfaces are found in the temperature, salinity, and density records made during TOGA COARE, using bow-mounted sensors (Soloviev and Lukas 1997; Wijesekera et al. 1999a; Soloviev et al. 2002).

Fig. 5.17 A sharp frontal line observed in the equatorial western Pacific warm pool from the *R/V Kaiyo* on 13 August 1996. After Soloviev et al. (2002) with permission from Elsevier

5.4.1 Observations of Sharp Frontal Interfaces in the Western Pacific Warm Pool

The western equatorial Pacific warm pool region—the TOGA COARE domain—is characterized by heavy precipitation and generally light winds. As a result, both heat and freshwater fluxes contribute substantially to the buoyancy influx to the top of the surface mixed layer, and both temperature and salinity stratification are found in the upper ocean (Lukas and Lindstrom 1991). The thermohaline fields in the warm pool area are heterogeneous and nonstationary to a surprising degree (Huyer et al. 1997); there are numerous instances of sharp fronts in the surface layer of the ocean (Soloviev and Lukas 1997).

Figure 5.17 shows a sharp front in a photograph taken from the bridge of the R/V *Kaiyo* in the western equatorial Pacific warm pool during a TOCS cruise. (This is believed to be the same type of front as in the image from space shown in Fig. 5.16). A description of the upper ocean currents, thermohaline structure, and atmospheric forcing during TOCS can be found in Matsuura (2002).

The sharp frontal line in Fig. 5.17 is roughly aligned in the east–west direction and extended from one horizon to the other. The front is clearly seen in the photograph because the wind waves to the north of the front break much more intensively than those to the south of the front. There is also some difference in ocean color across the front.

Conductivity, Temperature, Depth (CTD) stations made along 156°E from 8°N to 3°S (prior to crossing the front) reveal a surface salinity minimum at about 5°N and the related meridional salinity gradient at the equator (Fig. 5.18). A CTD station taken just north of the front (see map in Fig. 5.19) reveals a nearly isothermal layer 71 m deep (as determined from the criteria $T(1) - T(h) = 0.5^{\circ}C$) and a shallow halocline, starting from ~12 m (Fig. 5.18).

The shallow halocline was presumably related to the front. In Fig. 5.20, the thermohaline structure of the upper 71 m at this CTD station is shown in more detail. The layer between the top of the shallow halocline (the well-mixed layer) and the

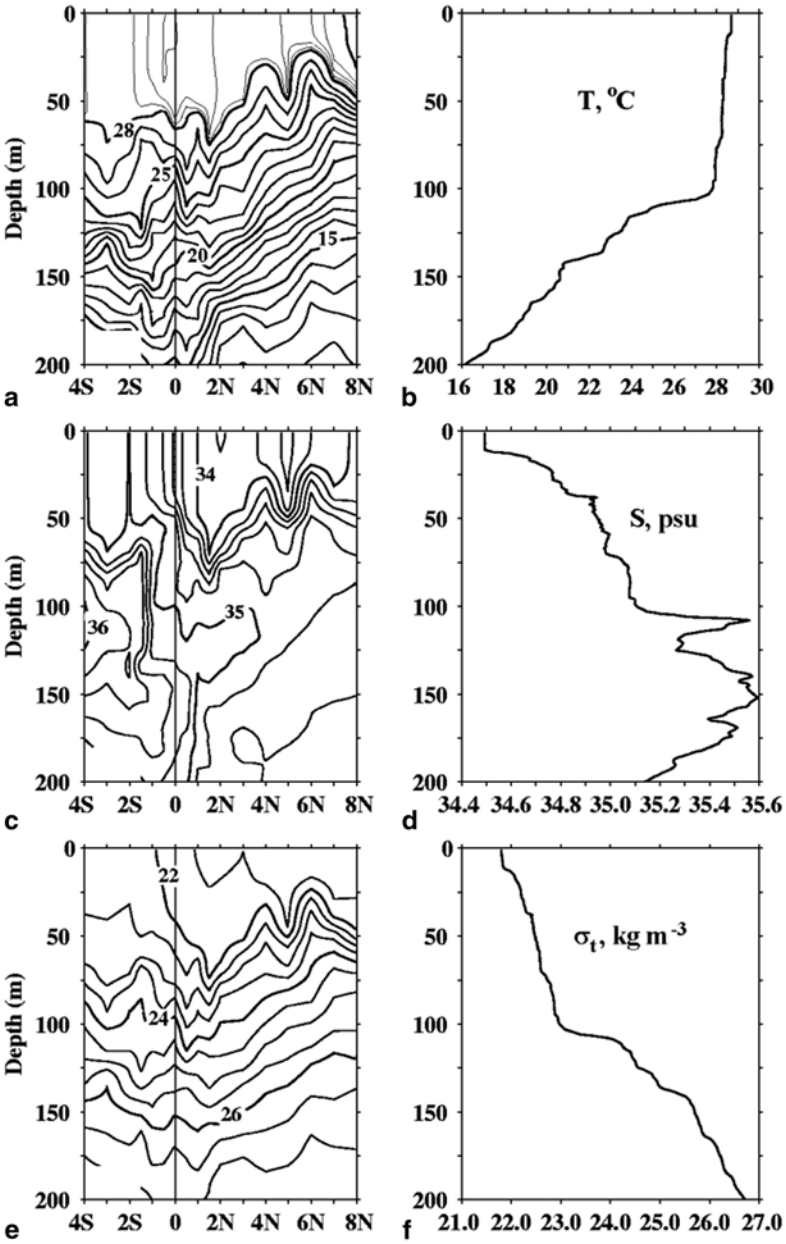

Fig. 5.18 Contour plots of (**a**) temperature, (**c**) salinity, and (**d**) density during the R/V *Kaiyo* section along 156° E. Vertical profiles of (**b**) temperature, (**d**) salinity, and (**f**) density calculated from the CTD station taken north of the surface front (see Fig. 5.19 for the position of the station relative to front). There is a 4° difference in longitude between the meridional section and the CTD station. The contour interval in plot (**a**) is 0.2°C for $T > 28\,°C$ and 1.0 °C for $T < 28\,°C$. After Soloviev et al. (2002) with permission from Elsevier

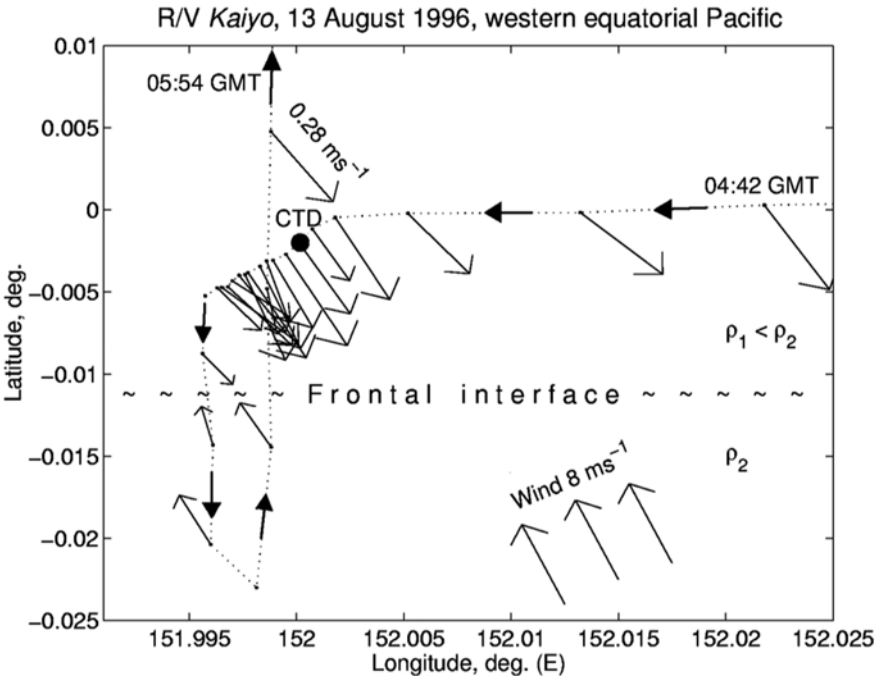

Fig. 5.19 Track of the R/V *Kaiyo* on 13 August 1996 (during intersection of the sharp surface front shown in Fig. 5.17) is given with dotted line; bold arrows indicate direction of ship. The time marks are on the upper right and left corners. The ADCP velocity shear vector $\Delta U = U_{16} - U_{24}$ is shown along the ship track, where U_{16} and U_{24} are the horizontal velocity vectors for the 16 and 24 m bins, respectively. The scale for the velocity shear vector can be found in the upper left corner. Position of the CTD station (Fig. 5.18b, d, and 5.20) is marked with a bold circle. After Soloviev et al. (2002) with permission from Elsevier

bottom of the nearly isothermal layer (the top of the thermocline) resembles a barrier layer, the feature often found in the western Pacific warm pool (Lukas and Lindstrom 1991). This particular case has a temperature gradient reinforcing salinity stratification, though it is only approximately 1/2 of the salinity contribution to the stratification of the barrier layer.

There is a well-mixed near-surface layer in the upper 12 m of the ocean (Fig. 5.20). Laboratory experiments described in Simpson (1987) suggest that the speed of a gravity current U_b developing due to the density anomaly $\Delta\rho$ is controlled by the Froude number, $Fr = U_b / \sqrt{g' h_0}$, where g' is the reduced gravity $(g\Delta\rho/\rho_0)$ and h_0 is the effective depth of the near-surface density anomaly. Following Whitham (1974), we will use Favor's (cited from Whitham 1974) critical value $Fr = 1.2$. Simpson (1987) found that the critical Froude number could depend on h_0/H, where H is the depth of the nearly isothermal layer. For crude estimates, we will ignore this dependence.

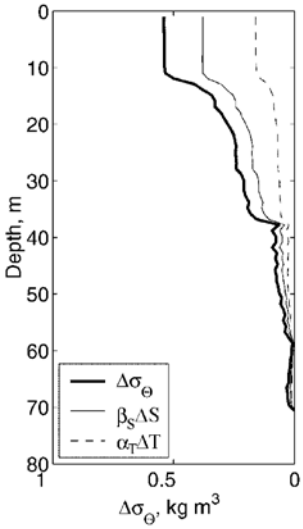

Fig. 5.20 Vertical distribution of potential density (σ_Θ) relative to the top of the thermocline (bottom of nearly isothermal layer) and the impact of salinity (S) and potential temperature (Θ) on stratification within the upper ocean from the CTD station indicated in Fig. 5.19. Here, α_T and β_S are the respective thermal expansion and salinity contraction coefficients; Δ is the difference operator (with respect to the bottom of the nearly isothermal layer). The depth of the nearly isothermal layer, $H=71$ m, is determined from criteria $T(1)-T(H)=0.5^\circ$C. After Soloviev et al. (2002) with permission from Elsevier

Assuming that in the example shown in Fig. 5.20 $h_0=12$ m, $H=71$ m, $\Delta\rho=0.54$ kg m^{-3}, $\rho_0=1024$ kg m^{-3}, and $Fr=1.2$, the speed of the gravity current due to the observed density anomaly within the mixed layer is estimated as $U_b\approx0.30$ m s^{-1}. This is in fact a lower estimate, since the effective thickness of the near-surface density anomaly layer driving the gravity current is larger than 12 m. The effective thickness calculated as $h_0=(\rho(0)-\rho(h))^{-1}\int_0^h(\rho(z)-\rho(h))dz\approx27$ m results in $U_b=0.44$ m s^{-1}, which is an upper estimate. (However, both estimates do not account for the opposing wind stress.)

The acoustic Doppler current profiler (ADCP) record from the 16 m bin shows a jump of the relative velocity, $\Delta U=U_{16}-U_{24}$, of approximately 0.4 m s^{-1} atthe intersection of the front (Fig. 5.19). This is within the range of the preceding estimates for the gravity current speed. (Note that the shipboard ADCP data start only from 16 m.) The contour plot of the northward velocity component during the subsequent meridional section of the R/V *Kaiyo* along 152°E (Fig. 5.21) reveals signatures of a strong South-southeast (SSE) near-surface current. The sharp front visually observed in Fig. 5.17 can be associated with the leading edge of this near-surface current. According to the shipboard ADCP and meteorological observations, an 8 m s^{-1} SSE wind opposed the buoyant spreading of the front (Fig. 5.19).

There is a jump in the horizontal velocity component normal to the front (Fig. 5.19). The breaking of surface waves observed north of the front (Fig. 5.17) can be ascribed to the effect of surface wave–current interactions.

Another observation of the sharp frontal interface is presented in Fig. 5.22. This is an east–west section from the R/V *Wecoma* during TOGA COARE. Visual observations of the ocean surface were not conducted for this section, but evidence

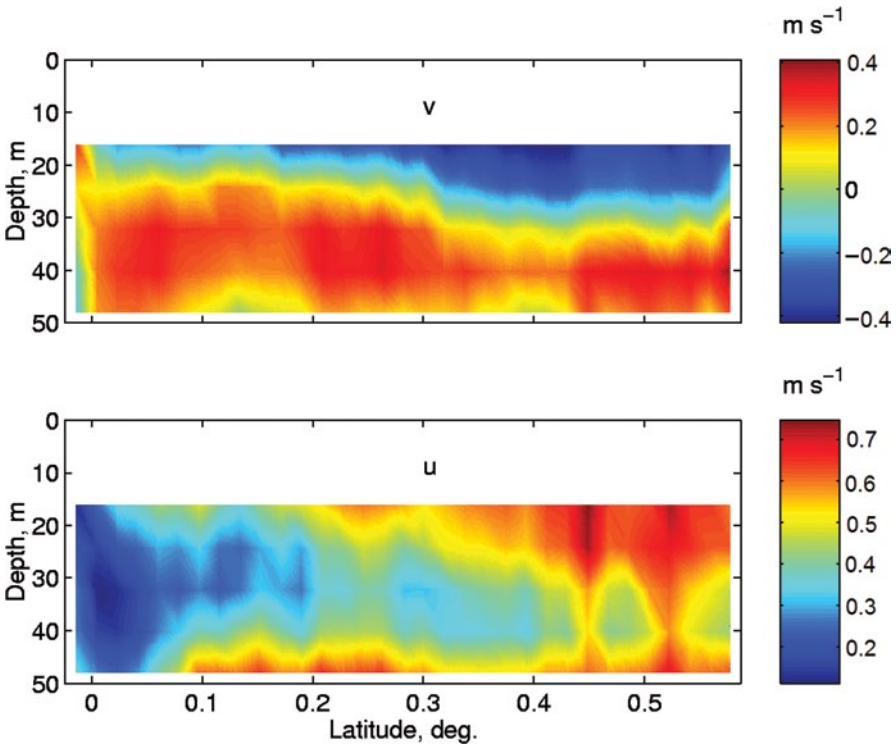

Fig. 5.21 ADCP velocity contour plots for north v and east u components during the meridional section of the R/V *Kaiyo* on 13 August 1996 (corresponds to the northbound part of the ship trajectory in Fig. 5.19)

of convergence lines was seen in sections during the preceding and following days. The data from the CTD sensor mounted on the bow of the vessel at 2 m mean depth (Wijesekera et al. 1999a) provided high-resolution data in the horizontal direction, and the data from a towed undulating CTD (SEASOAR) provided information on the upper ocean stratification during this case study. The 3 km horizontal grid of the interpolated SEASOAR and ADCP data is, however, too coarse to resolve small-scale horizontal features. In particular, the internal-wave train that presumably can accompany the propagation of the gravity current cannot be resolved with 3 km data since the theoretical wavelength of the wave train (see Sect. 5.4.4) is only $\lambda \approx 6h_0 \sim 10^2$ m.

A sharp front is clearly seen in the bow record of density at 45.6 km (Fig. 5.22a), associated with a rain-formed freshwater surface lens. Note that only one boundary of this lens is sharp. The density and velocity contour plots for the upper 100 m of the ocean from SEASOAR and ADCP measurements (Fig. 5.22b–d) reveal a density anomaly and signatures of the near-surface current associated with this frontal structure. Between 25 and 50 km, this density anomaly has cyclonic vorticity, which appears to have been caused by the inertial spin-down of an eastward equatorial jet (Feng et al. 2001).

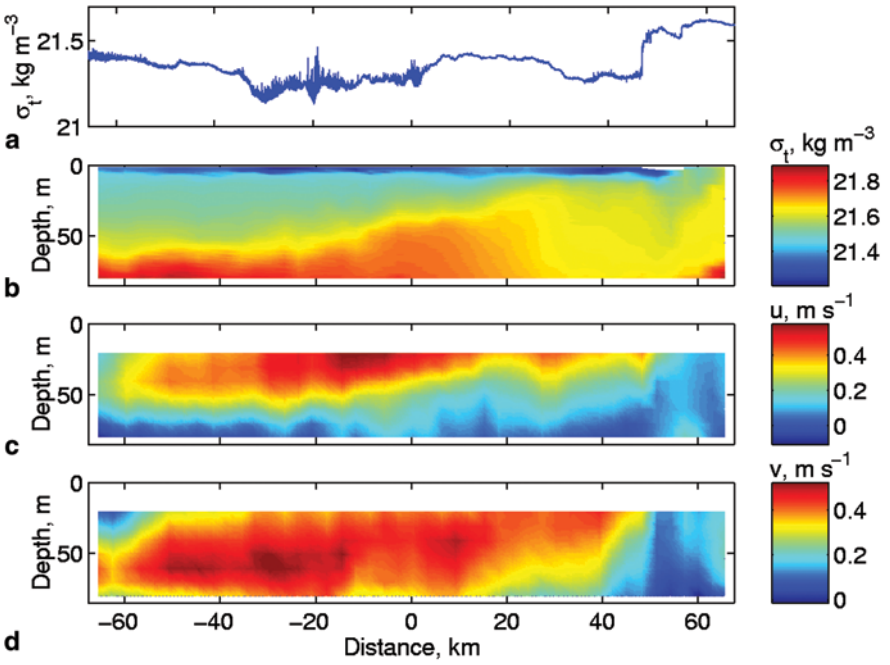

Fig. 5.22 **a** Sharp frontal interface in the near-surface density field measured at 2 m mean depth by a bow-mounted CTD, **b** density contour plot calculated from a towed undulating vehicle and **c**, **d** eastward and northward velocity contour plots. After Soloviev et al. (2002) with permission from Elseviers

Several factors complicate shipboard observations of the sharp frontal interfaces. Such fronts are very localized in space; the moments of their intersection are usually unknown in advance. For their study, high-resolution measurements over a relatively long time period are therefore necessary. There are no conventional techniques for such measurements. (Remember that standard shipboard TSGs usually do not resolve features with scales less than several hundred meters.) Moreover, the magnitude of the cross-frontal difference in temperature (T) and salinity (S) is typically only of the order of 0.01 °C or psu. Such frontal interfaces may be strongly masked at the surface by diurnal warming or precipitation effects in the near-surface layer of the ocean. In measurements by moored sensors, the fronts can be detected only for extreme situations, because the frequency range of the signal from frontal passages substantially overlaps the frequency range of the diurnal warming/precipitation variability. High-resolution towed measurements, however, do reveal the sharp frontal interfaces due to the horizontal scale separation.

During TOGA COARE, fast-response temperature, conductivity, pressure (depth), and turbulence probes were mounted on the bow of the R/V *Moana Wave* at a nominal depth of 1.7 m (Section 3.3.5 and Soloviev et al. 1998, 1999). The data

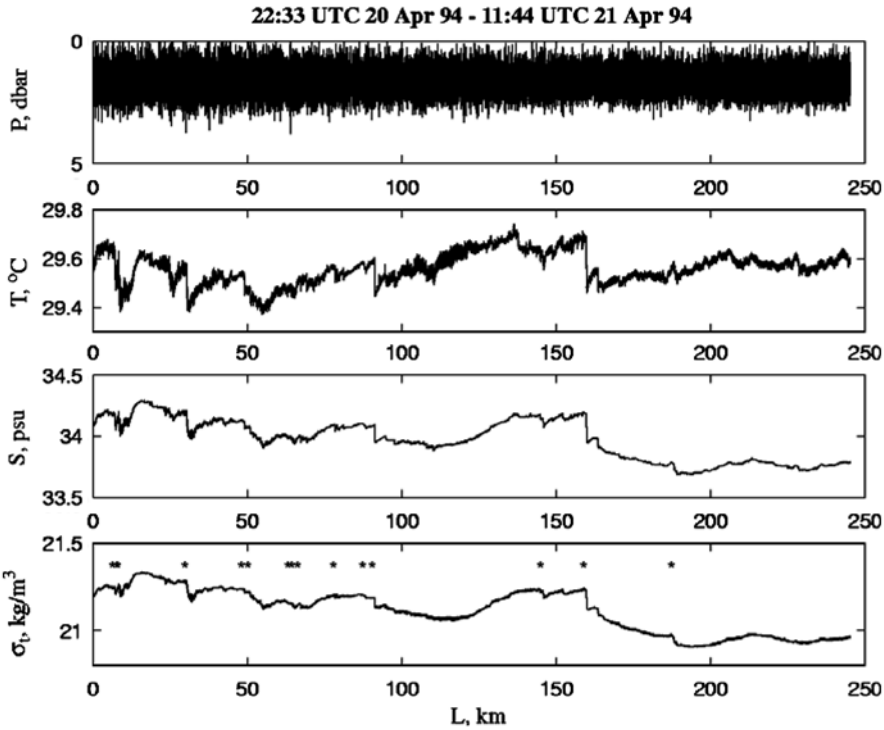

Fig. 5.23 Example of repeating asymmetrical structure in the near-surface layer of the ocean in the western equatorial Pacific warm pool (1 dbar = 0.98 m). This is a 13-hour record obtained by bow sensors from 7°05' S, 164°21' E to 5°00' S, 163°12' E (ship heading ~330°). Sharp frontal interfaces detected in σ_t with the algorithm described in Sect. 5.4.2 are marked by asterisk signs. After Soloviev and Lukas (1997). Copyright © 1997 American Meteorological Society. Used with permission

were collected almost continuously during several cruises, which provided representative statistics of frontal interfaces.

It is intriguing that the frontal interfaces often appear in groups. Figure 5.23 shows an example of such variation. The temperature, salinity, and density series reveals a quasi-periodic structure of about 10–60 km wavelength observed on the background of the mean horizontal density gradient of about 0.001 kg m^{-3} km^{-1}. A feature of this structure is its strong asymmetry. A gradual rise of density is followed by its abrupt reduction.

Frontal interfaces can presumably interact with the wind drift current (Soloviev and Lukas 1997). Figures 5.24–5.26 depict three examples of sharp frontal interfaces observed in the warm pool area during the R/V *Moana Wave* COARE EQ-3 cruise. In addition to high-frequency signals from the bow sensors, the corresponding records of temperature and salinity from the ship's TSG system are also shown.

There are dramatic changes in the turbulence dissipation rate associated with the frontal interface in the cases shown in Figs. 5.24 and 5.25, while there are no

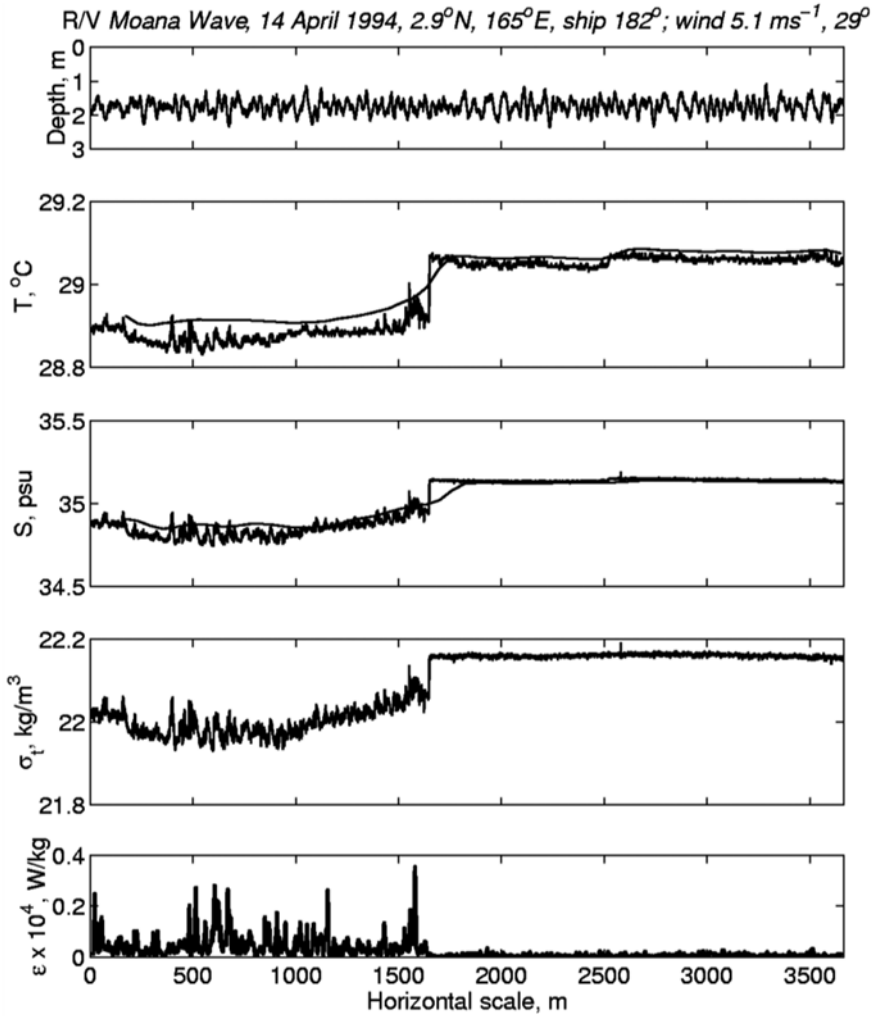

Fig. 5.24 The depth (pressure), temperature (T), salinity (S), density (σ_t), and the dissipation rate of turbulent kinetic energy (ε) from bow sensors for the case of wind stress opposing the buoyant spreading of front. Corresponding records of temperature (bow thermistor at 3 m intake) and salinity (ship's thermosalinograph system) are shown with smooth lines. After Soloviev et al. (2002) with permission from Elsevier

signatures of turbulence variation related to the interface in the example shown in Fig. 5.26. In Fig. 5.24, the wind stress opposes the buoyant spreading of the front; the turbulence signal is substantially increased on the downwind side of the interface. In Fig. 5.25, the wind stress is almost tangential to the front. There is a very localized increase in the turbulence signal associated with this frontal interface. Note that this front is relatively weak. Figure 5.26 represents a case where the wind

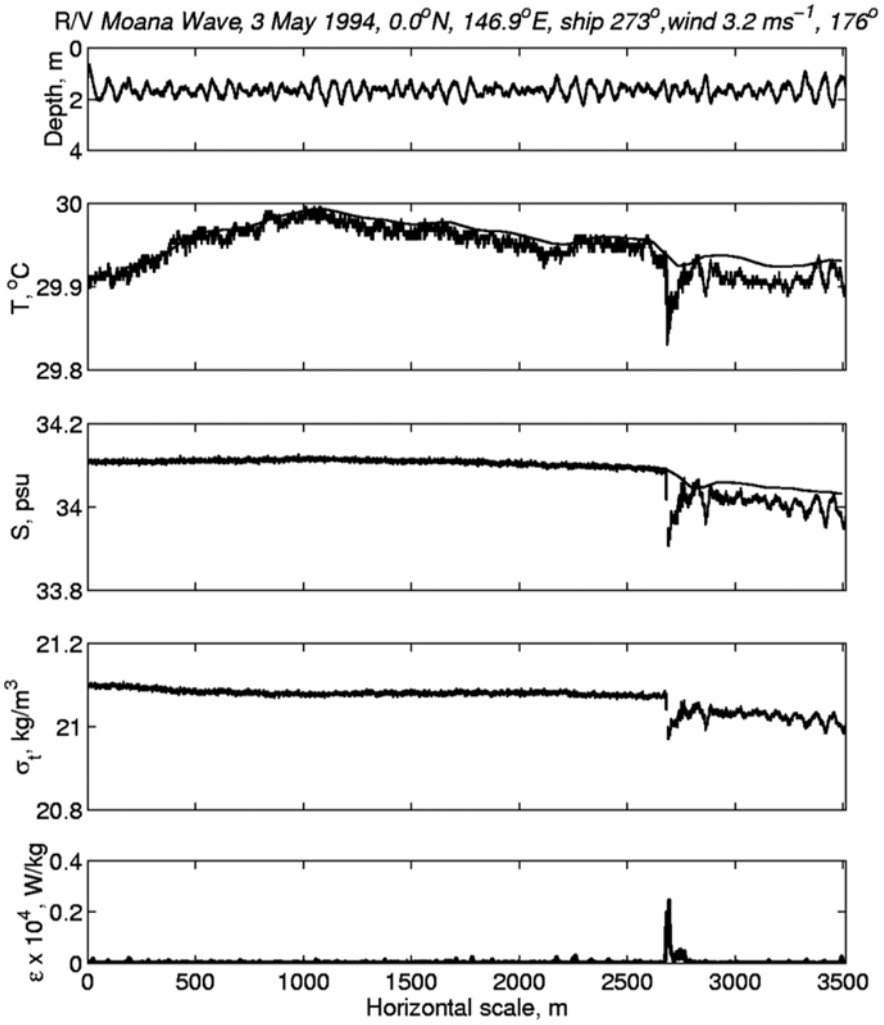

Fig. 5.25 Same as in Fig. 5.24 but for a case where the wind stress was directed along frontal line. After Soloviev et al. (2002) with permission from Elsevier

stress was in the same direction as the direction of the buoyant spreading of the front. The turbulence dissipation level does not change at the interface intersection.

These three cases represent noncompensated fronts. The differences in the turbulence signals in the vicinity of the fronts are possibly associated with the interaction of frontal interfaces with wind stress. Figure 5.24 suggests that when the wind stress opposes the buoyant spreading of a sharp front, intensive mixing occurs at the front. It should be stressed that in most cases, however, the turbulence signals could not be confidently associated with the presence of sharp frontal interfaces. We also do not know the exact orientation of the front with respect to the ship track or wind.

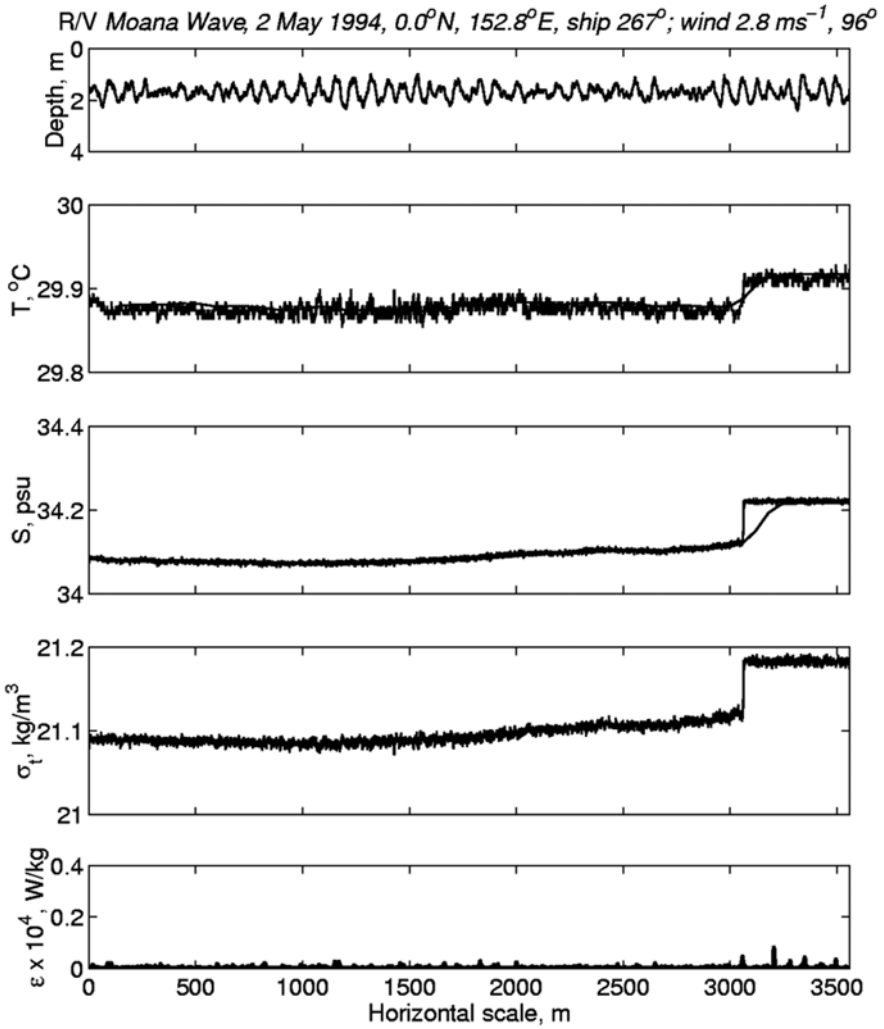

Fig. 5.26 Same as in Fig. 5.24 but for a case with the wind stress directed from lighter to denser water. After Soloviev et al. (2002) with permission from Elsevier

A special survey in which the ship followed a snake-like trajectory was performed to determine the orientation of a particular frontal structure to the wind direction (Fig. 5.27). The front was curved and oriented approximately 45–80° to the wind direction. A reciprocal course was run at slower ship speed in order to obtain data at higher resolution while crossing the front.

Figure 5.28 shows the individual intersections of the front on a high-resolution distance scale. Intersections 2, 4, and 6 are plotted in the inverse direction because of the reciprocal course of the ship at these intersections. For intersections 5, 6, and 7, the horizontal scale is multiplied by 0.15, 0.5, and 0.5, respectively, to correct for the oblique angle of intersection with the front. A feature of this front is that it

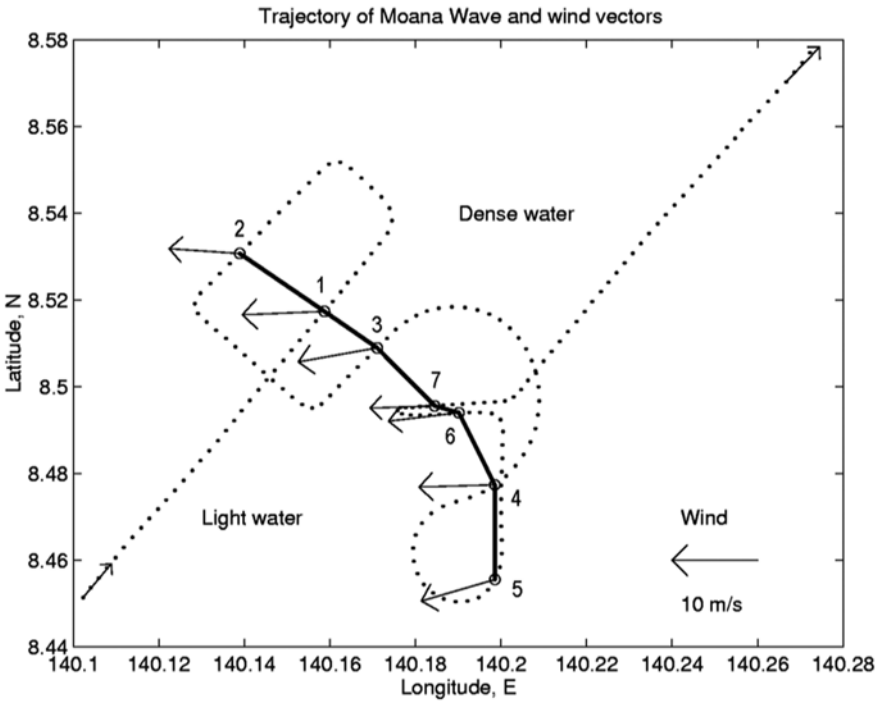

Fig. 5.27 Snake-like trajectory of the ship and locations of intersection of the front. Position of the ship is shown by points; the time interval between points is 1 min. The front as determined by the points of its intersection (circles numbered from 1 through 6) is shown by a solid line. Corresponding values of the wind vectors from the ship's measurements are also shown. After Soloviev and Lukas (1997). Copyright © 1997 American Meteorological Society. Used with permission

is seen in the σ_t record only at intersections 1, 2, and 3. For the intersections 4, 5, 6, and 7, the frontal interface is almost compensated in the density field but is still seen in the T and S records. The front shown in Fig. 5.28 is of about one order of magnitude wider than that shown in Fig. 5.26. We ascribe this difference to the wind stress direction opposing the buoyant spreading of the front in the former case.

Figure 5.29 demonstrates how the temperature–salinity relationship across this front evolved over time with the wind stress opposing the buoyant spreading of front. During several hours, the ship crossed back and forth across this front (Fig. 5.27). The front appears to degrade considerably during the time period; the temperature–salinity relationship tends toward the equilibrium state, which is characterized by density ratio,

$$R = \alpha_T \Delta T / \beta_S \Delta S = 1, \tag{5.25}$$

where $\alpha_T = (\partial_t \rho / \partial T)\big|_{p,S}$ and $\beta_S = (\partial \rho_t / \partial S)\big|_{p,T}$ are the expansion coefficients of temperature and salinity in units of kg m^{-3} °C^{-1} and kg m^{-3} psu^{-1}, and the temperature and salinity differences ΔT and ΔS are taken across the frontal interface.

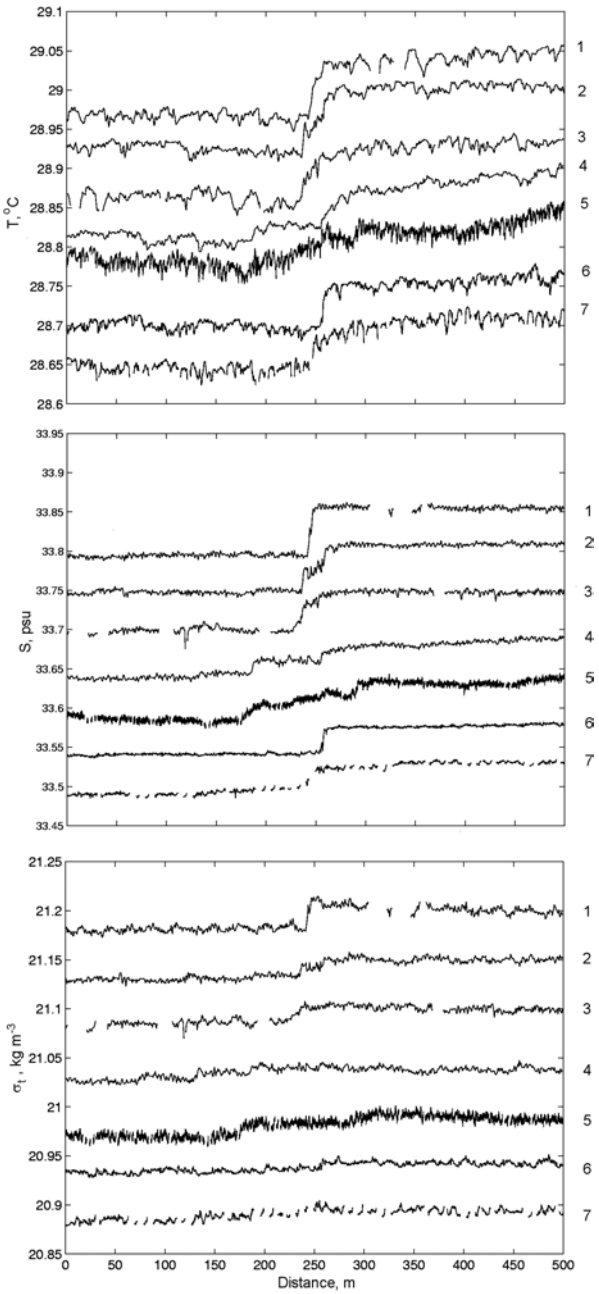

Fig. 5.28 Small-scale structure of the sharp frontal interface shown in Fig. 5.27. Blank spaces on S and σ_t profiles correspond to surfacing of the probes due to ship pitching. After Soloviev and Lukas (1997). Numbers along right axes indicate the successive cross-frontal sections. Copyright © 1997 American Meteorological Society. Used with permission

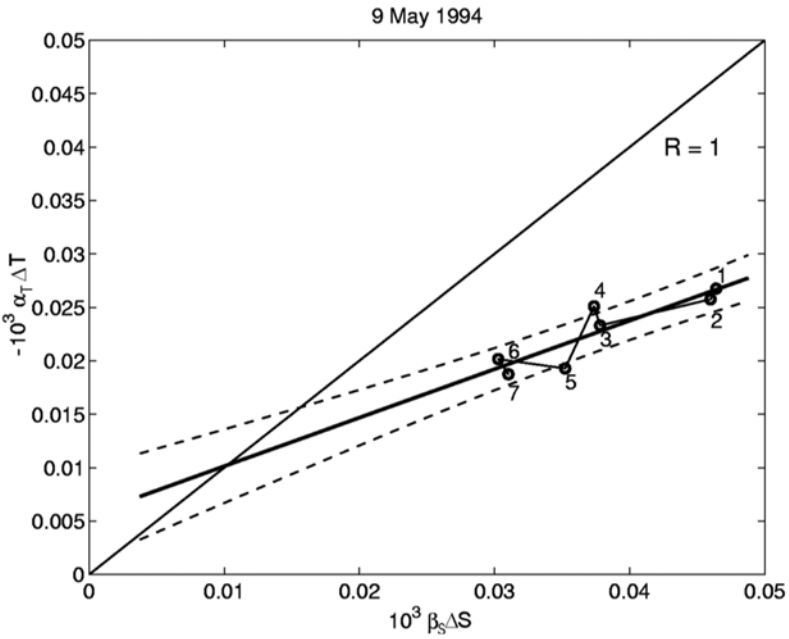

Fig. 5.29 Evolution of the temperature–salinity relationship during multiple intersections of a sharp front in the warm pool area during the R/V *Moana Wave* COARE EQ-3 cruise. The successive frontal intersections are numbered from 1 to 7 (for more details see Fig. 5.27). These points are linearly extrapolated (bold straight line) up to the intersection point with line $R=1$, while the space between dashed lines contain at least 50 % of the predictions. After Soloviev et al. (2002) with permission from Elsevier

Equation (5.25) is shown by the straight diagonal line in Fig. 5.29. (Note that some contribution from spatial variation of the front is possible in Fig. 5.29). According to the linear interpolation of the *T*–*S* tendency (Fig. 5.29), the compensated state for this frontal interface could be achieved at $\alpha_T \Delta T \approx 1{\cdot}10^{-5}$ and $\beta_S \Delta S \approx 1{\cdot}10^{-5}$, which corresponds to $\Delta T \approx -0.030^{\circ}\mathrm{C}$ and $\Delta S \approx 0.013$ psu.

After the interface achieves the compensated state ($R=1$), it is no longer affected by wind stress (see Sect. 5.4.4). The density ratio *R* is therefore an important parameter characterizing the dynamics of sharp frontal interfaces.

5.4.2 *Statistics of Sharp Frontal Interfaces in the Western Pacific Warm Pool*

The presence of sharp frontal interfaces is associated with the subduction process in the surface mixed layer, which is important in forming the barrier layer in the warm pool area. The cases of sharp fronts described in the previous section represent extreme situations. In many other cases, the temperature, salinity, and density

differences across fronts are relatively small. Thus, these fronts cannot be seen visually on the ocean surface as in the case shown in Fig. 5.17, they may not be detected from the available ADCP measurements because they are often shallower than 16 m (Figs. 5.21 and 5.22), and they cannot be seen in the bow turbulence records as in the case shown in Figs. 5.24–5.26. These frontal interfaces, however, can be detected in the bow density, salinity, and temperature records due to huge local gradients within the interfaces.

Soloviev and Lukas (1997) developed an algorithm for the automatic detection of sharp frontal interfaces. The sharp frontal interface is detected in a scalar property C when $|dC/dx| > n \cdot std(dC/dx)$. In order to detect the sharpest frontal interfaces, Soloviev and Lukas (1997) recommend to set $n=4$.

The ability to detect an interface depends on the ratio of the maximum gradient within the interface to the level of background fluctuations. Background fluctuations depend strongly on environmental conditions such as the wind speed, heat fluxes, presence of rain, diurnal warming, and so on. An interface may be clearly seen, for example, in the salinity record but fall below the detection level in the temperature and/or density record(s). Some interfaces are therefore found simultaneously in two or three of these variables, while others appear clearly in only one variable. We will hereafter refer to the sharp frontal interfaces found in density, salinity, and temperature records as the *density*, *salinity*, and *temperature interfaces*, respectively.

In Fig. 5.30, the statistical properties of the density, salinity, and temperature interfaces obtained from bow records during four TOGA COARE cruises of the R/V *Moana Wave* are summarized in the form of histograms. The first, second, and third rows in Fig. 5.30 correspond to the density, salinity, and temperature interfaces. The total number of sharp fronts found in density, $N_\rho = 326$, in salinity, $N_S = 751$, and in temperature, $N_T = 412$. The statistics presented in Fig. 5.30 include the cross-front difference of density, salinity, and temperature (left column) and the density ratio R for the density, salinity, and temperature interfaces expressed in terms of the Turner angle (the right column).

In the oceanographic literature, $Tu = \arctan(R)$ is known as the Turner angle (Ruddick and Turner 1979), where R is defined as in (5.25). The Turner angle is positive when temperature and salinity tend to compensate each other in density. For compensated fronts, $R=1$ and $Tu=\pi/4$. For fronts with no temperature difference ($\Delta T=0$), $R=0$ and $Tu=0$, while for fronts with no salinity difference ($\Delta S = 0$), $R = \infty$ and $Tu=\pi/2$.

As emphasized by Ferrari and Rudnick (2000), the advantage of using the Turner angle instead of the density ratio number is that the infinite scale of R is replaced by a finite one running from $-\pi/2$ to $\pi/2$. In addition, the temperature-dominated regions $(1 < |R| < \infty)$ and salinity-dominated regions $(0 < |R| < 1)$ occupy the same space on the Tu scale, which in particular means that the ensemble averaging over Tu may be more accurate than that over R.

According to Fig. 5.30, the average density ratio number defined as $<R>=tan(<Tu>)$ is relatively small for density interfaces ($<R>=0.2$), is larger for salinity interfaces ($<R>=0.5$), and approaches unity for temperature interfaces ($<R>=0.9$).

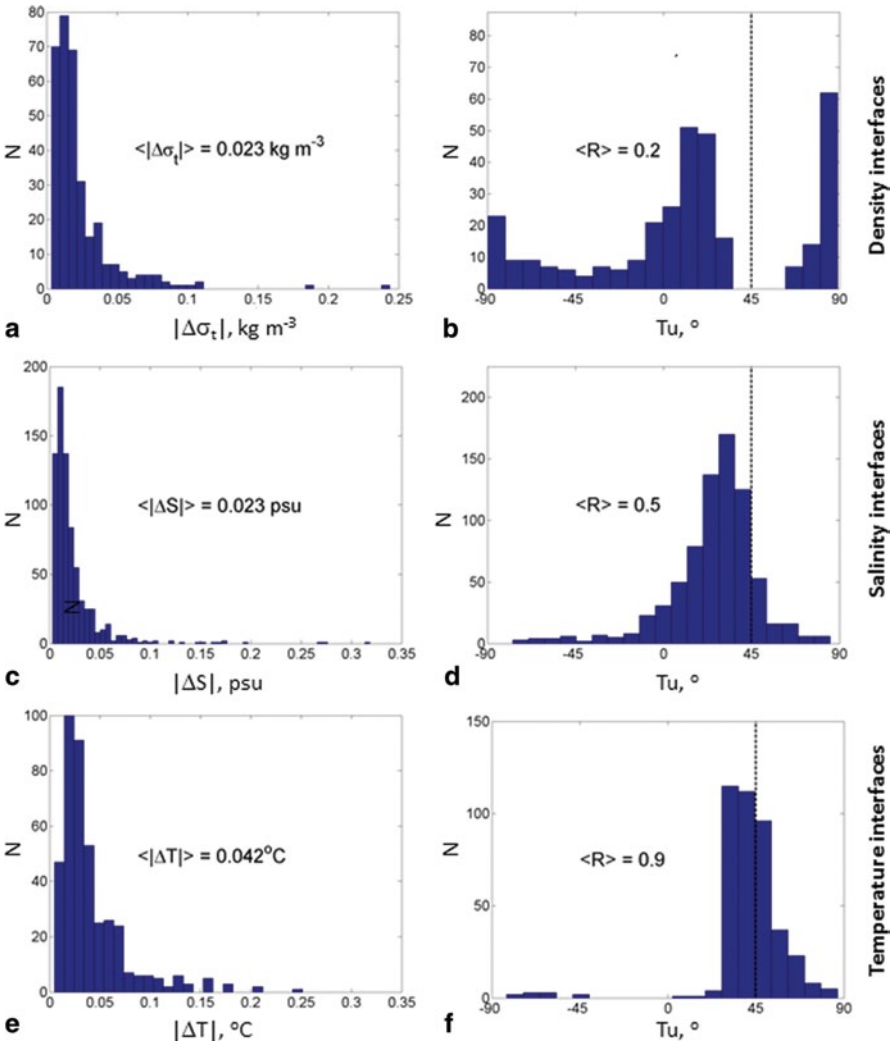

Fig. 5.30 Statistics of sharp frontal interfaces acquired with bow sensors during four TOGA COARE cruises of the R/V *Moana Wave*. Histograms of cross-front differences for the sharp frontal interfaces detected in **a** density, **c** salinity, and **e** temperature data and respective histograms (**b**, **d**, and **f**) for the Turner angle. After Soloviev et al. (2002) with permission from Elsevier

(The operator <> here denotes ensemble averaging.) The interpretation is that all density interfaces and a part of the salinity interfaces are not compensated interfaces, while the majority of the temperature interfaces appear to be compensated interfaces.

Figure 5.31 shows the dependence of sharp frontal interfaces on the wind-to-ship angle, θ (the left column), and on the wind speed, U_a (the right column), separately for the density, salinity, and temperature interfaces (the first, second, and third rows,

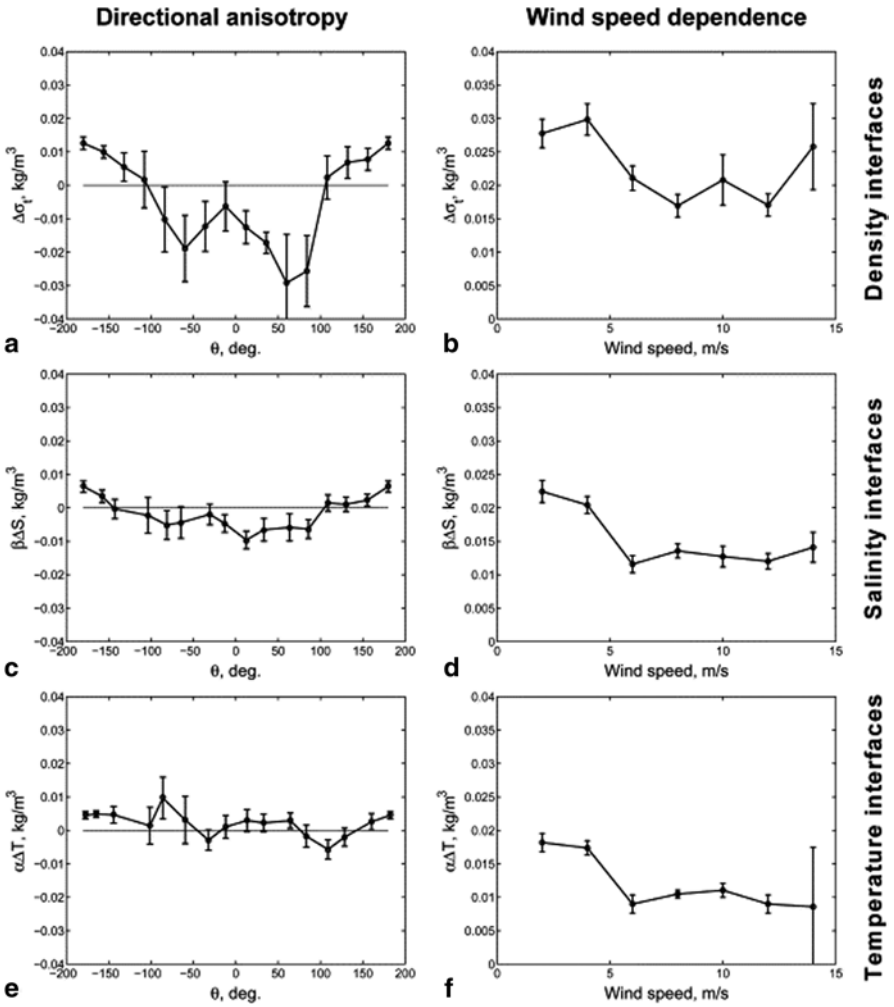

Fig. 5.31 Directional and wind speed dependence of the sharp frontal interfaces detected in the (**a**, **b**) density, (**c**, **d**) salinity and (**e**, **f**) temperature bow data, respectively. The data are from four TOGA COARE cruises. The temperature and salinity differences are shown as the equivalent density differences to simplify their visual comparison with the density differences in **a**) and **b**). The vertical bars represent one standard error confidence limits calculated from Student's distribution. After Soloviev et al. (2002) with permission from Elsevier

respectively). Salinity and temperature differences in Fig. 5.31c–f are multiplied by the corresponding expansion coefficients, α_T or β_S, to have comparable (density) units on all graphs. Figure 5.31 represents the bow data sets collected during the four COARE cruises of the R/V *Moana Wave* (same as in Fig. 5.30). The data in Fig. 5.31 are averaged over θ within ±24° and U_a within ±2 m s^{-1}. The vertical bars

represent one standard error confidence limits calculated on the basis of Student's distribution (Rabinovich 1995).

At the intersection of a particular frontal interface, we do not know the intersection angle. Soloviev and Lukas (1997) nevertheless showed that, in a statistical sense for the frontal interfaces detected with their algorithm, the average wind-to-front angle, $<\phi>$, can be replaced with the average wind-to-ship angle, $<\theta>$ where $\theta = \beta - \gamma$, β is the wind direction (we use the meteorological convention), and γ is the ship's course. The front vector is defined here as a vector that is normal to the frontal line. The vector direction is positive from less to more dense water (*i.e.,* coinciding with the direction of the gravitational spreading of the front).

According to Fig. 5.31, the density and salinity interfaces (which are mostly not compensated fronts) appear to depend on the wind-to-front angle. The spatial anisotropy is pronounced for the density interfaces (Fig. 5.31a), is less pronounced (but still statistically significant) for the salinity interfaces (Fig. 5.31c), and is practically non-resolvable for the temperature interfaces (Fig. 5.31e).

It is remarkable that the density fronts do not seem to depend much on the wind speed magnitude (Fig. 5.31b), while the salinity and temperature interfaces degrade with increasing wind speed. Larger error bars in Figs. 5.31b and 5.31 f at 14 m s^{-1} average wind speed are primarily due to a relatively small number of observations of the density and temperature fronts under high wind speed conditions (10 and 3, respectively). For the salinity interfaces, this number is larger (37), and the confidence limits for the 14 m s^{-1} bin are smaller (Fig. 5.31d).

Based on the theory developed in Sect. 5.4.4, the fronts that do not satisfy inequality (5.43) (*i.e.*, cannot interact with wind stress) are removed from the ensemble averaging in Fig. 5.31. The removal of this relatively small number of interfaces (see histogram in Fig. 5.37b) results in some reduction of error bars but does not modify the main conclusions about directional anisotropy and wind speed dependence of the sharp frontal interfaces.

5.4.3 Internal Wave–Shear Flow Interaction as a Cause of Repeating Frontal Interfaces

Soloviev and Lukas (1997) hypothesized that the sharp frontal interfaces may occur as a result of nonlinear buoyant adjustment of the stably stratified near-surface layer of the ocean to external forcing. The external forcing includes the variable buoyancy flux and wind stress at the ocean–air interface, tidal motions, and so forth. Relatively small thickness of the near-surface anomalies is favorable for the development of nonlinear interactions. The frontal interfaces are often found in groups (as in the example shown in Fig. 5.23). This feature of the frontal interfaces was explained using a "buoyant" asymptotic of the problem (*i.e.*, neglecting rotational effects).

Laboratory studies indicate that any density anomaly in the upper layer tends to spread horizontally. The leading edge of the gravity current along a boundary

through a uniformly stratified medium can generate several different modes of internal waves. According to a laboratory observation described by Simpson (1987), "… These waves affected the form of the gravity current behind the head in a rhythmical manner. The fluid in the original head was cut off from the flow, which formed a second head. The process was repeated and later a third new front appeared…" However, this striking effect was observed only when the Froude number,

$$Fr_0 = \frac{U_b}{NH} < \frac{1}{\pi} \tag{5.26}$$

and the fractional depth of the gravity current was less than 0.2 of the total depth H (here, U_b is the speed of the gravity current and N is the Brunt–Vaisala frequency of stratified surroundings). This is a resonant type of mechanism; it provides a plausible explanation for the appearance of upper ocean sharp frontal interfaces in groups.

In the equatorial region, the maximum spatial scale of buoyancy-driven anomalies is restricted by the baroclinic Rossby radius (Moore and Philander 1977). The equatorial baroclinic Rossby radius is

$$L_\beta = \left(\frac{c}{2\beta}\right)^{1/2}, \tag{5.27}$$

where $\beta = (\partial f / \partial y)_{\varphi=0} = 2.3 \times 10^{-11}$ m^{-1} s^{-1}, f is the Coriolis parameter, and c is the phase speed of internal perturbations. At $c = 0.1$–0.4 m s^{-1} (typical for weakly stratified mixed layer), $L_\beta = 50 - 100$ km, which correlates with the maximum horizontal distance between the sharp frontal interfaces observed in the western equatorial Pacific warm pool.

The nature of interaction between the near-surface current and the internal wave field has been described in several theoretical studies (Romanova 1984; Voronovich et al. 1998a). The vorticity and internal gravity waves interact and influence each other in the presence of density stratification. This influence is relatively weak when far from the resonance, but is greatly enhanced when the phase speed of the vorticity wave matches the celerity of one of the internal wave modes. The internal wave–shear flow resonance can lead to the splitting of the near-surface gravity current into a coherent series of frontal interfaces.

The sketch in Fig. 5.32 shows the flow geometry in the Romanova (1984) and Voronovich et al. (1998a) theory. The problem is formulated under a rigid-lid approximation. The shear is localized in the thin subsurface layer of thickness h and has no inflection points in the velocity profile U(z). The latter condition is to ensure that the flow is dynamically stable with respect to perturbations in the inviscid limit.

For resonance to occur in the flow configuration shown in Fig. 5.32, the typical frequency of the vorticity waves should be of the same order as that of the internal wave N_0

$$u_0 / H = c_N N_0 = \max(N), \tag{5.28}$$

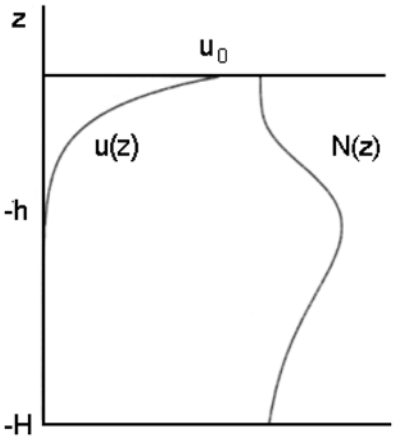

Fig. 5.32 Flow geometry and notation in the theory of shear waves. After Romanova (1984)

where Eq. (5.28) is formulated in dimensional variables and c_N is a dimensionless coefficient.

In an attempt to describe the nonlinear resonant interaction by means of an asymptotic analysis, Voronovich et al. (1998a) derived the set of two coupled equations for normalized wave amplitudes a and b of the internal and vorticity modes, respectively.

$$\begin{cases} a_t + \Delta a_x + a_{xxx} - b_x = 0, \\ b_t + 2bb_x - a_x = 0. \end{cases} \tag{5.29}$$

where Δ is a free parameter corresponding to a disparity in the coupled wave phase speeds.

Two types of solutions for plane solitary waves follow from (5.29). The first type of solutions ("supercritical") propagates with velocities greater than that of the current, which is expressed by inequality:

$$u_0 / H < c_N N_0. \tag{5.30}$$

The supercritical solution has amplitudes limited by the critical value (*i.e.*, the value at which the solitary wave exhibits a sharp corner at the crest—see also Fig. 5.33). This type of nonlinear instability leads to the formation of vertical slopes and, thus, to wave breaking in finite time. Solitary waves of the second type ("subcritical") have velocities smaller than the flow speed at the surface and are characterized by a series of smooth pulses.

It is easy to see that (5.30) is similar to (5.26). The supercritical solution following from the internal wave–shear flow interaction theory can therefore be identified as that describing the formation of repeating ageostrophic fronts. It should be noted that in contrast to the Kelvin–Helmholtz instability (Sect. 5.5.3) the critical layer

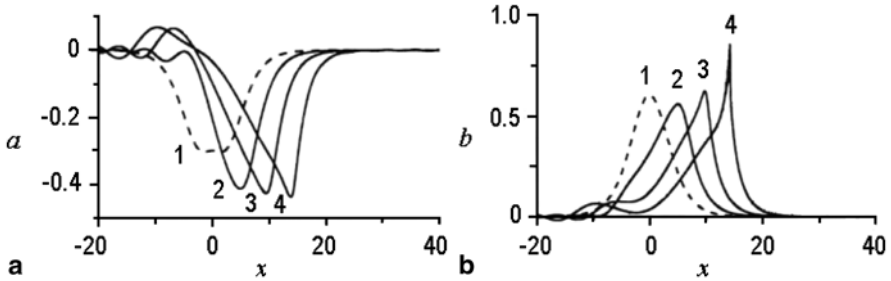

Fig. 5.33 Nonlinear evolution of an initial pulse of supercritical amplitude.Graphs (**a**) and **b** represent solutions of (5.29) (for variables a and b, respectively) at different dimensionless time t. After Voronovich et al. (1998a). Reproduced with permission from Cambridge University Press

contribution to the internal wave–vortex resonance is negligible. These are fundamentally different mechanisms.

This specific application of the internal wave–shear flow interaction theory described above has not yet been developed in detail. However, the effect of resonant interaction of propagating surface density plumes with environmental stratification has been reproduced in the numerical simulation using a computational fluid dynamics model (Matt et al. 2012). The model is initialized with a density (temperature) anomaly in the near-surface layer of the ocean (Fig. 5.34), which satisfies necessary conditions on the Froude and plume layer thickness conditions that are required for the resonant interaction (see Sect. 5.4.3). The low-density plume propagates in the upper layer of the water column as a buoyancy-driven current. The flow exhibits features of a classic gravity current, including the gravity current head and a tail region (compare to the example from TOGA COARE shown in Fig. 5.22b).

As the near-surface low-density plume propagates into the stratified environment, internal waves are excited in the thermocline. This then leads to a resonant interaction between the internal waves and the near-surface current, which results in a fragmentation of the low-density plume. The fragmentation becomes apparent as a banding pattern on the sea surface in the velocity field (Fig. 5.35). This pattern of alternating bands can also be seen in the sea surface signature in the simulated radar image calculated using the radar imaging model M4S (Romeiser 2008).

In the example shown in Fig. 5.35, a wind speed of 4 m/s along the x-axis is set in order to run the M4S model. The effect of wind stress on the plume hydrodynamics, however, was ignored in this example. We consider wind stress effects in the next section.

5.4.4 Interaction of Sharp Fronts with Wind Stress

High-resolution horizontal measurements in the open ocean thus reveal frontal interfaces of width less than 100 m. These sharp frontal interfaces have been observed in a wide range of wind speed conditions (0–15 m s^{-1}). The frontal interfaces of

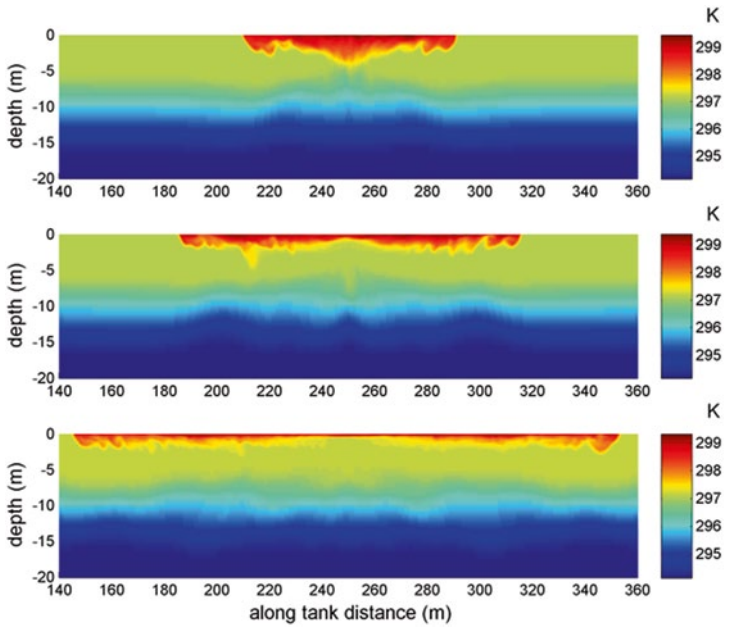

Fig. 5.34 A side view of temperature (in K) illustrates the propagation of the low-density plume in the near-surface layer and the internal waves generated in the thermocline. Time evolution is from top to bottom. *Top*: after time 300 s, middle: after 1500s, and *bottom*: after 2000s. After Matt et al. (2012)

less than ~100 m width reveal anisotropy with respect to the wind stress direction (Fig. 5.31).

Some of the frontal interfaces are narrow—sometimes only a few meters. Detailed analysis of the record shown in Fig. 5.26 reveals that the width of the frontal interface is only about 1.5 m; the absolute values of the horizontal temperature, salinity, and density gradients within this interface reach 137.8°C km^{-1}, 125.8 psu km^{-1}, and 47.96 kg km^{-1}, respectively. In particular, the density gradient within the interface is about 5×10^4 times larger than the mean horizontal density gradient (which is ~0.001 kg m^{-3} km^{-1}). This interface looks pretty much like a discontinuity or a "wall" in the upper ocean.

How can such discontinuities survive in the turbulent ocean? Soloviev and Lukas (1997) suggested that this happens because noncompensated fronts narrower than 100 m could interact with the wind stress. When the wind stress is directed toward lower density, gravitational instability may trigger intensive vertical and cross-frontal mixing. In the process of mixing, the interface may either reach the compensated state or entirely disappear; in both cases, the interface is no longer prominent in the density field. When the wind stress is directed toward higher density, vertical stratification develops due to tilting, which inhibits mixing. As a result, the sharp interface "freezes" and can drift downwind until the wind substantially changes either its direction or itsspeed with respect to the front. The lifetime of the

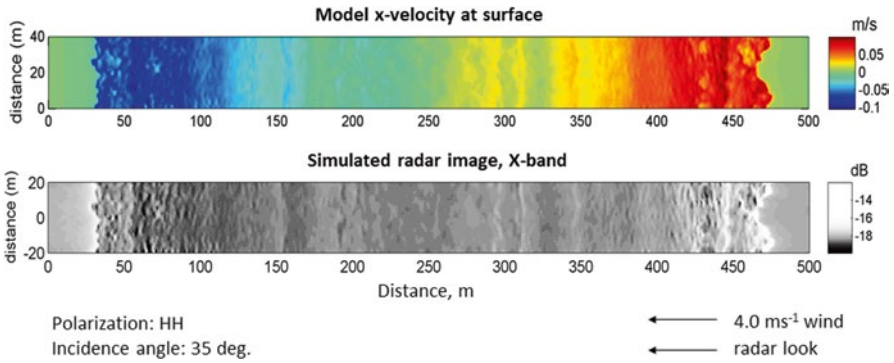

Fig. 5.35 Surface signature of low-density plume in the velocity field (top, in m/s) and radar backscatter intensity map (bottom; NRCS, db values here should be taken as relative). x-axis shows along-tank distance; y-axis is across-tank distance (in m). Taken at time t = 2850s. The surface velocity field from the hydrodynamic model is used as input for the radar model. After Matt et al. (2012)

sharp frontal interfaces can therefore be linked to the synoptic timescale for atmospheric processes (~5 days).

Soloviev et al. (2002) later identified this mechanism of the interaction between a sharp front and wind stress as Stommel's overturning gate (Fig. 5.36). According to Stommel (1993):

"Future observational study of the three-dimensional structures within the 'mixed' layer may show that direct driving of shear within the layer by wind overwhelms the hypothetical density-driven exchanges of thermohaline regulations (…) In the presence initially of a horizontal density gradient in the direction of the displacement, one of two events will ensue. If the displacement is toward larger mixed-layer density, then vertical stratification develops. Vertical mixing eventually occurs. There is a horizontal exchange of properties. On the other hand, if the wind-forced displacement of the surface half of the mixed layer is toward smaller density below, rapid gravitational instability will mix the two halves immediately, effectively short cutting the horizontal exchange (…) Therefore, there is a form of gate that opens or closes to allow horizontal flux of properties in the mixed layer, and it depends on the joint signs of displacement and local horizontal density gradient. For convenience this phenomenon may be called the *overturning gate*."

Stommel's overturning gate is open when the surface wind drift current is directed toward higher density and closed when directed toward lower density, as it is schematically illustrated in Fig. 5.36a, b. In case b, the wind drift current stabilizes the sharp frontal interface, which then resembles an arrested wedge.

The spatial anisotropy of noncompensated interfaces (Fig. 5.31a, c) can therefore be explained by the fact that most sharp frontal interfaces are observed when the wind stress is directed toward higher density (the overturning gate is opened). When the wind stress is toward lower density (the overturning gate is closed), the intensive mixing effectively eliminates noncompensated sharp frontal interfaces (this

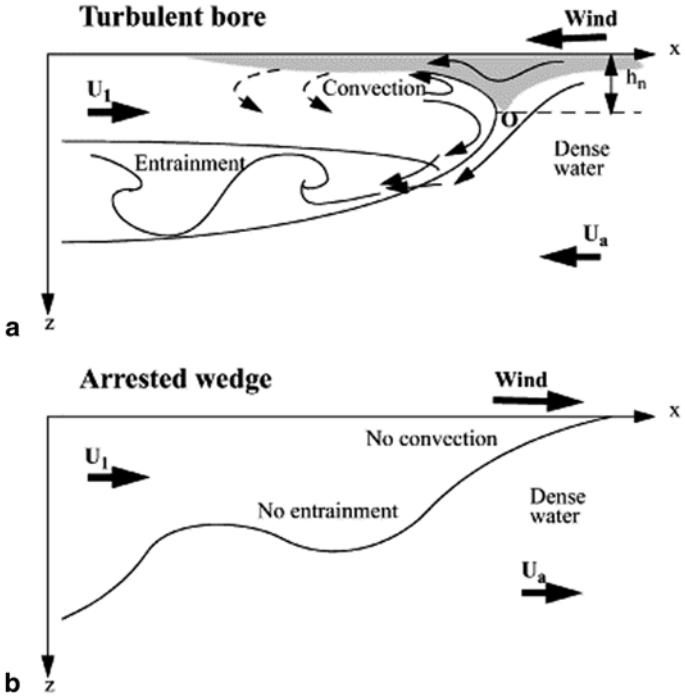

Fig. 5.36 Interaction of sharp frontal interface with wind stress: **a** Stommel's overturning gate is closed; **b** Stommel's overturning gate is opened. After Soloviev et al. (2002) with permission from Elsevier

process is illustrated in Fig. 5.28). The lifetime of a noncompensated sharp frontal interface opposing the wind stress is relatively small; the probability of its observation is reduced.

Stommel's overturning gate is a complicated nonlinear problem. Its faithful solution in the framework of the hydrodynamics equations is not feasible now, though the internal wave–shear flow interaction theory described in the previous section has a good chance to succeed in this direction.

At the same time, the structural form of the sharp frontal interfaces has some similarity to that of the internal surge previously observed in long stably stratified lakes (Thorpe 1971; Hunkins and Fliegel 1973; Farmer 1978). The evolution of an initially smooth perturbation with wavelength $\lambda >> h_0$ into an asymmetric shockwave structure can be described in the framework of the shallow water theory similar to the analysis of Farmer (1978) for a long stably stratified lake; however, in our case, h_0 is the depth of the intermediate thermocline associated with the front.

At the stage when the internal perturbation's slope becomes very steep, dispersion and dissipation effects are important in this nonlinear system. Whitham (1974) and Barenblatt and Shapiro (1984) applied an equation of Korteweg–de Vries–

Burgers type to explore a simple nonlinear system with dispersion and dissipation. Applied to a two-layer upper ocean with an infinitely deep lower layer, this equation is as follows:

$$\eta_t + c_0\left(1+\frac{3}{2}\frac{\eta}{h_0}\right)\eta_x + \frac{1}{6}c_0 h_0{}^2\eta_{xxx} = \nu_e\eta_{xx}, \tag{5.31}$$

where η is the displacement of streamlines, t is time, x is the horizontal coordinate in the direction of propagation, h_0 is the undisturbed depth of the near-surface pycnocline, $c_0 = (g'h_0)^{1/2}$ is the phase speed of the disturbance, g' is the reduced gravity, and ν_e is the effective (turbulent) viscosity.

The Korteweg–de Vries–Burgers equation is a convenient tool in exploring the relative importance of dissipation and dispersion in a weakly stratified mixed layer of the ocean, since this equation represents the simplest form of nonlinear evolution including both dispersion and dissipation. (Some caution should however be exercised here because Whitham (1974) and Barenblatt and Shapiro (1984) did not derive (5.31) directly from the Navier–Stokes equation.)

Steady propagating solutions of (5.31) are of the form $\eta = h_0\zeta(X)$, $X = x - Ut$, where U is the propagation speed of the disturbance. The integration of Eq. (5.31) results in (Whitham 1974)

$$\frac{1}{6}h_0{}^2\zeta_{xx} - \frac{\nu_e}{c_0}\zeta_x + \frac{3}{4}\zeta^2 - \left(\frac{U}{c_0}-1\right)\zeta = 0, \tag{5.32}$$

which can be normalized in the following way:

$$z_{\xi\xi} - mz_\xi + z^2 - z = 0, \tag{5.33}$$

where $\xi = 6\left[(Fr-1)\right]^{1/2}\frac{X}{h_0}$, $z = \frac{3}{4(Fr-1)}\zeta$, $F = \frac{U}{c_0}$

$$m = \left(\frac{6}{Fr-1}\right)^{1/2}\mathrm{Re}_*^{-1}, \tag{5.34}$$

$$\mathrm{Re}_* = h_0(g'h_0)^{1/2}\nu_e^{-1}. \tag{5.35}$$

Here, Re_* is the dimensionless Reynolds number, which defines the relationship between the dissipative and dispersive properties of this nonlinear system (Barenblatt and Shapiro 1984). According to Whitham (1974), for $m<2$ the solution is a wavelike (soliton) type, while for $m>2$, it is a shockwave (dissipative) type. The critical value of $m=2$ at $Fr=1.2$ corresponds to $\mathrm{Re}_* = \mathrm{Re}_{cr} = 2.74$. This means that the solution of (5.31) is wavelike in nature (and finally evolves into a wavelike bore) for

$\mathrm{Re}_* > \mathrm{Re}_{cr}$ and is turbulent in nature (and finally evolves into a turbulent bore) for $\mathrm{Re}_* < \mathrm{Re}_{cr}$.

The wavelength of the wave train that occurs at $\mathrm{Re}_* < \mathrm{Re}_{cr}$ can be estimated using Whitham's (1974) solution of (5.33) as follows: $\lambda \approx 6.5\left[6(F-1)\right]^{-1/2} h_0$. At $Fr = 1.2$ and $h_0 = 20$ m, this results in a 120 m wavelength.

One problem emphasized by Whitham (1974) is that the effective viscosity that can be obtained by parameterization via the mean shear flow is about 10 times smaller than that necessary to achieve the critical value of Re_*. This problem, however, can be resolved by incorporating Stommel's concept of the overturning gate. When the wind stress opposes buoyant spreading of the sharp front, the convective overturning enhances the effective viscosity at the sharp frontal interface. Soloviev and Lukas (1997) parameterized the effective viscosity entering (5.35) as a sum of shear (ν_{shear}) and convectively (ν_{conv}) induced turbulent viscosity:

$$\nu_e \approx \nu_{shear} + \nu_{conv} = \nu_{shear} f_c, \tag{5.36}$$

where $\nu_{shear} = \kappa u_* h_0$, $f_c = 1 + \nu_{conv} / \nu_{shear} \approx 1 + \left[30 \frac{h_0}{L}\left(\cos\phi + |\cos\phi|\right)\right]^{1/3} \frac{Ri_*^{1/6}}{\kappa}$ is the factor describing convective enhancement of mixing in the frontal zone, L is the width of the frontal interface, $Ri_* = g' h_0 / u_*^2 = (c_0 / u_*)^2$, c_0 is the phase speed of internal disturbances, u_* is the friction velocity in water, κ is von Karman's constant ($\kappa = 0.4$), and ϕ is the wind direction relative to the direction of buoyant spreading of the front. For $\phi > 90°$ or $\phi < -90°$ and $f_c \equiv 1$, no convective instability is possible (Stommel's overturning gate is opened), while for $-90° < \phi < 90°$ and $f_c > 1$ convective instability at the leading edge of the gravity current can develop (Stommel's overturning gate is closed).

Incorporation of parameterization (5.36) into (5.35) leads to the following relationship:

$$\mathrm{Re}_*\left(Ri, \phi\right) \approx \frac{\kappa^{-1} Ri_*^{1/2}}{\left\{1 + \left[30\left(\cos\phi + |\cos\phi|\right) h_0 / L\right]^{1/3} \kappa^{-1} Ri_*^{1/6}\right\}}, \tag{5.37}$$

which is shown in Fig. 5.37. The horizontal plane in Fig. 5.37 corresponds to the relationship

$$\mathrm{Re}_* = \mathrm{Re}_{cr} = 2.74 \tag{5.38}$$

which separates the arrested wedge and turbulent bore regimes.

A two-dimensional version of Fig. 5.37 is given in Fig. 5.38, which shows (5.37) for $h_{0=}10$ m, $L = 20$ m, and $\Delta\sigma_t = 0.05$ kg m^{-3} for the friction velocity range 0.001 m s$^{-1} < u_* < 0.01$ m s^{-1}. A turbulent bore solution is possible when the wind opposes the buoyant spreading of the front. Under light winds or in the case when

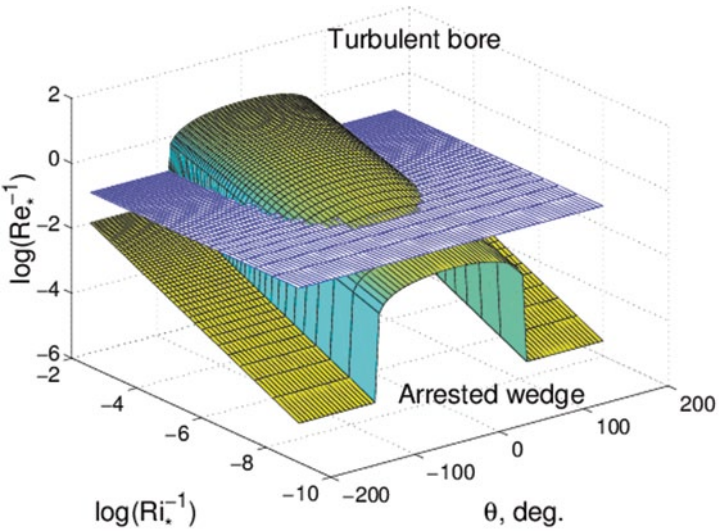

Fig. 5.37 Diagram for the two regimes of wind–front interaction according to (5.37)-(5.38). After Soloviev et al. (2002) with permission from Elsevier

the wind velocity is directed along the direction of buoyant spreading of the front, $\mathrm{Re}_* > \mathrm{Re}_{cr}$, and the solution is of the wave train type

For the case shown in Figs. 5.17–5.21, $\mathrm{Re}_* \approx 2-4$; the sharp front is close to the regime of the internal turbulent bore. For the case shown in Fig. 5.22, $\mathrm{Re}_* \approx 60$; the sharp frontal interface is in the arrested wedge regime. Since dispersion dominates over dissipation in the arrested wedge regime, an internal wave train may develop. However, the horizontal grid for the SEASOAR and ADCP data (3 km) is not sufficient to resolve short internal wave trains. Soloviev et al. (2002) speculated that from the bow data it is possible to see these shortwave oscillations at the front intersection only when the surface plume depth is relatively shallow (with respect to the sensor depth, which is ~2 m). In the cases presented in Figs. 5.17–5.21, the plume depth was much larger than 2 m.

When the wind stress direction coincides with the buoyancy-driven propagation of the front (θ=180°), (5.37) reduces to

$$\mathrm{Re}_*(Ri, 180^o) = \kappa^{-1} Ri_*^{1/2}. \tag{5.39}$$

Since $Ri_* = (c_0/u_*)^2$ and $c_0 >> u_*$, the development of a turbulent bore in this situation is practically impossible.

When the wind stress opposes the buoyant spreading of the front (ϕ=0°), (5.37) correspondingly reduces to

$$\mathrm{Re}_*(Ri_*, 0) = \frac{\kappa^{-1} Ri_*^{1/2}}{\left\{1 + (60h/L)^{1/3} \kappa^{-1} Ri_*^{1/6}\right\}}. \tag{5.40}$$

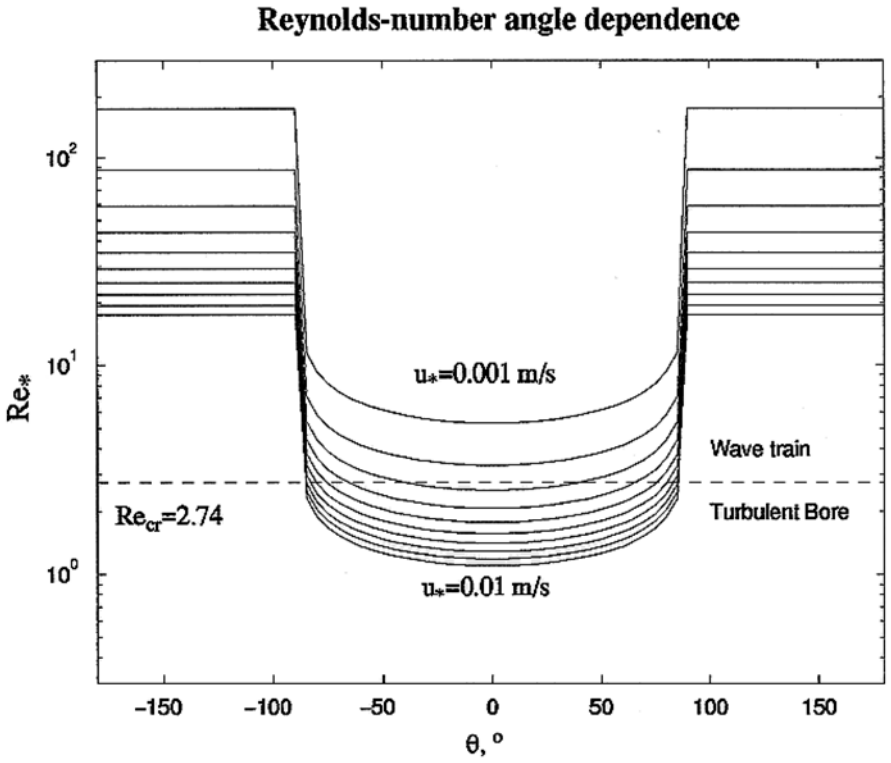

Fig. 5.38 Dependence of Reynolds number Re_* on wind direction relative to the direction of the buoyant spreading of the front θ, calculated for friction velocity u_* from 0.001 to 0.01 m s^{-1} in steps of 0.001 m s^{-1}. Dashed line represents critical value of the Reynolds number. After Soloviev and Lukas (1997). Copyright © 1997 American Meteorological Society. Used with permission

Estimates show that the condition for the development of an internal turbulent bore,

$$\mathrm{Re}_*(Ri_*, 0) < \mathrm{Re}_{cr}, \tag{5.41}$$

can be easily satisfied for a weakly stratified mixed layer. For the seasonal thermocline, however, it is practically impossible to satisfy (5.41) due to considerable stratification and larger depth. The response to wind forcing in the form of an internal turbulent bore is therefore possible for weakly stratified mixed layers but not possible for the seasonal thermocline (perhaps except during hurricane conditions).

Since for most practical situations, $(60h/L)^{1/3}\kappa^{-1}Ri_*^{1/6} >> 1$, formula (5.40) can be simplified as follows:

$$\mathrm{Re}_*(g', u_*, 0) \approx \frac{1}{60^{1/3}}(g'L/u_*^2)^{1/3} = \mathrm{Re}_L, \tag{5.42}$$

which contains only parameters that are readily available from the ship's underway measurements ($g' = g\Delta\rho/\rho$ is the reduced gravity, $\Delta\rho$ the density difference across the frontal interface, L the interface width, and u_* the frictional velocity). Re_L exceeds Re_* by 7% on average for $h_0 = 10$ m and by 16% for $h_0 = 2$. The difference between Re_L and Re_* increases with decreasing h_0. Recall that the algorithm for sharp frontal interface detection (see Sect. 5.4.2) does not detect the interfaces associated with plumes of less than approximately 2 m depth, as these plumes are above the mean depth of the bow sensors.

It is remarkable that no measurement of the intermediate pycnocline depth, h_0, is required to calculate the *frontal Reynolds number*, Re_L, defined by formula (5.42). This number can therefore be estimated practically for all observations of sharp frontal interfaces made during TOGA COARE (Fig. 5.39b). According to the theory considered here, Stommel's mechanism of the overturning gate (including the development of an internal bore) is possible in principle at

$$\mathrm{Re}_L < \mathrm{Re}_{cr}. \tag{5.43}$$

This is, however, only a necessary but not sufficient condition for the internal bore regime (remember that Re_L is an asymptote of (5.40). It does not account for the wind-to-front angle dependence described with (5.37)).

In terms of the interface width, (5.43) transforms into inequality

$$L < L_{cr}. \tag{5.44}$$

From (5.38) and (5.42), the critical width of the frontal interface is $L_{\mathrm{cr}} = 1234\, u_*^2/g'$. Inequality (5.44) means that only very sharp frontal interfaces (typically of less than 100 m width) can interact with wind stress.

As we already mentioned in Sect. 5.4.2, condition (5.43) had been applied to the data shown in Fig. 5.31; as a result, the error bars for the directional dependence reduced. In fact, only 10% of the density interfaces detected from the COARE bow data with the algorithm described in Sect. 5.4.2 do not satisfy condition (5.43); according to the theory developed here, these interfaces cannot interact with wind stress at any wind-to-front angle.

As follows from relationship (5.37), the transition from the wavelike to the turbulent regime occurs (if it occurs at all) almost sharply at $\phi = \pm 90°$ (Fig. 5.37). If a turbulent bore does develop, the frontal interface is intensively mixed and may disappear or reach a compensated state quickly. If no turbulent bore develops then the situation has some analogy to the arrested wedge, and the frontal interface may exist for a relatively long time, drifting with the wind. This means that the observed fronts are mainly arrested frontal interfaces, which can explain their spatial anisotropy with respect to wind direction (Figs. 5.31a, c).

Because the transition from turbulent to arrested front occurs when convective overturning starts, there should be dependence on the angle rather than on wind

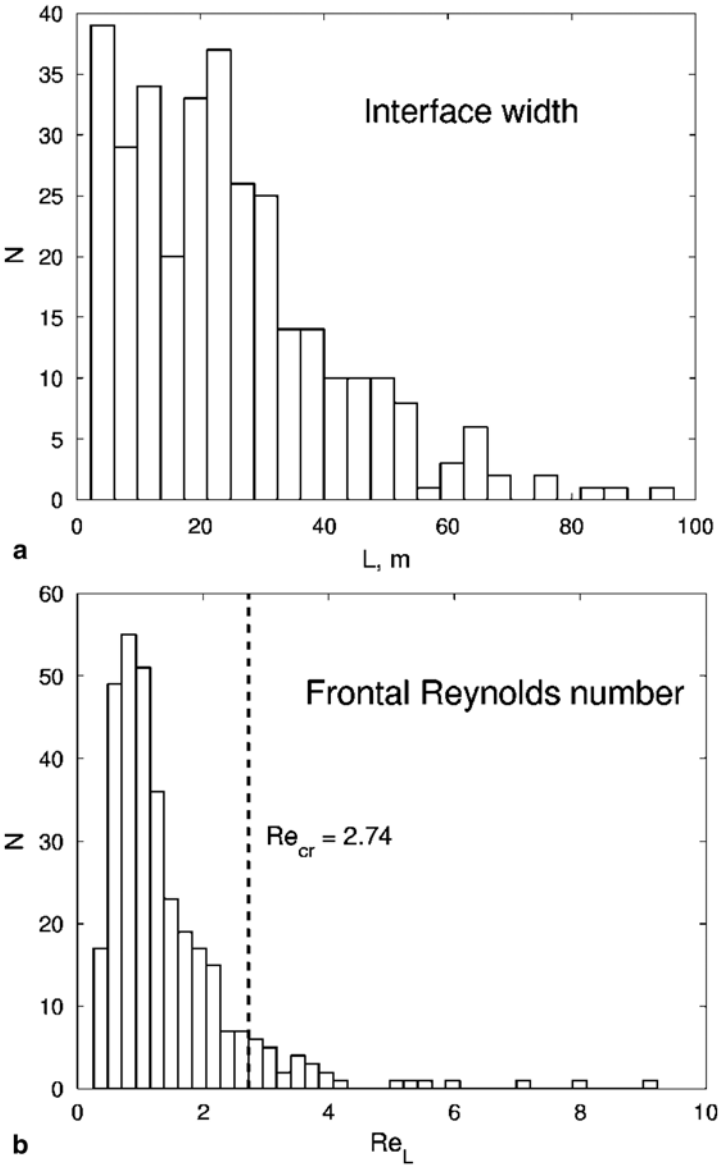

Fig. 5.39 Histograms of (**a**) width, L, and (**b**) frontal Reynolds number, Re_L, for the sharp frontal interfaces detected in the bow density data for four TOGA COARE cruises of the R/V *Moana Wave*. After Soloviev et al. (2002) with permission from Elsevier

speed, which is consistent with observations (Fig. 5.31b). This is because convection triggers the development of billows, which are relatively large eddies providing an effective mixing mechanism.

In the case of compensated fronts, there is no interaction between the frontal interface and wind stress, and no spatial anisotropy is expected. This is consistent with observed temperature interfaces (Fig. 5.31e), which are mostly compensated. Some dependence on wind speed observed in Fig. 5.31f can be explained by the fact that the wind-induced turbulent mixing increases with wind speed, thus affecting the erosion of compensated frontal interfaces.

The sharp frontal interfaces discussed here are different from the so-called *ramp-like* coherent structures. The ramp-like structures are described in Sect. 5.6.

5.4.5 Parameterization for Cross-Frontal Exchange

From the concept of Stommel's overturning gate (Fig. 5.36), a sharp frontal interface may evolve into:

a. an arrested wedge, which "freezes" the frontal structure or
b. a bore-like structure, which dramatically intensifies the cross-frontal exchange and leads to a rapid elimination of the density difference across the interface.

According to the laboratory experiment of Simpson (1987), the gravitational instability induced at the leading edge of a surface gravity current by an opposing surface stress (wind stress in our case) may trigger Kelvin–Helmholtz instability and billowing in tale part of the gravity current head. The entrainment flux associated with this instability achieves a relatively large value, estimated by Simpson (1987) as 0.15 times the mass flux of the gravity current itself. These considerations lead to the following parameterization of the cross-frontal mass exchange (Soloviev et al. 2002):

$$\overline{u'\rho'} = \begin{cases} c_e V_g \Delta\rho, & \text{for } \mathrm{Re}_* \le \mathrm{Re}_{cr} \\ \sim 0, & \text{for } \mathrm{Re}_* > \mathrm{Re}_{cr} \end{cases}, \tag{5.45}$$

where u' and ρ' are deviations from the temporal or spatial mean cross-front velocity and density, $\Delta\rho$ is the density difference across the frontal interface, $c_e \approx 0.15$ is an empirical constant, and V_g is the speed of the gravity current estimated here in the same way as in Sect. 5.4.1: $V_g = F(g'h_0)^{1/2} \approx 1.2(g'h_0)^{1/2}$. In accordance with (5.37) (see also Fig. 5.37):

$$\mathrm{Re}_*(Ri,\phi) \approx \kappa^{-1} Ri_*^{1/2} / \left\{1 + \left[30\left(\cos\phi + |\cos\phi|\right) h_0 / L\right]^{1/3} \kappa^{-1} Ri_*^{1/6}\right\}, \; Ri_* = g'h_0 / u_*^2,$$

and $\mathrm{Re}_{cr} \approx 2.74$. Similar formulas can be derived for the heat, salinity, and chemical substance flux by replacing the density in (5.45) with the temperature, salinity, or concentration, respectively.

Increased scatter of the experimental points near $\theta = -90°$ and $\theta = 90°$ in Fig. 5.31a possibly indicates that there are some processes that are not controlled by Stommel's overturning gate mechanism. (The increased scatter may also be due to the uncertainty of the front alignment relative to the wind, which makes the sign of the cross-front component unknown when the wind is close to alignment with the front.) In particular, the tangential shear that is often observed at sharp fronts (see Figs. 5.21 and 5.22) may result in the formation of quasi-geostrophic eddy pairs, advection within these eddies, and the ultimate destruction of eddies with subsequent dissipation of the thermohaline structure. For mid-latitudes and high latitudes, this mechanism can be parameterized as follows (Spall and Chapman 1998):

$$\overline{u'\rho'} = c_e V_m \Delta \rho \tag{5.46}$$

where V_m is a scale for the along-front velocity and $c_e \approx 0.045$ is an empirical constant. (Though constant c_e does not appear to depend on rotation effects explicitly, the validity of parameterization (5.46) for low latitudes has not yet been proven.)

Parameterization (5.46) has a structure similar to (5.45). The ratio of the constants, $c_b/c_e \sim 3$, and of the velocity scales, $V_g/V_m \sim 1$, suggests that the cross-frontal exchange due to an internal bore is comparable to, or perhaps exceeds, the cross-frontal exchange due to eddies.

5.4.6 Implications for the T–S Relationship in the Mixed Layer

As follows from the discussion in Sects. 5.4.4 and 5.4.5, on horizontal scales less than approximately 100 m the temperature–salinity relationship in the mixed layer of the ocean depends on the relative angle between the horizontal density gradient and the wind stress vector.

Ferrari and Rudnick (2000) found that the horizontal density ratio R in the subtropical Pacific mixed layer is close to 1 for horizontal scales >100 m. Statistics for 1 month of low-latitude observations acquired during TOGA COARE (see Fig. 5.30) indicate that there are numerous cases of noncompensated density fronts (*i.e.*, $R \neq 1$). These statistics, however, relate to the sharp interfaces only (*i.e.,* those less than ~100 m width) and are therefore not contradictory to the results of Ferrari and Rudnick (2000).

5.4.7 Observations of Sharp Frontal Interfaces in Mid-Latitudes and High Latitudes

The substantial observational statistics of the sharp frontal interfaces reported here are from tropical latitudes only. Sharp fronts have been observed in mid-latitudes as well. To our knowledge, there are only a few cases of shipboard observations (Zenk

and Katz 1975; Soloviev and Zatsepin 1992); no representative statistics have been obtained in mid-latitudes.

In high latitudes, sharp frontal interfaces are expected to be present in the marginal ice zone during periods of ice melting. To the best of our knowledge, there have been no horizontal microstructure measurements in the near-surface layer of the ocean in polar seas.

At this point, we do not know exactly how the sharp frontal interfaces are affected by the Earth's rotation. From general considerations, the rotation should not directly affect the internal structure of sharp fronts because their width is so small. Fronts, nevertheless, are associated with larger scale anomalies; these anomalies may depend on the Earth's rotation even near the equator. In particular, the sharp front shown in Fig. 5.22a was found at the edge of a density anomaly with cyclonic vorticity, that appears to be caused by the inertial spin-down of an eastward equatorial jet (Feng et al. 2001). In mid-latitudes, mesoscale eddies wind the sharp fronts into spirals (Munk and Armi 2001).

5.5 Internal Waves in the Near-Surface Pycnocline

As described in Sect. 4.2.3, the shallow diurnal thermocline and rain-formed halocline are subject to perturbations in the form of internal waves. In some instances, these internal waves become large, transform into billows or rolls, and can produce signatures in SST and on synthetic aperture radar (SAR) images.

5.5.1 Large-Amplitude Internal Waves

The terminology "large-amplitude" internal wave in this context means that the amplitude of the internal wave is of the order of the distance to the surface (depth). Soloviev and Lukas (1996) reported an observation of a packet of large-amplitude internal waves in the diurnal thermocline (Fig. 5.40). The observation was made with bow-mounted sensors (see Sect. 3.3.5) while steaming at 10–11 knots.

CTD profiles made before and after this section revealed a barrier layer above the thermocline with a salinity difference of ~0.6 to ~1.0 psu from the top of the thermocline to the base of the mixed layer. The depth of the upper quasi-homogeneous layer identified in the CTD temperature profiles was 40 m before and 80 m after the section, respectively. Horizontal variability of the salinity in Fig. 5.40 was presumably because of the previous surface forcing (rainfall) or the spatial variability of the underlying barrier layer.

Figure 5.41 documents the evolution of averaged vertical profiles of T, S, and σ_t on the same day (22 April 1994) from early morning until late afternoon. At 8:37 LT, the profiles of T, S, and σ_t showed a well-mixed near-surface layer (within the 3 m depth variation range of the bow sensors). Wind speed was 2.2 m s^{-1}. The

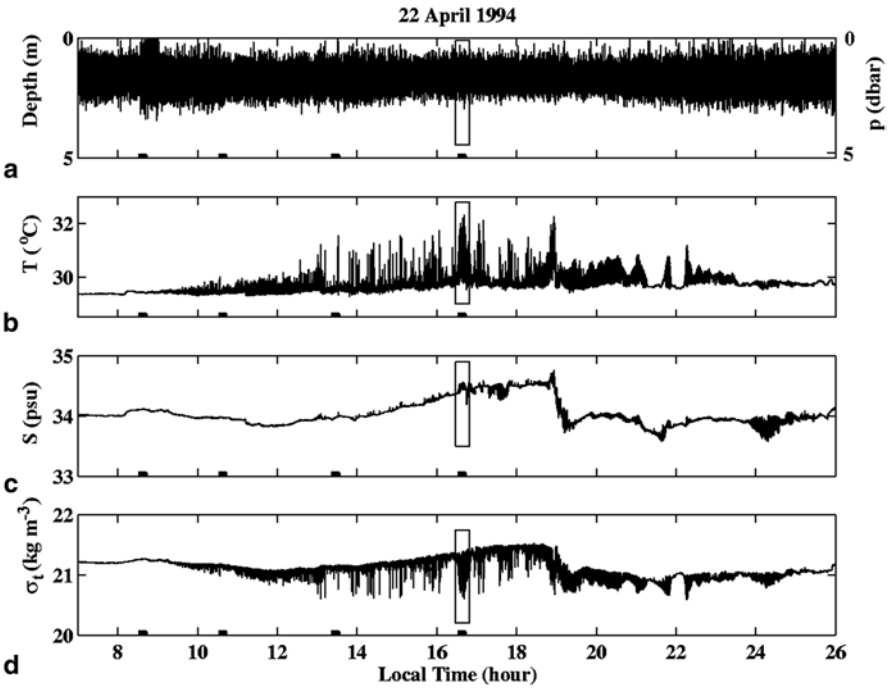

Fig. 5.40 Example of records of (a) depth (pressure), (b) temperature, (c) salinity, and (d) sigma-t density made by bow sensors in the western Pacific warm pool during a strong diurnal warming event. Segments marked by rectangles are shown in more detail in Fig. 5.42. Solid segments on the time axis correspond to 10 min averaging intervals for calculation of vertical profiles of *T, S*, and s_t shown in Fig. 4.7. After Soloviev and Lukas (1996). Copyright © 1996 American Meteorological Society. Used with permission

temperature profile at 10:37 LT indicated that the diurnal warming of the upper ocean layer had started; because of low wind speed conditions (1.5 m s^{-1}), the diurnal thermocline was within the upper meter of the ocean surface. At 13:27 LT, the diurnal thermocline was still in the upper 1 m because of calm conditions (0.9 m s^{-1} wind speed); the temperature difference reached ~2°C. There was also ~0.1 psu salinity difference across the diurnal thermocline as a result of evaporation from the ocean surface and accumulation of the excess salinity within the diurnal mixed layer.

At 16:37 LT (Fig. 5.41), the beginning of the evening deepening of the diurnal thermocline, vertical profiles reveal increased scatter. This time interval is analyzed further in the contour plot shown in Fig. 5.42. The corresponding section of the records is denoted in Fig. 5.40 by a rectangle. There are high-frequency oscillations of *T*, *S*, and σ_t in this record (Fig. 5.42, b–d) because of the depth variation of the probes (Fig. 5.42a). There are also variations in temperature of about 2°C in *b*, which are visible over several kilometers. The $\sigma_t - p$ contour plot (Fig. 5.42d) reveals wavelike disturbances of the diurnal thermocline with a typical scale beginning from ~200 m.

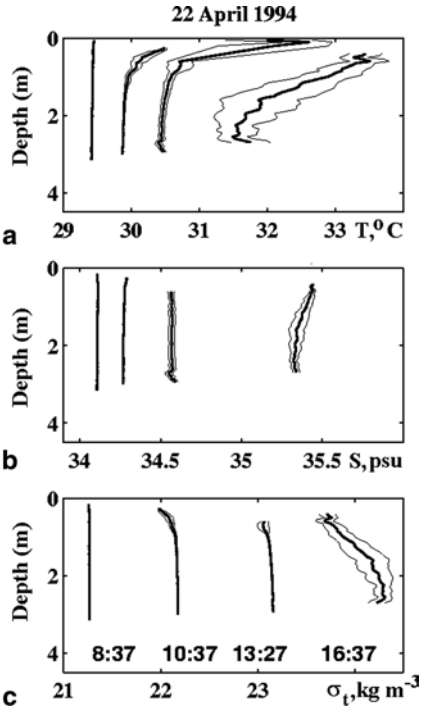

Fig. 5.41 Vertical profiles of temperature, salinity, and density obtained by averaging 10 min intervals of the bow sensor data within 0.1 dbar pressure ranges. Each successive profile is shifted by 0.5° C in temperature, by 1.2 psu (in subplot a) and 0.3 psu (in subplot b) in salinity, and by 1.0 in σ_t. The local time below each profile corresponds to the middle of the 10 min segment. Thin lines represent one standard deviation. After Soloviev and Lukas (1996). Copyright © 1996 American Meteorological Society. Used with permission

The $T - \sigma_t$ contour plot in Fig. 5.42e reveals an asymmetric anomaly between 5300 and 6000 m associated with a salinity feature (Fig. 5.42d). It is not clear, however, whether it has any connection with the large-amplitude shortwave train observed in the $\sigma_t - p$ contour plot (Fig. 5.42d).

The $\sigma_t - p$ contour plot in Fig. 5.42d shows an intermittent wavelike pattern. The intermittence in space and time, with energy predominantly in the first mode, is a typical feature of short-period internal waves trapped in the thermocline that is close to the surface (Brekhovskikh et al. 1972). There is also asymmetry in the perturbations in Fig. 5.42d. When a thermocline is close to the surface, it is typical for the wave crest to flatten and the troughs to become sharper (Thorpe 1968).

These observations revealed a near-surface spatial structure that looks like a packet of large-amplitude internal waves. For the data shown in Fig. 5.42d, the amplitude of the wavelike perturbations is much larger than the uncertainty of the pressure-to-depth conversion (~0.1 m). The 30-day data set analyzed by Soloviev and Lukas (1996) contained several other cases of large-amplitude internal waves within the diurnal thermoclineto the amplitude comparable with the depth of the thermocline.

For comparison, Voropaev et al. (1981) observed a wavelike perturbation of the diurnal thermocline of ~200 m length and ~1 m height under 5 m s^{-1} wind speed. Imberger (1985) presented detailed near-surface measurements from a freshwater lake during 21.5 hours, including the observation of internal waves of ~1 m amplitude and billows associated with the diurnal thermocline.

Wijesekera and Dillon (1991) and Lien et al. (1996) observed packets of internal waves with approximately 200 m wavelength associated with diurnal cycling. Interestingly, Wijesekera and Dillon (1991) found for a large-amplitude wave packet that the wave-induced Reynolds stress below the mixed layer was of the same order of magnitude as the surface wind stress.

Mack and Hebert (1997) found large-amplitude internal waves in the upper layer of the eastern equatorial Pacific Ocean from towed thermistor-chain measurements. Occurrences of large-amplitude internal waves were consistent with solutions to the Taylor–Goldstein equation for shear flow instability (see Sect. 5.5.3). This instability is due to changes in the vertical structure of the mean horizontal velocity and density associated with diurnal cycling.

The two mechanisms presumably important for the generation of internal waves on the near-surface pycnocline are (a) resonant interactions between the internal mode and a pair of surface waves with almost equal frequency and direction and (b) the shear instability produced by the diurnal jet at the evening deepening due to convection. Below, we discuss both mechanisms in more detail.

5.5.2 *Surface–Internal Wave Resonant Interactions*

Nonlinear interaction of surface gravity waves can cause the excitation of internal waves in stratified near-surface layers. Observations of Apel et al. (1975), Briscoe (1983), and others suggest that a strong ocean swell can generate internal waves. A pair of surface waves with almost equal frequency and direction and an internal wave may satisfy the necessary conditions of the resonant triad (Phillips 1977):

$$\vec{k} = \vec{k}_1 - \vec{k}_2 \text{ and } \omega(\vec{k}) = \omega(\vec{k}_1) - \omega(\vec{k}_2), \tag{5.47}$$

where $\vec{k}_1$ and $\vec{k}_2$ are the wavenumber vectors, $\omega_1 = \omega(\vec{k}_1)$ and $\omega_2 = \omega(\vec{k}_2)$ are the frequencies of the pair of surface waves, $\vec{k}$ is the wavenumber vector, and ω is the frequency of the internal wave.

Brekhovskikh et al. (1972) and Watson et al. (1976) used a *locked-phase approximation* to theoretically describe two surface waves interacting with an internal wave. This mechanism is relatively strong, predicting the internal-wave growth timescale of the order of a few hours. It requires, however, a special situation: Each of the two surface waves must have a deterministic phase relationship for as long as it takes to generate the internal wave. This is possible for a narrow-band long ocean swell.

Models of *spontaneous creation mechanism* (Olbers and Herterich 1979) and *modulation mechanism* (Dysthe and Das 1981) are based on incoherent or statistical three-wave interactions. According to Olbers and Herterich (1979), the spontaneous creation mechanism may play an important role if there is strong stratification. Watson (1990) concluded that, except for winds > 20 m s^{-1}, only the modulation mechanism is of practical significance (but with energy flow from the internal to the surface waves). In contrast to this result for the wind waves, Watson (1990) also found that a strong, narrow-band ocean swell can lead to rapid growth of high-frequency internal

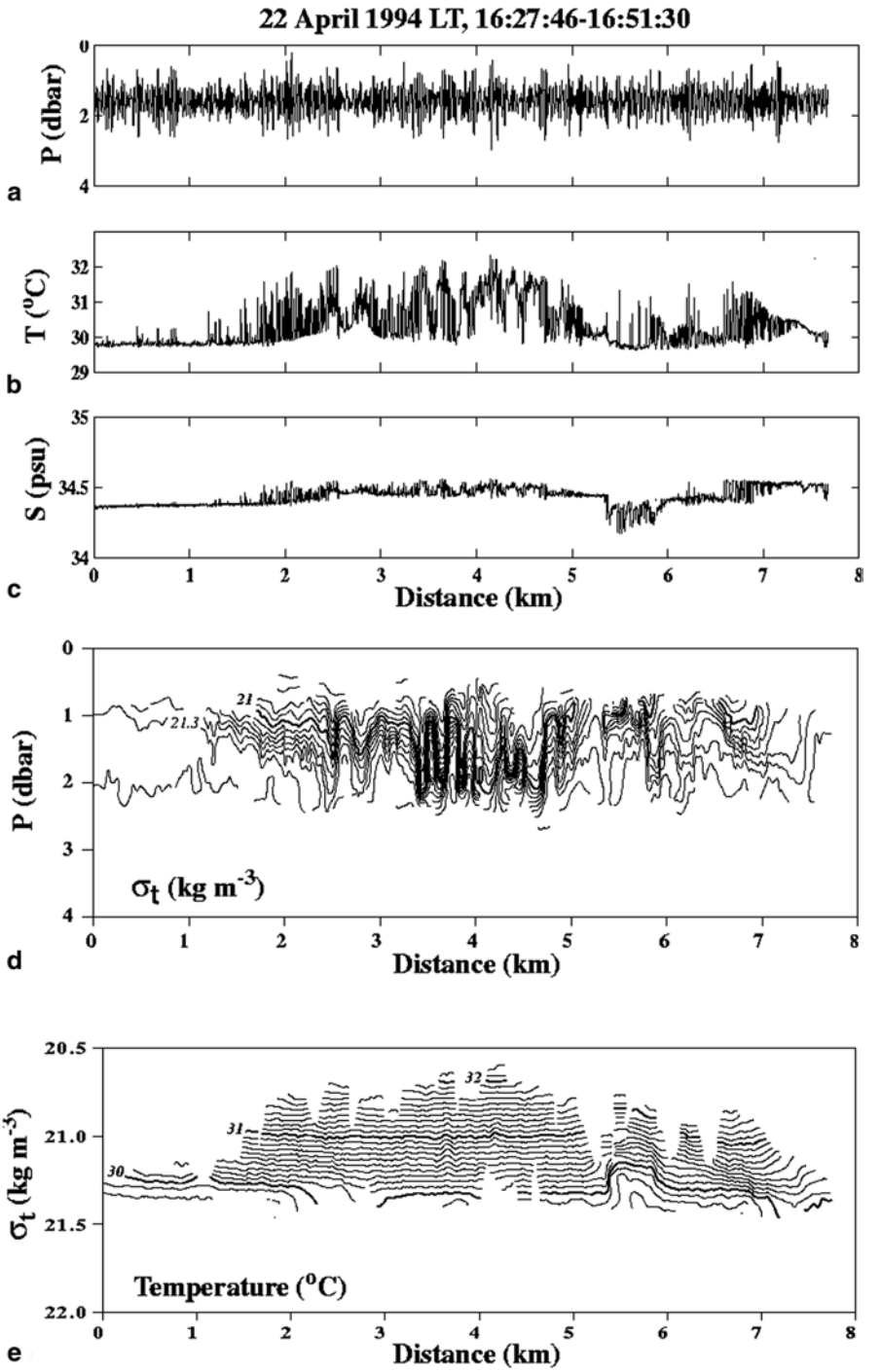

waves. The application of the theoretical models cited above, however, demands advanced measurement for both internal and surface wave components, which has not yet been done.

5.5.3 Kelvin–Helmholtz Instability of a Sheared Stratified Flow

The kinetic energy accumulated by the diurnal jet during a period of intensive warming is a possible source of mechanical energy for the generation of internal waves and billows in the diurnal thermocline. During a period of intensive solar heating, the turbulent friction in the diurnal thermocline is substantially reduced due to buoyancy forces (Kudryavtsev and Soloviev 1990). The shallow diurnal jet accumulates the momentum transferred from the wind. In the evening, the net surface buoyancy flux at the ocean–air interface decreases, and when it becomes negative convection develops (see Sect. 5.8.3); the slippery conditions within the diurnal thermocline disappear and the momentum flux at the lower boundary of the diurnal jet increases. This provides favorable conditions for the Kelvin–Helmholtz instability. The atmospheric forcing may significantly vary during the day (*e.g.,* because of clouds) producing short-term conditions for Kelvin–Helmholtz instability in the diurnal thermocline (see an example in Fig. 4.20).

The instability of a continuously stratified shear flow can be described with the Taylor–Goldstein equation (Taylor 1931; Goldstein 1931). The Taylor–Goldstein equation is derived under the assumption of an inviscid, Boussinesq fluid; the vertical structure equation is linearized around the vertical profiles of horizontal velocity and density representing the basic state. The upper equatorial ocean typically has strong mean shear, which in general may not coincide with the direction of the diurnal jet (the latter largely depends on wind stress direction). Mack and Hebert (1997) generalized this equation for a three-dimensional case in the following way:

$$\partial_{zz}^2 w + \left[\frac{\left|\vec{k}\right|^2 N^2}{\left(\vec{k}\cdot\vec{u}-\omega\right)^2} - \frac{\vec{k}\cdot\vec{u}_{zz}}{\vec{k}\cdot\vec{u}-\omega} - \left|\vec{k}\right|^2 \right] w = 0 \tag{5.48}$$

where $w(z)$ is the vertical structure of vertical velocity, $\vec{u} = \{u(z), v(z)\}$ is the mean horizontal velocity vector consisting of zonal $u(z)$ and meridional $v(z)$ components, $\vec{k} = \{k, l\}$ is the horizontal wavenumber vector consisting of the zonal k and meridional l components, ω is the complex frequency, $N^2(z) = -g\partial_z \overline{\rho} / \rho_0$ is the mean squared buoyancy frequency, and $\overline{\rho}$ and ρ_0 are the horizontal mean and the overall

Fig. 5.42 Observations during strong diurnal warming near 2.2° S, 161.7°E during COARE cruise EQ-3. The upper part of the figure shows records of **a** pressure, **b** temperature, and **c** salinity. The lower part shows corresponding contour plots **d** of σ_τ versus P and **e** of T versus σ_τ. Wind speed is 0.5 m s^{-1} – 1.0 m s^{-1}, direction 297–339°; ship speed is 5.5 m s^{-1}, direction 338°; height of swell waves observed from the bridge ~1 m, direction ~50°. After Soloviev and Lukas (1996). Copyright © 1996 American Meteorological Society. Used with permission

mean densities, respectively. The solution for (5.48) is sought in the form of a plane wave:

$$W(x,y,z,t) = w(z)\exp\left[i(kx+ly-\omega t)\right] \tag{5.49}$$

For complex frequency $\omega = \omega_r + i\omega_i$, the exponential in (5.49) has a real and growing part (for $\omega_i > 0$), so that all wave variables have a growth rate ω_i.

The Howard (1961) theorem states that the complex phase speed of any unstable modal solution in parallel flows of an inviscid fluid must lie inside the semicircle in the upper half of the complex phase speed plane, which has the range of the mean flow as the diameter. Mack and Hebert (1997) altered slightly this theorem in application to the three-dimensional version of the Taylor–Goldstein Eq. (5.48) to obtain the following criteria for instability:

$$\begin{aligned}&\left\{\omega_r - \frac{1}{2}\left[\max\left(\vec{k}\cdot\vec{u}\right)+\min\left(\vec{k}\cdot\vec{u}\right)\right]\right\}^2 + \omega_i^2 \\ &\le \left\{\frac{1}{2}\left[\max\left(\vec{k}\cdot\vec{u}\right)-\min\left(\vec{k}\cdot\vec{u}\right)\right]\right\}^2\end{aligned} \tag{5.50}$$

$$\omega_i > 0 \tag{5.41}$$

Mack and Hebert (1997) found that solutions were almost completely determined by the mean density and velocity profiles, which was in agreement with most of their field data (unfortunately, there was no information on velocity in the upper 20 m layer of the ocean). A necessary criterion for instability of a stratified parallel flow was a gradient Richardson number, $Ri = N^2/(u_z^2 + v_z^2) < 1/4$. The fastest growing, unstable first-mode solutions had e-folding growth times of less than 10 min.

For a two-dimensional, two-layer model the criteria of instability is as follows (Turner 1973):

$$\lambda < \pi(\Delta u)^2 / g' \tag{5.52}$$

where λ is the wavelength, Δu is the vertical velocity jump, and $g' = g\Delta\rho/\rho_0$ is the reduced gravity. For the large-amplitude internal wave observations of Soloviev and Lukas (1996) (Fig. 5.42), $\Delta\rho/\rho_0 \approx 5\times10^{-4}$. The typical velocity of the diurnal jet is 0.2–0.3 m s^{-1}. In the equatorial ocean, however, there is substantial background shear. For a total velocity difference $\Delta u \sim 0.5 - 0.7$ m s^{-1}, formula (5.52) results in an estimate $\lambda < 160 - 310$ m. The σ_t–P contour plot in Fig. 5.42d reveals wavelike disturbances of the diurnal thermocline with a typical scale beginning from ~200 m, which is consistent with the above estimate.

Observations from satellite images of strong diurnal warming events near the California coast (Flament et al. 1994) indicated the formation of coherent streaks, associated with the erosion and decay of the warming layers during the night

following strong diurnal warming. The horizontal spacing of the streaks, observed at 1 km resolution, was ~4–8 km. This is consistent with Fig. 5.42 in which it is possible to trace a several-kilometer scale variation of the near-surface temperature of ~2°C. Internal waves of ~200 m wavelength cannot be resolved in the available satellite images. The patterns between the two successive images separated by 5 h 26 min (Flament et al. 1994, Fig. 12b and c) look stationary, but appear consistent with internal waves propagating at ~0.1 m s^{-1} in the diurnal thermocline.

The horizontal spacing of the streaks of 4–8 km observed by Flament et al. (1994) is probably too large for the Kelvin–Helmholtz instability because of the limitation on the maximum wavelength imposed by (5.52). The internal wave–vortex resonance mechanism considered in Sect. 5.4.3 allows for perturbations with a wavelength of a few km to develop (but those perturbations are not of Kelvin–Helmholtz type).

Internal waves in the near-surface stably stratified layers could modulate the roughness of the ocean surface in the same way as the internal waves in the main thermocline, making them visible in SAR images. Nonlinear internal waves and billows in the near-surface layer of the ocean associated with diurnal thermocline or rain-formed halocline may also modulate SST producing specific spatial patterns seen in the infrared images of Walsh et al. (1998).

5.6 Ramp-Like Structures

As emphasized in many studies (*e.g.,* Thorpe 1985, 1988; Csanady 1984; Soloviev et al. 1988), the turbulent boundary layer at the ocean surface has some similarity to the atmospheric turbulent boundary layer. The atmospheric boundary layer exhibits spatially coherent organized motions in the form of "ramps" (Antonia et al. 1979; Phong-Anant et al. 1980). Ramp-like structures have also been found in the upper layer of the ocean under both stable (Thorpe and Hall 1987) and unstable (Soloviev 1990; Wijesekera et al. 1999b) stratification. Since the organized structures are of relatively large size (comparable to the boundary-layer thickness), they may appreciably contribute to the vertical transport of heat, mass, and momentum as well as air bubbles.

5.6.1 Phenomenology of Ramp-like Coherent Structures

The laboratory measurements of Brown and Thomas (1977), made in a coordinate system moving with the average convection velocity of coherent structures, suggest that the typical organized motion in the unstratified turbulent boundary layer resembles a three-dimensional horseshoe vortex that is inclined to the wall. Interaction of the velocity field in the vortex with the mean shear current leads to the vortex asymmetry. As a result of this asymmetry, the so-called ramp-like structure forms, which is schematically illustrated in Fig. 5.43. The velocity jump at the upstream

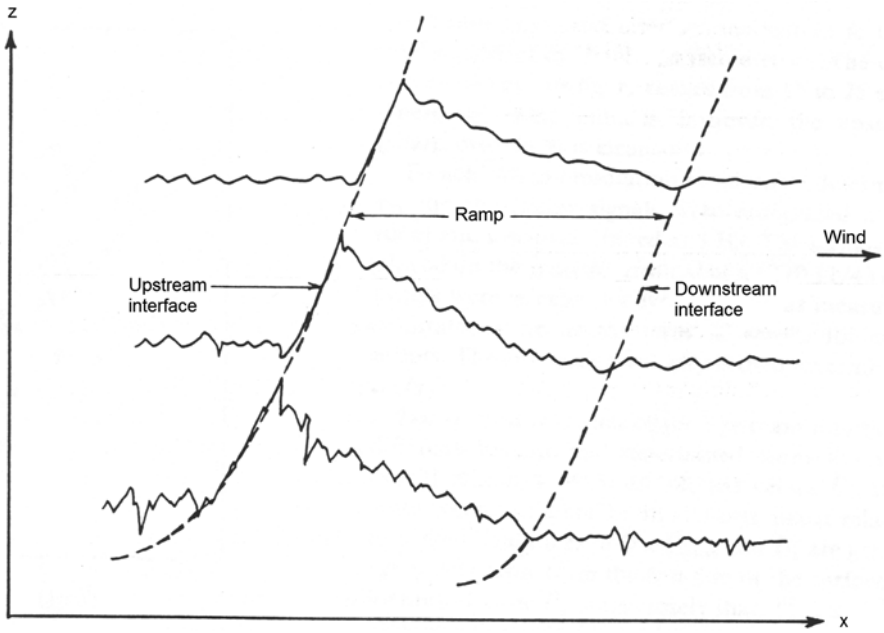

Fig. 5.43 Phong-Anant et al. (1980) schematic representation of temperature ramps measured simultaneously at different heights. Upstream and downstream interfaces are indicated by dashed lines. Continuous lines are isotherms. Reproduced with permission from American Geophysical Union

interface has a tendency to increase with distance from the wall and is of the same order of magnitude as the mean speed of the boundary-layer flow.

Temperature (density) features accompany vorticity features in stratified conditions. Observations of Phong-Anant et al. (1980) using a fixed probe in the convectively unstable atmospheric boundary layer confirms that temperature has a characteristic ramp profile—a gradual rise followed by a relatively sharp decrease. Temperature ramps in the atmospheric boundary layer were suggested to be a signature of organized large-scale motion (Phong-Anant et al. 1980). In the unstably stratified atmospheric turbulent boundary layer, the coherent structures of this type have vertical scale proportional to the Oboukhov length scale (L_O), while their horizontal size is an order of magnitude bigger than the vertical.

An important question concerns the size of the contribution of the coherent structures to the vertical Reynolds shear stress and heat flux. From measurements in the atmospheric boundary layer, Phong-Anant et al. (1980) estimated the contribution of the organized motion to the vertical heat flux for unstable stratification conditions as being over 40% of the average vertical heat flux and about 20% of the average Reynolds stress. The relative contribution to the average vertical heat flux and Reynolds stress is less than 10% for nearly neutral and moderately stable conditions.

There are good reasons to assume that ramp-like coherent structures are important in the dynamics of the upper ocean turbulent boundary layer as well (Thorpe 1985).

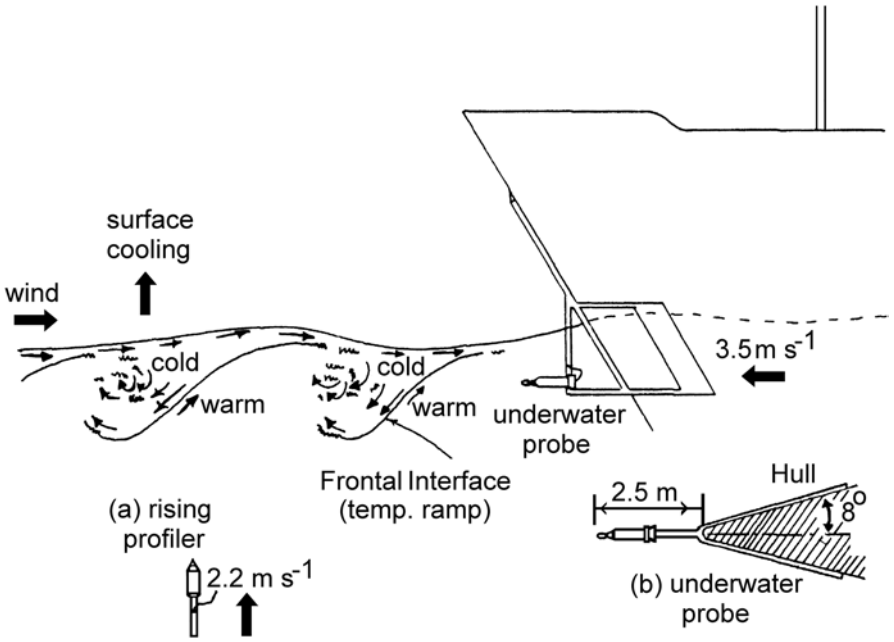

Fig. 5.44 Schematic representation showing spatially coherent organized motion in the upper ocean boundary layer under unstably stratified conditions and experimental techniques and devices in Soloviev's (1990) experiment: **a** free-rising profiler, **b** top view at the probe mount (2 m below the waterline). Reproduced with permission from *Nature*

At the same time, free-surface effects can modify the properties of the organized motion. Observation and theory of the coherent structures in the near-surface layer of the ocean are more complicated than in the atmosphere. One reason is that, due to significant difference in density and specific heat capacity in air and water, the boundary-layer temperature and velocity scales in the ocean are much smaller than in the atmosphere.

Thorpe (1985) observed ramp-like structures in the stably stratified near-surface ocean. Soloviev (1990) and Wijesekera et al. (1999b) reported the presence of ramp-like structures in the near-surface layer of the ocean under unstably stratified conditions as well. The next three subsections are devoted to the analysis of data on ramp-like structures taken in the upper ocean.

5.6.2 Observation of Ramp-like Coherent Structures with Bow-Mounted Sensors

A schematic diagram of Soloviev's (1990) experiment is shown in Fig. 5.44. The underwater probe was mounted on the bow of the research vessel *Akademik Kurchtov* at 2 m depth and it measured temperature and conductivity fluctuations ahead

Table 5.2 Case studies of ramp-like structures in the oceanic and atmospheric turbulent boundary layers under unstably stratified conditions. Here, U_{10} is the wind speed at 10 m height, τ_0 is the wind stress, h_s is the sensor depth (in the ocean) or sensor height (in the atmosphere), L_O is the Oboukhov length scale, $\langle|\Delta\theta|\rangle$ is the average temperature ramp magnitude, $T_* = Q_0/(c_p\rho u_*)$ is the friction temperature, Q_0 is the net surface cooling, and u_* is the friction velocity

Figure	Experiment	U_{10}, m s^{-1}	τ_0 N m^{-2}	h_s/L_O	$<\|\Delta\theta\|>/T_*$
Fig. 5.45a, b	Ocean—bow sensors Soloviev and Bezverkhny (1990)	3.4	0.015	−1.5	1.9
Fig. 5.49	Ocean—free-rising profiler Soloviev (1990)	4.1	0.019		
Fig. 5.46	Ocean—bow sensors Wijesekera et al. (1999b)	8	0.1	−0.1	2
Fig. 5.45c	Atmosphere—tower Antonia et al. (1979)	5.6	0.048	−0.8	2.9

of the moving vessel. Due to a "knife-edge" hull, the research vessel produced practically no bow wave ahead of itself, as confirmed by photographs and following from hydrodynamic estimates. In front of a moving sphere, streamlines are not appreciably disturbed at a distance greater than ~3 radii (see discussion of these techniques in Sect. 3.3.5b). At the probe mount location, the radius of curvature of the vessel's hull was ~10 cm with a frontal angle of 16° (Fig. 5.44). No turbulent or wave perturbations from the vessel's body were therefore expected in the measurement area. These measurements were made at 37°W between 1°N and 20°N in June 1985. Wijesekera et al. (1999b) performed a similar set of observations with a bow-mounted CTD in the western equatorial Pacific during TOGA COARE.

The observations reported here were made when it was not raining and outside frontal regions to simplify the identification of ramp-like structures. Information for the context of the observations is given in Table 5.2.

Figure 5.45, a and b, shows fragments of the bow temperature recordings at the nominal depth of 2 m, while the ship was steaming into the wind at 3.5 m s^{-1}. These measurements were taken during nighttime when the surface layer cools (unstable stratification). For comparison, a temperature record in the atmospheric boundary layer (at 12 m height) under unstable stratification is shown in Fig. 5.45c. There is a striking similarity between the ramp-like structures observed in the ocean and in the atmosphere. Although absolute temperature scales in the ocean and the atmosphere are very different, the dimensionless characteristics, like $\langle|\Delta\theta|\rangle/T_*$, are consistent (see Table 5.2).

For convenient comparison with the atmospheric boundary layer, the ocean temperature records (Fig. 5.45a and b) are plotted with time and temperature scales reversed. The reason for the temperature coordinate reversion is that unstable stratification in the upper ocean is caused by surface cooling, which is opposite to its atmospheric counterpart where the unstable stratification is due to warming of the underlying surface. The reason for the reversion of the time coordinate in the oceanic data series is that the ship was traveling into the wind; the bow sensors crossed the structures in the ocean layer in the direction opposite to the relative direction of

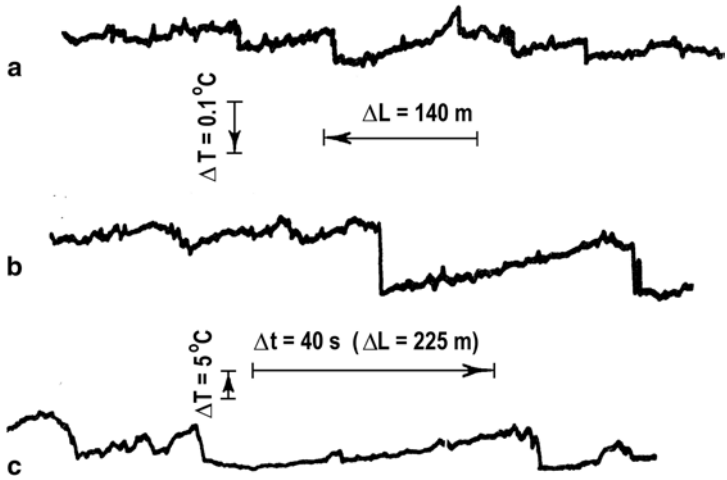

Fig. 5.45 Fragments of (**a**, **b**) horizontal temperature profiles obtained with the bow-mounted sensors in unstably stratified conditions in comparison with (**c**) temperature records in the unstably stratified atmospheric boundary layer. The ship was steaming into the wind. The scales for subplots (**a**) and (**b**) are the same. For the atmospheric measurements done from a fixed tower (curve c), the equivalent distance scale is also shown (which is calculated from formula $\Delta L = U_{10}\Delta t$). After Soloviev and Bezverkhny (1990)

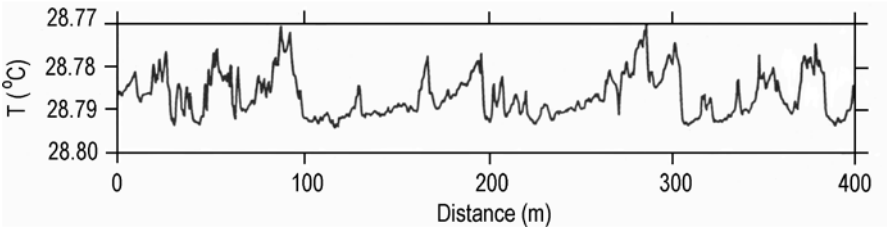

Fig. 5.46 A horizontal series of temperature observed at 2 m during the night of December 31, 1992 from the R/V *Wecoma* moving downwind at 4 m s^{-1}. Wind stress (westerly) is about 0.1 N m^{-2}, net surface cooling about 250 W m^{-2}, the stability parameter, z_s/L_O=-0.1, where L_O is the Monin–Oboukhov scaling length, and average bow sensor depth z_s=2 m. After Wijesekera et al. (1999b)

the air flow during the measurements with a fixed sensor in the Antonia et al. (1979) experiment (Fig. 5.45c).

Figure 5.46 shows the horizontal temperature series taken during nighttime measurements with bow sensors mounted at 2 m depth (nominal) by Wijesekera et al. (1999b). In order to compare this record with the data shown in Fig. 5.46, the temperature scale is reversed. The distance scale, however, does not require reversion, because this measurement is made in the downwind direction. The temperature series in Fig. 5.46 reveals ramp-like structures similar to those in Fig. 5.45

Patterned on Fig. 4 of Thorpe and Hall (1987), which shows processes of the vertical transport in a stably stratified shear boundary layer of the upper ocean, Fig. 5.44 reconstructs water circulation in unstably stratified conditions. As the ship moves upwind, the ramps are observed as the probe passes from the "warm water" to the "cold water" side of the inclined sharp interfaces (Fig. 5.44). The ramps on the temperature record shown in Figs. 5.45a, b and 5.46 are consistent with this sketch.

5.6.3 Skewness of temperature derivative

The presence of ramp-like structures in the temperature records leads to asymmetry of the probability distribution function (PDF) for the temperature derivative (Thorpe 1985). A measure of PDF asymmetry is the skewness, μ_3, which is defined as follows:

$$\mu_3 = M_3 / M_2^{3/2}, \tag{5.53}$$

where $M_3 = \left\langle (\partial T/\partial \alpha - \langle \partial T/\partial \alpha \rangle)^3 \right\rangle$, $M_2 = \left\langle (\partial T/\partial \alpha - \langle \partial T/\partial \alpha \rangle)^2 \right\rangle$, and $\partial T/\partial \alpha$ denotes the temperature derivative either over time, $\alpha = t$, for fixed-sensor measurements, or over the horizontal coordinate, $\alpha = x$, for towed measurements.

The skewness of the oceanic temperature derivative for the upwind direction of the ship in the observations of Soloviev (1990) under convectively unstable near-surface conditions of the ocean falls in the range -0.7 to -1.0. In the convectively unstable atmospheric boundary layer, the skewness in the presence of coherent structures falls in a similar range (Thorpe and Hall 1987).

As mentioned before, based on the results of laboratory experiments the vortex motion associated with a ramp-like structure in the upper ocean has the rotation axis oriented perpendicular to the wind direction or, more exactly, to the wind drift current direction. As a result, the mean value of μ_3 depends on the direction of the ship's motion relative to the wind. The directional dependence of μ_3 on the wind heading relative to ship heading measured by Wijesekera et al. (1999a) is shown in Fig. 5.47.

The dependence of the temperature derivative skewness on the relative wind directionfor mid-latitudes, including both stable and unstable upper ocean stratification, is shown in Fig. 5.48. During the daytime when the stratification is stable, μ_3 is positive. In order to account for the sign of stratification, the skewness coefficient in Fig. 5.48 is multiplied by the sign of the Monin–Oboukhov stability parameter z_s/L_O.

The full series of measurements made in January 1990 in the Atlantic Ocean by Soloviev (1990) is compared in Fig. 5.48 with the data obtained by Thorpe (1985) under stable stratification conditions, and by Thorpe (1988) under unstable stratification conditions in the North Atlantic. These data sets also include a range of relative wind directions. They reveal the directional anisotropy of the coherent structures of this type with respect to the wind stress direction. The magnitudes of μ_3 in Soloviev (1990) are near those reported by Thorpe (1985) and Thorpe and Hall (1987) at similar winds and towing angles.

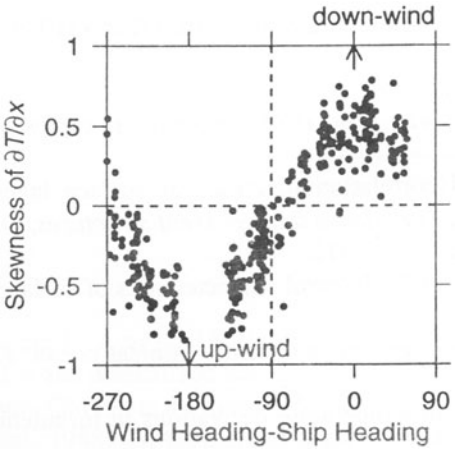

Fig. 5.47 Skewness of $\partial T / \partial x$ versus the relative angle between the wind and ship heading under unstably stratified conditions in the western equatorial Pacific Ocean. After Wijesekera et al. (1999b)

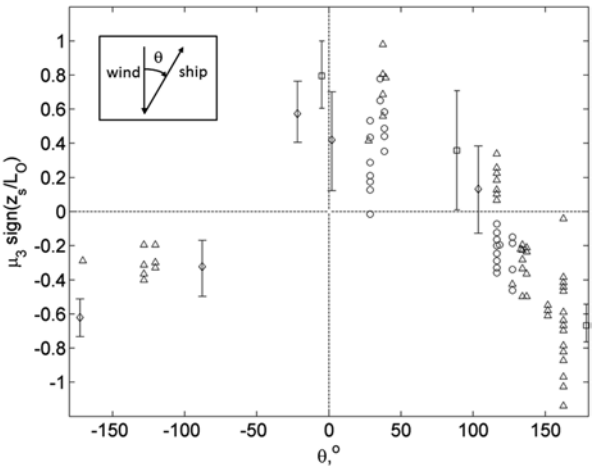

Fig. 5.48 Skewness of $\partial T / \partial x$ multiplied by the sign of the Monin–Oboukhov stability parameter z_s/L_O versus the relative wind direction according to Soloviev and Bezverkhny (1990), where zs is the depth of the temperature sensor. Triangles and circles represent measurements at zs = 1.5 m average depth during nighttime ($L_O<0$) and daytime ($L_O>0$) conditions, respectively. For comparison, data from Thorpe (1985) and (1988) squares and diamonds

The observations of ramp-like structures in the upper ocean obtained from different sources under various wind speed and stratification conditions appear to be consistent. The difference between equatorial (Fig. 5.47) and mid-latitude (Fig. 5.48) directional diagrams is that, in mid-latitudes, the maximum of the skewness seems to be shifted to the right by 10–20°.This can be explained by the fact that away from the equator the wind drift current direction differs from the wind velocity vector direction because of the Ekman spiral (see Sect. 1.7.1). Data scatter in both figuresis, however, marginal for making final conclusions.

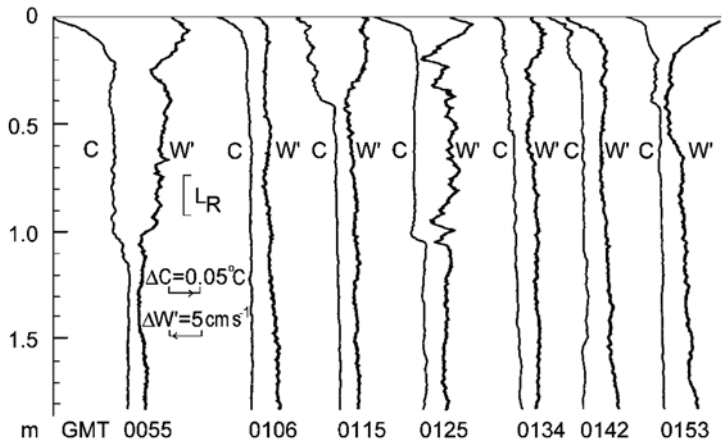

Fig. 5.49 Vertical profiles of temperature (C, calculated from conductivity profiles assuming constant salinity) and vertical component of velocity fluctuation (W') in the upper ocean in convectively unstable conditions (nighttime). A positive $\Delta W'$ indicates a positive velocity change of the flow along the profiler. The vertical length scale (L_R) represents the relaxation time of the fluctuation velocity sensor. After Soloviev (1990). Reproduced with permission from *Nature*

5.6.4 Vertical Profiles

Additional insight into spatially coherent organized motions in the near-surface layer of the ocean has been obtained from the analysis of free-rising profiler data (Fig. 5.44). The profiler measured vertical velocity profiles of conductivity and the vertical component of velocity fluctuations in the frequency range 2–250 Hz. The rise speed of the profiler was 2.2 m s^{-1}. Temperature profiles were calculated from the conductivity profiles neglecting salinity variation. For the convectively unstable near-surface layer of the ocean, these calculations resulted in only small error (see Sect. 2.3.1). The profiler tends to follow the wave-induced orbital motion in long surface waves (see Sect. 3.4.4). This reduces the influence of surface waves on turbulence measurements in the upper boundary layer of the ocean.

Figure 5.49 shows a series of measurements of temperature and vertical velocity fluctuations made by a free-rising profiler at 20° N, 37°W in the early morning hours. The weather conditions were similar to those during the measurements shown in Fig. 5.45. The time interval between successive measurements was ~10 min, and the vessel drift during this time period was several tens of meters. The structures investigated supposedly had time and space scales of the same order. From these data, it would then be difficult to trace any space–time connections between the successive vertical profiles in relation to ramp-like structures.

Figure 5.49 suggests that in a few cases the profiler crossed the temperature interfaces presumably related to ramp-like structures. In particular, in the profiles obtained at 00:55 and 01:25 UTC, the temperature interfaces were correlated with abrupt vertical velocity features. In the interpretation of the velocity profiles, it is

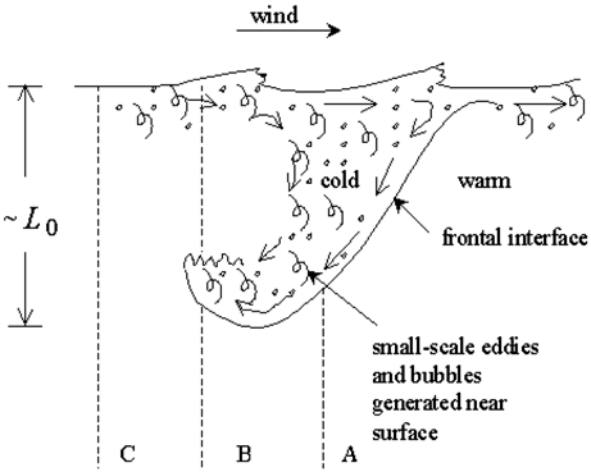

Fig. 5.50 Schematic representation of the cooled water, small-scale eddies, and bubble transport from the near-surface zone to deeper layers due to ramp-like coherent structure under convectively unstable conditions. Vertical dashed lines (A, B, and C) indicate some of the possible free-rising profiler trajectories with respect to the organized structure

important to remember that the sensor measured only velocity fluctuations within the frequency range 2–250 Hz. Since the profiler moved quickly with respect to the water (at a 2.2 m s^{-1} vertical speed), abrupt velocity changes were observed correctly.

Similar profiles obtained at 00:55 (Fig. 5.49), but having the opposite sign of vertical velocity change at 0.95 m depth and the same sign of temperature change as the profiles discussed above, may be interpreted as the result of intersection of a region where cold water was moving along the frontal interface toward the ocean surface. This corresponds to profiler trajectory B in Fig. 5.50.

The profiles obtained at 01:06 GMT have no substantial changes either in temperature or in the vertical component of velocity. These profiles might be located in the space between the large-scale eddies (trajectory C in Fig. 5.50). The other four pairs of profiles shown in Fig. 5.49 are supposedly related to the cases when the profiler passes through less-pronounced regions of the vortex structure.

The vertical profiles shown in Fig. 5.49 are thus consistent with the presence of ramp-like coherent structures in the near-surface layer of the ocean. This is, however, fragmentary information; alternate interpretations are not excluded.

Before moving on to theoretical aspects of the problem of ramp-like coherent structures, we would like to point the reader to one unresolved question relating to the problem of organized motions in the upper ocean. The field study performed by Thorpe et al. (2003) using an autonomous underwater vehicle suggests that both types of coherent structures do coexist. How can ramp-like structures coexist with Langmuir circulations? Vortices associated with ramp-like structures have transverse axes, while Langmuir circulations have a longitudinal axis, relative to the wind. Moreover, both phenomena have similar space and timescales. Each of these motions in isolation is two-dimensional. However, two uncorrelated two-dimensional motions with mutually perpendicular axes represent a three-dimensional motion, which, according to principles of self-organization, should have a tendency to randomization rather than organization. At first glance, the ramp-like structure

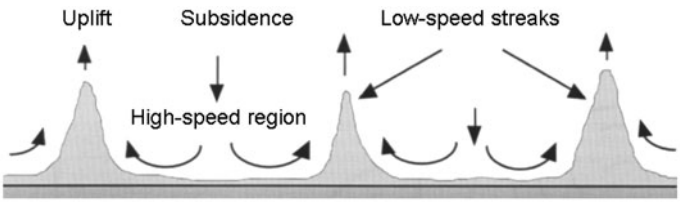

Fig. 5.51 Schematic cross-flow section of the low-speed streaks near the ground. After Smith and Walker (1997) With permission by WIT Press

and Langmuir circulations should not coexist at all. This appears possible only if they are synchronized in some way in space and time.

Microstructure measurements in the near-surface layer of the ocean are still very rare. Further studies will have to address the question posed above, as well as some other important questions relating to the problem of coherent structures in the upper ocean. Though previous studies in the atmospheric boundary layer can provide guidance to ocean boundary-layer studies, the analogy between the atmospheric and oceanic boundary layers, however, is not exact. The oceanic turbulent boundary layer differs from its atmospheric analog due to the presence of a free surface. The importance of free-surface effects (including breaking waves) increases toward the surface. Processes in the near-surface layer are therefore crucial to understanding the coherent structures in the upper ocean turbulent boundary layer and must be sampled adequately.

5.6.5 Townsend's Hypothesis and Ramp-Like Structures

Townsend (1961) conditionally divided the turbulence near a wall into two parts—an active part, which transports momentum, and an inactive part, which does not. In addition, he hypothesized that these two types of turbulent motion do not interact. In Townsend's (1961) model, active turbulence is generated by wind shear; its properties can be scaled by local parameters of the flow. Inactive turbulence is the product of energetic processes remote from the surface; its properties are scaled with the outer-layer parameters. The Monin–Oboukhov similarity theory, which is formulated in terms of local parameters, can apply to active motions only.

McNaughton and Brunet (2002) proposed a mechanism for how inactive motions could initiate active, coherent ejection/sweep structures that carry much of the momentum and heat (Fig. 5.51). They found evidence that the inactive motions take the form of streak patterns of faster and slower air, which are aligned with the surface wind. The streaks are induced by the pressure effect of the large eddies passing overhead. Sharp convergence lines of uplifted, slower air are created in the flow by the high-speed streams of subsiding air spreading laterally. The slow streaks are therefore narrower than the subsiding zones between (Fig. 5.51).

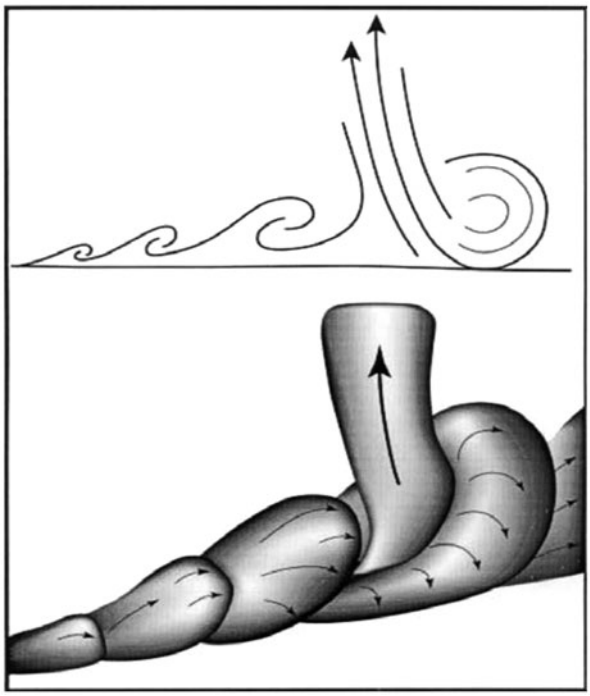

Fig. 5.52 Schematic diagram of a series of vortices forming across the spine of a low-speed streak. The upper panel shows a longitudinal section down the streak while the lower panel represents an outline of the air of the streak as the vortices form. The vortices lying across the spine of the streak take on a 'horseshoe' or 'hairpin' shape where the streak is sufficiently upright, and these can grow to the point where they contact the ground and cause a vigorous ejection of fluid. After McNaughton and Brunet (2002). Reproduced with permission from Springer

The difference in speeds of the various parts of the flow thus creates convergence zones where the high-speed streams overtake the slower moving streaks. In each of these zones, the faster air stream at first simply passes about the slower streak, creating a zone of strong shear between the faster and slower air streams. The velocity profile along normals to this interface is strongly inflected, forming a classic source of instability in the flow. It initiates a series of transverse roll vortices, just as similar inflections do in plane mixing layers, but here the roll vortices are draped across the spine of the engulfed streak. These vortices describe gentle arcs where the streak is low and board, but become croissant- or horseshoe vortices over taller, more upright parts of streaks. Well-formed horseshoe vortices can then assume a life of their own, continuing to grow by taking vorticity and turbulent kinetic energy (TKE) from the mean flow itself. The mean shear also rotates these coherent vortices forward until, by a combination of growth and rotation, they contact the ground to form a dam with strong inflows along the ground produced by the rotation of the vortex arms and the main flow presenting pressing in from behind. With nowhere else to go, the trapped air squirts backward and outward into the flow. This squirt is usually described as an ejection/sweep event. Figure 5.52 illustrates a schematic of the first ejection formation on a streak.

McNaughton and Brunet (2002) assume that their model is consistent with information from many sources and provide a historical excursion into studies of the bursting process. Theodorsen (1952) was probably the first who gave theoretical

arguments for initiation of horseshoe vortices about slow-moving masses of fluid attached to the ground, with subsequent vortex roll-up and ejection. In the 1950s, he could not know of wall streaks nor appreciate the power of the ejection. In a series of laboratory experiments, Kline et al. (1967) discovered wall streaks and described their oscillation and breakup with sudden ejection of fluid from very near the wall. Kline et al. (1967) did not detect the overtaking fluid or the horseshoe vortices. Corino and Brodkey (1969) observed the colliding masses of fluid and realized the power of the ejections in the boundary-layer dynamics; their visualization methods unfortunately could not detect the formation of horseshoe vortices. Hinze (1975) and Offen and Kline (1975) proposed a relationship between wall streaks and horseshoe vortices. Hagen and Kurosaka (1993) were the first who demonstrated the connection between horseshoe vortices and powerful ejections. From a large-eddy simulation (LES) of a convective atmospheric boundary layer, Lin (2000) deduced a sequence of horseshoe eddies followed by a vigorous ejection. Finally, McNaughton and Brunet (2002) used his results to develop the schematic diagram shown in Fig. 5.52.

McNaughton and Brunet's mechanism thus appears to be consistent with a wide range of results from laboratory and atmospheric boundary-layer experiments. The new element introduced by these researchers is the pressure mechanism for streak formation. This mechanism has an important consequence, since it allows the wall streaks to form within fully turbulent layers. Previously, wall streak formation has been associated only with viscous sublayers, though the importance of pressure rather than vorticity in creating motions near the ground was shown from LES results by Moeng (see Peltier et al. 1996).

The phenomenological model of McNaughton and Brunet (2002) justifies some important underlying assumptions made in the theory of coherent structures as vorticity waves described in the next section (Sect. 5.6.6):

1. wall streaks can form within fully turbulent layers;
2. a zone of strong shear is created between the faster and slower air streams; and
3. on certain timescales the viscosity effects are negligible.

Since temperature transport is significantly affected, the dimensional assumptions of the Monin–Oboukhov theory are undermined. This circumstance has important application for mixing parameterizations, which can no longer rely on local diffusion only but must include nonlocal transport due to coherent structures.

5.6.6 Vorticity Waves in Shear Flows

The vorticity waves introduced in Sect. 5.4.3 for a stratified ocean (in relation to sharp frontal interfaces) can also exist in a uniform density fluid (Lin 1966). In stratified flows, the vorticity waves are not directly affected by stratification, though the presence of stratification may affect the vorticity waves indirectly, via modifying the mean velocity profile or due to resonance with the internal waves that can develop in the underlying stratified layer (Sect. 5.4.3).

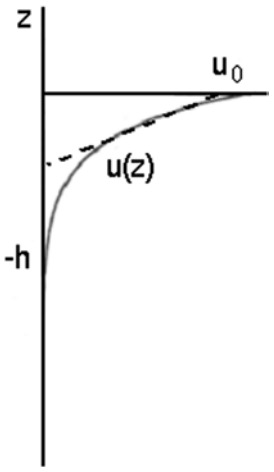

Fig. 5.53 Schematic representation of the wind drift current in the surface layer of the ocean. After Voronovich et al. (1998b). Reproduced with permission from Wiley-Blackwell

The theoretical analysis below is based on the hypothesis that ramp-like structures are associated with vorticity waves. Ramp-like structures have been observed within the actively mixed turbulent boundary layer (*i.e.*, at $Ri < Ri_{cr} = 1/4$) that, according to condition (5.26) (or (5.28)), can be far from internal wave–shear resonance. The system of equations describing the internal wave–shear flow resonance in Sect. 5.4.3 is replaced with a single nonlinear evolution equation (Shrira 1989; Voronovich et al. 1998b):

$$\partial_\tau A - \alpha A \partial_x A - \beta \hat{G}\left[\partial_x A\right] = 0, \tag{5.54}$$

where $\alpha = u'|_{z=-0}$, $\beta = (u^2/u')|_{z=0}$, and $\hat{G}$ is an integral operator of the form

$$\hat{G}\left[\varphi(\vec{r})\right] = \frac{1}{4\pi^2}\int_{-\infty}^{\infty} Q\left(\vec{k}\right)\varphi(\vec{r}_1)\exp\left(i\vec{k}\left(\vec{r}-\vec{r}_1\right)\right)d\vec{k}\,d\vec{r}_1 \tag{5.55}$$

This class of evolution equation is specified by the kernel $Q(\vec{k})$ that depends on the structure of eigenfunctions of the boundary-layer problem. In the two-dimensional case, Eq. (5.54) reduces to the well-known equation of the Benjamin–Ono type (previously derived in a similar context by Romanova (1984)). The coefficients of the related Benjamin–Ono equation appear to be finite only when the condition $u(z) \sim \alpha z$ is satisfied at $z \sim 0$. For this special case of the linear velocity profile (see dashed line in Fig. 5.53) and $N = 0$, the Romanova (1984) solution represents a vorticity wave, which is defined as a long wave having the maximum of its modal function at the vorticity jump at $z = h$.

For a smooth shear profile localized near the surface (see continuous line in Fig. 5.53), the solution is much more complicated but still preserves some basic properties of the simplest model. Voronovich et al. (1998b) demonstrated that on horizontal length scales $L >> h\,\mathrm{Re}^{1/4}$ arbitrary wave perturbations still behave like

discrete modes in Romanova's solution, while the viscous terms are negligible on length scales $L << h\,\mathrm{Re}^{1/2}$. Here, $\mathrm{Re} = u_0 h / \nu$, where velocity u_0 and depth h scales are defined as shown in Fig. 5.53 and ν is the molecular coefficient of kinematic water viscosity.

The waves of the continuous spectrum thus form an intermediate asymptotic solution; its leading terms coincide with the solution for the simplest model of Romanova (1984). A continuous spectrum replaces the discrete modes on intermediate times

$$h\,\mathrm{Re}^{1/4} << L << h\,\mathrm{Re}^{1/2}. \tag{5.56}$$

For $h = 1$ m, $u_0 = 0.1$ m, and $\nu = 10^{-6}$ m^2 s^{-1}, inequality (5.56) corresponds to the range of horizontal scales, 18 m << L << 316 m, which is consistent with the typical horizontal scales of ramp-like structures in the upper ocean (see Figs. 5.45b and 5.46).

The dispersion relationship for the linear analog of Eq. (5.54) is as follows:

$$\omega = (c - \beta\left|\vec{k}\right|)k_x, \tag{5.57}$$

where $c = U|_{z=0}$. For a two-dimensional case $k = k_x$; the spectrum of $\omega(k)$ in (5.57) is "nondecaying" because the conditions for three-wave synchronization $\omega(k_3) = \omega(k_1) + \omega(k_2)$ at $k_3 = k_1 + k_2$ are never fulfilled. At the same time for three-dimensional waves, the synchronism conditions can be satisfied for certain oblique perturbations (Voronovich et al. 1998b). Plane (three-dimensional) solitary waves in infinitely deep water appear to be unstable with respect to transverse perturbations (Pelinovsky and Shrira 1995).

The properties of the intermediate asymptotic solution of Eq. (5.55) are consistent with the qualitative scheme of Townsend (1961) discussed in the previous section (Sect. 5.6.5). Perturbations that develop across the spine of a low-speed streak (Fig. 5.52) are apparently long enough to satisfy the left side of inequality (5.56). The fact that the three-dimensional solution of (5.54) is unstable with respect to transverse perturbations is also qualitatively consistent with the McNaughton and Brunet (2002) phenomenology stating (see Fig. 5.52) that the flow instability is initiated by transverse roll vortices

The active motions are dissipative; the viscosity effects can therefore no longer be ignored. This imposes an upper bound on the horizontal length scale, which is determined by the right side of inequality (5.56).

The interpretation of the ramp-like coherent structures as nonlinear wavelike perturbations in shear flow due to the inhomogeneous mean vorticity field is consistent with observational data. The theory of vorticity waves can therefore serve as the basis for the interpretation of the ramp-like coherent structures. This theory, however, describes the evolution of weakly nonlinear waves only and cannot handle the dynamics of the horseshoe vortex.

5.7 Langmuir Circulations

5.7.1 Phenomenology

Long before oceanography developed as a distinct branch of science, sailors and seafarers noted long narrow "bands," "streaks," or "lanes" on the sea surface, which were often nearly aligned with wind. This phenomenon appears in the notes of Charles Darwin from his voyages on the *Beagle* (Leibovich 1983). In 1938, Langmuir came to the conclusion that the streaks or "windrows" are the visible manifestations of a parallel series of counter-rotating vortices in the surface layers of the water with axes nearly parallel to the wind. At present, while the existence and many features of Langmuir circulations are generally accepted, their role in the mixed layer dynamics is still ambiguous.

Different floating substances ranging from seaweed and marine organisms to organic films and foam from breaking waves tend to concentrate in the convergence zones. Flotsam makes the bands visible directly. These bands are sometimes observed even in the absence of floating objects—compressed films make them visible due to suppressing capillary waves, thereby giving the bands a smoother appearance in surface reflectance. In some cases, the amplitude of the surface gravity waves increases in convergence zones leading to wave breaking. Though convergences at the ocean surface can be caused by different factors including internal waves, oceanic fronts, convection, etc., Langmuir circulations are an important and frequent cause of the near-surface convergence lines.

The convergence zones are sometimes seen in infrared imagery through their interaction with the ocean's cool skin. The infrared imagery shown in Fig. 5.54 depicts long, dark (cool) streaks associated with Langmuir circulations (Marmorino et al. 2005). Surface convergences between successive pairs of Langmuir cells interact with the cool skin producing the cool streaks in the imagery. This observation was made from an aircraft flying over the inner West Florida continental shelf where the water depth was only 3 m. A wind of about 5 m s^{-1} was blowing nearly parallel to the streaks. The spacing of the streaks in Fig. 5.54 is 10–20 m, which gives each cell an unusually large width-to-height aspect ratio of about 2.5. In the open ocean, the aspect ratio of the largest Langmuir cells is believed to be close to unity.

The Langmuir cells are parallel and oriented nearly downwind with alternating longitudinal vorticity (Fig. 5.55), producing convergence and divergence zones. The downwelling zones are substantially narrower than the upwelling zones. The typical distance between the Langmuir vortices is from a few meters to a few hundred meters.

Langmuir circulations appear to be a transient and variable process. A hierarchy of Langmuir circulations is often observed with smaller, more irregular, and less well-defined streaks occurring between stronger and more widely spaced streaks. In the hierarchy of spacings between the lanes, the small cells continually form and gradually merge into the more permanent larger cells (Thorpe 1992). Evidence for

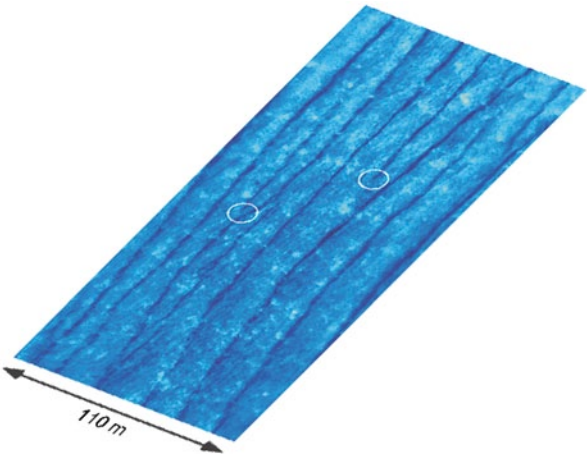

Fig. 5.54 Langmuir cells (*dark streaks*) in nighttime infrared imagery. The streaks are about 0.2 °C cooler than the ambient surface water. The circle on the right highlights the termination of one streak. The left circle indicates where two streaks merge. Such features persisted over several minutes and drifted with the downwind surface current. Bright (warm) spots occurring throughout the image represent microscale wave breaking events. (This image is from the public domain of the Naval Research Laboratory Web Site http://www.nrl.navy.mil.)

the adjacent streaks merging and individual streaks terminating can also be found in the infrared imagery shown in Fig. 5.54 (two circled areas).

According to observations, the speed of near-surface current in the wind direction is maximal in convergence zones, reaching 0.2 m s^{-1} with respect to the current speed in divergence zones. The typical speed of downwelling in the convergence zones is of the order of several cm s^{-1} near the surface according to some investigators. At the same time, downward vertical velocities estimated by Weller and Price (1988) appear to be even larger, perhaps because the vertical velocity increases with depth to some point $\sim h/2$. Interestingly, D'Asaro et al. (1996) attempt to identify motions below the surface as Langmuir circulations using Lagrangian tracking did not provide clear evidence for the presence of circulatory flows.

The Langmuir circulations form within a few minutes of onset of a wind of 3 m s^{-1} or faster (Pollard 1977). Langmuir circulations are observed regardless of surface heating or cooling. Nevertheless, under conditions of surface cooling (unstable stratification), the Langmuir circulations may form at a lower wind speed. For wind speeds exceeding 3 m s^{-1}, surface fluxes (cooling or heating) do not appear to appreciably modify their strength and form.

Under high wind speed conditions, the Langmuir cells are not clearly seen on the ocean surface because of wave breaking though they may still exist (Leibovich 1983). Most observations of Langmuir circulations are reported in the wind speed range from 3 to 10 m s^{-1}, although there are observations of the Langmuir-type streaks at wind speeds less than 3 m s^{-1}.

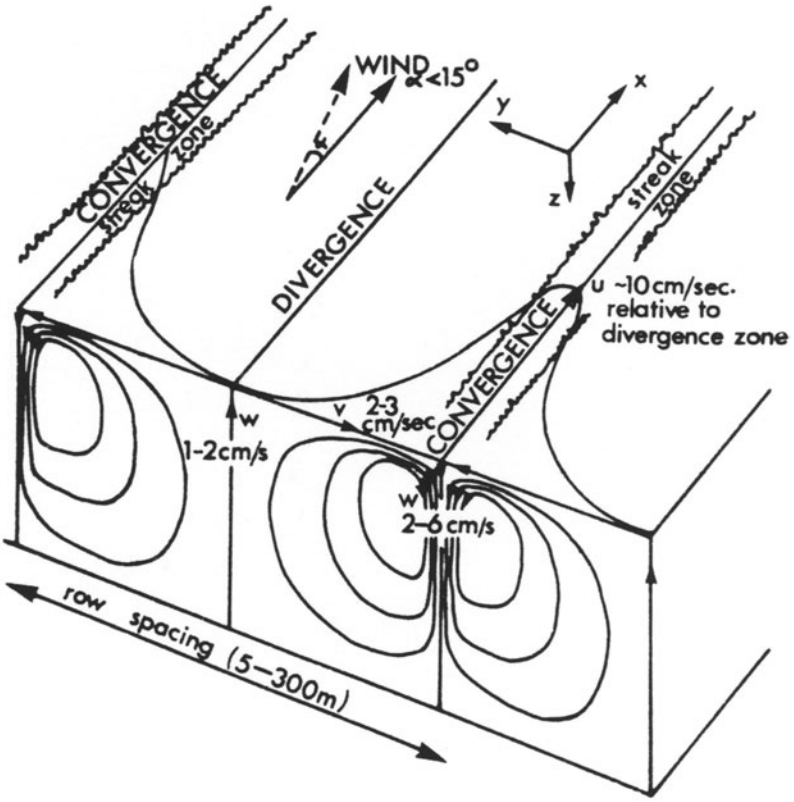

Fig. 5.55 Pollard's (1977) sketch of Langmuir circulations

Weller and Price (1988) found that Langmuir cells rapidly destroy the surface thermal stratification in shallow diurnal mixed layers. They, however, could not find evidence that Langmuir vortices directly participate in mixing in the deeper parts of the oceanic mixed layer.

Craik and Leibovich (1976) developed a list that abstracts a minimum of qualitative features than any viable theory of Langmuir circulations must be able to reproduce:

1. A parallel system of vortices must be nearly aligned with the wind.
2. A means must be given by which these vortices are driven by the wind.
3. The resulting cells must have the possibility of an asymmetric structure with downwelling speeds larger than upwelling speeds.
4. Downwelling zones must be under lines where the wind-directed surface current is greatest.
5. The Langmuir circulations must have maximum downwelling speeds comparable to the mean wind-directed surface drift.

Apparently, this checklist helped Craik and Leibovich to develop their famous theory of Langmuir circulations.

5.7.2 Concepts and Theories

Many mechanisms for Langmuir circulations have been proposed since the publication of the pioneer work of Langmuir in 1938. An overview of the early ideas concerning the mechanism of the Langmuir circulations can be found in Leibovich (1983). Potentially important mechanisms can be grouped as follows: (1) convection, (2) wind forcing, (3) action of surface gravity waves,and (4) joint influence of wind and waves. Most of these mechanisms have been shown to be nonessential to or incompatible with the phenomenon and therefore have been dismissed. A combination of theories, field, and laboratory observations pointed out an interaction between wave motions and surface-sheared currents as a mechanical cause for the phenomenon.

In the 1970s, Garrett, Craik, and Leibovich developed a theory capable of predicting observable features of Langmuir circulations. The theory involved the distortion of vortex lines in the current by the action of surface waves. This theory was based upon a set of nonlinear equations derived from the Navier–Stokes equations by perturbation procedure. Craik–Leibovich or "CL" theories described circulatory motions by two distinct theoretical mechanisms, which are considered below. Both mechanisms depended on wave–current interactions.

The orbital motion of irrotational surface gravity waves usually dominates the instantaneous velocity field in the near-surface layer of the ocean. An important component of CL models is the Stokes drift associated with the surface waves,

$$\vec{U}_s = \overline{\int_t \vec{u}_w dt \cdot \nabla \vec{u}_w}. \tag{5.58}$$

The Stokes drift results from the nonlinear rotational component of the surface wave field and is defined in (5.58) following Phillips (1977). The overbar in (5.58) corresponds to a proper averaging operator; $\vec{u}_w$ is the velocity vector of the orbital motion induced by the waves.

The surface wind stress is an important source of vorticity in the surface layer of the ocean. Vorticity in the surface layer of the ocean may also arise from shear currents driven by horizontal pressure gradients, which are not necessary directly related to the surface stress. The surface waves (that develop due to a prolonged action of the wind stress on the sea surface) perturb the vorticity field in the near-surface layer of the ocean. In particular, surface waves stretch and rotate vortex lines. The rectified (*i.e.*, irreversible) effects of the waves arise from additional advection and stretching of mean vorticity by the wave-induced Stokes drift (Leibovich and Ulrich 1972).

The governing equations in the model for the rectified water motion under the Boussinesq approximation are based on the assumption of constant eddy diffusivity of momentum (ν_T) and heat (χ_T) and are as follows (Leibovich 1977b):

$$\begin{aligned}
&\frac{\partial \vec{u}}{\partial t}+\vec{u}\cdot\nabla\vec{u}=-\nabla\pi+\vec{U}_s\times curl\,\vec{u}+\alpha_T g\theta\vec{k}+\nu_T\nabla^2\vec{u},\\
&\frac{\partial\theta}{\partial t}+\vec{u}\cdot\nabla\theta=-w\frac{\partial\overline{T}(z)}{\partial z}+\chi_T\nabla^2\theta,\ \ \nabla\cdot\vec{u}=0,
\end{aligned} \tag{5.59}$$

where $\overline{T}(z)$ is the temperature distribution in the absence of circulations, θ is the perturbation of temperature, α_T is the coefficient of thermal expansion, g is the acceleration of gravity, $\vec{u}$ is the mean velocity vector in the current, and π is a modified pressure term that includes the mean pressure as well as terms involving wave kinetic energy.

The boundary conditions for the equation system (5.59) are as follows:

$$\frac{\partial u}{\partial z}=u_*^2\,/\,\nu_T;\ \frac{\partial v}{\partial z}=0;\ w=0;\ \theta=0 \text{ at } z=0; \tag{5.60}$$

$$\vec{u}\to 0,\ \theta\to 0 \quad \text{as } z\to-\infty, \tag{5.61}$$

where u_* is the friction velocity in water. The ocean at the initial moment is motionless, except that surface waves are present. The wind drift current does not change in the longitudinal direction x. If the wave–mean current interactions are ignored (which means that the currents may be specified in advance), then the Stokes drift is given a priori; the system of Eq. (5.59) is closed.

This model is able to address the problem of the generation of Langmuir circulations from the motionless state. It meets the criteria of Craik and Leibovich (Sect. 5.7.1) and thereby explains many observable features of the Langmuir circulations.

Leibovich (1977a, b) further extended the CL model to allow time development of the currents and density stratification under the Boussinesq approximation. These works, however, greatly simplified the problem by parameterizing the effects of turbulent fluctuations by constant eddy diffusivities. More sophisticated turbulence models like those described in Chap. 3 were not yet available in the 1970s.

A remarkable feature of (5.59) is the presence of a vortex force:

$$\vec{f}_v=\vec{U}_s\times\vec{\omega} \tag{5.62}$$

where $\vec{\omega}$ is the mean vorticity. Note that as $\vec{U}_s\to 0$ (which is achieved, for instance, when $z\to\infty$), the vortex force term (5.62) vanishes and Eqs. (5.59) reduce to the classical Navier–Stokes equations of a Boussinesq fluid.

In order to explore the role of the vortex force term (5.62), let us follow Leibovich (1983) and assume that the wind blows in a fixed direction over initially undisturbed water of unlimited horizontal extent and depth. Only one fixed direction is involved in the problem formulation, thereby symmetry dictates the development

of a surface wave field with unidirectional Stokes drift aligned with the wind or $\vec{U}_s = U_s \vec{e}_1$. Since this is a two-dimensional hydrodynamic system, it has a tendency to self-organization.

For simplicity, Coriolis acceleration is neglected; the total momentum transferred to the surface layer of the ocean is in the same direction as the Stokes drift velocity vector. The horizontally averaged velocity is $\vec{u} = u(z,t)\,\vec{e}_1$, while the positive y-vorticity is $\vec{\omega} = (\partial T / \partial z)\vec{e}_2$. It is remarkable that the vortex force

$$\vec{f}_v = \vec{e}_3\, U_s\, \partial u / \partial z, \tag{5.63}$$

is oriented vertically upward and is formally analogous to the buoyancy force in (5.59). Here, $\vec{e}_1, \vec{e}_2, \vec{e}_3$ are the unit coordinate vectors $(\vec{e}_3 = \vec{e}_1 \times \vec{e}_2)$.

If the Stokes drift U_s would depend only on depth z, then the vortex force could be balanced by the analog of a hydrostatic pressure gradient (developing unidirectional current). If for any reason the Stokes drift varies across the wind (in the y^-, or transverse direction), the vortex force cannot be balanced just by pressure gradients, and an overturning is possible.

Longuet-Higgins (1962) exploited the fact that the directional spectrum of wind-generated surface waves in a "short-crested" sea is bimodal and symmetric with respect to the wind. If the spectrum is bimodal (with peaks of wave energy at angles $+/-\theta$ with respect to the wind), and if the wave spatial structure remains coherent long enough for the rectification responsible for the Stokes drift to take place (many times a typical wave period), then the Stokes drift would be spatially periodic with a cross-wind wave number of 2 k *sin* θ, where k is the characteristic wave number of the surface waves. This horizontally periodic wave drift produces a torque due to horizontal variations of vortex force that drives the roll motions (Craik and Leibovich 1976). This mechanism is known in the literature as the Craik–Leibovich 1 (CL1) mechanism.

Leibovich and Ulrich (1972) proposed an alternate, kinematic interpretation of the CL1 mechanism. In this interpretation, the Stokes drift deforms the vortex lines associated with the current and produces the streamwise vorticity periodically (in y) altering in sign.

Figure 5.56 summarizes both the dynamic and kinematic interpretations of the CL1 mechanism. This figure also includes a schematic diagram of idealized "cross-wave trains" assumed in the CL1 mechanism.

Leibovich (1977a) extended the CL1 theory to include time evolution of the coupled (wind-directed) currents and circulations. He formulated the problem as an initial-value problem, with currents and circulations initially zero and initiated by a step function in surface stress, which resulted in a well-posed mathematical problem. Since by assumption the wave field is steady and invariant in the x-(wind) direction and symmetric with respect to the x-axis, the problem is independent of x and any emerging circulations appear in the form of rolls. This initial-value problem depends upon an angle representing the directional properties of the waves and a single dimensionless parameter called the *Langmuir number*,

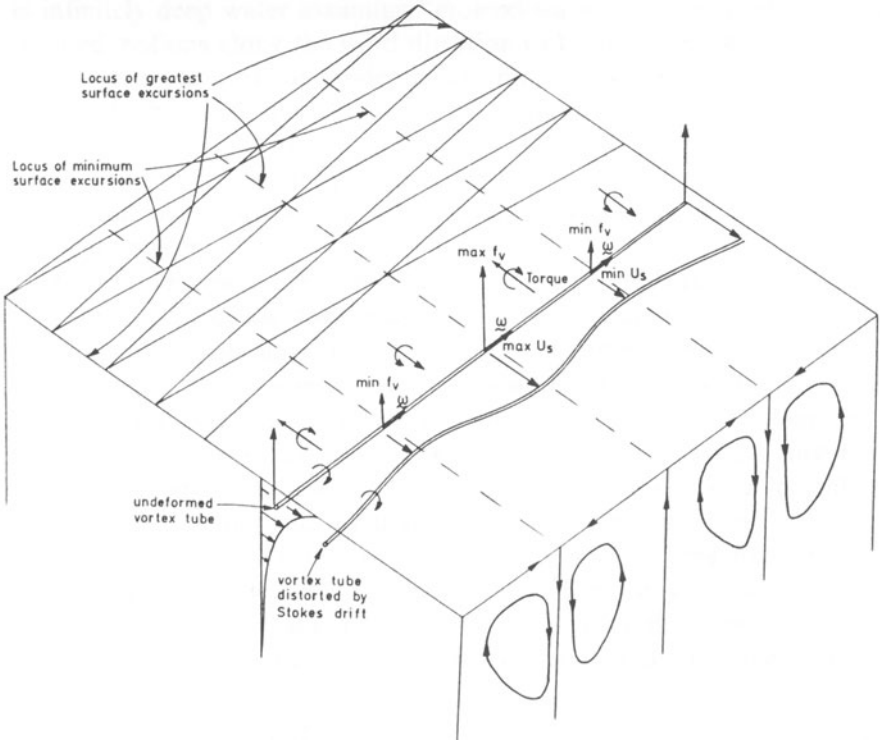

Fig. 5.56 Sketch illustrating the direct-drive generation mechanism for Langmuir circulation. Wave crests of the assumed crossed-wave pattern are shown; the Stokes drift variations distort vortex lines of the primary current. The resulting variations of vortex force create a torque leading to overturning. After Leibovich (1983) Reprinted with permission by Annual Reviews www.annualreviews.org

$$La = (v_T^3 k^2 / \sigma a^2 u_*^2)^{1/2} \tag{5.64}$$

where u_* is the friction velocity (corresponding to a constant wind stress for t≥0); v_T is the eddy viscosity; and σ, k, and a are the characteristic surface wave frequency, wave number, and amplitude, respectively. The Langmuir number describes the balance between the rate of diffusion of streamwise vorticity and the rate of production of streamwise vorticity by the vortex stretching accomplished by the Stokes drift. This number can also be interpreted as an inverse Reynolds number.

The formation of a periodic Stokes drift pattern, which is basic to the CL 1 theory, requires a given wave pattern to be phase-locked for several wave periods. Moreover, the formation of a well-developed circulation by the CL1 mechanism seems to require that the Stokes drift pattern remain fixed for times of the order of hundreds of wave periods. Phase locking for times as long as this is not expected in

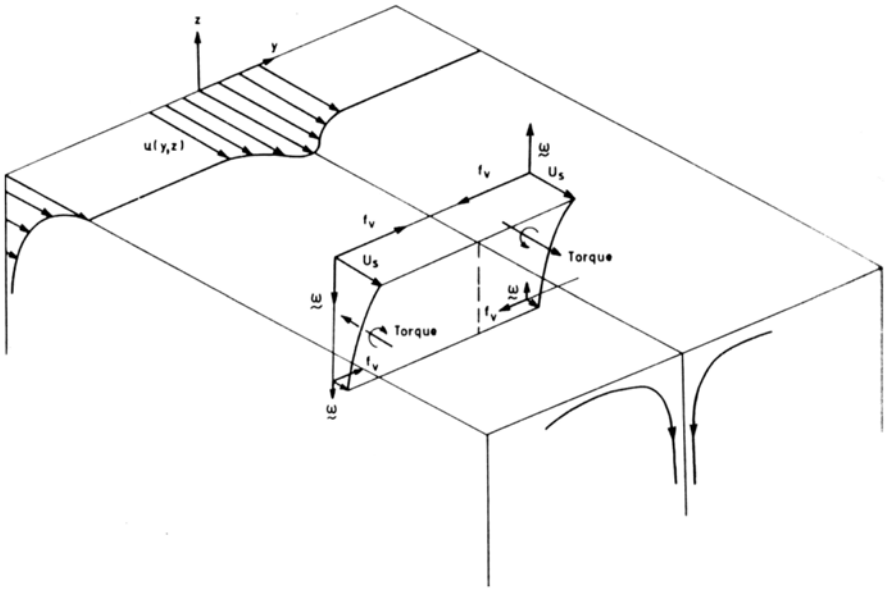

Fig. 5.57 Sketch illustrating the Craik and Leibovich instability mechanism of Langmuir-circulations generation. The Stokes drift is horizontal but decays in depth. Streamwise vorticity is induced by the current. Variations of vortex force caused by the current perturbation create torques leading to overturning. After Leibovich (1983) Reprinted with permission by Annual Reviews www.annualreviews.org

a wind-generated sea; it has, however, been achieved in the laboratory (Faller and Caponi 1978).

Craik (1977) and Leibovich (1977b) proposed another mechanism for Langmuir circulations, which does not require the presence of a coherent surface-wave pattern. It is known in the literature as the CL2 mechanism. The linear stability of a unidirectional sheared current in the presence of a parallel, spanwise uniform Stokes drift is the basis of the CL2 mechanism.

The Langmuir cells are produced via the vortex force as an inviscid instability of the unidirectional current. The vortex force represented by (5.62) in this case is balanced by a vertical pressure gradient. Assuming that U_s and u and the vortex force typically decrease monotonically with depth below the surface, the joint effect of the typical distributions of U_s and u with depth appears to be analogous to a statically unstable vertical density distribution (Leibovich 1983). If dissipation is sufficiently weak, the rectilinear current could become unstable. It is interesting that, if the waves and current are opposed, then the vortex force is stabilizing and Langmuir circulations cannot be generated by the CL2 mechanism.

Figure 5.57 illustrates both the dynamics and kinematics of the CL2 mechanism. If a horizontally uniform current $u(z)$ has an infinitesimal spanwise irregularity $u(y,z,t)$, this produces vertical vorticity $\omega_z = -(\partial u/\partial y)$ and a horizontal

vortex-force component $-U_S \omega_z \vec{j}$. The horizontal vortex-force component is then directed toward the planes of maximum u. The converging horizontal forces cause acceleration toward these planes, where, by continuity, the fluid must sink. Under the assumption that $\partial u/\partial z > 0$ and shear stresses are vanishing, conservation of x-momentum for a thin slab of fluid centered on the convergence plane shows that, as the fluid sinks, u must increase. Thus, a current anomaly will lead to convergence and therefore be amplified, which in turn further amplifies the convergence. This positive feedback results in the development of Langmuir-type circulations. Frictional effects are included in this conceptual mechanism. A kinematic interpretation of the CL2 mechanism is that the vertical vorticity is rotated and stretched by the Stokes drift, leading to convergence and amplification of the anomaly (Leibovich 1983).

Craik (1977) and Leibovich (1977b) suggested an interesting analogy between the Langmuir instability induced in stably stratified flow and turbulent flows in the regime of marginal stability. These authors concluded that an inviscid, non-heat-conducting fluid of infinite depth is stable if

$$M(z) = \frac{\partial U_S(z)}{\partial z}\frac{\partial u(z)}{\partial z} - N^2(z) \tag{5.65}$$

is everywhere negative, and it is unstable otherwise. Here, $N^2 = -\alpha_T g \partial \overline{T}(z)/\partial z$ is the Brunt–Vaisala frequency of the basic state; $\partial U_S/\partial z$ and $\partial u/\partial z$ are vertical gradients of the Stokes drift and of the shear currents. In an unstable system with a stable density stratification, $N^2 \geq 0$, no disturbances penetrate below some characteristic depth. As it follows from (5.65), stability for the inviscid case occurs for

$$Ri_* = \min\left[N^2(z)/\left(\frac{\partial U_S}{\partial z}\frac{\partial u}{\partial z}\right)\right] > 1, \tag{5.66}$$

when the minimum is taken over depth. Ri_* resembles a gradient Richardson number, with the geometric mean of $\partial u/\partial z$ and $\partial U_S/\partial z$ replacing the usual shear.

McWilliams and Sullivan (2000) proposed a modest generalization of the K-profile parameterization (KPP) model for the regime of weakly convective Langmuir circulation. It is interesting that the appearance of the gradient Richardson number in the theory of Langmuir circulations for a stably stratified ocean layer opens an opportunity to parameterize the mixing produced by Langmuir circulation with a simple, first moment closure scheme based on the gradient Richardson number (Soloviev et al. 2001) and described in Sect. 3.6.2.

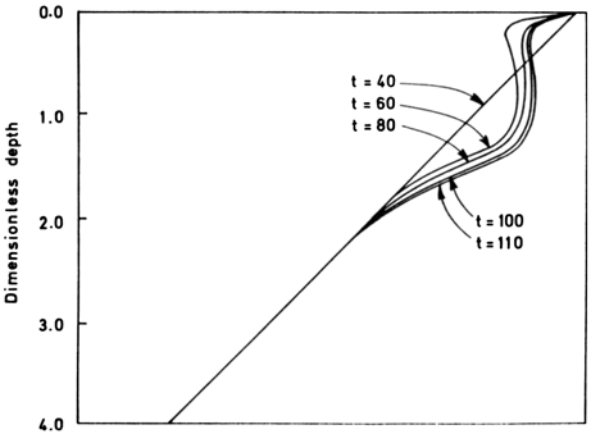

Fig. 5.58 Horizontally averaged temperature at various times after onset of Langmuir circulations by the instability mechanism. After Leibovich and Lele (1982). Reproduced with permission from Sydney Leibovich

5.7.3 Numerical Models of Langmuir Circulations

Realistic simulations of the upper ocean turbulence in the presence of free surface are still a computational challenge. The Craik–Leibovich term is introduced in the equations of motion (5.59) to compensate for the replacement of the free surface with ridged-wall boundary conditions (5.60)–(5.61). This replacement substantially simplifies numerical simulations. At this point, the validity range of this approximation, however, is not completely clear.

Models explicitly incorporating free surface are able to reproduce Langmuir-type circulations without surrogate terms in the equations of motion (Dhanak and Si 1999; Tsai 2001; Soloviev et al. 2012). The numerical simulations with these models, however, have been done only on relatively small spatial scales.

a) Direct numerical simulation (DNS)

Leibovich and Lele (1982) computed cases with constant N, together with other examples with variable N simulating preexisting mixed layers bounded by a thermocline. Figure 5.58 demonstrates how the horizontally averaged temperature evolves into a sharp thermocline from an initially linear profile due to developing cellular circulation motion. For gradient Richardson numbers $Ri_* > 0.125$, growth rates were smaller and the unstable motions were oscillatory. Surprisingly, the motions appear qualitatively to be a mixture of monotonically growing circulations in homogeneous water and internal waves. Apparently, the internal waves support a nonlocal transport of the kinetic energy away from the near-surface layer.

The amount of TKE transformed into internal wave motions is an important unresolved question in modeling turbulent mixing in the upper ocean (Kantha 2006). Unfortunately, experiments on mixing in the ocean, in which internal wave and turbulence kinetic energies are separated out and measured as a function of time, are

a challenge. In this connection, it is interesting to mention the work of Zilitinkevich and Calanca (2000) who included internal waves in a mixed-layer parameterization for the atmospheric boundary layer. Experimental data of this type in the atmospheric boundary layer are readily available (Zilitinkevich and Esau 2005). The Zilitinkevich and Calanca (2000) theory is pending implementation for upper ocean mixed layer dynamics (V.M. Kamenkovich, private communication).

For $Ri_* \geq 1/4$, but well below the inviscid criterion (5.66), the system appears to be stable at the Langmuir number of 0.01 used in the calculations. Leibovich and Lele (1982) found that sufficiently thick preexisting thermoclines with sufficiently strong temperature gradients act as an impenetrable "bottom" for the induced circulations. This is in accordance with Langmuir's (1938) ideas.

b) Large Eddy Simulation (LES)

Skyllingstad and Denbo (1995) performed LES studies of Langmuir circulation under a variety of conditions. These conditions included wind- and convection-driven mixing with and without Stokes drift to highlight their importance in the structure of the upper layers. They indicated the limited effect of surface heating and cooling on the near-surface structure of Langmuir circulations during their simulation. Cases with the wind- and wave-forced simulations (with or without cooling or heating) reveal the organized structure; conversely, runs without surface wave forcing do not reveal this type of organization. Remarkably, the characteristic elongated structures associated with Langmuir cells were evident in the near-surface layer only but not at greater depths in the upper ocean mixed layer. The increase of vertical velocity variance and entrainment heat flux in the case with Stokes drift relative to the case with no Stokes drift led Skyllingstad and Denbo (1995) to the conclusion that Langmuir circulations might be important to the dynamics of the upper ocean mixed layer.

McWilliams et al. (1997) added Coriolis and pressure terms to the mean momentum equation for Stokes drift that was ignored by Skyllingstad and Denbo (1995). McWilliams et al. (1997) performed LES studies with the improved model formulation and demonstrated an elevated TKE and dissipation rate of TKE in the mixed layer, especially in the upper part, as well as a significant increase in eddy viscosity. The vertical velocity profiles in the Ekman layer were more homogeneous in the case with Langmuir circulation. Based on this numerical study, these authors introduced a concept of "Langmuir turbulence." This concept has been explored with LES in a number of subsequent studies. Field verifications are, however, still a challenge. In a strange way, one of the most visible parameters of Langmuir cells—spanwise size of cells—has practically never been quantified in the LES simulations (in order to compare with available observations under different wind-wave conditions).

The LES simulation (e.g., McWilliams et al. 1997; McWilliams and Sullivan 2000) shows significant increase of the dissipation rate in the upper ocean mixed layer due to Langmuir circulation, which is puzzling. Organization should not increase, but rather reduce chaos and thus reduce dissipation in the system (while increasing transport of properties by adding a nonlocal component). It is, therefore,

not clear how the term "turbulence" is applicable to a spatially coherent organized motion like Langmuir circulation.

In summary, the LES models of Langmuir circulation are now quite sophisticated; these models incorporate stratification, bubble dynamics, and bubble-mediated gas transport (*e.g.*, Liang et al. 2011, 2012). However, these modeling results still pose some questions:

1. Langmuir circulation is an organized structure. Any organization increases effectiveness of the transport and reduces dissipation in the system. Why do the existing LES models in fact produce the increase of dissipation in the presence of Langmuir circulation?
2. Is the term Langmuir turbulence proper for characterizing Langmuir circulation?
3. Do the periodic boundary conditions in the presence of the Coriolis force, which deviates the current from the wind direction (Ekman spiral), impose artificial periodicity, which may look like Langmuir circulation but, in fact, determined by the size of the numerical domain and value of the Coriolis parameter (see Chap. 1, Sect. 1.3.1)?

An answer to these questions is important for development of realistic models of the upper ocean dynamics.

5.7.4 An Alternative Mechanism of Langmuir Circulation

The Craik–Leibovich mechanism may not be the only one that results in the generation of Langmuir circulation. Gargett (2009) suggested that"Couette circulations" (which are not related to surface waves) have the same downwind-elongated counter-rotating vortex pairs as do Langmuir circulations, leading to identical patterns of convergences alternating with divergences. The circulations of this type develop in the boundary layer near the rigid wall. Lesieur (2008) calls them "streaks." Rolls in the atmospheric boundary layer are another example of a similar coherent structure, which are not related to surface waves as well. Streak-like structures have also previously been reported from numerical simulations below the free surface with no waves (Dhanak and Si 1999; Tsai 2001; Soloviev et al. 2012).

According to Lesieur (2008), near the rigid wall the streaks are observed in the buffer layer between the viscous sublayer and the area of developed turbulence. The spanwise size of these streaks is $l \sim 10\,\delta_\nu$, where

$$\delta_\nu = 10\,\nu/u_*$$

is the thickness of the viscous sublayer and u_* is the friction velocity.

In the presence of breaking waves, the turbulent mixing coefficient in the wave-stirred layer can be treated as a constant (resembling the molecular viscosity but of much higher value). The thickness of the wave-stirred layer is O(H_s), where H_s is the significant wave height (see Chap. 3). By hypothesizing an analogy between the turbulent mixing coefficient in the wave-stirred layer and the molecular viscosity

coefficient in the viscous sublayer, the spanwise size of streaks in this case can be scaled with depth of the wave-stirred layer (Soloviev et al. 2012).As a result, the spacing between the streaks is O($10H_s$), which will range from a few meters under low wind speed conditions to hundreds of meters under high wind speed conditions.

Finally, it should be noted that the streaks are subject to Tollmien–Schlichting instability, which results in intermittent ejections of fluid from the boundary layer. This is presumably the mechanism forming ramp-like structures in turbulent boundary layers (see Sect. 5.6.3). The alternative theory, thus, can potentially explain the coexistence of Langmuir cells and ramp-like structures, at least under not very high wind speed conditions. Tsai and Hung (2007) assumed that streaks are observed at relatively low wind speeds, while the Craik–Leibovich mechanism takes over under high winds.

5.8 Convection

Free convection is fluid motion due to unbalanced buoyancy forces. Free convection, also referred to as simply *convection*, is driven by the static instability that results when relatively dense fluid lies above relatively light fluid. In the ocean, greater density is associated with colder and/or saltier water, and it is possible to have *thermal convection* due to the vertical temperature gradient, *haline convection* due to the vertical salinity gradient, or *thermohaline convection* due to the combination.

Since convection has a preferred direction (determined by the gravity force), it is a two-dimensional hydrodynamic process, which, therefore, has a tendency to self-organization. Soloviev and Klinger (2001) provided a comprehensive review of convection in the upper layer of the ocean. Here, we focus on the coherent properties of convection.

Since seawater is about 1,000 times denser than air, the air–sea interface from the waterside can be considered a free surface. The so-called *thermo-capillary (Marangoni) convection* can develop near this surface due to the dependence of the surface tension coefficient on temperature. There are experimental indications that, in the upper ocean layer more than 2 cm deep, buoyant convection dominates. Surfactants, however, may substantially affect the surface renewal process (see Sect. 2.3.7). Here, we consider convection without these capillary effects.

Convection is one of the key processes driving mixed layer turbulence, though mechanical stirring driven by windstress and other processes are also important. Therefore, understanding convection is crucial to understanding the mixed layer as well as property fluxes between the ocean and the atmosphere.

Thermal convection is associated with the cooling of the ocean surface due to sensible (Q_T), latent (Q_E), and net longwave radiation (Q_L) heat fluxes. Q_T may have either sign; its magnitude is, however, much less than that of Q_E or Q_L (except perhaps in some extreme situations such as cold air outbreaks over warm western boundary currents). The top of the water column becomes colder and denser than the water below, and convection begins. In this way, cooling is associated with the homogenization of the water column and the deepening of the mixed layer.Warm-

ing due to solar radiation occurs in the surface layer of the ocean and is associated with re-stratification and reduction in mixed layer depth (see Chap. 4). The most prominent examples of this mixing/re-stratification process are the diurnal cycle (nighttime cooling and daytime warming) and the seasonal cycle (winter cooling and summer warming).

There are also important geographical variations in convection, with net cooling of relatively warm water occurring more at higher latitudes and a net warming of water occurring closer to the equator. For this reason, mixed layer depth generally increases toward the poles, though at very high latitudes ice melt can lower the surface salinity enough to inhibit convection. Over most of the ocean, annual average mixed layer depths are in the range of 30–100 m, though very dramatic convection in such places as the Labrador Sea, Greenland Sea, and western Mediterranean Sea can deepen the mixed layer to thousands of meters. The deep convection can be significantly affected by the rotation of the Earth.

Convection directly affects several aspects of the near-surface ocean. Most obviously, the velocity patterns of the turbulent flow are influenced by the presence of convection, as is the velocity scale.The convective velocity field then controls the vertical transport of heat (or more correctly, internal energy), salinity, momentum, dissolved gases, and other properties, and the vertical gradients of these properties within the mixed layer. Convection helps to determine property exchanges between the atmosphere and ocean and the upper ocean and the deep ocean. The importance of convection for heat and gas exchange has implications for climate studies, while convective influence on the biologically productive euphotic zone has biological implications as well.

5.8.1 Phenomenology

The classical problem of free convection in the ocean is to determine the motion in a layer of fluid in which the top surface is kept colder than the bottom surface (Soloviev and Kilnger 2001). This is an idealization of such geophysical examples as an ocean being cooled from above or the atmosphere being heated from below. The classical problem ignores such complications as wind stress on the surface, waves, topographic irregularities, and the presence of a stably stratified region below the convection region. The study of convection started in the early twentieth century with the experiments of Benard and the theoretical analysis of Rayleigh. One might expect that heavier fluid would necessarily exchange places with lighter fluid below due to buoyancy forces. This happens by means of convective cells or localized plumes of sinking dense fluid and rising light fluid. However, such cells or plumes are retarded by viscous forces and are also dissipated by thermal diffusion and entrainment as they fall or sink into an environment with a different density. When the buoyancy force is not strong enough to overcome the inhibitory effects, the heavy-over-light configuration is stable and no convection forms. The relative strengths of these conflicting forces is measured by the Rayleigh number, a nondimensional number given by

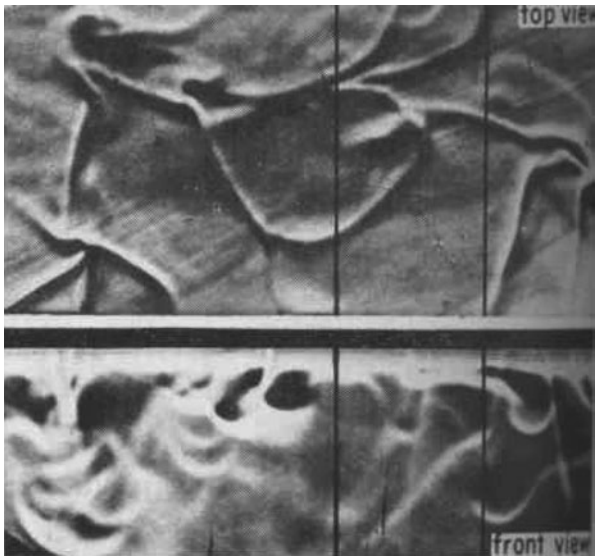

Fig. 5.59 Orthogonal views of convective streamers in the warm water that is cooling from the surface. The constantly changing patterns appear as intertwining streamers in the side view. Adopted from Spangenberg and Rowland (1961) with permission from the American Institute of Physics

$$Ra = g\alpha_T \Delta T h^3 / (k_T \nu), \tag{5.67}$$

where g is the acceleration of gravity, α is the thermal expansion coefficient of seawater ($\alpha_T = -2.6 \cdot 10^{-4^\circ}\,\mathrm{C}^{-1}$ at $T = 20$ °C and $S = 35$ psu), ΔT is the temperature difference between the top and bottom surfaces, h is the convective layer thickness, and ν and k_T are the molecular coefficients of viscosity and thermal diffusivity, respectively ($\nu = 1.1 \cdot 10^{-6}$ m^2 s^{-1} and $k_T = 1.3 \cdot 10^{-7}$ m^{2}s^{-1} at $T = 20$ °C and $S = 35$ psu). The term, $\alpha_T \Delta T = \Delta\rho/\rho$, represents the relative density difference between top and bottom.

Turbulent convection is usually characterized by the formation of descending parcels of cold water. In laboratory experiments, it has been found that water from the cooled surface layer collects along lines producing thickened regions that become unstable and plunge in vertical sheets (Fig. 5.59). In analogy to the atmospheric convection, we will call these parcels *thermals*, although, in contrast to the atmosphere, in the ocean they are colder than the surrounding fluid. Howard (1966) formulated a phenomenological theory that represented turbulent convection as the following cyclic process.The thermal boundary layer forms by diffusion, grows until it is thick enough to start convecting, and is destroyed by convection, which in turn dies down once the boundary layer is destroyed. Then the cycle begins again. This phenomenological theory has implications for the development of parameterizations for the air–sea heat and gas exchange under low wind speed conditions with a renewal model (see Chap. 2).

The descending parcels of water have a mushroom-like appearance. In the process of descending to deeper layers, the descending parcels join and form larger mushroom-like structures. The latter descend faster and eventually form bigger structures. This cascade process produces a hierarchy of convective scales, which is

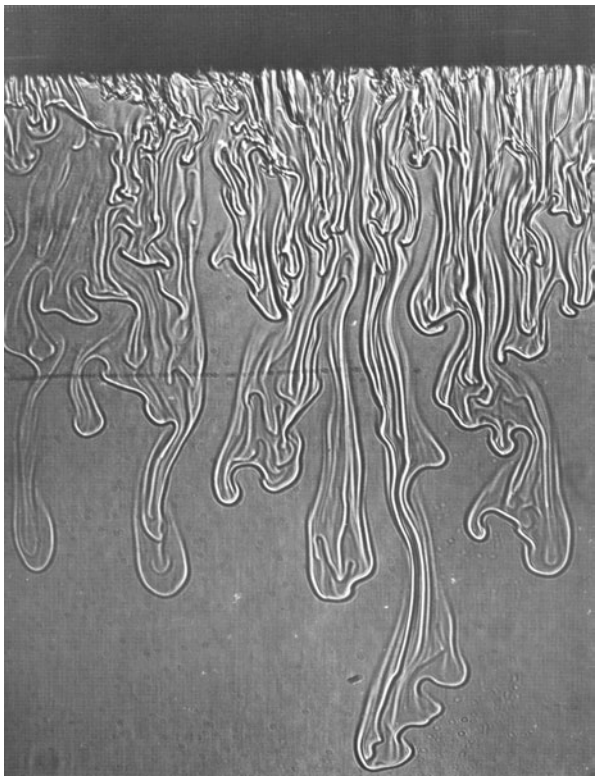

Fig. 5.60 Shadowgraph picture of the development of secondary haline convection. Adopted from Foster (1975)

illustrated in Fig. 5.60 for the example of haline convection. As a result, the energy cascades to larger scales. This is consistent with the fact that the free convection represents a type of two-dimensional hydrodynamic system and thus has a tendency to self-organization.

The size of convective parcels of cooler water increases with depth. If the mixed layer is deep, as in the example from the Labrador Sea shown in Fig. 5.61, the horizontal size of the convective cells can exceed one hundred meters. In this experiment the depth of the convective mixed layer is equal to 350 m (Fig. 5.61b). The horizontal profile of the vertical velocity taken at 250 m (Fig. 5.61c) reveals quasiperiodic structure. Zhang et al. (2001) identified this structure as convection. The peak in the spectrum calculated from the velocity record is at 0.007 Hz, which corresponds to a 143 m wavelength for AUV speed 1 m s^{-1}.

5.8.2 Penetrative Convection

The unstable stratification of the mixed layer is usually bounded below by a stratified pycnocline. One can imagine the mixed layer growing in depth with thermals

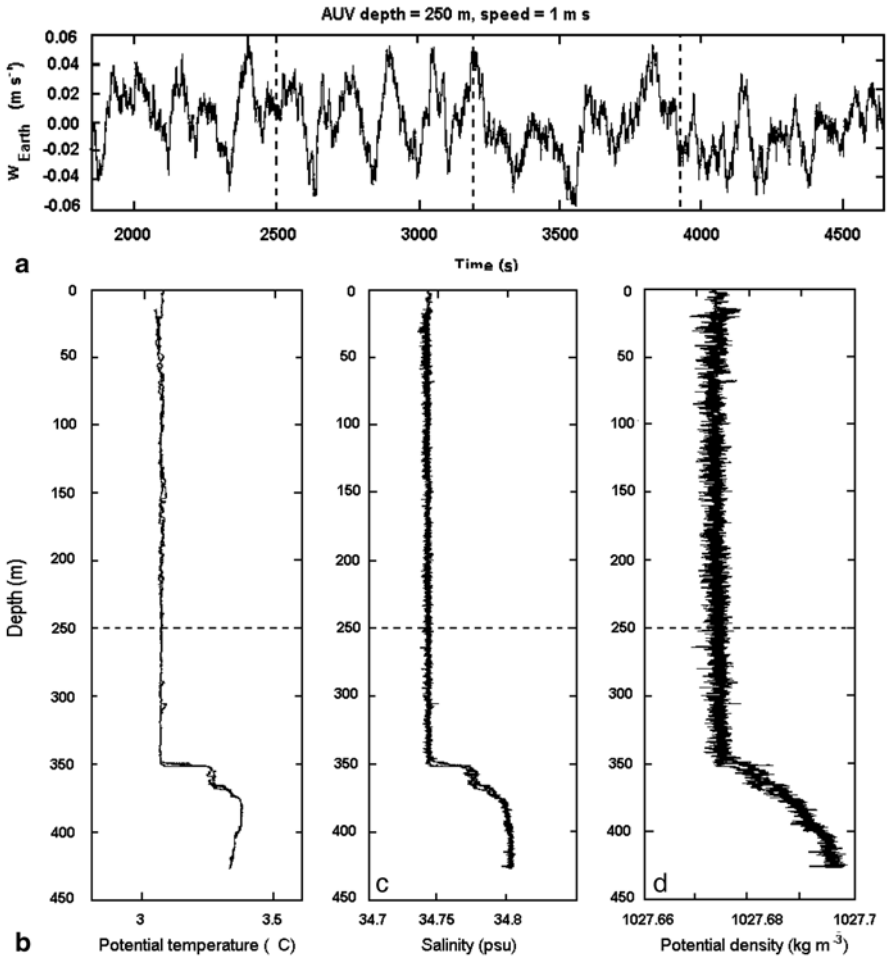

Fig. 5.61 **a** The Earth-referenced vertical flow velocity w_{Earth} at 250 m depth measured during an autonomous underwater vehicle (AUV) mission in the Labrador Sea. The vertical dashed lines show the AUV 90° turning points. The profiles of potential temperature, salinity, and potential density during this AUV mission are shown on panel **b**, **c**, and **d**, respectively. The depth of the AUV mission is shown by a horizontal dashed line. After Zhang et al. (2001) © 2001 IEEE

confined to the statically unstable depth range. In reality, the largest thermals acquire enough kinetic energy as they fall through the mixed layer that they can overshoot the base of the mixed layer, working against the stratification. This is penetrative convection, which is a type of organized motion. The penetrative convection produces a counter-gradient flux that is not properly accounted for if convective mixing is modeled as merely a very strong vertical diffusion.

The cooling of the ocean from its surface is countered by the absorption of solar radiation. The latter is a volume source for the upper meters of the ocean. The ther-

mals from the ocean surface, as they descend deeper into the mixed layer, produce heat flux that is compensated by the volume absorption of solar radiation.. This is another type of penetrative convection in the upper ocean, which is considered in more detail in Sect. 4.6.1.

5.8.3 Diurnal and Seasonal Cycle of Convection

Below the wave-turbulent layer shear and convection are the main sources of turbulent mixing (Sect. 3.2.4). Experimental studies conducted in the atmospheric boundary layer show that for $|z|/L_O < -0.1$ the flow is primarily driven by buoyant convection, where $L_O = u_*^3 / \left[\alpha_T g Q_0 \kappa / (c_p \rho) \right]$ is the Obouk-hov buoyancy length scale.

For 5 m s^{-1} wind speed and net surface cooling $Q_0 = 100$ Wm^{-2}, the Oboukhov length scale in the upper ocean is $L_O \sim -15$ m. This means that the shear driven turbulent flow is confined within the upper approximately 1.5 m. In a 50 m deep mixed layer 97% of its depth will be driven by buoyant convection during nighttime.

For much of the year, most of the ocean experiences a cycle of daytime heating and night-time cooling which leads to a strong diurnal cycle in convection and mixed layer depth. Such behavior is illustrated in Fig. 5.62. At night, when there is cooling, the convective plumes generally reach the base of the mixed layer. During the day, convection is inhibited within the bulk of the mixed layer but may still occur near the surface, even if the mixed layer experiences a net heat gain. This is because the solar radiation is a volume source of heat (see Chap. 4).

Usually, the rate of TKE production in the mixed layer is dominated by the convective term at night, but by the wind stress term during most of the day. Because the compensation depth (see Sect. 4.6.1 for definition) is generally quite small, TKE generated by convection during daytime makes no contribution to turbulent entrainment at the bottom of the mixed layer, which lies much deeper.

Stable stratification inhibits turbulent mixing below the relatively thin near-surface convection layer. Vertical mixing of momentum is confined to the shallow diurnal mixed layer, so that, during the day, flow driven directly by the wind stress is confined to a similarly thin current known as the diurnal jet. In the evening, when convection is no longer confined by the solar radiation effect, convective thermals penetrate deeper into the mixed layer, increasing the turbulent mixing of momentum at the bottom of the diurnal jet. The diurnal jet then releases its kinetic energy during a relatively short time period. This process is so intense that the kinetic energy released cannot be dissipated locally. As a result, a Kelvin–Helmholtz type of instability is formed, which generates billows—another type of organized structure. The billows intensify the deepening of the diurnal mixed layer. The theoretical basis for this mechanism is described in Sect. 5.5.3.

Although the energy of convective elements is relatively small, it serves as a catalyst for the release of the kinetic energy by the mean flow. In most of the equatorial ocean, the Equatorial Undercurrent intensifies the shear in the upper ocean;

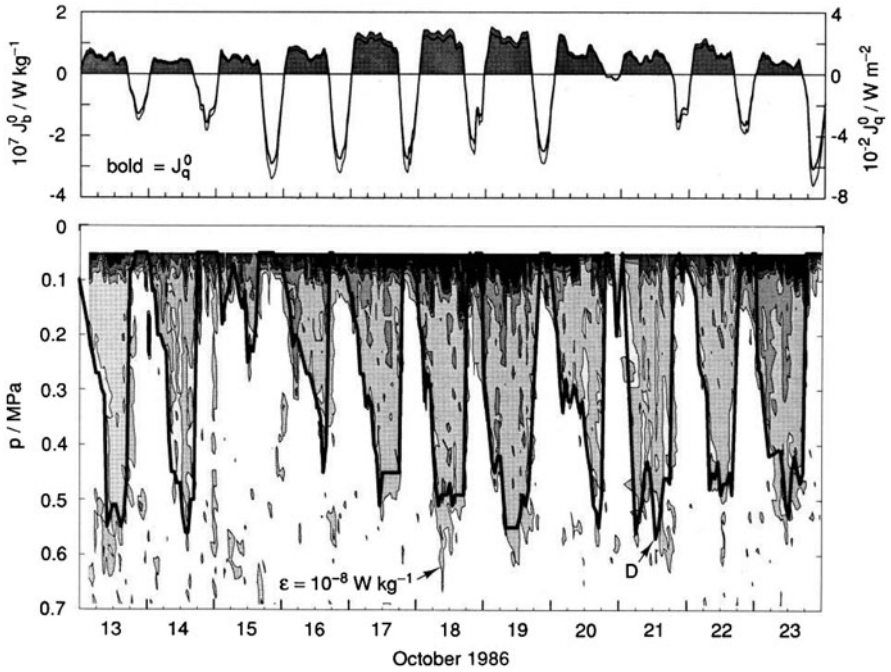

Fig. 5.62 Diurnal cycles in the outer reaches of the California Current (34° N, 127° W). Each day the ocean lost heat and buoyancy starting several hours before sunset and continuing until a few hours after sunrise. These losses are shown by the shaded portions of the surface heat and buoyancy fluxes in the top panel. In response, the surface turbulent boundary layer slowly deepened (lower panel). The solid line marks the depth of the surface turbulent boundary layer, and the lightest shading shows 10^{-8} W kg^{-1} < ε < 10^{-7} W kg^{-1}. The shading increases by decades, so that the darkest shade is ε > 10^{-5} W kg^{-1}. Note that 1 MPa in pressure p corresponds to approximately 100 m in depth, $J_b^0 = -B_0$, and $J_q^0 = -(Q_0 + I_R)$, where I_R is the solar radiation flux penetrating the ocean surface. After Shay and Gregg (1986). Copyright © 1986 American Meteorological Society. Used with permission

the evening deepening of the diurnal jet is therefore sometimes so intense that it resembles a shock wave, which radiates very intense high-frequency internal waves in the underlying thermocline.

The diurnal cycle is often omitted from numerical ocean models for reasons of computational cost. However, the mixed layer response to daily-averaged surface fluxes is not necessarily the same as the average response to the diurnal cycle (Shinoda et al. 1998; McCreary et al. 2001). Neglecting the diurnal cycle replaces periodic nightly convective pulses with chronic mixing that does not reach as deep.

Upper ocean convection is a mechanism effectively controlling the seasonal cycle in the ocean as well (Woods and Barkman 1986). Resolution of diurnal changes is usually uneconomical when the seasonal cycle is considered. Because of the nonlinear response of the upper ocean to atmospheric forcing, simply averaged heat fluxes cannot be used to estimate the contribution of convection on the seasonal

scale. The sharp transition between the nocturnal period, when convection dominates mixing in the surface layer, and the daytime period, when the Sun severely limits the depth of convection leaving the wind stress to control mixing, may in fact simplify the design of models for the seasonal cycle of the upper ocean. Parameterization of the convection on the seasonal and global scale is an important task for the prediction of climate and its changes.

Though free convection is probably one of the most studied types of organized motion, many intriguing questions regarding convection in the open ocean still remain. Some of them, like the role of penetrative convection in mixed layer dynamics, are of crucial importance for the improvement of global ocean circulation modeling. Others, like the role of surfactants in the surface renewal process, are of substantial interest for studying the air–sea exchange and global balance of *greenhouse gases* like CO_2.

5.9 Conclusions

Spatially coherent organized motions are an inherent part of the upper ocean turbulent boundary-layer dynamics. These motions perform nonlocal transport of properties.

Observation of coherent structures in the open ocean is not a simple experimental task. Though several types of these structures have been observed in oceanic turbulence studies, most of our knowledge of this phenomenon in the ocean is either fragmentary or mainly based on the analogy between atmospheric and oceanic boundary layers, and on laboratory studies. A major problem of applying the knowledge acquired in the atmospheric boundary layer to its oceanic counterpart is in the huge difference between the air and water densities. In particular, the air–sea interface from the waterside behaves like a free surface (which, in particular, requires different surface boundary conditions.)

The elements of the theory for the coherent structures in the upper ocean do exist, but they often come from different areas of science and still require substantial efforts to apply them to the upper ocean situation. The theoretical models of organized structures are often detached from real observations, while the existing observations could validate theories only in a few successful cases. This is an indication that this area of physical oceanography requires special attention.

References

Ando K, McPhaden MJ (1997) Variability of surface layer hydrography in the tropical Pacific ocean. J Geophys Res 102(C10):23063–23078

Antonia RA, Chambers AJ, Friehe CA, Van Atta CW (1979) Temperature ramps in the atmospheric surface layer. J Atmos Sci 36:99–108

Apel JR, Byrne HM, Proni JR, Charnell RL (1975) Observations of oceanic internal and surface waves from the earth resources technology satellite. J Geophys Res 80:865–881

Barenblatt GI, Shapiro GI (1984) A contribution to the theory of the wave fronts in dispersive media. Izvestiya, Akad Nauk SSSR, Atmos Oceanic Phys 20(4):277–284
Batchelor GK (1969) Computation of the energy spectrum in homogeneous two-dimensional turbulence. The Physics of Fluids, Suppl. II, 12:233–239
Belcher SE, Vassilicos JC (1997) Breaking waves and the equilibrium range of wind wave spectra. J Fluid Mech 342:377–401
Belkin I, Cornillon P, Shan Z (2001) Global survey of ocean fronts from Pathfinder SST data. The oceanography society biennial scientific meeting, 2–5 April, 2001, Miami Beach, Florida USA. Oceanography 14(1):10
Boubnov BM, Golitsyn GS (1990) Temperature and velocity field regimes of convective motions in a rotating fluid layer. J Fluid Mech 219:215–239
Branover H, Eidelman A, Golbraikh E, Moiseev S (1999) Turbulence and structures. Chaos, fluctuations, and self-organization in nature and in the laboratory. Academic Press, San Diego, p 270
Brekhovskikh LM, Goncharov VV, Kurtepov VM, Naugol'nykh KA (1972) Resonant excitation of internal waves by nonlinear interaction of surface waves Izvestiya,. Atmos Ocean Phys 8:192–203
Briscoe MG (1983) Observations on the energy balance of internal waves during JASIN. Philos T Roy Soc London A308:427–444
Brown GL, Thomas ASW (1977) Large structure in a turbulent boundary layer. Phys Fluids 20:S243–S252
Cabanes O (1999) Modulation of mixed layer thermodynamics by equatorial waves in the tropical western Pacific. report. ENM Meteo France and SOEST University of Hawaii, p 74
Corino ER, Brodkey RS (1969) A visual investigation of the wall region in turbulent flow. J Fluid Mech 37: 1–30
Craik ADD (1977) The generation of Langmuir circulations by an instability mechanism. J Fluid Mech 81:209–223
Craik ADD, Leibovich S (1976) A rational model for Langmuir circulations. J Fluid Mech 73:401–426
Csanady GT (1984) The free surface turbulent shear layer. J Phys Oceanogr 14:402–411
D'Asaro EA, Farmer DM, Osse JT, Dairiki GT (1996) A Lagrangian float. J Atmos Ocean Tech 13:1230–1246
Delcroix T, Eldin G, Henin C, Gallois F, Grelet J, Inal M, Keene S, Langlade M.-J, Menkes C, Masia F, Richards K (1993) Campagne COARE-POI a bord du N.O. Le Noroit, 1 Dec 92–2 Mar 93. Technical Report, ORSTOM, BP A5, Noumea, New Caledonia. Rapports de Missions, Sci Mer Oceanogr Phys 10:338
Dhanak MR, Si C (1999) On reduction of turbulent wall friction through spanwise wall oscillations. J Fluid Mech 383:175–195
Dobrokhotov S, Semenov E, Tirozzi B (2003) Hugoniot–Maslov chains for singular eddy solutions of quasilinear hyperbolic systems and tayphoon trajectories. Sovrem Mat Fund Napr 2:5–44 (in Russian).
Dysthe TH, Das KP (1981) Coupling between a surface wave spectrum and an internal wave: modulation interaction. J Fluid Mech 104:483–503
Einstein A (1905) On the motion of small particles suspended in liquids at rest required by the molecular-kinetic theory of heat. Annalen der Physik 17:549–560
Eldevik T, Dysthe K (2002) Spiral Eddies. J Phys Oceanogr 32(3):851–869
Faller AJ, Caponi EA (1978) Laboratory studies of wind-driven Langmuir circulations. J Geophys Res 83:3617–3633
Farmer DM (1978) Observations of long nonlinear internal waves in a lake. J Phys Oceanogr 8(1):63–73
Fedorov KN (1986) The physical nature and structure of oceanic fronts. Springer-Verlag, Berlin
Feng M, Lukas R, Hacker P, Weller RA, Anderson SP (2000) Upper ocean heat and salt balances in the western equatorial Pacific in response to the intraseasonal oscillation during TOGA COARE. J Climate 13:2409–2427

Feng M, Lukas R, Hacker P (2001) Spin-up of a sub-mesoscale eddy in the TOGA COARE Intensive flux array during the spin-down of an intense eastward jet. J Phys Oceanogr 31(3):711–724
Ferrari R, Paparella F (2003) Compensation and alignment of thermohaline gradients in the ocean mixed layer. J Phys Oceanogr 34:247–257
Ferrari R, Rudnick DL (2000) Thermohaline variability in the upper ocean. J Geophys Res 105(C7):16,857–16,883
Ferrari R, Young WR (1997) On the development of thermohaline correlations as a result of nonlinear diffusive parameterizations. J Mar Res 55:1069–1101
Ferrari R, Paparella F, Rudnick DL, Young WR (2001) The temperature-salinity relationship of the mixed layer. In: Peter Muller, Diane Henderson (eds) Proceedings, Hawaiian winter workshop, University of Hawaii at Manoa, January 16–19, 2001. SOEST Special Publication 2001, pp 95–104
Flament P, Firing J, Sawyer M, Trefois C (1994) Amplitude and horizontal structure of a large diurnal sea surface warming event during the coastal ocean dynamics experiment. J Phys Oceanogr 24:124–139
Foster TD (1975) The hierarchy of convection, Colloques Internationaux du C.N.R.S. N215.—Processus de Formation Des Eaux Oceaniques Profondes, pp 235–241
Gargett AE (2009) Couette vs. Langmuir circulations: Comment on "On the helical flow of Langmuir circulation—Approaching the process of suspension freezing" by Dethleff, Kempema, Koch and Chubarenko. Cold Reg Sci Techn 56:58–60
Goldstein S (1931) On the stability of superposed streams of fluids of different densities. Proc Roy Soc A 132:524–548
Golitsyn S (2008) Polar lows and tropical hurricanes: Their energy and sizes and a quantitative criterion for their generation. Izv., Atmos Ocean Phys 44(5):537–547
Golitsyn GS (2012) On the nature of spiral eddies on the surface of seas and oceans. Izvestiya, Atmos Oceanic Phys 48(3):350–354
Grabowski WW, Smolarkiewicz PK (1999) CRCP: a cloud resolving convection parameterization for modeling the tropical convecting atmosphere. Physica D 133:171(178)
Hagen JP, Kurosaka M (1993) Corewise cross-flow transport in hairpin vortices–the "Tornado Effect." Phys. Fluids A 5:3167–3174
Hasegawa A (1985) Self-organization processes in continuous media. Advan Phys 34:1–42
Hinze J (1975) Turbulence. McGraw-Hill, New York, p 790
Howard LN (1961) Note on a paper of John Miles. J Fluid Mech 10: 509–512
Howard LN (1966) Convection at high Rayleigh number. Proc of the Eleventh Intern. Congress of Applied Mechanics, Munich, pp 1109–1115
Hunkins K, Fliegel MJ (1973) Internal undular surges in Seneca Lake: Natural
Huyer A, Kosro PM, Lukas R, Hacker P (1997) Upper ocean thermohaline fields near 2°S, 156°E, during the coupled ocean-atmosphere response experiment, November 1992 to February 1993. J Geophys Res 102:12,749–12,784
Imberger J (1985) The diurnal mixed layer. Limnol Oceanogr 30(4):737–770
Kamal JC, Wyngaard JC, Izumi Y, Cote OR (1972) Spectral characteristics of surface-layer turbulence, Q J Roy Meteor Soc 98:563–589
Kantha L (2006) Comments on "Second-order turbulence closure models for geophysical boundary layers: a review of recent work". Cont Shelf Res 26:819–822
Kline SJ, Reynolds WC, Schraub FA, Runstadler PW (1967) The structure of turbulent boundary layers. J Fluid Mech 30:741–773
Kraichnan RH (1967) Inertial ranges in two-dimensional turbulence. Phys Fluids 10:1417–1423
Kraichnan RH (1975) Statistical dynamics of two-dimensional flow. J Fluid Mech 67:155–175
Kudryavtsev VN, Soloviev AV (1990) Slippery near-surface layer of the ocean arising due to daytime solar heating. J Phys Oceanogr 20:617–628
Landau LD, Lifshitz EM (1993) Fluid mechanics, 2nd edn. Pergamon Press, New York, p 593
Langmuir I (1938) Surface motion of water induced by wind. Science 87(2250):119–123
Large WG, Danabasoglu G, McWilliams JC, Gent PR, Bryan FO (2001) Equatorial circulation of a global ocean climate model with anisotropic horizontal viscosity. J Phys Oceanogr 31:518–536

Leibovich S (1977a) On the evolution of the system of wind drift currents and Langmuir circulations in the ocean. Part I. Theory and the averaged current. J Fluid Mech 79:715–749
Leibovich S (1977b) Convective instability of stably stratified water in the ocean. J Fluid Mech 82:561–585
Leibovich S (1983) The form and dynamics of Langmuir circulations. Ann Rev Fluid Mech 15:391–427
Leibovich S, Lele SK (1982) Thermocline erosion and surface temperature variability due to Langmuir circulations. FDA Rep. #82–07, Sibey School Mech & Aerosp. Eng. Cornell Univ., Ithaca
Leibovich S, Ulrich D (1972) A note on the growth of small scale Langmuir circulations. J Geophys Res 77:1683–1688
Lesieur M (2008) Turbulence in fluids, fourth revised and enlarged edition. Springer. p 148.
Liang J-H, McWilliams JC, Sullivan PP, Baschek B (2011) Modeling bubbles and dissolved gases in the ocean, J Geophys Res 116:C03015
Liang J-H, McWilliams JC, Sullivan PP, Baschek B (2012) Large eddy simulation of the bubbly ocean: New insights on subsurface bubble distribution and bubble-mediated gas transfer, J Geophys Res 117:C04002
Lien R-C, McPhaden MJ, Gregg MC (1996) High-frequency internal waves at 0°, 140°W and their possible relationship to deep-cycle turbulence. J Phys Oceanogr 26:581–600
Lin CC (1966) The theory of hydrodynamcis stability. Cambridge Univ. Press, p 155
Lin C-L (2000) Local pressure transport structure in a convective atmospheric boundary layer. Phys Fluids 12:1112–1128
Longuet-Higgins MS (1962) Resonant interaction between two trains of gravity waves. J Fluid Mech 12:321–332
Lukas R, Lindstrom E (1991) The mixed layer of the western equatorial Pacific Ocean. J Geophys Res C96(Supplement):3343–3358
Mack AP, Hebert D (1997) Internal gravity waves in the upper eastern equatorial Pacific: Observations and numerical solutions. J Geophys Res 102(9):21,081–21,100
Marmorino GO, Smith GB, Lindemann GJ (2005) Infrared imagery of large-aspect-ratio Langmuir circulation. Continental Shelf Res 25:1–6
Maslov VP (1980) Three algebras meeting nonsmooth solutions of systems of quasilinear hyperbolic equations. Uspekhi Mat Nauk 35(2):252–253 (in Russian)
Matsuura H (2002) Observed variations of the upper ocean zonal currents in the western equatorial Pacific and their relation to local wind. J Geophys Res 107:3210
Matt S, Fujimura A, Soloviev A, Rhee SH, Romeiser R (2012) Fine-scale features on the sea surface in SAR satellite imagery—Part 2: Numerical modeling. Ocean Sci Discuss 9:2915–2950
McCreary JP Jr, Kohler KE, Hood RR, Smith S, Kindle J, Fischer AS, Weller RA (2001) Influences of diurnal and intraseasonal forcing on mixed-layer and biological variability in the central arabian sea. J Geophys Res 106:7139–7155
McNaughton KG, Brunet Y (2002) Townsend's hypothesis, coherent structures and Monin-Obukhov similarity. Bound-Layer Meteor 102:161–175
McWilliams J (1984) The emergence of isolated coherent vortices in turbulent flow. J Fluid Mech 146:2–43
McWilliams JC. Sullivan P (2000) Vertical mixing by Langmuir circulations. Spill Sci Techn Bull 6(3/4):225–236
McWilliams JC, Sullivan PP, Moeng C-H (1997) Langmuir turbulence in the ocean. J Fluid Mech 334:1–30
Moffatt HK, Tsinober A (1992) Helicity in laminar and turbulent flow. Ann Rev Fluid Mech 24:281–312
Moncrieff MW, Krueger SK, Gregory D, Redelsperger J-L, Tao W-K (1997) GEWEX Cloud System Study (GCSS) Working Group 4: Precipitating convective cloud systems. Bull Am Meteorol Soc 78:831–845
Moore DW, Philander SGH (1977) Modeling the equatorial oceanic circulation. In: The Sea, Vol. VI, Wiley Interscience, New York, pp 319–361

Munk W, Armi L (2001) Spirals on the sea: A manifestation of upper-ocean stirring. In: From stirring to mixing in a stratified ocean, Proceedings 'Aha Huliko'a Hawaiian Winter Workshop. University of Hawaii at Manoa, January 16–19, 2001, SOEST Special Publication, p 81–86
Nicolas G, Prigogine I (1977) Self-organization in nonequilibrium systems: From dissipative structures to order through fluctuations. Wiley, New York, p 491
Offen GR, Kline SJ (1975): A proposed model of the bursting process in turbulent boundary layers', J Fluid Mech 70:209–228
Olbers DJ, Herterich K (1979) The spectral energy transfer from surface waves to internal waves. J Fluid Mech 92:349–380
Özgökmen TM, Piterbarg LI, Mariano AJ, Ryan EH (2001) Predictability of drifter trajectories in the tropical Pacific Ocean. J Phys Oceanogr 31(9):2691–2720
Pelinovsky DE, Shrira VI (1995) Collapse transformation for self-focusing solitary waves in boundary-layer type shear flows. Phys Lett A: Math Gen 206:195–202
Peltier LJ, Wyngaard JC, Khanna S, Brasseur J (1996) Spectra in the unstable surface layer. J Atmos Sci 53:49–61
Phillips OM (1977) The dynamics of the upper ocean. Cambridge University Press, p 366
Phong-Anant D, Antonia RA, Chamber AJ, Rajagopalan S (1980) Features of the organized motion in the atmospheric surface layer. J Geophys Res 424–432
Pinkel R (2000) Internal solitary waves in the warm pool of the western equatorial Pacific. J Phys Oceanogr 30:2906–2926
Pollard RT (1977) Observations and theories of Langmuir circulations and their role in near surface mixing. In: Angel M (ed) A voyage of discovery: George Deacon 70th anniversary volume, Pergamon Press, Oxford, p 696
Price JF, Sanford TB, Forristall GZ (1994) Forced stage response to a moving hurricane. J Phys Oceanogr 24:233–260
Rabinovich SG (1995) Measurement errors: theory and practice. American institute of physics, Woodbury, New York, p 279
Randall D, Khairoutdinov M, Arakawa A, Grabowski A (2003) Breaking the cloud parameterization deadlock, Bull Amer Meteor Soc 84(11):1547–1564
Redelsperger JL, Brown PRA, Guichard F, Hoff C, Kawasima M, Lang S, Montmerle Th, Nakamura K, Saito K, Seman C, Tao WK, Donner LJ (2000) A GCSS model intercomparison for a tropical squall line observed during TOGA-COARE. I: Cloud-resolving models. Q J Roy Meteor Soc 126:823–864
Rhines PB (1975) Waves and turbulence on a beta-plane. J Fluid Mech 69:417–443
Roemmich D, Morris M, Young WR, Donguy JR (1994) Fresh equatorial jets. J Phys Oceanogr 24:540–558
Romanova NN (1984) Long nonlinear waves on layers having large wind velocity gradients. Izvestiya, Akad Nauk SSR, Fizika Atmos I Okeana 20:469–475 (Translation: Izv Acad Sci USSR, Atmosph Ocean Phys 20:452–456)
Romeiser R (2008) M4S 3.2.0 User's manual. University of Hamburg, Hamburg
Ruddick BR, Turner JS (1979) The vertical length scale of double-diffusive intrusions. Deep sea research Part A. Oceanogr Res Papers 26(8):903–913
Rudnick DL, Luyten JR (1996) Intensive surveys of the Azores Front 1. Tracers and dynamics. J Geophys Res 101: 923–940
Sandstrom H, Oakey NS (1995) Dissipation in internal tides and solitary waves, J Phys Oceanogr 25:604–614
Shay TJ, Gregg MC (1986) Convectively driven turbulent mixing in the upper ocean, J Phys Oceanogr 16:1777–1798
Shinoda T, Lukas R (1995) Lagrangian mixed layer modeling of the western equatorial Pacific. J Geophys Res 100(C2):2523–2541
Shinoda T, Hendon HH, Glick JD (1998) Mixed layer modeling of intraseasonal sea surface temperature variability in the tropical western Pacific and Indian ocean. J Climate 11:2668–2685
Shrira VI (1989) On the 'sub-surface' waves of the mixed layer of the upper ocean. Dokl Akad Nauk SSSR 308:732–736 (Trans USSR Acad Sci, Earth Sci Section 308:276–279)

Short DA, Kucera PA, Ferrier BS, Gerlach JC, Rutledge SA, Thiele OW (1997) Shipborne radar rainfall patterns within the TOGA/COARE IFA. Bull Amer Meteor Soc 78(12):2817–2836
Simpson JE (1987) Gravity currents: In the environment and the laboratory. Ellis Horwood Limited, New York, p 244
Simpson JE, Linden PF (1989) Frontogenesis in a fluid with horizontal density gradients. J Fluid Mech 202:1–16
Skyllingstad ED, Denbo DW (1995) An ocean large-eddy simulation of Langmuir circulations and convection in the surface mixed layer. J Geophys Res 100:8501–8522
Smith CR, Walker JDA (1997) Sustaining mechanisms of turbulent boundary layers: the role of vortex development and interaction. In: Panton RL (ed) Self-sustaining mechanisms of wall turbulence, Advances in fluid mechanics 15, Computational Mechanics Publications, Southampton, pp 273–308
Soloviev AV (1990) Coherent structure at the ocean surface in the convectively unstable conditions. Nature 346:157–160
Soloviev AV, Bezverkhny VA (1990) Coherent structure in the near-surface turbulent boundary layer of the ocean. Doklady Akademii Nauk SSSR 312(1):218–222
Soloviev A, Klinger B (2001) Open ocean convection. In: Encyclopedia of ocean sciences, Academic Press, UK, pp 2015–2022
Soloviev A, Lukas R (1996) Observation of spatial variability of diurnal thermocline and rain-formed halocline in the western Pacific warm pool. J Phys Oceanogr 26(11):2529–2538
Soloviev A, Lukas R (1997) Sharp frontal interfaces in the near-surface layer of the ocean in the western equatorial Pacific warm pool. J Phys Oceanogr 27(6):999–1017
Soloviev AV, Zatsepin AG (1992) Response of density depression pool to wind forcing. Abstract, 24th International Liege colloquium on ocean hydrodynamics: "Sub-Mesoscale Air-Sea Interaction," Liege, Belgium, May 4–8, 1992. GHER/Model Environment, pp 99–100
Soloviev AV, Vershinsky NV, Bezverchnii VA (1988) Small-scale turbulence measurements in the thin surface layer of the ocean. Deep-Sea Res 35:1859–1874
Soloviev A, Lukas R, DeCarlo S, Snyder J, Arjannikov A, Turenko V, Baker M, Khlebnikov D (1998) A near-surface microstructure sensor system used during TOGA-COARE. Part I: Bow measurements. J Atmos Ocean Tech 15:563–578
Soloviev A, Lukas R, Hacker P, Baker M, Schoeberlein H, Arjannikov A (1999) A near-surface microstructure sensor system used during TOGA COARE. Part II: Turbulence measurements. J Atmos Oceanic Tech 16:1598–1618
Soloviev A, Lukas R, Hacker P (2001) An approach to parameterization of the oceanic turbulent boundary layer in the western pacific warm pool. J Geophys Res 106:4421–4435
Soloviev A, Lukas R, Matsuura H (2002) Sharp frontal interfaces in the near-surface layer of the tropical ocean. J Mar Syst–Spec Issue Ocean Front 37(1–3):47–68
Soloviev A, Fujimura A, Matt S (2012) Air-sea interface in hurricane conditions, J Geophys Res 117:C00J34
Spall M, Chapman D (1998) On the efficiency of baroclinic eddy heat transport across narrow fronts. J Phys Oceanogr 28(11):2275–2287
Spangenberg WG, Rowland WR (1961) Convective circulation in water induced by evaporative cooling. Phys Fluids 4:743–750
Stevenson RE (1985) Oceanography in orbit. In: 1985 Yearbook and the future. Encyc Brit Chicago IL, p 190–205
Stevenson RE (1998) Spiraleddies: The discovery that changed the face of the oceans. 21st Century Sci Tech 11:58–71
Stevenson RE (1999) A view from space: The discovery of nonlinear waves in the ocean's near surface layer. 21st Century Sci Tech 18:36–47
Stommel H (1993) A conjectural regulating mechanism for determining the thermohaline structure of the oceanic mixed layer. J Phys Oceanogr 23(1):142–148
Stuart JT, (1967) On finite amplitude oscillations in laminar mixing layers. J Fluid Mech 29:417–440
Tandon A, Garrett C (1995) Geostrophic adjustment and restratification of a mixed layer with horizontal gradients above a stratified layer. J Phys Oceanogr 25:2229–2241

Taylor GI (1931) Effect of variation in density on the stability of superposed streams of fluid. P Roy Soc Lon A 132:499–523
Theodorsen T (1952) Mechanism of turbulence. In: Proceedings of the second midwestern conference on fluid mechanics, Columbus, Ohio, Ohio State University, pp 1–18
Thorpe SA (1968) On the shape of progressive internal waves. Phil Trans Roy Soc Lon Ser A 263:563–614
Thorpe SA (1971) Asymmetry of the internal seiche in Loch Ness. Nature 231(5301):306–308
Thorpe SA (1985) Small-scale processes in the upper ocean boundary layer. Nature 318:519–522
Thorpe SA (1988) The dynamics of the boundary layers of the deep ocean. Sci Prog Oxf 72:189–206
Thorpe SA (1992) The break-up of Langmuir circulation and the instability of an array of vortices. J Phys Oceanogr 22:350–360
Thorpe SA, Hall AJ (1987) Bubble clouds and temperature anomalies in the upper ocean. Nature 328:48–51
Thorpe SA, Jackson JFE, Hall AJ, Lueck RG (2003) Measurements of turbulence in the upper ocean mixing layer using Autosub. J Phys Oceanogr 33:122–145
Tomczak M (1995) Salinity variability in the surface layer of the tropical western Pacific ocean. J Geophys Res 100(C10):20,499–20,515
Townsend A (1961) Equilibrium layers and wall turbulence. J Fluid Mech 11:97–120
Tsai W (2001) On the formation of streaks on wind-driven water surfaces. Geophys Res Lett 28(20):3959–3962. doi:10.1029/2001GL013190.
Tsai W-T, Hung L-P (2007) Three-dimensional modeling of smallscale processes in the upper boundary layer bounded by a dynamic ocean surface, J Geophys Res 112:C02019, doi:10.1029/2006JC003686
Turner JS (1973) Buoyancy effects in fluids. Cambridge Univ. Press, New York
Van Heijst GJF (1993) Self-organization of two-dimensional flows. Nederlands Tijdschrift voor Natuurkunde 59:321–325
Van Heijst GJF, Flór JB (1989) Dipole formation and collision in a stratified fluid. Nature 340(6230):212–215
Van Heijst GJF, Kloosterziel RC (1989) Tripolar vortices in a rotating fluid. Nature 338(6216):569–570
Vialard J, Delecluse P (1998) An OGCM study for the TOGA decade. Part II: Barrier layer formation and variability. J Phys Oceanogr 28(C6):1089–1106
Voronovich VV, Pelenovsky DE, Shrira VA (1998a) On internal wave-shear flow resonance in shallow water. J Fluid Mech 354:209–237
Voronovich VV, Shrira VI, Stepanyants YuA (1998b) Two-dimensional models for nonlinear vorticity waves in shear flows. Stud Appl Math 100:1–32
Voropayev SI, Afanasyev Ya D, Filippov IA (1991) Horizontal jets andvortex dipoles in a s Voronovich, V.V., D.E. Pelenovsky, and V.A. Shrira, 1998a: On internal wave-shear flow resonance in shallow water. J Fluid Mech 354:209–237
Voropaev SI, Gavrilin BL, Zatsepin AG (1981) On the structure of the surface layer of the ocean. Izvestiya: Akad Nauk SSSR. Atmos Ocean Phys 17:378–382
Walsh EJ, Pinkel R, Hagan DE, Weller RA, Fairall CW, Rogers DP, Burns SP, Baumgartner M (1998) Coupling of internal waves on the main thermocline to the diurnal surface layer and sea surface temperature during the tropical ocean global atmosphere coupled ocean-atmosphere response experiment. J Geophys Res 103:12,613–12,628
Watson KM (1990) The coupling of surface and internal gravity waves: revisited. J Phys Oceanogr 20:1233–1248
Watson KM, West BJ, Cohen BI (1976) Coupling of surface and internal gravity waves: A mode coupling model. J Fluid Mech 77:185–208
Weller RA, Price JF (1988) Langmuir circulation within the oceanic mixed layer. Deep-Sea Res 35:711–747
Wijesekera HW, Dillon TM (1991). Internal waves and mixing in the upper equatorial pacific ocean. J Geophys Res 96:7115–7125

Wijesekera HW, Paulson CA, Huyer A (1999a) The effect of rainfall on the surface layer during a westerly burst in the western equatorial Pacific. J Phys Oceanogr 29(4):612–632
Wijesekera HW, Paulson CA, Huyer A (1999) Spectra and skewness of near-surface turbulent temperature fluctuations forced by surface cooling and wind stress, Proceeding COARE98, Boulder, Colorado, USA, 7-14 July 1998, World Climate Research Programme, pp.287-288.
Wijesekera HW, Paulson CA, Huyer A (2001) Horizontal wave number spectra of temperature in the unstably stratified oceanic surface layer. J Geophys Res 106:16,929–16,946
Whitham GB (1974) Linear and nonlinear waves. Wiley, New York
Woods JD (1980) The generation of thermohaline fine structure of fronts in the ocean. Ocean Model 32:1–4
Woods JD, Barkmann W (1986) The response of the upper ocean to solar heating. I: The mixed layer. Q J Roy Meteor Soc 112:1–42
You Y (1995) Salinity variability and its role in the barrier-layer formation during TOGA COARE. J Phys Oceanogr 25:2778–2807
Yoder JA, Ackleson SG, Barber RT, Flament P, Balch WM (1994) A line in the sea. Nature 371:689–692
Young WR (1994) The subinertial mixed layer approximation. J Phys Oceanogr 24:1812–1826
Zenk W, Katz EJ (1975) On the stationarity of temperature spectra at high horizontal wave numbers. J Geophys Res 80(27):3885–3891
Zhang Y, Baggeroer AB, Bellingham JG (2001) Spectral-feature classification of oceanographic processes using an autonomous underwater vehicle. IEEE J Ocean Eng 26:726–741
Zilitinkevich SS, Calanca P (2000) An extended similarity-theory for the stably stratified atmospheric surface layer. Q J Roy Meteorol Soc 126:1913–1923
Zilitinkevich SS, Esau IN (2005) Resistance and heat/mass transfer laws for neutral and stable planetary boundary layers: old theory advanced and re-evaluated. Quart J Roy Met Soc 131:1863–1892

Chapter 6
High Wind Speed Regime

Abstract Under high wind speed conditions breaking waves disrupt the air-sea interface producing a two-phase zone—air bubbles in water and sea spray in air. This mixed-phase environment changes the regime of air-sea interaction. In this chapter, after reviewing dynamics of air-bubbles and sea spray droplets in detail, the reader is exposed to the idea that under strong winds Kelvin-Helmholtz instability is the likely mechanism for the intense production of spume and formation of a two-phase transition layer. The resulting two-phase environment eliminates short wind-waves, including some responsible for a substantial part of the surface wind stress. Amazingly, this concept provides an explanation for the rapid intensification of some storms to major tropical cyclones and observed bi-modal distribution of tropical cyclone maximum intensity. A long overdue implementation of sea surface micro-physics into operational models is expected to improve predictions of tropical cyclone intensity and the associated wave field.

Keywords Whitecaps • Sea spray • Spume • Air bubbles • Marine aerosol • Drag coefficient • Kelvin-Helmholtz instability • Tollmien-Schlichting instability • Two-phase environment • Transition layer

6.1 Introduction

With increasing wind speed, the sharp interface between the air and water disappears for longer intervals and over larger area (Fig. 6.1). Under high winds, the concept of the air-sea interface becomes problematic. A two-phase environment with transition from bubble-filled water to spray-filled air is formed. In very high winds, a distinct layer of foam is observed.

The effects of bubbles and sea spray appear to be of crucial importance for air–sea exchanges in tropical cyclones. In particular, modification of short surface waves by two-phase environment may have appreciable consequences for the air–sea drag coefficient. These effects can also be important for extratropical winter storms.

In Sect. 6.1 of this chapter, we consider air bubbles in the near-surface layer of the ocean. Effects of the bubbles produced by breaking surface waves include the modification of upper ocean turbulence by rising bubbles, their contribution to

A. Soloviev, R. Lukas, *The Near-Surface Layer of the Ocean,* Atmospheric and Oceanographic Sciences Library 48, DOI 10.1007/978-94-007-7621-0_6,

air–sea gas exchange, and to the acoustic and optical environments. Sea spray and marine aerosol generation is the subject of Sect. 6.2. Section 6.3 discusses the issues of modeling air–sea exchanges in high wind conditions and intends to explain the recently discovered phenomenon of the limiting state of the aerodynamic roughness under hurricane conditions. Section 6 concludes this chapter.

6.2 Air Bubbles in the Near-Surface Turbulent Boundary Layer

6.2.1 Active and Passive Phases in Bubble Life

The high wind speed regime is associated with energetic wave-breaking events. The fraction of the ocean surface covered with wave breakers rapidly increases with wind speed though, according to recent data, does not seem to exceed 10 % even under very strong winds (Holthuijsen et al. 2012).

Breaking waves entrain air and create bubble plumes, which are highly transient and localized phenomena. Based on laboratory experiments of Leifer and de Leeuw (2001), the lifetime of wave-generated bubbles can be divided into four phases (1) formation, (2) injection, (3) rise, and (4) senescence. The first phase is observed to occur during the first 0.1 s or less. During the second phase, the plume rapidly descends, initially at roughly a 30° angle, then tilting toward the vertical. The second (injection) phase ends at the maximum penetration depth; it is followed by the third phase, when the mass of bubbles rises toward the surface. The injection and rise phases last roughly the same time. Once the bubble creation process ceases, a newly formed bubble plume becomes acoustically quiescent and evolves under the influence of turbulent diffusion, advection, buoyant degassing, and dissolution. This is the fourth, senescence, phase, which corresponds to typical bubble observations (that is the background distribution). During the senescence phase the plume consists of the smaller, mostly $r < 0.2$ mm bubbles.

Size-dependent bubble rise velocity mainly determines the residence time of larger bubbles, but the residence time of smaller bubbles may also be affected by the turbulent flow in the near-surface layer. Bubble plumes consisting of small bubbles can extend well into the mixed layer. As a result, the smaller bubbles act as tracers and map out the surface signatures of Langmuir cells (Farmer and Li 1995), or the edges of current fronts and rips (Marmorino and Trump 1996).

6.2.2 Bubble Rise Velocity

Bubble hydrodynamics depend on bubble size, temperature, and the presence of surfactants (Leifer et al. 2000). Depending on size, the bubble form varies from

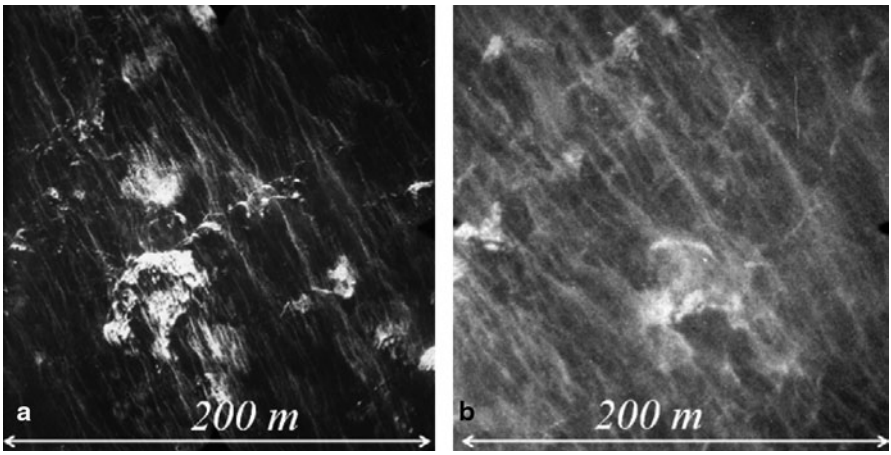

Fig. 6.1 Ocean surface foam streaks observed on photographic images of the sea surface in a hurricane: **a** Wind speed 28 m s^{-1} and **b** wind speed 46 m s^{-1}. After Black et al. (2006)

spherical to spheroid for small bubbles ($r<0.5$ mm) to ellipsoid for larger bubbles ($r>0.5$ mm). The radius of transition between the spheroidal and ellipsoidal form depends on the temperature and on the presence of surfactants. Small bubbles are nearly perfect spheres because surface tension dominates over the drag stress that acts upon the rising bubble. The surface tension force, however, decreases inversely proportional to the bubble radius. At the same time, the drag force increases since larger bubbles rise faster and have larger effective cross-sectional area. Bubbles with radius larger than approximately 0.7 mm (at $T=20°C$) can oscillate, in both path and shape, affecting the rise velocity. The trajectory oscillations (zigzag or helical) are important for bubbles that just start oscillating and reduce their speed. For large bubbles ($r>3.5$ mm), the shape or deformation oscillations are more important. The latter results in the reduction of the drag coefficient and thus an increase of rise speed.

The important factor in bubble hydrodynamics is the presence of surfactants, which can partially immobilize the surface, increasing drag and decreasing rise velocity. In the bubble radii range from approximately 0.25 mm to 10 mm, clean bubbles have different hydrodynamics from *dirty* (i.e., surfactant covered) bubbles.

Thorpe (1982) proposed a formula for the buoyant rise speed of bubbles:

$$w_b(r)=\left(\frac{2r^2g}{9\nu}\right)\left[\left(y^2+2y\right)^{1/2}-y\right] \tag{6.1}$$

where $y=10.82\nu^2/\left(gr^3\right)$. This equation is derived for dirty bubbles (small bubbles become covered with surfactants within a short time period).

Patro et al. (2001) proposed an analytical parameterization formula for clean non-oscillating bubbles:

Table 6.1 Coefficients for Eq. (6.2) parameterizing the rise velocity for clean non-oscillating bubbles. (After Patro et al. 2001)

Re	r (μm)	c	d	n
<1	<60	0.666	2.0	−1.00
1–150	60–500	0.139	1.372	−0.64
150–420	550–660	11.713	2.851	−0.64
420–470	660–700	0.156	1.263	−0.64
470–540	700–850	0.021	0.511	−0.64

Table 6.2 Coefficients for Eq. (6.3) parameterizing clean oscillating bubbles. (After Patro et al. 2001)

H_1	K_1	r_C	w_{bm}	m_1	m_2
-4.792×10^{-4}	0.733	0.0584	22.16	−0.849	−0.815

$$w_b = \frac{c}{3} g r^d v^n \tag{6.2}$$

where the coefficients c, d, and n for this equation are given in Table 6.1.

For clean oscillating bubbles, Patro et al. (2001) developed the following analytic parameterization:

$$w_b = \left[w_{bm} + H_1 \left(r - r_c \right)^{m_1} \right] \exp\left[K_1 \left(r - r_c \right)^{m_2 T} \right] \tag{6.3}$$

where the coefficients H, K, m_1, and m_2 and the critical radius r_C (below which the parameterization suggests that bubbles do not oscillate for any temperature T), and the minimum velocity w_{bm} for oscillating bubbles are given in Table 6.2. Parameterization (6.3) is applicable for oscillating bubbles for $0\,^0\mathrm{C} < T < 30\,^0\mathrm{C}$ and $r_p < r < 4$ mm. The radius r for the onset of oscillation varies with temperature T according to the parameterization relationship,

$$r_p = 1086 - 16.05\, T_p \tag{6.4}$$

where r_p and T_p are the peak radius and temperature, respectively.

A comparison of observed bubble rise velocities in clean and natural waters is shown in Fig. 6.2, together with the parameterizations for clean and dirty bubbles (Clift et al. 1978). The parameterization for clean bubbles demonstrates a monotonic increase of w_b with radius r until the onset of oscillation, after which w_b decreases to some level and then starts increasing again. In contrast, the parameterization for dirty bubbles shows a monotonic increase with r.

The observational data given by Clift et al. (1978) suggest that the rise velocity for seawater bubbles with radii larger than approximately 0.6 mm is close to that of hydrodynamically clean bubbles. An explanation is that larger bubbles rise quickly to the surface and thus do not have sufficient time to collect surfactants (Keeling

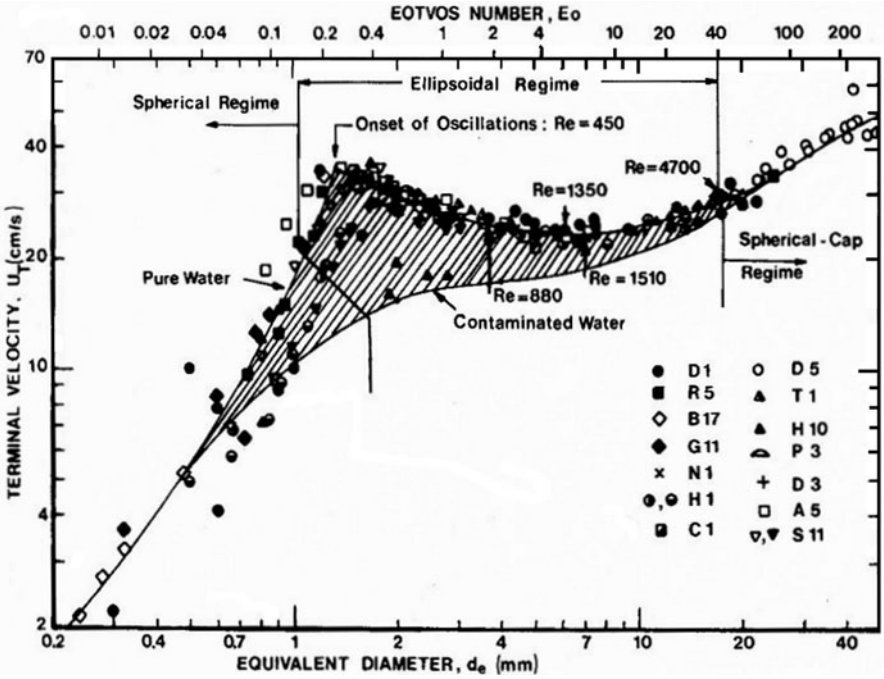

Fig. 6.2 The bubble rise velocity for hydrodynamically clean and dirty bubbles as a function of the bubble size. After Clift et al. (1978)

1993; Woolf 1993). Small bubbles (less than approximately 0.3 mm radius) are assumed to perform hydrodynamically as dirty bubbles (Woolf and Thorpe 1991). Their surface becomes covered with surfactants almost instantaneously.

Patro et al. (2001) proposed to treat small bubbles in seawater as dirty and large bubbles as clean with a transition at circa 0.6 mm. The transition radius somewhat increases with the increase of the bubble residence time in the water column. The assumption about clean and dirty bubbles is, however, somewhat uncertain. Adding to the uncertainty is the interaction among bubbles and their collective behavior in bubble clouds.

The presence of a persistent air bubble layer near the surface depends on the terminal velocity of bubbles, w_b, and the root mean square (RMS) vertical turbulence velocity, w_{RMS}. When $w_b < w_{RMS}$. The bubbles may remain in suspension for a timescale comparable to the average time interval between wave-breaking events at that location, thus forming a persistent background air bubble layer (Deane 2012). According to Deane's estimate, for winds above 13 m s^{-1}, the flat bubble terminal velocity dependence results in a rapid increase in the size of bubbles in the near-surface layer, leading to acoustic screening of the ocean surface from below by bubbles.

6.2.3 Bubble Size Distribution Function

The bubble-mediated component of air–sea gas exchanges, production of spray droplets and aerosols, optical properties of the sea surface, generation of ambient noise and sound transmission within the oceans, and scavenging of biological surfactants essentially depend on the size distribution of bubbles. The size distribution of entrained bubbles is also an important factor in controlling turbulence and dynamics in wave breakers. In addition, bubbles of different sizes behave differently in the turbulent surface layer. Bubble size distribution data potentially lead to a dynamical description of air–sea interaction based on near-surface turbulence, advection, and other properties.

Different approaches for measuring bubble size spectra, from acoustical to optical, have been developed. Each technique has advantages and disadvantages and is effective over different size ranges and bubble density regimes (Leifer et al. 2003). Acoustic methods have played a definite role in observing bubble size distributions because bubbles have a high resonance quality factor leading to an acoustical cross section some three orders of magnitude greater than their geometrical cross section (Farmer et al 1998). This effect reaches a maximum typically around a frequency of 30 kHz, which corresponds to a bubble radius of 100 μm. Different sound frequencies excite bubbles of different radii, which allow an estimate of the bubble size distribution from acoustic measurements. However, acoustic methods have difficulties with large bubbles ($r > 0.5$–0.7 mm), which are nonspherical in turbulent flow, and for high bubble concentrations. Laser techniques are noninvasive but, in common with acoustic methods, have problems when multiple bubbles enter the beam (high bubble density) and with large bubbles ($r > 1$ mm), whose mean shape is elliptical and is subject to oscillations. The optical methods based on the analysis of video or photo images are able to measure at high bubble concentrations and over a wide range of bubble sizes. The optical methods are, however, invasive in general and may disturb the measurement area.

The initial bubble formation, breakup, coalescence, dissolution, vertical motion caused by buoyancy forces, and turbulent mixing are the processes that determine the bubble size distribution in the ocean. Air is initially entrained into relatively large bubbles as a wave breaks. These bubbles rapidly break into smaller bubbles. During this active phase the bubble fragmentation process determines the bubble size distribution. Breaking waves directly inject air into the wave-stirred layer (see Fig. 3.1). As soon as the wave breaker expends its energy, the air entrainment ceases and the bubble creation process stops. The bubble size distribution then evolves rapidly because larger bubbles leave the area and surface more quickly than smaller ones.

The bubbles with radius $r > 0.7$ mm have rising velocities of the order of 0.2 m s^{-1}–0.4 m s^{-1} (Fig. 6.2); after the end of the wave-breaking process the remaining turbulence has little effect on their dynamics. The large bubbles immediately return to the surface, rarely penetrating below the wave-stirred layer. Note that the wave-stirred layer depth is typically less than one significant wave height (see

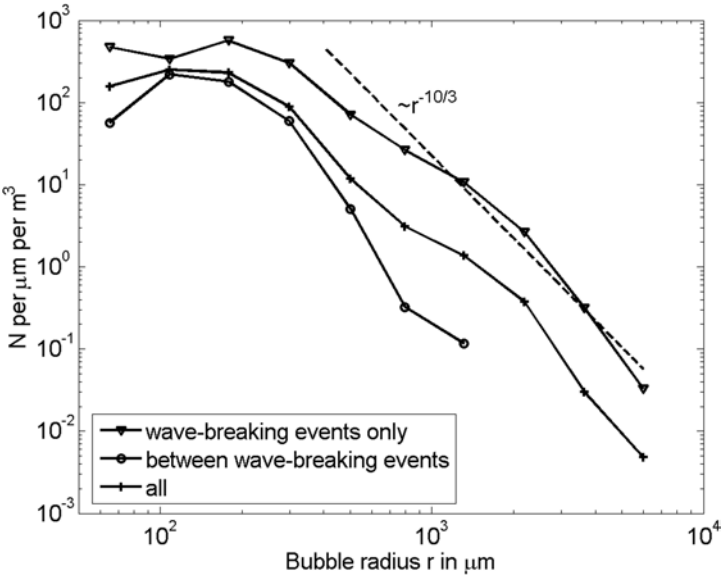

Fig. 6.3 Bubble size distributions at 0.6 m depth including and excluding wave-breaking events (Bowyer 2001). These measurements are taken at 11–13 m s^{-1} wind speed, 2.5 m wave height, and 15–120 km fetch. Reproduced by permission of American Geophysical Union

Chap. 3, Fig. 3.19). Smaller bubbles ($r \sim 0.1$ mm) have terminal velocities of the order of 0.01 m s^{-1}. The background turbulence as well as organized structures (see Chap. 5) can transport these small bubbles to greater depths.

The bubble size spectra can be separated into the regions within the wave-stirred layer and below the wave-stirred layer. The spectra within the wave-stirred layer can additionally be separated into those taken during wave-breaking events and those in between wave-breaking events.

Figure 6.3 shows averaged bubble spectra measured at 0.6 m depth including and excluding wave-breaking events. These observations are presumably in the wave-stirred layer. The density of bubbles, especially of large bubbles, is significantly higher during wave-breaking events. In this example, the slope of the spectrum for large bubbles changes in logarithmic coordinates from approximately −2.9 during wave-breaking events to approximately −4.3 between the wave-breaking events.

Two mechanisms for large bubble fragmentation are possible in the wave breaker: (1) turbulent fragmentation represented by the turbulent kinetic energy dissipation rate ε and (2) rising-bubble fragmentation, characterized by the rising velocity w_b and the collective behavior of rising bubbles.

From dimensional considerations, Garrett et al. (2000) derived a bubble size spectrum for the turbulent fragmentation mechanism

$$N(r) \propto Q\varepsilon^{-1/3} r^{-10/3} \tag{6.5}$$

where $N(r)$ is the number of bubbles per m^3 per mm radius increment (bubble density), Q is the volume of air entrained per volume of water per second (with dimension s^{-1}), and r is the bubble radius. The turbulent fragmentation mechanism is important during wave-breaking events. A theoretical spectrum (6.5) is compared in Fig. 6.3 with the field data of Bowyer (2001). For bubbles larger than approximately 1 mm, the slope of the theoretical spectrum is, in fact, consistent with the experimental spectrum averaged over wave-breaking events.

Spectrum (6.5) is based on the concept of turbulent fragmentation formulated by Kolmogorov (1949) and Hinze (1955). They pointed out that at high Reynolds number, a droplet of any different fluid or a gas bubble is likely to break up under the influence of differential pressure forces on its surface if these forces exceed the restoring forces of surface tension. Turbulent fragmentation thus depends on the ratio of these forces, which is characterized by the Weber number,

$$We = \left(\rho/\sigma_s\right)u^2 d \tag{6.6}$$

where ρ is the water density, σ_σ is the surface tension, u is the turbulent velocity fluctuation on the length scale of the bubble, and d is the bubble diameter. Within the Kolmogorov inertial sub-range, the fluctuation velocity relates to the dissipation rate of the turbulent kinetic energy as,

$$u \sim (\varepsilon d)^{2/3} \tag{6.7}$$

Turbulent bubble fragmentation is expected when the Weber number exceeds its critical value, We_{cr}. This condition corresponds to inequality $d > a_H$, where

$$a_H = We_{cr}^{3/5}\left(\sigma_s/\rho\right)^{3/5}\varepsilon^{-3/5} \tag{6.8}$$

is the *Hinze scale*, which is typically of the order of 1 mm. Hinze (1955) estimated the critical value of the Weber number as 0.2. More recent experiments by Lewis and Davidson (1982), Martinez-Bazan et al. (1999), and Deane and Stokes (2002) suggest that We_{cr} lies in the range from 3 to 4.7. Bubbles smaller than the Hinze scale are stabilized by surface tension, and the process of turbulent fragmentation is believed to be less important for these small bubbles.

Garrett et al. (2000) pointed out a major caveat for the turbulent fragmentation theory. Though the considerations leading to Eq. (6.5) are similar to those leading to Kolmogorov's inertial sub-range in the energy spectrum of isotropic turbulence, there is one significant difference. In the Kolmogorov cascade the energy ultimately cascades into eddies at the Kolmogorov scale $\eta_T = \left(\nu^3/\varepsilon\right)^{1/4}$ or less, and then dissipates into heat due to viscosity. In the case of bubbles, the input air fragments into smaller and smaller bubbles until surface tension halts the cascade at the Hinze scale. Air would thus tend to accumulate in a large spectral peak at the Hinze scale that would only slowly disappear since bubble dissolution is a relatively slow process. At the time of the Garrett (2000) publication, such a peak was not observed in either field or laboratory experiments.

Spectrum (6.5) is based on the assumption that the total air fraction is not large enough to have a feedback effect on the fragmentation process. At first glance, this assumption seems to be supported by the Deane and Stokes (2002) laboratory observation that "…the measured [bubble] separation velocity was always a factor of 5 or greater than the expected rise velocity of the bubble products, and the buoyancy effects were therefore assumed to be an unimportant source of bias." However, the Dean and Stokes experiment studied plunging breakers, which are not typical for open ocean conditions. In addition, the collective behavior of bubbles can result in significant fluctuations of the rising velocity of individual bubbles (Göz et al. 2001); the velocity fluctuations are mainly responsible for bubble fragmentation. The second mechanism, the rising-bubble fragmentation due to buoyancy forces, therefore cannot be completely discounted on the basis of the Deane and Stokes (2002) observation.

The spilling wave breaker resembles a turbulent bore (Sect. 1.6.4), which is an organized structure characterized by the regime of marginal stability in which the buoyancy and inertial forces are balanced in such a way that the Richardson number is close to its critical value (Turner 1973). The Kolmogorov cascade has to be replaced here with the concept of marginal stability in the bore-like wave breaker.

If we assume that the mechanism of bubble fragmentation due to buoyancy forces does dominate in spilling breakers and identify w_b as the determining parameter (replacing dissipation rate ε), then standard dimensional analysis leads to the following size spectrum:

$$N(r) \propto Q w_b^{-1} r^{-3} \tag{6.9}$$

An assumption that for large bubbles the rise velocity is approximately constant results in the -3 power law, which is close to the $-10/3$ power law in Eq. (6.5). Since bubble rise velocity w_b depends on the bubble radius r (Fig. 6.2), the power-law scaling in Eq. (6.9) can be different for different parts of the spectrum. Spectrum (6.9) should therefore be used with parameterization formulas (6.2) and (6.3).

Remarkably, Eq. (6.9) does not contain ε as a determining parameter. (From Chap. 3, the reader knows how difficult is to measure the dissipation rate in a breaking wave.)

Previously published distributions (Farmer et al. 1998; Bowyer 2001 and others) were unimodal. These averaged together many plumes of diverse types along with the background, thereby eliminating the multiple peaks. Leifer et al. (2003) and Leifer and de Leeuw (2006) developed a plume-type classification scheme. When analyzed separately, populations of different plume types (measured in a wind–wave tank) appeared to be multimodal. The wind–wave tank experiments, however, appear to produce the bubble size distributions that are quite different from those observed in the open ocean (Norris et al. 2013).

Figure 6.4 shows a comparison of bubble size spectra collected in the open ocean, surf zone, and laboratory tank. The laboratory data are neither representative of the surf zone nor of the open ocean. The bimodal distribution of spectra obtained from the laboratory experiment is not observed in any of the surf zone or open ocean

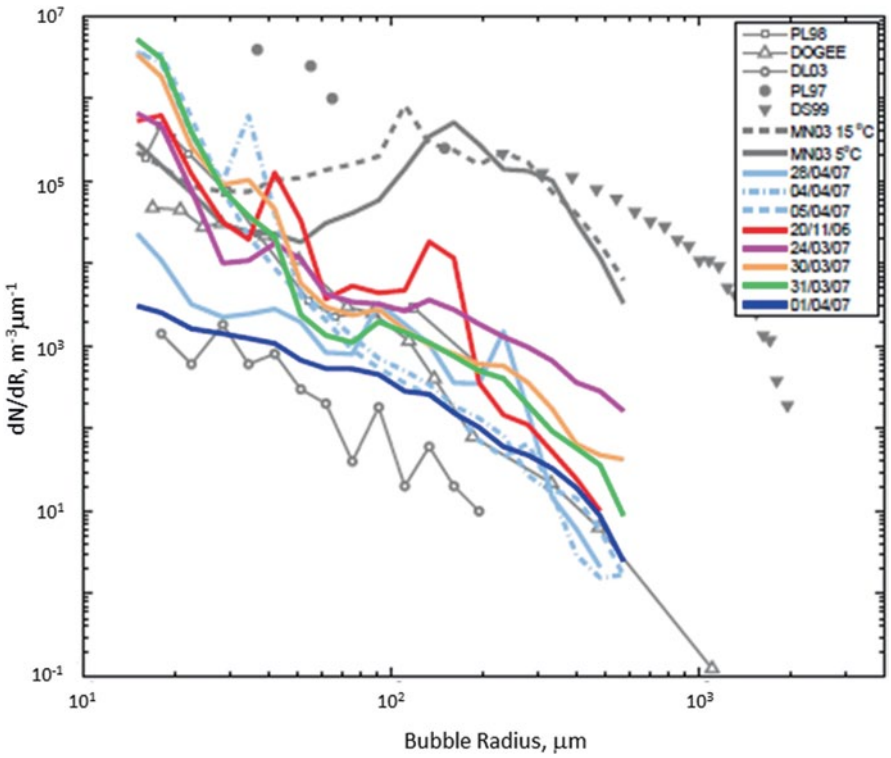

Fig. 6.4 Averaged bubble population distributions from the open ocean buoy deployments by Norris et al. (2013) (colored lines) in comparison with surf zone and laboratory measurements. The open ocean bubble size spectra of de Leeuw et al. (2003) (DL03, $U = 5.8$ m s^{-1}), Phelps and Leighton (1998) (PL98, depth 0.5 m, U, 12–14 m s^{-1}), Brooks et al. (2009), and Pascale et al. (2011) (DOGEE, averaged over a depth of 0–3 m, $U = 13$ m s^{-1}) and the surf zone spectra (filled symbols) of Phelps et al. (1997) and Deane and Stokes (1999) (DS99) along with the laboratory results of Mårtensson et al. (2003) at 5°C (solid gray line) and 15°C (dashed gray line) are also shown. Note that the Deane and Stokes (1999) data relate only to actively breaking surf regions. After Norris et al. (2013)

bubble spectra. The surf zone bubble size spectra appear to be two or three orders higher than the open ocean spectra.

The Norris et al. (2013) open ocean data were taken only 8 m from the ship hull, which might have distorted the wind–wave field with unknown consequences for the bubble spectrum. Their data, nevertheless, are close to the measurements of bubble spectra with a free drifting buoy by Pascal et al. (2011).

6.2.4 Bubble Dispersion and Diffusion

A bubble plume injected in the near-surface layer of the ocean during a wave-breaking event is subject to dispersion and turbulent diffusion. Larger bubbles rise to the

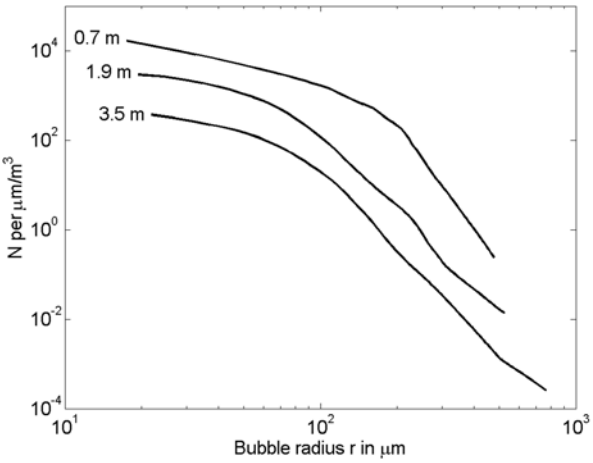

Fig. 6.5 The averaged bubble size spectrum at three depths below the surface, obtained at a wind speed of 11.9 m s^{-9}. After Garrett et al. (2000). Copyright © 2000 American Meteorological Society. Used with permission

surface within a few seconds, forming the whitecaps. Wave breaking also leaves numerous smaller bubbles that can persist for minutes.

Figure 6.5 shows averaged bubble size distributions acquired in the Gulf of Mexico by Farmer et al. (1998) and analyzed by Garrett et al. (2000) at depths 0.7 m, 1.9 m, and 3.5 m. The bubble density decreases with depth. The most significant drop for large bubbles ($r>200$ μm) is observed between 0.7 m and 1.9 m depths. A plausible explanation is that the 0.7 m depth is within the wave-stirred layer, while the observations at 1.9 m depth are outside this layer.

The spectra shown in Fig. 6.5 are averages over a sufficiently large time period (30 min). Since this time period included different types of wave-breaking events, possible bimodal spectral structures (like those shown in Fig. 6.4) could not be revealed.

Garrettson (1973) derived an equation governing the size distribution N of a cloud of bubbles at depth z. Thorpe (1982) simplified this equation by considering the cloud composed of small bubbles of a single gas (for instance, nitrogen) and of almost equal size. Ignoring acceleration and volume source terms (but retaining the dissolution term), and assuming horizontal isotropy transport Eq. (1.12) in application to bubbles takes the following form:

$$\frac{\partial C}{\partial t} = \frac{d}{dz}\left(K_B \frac{dC}{dz}\right) - w_b \frac{dC}{dz} - \sigma_* C \tag{6.10}$$

where C is the volume concentration of bubbles, w_b is the bubble rise speed, σ_* is the bubble dissolution rate, and K_B is the turbulent diffusion coefficient for bubbles.

The terms on the right side of Eq. (6.10) represent the downward turbulent diffusion of bubbles from the surface wave-breaking zone, the vertical rise of bubbles

toward the surface, and the dissolution and decay of bubbles, respectively. In the Thorpe (1982) model, an additional assumption is that the total number of bubbles decreases at the same rate as the radius decreases.

With a simplified parameterization for the turbulent mixing coefficient

$$K_B = \kappa u_* |z| \tag{6.11}$$

and the bubble decay rate

$$\sigma_* = \alpha z / (1 + |z| / H_0) \tag{6.12}$$

(here $H_0 = p_0 / g\rho \approx 10$ m, where p_0 is the atmospheric pressure), Thorpe (1982) obtained the following solution of (6.10):

$$N / N_0 = (\mu |z|)^{-\lambda/2} H_{\lambda/2}(\mu |z|^{1/2}) \tag{6.13}$$

where $H_{\lambda/2}$ is the modified Bessel function chosen so that $N \to 0$ as $z \to -\infty$, $\lambda = w_b / (\kappa u_*)$, $\mu = (\alpha / (\kappa u_*))^{1/2}$, and N_0 is a constant.

Since wave-breaking turbulence is not included in the mixing parameterization, there is a singularity of the air bubble flux at $z = 0$. In order to preserve the flux of bubbles, the value $\partial N / \partial z \to \infty$ was avoided by selecting the initial depth $z_0 = 0.5$ m and the maximum depth $z_{max} = 10$ m. This selection of initial depth away from the ocean surface also avoids discussion of the near-surface breaking wave zone where the assumed form of K_B is not valid. The solutions for bubbles with radius $a_0 = 50$ μm, $w_b = 0.54 \times 10^{-2}$ m s^{-1}, and $\alpha \approx 4 \times 10^{-3}$ s^{-1} m^{-1} were qualitatively consistent with the observations of Johnson and Cooke (1979). The assumptions about the mixing coefficient and choice of other parameter values were, however, tenuous and suspension of bubbles by the turbulent flow could not be included in the Thorpe (1982) pioneering work.

Recent developments in computational fluid dynamics methods have opened new opportunities for modeling of air bubble dynamics in the near-surface layer of the ocean. Liang et al. (2011) have developed a bubble concentration model and a dissolved gas concentration model for the oceanic boundary layer. The Liang et al. (2012) bubble model solves the extended version of Eq. (6.10) including a set of concentration equations for multiple gases in bubbles of different sizes; in addition, a dissolved gas concentration model simulates the evolution of dissolved gases and dissolved inorganic carbon. This sophisticated model based on the direct numerical simulation (DNS) method accounts for advection, diffusion, bubble buoyant rising, bubble size changes, gas exchange between bubbles and ambient water, and chemical reactions associated with the dissolution of CO_2. However, verification of numerical models with observational data is still a challenge.

In addition to dispersion and turbulent diffusion, small bubbles are drawn into the convergence zones produced by spatially coherent organized motions in the near-surface layer of the ocean (Chap. 5).

6.2.5 *Buoyancy Effects in Bubble Plumes*

The process of surface wave breaking and air entrainment have considerable dynamical coupling. A substantial part of the fluctuation energy during wave breaking may work against buoyancy forces (Woolf 1997).

Buoyancy effects in a two-phase environment can be understood from the classic budget equation for turbulence kinetic energy (TKE), similar to that in the theory for the flow with suspended particles developed by Barenblatt and Golitsyn (1974) for modeling dust storms. This theory predicts reduction of the turbulent drag coefficient in the suspension flow. Application of the Barenblatt and Golitsyn theory to the air bubble plumes produced by breaking waves, however, is not straightforward. In particular, the Kolmogorov number criteria (which is the analog of the Richardson number introduced for suspension flows) cannot be applied directly to the bubble-saturated upper ocean because the near-surface turbulence is produced by breaking waves rather than by mean horizontal shear (as in dust storms). The discussion in this section is therefore mainly qualitative rather than quantitative. Another aspect of this theory is that it does not explicitly include bubble size distribution. However, only relatively small bubbles can be entrained by the upper ocean turbulence and provide buoyant (negative) feedback on turbulence levels. Larger bubbles by themselves can induce turbulence in the near-surface layer of the ocean. Bubbles with radius exceeding approximately 1 mm shed unsteady vortices; the bubble trajectory also becomes unstable, changing from rectilinear to zigzag trajectories (Lima-Ochoterena and Zenit 2003). Generally, the bubble-induced water turbulence and the rise velocity of bubble swarms are different from those of single bubbles, due to bubble interactions (Göz et al. 2001).

The average void fraction of air due to bubbles from field measurements is given in Table 6.3 as a function of depth. In its contribution to the buoyancy, the maximum air fraction of 0.016% observed at 0.1 m depth is equivalent approximately to a 0.5°C change in water temperature. The average air fraction rapidly drops with depth (Table 6.3).

During an active phase, the bubble plume may contain a volume fraction of air that is much greater than the average over many wave periods. For comparison, the observations of Bowyer (2001) averaged over wave-breaking events gives the volume air fraction of as much as 0.12%, which is equivalent to a 3.75°C change in water temperature in terms of buoyancy.

The relatively high concentration of bubbles that is required for buoyancy effects to be important is primarily observed in wave breakers and convergence zones (e.g., due to Langmuir circulations). A high void fraction due to air bubbles is present in the transition layer between air and water under very high wind speed conditions (Sect. 6.4.3).

The vertical profiles of air-fraction obtained with bow sensors in the upper 2 m of the ocean under relatively strong winds are shown in Fig. 6.6. The idea of extracting this type of profile from bow sensors emerged during communication of one of the authors (Soloviev) with Kennan Melville from Scripps Institution of Oceanography.

Table 6.3 Average void fraction for the conditions of developed seas. The measurements are taken from wave-following buoys.

Source	Depth (m)	Void fraction (%)	Wind speed ($m\ s^{-1}$)	Wave height (m)	Fetch
Bowyer (2001)	0.1	0.016	10–12	2	Unlimited
Bowyer (2001)	0.6	0.0054	11–13	2.5	15–120 km
Farmer et al. (1998) and Garrett et al. (2000)	0.7	0.0060	12		>100 km
Farmer et al. (1998) and Garrett et al. (2000)	1.9	0.00030	12		>100 km
Farmer et al. (1998) and Garrett et al. (2000)	3.5	0.000044	12		>100 km

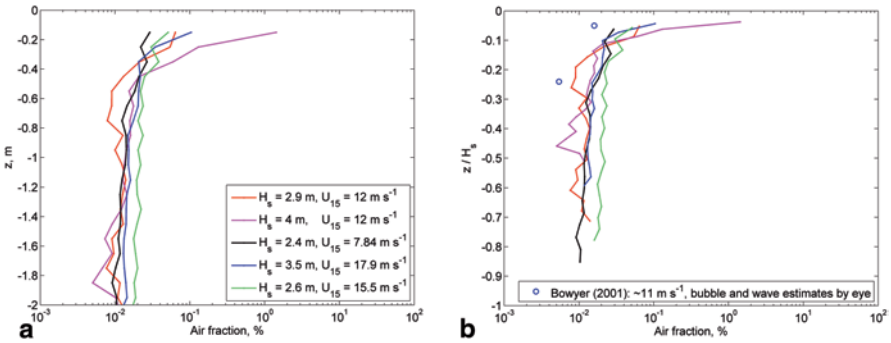

Fig. 6.6 **a** Average vertical air-fraction profiles in the near-surface layer of the ocean obtained by the authors of this monograph with the conductivity sensor installed on the bow of the vessel during the TOGA COARE experiment (more details in Sect. 3.3.5). The wind speed range is from 8 m s^{-1} to 15.5 m s^{-1}. Depth is calculated as distance from the "instantaneous" position of the sea surface. **b** Data from the bow sensor from the upper 1 m of the ocean normalized by significant wave height in comparison with the Bowyer (2001) data (shown as open circles).

The data shown in Fig. 6.6 suggest that the air concentration close to the sea surface can exceed 1 %. Note that in terms of contribution to buoyancy, a 1 % difference in water density is equivalent to a 30°C temperature difference.

Under moderate wind speeds, wave-breaking events last only about 1 s; the whitecap area associated with the wave breaker occupies a relatively small fraction of the sea surface. The whitecap coverage increases rapidly with wind speed. According to Monahan and O'Muircheartaigh (1980), the fractional coverage of the stage B whitecaps, which are the surface expression of decaying bubble plumes, is a strong function of wind speed:

$$W_c \approx 3.84 \times 10^{-4} U_{10}^{3.41} \tag{6.14}$$

where U_{10} is the wind speed at 10 m height. Bortkovskii ((1983) found that the whitecap coverage varies with temperature (though he offered no parameterization for its temperature dependence).

Equation (6.14) predicts that $W_c = 1$ at $U_{10} = 38.7$ m s^{-1}. Extrapolation of Eq. (6.14) to such high wind speed, of course, does not make sense. In fact, the Anguelova and Webster (2006) analysis shows that the whitecap coverage does not exceed 10% even in hurricane conditions. Nevertheless, sea state photographs taken during a hurricane (Fig. 6.1) show that above $U_{10} = 40$ m s^{-1}, the sea surface in fact becomes completely covered with the "whiteout" consisting of foam and streaks (Holthuijsen et al. 2012). This suggests that mechanisms other than whitecapping dominate production of the whiteout during hurricanes (see Sect. 6.4.3).

So far neither the bubble buoyancy effects on near-surface turbulence nor the bubble-induced turbulence has been investigated thoroughly in the open ocean.

6.3 Sea Spray Aerosol Production

6.3.1 Introduction

The ocean surface layer is a source of *sea spray* and *marine aerosols*. According to estimates given in Monin and Krasitskii (1985), about 0.3% of the world ocean surface is covered with breaking waves and the total salt flux into the atmosphere is about 10^{12} kg per year.

The sea spray is an important factor in the air–sea transfer of heat, moisture, and momentum under high wind speed conditions. The primary marine aerosol is composed of seawater enriched with chemical compounds, insoluble organic matter as well as living microorganisms (bacteria, viruses). Both natural and anthropogenic compounds, dissolved in the near-surface layer of the ocean or as a thin film on the ocean surface, contribute to the content of marine aerosols. Large spray drops return to the ocean before evaporating, so these compounds are also returned. Smaller drops are entrained into the turbulent air flow in the marine boundary layer and, under favorable conditions, completely evaporate producing sea-salt aerosol particles, which are effective cloud condensation nuclei. Influencing the development and albedo of clouds, sea-salt aerosols can influence climate.

Sea-salt particles are an important part of the atmospheric sulfur cycle (Chamides and Stelson 1992). According to O'Dowd et al. (1999), natural and anthropogenic sulfate aerosols influence the climate. The Intergovernmental Panel on Climate Change (2001) estimated the direct and indirect radiative forcing of sulfate aerosols to be in the range –0.2 to –0.8 W m^{-2} and 0 to –1.5 W m^{-2}, respectively. This is comparable in magnitude to the radiative forcing of anthropogenic greenhouse gases. It is important that sulfate aerosols produce a radiative effect that is opposite in sign to that of anthropogenic greenhouse gases.

In addition to affecting climate, marine spray and aerosols transfer pollutants from the ocean to the atmosphere, serve as a tracer in the climate record of Arctic and Antarctic snow and ice cores, play a role in corrosion, and cause vegetation stress in coastal regions. The optical properties of the marine boundary layer depend substantially on the type and concentration of aerosols.

Note here that some studies cited below, like that of Andreas (1998), use the diameter of wet particles (i.e., of droplets), while others, like that of Mårtensson et al. (2003), use the diameters of dry particles. This can be attributed to different applications of marine aerosol results. Air–sea interaction scientists are interested in the influence of marine aerosols on the air–sea fluxes, while climatologists are mostly concerned with the presence of dry aerosol particles in the atmosphere. Respectively, different definitions for the sea spray and aerosol generation functions can be found in the literature. In particular, A convention of specifying the size of sea spray particles and dry aerosol particles can be found in de Leeuw et al. (2011).

6.3.2 Mechanisms of Sea Spray Production

There are basically three varieties of spray droplets: film droplets, jet droplets, and spume droplets. We first consider film and jet droplets.

Bursting air bubbles create film and jet droplets. Bubbles are primarily generated through entrainment by breaking waves (Thorpe 1986). After being carried to some depth by a plunging wave jet, a bubble then rises to the surface where it bursts. The process of bursting is schematically illustrated in Fig. 6.7. As the bubble emerges from the water, a thin film forms at the upper surface of the bubble; the film thins by drainage and eventually ruptures. When the bubble film opens, the rim of the receding film cap ejects tens to hundreds of film droplets with radii ranging roughly from 0.5 to 5 μm (Spiel 1998). The collapsing bubble cavity shoots up a jet of water from its bottom. Due to velocity differences along this jet, it soon breaks up into a few jet droplets with radii typically ranging from 3 to 50 μm, depending on the size of the bubble that created them.

The number and size distribution of film and jet drops are connected to the bubble size distribution. Small bubbles produce only jet drops. The size of the jet drops is about 1/10 of the parent bubble diameter size; the bursting bubble produces a maximum of six jet droplets; bubbles larger than 3.4 mm produce no jet drops (Spiel 1997). Jet drops, hence, dominate in the super-micrometer aerosol range.

In addition to film and jet droplets, spume drops are produced by direct "tearing of water" from wave crests at wind speeds higher than about 9 m s^{-1} (Monahan et al. 1983). The spume drops are the largest spray droplets; minimum radii are generally about 20 μm and there is no definite maximum radius. Spume generation is associated with eliminating the clearly defined air–sea interface under high wind speed conditions. Koga (1981) and Veron et al. (2012) have shown from observations in a wind–wave tank that near the crest of the wave, where the wind stress is generally the highest, small projections develop, which then break up to form spume droplets.

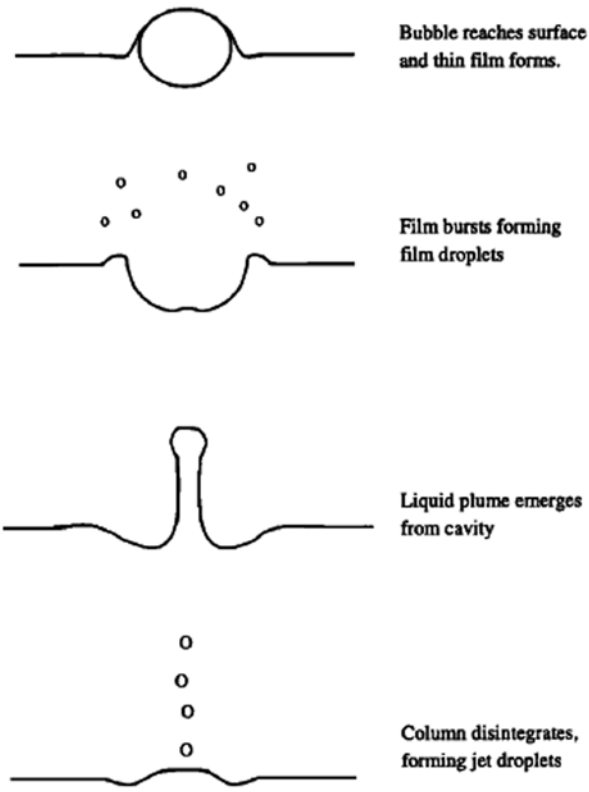

Fig. 6.7 Creation of droplets by bursting bubble at water surface. After Pattison and Belcher (1999). Reproduced by permission of American Geophysical Union

The maximum diameter of these droplets was about 3 mm. The projections presumably develop due to Kelvin–Helmholtz (KH) instability of the air–sea interface, which is discussed later in this chapter.

Droplets with radii in the range 10–500 μm contribute most to the heat fluxes at high wind speeds (Andreas 1992). This size range is dominated by spume droplets, implying that spume generation is the most important mechanism of droplet generation for mediating fluxes under very high wind speed conditions.

The terminal velocity of the largest drop that is stable in the gravitational field (assuming an oblate-spheroid shape of the droplet) scales according to Pruppacher and Klett (1978) as follows:

$$w_t \approx \left(\frac{4\pi b_a}{3aC_D}\right)^{1/2}\left(\frac{\rho g\sigma_s}{\rho_a^2}\right)^{1/4}, \tag{6.15}$$

where b_a is the axial ratio of the oblate spheroid ($b_a \approx 0.55$), C_D is the drag coefficient ($C_D \approx 0.85$), and σ_s is the surface tension at the air–sea interface. For air-temperature of 20 °C and normal atmospheric pressure of 101.3 kPa, the terminal velocity is equal to $w_t \approx 7.8$ m s^{-1}. Equation (6.15) is relevant for drops $r > 2$ mm.

The transport equation for a large droplet in an equilibrium thermodynamics state and in a statistically steady and horizontally homogeneous marine boundary layer is as follows (Iida et al. 1992):

$$w_t \frac{dC}{dz} + \frac{d}{dz}\left(K_D \frac{dC}{dz} \right) = 0. \tag{6.16}$$

A plausible parameterization for the turbulent diffusion coefficient in a coordinate system connected to the sea surface is

$$K_D = Sc_T^{-1} \kappa \left(z + z_{0a} \right) u_{*a}, \tag{6.17}$$

where Sc_T is the turbulent Schmidt number for water droplets (of the order of unity) and z_{0a} is the surface roughness parameter from the air-side of the air–sea interface, for instance, expressed via Charnock's (1955)-type parameterization,

$$z_{0a} = 0.0185 u_{*a}^2 / g. \tag{6.18}$$

The solution for Eqs. (6.16) and (6.17) for C are as follows:

$$C = C_0 \left(1 + z / z_{0a} \right)^{-w_t / \kappa u_{*a}}, \tag{6.19}$$

where C_0 is some reference concentration at $z = 0$.

At $u_{*a} = 2$ m s^{-1} (corresponding to $U_{10} \approx 40$ m s^{-1}), the terminal velocity for the largest spray droplets $w_t \approx 8$ m s^{-1}: $w_t / \left(\kappa u_{*a} \right) \approx 10$. From Eq. (6.19), it follows that the droplet concentration should decrease at $z = z_{0a}$ by a factor $2^{10} \approx 10^3$ relative to the reference concentration, C_0. The surface roughness length scale, z_{0a}, following from the Charnock (1955) parameterization is of the order of 1 cm. As a result, in a purely diffusive model, the concentration of the largest droplets should drop dramatically with distance from the sea surface.

Though the turbulent diffusion mechanism apparently is not effective for the largest droplets, these droplets after tearing from the wave crest are taken up by the wind and typically fly some distance in the horizontal direction before reentering the ocean surface.

6.3.3 Sea Spray Source Function

The sea spray source or generation function, defined as the rate at which spray droplets of any given size are produced at the sea surface, is essential for many applications. The sea spray generation function, commonly denoted as dF_0 / dr_0 (e.g.,

Monahan et al. 1986), where F_0 is total droplet flux from the ocean and r_0 is the radius of a droplet at its formation, has units of number of droplets produced per square meter of surface per second per micrometer increment in droplet radius. For the consideration of spray momentum, heat, and moisture transfer, the generation function expressed as a volume flux, $\left(4\pi r_0^3/3\right)dF_o/dr_0$, is more suitable.

Andreas (1998) compared the results of different authors only to find that the existing parameterizations of the primary marine aerosol source differ by 6–10 orders of magnitude (Fig. 6.8). He nevertheless found some consistency in the estimated shape of the spray generation function. The volume flux is relatively small for droplets with radii less than 2 μm or exceeding 500 μm; there is a 2–3 order-of-magnitude peak in the spray generation function between approximately 10 μm and 200 μm. This peak appears in the spume droplet region, which contributes most to the heat and momentum fluxes at high wind speeds. Parameterization of spume droplet production is therefore essential for evaluating the effects of spray on air–sea heat and moisture transfer.

The estimated generation rates differ so greatly mainly due to the use of different sets of droplet concentration data and differences in the assumptions made regarding droplet trajectories. The process of droplet evaporation also adds to the uncertainty. Ultimately, Andreas (1998) discounts some of the parameterizations shown in Fig. 6.8 based on different grounds and ultimately focuses his analysis on the results of Smith et al. (1993) and Monahan et al. (1986) to produce the following parameterization:

$$\frac{dF_{MS}}{dr_0} = 3.5\frac{dr_{80}}{dr_0}\frac{dF_s}{dr_{80}},$$

$$\text{where } \frac{dF_s}{dr_{80}} = \begin{cases} C_1\left(U_{10}\right)r_{80}^{-1}, & 10 \le r_{80} \le 37.5\ \mu\text{m} \\ C_2\left(U_{10}\right)r_{80}^{-2.8}, & 37.5 \le r_{80} \le 100\ \mu\text{m} \\ C_3\left(U_{10}\right)r_{80}^{-8}, & 100 \le r_{80} \le 250\ \mu\text{m} \end{cases} \tag{6.20}$$

in which the spume extrapolation (third line) is based on droplet concentration data obtained within 0.2 m of the surface by Wu (1984). Here C_1, C_2, and C_3 are the wind-speed dependent coefficients ($\sim U_{10}^3$) that are evaluated by matching wind-dependent coefficient C_1 to the Smith et al. (1993) parameterization at $r_{80} = 10\ \mu\text{m}$, where r_{80} is the radius of spray droplets in equilibrium at a relative humidity of 80 %. Coefficient C_2 is determined from the continuity condition at $r_{80} = 37.5\ \mu\text{m}$. Coefficient C_3 is then similarly found at $r_{80} = 100\ \mu\text{m}$. The relationship between r_{80} and r_0 (the radius of a droplet at its formation) is as follows:

$$r_{80} = 0.518 r_0^{0.976} \tag{6.21}$$

The parameterizations that are currently in use for various applications are still with a few orders of magnitude differences (Andreas et al. 2010; de Leeuw et al. 2011). Furthermore, the existing data do not cover hurricane wind conditions (U_{10}>30–40 m s^{-1}). As a result, the sea spray generation function for hurricane conditions

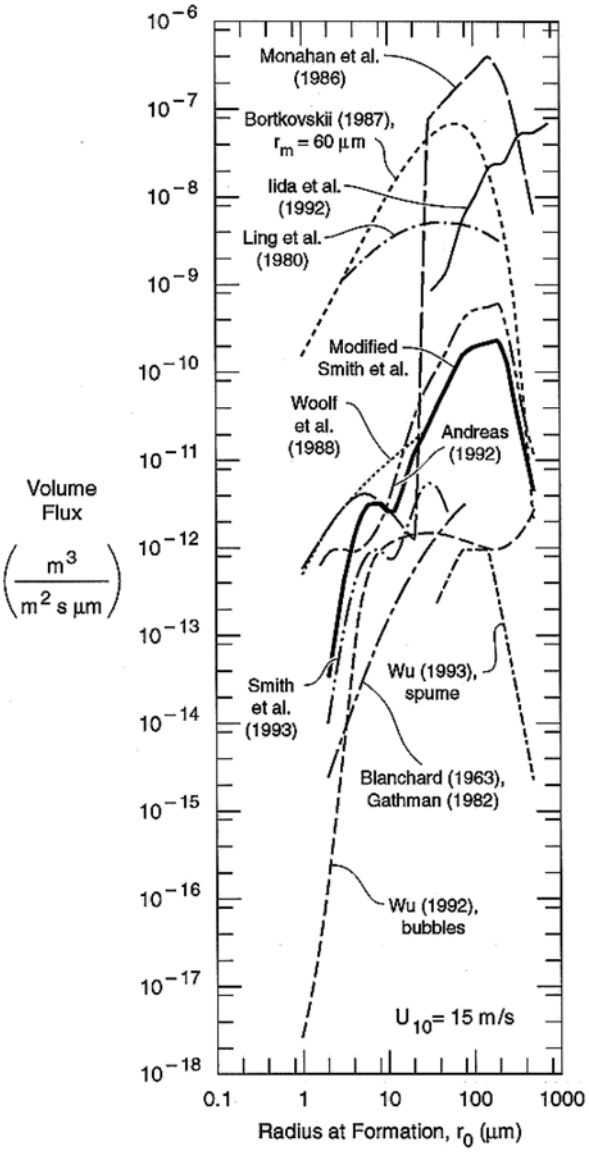

Fig. 6.8 Various estimates of the sea spray generation function expressed as the volume flux, $\left(4\pi r_0^3/3\right)dF/dr_0$, for U_{10} of 15 m s^{-1}. After Andreas (1998). Copyright © 1998 American Meteorological Society. Used with permission

remains practically unknown. Andreas (1998) has concluded that there is no trustworthy spray generation function even for a wind speed exceeding 20 m s^{-1}. Extrapolation of parameterization to hurricane conditions undertaken by some authors is not based on any data.

The dynamics of large droplets is a critical issue in developing the spray generation function for high wind speed conditions. After the initial ejection or splashing from the wave crest region these droplets fall quickly and do not diffuse to any significant height above the ocean, though can be taken up by the wind gust and fly some distance in the horizontal direction before reentering the ocean surface (Koga 1981; Veron et al. 2012). The largest droplets may therefore have eluded complete characterization during previous field experiments.

6.3.4 Primary Aerosol Number Distributions

Marine aerosol production is a major contributor to global natural aerosol systems (Lewis and Schwartz 2004; O'Dowd and Leeuw 2007; Clarke et al. 2006; de Leeuw 2011). The Earth's radiative budget, biogeochemical cycling, visibility, remote sensing, impacts on ecosystems, and regional air quality significantly depend on the contribution from marine aerosol. Marine aerosols include primary components, which are a result of air–sea interactions, and secondary components, which result from gas-to-particle conversion process. We consider here the mechanisms of the primary marine aerosol production. Reviews of the secondary aerosol production can be found in Lewis and Schwartz (2004) and O'Dowd and Leeuw (2007).

The size distribution function of bubbles in the upper ocean, which are the primary source of marine aerosols, depends on wave-breaking parameters, on temperature, salinity, and presence of surfactants. The primary marine aerosol generation is expected to depend on these parameters as well. Figures 6.9 and 6.10 show results of a laboratory experiment for quantifying the salinity and temperature dependence of primary marine aerosol generation.

Figure 6.9 illustrates the effect of salinity on the dry aerosol number concentration (N_p). For the interpretation of this graph recall that for a similar drop size spectrum at formation, the less saline droplets produced at the lower salinity will evaporate to particles with smaller dry particle diameter D_p. The ratio between the diameters of dry particles resulting from 33.0 and 9.2‰ salinity following from simple considerations is determined as $(33.0/9.2)^{1/3} \sim 1.5$.

For aerosols generated by bubbles in the saltwater solutions ($S_w = 9.2$‰ and 33.0‰), two modes are observed depending on the particle size (Fig. 6.9). For the higher salinity, the small particle mode appears as a peak at ~0.1 μm D_p, whereas for the lower S_w, the small particle mode appears as a peak that is roughly a factor 1.5 smaller. This is consistent with the above ratio estimate for the dry particle diameters evaporated from the same size wet particle but with different sea-salt concentration. For particles from the $D_p < 0.2$ μm range, the total volume varies approximately proportionally to the water salinity.

On the other hand, for $D_p > 0.2$ μm (with a peak at ~2 μm), the aerosol spectra have a similar shape for both salinities; the concentrations, however, are an order of magnitude different. This leads to the conclusion that for $D_p < 0.2$ μm, salinity does not affect the original droplet production, just the size of the residual dry aerosol.

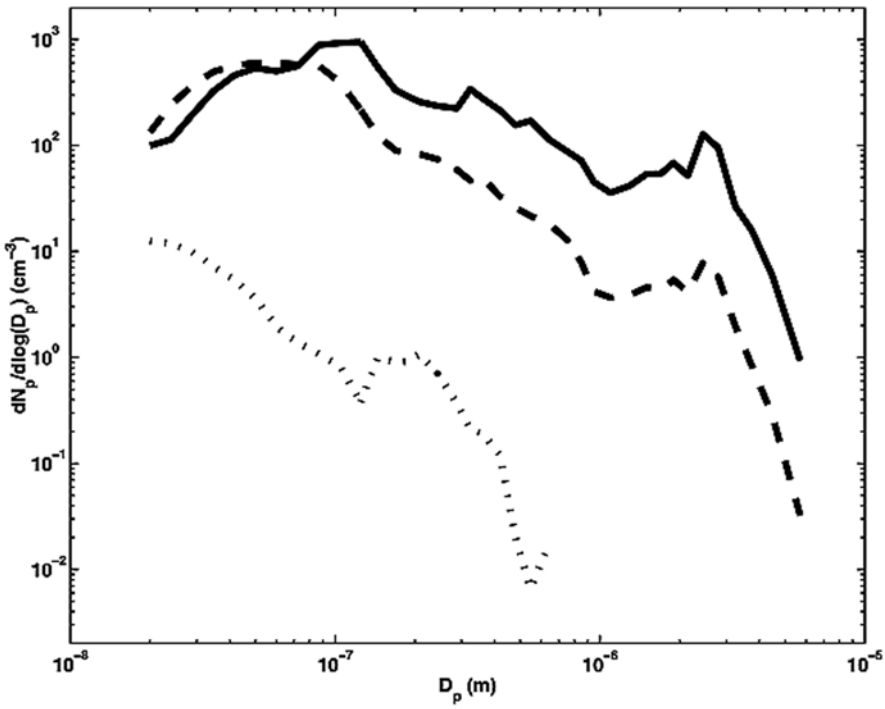

Fig. 6.9 Number distributions of primary aerosols produced from bubbles in water with salinity of 0.0‰ (dotted line), 9.2‰ (dashed line), and 33.0‰ (solid line) in a laboratory experiment. Water temperature was 23 °C. After Mårtensson et al. (2003). Reproduced by permission of American Geophysical Union

Note that at formation, droplets are assumed to have the salinity of the seawater (Andreas 1998). Figure 6.9 thus indicates different droplet formation processes for particles with D_p smaller than ~0.2 μm and for particles larger than this size.

Aerosol number size distributions for four water temperatures are presented in Fig. 6.10. For $D_p > 0.35$ μm, the number concentration increases with increasing temperature, and the shapes of the size distributions are similar at all temperatures. For $D_p < 0.07$ μm, the number concentration decreased with increasing temperature. The curves cross in a transitional range $0.07 < D_p < 0.35$ μm; however no clear trend with water temperature has been revealed for this transition. Similar to the salinity dependence (Fig. 6.9), the temperature dependence in Fig. 6.10 indicates different droplet formation processes, in this case below and above 0.07–0.35 μm D_p.

6.3.5 *Parameterization of Sea Spray Aerosol Production Flux*

De Leeuw et al. (2011) have analyzed different parameterizations for the production flux of sea-salt aerosol particles based on laboratory experiments and field

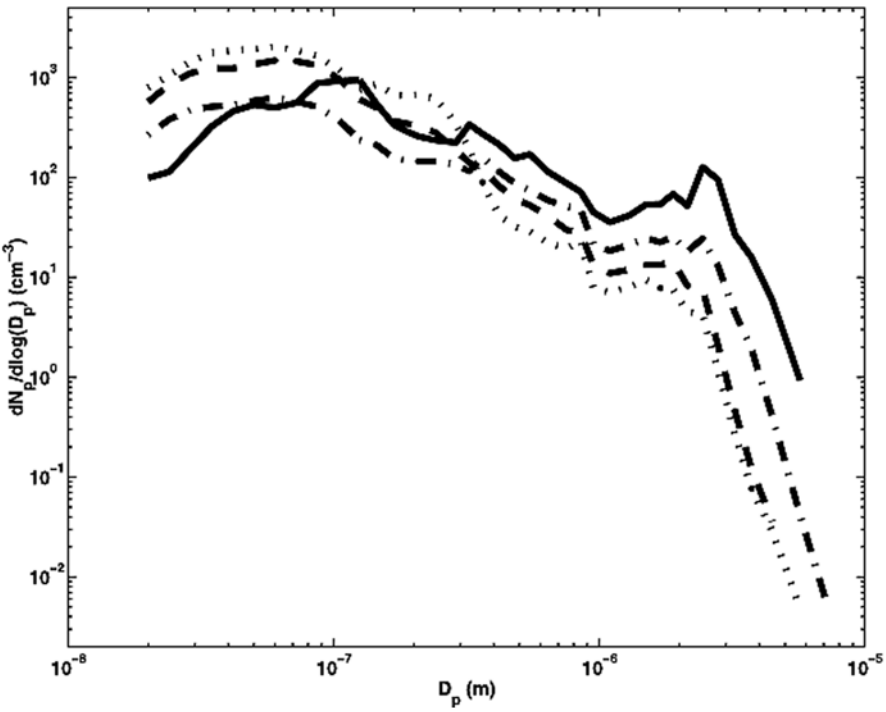

Fig. 6.10 Number distributions of primary aerosol produced at water temperatures of –2 °C (dotted line), 5 °C (dashed line), 15 °C (dot-dashed line), and 23 °C (solid line) in laboratory conditions. The salinity was 33‰. After Mårtensson et al. (2003). Reproduced by permission of American Geophysical Union

measurements, in the surf zone and in the open ocean (Fig. 6.11). The surf zone and laboratory results, however, are not representative of open ocean whitecapping processes, bubble size spectra, and sea spray aerosol flux. In fact, the wave-breaking turbulence and bubble plume dynamics in the open ocean are quite different from those in the surf zone and laboratory facilities (Norris et al. 2013).

For small particle sizes, contributions of organic matter to sea spray aerosol in areas with high biological productivity are important and may dominate for particle sizes $r_{80} < 0.25$ µm (Lewis and Schwartz 2004). Notably, this may also be applicable to hydrocarbon dispersion in the form of aerosol particles from oil spills into the atmosphere under strong winds and breaking waves.

Order-of-magnitude variation remains in estimates of the size-dependent production flux per whitecap area, the quantity central to formulations of the production flux based on the whitecap method. This uncertainty indicates that the production flux may depend on quantities such as the volume flux of air bubbles to the surface that are not accounted for in current models. Variation in estimates of the whitecap fraction as a function of wind speed contributes additional, comparable uncertainty to production flux estimates (de Leeuw et al. 2011; Holthuijsen et al. 2012).

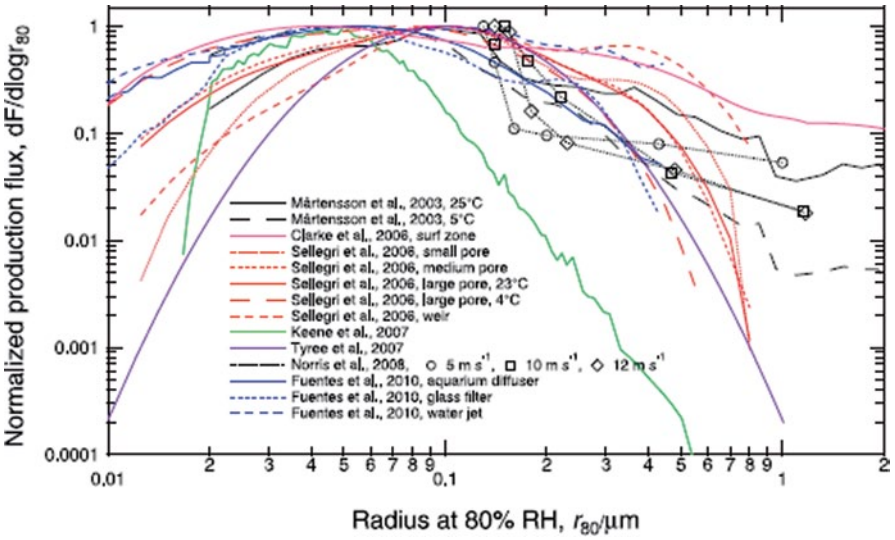

Fig. 6.11 Parameterization of sea spray aerosol production flux (normalized to maximum of size distribution) from the laboratory and field experiments discussed in de Leeuw et al. (2011) Copyright © 1999-2013 John Wiley & Sons, Inc.

Despite significant advances, the uncertainty in the sea spray aerosol production function remains very large. As a consequence, there is an almost two orders of magnitude spread in current estimates of global annual sea spray aerosol emissions (de Leeuw et al. 2011). The present knowledge of the aerosol production function limits the representation of emissions of sea spray aerosols in pollution transport models (e.g., for oil spill dispersion) or advanced climate models.

6.4 Air–sea Exchange During High Wind Speeds

6.4.1 Effect of Spray on Air–Sea Exchanges

Spray droplets that eventually become the main component of the marine aerosol are typically smaller than those that most influence air–sea heat and moisture transfer. Spume droplets, which are relatively large, are particularly important for the fluxes carried by sea spray. Andreas (1998) and Andreas and Emanuel (2001) estimated the effects of the sea spray on heat, moisture, and momentum transfer using a sea spray generation function that was extended into the range of spume droplet sizes. These authors employed a sea spray generation function valid in the droplet radius range from 2 µm to 500 µm based on the Andreas (1992) and modified Smith et al. (1993) parameterizations.

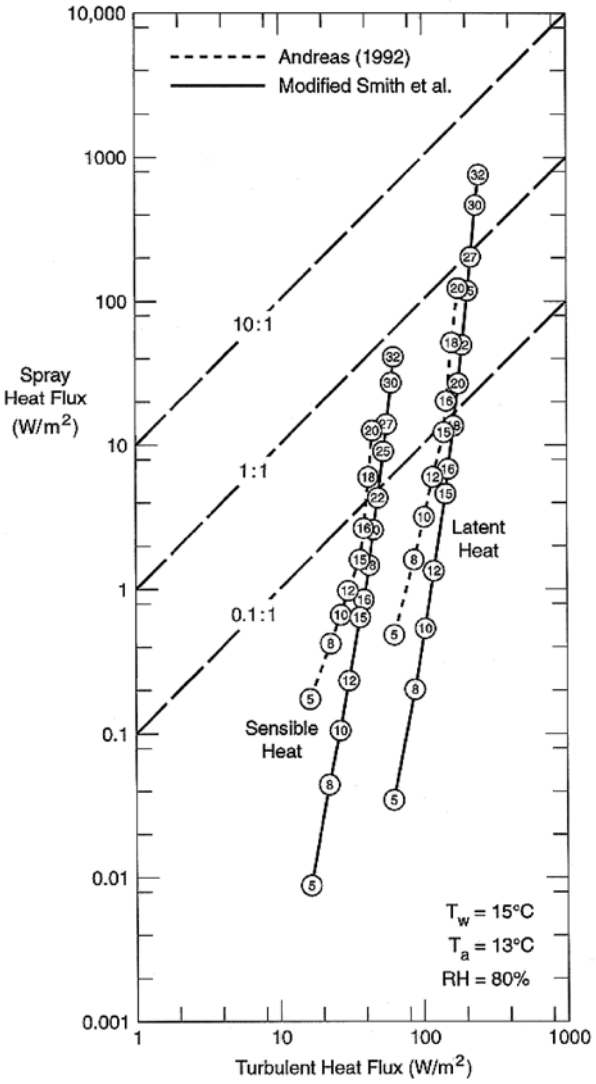

Fig. 6.12 Estimates of the sensible and latent heat fluxes from the Andreas (1992) spray model and two formulations for the spray generation function. The turbulent heat fluxes are estimated from bulk aerodynamic formulas. The surface water temperature (which is the initial temperature of the spray droplets) is T_w, the air temperature is T_a, and the relative humidity is RH. The number in each circle is the 10 m wind speed in m s^{-1}. The *diagonal lines* indicate where the spray and turbulent fluxes are equal (1:1), where the spray flux is 10% of the turbulent flux (0.1:1), and where the spray flux is 10 times the turbulent flux (10:1). After Andreas (1998). Copyright © 1998 American Meteorological Society. Used with permission

Figure 6.12 shows estimates of the magnitude of the sensible and latent heat fluxes based on the Andreas (1992) spray model and two formulations for the spray generation function—the one developed in Andreas (1992) and the modified param-

eterization of Smith et al. (1993). Differences between these generation functions are observed only for $U_{10} < 15$–16 m s^{-1}, when the contributions of sea spray to air–sea fluxes of heat and moisture are small. Figure 6.12 suggests the possibility of extremely large contributions of sea spray to heat and moisture transfer during storms.

Sea spray represents a volume source of heat and moisture in the marine boundary layer. The temperature and humidity profiles can be so strongly modified near the surface by the effects of evaporating spray that additional feedbacks may occur (Katsaros and de Leeuw 1994). The contribution of this feedback is still largely unknown due to the lack of reliable field data under very high wind speed conditions. Andreas' (1998) estimate does not include this feedback, though Fairall et al. (1994) have made an attempt to quantify the resulting sensible and latent heat flux above the droplet evaporation layer.

An important feature of the spray thermodynamics is that the processes of heat and mass exchange of a spray droplet with the air are decoupled. Figure 6.13 demonstrates this for a 100-μm radius spray droplet ejected into typical tropical cyclone conditions. The initial droplet temperature equal to the sea surface temperature drops from 28°C to its equilibrium temperature within 1 s, while only 1 % of the droplet mass must evaporate for the droplet to reach this equilibrium temperature (Andreas and Emanuel 2001). Remarkably little evaporation occurs until at least 40–50 s after droplet formation.

After spray is ejected into the atmosphere, wind can accelerate it. The time required for sea spray droplets starting with no horizontal speed to accelerate to within e^{-1} of the nominal wind speed U_{10} is shown in Fig. 6.14. This exchange extracts momentum from the flow, which is transferred to the ocean when spray droplets land back in the water (Andreas and Emanuel 2001). In surface-level winds of 10 m s^{-1} and higher, droplets with radii up to 500 μm reach a speed equal to the local speed within 1 s. An estimate of droplet residence time for all droplets up to 500 μm in radius suggests that this time is sufficient to accelerate to the local wind speed.

Thus, spray droplets with relatively short atmospheric residence time (the reentrant spray) effectively transfer momentum flux and sensible but not latent heat flux. Note that the latent heat flux is usually much larger than the sensible heat flux.

The spray momentum τ_{sp} and buoyancy B_{sp} vertical fluxes are defined from the following formulas (Andreas and Emanuel 2001):

$$\tau_{sp} = \frac{4\pi}{3}\rho_w U \int_{r_{lo}}^{r_{hi}} r_0^3 \frac{dF_0}{dr_0} dr_0, \tag{6.22}$$

where dF_0/dr_0 is the sea spray generation function and U is the wind speed at one significant wave height above the mean sea level. Equation (6.22) implies that all droplets reach this level. Some justification for this assumption comes from the fact that the droplets that contribute most to the spray momentum flux are the large ones torn right off the wave crests.

Equation (6.22) is nevertheless only an upper bound on the surface stress and vertical buoyancy flux that falling spray droplets produce on the ocean surface layer. In fact, some small spray droplets are entrained in the turbulent flow and never

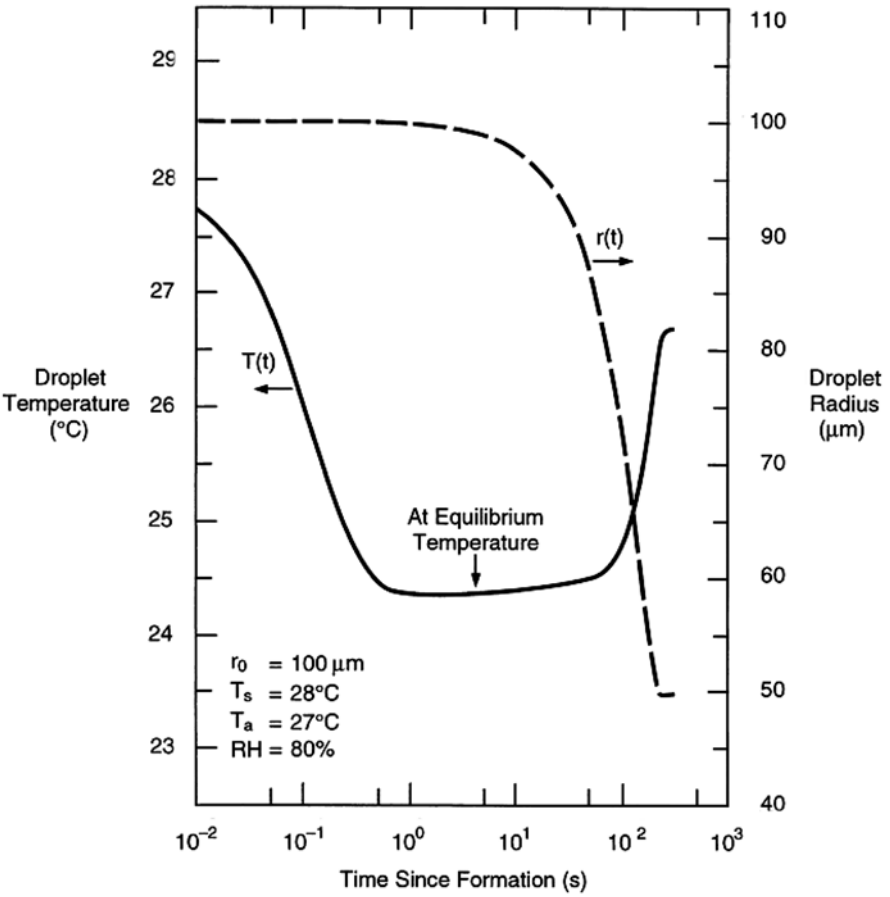

Fig. 6.13 Evolution of temperature and radius of a spray droplet of initial radius $r_0 = 100\ \mu$m, which is ejected from the sea surface at temperature $T_s = 28\,°$C into the air at temperature $T_a = 27\,°$C and relative humidity 80 %. The droplet has initial salinity 34 psu, and the barometric pressure is 1,000 mb. After Andreas and Emanuel (2001). Copyright © 2001 American Meteorological Society. Used with permission

return back to the ocean. The droplets that return to the sea partially evaporate and therefore have a reduced radius r_0, and thus reduced momentum.

Figure 6.15 shows the results of the estimation of τ_{sp} from Eq. (6.22) for two versions of the sea spray generation function in comparison with the total surface stress,

$$\tau = \rho_a u_{*a}^2, \tag{6.23}$$

where ρ_a is the air density and u_{*a} is the friction velocity in the air. The sea spray generation function has not yet been determined for friction velocities $u_{*a} \geq 2$

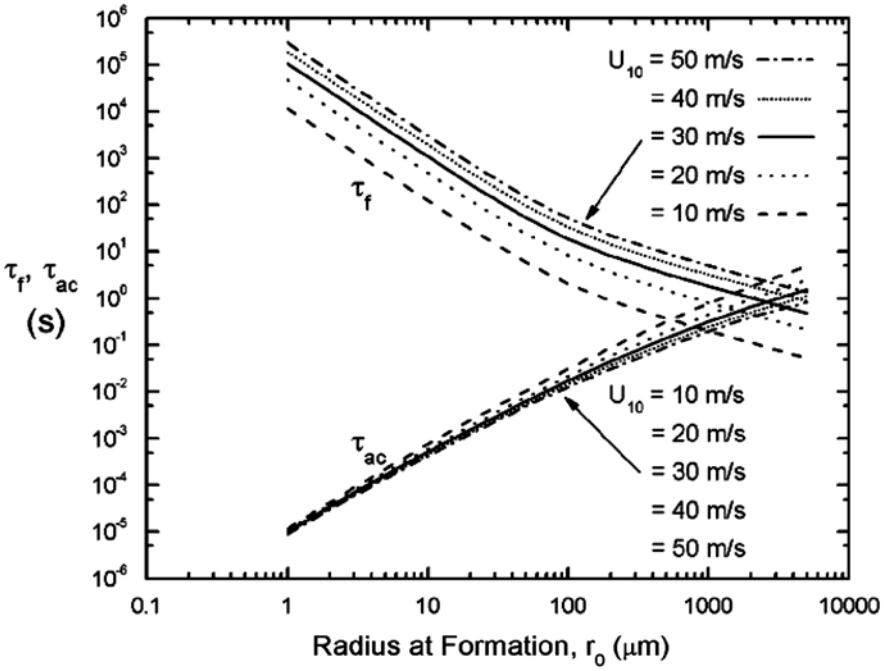

Fig. 6.14 Time τ_{ac} required for sea spray droplets to accelerate to wind speed U_{10}. Here, τ_f is the typical atmospheric residence time for droplets of initial radius r_0 at the indicated wind speed calculated from relation $\tau_f = A_{1/3}/w_t$, where $A_{1/3}$ is the significant wave amplitude determined as $A_{1/3} = 0.015U_{10}^2$ ($A_{1/3}$ is in m and U_{10} is in m s^{-1}). The air temperature is taken as 20 °C, and the barometric pressure as 1,000 hPa. After Andreas (2004). Copyright © 2004 American Meteorological Society. Used with permission

m s^{-1}. In the range $u_{*a} < 2$ m s^{-1}, τ_{sp} estimated with (6.22) is much less than τ. Nevertheless, the estimated spray stress increases approximately as the fourth power of u_{*a}, because $dF_0/dr_0 \sim u_{*a}{}^3$ and U is approximately linear in u_{*a}. At the same time, τ is just quadratic in u_{*a}. Andreas (2004) therefore assumes that when the winds reach hurricane strength, spray stresses may become comparable to the total stress. Andreas and Emanuel (2001) proposed the following parameterization for the spray stress,

$$\tau_{sp} = 6.2 \times 10^{-2} u_{*a}^4, \tag{6.24}$$

which gives τ_{sp} in N m^{-2}, when u_{*a} is in m s^{-1}. They call parameterization (6.24) "heuristic" because it is based on their intuition rather than on any data. According to Fig. 6.15, the sea spray stress becomes comparable to the interfacial wind stress at about 60 m s^{-1} wind speed, which is consistent with Soloviev and Lukas (2010). Note that the sea spray contribution to the sensible and latent heat fluxes becomes comparable to the corresponding interfacial fluxes at about 30 m s^{-1} wind speed.

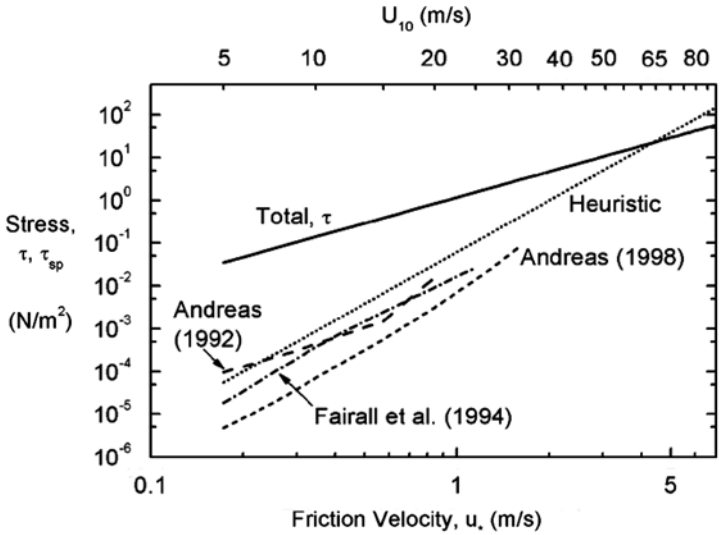

Fig. 6.15 Estimates of the total and sea spray stresses. The sea spray stresses are calculated from Eq. (6.22) for three versions of the sea spray generation function. The extent of these curves reflects the wind speed range over which the functions are appropriate. The total stress line is Eq. (6.23); the heuristic line is equation (6.24). After Andreas (2004). Copyright © 2004 American Meteorological Society. Used with permission

6.4.2 Dynamics of Suspension Flow

The spray-saturated atmospheric boundary layer can be represented as a suspension flow. The Barenblatt and Golitsyn (1974) theory for the flow with suspended particles in a dust storm can provide a theoretical basis for the analysis of the sea spray effects on the marine boundary layer. In this conceptual theory, a stationary turbulent flow of a dust–gas suspension is considered in the semi-infinite region $z \geq 0$ bounded from below by the horizontal plane $z = 0$. The suspension is a two-phase medium consisting of a gas with small particles; the concentration, volume, and weight of particles are small. The horizontal velocity components for the particles and gas are the same while the vertical components differ by the constant value a, which is the fall velocity of a single particle in unbounded space. Contributions due to particle interactions with the pressure and viscous stress are neglected due to the smallness of the particle concentration. Only density variations connected to the action of gravity are taken into account, which is the Boussinesq approximation. Under the Boussinesq approximation, the direct contribution of the solid phase to the momentum and momentum flux of the suspension are neglected. The analogy is of course not complete because in contrast to dust particles, sea spray experiences phase transformation (evaporation).

The laws of momentum and mass conservation for the suspension (Fig. 6.16) are as follows:

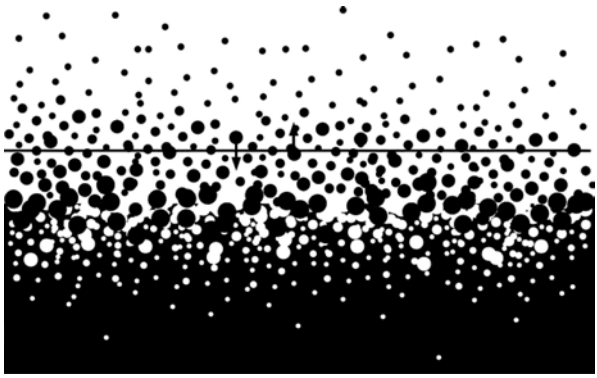

Fig. 6.16 Momentum and enthalpy transfer through an emulsion. Spray droplets are ejected upward and accelerate toward the free stream velocity, absorbing momentum from the atmosphere. After Emanuel (2003). Copyright © 2003 American Meteorological Society. Used with permission

$$-\rho\overline{u'w'} = \tau = \rho u_*^2 = const, \tag{6.25}$$

$$\overline{C'w'} = aC, \tag{6.26}$$

where C is the volume concentration of particles ($C = 4\pi r^3 n/3$), for which r is the particle radius, and n is the number of particles in the unit volume. Equation (6.26) reflects the fact that the vertical turbulent flux of the admixture is equal to its gravitational fallout.

The density of suspension is defined through its components:

$$\rho = \rho_g (1 - C) + \rho_p C \tag{6.27}$$

where ρ_g is the gas density and ρ_p is the particle density. The velocity vector $\vec{u}$ that consists of the longitudinal u and the vertical w components is defined in the following way:

$$\vec{u} = \left[\rho_g (1 - C)\vec{u}_g + \rho_p C\vec{u}_p\right] / \rho \tag{6.28}$$

where $\vec{u}_g$ and $\vec{u}_p$ are the gas and particle velocity vectors, respectively. For small volume ($C \ll 1$) and weight ($\sigma C \ll 1$) concentrations, the density fluctuations are:

$$\rho' = \sigma\rho C, \tag{6.29}$$

where

$$\sigma = (\rho_p - \rho_g) / \rho_g, \tag{6.30}$$

For water drops in the air $\sigma = (\rho - \rho_a) / \rho_a \approx \rho / \rho_a$.

The equation for the turbulent energy balance of the admixture is as follows:

$$\overline{\rho u, w,} du/dz + \overline{\rho' w'} g + \varepsilon = 0, \tag{6.31}$$

where ε is the dissipation rate of the turbulent kinetic energy. With Eq. (6.29), this equation can be presented in the form:

$$\overline{\rho u' w'} du/dz + \sigma \rho \overline{C' w'} g + \rho \varepsilon = 0 \tag{6.32}$$

The physical meaning of this equation is that the energy of turbulence generated by the mean shear flow is then spent partially for suspension and partially for dissipation. Introducing the nondimensional parameter,

$$K_t = \frac{g\overline{C' w'} \rho / \rho_a}{\overline{u' w'} du/dz} \tag{6.33}$$

which is known as the *Kolmogorov number*, Eq. (6.32) can then be presented in the following form:

$$\overline{u' w'} (du/dz)(1 - K_t) + \varepsilon = 0 \tag{6.34}$$

The solution of the problem appears to depend on a nondimensional parameter already familiar to us from Sect. 6.3.2:

$$\omega = w_t / (\kappa u_{*a}), \tag{6.35}$$

where w_t is the terminal velocity of the particle. For $\omega \geq 1$, the vertical distributions of the horizontal velocity u and concentration C are determined by the classical laws for the logarithmic boundary layer (Prandtl 1949):

$$u(z) = \frac{u_{*a}}{\kappa} \ln z + const_1, \quad C(z) = \frac{const_2}{z^{\omega}}, \tag{6.36}$$

which means that the particles do not affect flow dynamics.

For $\omega < 1$, the saturation-limited flow regime is possible, which is described by the following relation for the velocity and concentration profiles (Barenblatt and Golitsyn 1974):

$$u(z) = \frac{u_{*a}}{\kappa \omega} \ln z + const, \quad C(z) = \frac{a^2 K_t}{\sigma g z}, \tag{6.37}$$

For $\omega > 1$, the vertical mixing coefficient is defined as $K_m = \kappa u_{*a} z$, while for $\omega < 1$, it is given by equation

$$K_m = \omega \kappa u_{*a} z = w_t z, \tag{6.38}$$

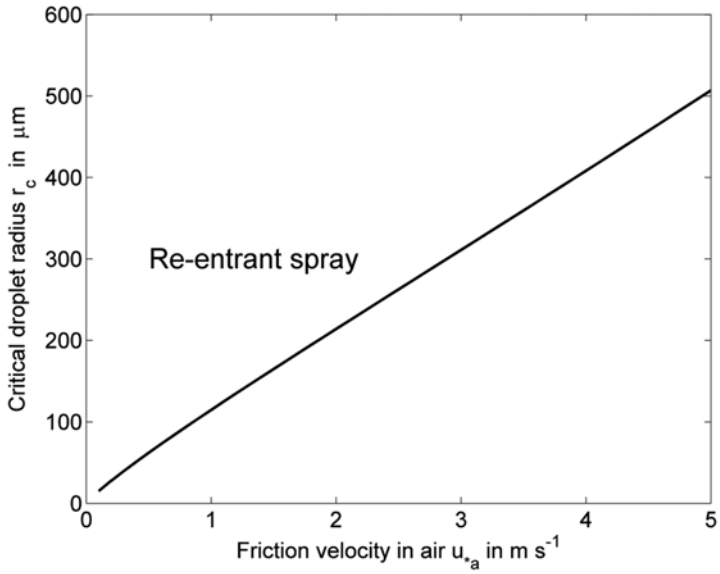

Fig. 6.17 Critical radius separating reentrant and entrained droplets according to the Barenblatt and Golitsyn (1974) theory

which means that the stratification effect reduces turbulent friction by a factor of ω^{-1}.

Equation (6.35) at $\omega = 1$ combined with the formula for the terminal velocity of raindrops (2.112) gives an equation for the droplet radius separating the two regimes according to the Barenblatt and Golitsyn theory. This critical droplet radius r_c is as follows:

$$r_c = r_v \left[1 - \ln\left(\kappa u_{*a} / w_t\right)\right]^{1/\lambda} \tag{6.39}$$

Dependence (6.39) is shown in Fig. 6.17 as a function of the friction velocity in air. Spray droplets with radii $r > r_c$ are the reentrant spray, while smaller droplets are effectively transported by turbulence. Note that for 15 m s^{-1} wind speed, which corresponds to the friction velocity in air $u_{*a} \approx 0.6$ m s^{-1}, the critical droplet radius is $r_c \approx 70$ μm. It is interesting that most of the spray generation functions shown in Fig. 6.8 reveal peaks around $r = 10^2$ μm, which may be an indication that the turbulent diffusion is not an effective mechanism for transporting these relatively large droplets. This, however, might also be an indication that the known spray generation functions underestimate the contribution of large droplets, because the largest droplets might elude detection during the measurements conducted at some distance from the sea surface.

The saturation-limited flow implies an infinite supply of particles from the boundary to the flow. If the particle supply is not infinite then at small distances

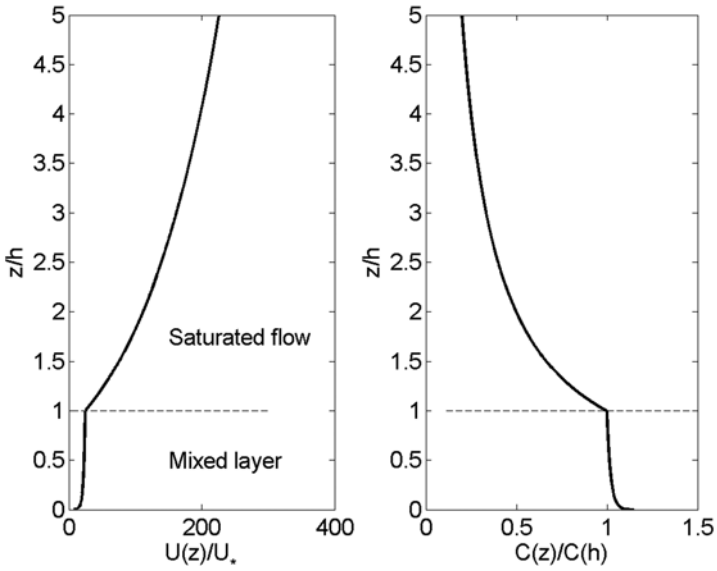

Fig. 6.18 Vertical profiles of velocity and concentration in the suspension-limited flow according to the Barenblatt and Golitsyn (1974) model

from the surface the velocity and concentration profiles follow the laws of the classic logarithmic boundary layer (6.36), while switching to the saturation-limited regime (6.37) at some distance h from the boundary. In the latter case, a new parameter enters the problem, the surface buoyancy flux of spray particles B_{sp}, and a new length scale appears:

$$L_* = \frac{u_{*a}^3}{\kappa B_{sp}}, \tag{6.40}$$

which is an analog to the Oboukhov buoyancy length scale in the thermally stratified turbulent boundary layer. A mixed layer with thickness $h \sim L_*$ would form in the atmospheric boundary layer if heat and moisture fluxes were ignored. This regime is schematically illustrated in Fig. 6.18 for $\omega = 0.1$.

The buoyancy flux due to sea spray can be estimated from the sea spray generation function (see Sect. 6.3.3) in the following way.

$$B_{sp} = -\frac{4\pi}{3}\rho g \int_{r_{lo}}^{r_{hi}} r_0^3 \frac{dF_0}{dr} dr_0, \tag{6.41}$$

where B_{sp} is in (kg m^{-3}) (m^2 s^{-3}).

A rough estimate of the Oboukhov-type length scale from (6.40) using sea spray generation function (6.20) for a 15 m s^{-1} wind speed is $L_* = -10^2$ m. The sea spray generation function dF_0/dr_0 defined from Eqs. (6.20)–(6.21) increases with friction

velocity as u_{*a}^3, which is the same dependence on friction velocity as in the numerator of Eq. (6.40). As a result, the above estimate for L_* does not change with wind speed.

According to the Monin–Oboukhov theory, the buoyancy effects are pronounced at a height $z \sim |L_*|$ and negligible for $z \langle 0.1 |L^*|$. Furthermore, length scale L^* is additive to the classical Oboukhov length scale determined by the heat and moisture fluxes in the atmospheric boundary layer, which can further diminish the buoyancy effect of sea spray.

Theoretically, the sea spray concentration in the marine boundary layer can reach the level at which the associated stratification may suppress turbulent fluctuations, reducing wind stress at the ocean surface. However, if the spray generation function (6.20)–(6.21) holds for very high wind speed conditions, then the influence of sea spray on the atmospheric boundary layer dynamics within the 10-m layer is relatively small even during hurricanes. As a result, the effect of sea spray buoyancy appears to be only marginal on the drag coefficient C_d referenced to a 10-m altitude. Sea spray buoyancy effects, nevertheless, can be more pronounced at larger altitudes (Bao et al. 2011).

6.4.3 The Air–Sea Interface Under Hurricane Conditions

Hurricanes take heat energy from the ocean and redeposit some as kinetic energy. How effective is the process of extraction of energy from the ocean and its dissipation in the ocean significantly depends on the properties and state of the sea surface.

Under low wind speed conditions, viscous stress at the air–sea interface supports the exchange of momentum between the atmosphere and ocean. Under moderate wind speed conditions, wind waves develop and the wave-induced stress becomes more important than the viscous stress. Breaking waves create whitecaps, which cover greater area with increasing wind speed. At very high wind speeds, the sea surface is dominated by streaks of foam and spray (Figs. 6.1).

Holthuijsen et al. (2012) have shown with extended analysis of observations from aerial reconnaissance films that whitecap coverage increases with wind, though, at very high wind speeds, saturates at 4% (Figs. 6.19, 6.20). The traditional assumption was that the whitecap coverage increases to 100% under hurricane conditions. However, the previous studies were limited by 23 m s^{-1} wind speed. At higher wind speeds, the "whiteout" is increasingly dominated by the streaks of foam and spray. At wind speeds above 40 m s^{-1}, the streaks merge into a whiteout with complete coverage (Fig. 6.1). The origin of whiteout is presumably a result of direct disruption of the air–sea interface by the KH and or Tollmien–Schlichting (TS) instability (Sect. 6.4.4).

The mixed-phase environment consisting of air bubbles in water and sea spray in air changes dynamics and thermodynamics of the air–sea interaction. Better understanding of the underlying physics is therefore fundamental to hurricane forecasting.

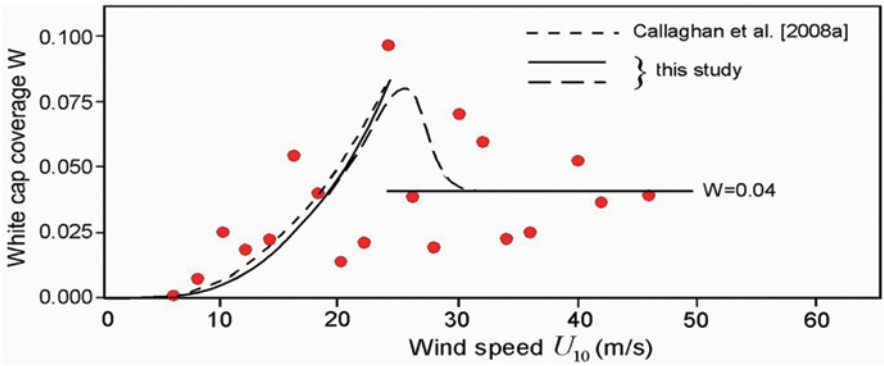

Fig. 6.19 The whitecap coverage obtained from the analysis of photos from low-level reconnaissance flights and approximated with a power law for wind speeds below 24 m s^{-1} and a constant above. A tanh capping with overshoot to a limiting value is shown with long dashes. Adapted from Holthuijsen et al. (2012). Reproduced by permission of American Geophysical Union

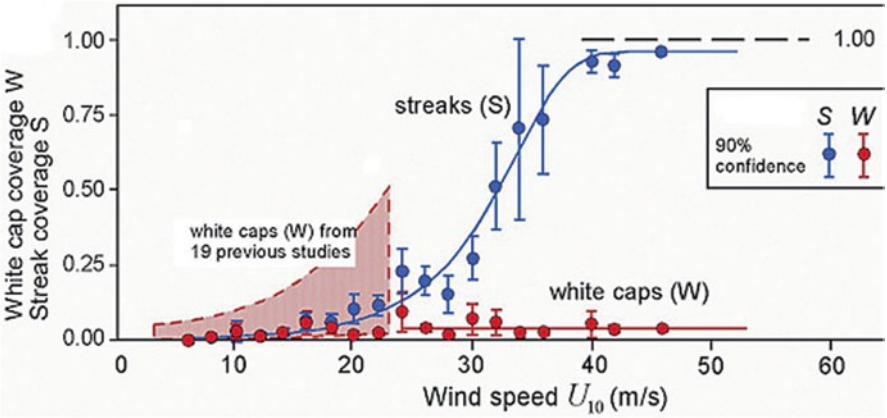

Fig. 6.20 Whitecap coverage W and streak coverage S as a function of wind speed. Blue and red dots represent observations, which are approximated with blue and red lines, respectively. Whitecap coverage W from 19 previous studies compiled by Anguelova and Webster (2006) is represented by shaded area. Adapted from Holthuijsen et al. (2012). Reproduced by permission of American Geophysical Union

6.4.4 Direct disruption of the air–sea interface

Whitecapping is not the most effective mechanism for disrupting the air–sea interface under very high wind speed conditions. More intense and widespread disruption of the interface between air and water under hurricane conditions can be achieved through the KH instability. The KH instability of the air–sea interface de-

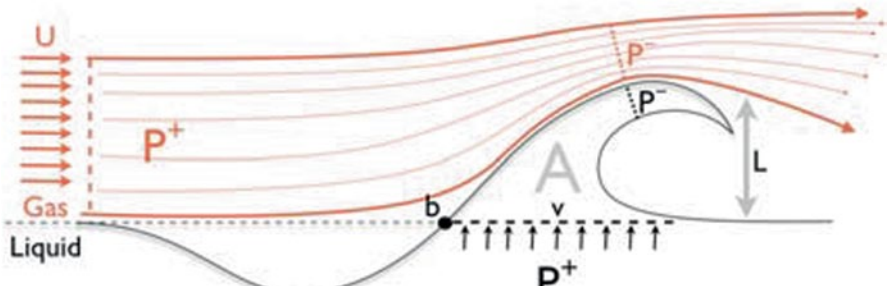

Fig. 6.21 Local perturbation of the KH instability. The wavelet that emerged due to the KH instability breaks the air–water interface when inequality (6.46) is satisfied. After Hoepffner et al. (2011). Copyright (2011) by the American Physical Society

velops within a very short time period (Kelly 1965). The TS instability (Yecko et al. 2002) is potentially another important process taking place at the air–sea interface under hurricane conditions.

The KH instability is the interfacial-type instability, while the TS instability develops in viscous sublayers in the air and/or water side. Note that similar processes take place during the atomization of liquid fuels in cryogenic and diesel engines (Yecko et al. 2002). Under hurricane conditions, the KH and TS instabilities initiate the tearing of short wavelet crests, ejection of spume, and creation of two-phase environment, with subsequent smoothing of the sea surface. The surface smoothing can explain saturation of the drag coefficient at the air–sea interface, an effect observed in the field and laboratory experiments (Powell et al. 2003; Donelan et al. 2004; Black et al. 2007; Troitskaya et al. 2010).

The KH mechanism in application to the air–sea interface is illustrated in Fig. 6.21. Acceleration of the air stream above a short wavelet induces a pressure drop across the air–water interface:

$$\Delta P = P^{+} - P^{-} = A\,\rho_a U^2 kL. \tag{6.45}$$

The pressure drop breaks up the interface if ΔP exceeds the combined restoring force of gravity and surface tension (Thomson (Lord Kelvin) 1871; Miles 1959):

$$\Delta P > \left(g\rho_w + \sigma_w k^2\right) L. \tag{6.46}$$

Here, σ_w is the surface tension, ρ_w is the water density, ρ_a is the air density, k is the wavelength, g is the acceleration due to gravity, and length scale L is proportional to the wave amplitude. The dimensionless coefficient entering Eq. (6.45) in Kelvin's theory is equal to A=1. Strictly speaking, Kelvin's wave generation theory is applicable to only infinitesimally small waves. In order to be consistent with Bernoulli's law, which is valid for finite value waves, A=2 might be more appropriate.

Combining Eqs. (6.45) and (6.46) results in the following threshold condition for the KH instability:

$$U^2 > U_{cr}^2 = A^{-1}\left(g\rho/k_m + \sigma_w k_m\right)/\rho_a = 2A^{-1}\sqrt{\sigma_w \rho g/\rho_a^2}. \tag{6.47}$$

where $k_m = \sqrt{\rho g/\sigma_w}$ is the wave number corresponding to the minimum phase speed of gravity-capillary waves. Finally, Eq. (6.47) can be expressed as follows:

$$U\Big/\left(\sigma_w \rho g/\rho_a^2\right)^{1/4} > (2/A)^{1/2}. \tag{6.48}$$

Due to appreciable change of the wind velocity with height, the interfacial velocity difference U that drives the KH instability is smaller than the wind speed at the reference height (U_{10}).

Soloviev and Lukas (2010) proposed the criteria for the KH instability at the air–water interface, using the friction velocity from the air side of the interface u_{*a} as a determining parameter, in the following way:

$$Ko = u_{*a}\Big/\left(g\sigma_w \rho/\rho_a^{\,2}\right)^{1/4}. \tag{6.49}$$

The instability occurs at $Ko > Ko_{cr}$, where $Ko_{cr} \approx 0.26$ as determined from the result of the Koga (1981) laboratory experiment, which corresponds to $U_{10} \approx 30$ m s^{-1} for air–water interface or $U_{10} \approx 25$ m s^{-1} for air–oil interface (for oil density 0.8 kg m^{-3} and air–oil surface tension 0.03 N m^{-1}).

It is easy to see that Eq. (6.49) is consistent with Eq. (6.48). However, using the friction velocity u_{*a} instead of the interfacial velocity difference U may have an advantage, since the friction velocity is related to the air–sea momentum flux ($\tau = \rho_a u_{*a}^2$), and thus can be defined in the framework of atmospheric circulation models.

Soloviev et al. (2012) demonstrated the possibility of direct disruption of the air–sea interface under hurricane force winds with an idealized 3D volume-of-fluid large eddy simulation (VOF-LES) model, which allowed simulation of the air–sea interface including effects of surface tension. For the case shown in Fig. 6.22, the wind stress $\tau = 4$ N m^{-2} (corresponding to $U_{10} \approx 40$ m s^{-1}) was applied at the upper boundary of the air layer. The Koga number $Ko = 0.38$ calculated from Eq. (6.49) in this case exceeded the critical value of $Ko_{cr} = 0.26$, which satisfied the condition for the development of the KH-type instability, $Ko > Ko_{cr}$. The disruption of the air–water interface resulted in the formation of a two-phase transition layer consisting of a fine mixture of the spray droplets and air bubbles (Fig. 6.22). The droplets in this model have densities ranging from the water density to the air density and can be interpreted as foam. Note that the model does not resolve the full size spectrum of spray droplets.

The numerical experiment with imposed short waves has demonstrated that the disruption of the air–sea interface and formation of spray take place predominantly near wave crests (Fig. 6.23). This is consistent with results of the Koga (1981) laboratory experiment where the KH-type instability of the air–water interface was observed near wave crests under hurricane force wind in the presence of an imposed monochromatic wave. The most characteristic feature of the wind–wave surface in such conditions was the appearance of small, isolated 3D projections on the air side of the interface (Fig. 6.24). Hoepffner et al. (2011) reported similar structures from a numerical simulation of the KH instability at a gas–liquid interface with relatively large (two orders of magnitude, but still one order less than air–water) density

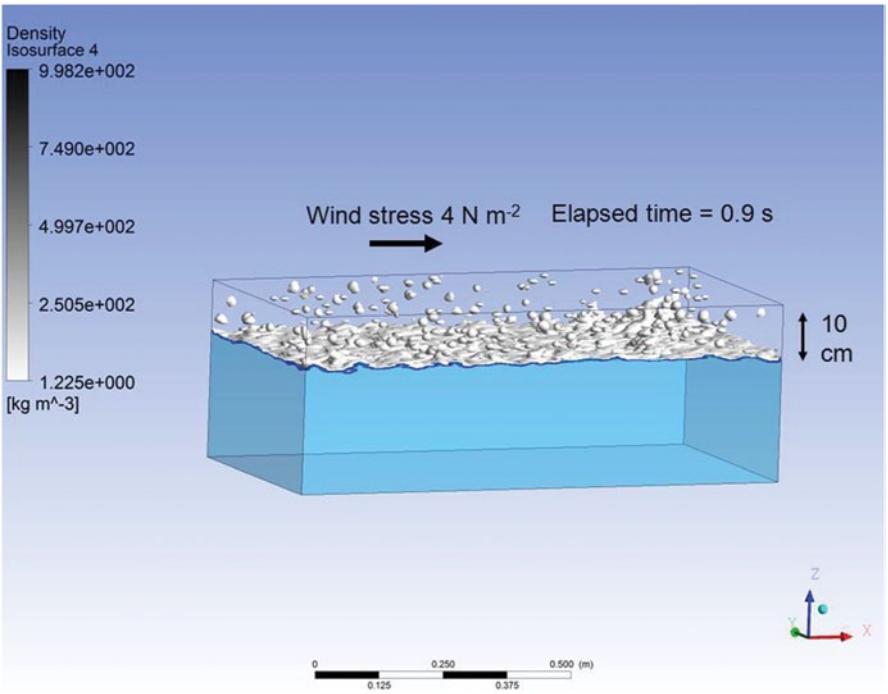

Fig. 6.22 The numerical experiment with an initially flat interface illustrates the possibility of the direct disruption of the air–water interface and formation of the two-phase environment under hurricane force wind. After Soloviev et al. (2012) by permission of John Wiley and Sons

difference. These authors observed the wave's tongue flaps that were fragile and periodically were torn into drops and thrown out to the fast gas stream. Such asymmetrical microstructure of the air–water interface is typical for the KH instability between liquids with very large density difference (e.g., the air–water interface).

Figure 6.25 shows a different view on the surface shown in Fig. 6.23, revealing intermittent streamwise structures with periodicity along the tops of wavelets. Streamwise coherent structures on the water surface in the form of streaks of spanwise size are on the order of a few centimeters wide. Similar streak-like structures have previously been reported from experiments and numerical simulations near the rigid wall (Lesieur 2008) and below the free water surface (Dhanak and Si. 1999; Tsai 2001). These streaks are subject to the TS instability. According to McNaughton and Brunet (2002), the nonlinear stage of the TS instability results in violent fluid ejections (see Fig. 5.52). The TS instability mechanism thus can contribute to the generation of spume and foam streaks in hurricane conditions.

Foam streaks are an observable feature on photographic images of the ocean surface under hurricane conditions (Fig. 6.1). At this point, however, it is difficult to conclude if the coherent structures observed in the numerical experiment (Fig. 6.25) and in the ocean are of the same nature, because the numerical model operates in

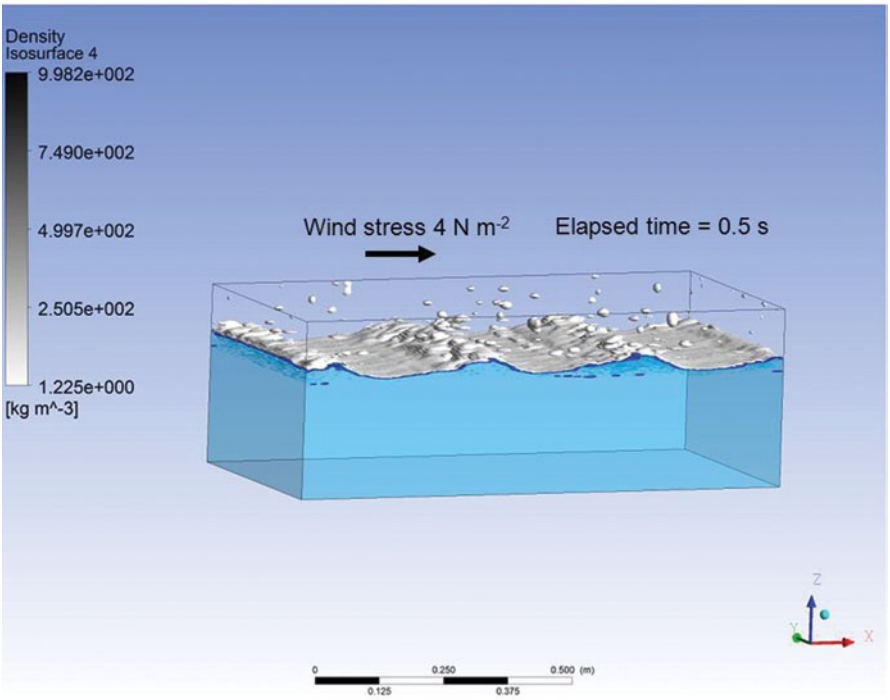

Fig. 6.23 Snapshot from a computational fluid dynamics experiment with imposed short waves demonstrates the tearing of wave crests, formation of water sheets and spume ejection into the air, 0.5 s after hurricane force wind stress is imposed at the top of the air layer. The two-phase mixture (density scale at left) of air and water covers the surface, and individual bubbles and spray droplets are also apparent. The length scale is indicated. After Soloviev et al. (2012) by permission of John Wiley and Sons

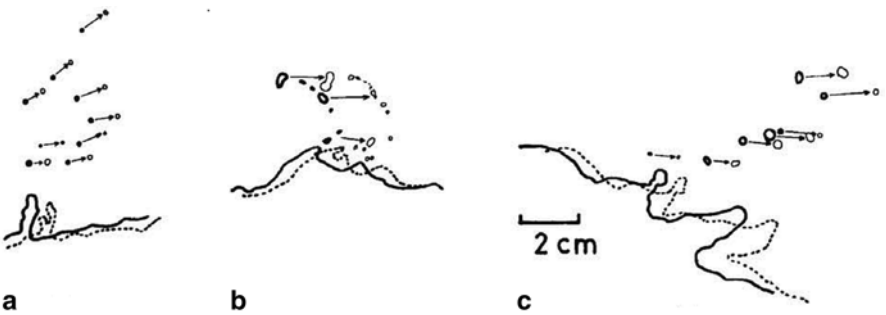

Fig. 6.24 Direct disruption of the air–water interface and production of droplets near the wave crest traced from two-color photographs in the Koga (1981) laboratory experiment at 16 m s^{-1} wind speed as measured at a reference height of 0.15 m above the water surface. Thick solid line represents first image and dotted or thin solid line represent second image. Cases **a**, **b**, and **c** represent situations at the windward slope near the crest, at the crest, and at the leading slope near the crest. After Koga (1981) by permission of Blackwell Publishing

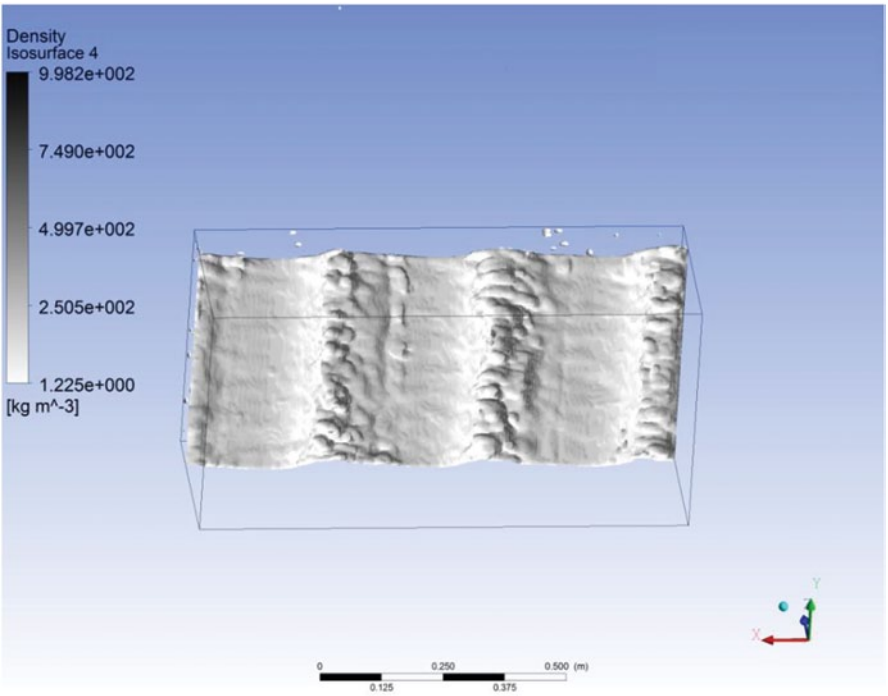

Fig. 6.25 View of the air–water surface shows quasi-periodic structures in the transverse direction along the top of wave crests. After Soloviev et al. (2012) by permission of John Wiley and Sons

a much smaller domain compared to the photo images of the sea surface shown in Fig. 6.1.

6.4.5 The Air–Sea Momentum Exchange in Very Strong Winds

The dynamics of cyclonic storms cannot be fully predicted without proper knowledge of the physical processes at the air–sea interface under high wind speed conditions. The drag coefficient formula of Large and Pond (1981) derived from field measurements, under low and moderate wind speed conditions, gives a linear increase of the drag coefficient with wind. There is evidence that this formula does not work in the high wind-speed regime. Figures 6.26 and 6.27 show the results of laboratory (Donelan et al. 2004) and in situ (Powell et al. 2003) evaluations of the drag coefficient under high wind speed conditions. Both data sets suggest that the drag coefficient does not increase (or perhaps even decreases) with wind speed starting from approximately 30 m s^{-1}.

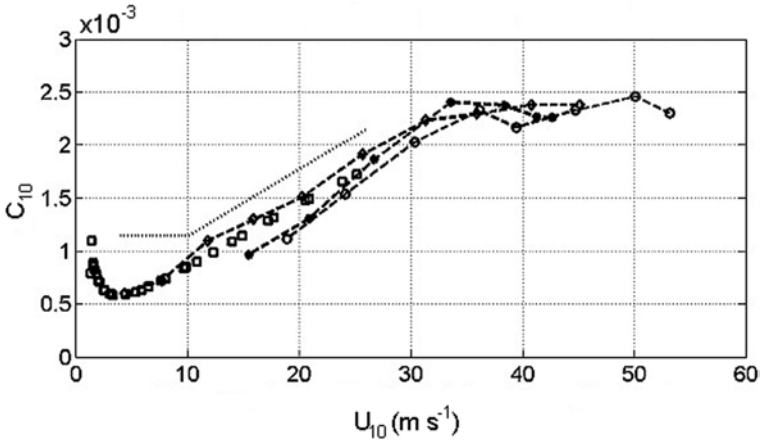

Fig. 6.26 Laboratory tank measurements of the neutral stability drag coefficient C_{10} referred to 10 m height by profile (asterisks), eddy correlation (diamonds), and momentum budget (circles) methods. The squares represent the data obtained in a different tank by Ocampo-Torres et al. (1994). The drag coefficient formula of Large and Pond (1981) derived from field measurements, under relatively low winds, is shown by dots. After Donelan et al. (2004) by permission of American Geophysical Union

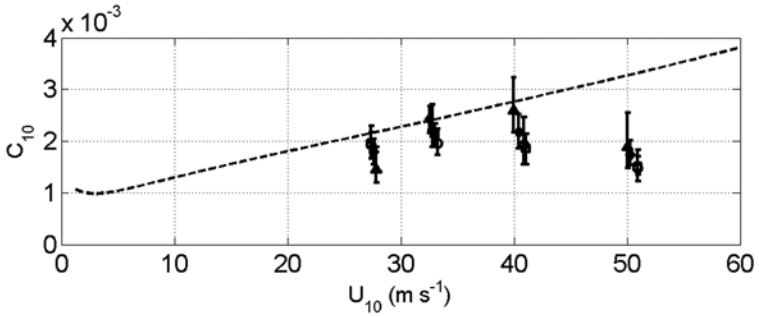

Fig. 6.27 Drag coefficient under high wind speed conditions. Dashed line is the Large and Pond (1981)-type parameterization derived by extrapolating relatively low wind speed measurements. Also shown are the experimental data of Powell et al. (2003) derived from GPS-sonde profiles and the corresponding 95% confidence limits. Reproduced with permission from Macmillan Publishers Ltd

According to the estimates described in Sect. 6.4.2, in the framework of the existing sea spray generation function, the buoyancy effect of spray by itself cannot explain the leveling off or reduction of the drag coefficient dependence on wind speed under very high wind speed conditions. Soloviev and Lukas (2010) proposed a different explanation of this effect, based on the Koga (1981) laboratory results

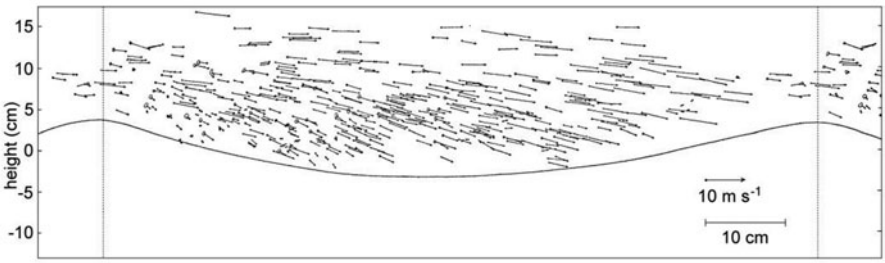

Fig. 6.28 Movements of directly produced droplets along the representative wave for the case of 16 m fetch at $u_{*a}=1.97$ m s^{-1}. Each droplet in the figure indicates actual size traced from photographs. Direction of the airflow and wave propagation is from left to right. Arrows indicate the droplet velocity vector in the coordinate system moving with the phase speed of the wave. After Koga (1981) by permission of Blackwell Publishing

that we discuss in more detail below. As discovered by Koga, the largest droplets are produced by the mechanism of direct splashing, which is initiated by the KH-type instability of the air–sea interface. Koga (1981) observed small projections, developing near wave crests where the wind stress is generally the highest and breaking up to form droplets. This observation is consistent with numerical simulations by Hoepffner et al. (2011) and Soloviev et al. (2012).

The spreading mechanism of the droplets in the Koga (1981) laboratory experiment varied according to the size of the droplets. For droplets with radius of 75 μm or more, representing the reentrant component of spray (see Fig. 6.17), the diffusion by air turbulence is not of primary importance. More important is the initial speed at the instant of the droplet production and the acceleration by wind.

Figure 6.28 shows the spatial distribution of the velocity vector of the splashing droplets relative to the wave profile in the Koga (1981) laboratory experiment. The experimental setup was able to resolve only droplets with radius larger than 0.4 mm. Most of these large droplets were produced on the leading slope near the wave crest with initial speeds of the same order, or somewhat larger than the speed of the projection (Fig. 6.24). The droplets spread upward and forward by the acceleration due to the drag of the pulsating wind flowing over the wave profile. Due to gravity, most of the droplets returned to the water surface on the windward slope near the crest of the next wave; their trajectories through the air make an angle of nearly 15 degrees with the horizontal. Most of the droplets collided with the wave surface when they were accelerated to about half the local wind speed. In some cases small droplets were jumping over the next crest, which usually took place when the steepness of the next crest was large. In this case, even large droplets sometimes jumped upward with some inclination over the next crest.

Andreas (2004) suggested that when the wind speed reaches about 30 m s^{-1}, the flux of spray droplets is equivalent to a heavy rainfall. As discussed in Chap. 2 (Sect. 2.6.5) rainfall damps some part of short surface waves, which contribute to the surface roughness and thus the drag coefficient. In analogy with rainfall, spray

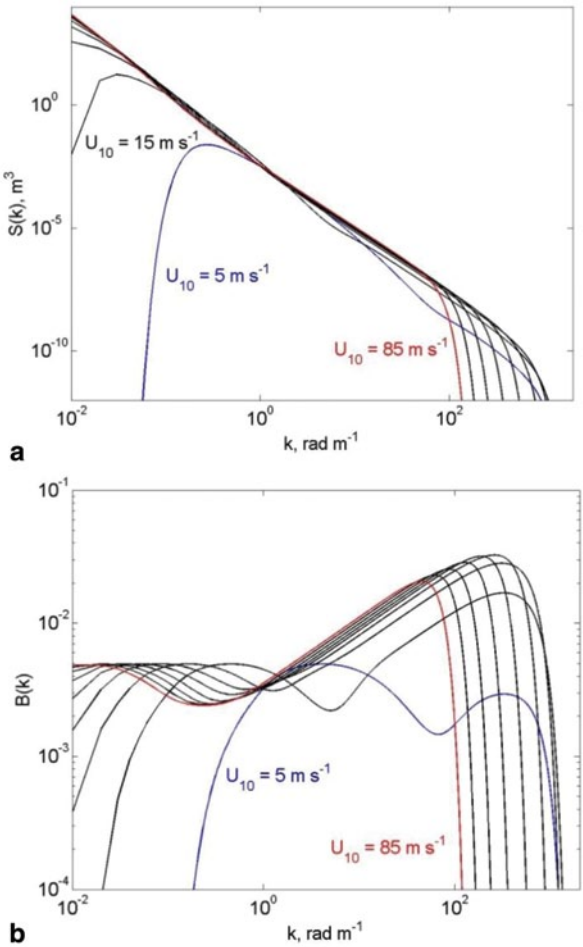

Fig. 6.29 Wave and curvature saturation spectra taking into account the suppression of short waves by two-phase environment under tropical cyclone conditions. Wind speed at a 10-m height (U_{10}) increases from 5 m s^{-1} to 85 m s^{-1} with 10 m s^{-1} increments. After Soloviev et al. (2013)

droplets generated by the KH or TS instability produce two-phase environment at the air–water interface, absorbing the energy of surface waves and smoothing the ocean surface.

Soloviev and Lukas (2010) analyzed the role of the two-phase transition layer that is formed by the reentrant spray and concluded that the two-phase environment has significant dynamic effect on short surface waves. In their conceptual framework, the two-phase environment developing at the air–sea interface eliminates a portion of the high wave number wind–wave spectrum, which is responsible for a substantial part of the air–sea drag coefficient, and thus can reduce the drag coefficient in hurricanes conditions. Furthermore, they concluded that under major

hurricane conditions (U_{10}>60 m s^{-1}), the increasing thickness of the two-phase transition layer may lead to the opposite effect—the increase of the drag coefficient limiting the maximum wind speed in tropical cyclones.

6.4.6 *Problem of Parameterization of the Air–Sea Drag Coefficient in Hurricane Conditions*

Hurricane track prediction has been steadily improving, while the intensity predictions have shown little or no progress during the last quarter century. A logical explanation of the intensity-forecasting problem comes from the method of elimination. Main factors contributing to hurricane intensity forecasting are computational power, observations, and physics. Computer performance is important for improved mesh resolution and operational forecasting. Observations contribute to the specification problem of the initial vortex initialization and the ocean–atmosphere environment and data assimilation. Physics are important for the theory of hurricanes and parameterization of unresolved spatial and temporal scales. During the last quarter century, the computer power increased by orders of magnitude and observations are now much more extensive and intense. Substantial improvements in computations and observations with no progress in intensity predictions suggest that unresolved physics are the weakest component in hurricane prediction models.

Tropical cyclone intensity is sensitive to relative strength of enthalpy and momentum fluxes between the ocean and the atmospheric boundary layer in the high wind core of the storm (Emanuel 1995). These fluxes are characterized by the corresponding air–sea exchange coefficients, C_k and C_d, which depend on the regime of air–sea interaction and the state of the air–sea interface. The laboratory experiment illustrated in Fig. 6.26 concluded that the drag coefficient increases with wind speed but levels off above approximately 33 m s^{-1} wind speed, which corresponds to the transition to a category 1 storm. Similar dependence has been obtained from field data (Fig. 6.27). This is an indication that the regime of air–sea interaction changes under tropical cyclone wind speeds. Another laboratory experiment (Jeong et al. 2012) suggests that the enthalpy exchange coefficient C_k may not have substantial dependence on wind speed.

The drag coefficient (C_d) dependence on wind speed under tropical cyclone conditions is therefore of critical importance for understanding and modeling storm intensity. In some publications, the leveling off of the drag coefficient in tropical cyclones had been linked to the suppression of near-surface turbulence by buoyancy forces due to spray loading in the atmospheric boundary layer. With the currently known sea spray generation function, the effect of sea spray buoyancy on the C_d when referred to 10 m height, however, appears to be relatively small (Soloviev and Lukas 2006; Ingel 2011; Kudrayvtsev and Makin 2011).

Soloviev et al. (2010) assumed that the change of the air–sea interaction regime under very high wind speed conditions is associated with direct disruption of the air–sea interface and formation of the two-phase transition layer consisting of air

bubbles and sea spray. However, the role of sea spray in Soloviev et al. (2010) is completely different from the explanation based on buoyancy effects. Rather, they assumed that the effect of sea spray on the air–sea drag coefficient under very high wind speed conditions is due to two-phase the transition layer suppressing short gravity-capillary waves. As a result, the relative contribution of short waves to the waveform drag gradually reduces with increasing wind speed.

Instability of the interface can be realized, for example, through the KH shear-layer instability (Kelley 1965). Our interpretation of the Kelley (1965) theoretical work is that the stochastic parametric KH instability contributes to microscale wave breaking. The microscale wave breaking as described by Banner and Phillips (1974) and Csanady (1990) is not able to disrupt the air–sea interface due to stabilizing gravity and surface tension forces. However, under very strong winds, the KH waves are able to overcome gravity and surface tension forces resulting in direct disruptions of the air–sea interface (Sect. 6.4.4). These disruptions are much more widespread than whitecapping. In addition to the interfacial-type KH instability, the TS instability taking place in the two viscous sublayers, on the water or air side of the interface, can contribute to the interface disruption. Coincidently, the air–water interface is close to the critical point where any of these instabilities can take place (Yecko et al. 2002). A result of the widespread break-up of the air–sea interface, by either KH or TS instability, is the formation of two-phase transition layer consisting of mixture of sea spray and air bubbles, which cannot support the shortest gravity-capillary waves.

Direct measurement of the gravity-capillary range of surface waves is a very difficult task under tropical cyclone conditions. Indirect data from microwave radar scattering studies appear to be helpful in verification of the wave models in the gravity-capillary range (Donelan and Pierson 1987; Bjerkaas and Reidel 1979; Apel 1994; Hwang et al. 2013). Laboratory experiments are also a valuable source of information on the dynamics of gravity-capillary waves (Jähne and Riemer 1990; Hara et al. 1994), though limited by the scale of the laboratory tank. Passive acoustic remote sensing is another potentially important source of information on the directional properties of gravity-capillary range of surface waves in the real ocean conditions, especially on the wave directional properties (Farrell and Munk 2008; Duennebier et al. 2012).

The main processes at the air–water interface that shape the long-wave component of the spectrum include wind input, nonlinear wave–wave interactions, dissipation by molecular viscosity of water, and wave breaking. The shorter wave components of the wave spectrum (the so-called high-frequencytail) are substantially determined by surface tension forces and depend on near-surface currents (Fan et al. 2009). The experimental (Hwang and Shemdin 1998) and theoretical (Banner and Mellville 1976) results reveal tendency of the high-frequency wave spectrum to saturate under high wind speed conditions, which has been incorporated in the wave model spectra of Elfouhaily et al. (1997) and Hwang et al. (2013).

Analysis based on the time-averaged wind velocity profile (Miles 1959) suggests that in the presence of wind waves, the KH instability cannot develop at the air–water interface (though can still develop at the air–oil interface). However, laboratory

(Koga 1981) and numerical (Soloviev et al. 2012) experiments, both conducted with monochromatic waves, have demonstrated that the KH instability of the air–water interface does take place, though predominantly near wave crests where the interfacial shear is higher and the local conditions for the KH instability development are more favorable. The timescale of the KH instability is much smaller than the period of energy containing wind waves (Kelley 1965). Consequently, the KH instability has sufficient time to develop within a relatively small portion of the wave period and, under very high wind speed conditions, locally disrupt the interface.

The KH mechanism is possible not only in the presence of a monochromatic surface wave but also in a more general case of the turbulent atmospheric boundary layer above the sea surface. A stochastic parametric KH instability can develop at the air–sea interface in the presence of wind waves even when it is prohibitive from the averaged air-flow conditions (Farrell and Ioannou 2008; Kudryavtsev and Makin 2011). The atmospheric boundary layer is typically turbulent and the associated characteristic wind field fluctuation is a phenomenon referred to as gustiness. Moreover, the stochastic gustiness-induced wave growth can be interpreted (Farrell and Ioannou 2008) in the framework of a generalized KH instability problem.

The Miles (1959) mechanism results in the wave growth exponential in time. It uses a linear laminar theory that has no direct role for turbulence. In the Phillips (1957) mechanism, the incoherent stochastic parametric forcing is essentially a result of the turbulence of the boundary layer. The stochastic forcing, entering additively in the Phillips theory, produces linear-in-time growth versus the exponential growth rate in the Miles theory. The stochastic forcing enters multiplicatively in the Farrell and Ioannou (2008) theory and produces an exponential growth, thus extending the Miles theory as the turbulence level increases.

Generation of wind-driven surface water waves can be interpreted as the shear stability problem in the presence of a flexible lower boundary. In the case of very high wind speed conditions, the KH instability results in extensive generation of sea spray and air bubbles. The two-phase environment suppresses short gravity-capillary waves and affects the aerodynamic drag of the sea surface under tropical cyclone conditions. Interestingly, by adding the two-phase environment under tropical cyclone conditions, we introduce substantial viscosity in the system, turning it into a rheological-type problem.

The disrupted interface cannot support very short waves. Equivalently, the dissipation of very short waves is sharply increased by turbulence associated with bubbles and spray, effectively damping such short waves. As wind speed increases, the thickness of the two-phase layer increases, eliminating increasingly longer waves in the high wave number range of the wave spectrum with consequent effect on the air–sea drag coefficient.

The bulk of the kinetic energy of surface waves is located within one-half wavelength (λ) of the surface. We correspondingly assume that the short gravity-capillary waves cannot be supported by the air–wave interface under condition $\lambda/2 < H$, where H is the thickness of the two-phase transition layer. Figure 6.30 demonstrates wave and curvature saturation spectra taking into account the suppression of short waves by two-phase environment under tropical cyclone conditions.

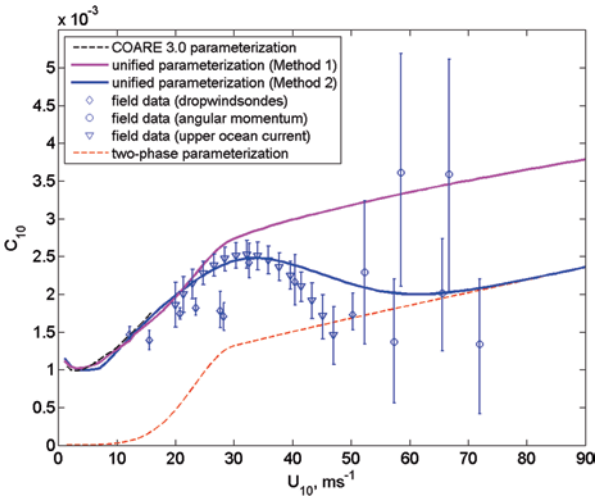

Fig. 6.30 Comparison of the unified air–sea drag parameterization calculated using Method 1 (Donelan and Person 1985) and Method 2 (Hsiao and Schemdin 1984) with the available field experiments. Field experiments (Powell et al. 2003, Black et al. 2007, Bell et al. 2012, Jarosz et al. 2012). The COARE 3.0 (Fairall et al. 2003) parameterization and two-phase (lower bound) layer parameterizations are also shown. After Soloviev et al. (2013)

Theoretical analysis of Farrell and Ioannou (2008) suggests that the stochastic parametric KH instability mechanism for the growth of surface water waves is sustained in a gusty turbulent flow above the random sea surface independently on the Miles wave generation mechanism (Miles 1959). Soloviev et al. (2013) therefore treated the waveform and two-phase layer stresses as independent entities. These stresses were then included in a unified model.

Unfortunately, the waveform stress calculation with existing theoretical models of wind–wave interaction is associated with an order of magnitude uncertainty. In operational wave models, this uncertainty is customarily compensated by introducing empirical coefficients, which are determined from field and laboratory experiments. It is, however, not clear how representative these models are under extreme, very high wind speed conditions. Furthermore, the stress due to two-phase environment at the air–sea interface, which is derived from the theoretical model, is supported by numerical simulations but has never been verified in the field.

Figure 6.30 shows calculations of the waveform stress, which are based on two different models of wind–wave interaction (Donelan and Pierson 1987 and Hsiao and Shemdin 1983, respectively). The unified parameterization denoted as "Method 1" is calculated by adding surface stresses. The unified parameterization denoted as "Method 2" operates with surface roughness length scales. We show both due to large uncertainty in the existing theories of wave generation and waveform stress estimation.

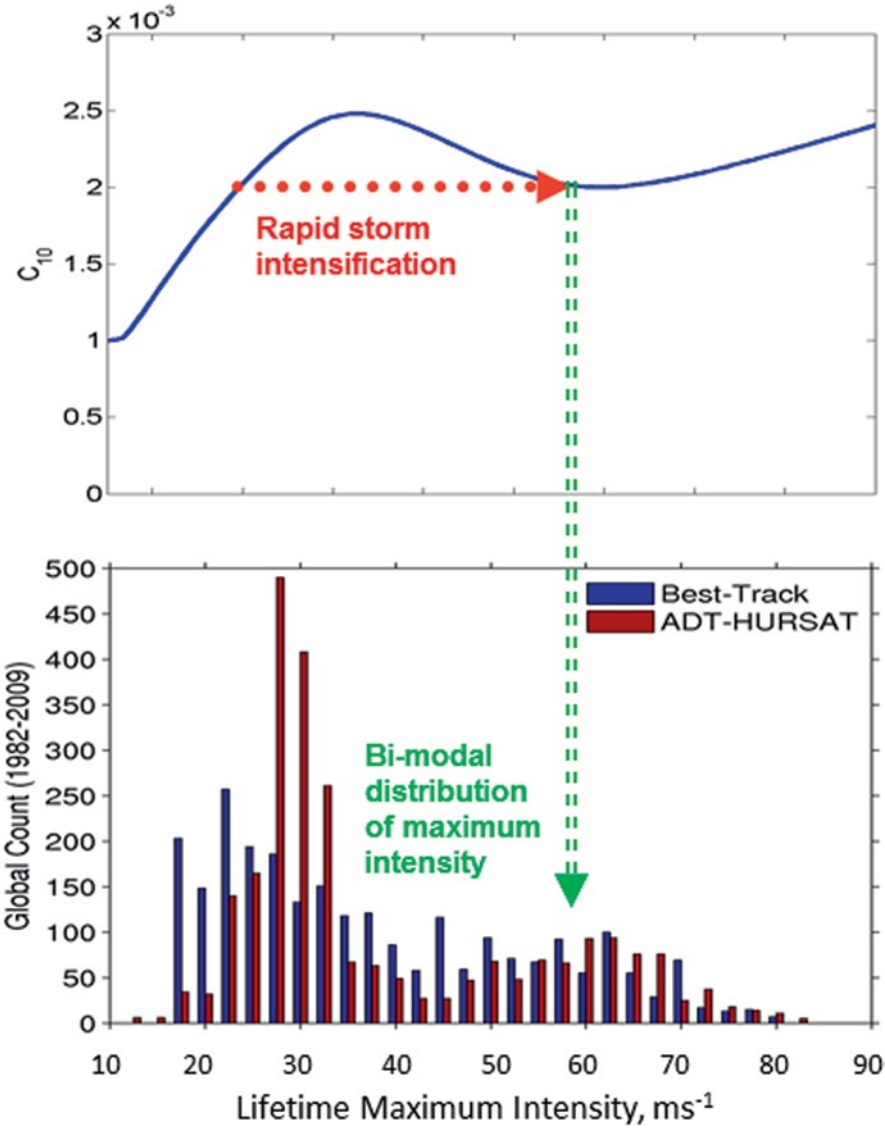

Fig. 6.31 The drag coefficient dependence on wind speed (a) may contribute to the rapid intensification from storms to major tropical cyclone and so may explain the observed (Kossin et al. 2013) bi-modal distribution of tropical cyclone intensity (b). After Soloviev et al. (2013)

The new unified drag coefficient parameterizations are compared with available data for very high wind speed conditions from field experiments. The lower bound on the drag coefficient estimates for tropical cyclone wind speeds is also shown. The unified parameterization in both cases exhibits the increase of the drag coef-

ficient with wind speed until approximately 30 m s^{-1} wind speed. Above this wind speed threshold, the drag coefficient either nearly levels off (Fig. 6.30, Method 1) or even drops and then starts again increasing above approximately 60 m s^{-1} wind speed (Fig. 6.30, Method 2). Remarkably, there is a local minimum of the drag coefficient wind speed dependence around 60 m s^{-1} for the Method 2 case.

The form of the unified parameterization reflects the fundamental change of the air–sea interface properties in tropical cyclone conditions. Here, this change is associated with the effect of direct disruption of the air–sea interface by the KH or TS instabilities, which leads to widespread production of sea spray and air bubbles. A two-phase transition layer made of a mixture of water droplets and air bubbles develops at the air–sea interface. In the model presented in this section, the two-phase environment developing at the air–sea interface eliminates some high-frequency waves, which affects the air–sea drag coefficient. With increasing wind speed, spray droplets take progressively larger potion of momentum from wind. As a result, above approximately 60 m s-1, the drag coefficient increases again with wind, which is in line with the heuristic model of Andreas (2004) discussed in Sect. 6.4.1.

The shape of the drag coefficient for high wind speeds should have consequences for hurricane dynamics and intensification. The leveling effect of the drag coefficient has been reported in a number of measurements done in the laboratory (Donelan et al. 2004) and ocean (Powell et al. 2003; Bell et al. 2012; Holthuijsen et al. 2012) during hurricane conditions. Notably, the mechanism of stochastic KH instability and the effect of two-phase environment on the short gravity-capillary waves are able to explain the leveling off of the drag coefficient (and even its reduction) under hurricane wind speeds (Fig. 6.30).

A negative slope in the C_d wind speed dependence shown in Fig. 6.30b above $U_{10} > 30$ m s^{-1} indicates that waveform drag may be reduced in certain wind speed, contributing to the rapid intensification of storms to major hurricanes. Note that the problem of rapid storm intensification has been a challenge for hurricane forecasters (Sampson et al. 2011). Despite a "sweet spot" in C_d, the subsequent slow increase of the drag coefficient with winds above 60 m s^{-1} serves as an obstacle for further intensification of a hurricane. This may explain the bimodal distribution of tropical cyclone intensity, which is an observable feature (Fig. 6.31). Other factors, however, may explain the bimodal distribution, though other explanation is also possible (Emanuel 2000).

References

Andreas EL (1992) Sea spray and the turbulent air-sea heat fluxes. J Geophys Res 97:11429–11441
Andreas EL (1998) A new sea spray generation function for wind speeds up to 32 m s^{-1}. J Phys Oceanogr 28:2175–2184
Andreas EL (2002) A review of sea spray generation function for the open ocean. In: Perrie W (ed) Atmosphere-Ocean interaction, Vol 1. WIT Press, Southampton, pp. 1–46
Andreas EL (2004) Spray stress revisited. J Phys Oceanogr 34:1429–1440

Andreas EL, Emanuel KA (2001) Effects of sea spray on tropical cyclone activity. J Geophys Res 58:3741–3751
Andreas EL, Jones KF, Fairall CW (2010) Production velocity of sea spray droplets. J Geophys Res 115:C12065
Anguelova MD, Webster F (2006) Whitecap coverage from satellite measurements: a first step toward modeling the variability of oceanic whitecaps. J Geophys Res 111:C03017
Apel JR (1994) An improved model of the ocean surface wave vector spectrum and its effects on radar backscatter. J Geophys Res 99(C8):16269–16291
Banner ML, Phillips OM (1974) On the incipient breaking of small scale waves. J Fluid Mech 65:647–656
Banner ML, Mellville WK (1976) Separation of air-flow over water waves. J Fluid Mech 77:825–842
Bao J-W, Fairall CW, Michelson SA, Bianco L (2011) Parameterizations of sea–spray impact on the air–sea momentum and heat fluxes. J Phys Oceanogr 139:3781–3797
Barenblatt GI, Golitsyn GS (1974) Local structure of mature dust storms. J Atmos Sci 31:1917–1933
Bell MM, Montgomery MT, Emanuel KA (2012) Air–sea enthalpy and momentum exchange at major hurricane wind speeds observed during CBLAST. J Atmos Sci 69:3197–3222
Bjerkaas AW, Reidel FW (1979) Proposed model for the elevation spectrum of a wind-roughened sea surface. Report APL-TG-1328–1–31, pp 31. Appl Phys Lab, Johns Hopkins University, Laurel, MD
Black PG, D'Asaro EA, Drennan WM, French JR, Niiler PP, Sanford TB, Terrill EJ, Walsh EJ, Zhang JA (2007) Air-Sea exchange in hurricanes: synthesis of observations from the coupled boundary layer air-sea transfer experiment. Bull Amer Meteor Soc 88(3):357–374
Bortkovskii RS (1983) Heat and moisture exchange between atmosphere and ocean under storm conditions. Hydrometeorological Publishing House, Leningrad, pp 160
Bowyer PA (2001) Video measurements of near-surface bubble spectra. J Geophys Res 106:14179–14190
Brooks IM, Yelland MJ, Upstill-Goddard et al (2009) Physical exchanges at the air-sea interface: field measurements from UK-SOLAS. Bull Amer Meteor Soc 90:629–644
Callaghan A, DeLeeuw G, Cohen L, O'Dowd CD (2008a) Relationship of oceanic whitecap coverage to wind speed and wind history. Geophys Res Lett 35:L23609. doi:10.1029/2008GL036165
Chamides WL, Stelson AW (1992) Aqueous-phase chemical processes in deliquescent sea-salt aerosols: a mechanism that couples the atmospheric cycles of S and sea salt. J Geophys Res 97:(20)565–20,580
Charnock H (1955) Wind stress on a water surface. Q J Roy Meteor Soc 81:639–640
Clarke AD, Owens SR, Zhou J (2006) An ultrafine sea-salt flux from breaking waves: Implications for cloud condensation nuclei in the remote marine atmosphere. J Geophys Res 111:D06202. doi:10.1029/2005JD006565
Clift R, Grace JR, Weber ME (1978) Bubbles drops and particles. Academic Press, New York, pp 380
Csanady GT (1990) The role of breaking wavelets in air-sea gas transfer. J Geophys Res 95:749–759
Deane GB (2012) Acoustic screening of the ocean surface by bubbles. Proceddings of underwater communications conference, 12–14 September 2012, Sestri Levante, Italy, p 7 (http://www.ucomms.net/proceedings.php)
Deane GB, Stokes MD (2002) Scale dependence of bubble creation mechanisms in breaking waves. Nature 418:839–844
de Leeuw G, Neele FP, Hill M, Smith MH, Vignati E (2000) Production of sea spray aerosol in the surf zone. J Geophys Res 105:(D24)29397–29409
de Leeuw G, Moerman M, Cohen L, Brooks B, Smith M, Vignati E (2003) Aerosols, bubbles and sea spray production studies during the RED experiments, Proceedings AMS conference, Long Beach, CA, 9–13 February, 2003

de Leeuw G, Andreas EL, Anguelova MD, Fairall CW, Lewis ER, O'Dowd C, Schulz M, Schwartz SE (2011) Production flux of sea spray aerosol. Rev Geophys 49:RG2001. doi:10.1029/2010RG000349

Deane GB, Stokes MD (1999) Air entrainment processes and bubble size distributions in the surf zone. J Phys Oceanogr 29:1393–1403

Dhanak MR, Si C (1999) On reduction of turbulent wall friction through spanwise wall oscillations. J Fluid Mech 383:175–195

Donelan MA, Pierson WJ (1987) Radar scattering and equilibrium ranges in wind-generated waves with application to scatterometry. J Geophys Res 92:4971–5029

Donelan MA, Haus BK, Reul N, Plant W, Stiassnie M, Graber H, Brown O, Saltzman E (2004) On the limiting aerodynamic roughness of the ocean in very strong winds. Geophys Res Lett 31:L18306

Duennebier FK, Lukas R, Nosal E-M, Aucan J, Weller RA (2012) Wind, waves, and acoustic background levels at station aloha. J Geophys Res 117:C03017

Elfouhaily T, Chapron B, Katsuros K, Vandemark D (1997) A unified directional spectrum for long and short wind-driven waves. J Geophys Res 102:15781–15796

Emanuel K (1995) Sensitivity of tropical cyclones to surface exchange coefficients and a revised steady-state model incorporating eye dynamics. J Atmos Sci 52:3969–3976

Emanuel K (2000) A statistical analysis of tropical cyclone intensity. Mon Weather Rev 128:1139–1152

Emanuel K (2003) Q similarity hypothesis for air-sea exchange at extreme wind speeds. J Atmos Sci 60:1420–1428

Fairall CW, Kepert JD, Holland GJ (1994) The effect of sea spray on the surface wind profile during conditions of strong wind. Bound -Lay Meteorol 55:305–308

Fan Y, Ginis I, Hara T (2009) The effect of wind-wave-current inter-action on air-sea momentum fluxes and ocean response in tropical cyclones. J Phys Oceanogr 39:1019–1034

Farmer DM, Li M (1995) Patterns of bubble clouds organized by Langmuir circulation. J Phys Oceanogr 25:1426–1440

Farmer DM, Vagle S, Booth AD (1998) A free-flooding acoustical resonator for measurement of bubble size distributions. J Atmos Ocean Tech 15(5):1132–1146

Farrell BF, Ioannou PJ (2008) The stochastic parametric mechanism for growth of wind-driven surface water waves. J Phys Oceanogr 38:862–879

Farrell WE, Munk W (2008) What do deep sea pressure fluctuations tell about short surface waves? Geophys Res Letters 35: L19605, doi:10.1029/2008GL035008

Garrett C, Li M, Farmer D (2000) The connection between bubble size spectra and kinetic energy dissipation rates in the upper ocean. J Phys Oceanogr 30:2163–2171

Garrettson GA (1973) Bubble transport theory with application to the upper ocean. J Fluid Mech 59:187–206

Gong SL, Barrie LA, Blanchet J-P (1997) Modeling sea-salt aerosols in the atmosphere: 1, Model development. J Geophys Res 102:3805–3818

Göz MF, Bunner B, Sommerfeld M, Tryggvason G (2001) Direct numerical simulation of bidisperse bubble swarms. Contribution to the international conference on multiphase flow, New Orleans, May 2001

Hara T, Bock EJ, Lyzenga D (1994) In situ measurements of capillary-gravity wave spectra using a scanning laser slope gauge and microwave radars. J Geophys Res 99(C6):12593–12602

Hinze JO (1955) Fundamentals of the hydrodynamic mechanism of splitting in dispersion process. AICHE J 1:289–295

Hoepffner J, Blumenthal R, Zaleski S (2011) Self-similar wave produced by local perturbation of the Kelvin-Helmholtz shear-layer instability. Phys Rev Lett 106(10):104502

Holthuijsen LH, Powell MD, Pietrzak JD (2012) Wind and waves in extreme hurricanes. J Geophys Res 117:C09003. doi:10.1029/2012JC007983

Hsiao SV, Shemdin OH (1983) Measurements of wind velocity and pressure with a wave follower during MARSEN. J Geophys Res 88:9841–9849

Hwang PA, Shemdin OH (1998) The dependence of sea surface slope on atmospheric stability and swell conditions. J Geophys Res 93:13903–13912
Hwang PA, Burrage DM, Wang DW, Wesson JC (2013) Ocean surface roughness spectrum in high wind condition for microwave backscatter and emission computations. J Atmos Oceanic Technol, in press
Iida N, Toba Y, Chaen M (1992) A new expression for the production rate of seawater droplets on the sea surface. J Oceanogr 48:439–460
Ingel LKh (2011) The effect of sea spray on the dynamics of marine atmospheric surface layer in strong winds. Izv Atmos Ocean Phys 47(1):119–127
Intergovernmental Panel on Climate Change (IPCC), Climate Change (2001) The scientific basis, contribution of working group I to the third assessment report of the intergovernmental panel on climate change. Cambridge University Press, New York
Jähne B, Riemer KS (1990) Two-dimensional wave number spectra of small-scale water surface waves. J Geophys Res 95(C7):11531–11546
Jeong D, Haus BK, Donelan MA (2012) Enthalpy transfer across the air–water interface in high winds including spray. J Atmos Sci 69:2773–2748
Johnson B, Cooke R (1979) Bubble populations and spectra in coastal waters: a photographic approach. J Geophys Res 84:3761–3766
Katsaros KB, de Leeuw G (1994) Comment on "Sea spray and turbulent air-sea heat fluxes" by Edgar L. Andreas. J Geophys Res 99:14339–14343
Keeling RF (1993) On the role of large bubbles in air-sea gas exchange and supersaturation in the ocean. J Mar Res 51:237–271
Kelly RE (1965) The stability of an unsteady Kelvin-Helmholtz flow. J Fluid Mech 22(3):547–560
Koga M (1981) Direct production of droplets from breaking wind-waves-Its observation by a multi-colored overlapping exposure technique. Tellus 33:552–563
Koga M, Toba Y (1981) Droplet distribution and dispersion process on breaking wind waves. Sci Rep Tohoku University, Sr. 5. Tohoku Geophys J 28:1–25
Kolmogorov AN (1949) O droblenii kapel v turbulentnom potoke. Dokl Akad Nauk USSR 66(15):825–828 (in Russian)
Kossin JP, Olander TL, Knapp KR (2013) Trend Analysis with a New Global Record of Tropical Cyclone Intensity. Journal of Climate, accepted
Kudryavtsev VN (2006) On the effect of sea drops on the atmospheric boundary layer. J Geophys Res 111:C07020
Kudryavtsev VN, Makin VK (2011) Impact of ocean spray on the dynamics of the marine atmospheric boundary layer. Bound -Lay Meteor 140:383–310
Large WG, Pond S (1981) Open ocean momentum flux measurements in moderate to strong winds. J Phys Oceanogr 11:324–336
Leifer I, de Leeuw G (2001) Bubble measurements in breaking-wave generated bubble plumes during the LUMINY wind-wave experiment. In: Saltzman ES, Donealn M, Drennan W, Wanninkhof R (eds) AGU monograph gas transfer at water surfaces, pp 303–309
Leifer I, de Leeuw G (2006) Bubbles generated from wind-steepened breaking waves: 1. Bubble plume bubbles. J Geophys Res 111:C06020. doi:10.1029/2004JC002673
Leifer I, de Leeuw G, Cohen LH (2000) Secondary bubble production from breaking waves: the bubble burst mechanism. Geophys Res Lett 27:4077–4080
LeMaire D, Sobieski P, Guissard A (1999) Full-range sea surface spectrum in nonfully developed state for scattering calculations. IEEE Trans Geosci, Remote Sensing 37:1038–1051
Leifer I, de Leeuw G, Cohen LH (2003) Optical measurement of bubbles: system design and application. J Atmos Oceanic Technol 20:1317–1332
Lesieur M (2008) Turbulence in fluids, fourth revised and enlarged edition. Springer. p 148.
Lewis DA, Davidson JF (1982) Bubble splitting in shear flow. Trans IChemE 60:283–291
Lewis ER, Schwartz SE (2004) Sea salt aerosol production: mechanisms, methods, measurements and models. Geophys Monogr Ser.152, pp 413, AGU, Washington, D.C
Liang J-H, McWilliams JC, Sullivan PP, Baschek B (2011) Modeling bubbles and dissolved gases in the ocean. J Geophys Res 116: C03015, doi:10.1029/2010JC006579

Liang J-H, McWilliams JC, Sullivan PP, Baschek B (2012) Large eddy simulation of the bubbly ocean: new insights on subsurface bubble distribution and bubble-mediated gas transfer. J Geophys Res 117:C04002
Lima-Ochoterena R, Zenit R (2003) Visualization of the flow around a bubble moving in a low viscosity liquid. Rev Mex Fis 49:348–352
Lohmann U, Feichter J, Penner J, Leaitch R (2000) Indirect effect of sulfate and carbonaceous aerosols: a mechanistic treatment. J Geophys Res 105:12193–12206
Marmorino GO, Trump CL (1996) High resolution measurements made across a tidal intrusion front. J Geophys Res 101(C11):25661–25674
Martinez-Bazan C, Montanes JL, Lasheras JC (1999) On the breakup of an air bubble injected into fully turbulent flow, part 2, size PDF of the resulting daughter bubbles. J Fluid Mech 401:183–207
Mårtensson EM, Nilsson ED, G de Leeuw, Cohen LH, Hansson H-C (2003) Laboratory simulations and parameterization of the primary marine aerosol production. J Geophys Res 108(D9):4297
McNaughton KG, Brunet Y (2002) Townsend's hypothesis, coherent structures and Monin-Obukhov similarity. Bound -Lay Meteor 102:161–175
Miles JW (1959) On the generation of surface waves by shear flows, part 3, Kelvin-Helmholtz instability. J Fluid Mech 6:583–598
Monahan EC, O'Muircheartaigh I (1980) Optimal power-law description of oceanic whitecap coverage dependence on wind speed. J Phys Oceanogr 10:2094–2099
Monahan EC, Fairall CW, Davidson KL, Boyle PJ (1983) Observed inter-relations between 10 m winds, ocean whitecaps and marine aerosols. Q J Roy Meteor Soc 109:379–392
Monahan EC, Spiel DE, Davidson KL (1986) A model of marine aerosol generation via whitecaps and wave disruption. In: Monahan EC, MacNiocaill G, (eds) Oceanic whitecaps and their role in air-sea exchange. D. Reidel, Dordrecht, pp 167–174
Monin AS, Krasitskii VP (1985) Phenomena on the ocean surface. Hydrometeoizdat, Leningrad, pp 376. (in Russian) Norris SJ, Brooks IM, BI. Moat BL, Yelland MJ, de Leeuw G, Pascal RW, and Brooks B (2013) Near-surface measurements of sea spray aerosol production over whitecaps in the open ocean. Ocean Sci. 9, 133-145
Ocampo-Torres FJ, Donelan MA, Merzi N, Jia F (1994) Laboratory measurements of mass transfer of carbon dioxide and water vapour for smooth and rough flow conditions. Tellus B 46: 16–32
O'Dowd CD, Smith MH (1993) Physiochemical properties of aerosols over the northeast Atlantic: evidence for wind-related submicron sea-salt aerosol production. J Geophys Res 98:1137–1149
O'Dowd CD, G de Leeuw (2007) Marine aerosol production: a review of the current knowledge. Phil Trans R Soc A 365:1753–1774. doi:10.1098/rsta.2007.2043
O'Dowd CD, Lowe JA, Smith MH (1999) Coupling sea-salt and sulphate interactions and its impact on cloud droplet concentration predictions. Geophys Res Lett 26:1311–1314
Pascal RW et al (2011) A spar buoy for high-frequency wave measurements and detection of wave breaking in the open ocean. J Atmos Oceanic Technol 28:590–605
Pattison MJ, Belcher SE (1999) Production rates of sea-spray droplets. J Geophys Res 104:18397–18407
Patro R, Leifer I, Bower P (2001) Better bubble process modeling: Improved bubble hydrodynamics parameterization. In: Saltzman ES, Donealn M, Drennan W, Wanninkhof R (eds) AGU monograph gas transfer at water surfaces pp 315–320
Phelps AD, Ramble DG, Leighton TG (1997) The use of a combination frequency technique to measure the surf zone bubble population. J Acoust Soc Am 101: 1981–1989
Phelps AD, Leighton TG (1998) Oceanic bubble population measurements using a buoy-deployed combination frequency technique. IEEE J Oceanic Eng 23:400–410
Phillips OM (1957) On the generation of waves by turbulent wind. J Fluid Mech 2:417–445
Powell MD, Vickery PJ, Reinhold TA (2003) Reduced drag coefficient for high wind speeds in tropical cyclones. Nature 422:279–283
Prandtl L (1949) Führer Durch die Strömngslehre, 3rd edn. F. Vieweg, Brawnschweig
Pruppacher HR, Klett JD (1978) Microphysics of clouds and precipitation. D. Reidel Publishing Company, Dordrecht, pp 714

Resch FR, Afeti G (1992) Sub-micron film drop production by bubbles in seawater. J Geophys Res 97:3679–3683
Sampson CR, Kaplan J, Knaff JA, DeMaria M, Sisko CA (2011) A deterministic rapid intensification aid. Wea Forecasting 26:579–585
Smith MH, Park PM, Consterdine IE (1993) Marine aerosol concentrations and estimated fluxes over the sea. Q J R Meteorol Soc 119:809–824
Soloviev A, Lukas R (2006) The Near-Surface Layer of the Ocean: Structure, Dynamics and Applications. Springer, Dordrecht, The Netherlands, 574 pp
Soloviev A, Lukas R (2010) Effects of bubbles and spray on air-sea exchange in hurricane conditions. Bound -Lay Meteorol 136:365–376
Soloviev A, Fujimura A, Matt S (2012) Air-sea interface in hurricane conditions. J Geophys Res 117:C00J34. doi:10.1029/2011JC007760
Soloviev A, Lukas R, Donelan M, Haus B, Ginis I (2013) The air-sea interface and surface stress under tropical cyclones. Nature Geoscience (manuscript for submission)
Spiel DE (1997) More on the births of jet drops from bubbles bursting on seawater surfaces. J Geophys Res 102:5815–5821
Spiel DE (1998) On the birth of film drops from bubbles bursting on seawater surfaces. J Geophys Res 103:24907–24918
Thomson W (Lord Kelvin) (1871) Hydrokinetic solutions and observations. Philosophical Magazine. Ser 4 42:pp 362–377
Thorpe SA (1986) Bubble clouds: a review of their detection by sonar, of realistic models, and of how may be determined. In: Monahan EC, MacNiocaill G (eds) Whitecaps and their role in air-sea exchange processes. D. Reidel, Norwell, pp 57–68
Thorpe SA (1982) On the clouds of bubbles formed by breaking wind-waves in deep water, and their role in air–sea gas transfer. P Trans Roy Soc Lon Ser A 304:155–210
Troitskaya YI, Sergeev DA, Kandaurov AA, Baidakov GA, Vdovin MA, and Kazakov VI (2012) Laboratory and theoretical modeling of air-sea momentum transfer under severe wind conditions. J Geophys Res. 117: C00J21, doi:10.1029/2011JC007778
Tsai W (2001) On the formation of streaks on wind-driven water surfaces. Geophys Res Lett 28(20): 3959–3962. doi:10.1029/2001GL013190.
Turner JS (1973) Buoyancy effects in fluids. Cambridge University Press, New York
Veron F, Hopkins C, Harrison EL, Mueller JA (2012) Sea spray spume droplet production in high wind speeds. Geophys Res Lett 39:L16602
Woolf DK (1993) Bubbles and the air-sea transfer velocity of gases. Atmos -Ocean 31:517–540
Woolf DK (1997) Bubbles and their role in air-sea gas exchange. In: Liss PS, Duce RA (eds) The sea surface and global change. Cambridge University Press, UK, pp 173–205
Woolf DK, Thorpe SA (1991) Bubbles and the air-sea exchange of gases in near-saturation conditions. J Mar Res 49:435–466
Black PG, D'Asaro EA, Drennan WM, French JR, Niiler PP, Sanford TB, Terrill EJ, Walsh EJ, Zhang JA (2007) Air-Sea Exchange in Hurricanes: Synthesis of Observations from the Coupled Boundary Layer Air-Sea Transfer Experiment. Bull Amer Meteor Soc 88(3): 357-374
Yecko P, Zaleski S, Fullana J-M (2002) Viscous modes in two-phase mixing layers. Phys Fluids 14:4115–4122

Chapter 7
Applications

Abstract In this final chapter, practical applications of the results obtained from the studies of the near-surface layer of the ocean are considered. These applications range from remote sensing and air–sea interactions to acoustics, optics, biophysical coupling, climate, ship wakes, and oil spill monitoring.

Keywords Remote sensing • Sea surface temperature • Surfactant • Oil spills • Acoustics • Optics • Chemistry • Sea surface salinity • Ship wake, profiling sonar • 3D sonar • SAR • Color imagery • Barrier layer • Ocean state • Coupled system

7.1 Introduction

The state of the sea surface and the near-surface layer of the ocean is a key factor in several important applications. Both remote and in situ sensing for ocean state estimation, ocean weather and climate prediction, pollution monitoring and prediction, and marine ecosystem monitoring and prediction are intimately related to understanding of processes taking place in the near-surface layer. These traditional applications of scientific understanding of the near-surface physics have been augmented by recent application developments in ocean color, acoustic sensing, and near-surface biology. Remote sensing of the sea surface from space can be efficiently complemented with remote sensing of the surface from inside the ocean. Optical and acoustical methods provide exciting opportunities in this direction.

Section 7.2 is devoted to the role of near-surface processes in remote sensing of the ocean from space. Synthetic aperture radar (SAR) and color imagery are characterized by relatively high spatial resolution revealing fine-scale features on the sea surface. These applications are described in separate sections (Sects. 7.3 and 7.4, respectively). Remote sensing of the ocean color is related to the inherent optical properties of the upper ocean, which we discuss in some detail in Sect. 7.5. Section 7.6 is devoted to the biochemistry of the near-surface layer of the ocean. Section 7.7 analyzes acoustic applications, and Section 7.8 is a discussion of parameterizing the near-surface layer processes for ocean and global climate modeling.

A. Soloviev, R. Lukas, *The Near-Surface Layer of the Ocean,* Atmospheric and Oceanographic Sciences Library 48, DOI 10.1007/978-94-007-7621-0_7,

7.2 Remote Sensing of the Ocean

Numerous satellites, as well as Space Shuttle, Mir, and International Space Station missions, have been devoted to collecting oceanographic data. These observations have revealed new phenomena, and have allowed studies of processes on unprecedented space and timescales compared to traditional in situ observations. Important data acquired with satellites include sea surface temperature (SST) and salinity, surface wind speed and direction, surface wave height and direction, sea level, ocean color, and sea ice thickness and extent. Remote sensing methods have found numerous applications in studies of the coastal and shelf waters adjacent to continental margins where inflow and mixing of river waters substantially contribute to the observed patterns. Obvious advantages of satellite remote sensing methods are in the frequent global coverage and generally have consistent accuracy of the data. However, the interpretation of the remotely sensed data often requires detailed knowledge of the processes at the air–sea interface.

7.2.1 Remote Sensing of Surface Winds

The forcing of the near-surface layer of the ocean and its resulting structures critically depend on the wind field and its variations. Surface waves and fluxes of mass, momentum, energy, heat, and gases all strongly depend on wind speed as well. The surface wind stress (as well as heat and moisture fluxes) over the global ocean represents the boundary condition for global circulation models (GCMs). Satellites provide exciting opportunities to measure wind stresses at the sea surface remotely, with global coverage and relatively high spatial resolution. Temporal resolution for a single polar orbiting satellite is determined by the revisit time, ranging from 3 to 30 days depending on the mission. The temporal resolution can, however, be reduced to several hours by using satellite constellations (Liu et al. 2008).

Passive (radiometric) and active (radar) ocean sensors have orbited and continue orbiting Earth, at various times since National Aeronautics and Space Administration (NASA)'s *Seasat* in 1978. NASA's Quick Scatterometer *(QuikSCAT)* has been one of the most sophisticated wind speed and direction satellites, equipped with the *Sea Winds* radar scatterometer. It completed its main mission in November 2009. *QuikSCAT* was capable of estimating wind speeds from surface roughness within the range of 3–20 m s^{-1} with an accuracy of 2 m s^{-1} and an accuracy of 20° for direction with 25 km resolution. NASA plans to replace *QuikSCAT* in 2015. The European Advanced Scatterometer (*ASCAT*) ocean surface winds system aboard the The European Organization for the Exploitation of Meteorological Satellites (EUMETSAT) METeorological OPerational (METOP) polar orbiting satellite has been providing a partial replacement for *QuikSCAT* surface winds during the interim period.

WindSat, a satellite-based polarimetric microwave radiometer developed by the US Navy, also provides ocean surface wind vector measurements (Geiser 2004). An example of the ocean surface wind map from *WindSat* is shown in Fig. 7.1. The wind

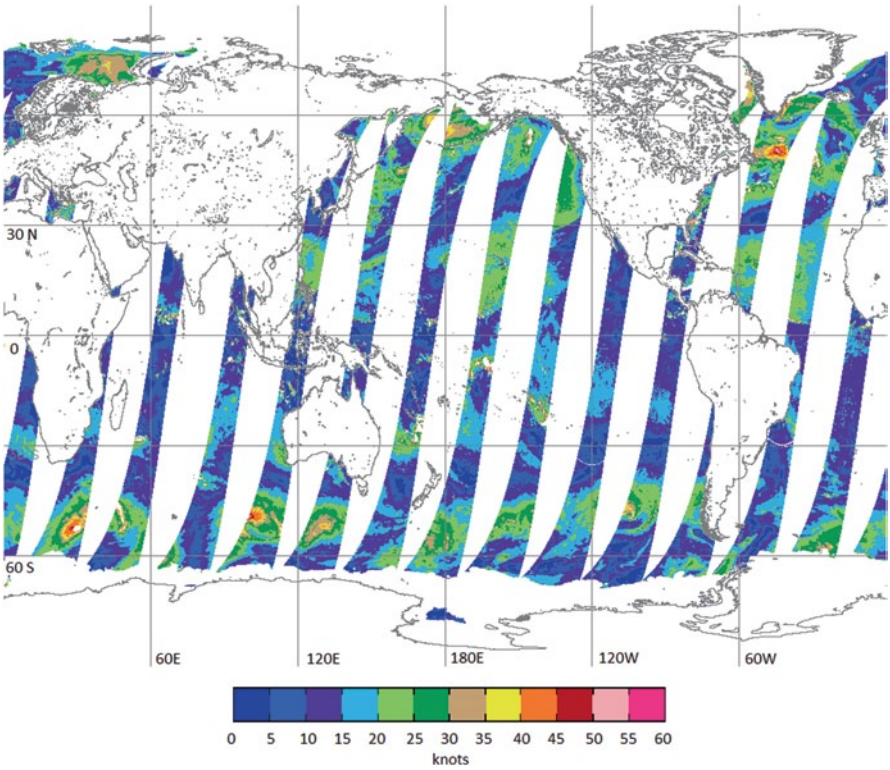

Fig. 7.1 A *WindSat* ocean surface wind map (ascending trajectory) for December 22, 2012. (http://www.nrl.navy.mil/WindSat/)

vector measurement accuracy of this passive sensor is comparable to that of *QuikSCAT* except for low wind speed or heavy rain conditions (Gentemann et al. 2010).

In order to utilize these remote measurements in the most effective way, understanding of both the detailed structure and dynamics of the ocean surface and the physics of electromagnetic wave scattering from the sea surface is required. The remote sensing of the wind velocity vector is possible due to the amplitude and directional correlation between the wind and sea-state parameters. The sea surface roughness almost entirely determines the scattering of radar signals. Gravity-capillary waves with wavelengths of ~0.01 m directly influence microwave scattering and radiance emission; a precise knowledge of the short-scale-wave roughness is therefore required (Janssen 2007). Due to nonlinear interactions, short waves are coupled with intermediate and long waves. Full wave number models of the surface roughness such as that of Donelan and Pierson (1987), Apel (1994), Elfouhaily et al. (1997), and Hwang (1997) have been widely used in microwave radar scattering studies. The problem, however, has not yet been completely solved because of the complex nature of the processes governing sea surface roughness and the

physics of electromagnetic wave interaction with the sea surface (Voronovich and Zavorotny 2001).

The problem of inverting the backscattered radar signal into useful information is related to (1) better understanding of how the variables of wind speed and direction, atmospheric thermal stability, SST, salinity, currents, rain, and bathymetry are related to the surface state, and (2) how the statistical properties of the sea surface can be extracted from backscattered radar signal. The first issue is inherently related to physics of the near-surface layer of the ocean. In particular, near-surface turbulence (Chap. 3), surface-intensified jets (Chap. 4), and the two-phase environment under very high wind speeds (Chap. 6) can affect gravity-capillary waves and, thus, the sea surface roughness. These effects may explain some discrepancies between theoretical and field results on electromagnetic scattering from the sea surface and have yet to be incorporated into remote sensing algorithms.

7.2.2 Sea Surface Temperature

SST is the primary ocean variable in air–sea interaction, and its space–time variability is closely tied to the atmosphere. SST is an important variable in many research and operational applications.

The wind–wave mixing, shear, and convection produce the surface mixed layer. The surface mixed layer participates in large-scale air–sea interaction, has substantial heat capacity, and is an important element of the weather and climate system. How the SST is connected to the temperature structure of the surface mixed layer is of interest for many practical applications, including the development of remote-sensing techniques for monitoring the climate and global carbon cycles. In fact, the SST differs from the temperature of the bulk of mixed layer due to the aqueous thermal molecular sublayer, the cool skin of the ocean (Sect. 2.2.2), surface-active materials (Sect. 2.3.7), diurnal warming (Sect. 4.2.1), and freshwater addition by precipitation (Sect. 2.6 and 4.2.4).

Thermal infrared (IR) imagery from satellites is an important source of information about the ocean. There are two atmospheric windows where absorption is a minimum (Fig. 7.2). The instruments deployed on aircraft usually utilize the 3–5 μm and 8–14 μm wavelength ranges, while the satellite-based sensors normally use the 3–4 μm and 10.5–12.5 μm windows. In the 10.5–12.5 μm range, radiant energy is absorbed by ozone. Water vapor and carbon dioxide absorb some of the radiation energy across the entire spectrum. As a result, both windows require corrections to account for atmospheric absorption. In addition to the water vapor absorption, the solar beams reflected from the ocean surface can contaminate the 3–4 μm window during daytime hours.

The primary IR sensor on US meteorological satellites has been the advanced very high-resolution radiometer (AVHRR). AVHRR has five measuring channels. Channel 3 (λ=3.55–3.93 μm), Channel 4 (λ=10.30–11.30 μm), and Channel 5

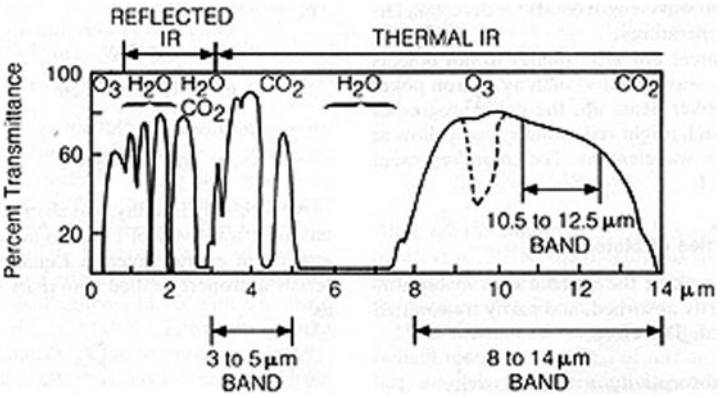

Fig. 7.2 Spectral plot of the atmospheric transmission in the infrared band. (Reproduced from Sabins, F.F., Remote Sensing Principles and Interpretation, 2nd ed. 449 PP. Copyright © 1987 WH Freeman & Co.)

($\lambda = 11.50–12.50$ μm) are in the window of atmospheric transparency and are used for SST measurements.

The Terra and Aqua satellites carry the moderate-resolution imaging spectroradiometer (MODIS), which is a 36-band spectroradiometer measuring, among other parameters, visible and IR radiation. The accuracy of the SST measurement with MODIS is several times higher than with AVHRR, approaching 0.1°K in favorable conditions. IR SST measurements are, however, strongly affected by the presence of clouds.

The temperature difference across the cool skin of the ocean is typically of the order of 0.2–0.3°C but can increase to 0.4–0.6°C under low wind speed conditions. Intense insolation at midday and/or air temperature exceeding water temperature can reverse the temperature gradient within the thermal molecular sublayer; the sea surface can become slightly warmer than the underlying water (Sect. 2.5). With the accuracy of the satellite techniques approaching 0.1°C, the aqueous thermal molecular sublayer has been included in some advanced remote-sensing algorithms starting from the pioneering work of Schlüssel et al. (1990).

Under light winds, the near-surface layer of the ocean is often re-stratified due to diurnal warming and/or precipitation effects. A thin near-surface mixed layer is formed. Its heat capacity is comparable to the heat capacity of the atmospheric boundary layer. Under these conditions, the near-surface layer of the ocean can rapidly respond to changes in the atmospheric state; as a result, both oceanic and atmospheric processes determine the SST.

Katsaros and DeCosmo (1990) hypothesized that the air–sea heat flux could control the interface temperature and result in smoothing of underlying spatial inhomogeneities of SST. This effect is illustrated in Fig. 7.3 with an example from the Florida Straits, which shows 3-day composite AVHRR during (a) winter and (b) summer. The Gulf Stream is clearly traced in the SST winter image, while it is almost completely masked in the SST image acquired during summer. Katsaros

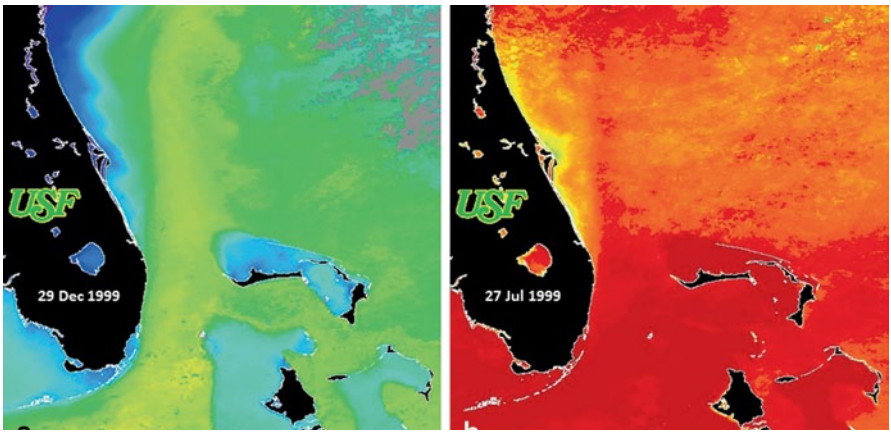

Fig. 7.3 Three-day composite Advanced Very High Resolution Radiometer (AVHRR) images of the Florida Straits during **a** winter and **b** summer. Note that the Gulf Stream clearly seen in the winter image is substantially masked by solar warming in the summer that not only produces the near-surface vertical temperature gradients but also diminishes the horizontal temperature gradients due to the effect of atmospheric regulation. (Adapted from Katsaros and Soloviev (2003) with permission from Springer Science and Business Media)

and Soloviev (2003) explain this observation as an effect of atmospheric regulation of diurnal SST amplitudes (see Sect. 4.6.3 for more details). The cooling of the sea surface by sensible and latent heat fluxes and net longwave radiation would be larger from the warmer water than from the cooler side of fronts or eddies, leading to greater diurnal heating on the cool side. This results in a decrease of the horizontal SST differences and possible erroneous conclusions about the ocean processes (Katsaros et al. 1983; Katsaros and Soloviev 2003; Katsaros et al. 2005). The atmospheric regulation can be additionally enhanced due to a positive correlation between SST and wind speed often observed on the mesoscale: regions with lower SST typically have lower winds, which leads to stronger diurnal warming. Interpretation of remotely sensed SSTs requires that this phenomenon becomes better understood and its frequency and importance in nature is assessed.

Clouds are the major obstacles in obtaining useful oceanographic information from satellite IR imagery. They may cover extended areas of the ocean up to 90% of time. Microwave thermal measurement of the ocean surface (for instance, with Special Sensor Microwave/Imager, SSM/I) is not affected by clouds, but its accuracy is far below that of IR sensors. Also, rains affect the microwave measurement by modification of the sea surface reflectance.

One approach to enhance capabilities of IR SST measurements is to combine the remote-sensing techniques with the mixed-layer models reproducing diurnal warming and precipitation effects (as well as the cool skin) and being forced with remotely sensed heat and momentum fluxes derived from microwave sensors (Soloviev and Schlüssel 2002). Several issues have yet to be resolved for this approach, which requires assimilation of multi-satellite and multi-sensor data in

order to have accurate estimates of surface fluxes. Notably, substantial progress has been made in the development of remote-sensing techniques for latent and sensible heat fluxes with accuracies of satellite products approaching the accuracy of buoy and shipboard bulk-flux measurements (Bentamy et al. 2003; Jo et al. 2004).

Another approach is to combine different types of satellite and in situ data. The in situ measurements are typically made at a few meter depths. The satellite SST comes either from a several micrometers thick layer (IR techniques) or from a few centimeters thick layer (microwave techniques) of the ocean. In order to reduce the effect of clouds, Martin et al. (2012) have combined IR and microwave data sets to produce global, continuous in time and space SST data sets using optimal interpolation techniques. Assimilation of in situ data may help to provide a better insight into the state of the upper ocean.

7.2.3 Sea Surface Salinity

Salinity is a major contributor to the ocean circulation, global water cycles, and climate variations (Fedorov 1991; Broecker 1991). Upper ocean salinity is an important parameter for El Niño Prediction (Ballabrera-Poy et al. 2002). Near-surface salinity structure strongly affects dynamics of tropical instability waves (Lee et al. 2012). Rapid intensification of hurricanes has been associated with the presence of the barrier layer observed over the Amazon River low-salinity plume (Grodsky et al. 2012).

The Global Ocean Data Assimilation Experiment requirement is to measure sea surface salinity with an accuracy of 0.1 psu in boxes of 200×200 km on a 10-day average. The measurement of the sea surface salinity from space can significantly improve understanding of ocean circulation, air–sea interaction, and the global climate as a result (Lagerloef et al. 1995). The water emissivity in the microwave range depends on salinity. In the long-wavelength end of the microwave spectrum (L- or C-band), the response due to changes in salinity is sufficiently strong to distinguish from the temperature dependence, though it is still a second-order effect. In order to obtain adequate resolution at the surface for longer wavelengths, large antennas must be placed in space.

The measurement of salinity from space became more practical with the emergence of aperture synthesis; this is the new microwave radiometer technology that does not require such large antennas. Le Vine et al. (1998) have shown the theoretical possibility of measuring sea surface salinity with airborne SAR. Figure 7.4 compares remote (airborne) and shipboard measurements of sea surface salinity made by these authors in the vicinity of the Delaware coastal current. The remote-sensing measurements were made from an aircraft with the Electronically Scanned Thinned Array Radiometer (ESTAR), which is an L-band synthetic aperture microwave radiometer. Both thermosalinograph- and microwave radiometer-derived salinity maps clearly show the freshwater signature of a coastal current and generally are in agreement to within about 1 psu.

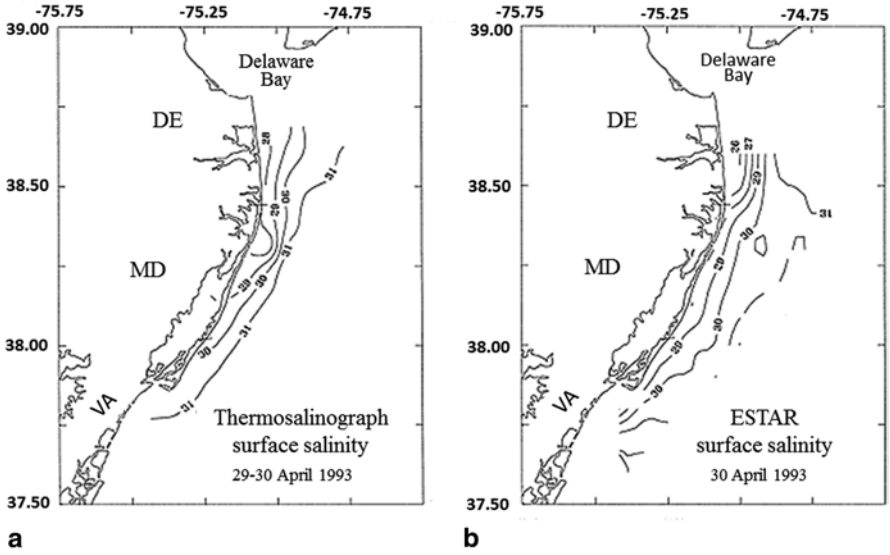

Fig. 7.4 Comparison of salinity fields obtained from **a** the thermosalinograph data and **b** from an airborne remote sensing instrument (ESTAR). (Reproduced from Le Vine et al. (1998). Copyright © 1998 American Meteorological Society. Used with permission)

Further progress in this direction has resulted in development of satellite technology, which is capable of measuring sea surface salinity on a global scale (Berger et al. 2002). The European Space Agency's Soil Moisture and Ocean Salinity (SMOS) satellite launched in 2009 uses the synthetic aperture concept. The NASA/Comisión Nacional de Actividades Espaciales (CONAE) Aquarius satellite launched in 2011 uses a large-size real-aperture antenna (Lagerloef 2012).

Salinity remote sensing from SMOS and Aquarius involves measuring the ocean's surface microwave emission in the L-band portion of the spectrum protected for radio astronomy. Dependence of the microwave emissivity on salinity decreases with reducing temperature; as a result, the salinity retrieval error increases toward the poles. Uncertainty in the sea surface roughness is the largest error source in the salinity retrieval. For wind speeds above 12–15 m s^{-1}, salinity retrieval becomes a major challenge (see Chap. 6 for discussion of wave spectrum under strong winds).

According to Boutin et al. (2012), over selected regions far from land and sea ice borders and after mean bias removal, the uncertainty on sea surface salinity retrieved from SMOS and averaged over 100×100 km and 10 days is between 0.3 psu and 0.5 psu. Aquarius, in addition, measures radar backscatter and therefore is potentially better suited to correct for the emission variations due to surface roughness (Yueh et al. 2010). The goal of these two missions is to achieve accuracy of the sea surface salinity averaged over 150–200 km and 1 month of ~0.2 psu (Boutin et al.

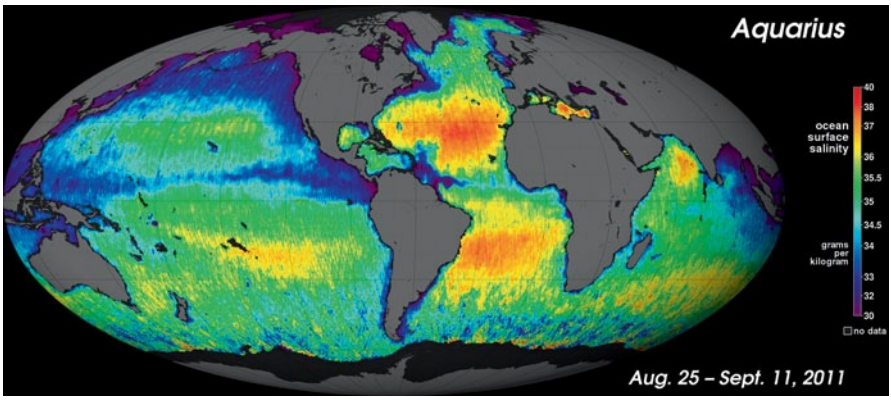

Fig. 7.5 **a** Mean global image for the first two and half weeks of Aquarius satellite sea surface salinity measurements. The north–south striped patterns are artifacts of small residual calibration errors. Values adjacent to coastlines, islands, and ice edges are biased low by the land–ice proximity. The image from the public domain of the National Aeronautics and Space Administration (NASA) Website (http://aquarius.umaine.edu/cgi/gallery.htm)

2012; Lagerloef 2012). Although there are still some challenges ahead, early results are promising.

The sensors working in the L-band ($\lambda = 24$ cm) receive signals from the upper centimeters of the ocean. Improving interpretation of salinity remote sensing therefore requires incorporation of detailed knowledge of near-surface salinity structure into the analysis. For instance, appreciable salinity difference in the near-surface layer of the ocean can develop due to rainfalls (Sect. 2.6 and 4.2).

Figure 7.5 shows mean composite global images of Aquarius salinity measurements averaged from the initial two and half weeks of data of data, 25 August to 11 September 2011 (Lagerloef et al. 2012). The global salinity map contains the well-known oceanographic features associated with salinity. In particular, it shows higher salinity in subtropical gyres, lower average salinity in the Pacific Ocean and Indian Ocean subtropical gyres relative to the Atlantic Ocean subtropical gyre, and lower salinity in the Intertropical Convergence Zone (ITCZ) and the western Pacific warm pool area. (Salinity retrievals in the Southern Ocean are, however, difficult because of high winds and low water temperatures.) The low-salinity plume from the Amazon River and the tropical instability waves in the equatorial Pacific can also be identified in Fig. 7.5.

Knowledge of the precipitation distribution will be helpful for the interpretation of remotely sensed salinity (as well as for many other applications). The first specialized satellite for precipitation measurements was the Tropical Rainfall Mapping Mission (TRMM). The results of the intercomparison between this satellite and the Tropical Ocean-Global Atmosphere Coupled Ocean-Atmosphere Response Experiment (TOGA COARE) rain radar shown in Fig. 7.6 are very promising. Note that the satellite-derived rain rates can be used to force the mixed-layer model aimed at enhancing the remote sensing of SST (see discussion in the previous section).

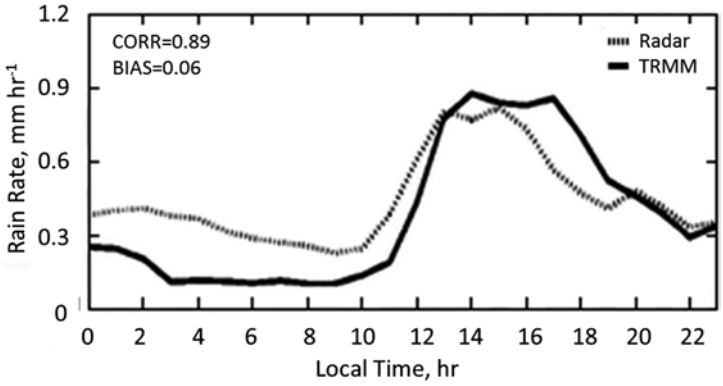

Fig. 7.6 The composite diurnal cycle from rainfall measurements during the Tropical Rainfall Measuring Mission (TRMM) using the microwave imager and precipitation radar, compared with the composite diurnal cycle from the TOGA COARE rain radar. The correlation coefficient and bias between the radar and satellite data are shown in the upper left corner of the graph. (Reproduced from Sorooshian et al. (2002). Copyright © 2002 American Meteorological Society. Used with permission)

The Global Precipitation Measurement (GPM) satellite is scheduled for launch in 2014 as a successor of TRMM. The GPM mission will include an advanced TRMM's microwave imager and dual-frequency precipitation radar. This NASA satellite is expected to extend coverage beyond the tropics to the Arctic and Antarctic.

7.2.4 Surface Ocean Currents

Ocean currents play a major role in the global heat transport and weather and climate (Broecker 1991). Practical applications of the remote-sensing data on currents are numerous including marine navigation, search and rescue operations, propagation of water pollutants (including oil spills), and health of marine ecosystem (see, e.g., recent reviews in Purkis and Klemas 2011; Klemas 2012). Remote sensing of the ocean currents provides important opportunities for studying ocean dynamics, (space) estimating the state of the ocean, and testing forecast models.

The ocean drifters that are tracked from satellites can provide the speed and direction of near-surface currents. The movements of natural surface features can be identified from satellites in temperature, color, or in the visual wavelength band, and, to some extent, provide information on the ocean current direction and velocity. Satellite-based altimeters provide information on surface currents from geostrophic balance calculations. These calculations combined with winds and the Ekman theory yield useful operational near-global surface layer current products (Lagerloef et al. 2003).

Ocean surface currents can be measured remotely with high-frequency (HF) radio waves due to the Bragg scattering effect. This effect results from coherent

reflection of the transmitted energy by ocean surface waves whose wavelength is exactly one-half of the transmitted radar waves (Paduan and Graber 1997). These coherent reflections produce a strong peak in the backscatter spectrum. Note that scatterometers exploit Bragg scattering from capillary waves (~1 cm) to obtain information about winds. HF radars exploit Bragg scattering from surface gravity waves ($\lambda \sim 10$ m) to obtain information about currents (as well as waves and winds). On combining simultaneous measurements from two separated sites, maps of surface current vectors can be created.

HF radar provides information about currents from the near-surface layer of the ocean with effective thickness equal to one-half of the radio wavelength, $\lambda/2 \sim 5$ m. The surface-intensified jets developing due to diurnal or freshwater influx in the near-surface layer of the ocean (Chap. 4) can affect the interpretation of the HF radar data.

At this point, HF radars have found important applications in coastal ocean studies (Shay et al. 2002; Flores-Vidal et al. 2013). There have also been attempts to employ the HF radar for offshore surface current measurements (Peters and Skop 1997). Ship-based HF observations, however, suffer from motion of the ship, which complicates the measurement due to the degradation of spectral returns.

However, the Wave and Surface Current Monitoring System (WaMoS) is able to produce directional ocean wave spectra and current velocity vector both from fixed platforms and moving ships (Borge et al. 2004). WaMoS uses the output from marine X-band radar and provides the essential wave parameters (significant wave height, peak wave period, and peak wave direction) as well as surface current speed and current direction.

Determination of surface currents is also possible from SAR imagery, which opens a new exciting opportunity to study global ocean circulation from space (Chapron et al. 2004). The following two techniques have been developed for the direct retrieval of line-of-sight surface current fields from SAR data: along-track interferometry (ATI) and Doppler-based centroid estimation. ATI requires two satellite antennas, while the Doppler-based centroid techniques use conventional SAR raw data (though with lower spatial resolution).

At this point, the SAR techniques can measure only the strong currents that have a favorable direction with respect to the satellite track, which is a signal-to-noise issue. However, the spaceborne Doppler-based techniques and ATI seem to have the potential to develop into a widely used remote-sensing method (Romeiser et al. 2010).

7.3 High-Resolution Microwave Imagery of the Sea Surface

In Chap. 5, we have seen that fine horizontal features on scales less than the typical scale of the upper ocean mixed layer depth (1–100 m) are often associated with 3D processes. Microwave imagery appears to be a useful tool for studying surface signatures of such processes.

The new generation of SAR satellites (*TerraSAR-X*, *RADARSAT-2*, *ALOS PALSAR*, *COSMO-SkyMed*) provides imagery of the sea surface starting from meter scale, also in dual or quad polarization (Biao and Perrie 2012). Satellite-based SAR has the advantage of penetrating through clouds and is independent of the time of day. As the SAR technology continues to advance, it produces better and higher resolution images of the ocean surface. These technological achievements open new opportunities to study physical processes in the upper ocean.

Airborne SAR can provide repeat-pass measurements at timescales much smaller than satellite SAR. An uninhabited aerial vehicle SAR (UAVSAR) was useful for monitoring the Deepwater Horizon oil spill in the Gulf of Mexico. The UAVSAR's significantly higher signal-to-noise ratio allowed discrimination of oil slick thickness, fractional surface coverage, and emulsification (Leifer et al. 2012).

The SAR techniques exploit electromagnetic waves of a several-centimeter or decimeter wavelength and are based on the Doppler shift in the radio signal reflected from the surface waves of comparable wavelength (Bragg scattering waves). The short surface waves are affected by the near-surface shear and orbital velocities of longer waves. In addition, the atmospheric wind patterns, the surface-intensified jets (Sect. 4.3), the aqueous viscous sublayer (Sect. 2.2.1), and the shape of the short wave portion of the wave spectrum appear to be of importance for extracting useful information about ocean currents from SAR imagery. Interpretation of SAR images is therefore a complex problem including upper ocean dynamics, presence of surface-active materials, wind–wave interactions, atmospheric forcing, and parameters of the satellite antenna.

The fine-scale features observable in SAR include the surface signature of natural processes, such as sharp frontal interfaces, freshwater plumes, and internal waves, as well as the signature of human activity, such as ship wakes and oil spills. The presence of natural or anthropogenic surfactants, which concentrate in convergence zones, can enhance or mask the visibility of these features. Atmospheric phenomena such as rain, atmospheric fronts, and atmospheric internal waves can also leave signatures on the sea surface, which complicate the interpretation of SAR imagery (Alpers and Huang 2011; Soloviev et al. 2012b).

Observations of oceanic fronts in SAR have been reported in a number of studies including Bulatov et al. (2003), Johannessen et al. (2005), and Soloviev et al. (2012b). Surface signatures of internal waves were discovered in the images received from the first SAR satellite (SEASAT) launched by NASA in 1978 (Fu and Holt 1982). Centerline wakes of ships are sometimes traced tens of miles behind the ship in SAR imagery (see, e.g., Reed and Milgram 2002; Soloviev et al. 2011 and others). Propagating freshwater plumes can also create fine-scale features on the sea surface visible in SAR images (Nash and Moum 2005; Matt et al. 2012a).

For ocean applications, SAR responds to patterns of surface gravity-capillary waves in the range from a few centimeters to a few decimeters, depending on the selected band of electromagnetic wave frequency. The gravity-capillary waves can be affected by convergence–divergence zones on the sea surface due to internal oceanic processes, by atmospheric processes (rain, wind gusts, coherent structures, and stratification in the marine boundary layer), and by the presence of surfactants or oil spills.

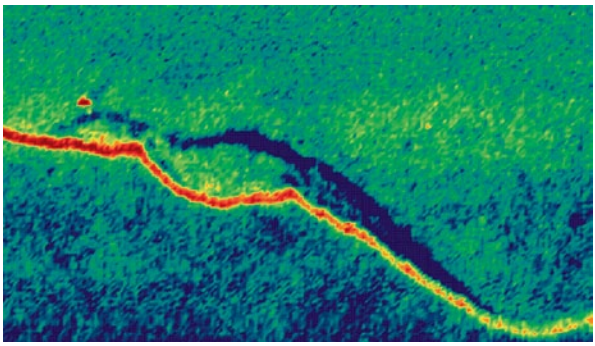

Fig. 7.7 Convergent front on the continental shelf detected by airborne radar. This X-band radar image (~2.25×1.25 km) was one of several collected by Farid Askari (NRL) near Cape Hatteras, NC, during the first high resolution remote sensing experiment. (This image is from the public domain of the Noval Research Laboratory Website http://rsd-www.nrl.navy.mil/7250/)

The role of surfactants in remote sensing of the sea surface with SAR has been extensively studied for several decades (see, e.g., Alpers and Hühnerfuss 1989; Hühnerfuss et al. 1996; Gade et al. 1998; Ermakov et al. 2002; see also Gade et al. 2006 for an extensive review). In a study including numerical simulation and laboratory experiments, Soloviev et al. (2011) and Matt et al. (2011) have found that the suppression of turbulence below the sea surface by surfactants resulted in an increase of temperature difference across the millimeter-scale thermal molecular sublayer by a factor of 2 (see Chap. 2). This can affect high-resolution sea surface imagery in IR and provide a link between SAR and IR features, since surfactants appear to simultaneously modify gravity-capillary waves, near-surface turbulence, and the aqueous thermal diffusion sublayer (cool skin).

7.3.1 Surface Features of Natural Origin

A variety of the oceanic structures such as fronts, meanders, eddies, and river plumes can be studied using the microwave imagery of their surface signatures. Figure 7.7 shows a convergent front on the continental shelf detected by airborne X-band radar operating in the 2.4–3.8 cm wavelength range. This is an image collected by Farid Askari (Naval Research Laboratory, NRL) near Cape Hatteras, NC, during the first high-resolution remote-sensing experiment. This converging front (rip) developed at the shoreward boundary of a Gulf Stream meander and the continental shelf waters. The red line indicates high backscatter, while the dark blue line supposedly corresponds to low backscatter due to an accumulation of surfactants on the north side of the rip.

The appearance of sharp frontal interfaces is usually an indication of an active subduction process (Chap. 5). Remotely sensed images of sharp frontal interfaces may therefore potentially contain information about the vertical structure of the upper ocean.

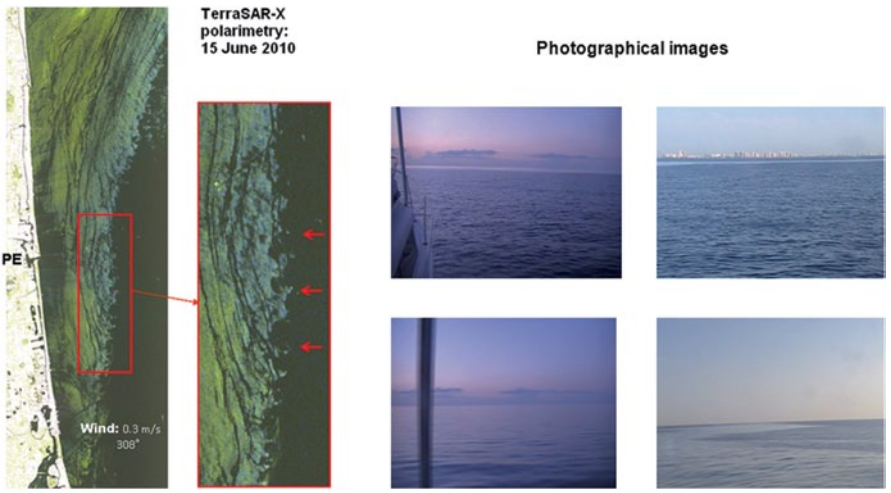

Fig. 7.8 The Gulf Stream front and expanded view showing slick lines and submesoscale frontal eddies in *TerraSAR-X* imagery. These features were seen throughout the coastal area and were confirmed with the photos taken from the R/V *Panacea* before this satellite overpass. (After Soloviev et al. 2012b)

Figure 7.8 shows results of an experiment during very low wind speed conditions. The SAR images suggest that the ocean surface in the core of the Gulf Stream is practically smooth. The coastal area on the western flank of the Gulf Stream is, however, intermittently covered by ripples. This coastal area includes elongated slick lanes, which are predominately directed along the coastline. The nature of these slick areas is not completely clear. One possibility is that it was due to a difference in the SST between the Gulf Stream and coastal water. During this experiment in July, the SST in the coastal waters near Ft. Lauderdale, FL, was higher than in the Gulf Stream. This could result in the convection motions above the coastal waters inducing short gravity-capillary waves on the sea surface.

Another possibility is that because this experiment was coincidently conducted during the Deepwater Horizon oil spill in the Gulf of Mexico, some undetected oil spill products containing surface-active materials (e.g., dispersants) could be transported by the Gulf Stream through the Straits of Florida in a diluted form during this time. Note that the bacterial content of the near-surface layer sampled during this time period included increased the presence of oil-transforming and surfactant-associated bacteria (Kurata et al. 2013).

The elongated slick areas in the coastal waters could be caused by internal waves generated due to bottom topography or by the freshwater plume discharging from the Port Everglades channel. The latter mechanism has been conceptually modeled y Matt et al.(2012a).

The sonar transect and vertical temperature profile taken just after the satellite overpass time are shown in Fig. 7.9. The sonar transect was conducted by profiling the water column. The vessel was moving in an approximate east-to-west direction

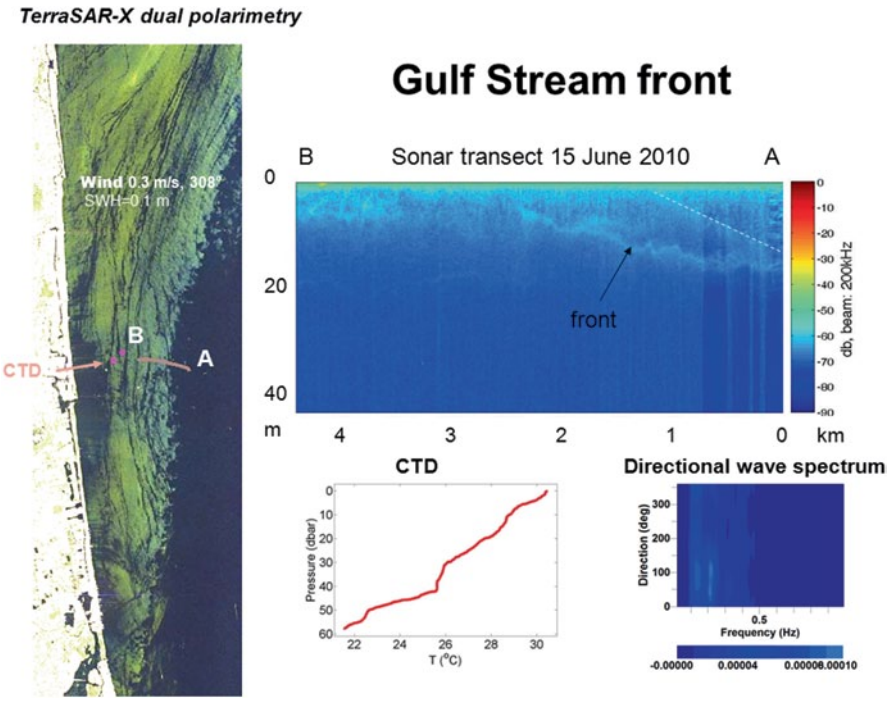

Fig. 7.9 (*Left*) *TerraSAR-X* image with location of CTD cast marked by red dot and trajectory of the research vessel for the horizontal transect marked by the pink line from A to B. A sharp front on the western flank of the Florida Current observed in the SAR image is presumably associated with an inclined front visible in the horizontal sonar transect. The dashed white line on the sonar contour plot is an acoustic artifact (late echo). The temperature profile measured from the CTD cast taken at a location as indicated by the red dot (N26°07.030 W80°04.154) and directional wave spectrum from the bottom-mounted AWAC instrument are shown at the bottom of the figure. (After Soloviev et al. 2012b)

from point A to point B on the map. This is also indicated in the sonar plot from A to B.

During this transect, a frontal feature observed with sonar approached the surface in approximately the same area as the front observed in the SAR image. Vertical temperature profiles obtained inshore of this area confirmed the presence of thermal stratification in the upper ocean layers.

Internal waves can have signatures in SAR imagery (Alpers 1985). Figure 7.10a demonstrates a COSMO-SkyMed SAR image taken during an experiment in the Straits of Florida, which reveals a wave-like pattern. This pattern is presumably due to internal waves developing in the thermocline.

Atmospheric internal waves and atmospheric boundary-layer rolls can also produce a wave-like pattern in SAR image. However, the structure of the wave-like pattern shown in Fig. 7.10a is consistent with oceanic internal waves (Alpers and Huang 2011). Note that large-amplitude internal wave solitons are an observable

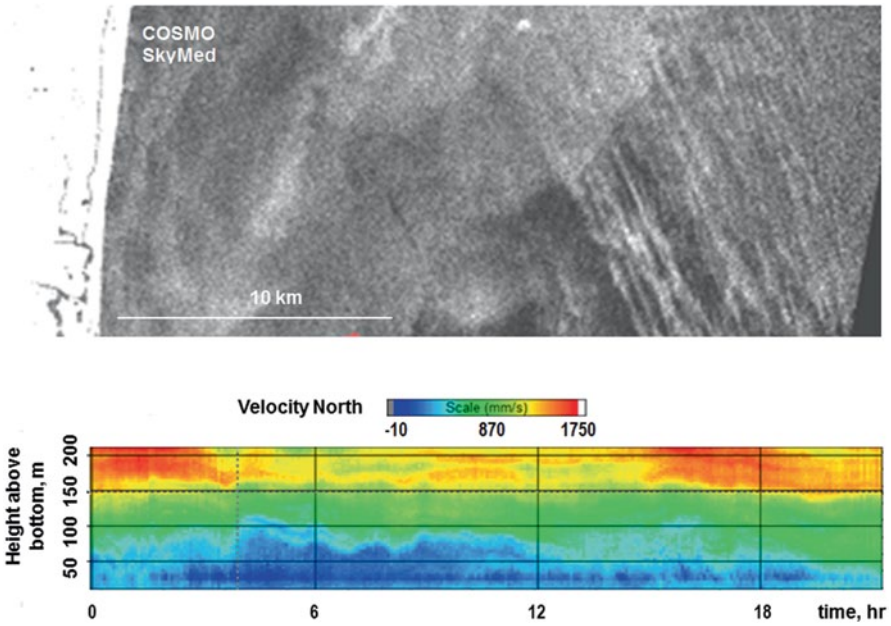

Fig. 7.10 Internal wave soliton in the Straits of Florida observed in SAR imagery and in situ measurements with a bottom acoustic Doppler current profiler deployed on Miami Terrace at a 245-m isobath

feature in the area of our experiments. Figure 7.10b shows such an example obtained around the time of the SAR satellite overpass.

Propagating freshwater plumes can produce prominent signatures in SAR images due to generation of internal waves. Figure 7.11 shows an example of the SAR signature of a freshwater plume. Simultaneous sonar measurements revealed the train of large-amplitude internal waves (Fig. 7.12). Matt et al. (2012a) demonstrated that such internal waves observable in SAR could be due to resonant interaction of freshwater plume propagating as gravity currents with environmental stratification (see also Chap. 5).

7.3.2 Wakes of Ships

A typical ship wake consists of a bow Kelvin wave, stern Kelvin wave, transverse Kelvin wave, centerline wake, and a turbulent region adjacent to the ship (Fig. 7.13). Often, one or more features of the wake could not be found in the satellite SAR images (Eldhuset 1996; Reed and Milgram 2002; Hennings et al. 1999). The centerline ship wake usually appears in SAR images as a dark scar. This feature is often the most prominent part of the wake image in SAR (Reed and Milgram 2002). The centerline wake can be traced behind the ship for tens of kilometers (Fig. 7.14a). However, in other cases, the ship wake quickly disappears (Fig. 7.14b).

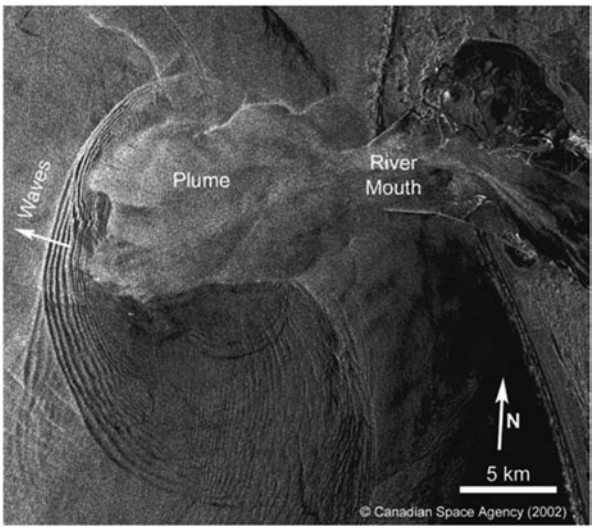

Fig. 7.11 SAR image of the Columbia River plume. (After Nash and Moum (2005) by permission of Nature)

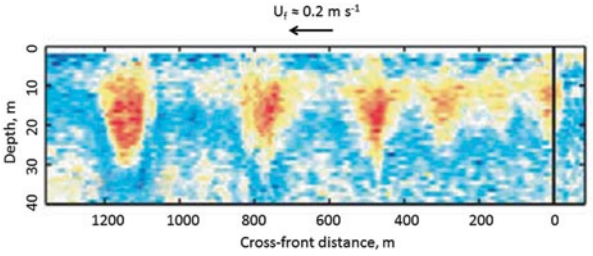

Fig. 7.12 Sonar image of a propagating train of internal waves associated with the plume shown in Fig. 7.11. (After Nash and Moum (2005) by permission of Nature)

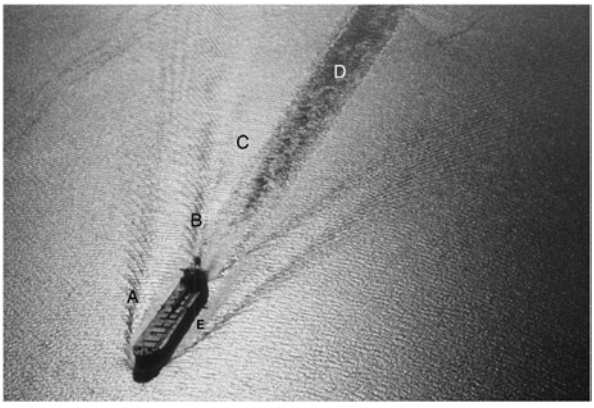

Fig. 7.13 Photograph of a ship and its wake in Chesapeake Bay near Annapolis, MD, showing classic Kelvin and turbulent wakes. Wake components: **a** bow wave, **b** stern wave, **c** transverse wave, **d** turbulent wake, and **e** turbulent region adjacent to ship, After Pichel et al. (2004). (Copyright © 2004 NOAA)

For detection and surveillance purposes, the ship wake creates additional opportunities because of its size and shape and additional parameters of the ship including direction, speed, and perhaps some additional information pertaining to the ship (see, e.g., Brusch et al. 2011). The appearance of the centerline wake is associated

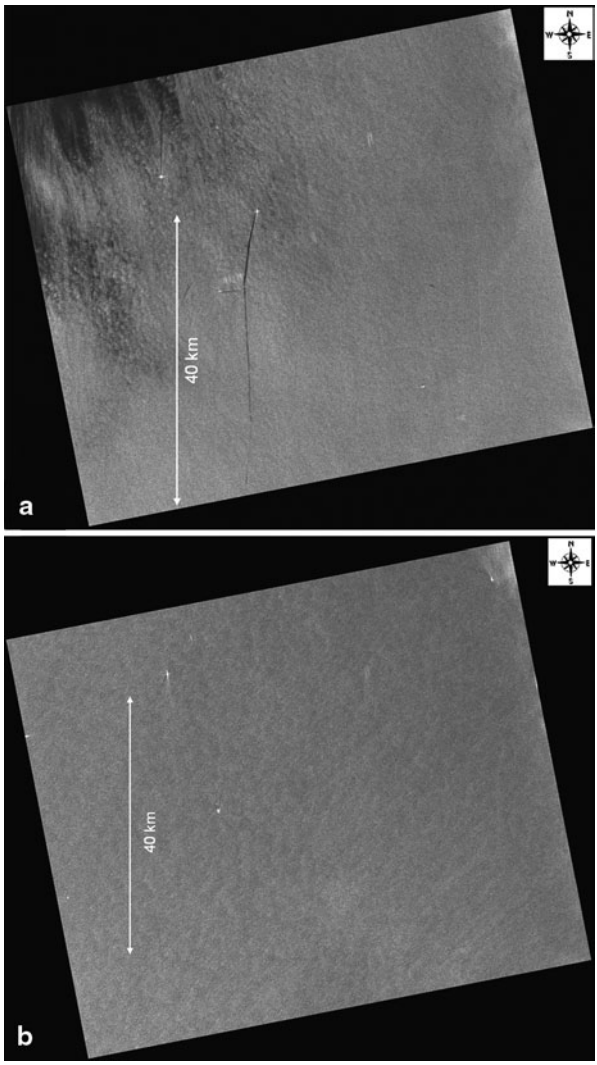

Fig. 7.14 ALOS PALSAR images taken in the Straits of Florida with **a** prominent and **b** almost invisible wakes behind moving ships. (After Soloviev et al. (2012a). Copyright © 2012 American Meteorological Society. Used with permission)

with the reduction of surface roughness due to the suppression of short (Bragg scattering) surface waves by surfactants, wave–current interactions, and turbulence in the wake (Fig. 7.15). The topic of ship detection is extensively covered in reviews by Milgram et al. (1993), Peltzer et al. (1992), Crisp (2004), Greidanus and Kourti (2006), and Brusch et al. (2011).

Gilman et al. (2011) analyzed a large data set of high-resolution photographic images of the far wake of a volunteer observing ship (Royal Caribbean's *Explorer of the Seas*) under various meteorological conditions and ship operation modes. This cruise ship is equipped with the state-of-the-art atmospheric and oceanic science laboratories, which are managed by the University of Miami's Rosenstiel School of

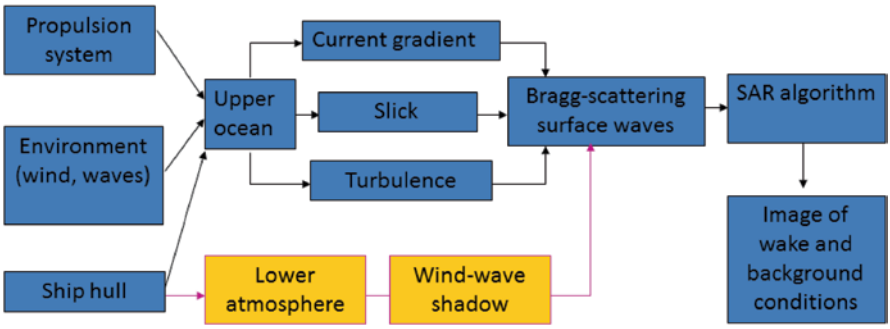

Fig. 7.15 SAR imaging of ship wakes. Effects of stratification, screening of the wind field by the ship superstructure, long/short wave modulation, and coherent structures add more complexity to these schematics. An example of the wind-wave shadow wake is shown in Fig. 7.23

Marine and Atmospheric Science. An astern-looking digital camera with a telephoto lens was installed on the top of a mast to obtain high-resolution images of the ship's wake during an approximately 1-year period. During this experiment, the ship was sailing from Miami and New Jersey to the Caribbean, Bermuda Islands, New England, and Eastern Canada.

Figure 7.16 presents two SAR images of the wake of the Royal Caribbean's *Explorer of the Seas* obtained from the RADARSAT-1 satellite. The big bright speckle on both images is the *Explorer of the Seas*. The centerline wake appears as a dark scar due to the suppression of roughness by the wake currents and surface films. The pairs of white dots are superimposed on the image at the positions corresponding to the averaged experimental values of pairs obtained from the *Explorer of the Seas* photographic measurements (Gilman et al. 2011). While these two cases represent different ship speeds, the shape of both wakes in radar images is consistent with the averaged shape measured from the photographic images.

Figure 7.17 shows the ship wake profile in SAR intensity cross section through the centerline wake. The average wake width obtained from the photographic images is indicated by a pair of vertical dashed lines. These plots suggest a good correlation between satellite-borne and ship-based measurements.

Another feature of the centerline wake is its asymmetry with respect to wind direction observed in *Seasat* SAR images (Lyden et al. 1988) and, more recently, in in SAR (Soloviev et al. 2011) and photo images of ship wakes (Fig. 7.18). Gilman et al. (2011) studied the correlation between wake asymmetry and relative wind direction using photo images taken from the top of a mast during a year-long experiment on the Royal Caribbean *Explorer of the Seas*. The wake asymmetry is found to be strongly correlated to the wind direction relative to the ship course. The plots in Fig. 7.18 show that if only one boundary of the wake is sharp, it is more often the leeward (downwind) boundary than the opposite. This asymmetry effect seems to be also sensitive to the wind speed: for the moderate wind speeds, the above correlation persists. These observations suggest that wake asymmetry can be a result of wind–wake interaction.

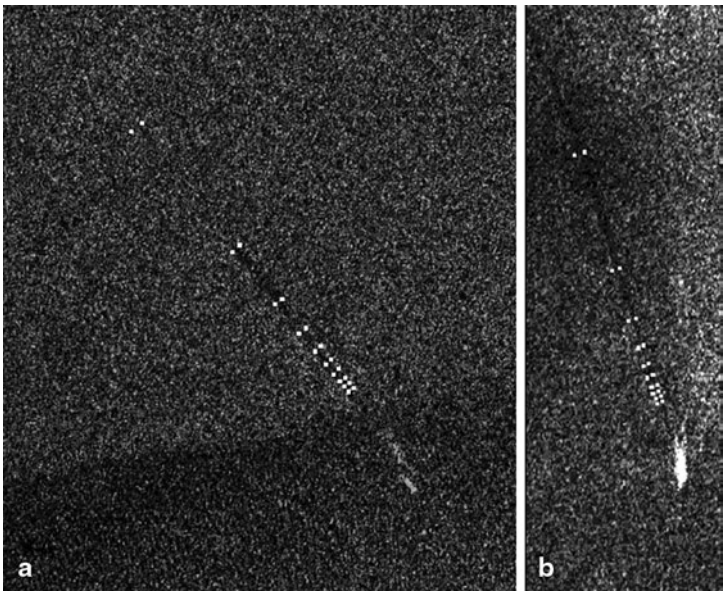

Fig. 7.16 SAR images of the Royal Caribbean *Explorer of the Sea's* and its wake. **a** *RADARSAT-1* beam (12.5 m resolution), image time 10:51:34 UTC 21 May 2007, ship at 37.6114°N, 70.3133°W, speed 21.6 kt, course 133.4°, wind speed 14.8 kt, direction 314.4 and **b** *RADARSAT-1* ScanSAR (25 m resolution), image 10:41:42 UTC 08 Sep 2007, ship at 41.0939°N, 69.2078°W, speed 10.6 kt, course 151.6°, wind speed 20.2 kt, direction 238.9°. White dots represent average wake width calculated from simultaneous photographic measurements taken from *the Explorer of the Seas*. After Gilman et al. (2011). Copyright © 2011 American Meteorological Society. Used with permission.

Figure 7.19 demonstrates two SAR images of ship wakes with 3 m spatial resolution taken with the new-generation satellite *TerraSAR-X*. Note an asymmetry of the centerline wakes relative to wind direction. The upwind side of these wakes is bright, while the downwind side is dark. This is consistent with previous observations in SAR and with the results of photo image analysis presented in Fig. 7.18. This type of asymmetry of the centerline ship wake in SAR imagery is explained by the hydrodynamic modulation of short wind waves due to convergence–divergence zones developing in the wake (Lyden et al. 1988; Soloviev et al. 2010). This effect of wind–wake interaction has been numerically reproduced by Fujimura et al. (2010, 2013).

Note that the SAR images of ship wake presented in Fig. 7.16b were taken when wind direction was across the wake. This image, however, did not reveal asymmetry of the centerline wake. The 25-m spatial resolution of the *RADARSAT-1* image was apparently not sufficient to resolve such fine feature of the wake as its asymmetry due to wind–wake interaction.

Figure 7.20 shows the *TerraSAR-X* image (left panel) and the simultaneous sonar measurements (right panel) in the wake of the *Eurus Paris* container ship on

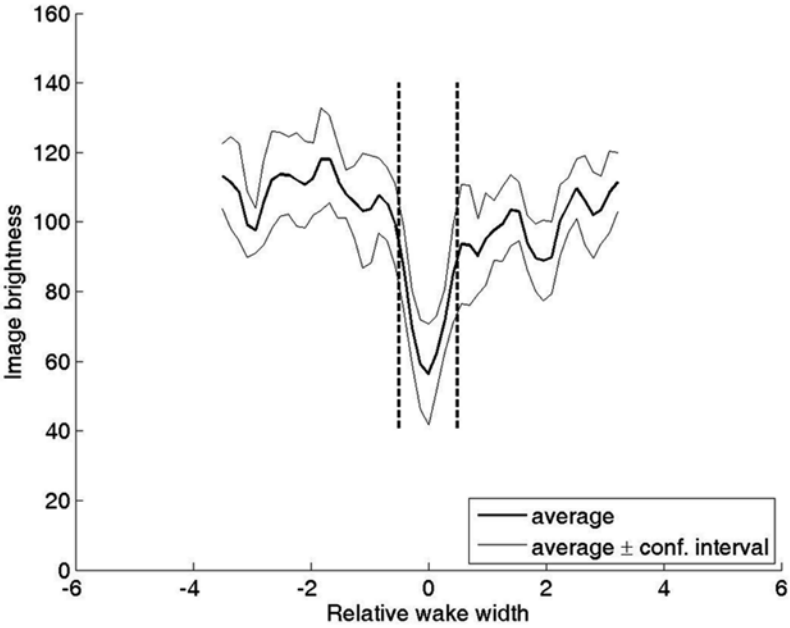

Fig. 7.17 Average cross-wake plot of image brightness (arbitrary units) and 95% confidence interval through the visible centerline wake in Fig. 7.16a. The dashed vertical lines plotted at abscissa values ±0.5 represent the normalized wake width from photographic measurements from the *Explorer of the Seas*. (After Gilman et al. (2011). Copyright © 2011 American Meteorological Society. Used with permission)

June 9, 2008. The wake is clearly seen in the SAR image. Four wake crossings with sonar were made while the wake could be resolved in acoustic imagery. In the SAR image, the equivalent distance from the ship for each of the sonar contour plots is schematically shown by the rectangles. This distance has been estimated using the ship speed and the time since the ship's passage. The wake on the SAR image faded when the sonar profile indicated disappearance of the acoustic signature of the wake in water. The plausible explanation is as follows: the sonar responds to bubbles; the same bubbles bring surface-active materials to the surface, which suppress short gravity-capillary waves, thus providing a link between the wake's visibility in sonar and in SAR. With increasing distance from the ship, the wake weakens and the concentration of ship-generated bubbles reduces. Correspondingly, supply of surfactants by raising bubbles reduces and cannot completely compensate the surfactant loss at the sea surface due to turbulent dispersion. As a result, the wake disappears from both sonar and SAR.

Surfactants, however, are not the only factor resulting in ship wake visibility in SAR. Other important factors include convergence–divergence circulation, turbulence, and wind–wave interactions in the ship wake, all of which have effect on short-gravity-capillary waves.

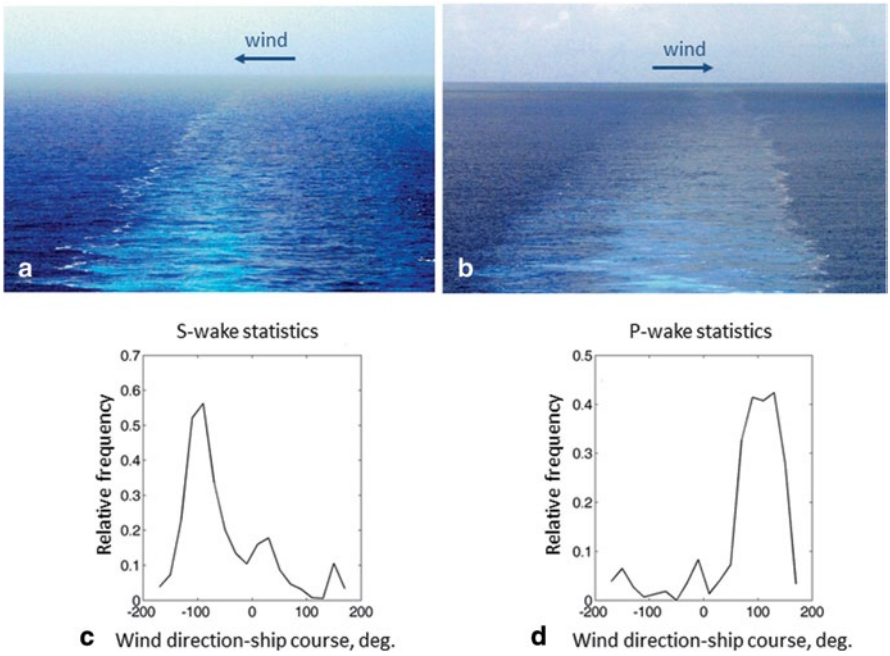

Fig. 7.18 Wake asymmetry vs. relative wind direction. *Top* row—examples of asymmetric wakes (the arrow shows the wind direction relative to the wake). **a** S-wake: 16:30:03 UTC 23 Jul 2007, ship course 176.1°, ship speed 22.2 kt, wind direction 91.9°, speed 18.5 kt and **b** P-wake: 16:37:57 UTC 27 Jul 2007, ship course 342°, speed 22.4 kt, wind direction 120.7°, speed 12.9 kt. *Bottom* row—relative frequency (see the text) of S- and P-wake as a function of relative wind direction (notice sharp peaks about ±90°), angular bins are 20°. (After Gilman et al. (2011). Copyright © 2011 American Meteorological Society. Used with permission)

The centerline ship wake in the presence of stratification in the near-surface layer of the ocean may produce a thermal signature on the sea surface due to mixing with cooler (or warmer and saltier) underlying water masses. In the example shown in Fig. 7.21, the research vessel consequently crossed the wake of a big ship three times. The centerline wake is well seen on the sonar contour plot. The sonar data also indicate the presence of a shallow thermocline. The temperature data taken at 1 m depth from the research vessel show negative anomalies associated with the first and second intersections of the wake but not with the third one. According to the sonar record, during the first and second intersections, the centerline wake penetrated the shallow thermocline, which resulted in bringing colder water to the surface. During the third intersection, the wake was weaker and could not reach the depth of thermocline; as a result, there was no specific thermal signature in the temperature record. Interaction of ship wake with a shallow thermocline has been conceptually reproduced by Matt et al. (2012a).

It should, however, be noted that temperature contrasts in SST within the ship wake when measured with IR sensors (Garrett and Smith 1984) could also be due to

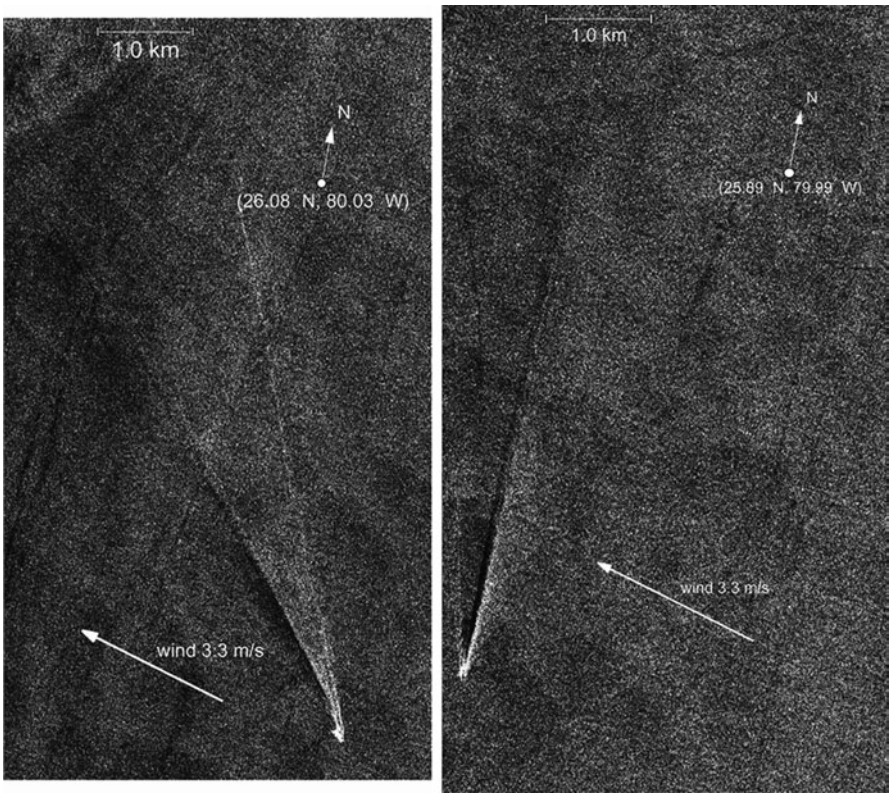

Fig. 7.19 Asymmetry of the centerline ship wake: fragments from the *TerraSAR-X* image on June 9, 2008 (in range–azimuth coordinates). (*Left*) Close-up of the wake of *Eurus Paris*. (*Right*) Wake of another ship in the same area (the ship identity and parameters are unknown). (Reproduced from Soloviev et al. (2012b) by permission of Kyoto University Press)

the effect of surfactants on the aqueous thermal molecular sublayer (cool skin). Garrett and Smith (1984) conducted a series of experiments to show that the contrast of the ship wake in IR imagery can be due to upwelling motion in the wake brining water with a different temperature to the surface as well as due to cool skin. The latter effect has been explained by suppression of turbulent and spatially coherent streak-like structures in the near-surface layer of the ocean due to viscoelastic properties of the sea surface enriched with surfactants (Soloviev et al. 2011; Matt et al. 2011).

An example of the "shadow-type" ship wake in SAR imagery (an effect represented in the schematic diagram in Fig. 7.15) is shown in Fig. 7.22. The shadow-type features are at least as prominent (in terms of size and contrast) as other features of the same wake. The vector diagrams show that the direction of the shadow-type wake coincides with the apparent wind direction for both ships in Fig. 7.22. According to Soloviev et al. (2010), this type of wake has surface signature, observable in SAR, but no underwater signature, which could be identified with sonar. The explanation is that this wake is due to a shadow in the wind field produced by

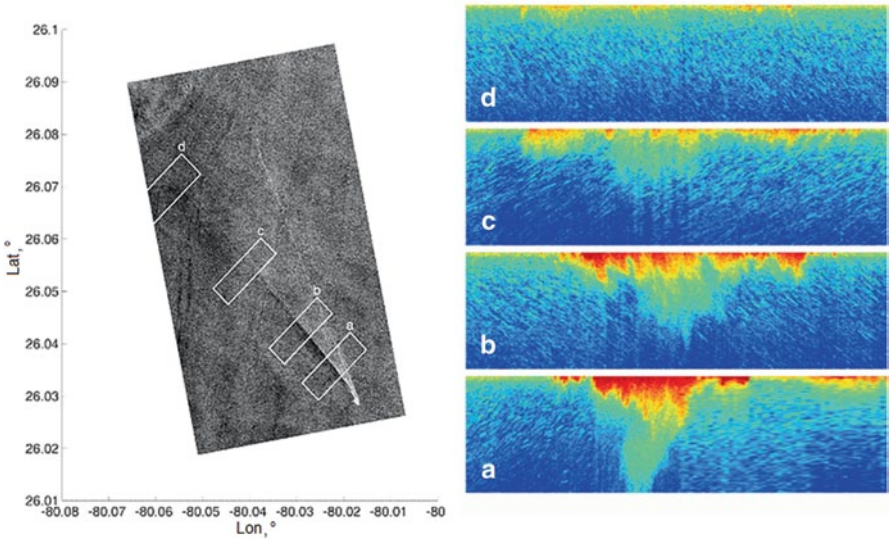

Fig. 7.20 (*Left*) SAR image of the wake of a moving ship, *Eurus Paris* (June 9, 2008). The rectangles on the image show the wake areas with wake age corresponding to the four crossings of the wake, which are shown in the right panel. (*Right*) Plots of the sonar return; the panels for east-to-west crossings (a and c) are flipped horizontally to achieve the same "geographical" orientation of all four panels. The depth ranges from 2 to 18 m. (Reproduced from Soloviev et al. (2010) by permission of IEEE)

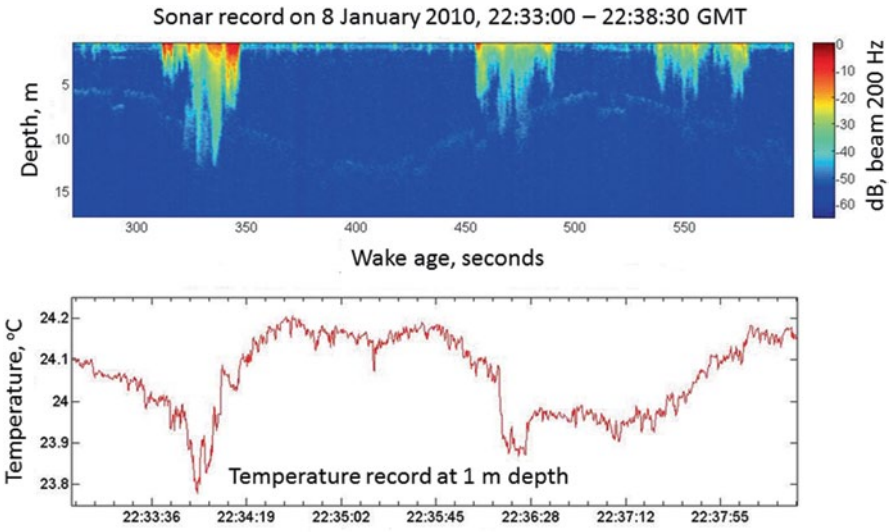

Fig. 7.21 Sonar and temperature record during ship wake crossing. Note a shallow thermocline also visible on the sonar record. (After Soloviev et al. 2012b)

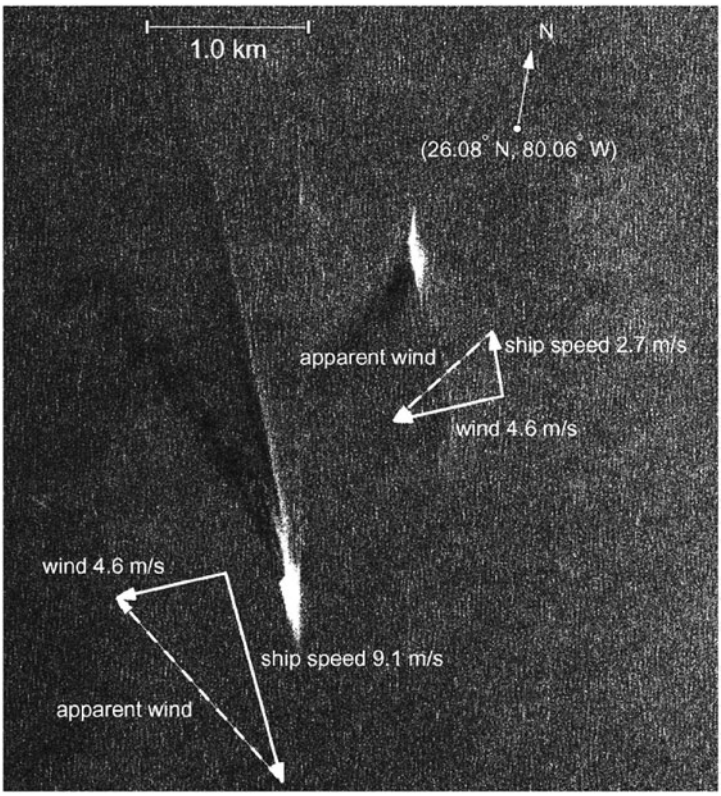

Fig. 7.22 Clip from the image made on June 14, 2008: the vector diagrams show the direction of the apparent wind coinciding with the direction of the shadow-type wake; the ship on the left is *Enchantment of the Seas* (notice also the wind asymmetry of its wake); the ship on the right is *Dole Colombia*. (Reproduced from Soloviev et al. (2010) by permission of IEEE)

the ship superstructure. This type of wake has the same nature as the wakes behind islands often observed in SAR. The difference is in the geometrical size of the wind shadow. The wind–shadow wakes originating from ships were for the first time identified by Soloviev et al. (2010).

7.3.3 Atmospheric Influences

Short gravity-capillary waves on the sea surface are primarily generated by wind stress and can be modulated by oceanic and atmospheric processes. A series of SAR images taken under different wind speed conditions (Fig. 7.23) suggests that with increasing wind speed, the visibility of signatures of natural fine-scale features in SAR decreases, while signatures, such as ship wakes or artificial-oil releases, are still detectable even under moderate wind speed conditions (Fig. 7.23).

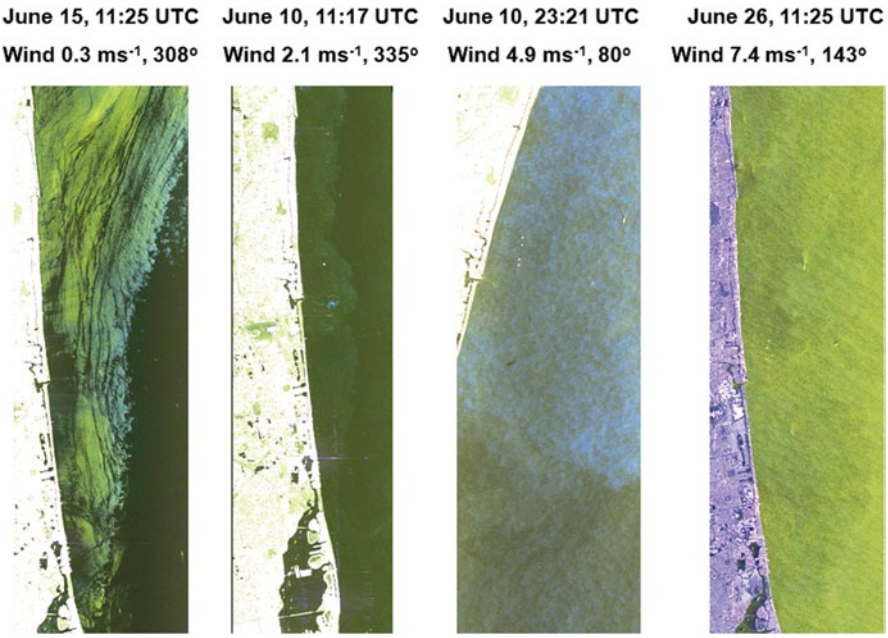

Fig. 7.23 *TerraSAR-X* polarimetric images. Natural slicks are prominent under very low wind speed conditions and disappear with increasing wind speed; artificial features can be seen even under moderate wind speed conditions. (After Soloviev et al. 2012b)

Figure 7.24 reveals a strong rain signature in a polarimetric SAR image. The area of rain is identifiable in the weather radar map and is consistent with a pronounced feature in SAR. The effect is due to gravity-capillary waves generated by the impact of rain droplets on the sea surface.

As already mentioned in Sect. 7.3.1, atmospheric internal waves and atmospheric boundary-layer rolls can produce signatures in SAR. These signatures may look similar to the signatures of the oceanic internal waves. Alpers and Huang (2011) have provided a qualitative guidance on distinguishing between atmospheric and oceanic wave-like signatures in SAR.

7.3.4 Numerical Simulation of Natural and Artificial Features in Radar Imagery

A combination of the numerical model based on computational fluid dynamics (CFD) with a radar imaging algorithm results in an effective approach for linking observed fine-scale structures such as ship wakes, internal wave solitons, spreading freshwater lenses, and sharp frontal interfaces with their SAR signatures (Fujimura et al. 2013; Matt et al. 2012a). Figure 7.25 provides an example of numerical simulation of the radar image of a ship wake. The surface velocity field produced by a CFD model was entered in a radar imaging algorithm (Romeiser 2008). The spatial

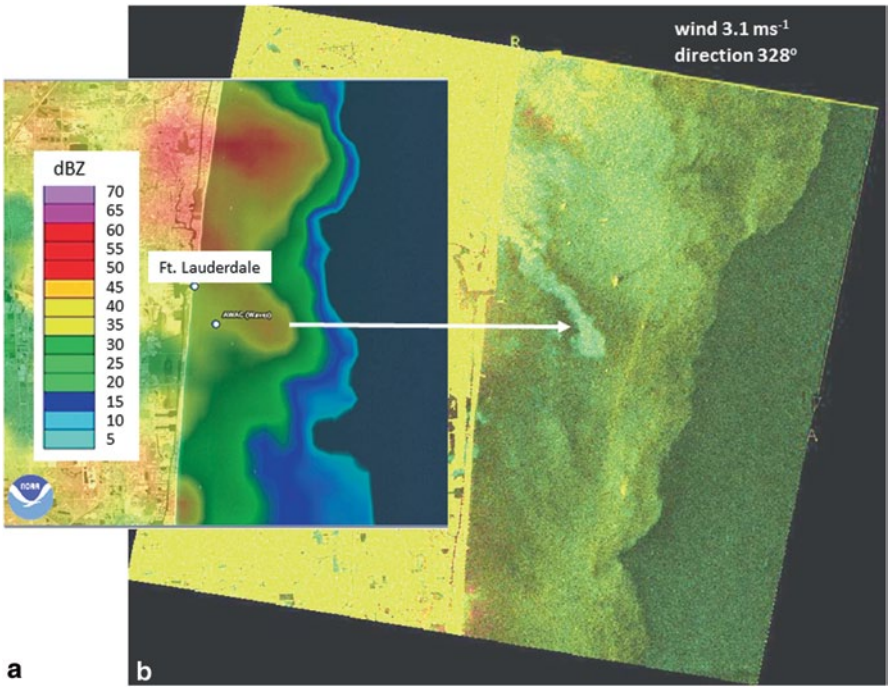

Fig. 7.24 **a** NOAA weather radar from the Miami, FL, NEXRAD station on June 30, 2010 11:13 UTC. The entrance to Port Everglades is indicated on the map for geographical reference. **b** *RADARSAT-2* image acquired June 30, 2010 11:14 UTC. Signatures of rain cells and atmospheric fronts are denoted on the image. (After Soloviev et al. 2012b)

resolution of the original CFD model was degraded to the 3 m by 3 m resolution of the *TerraSAR-X* imagery (Strip Mode). The numerical simulation is able to reproduce the observed (Fig. 7.25) asymmetry of the wake in the radar image relative to the wind direction. The upwind side of the wake is brighter than the downwind side of the wake. This asymmetry is explained by the interaction of the gravity-capillary waves with the convergent–divergent circulation within the ship wake (Fujimura et al. 2010).

Figure 7.26 shows model results for a wind–shadow-type wake, qualitatively consistent with the wind–shadow wake shown in Fig. 7.22. Results of numerical simulation of internal wave soliton (Fig. 7.27) and its signature in SAR and induced magnetic field are shown in Fig. 7.28.

7.4 Remote Sensing of Oil Spills

Oil spills in the ocean are caused by vessel operations, tanker vessel accidents, pipeline leaks, oil platform disasters, river run-off, and natural seeps (NRC 2003). Oil spills evolve rapidly and may age on a day-to-week timescale. Dynamic processes

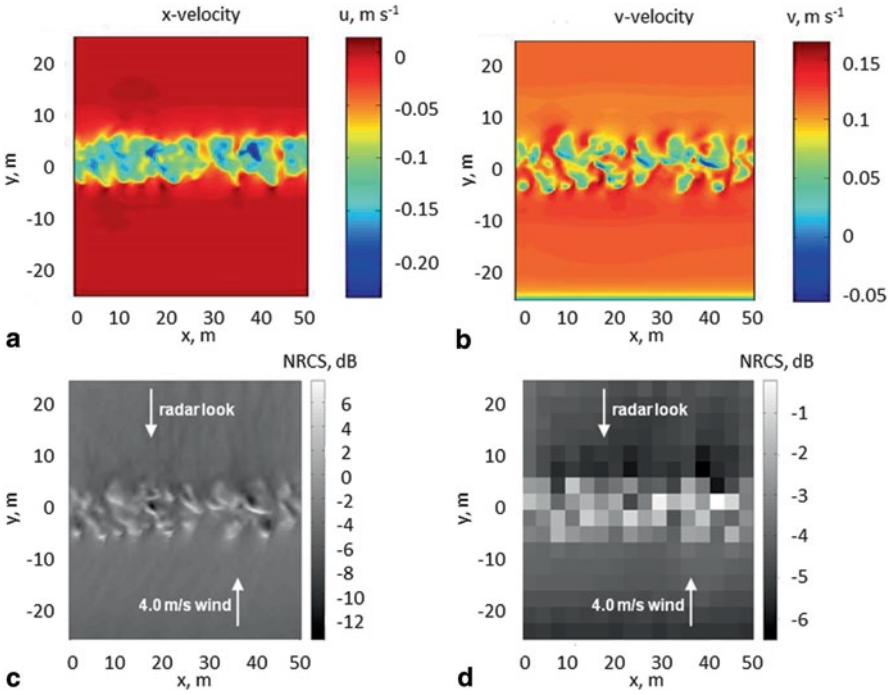

Fig. 7.25 Surface contours of **a** x-velocity and **b** y-velocity produced by CFD model simulation and simulated X-band NRCS maps in **c** original resolution (0.5×0.2 m) and in **d** reduced resolution (3×3 m). (After Fujimura et al. 2013)

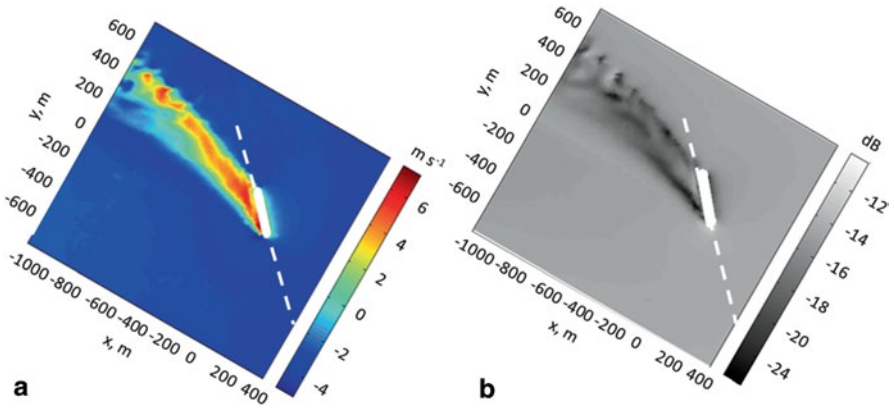

Fig. 7.26 **a** Numerical model of the wind field around a moving ship and **b** the simulated radar image (compared to Fig. 7.22). The ship course is indicated by dashed line. (After Matt et al. 2012b)

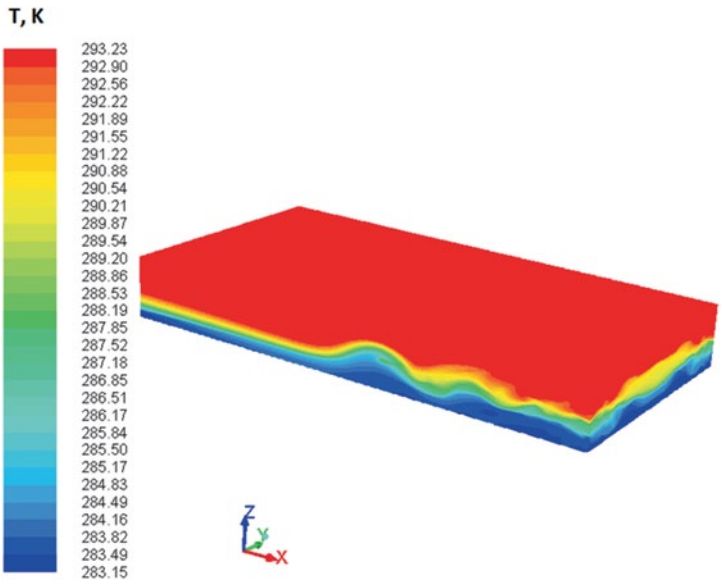

Fig. 7.27 Numerical simulation of internal wave soliton (3-D snapshot of the temperature field). Domain length—2 km. Domain width 1 km, depth 250 m, *horizontal* resolution 10 m, and *vertical* resolution 2 m (increased resolution in thermocline). Thermal stratification is similar to that observed on the South Florida shelf. (After Matt et al. 2012a)

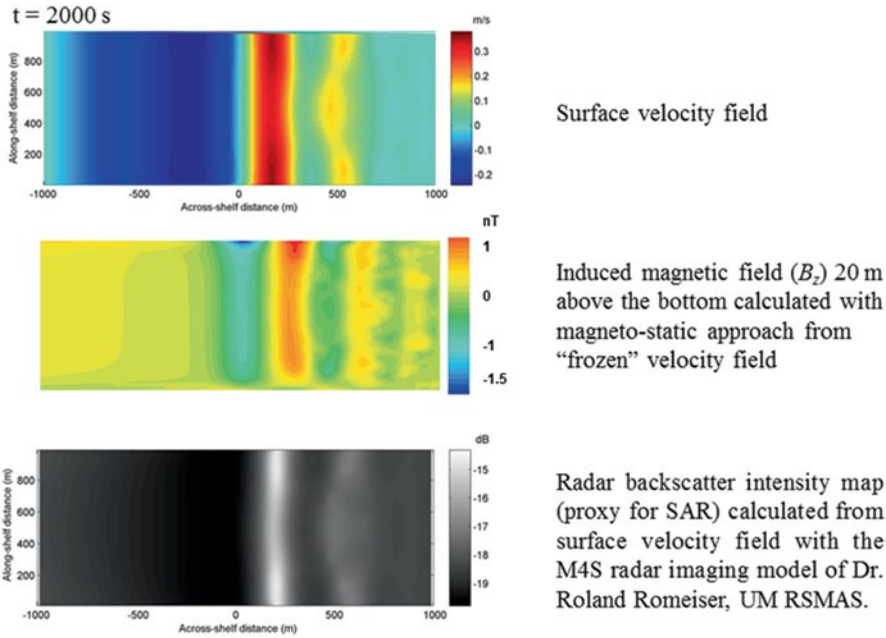

Fig. 7.28 Internal wave signature in surface velocity and magnetic fields and in SAR (top view). (After Matt et al. 2012a).

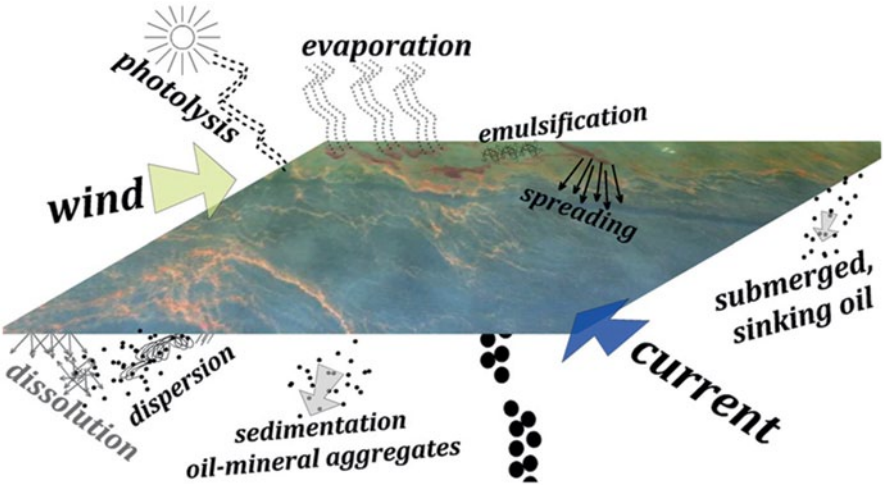

Fig. 7.29 Early oil spill processes on time-scales up to several days. The sketch incudes an image from the Deepwater Horizon oil spill. (After Leifer et al. (2012) by permission of JPL)

in the near-surface layer of the ocean, considered throughout this monograph, significantly determine the fate of oil spills. Figure 7.29 shows a schematic diagram of the early oil spill processes including wind–wave advection, formation of wind rows or narrow lines, horizontal spreading, and surface diffusion. Non-advective processes, involving sedimentation of hydrocarbon products into the water column, dissolution, emulsification, evaporation, and photochemical and biological degradation, lead to oil spill weathering (Leifer et al. 2012). Wind–wave turbulence actuates the oil–water mixing and formation of emulsions, which have distinct properties including high molecular viscosity (ACE 1996). Spatially coherent organized motions in the near-surface layer of the ocean accumulate oil spills into lines on the sea surface (Lehr and Simecek-Beatty 2000). In addition, oil spills damp short gravity-capillary waves and therefore are visible in SAR.

Extensive SAR imagery from observations of natural and man-made oceanic phenomena has been presented in Fu and Holt (1982), Alpers et al. (1999), and in SAR Marine User's Manual (2004). However, it is often difficult to distinguish between the signatures of natural (slicks, atmospheric fronts, rain cells) and man-made (ship wakes, oil spills) phenomena.

Migliaccio et al. (2009) and Velotto et al. (2010) proposed a new approach to distinguish between oil spills and look-alikes in SAR images of the ocean surface. This approach is based on the analysis of the co-polarized phase difference (CPD), defined as phase difference between complex horizontal transmit and horizontal receive (HH) and vertical transmit and vertical receive (VV) channels. Mineral oil spills damp the short resonant Bragg waves, which results in a high random scattering mechanism and as a consequence, in a low HH–VV correlation (Nunziata et al. in press). In contrast, a natural surfactant monolayer covering the sea surface produces relatively weak damping. The HH–VV correlation in the case of a surfactant

monolayer is relatively high and almost the same as for the clean surface (Migliaccio et al. 2009). Consequently, the phase difference between HH and VV channels allows distinguishing between areas covered by mineral oil spills and a broad class of look-alikes, which are characterized by weaker damping properties. This result has been implemented by Migliaccio et al. (2009) and Velotto et al. (2010) in the form of the CPD filter, which is based on the phase difference between the complex HH and VV channels.

The basic ideas pursued in this approach were investigated in the Ph.D. theses of F. Feindt (University of Hamburg 1985) and M. Gade (University of Hamburg 1996). Gade carried out very detailed studies using data of airborne and spaceborne radar sensors working in different bands. Gade inferred very complex conclusions from his data sets. At different bands and in the presence of different crude oil species, different artificial sea slicks, and different biogenic slicks, dramatic differences between the polarization ratios were observed. However, the technology of the 1990s did not allow conclusions that were on a sufficiently reliable statistical base. Obvious "tendencies" were observed; however, higher resolutions had been necessary to form a solid base for Gade's "tentative conclusions."

The CPD filter was tested with SAR images of artificial fish oil slicks, natural slicks, ship wakes, an atmospheric frontal line, and rain signatures, collected in the Straits of Florida. Figure 7.30 shows an SAR image taken during a fish oil release experiment in the Straits of Florida. Besides two artificial slicks created by the release of fish oil, this image also contains signature of several ship wakes, atmospheric front, and natural slick of unknown origin. The results of processing the SAR image of the fish oil slicks with the CPD filter are shown in Fig. 7.31. After applying the CPD filter, the areas covered with fish oil appear as bright features (Fig. 7.31).

The CPD filter has also been applied to the signature of a natural slick of unknown origin and a ship wake identified in Fig. 7.30. These features practically disappear from the image after applying the filter (Fig. 7.32).

Figure 7.33 demonstrates another case from the Straits of Florida, which is characterized by the presence of an atmospheric front (squall line) and the signature of rain in the SAR image. The atmospheric front in the form of a squall line was identified from a photo taken during the experiment. The rain signature was identified from the National Oceanic and Atmospheric Administration (NOAA) composite reflectivity radar image. Similarly to the case of natural slick and ship wake, the atmospheric frontal signature disappears after applying the CPD filter. The rain cell signature is, however, visible after processing with the CPD filter (Fig. 7.33). In contrast to the oil spill signature, the rain signature transforms into a dark feature.

Analysis of the cases presented in Figs. 7.31–7.33 suggests that the CPD filter is potentially an effective tool for distinguishing between the slicks produced by oil and other types of surface features. This filter is, however, most effective for X-band and C-band SAR, which responds to centimeter-scale surface waves. The L-band SAR, which responds to decimeter-scale surface waves, appears to be less sensitive to polarization differences (Minchew et al. 2012).

The new generation of high-resolution SAR satellites (*TerraSAR-X*, *Tandem-X*, *RADARSAT-2*, *COSMO-SkyMed*, *ALOS PALSAR*) opens new opportunities in the

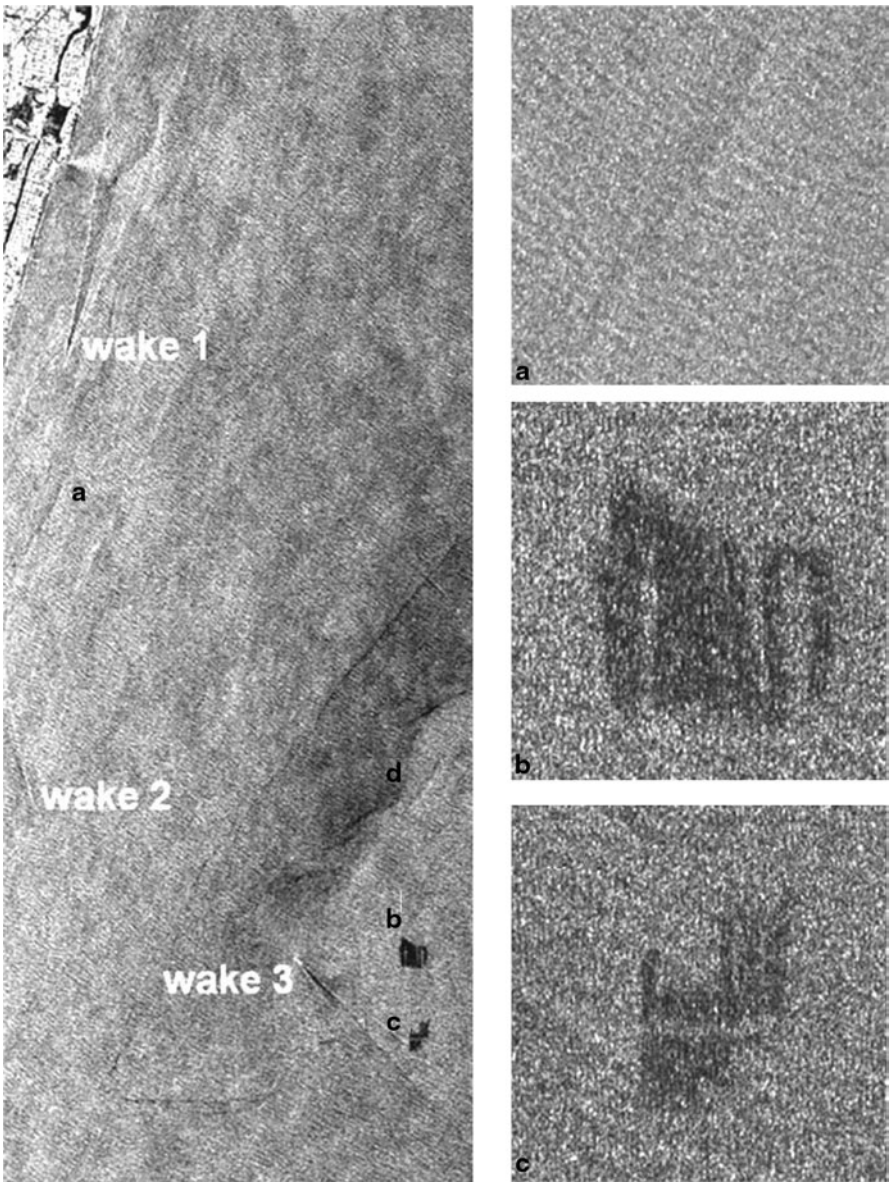

Fig. 7.30 A *TerraSAR-X* Stripmap image taken on 23:13 UTC 25 September 2009 (HH channel) off the coast of Ft. Lauderdale, Florida. The image reveals different features on the ocean surface: **a** oceanic front; **b** artificial slick, average age 80 min; **c** artificial slick created with fish oil, average age 30 min, a horizontal cut through the slick made by the passage of a boat is visible and **d** natural slick of unknown origin. Features a, b, and c are shown in more details in the right column. A few wakes of ships are also visible (wakes *1*, *2*, and *3*). (After Soloviev et al. 2012b)

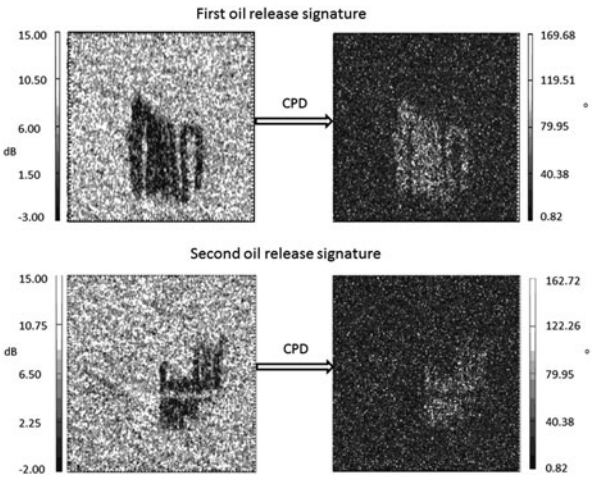

Fig. 7.31 Signature of a controlled oil spill releases in TerraSAR-X image and after applying the co-polarized phase difference (CPD) filter: CPD standard deviation for a 3×3 window filter for the slicks made by the release of fish oil (see Fig. 7.30, feature "b" for the first fish oil release and "c" for the second fish oil release). (After Soloviev et al. 2012b)

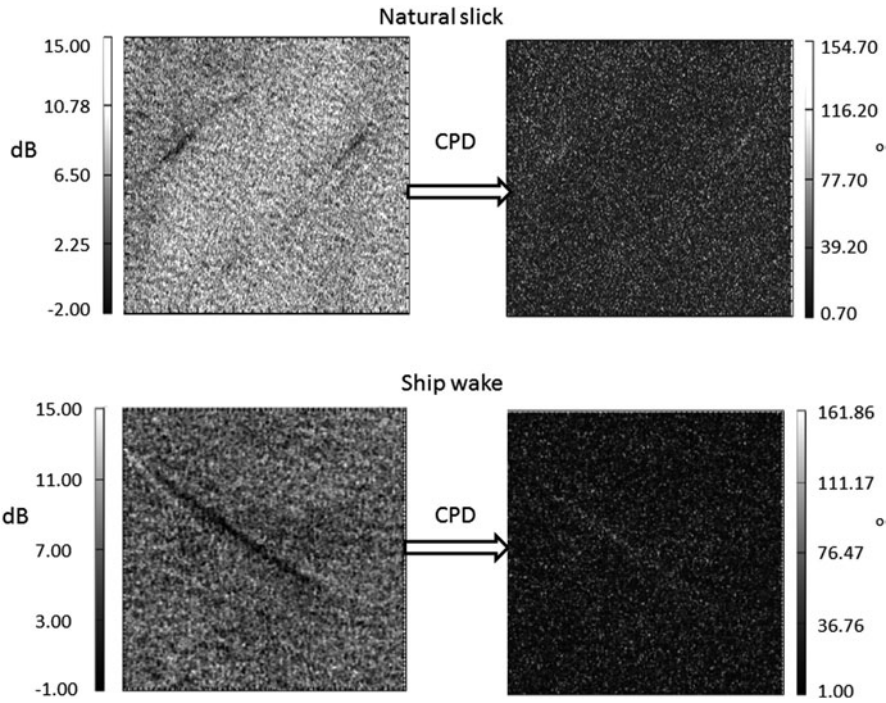

Fig. 7.32 Same as in Fig. 7.31 but for natural slick (feature "d" in Fig. 7.30) and ship wake (feature "wake 3" in Fig. 7.30)

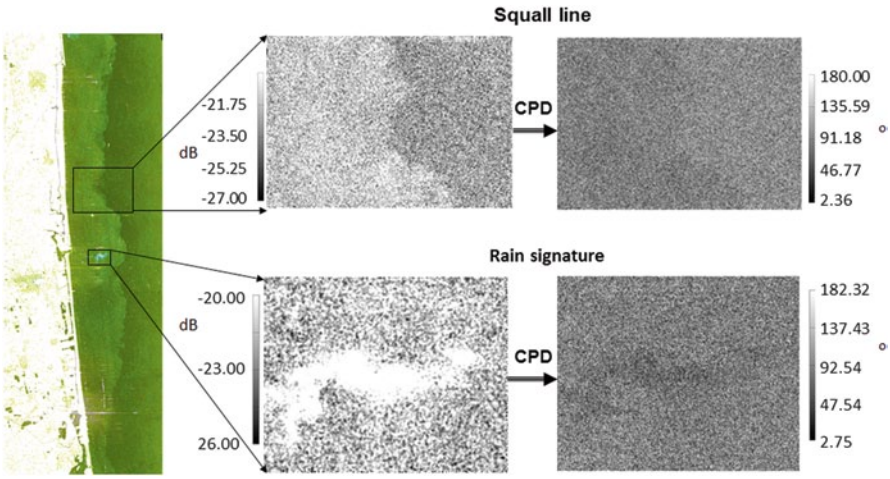

Fig. 7.33 Same as in Fig. 7.31 but for the atmospheric squall line and rain signature. The atmospheric squall line was also seen on a photo taken during this experiment; the rain feature was seen on the NEXRAD rain radar. (After Soloviev et al. 2012b)

oil spill detection and monitoring on a global scale. Airborne SAR can map areas of interest at high spatial resolution, with faster repeat times than SAR satellites. The airborne SAR can produce high signal-to-noise ratio, which allows discrimination of oil slick thickness, fractional surface coverage, and emulsification (Leifer et al. 2012).

SAR, airborne and satellite based, complements the other active and passive remote sensing tools and numerical models that are now available for oil spill detection and monitoring (see Liu et al. 2011; Özgökmen and Fischer 2012; Leifer et al. 2012 for comprehensive review). SAR is effective in cloudy conditions and nighttime, when application of other instruments is restricted. SAR techniques, however, have limitations—they are effective only within a limited wind speed range, from approximately 2 m/s to 5–8 m/s, depending on the wavelength band.

7.5 Marine Optics

7.5.1 Monochromatic and Color Imagery

Monochromatic aerial photography was the first method to trace spatial structures manifested on the ocean surface (Cox and Munk 1956). Introduction of color photography provided wider opportunities for studying and monitoring the ocean from space.

In addition to photographic methods, nonphotographic sensor systems and space imaging systems have been developing rapidly. Several types of color sensors have been implemented on polar orbiting satellites (e.g., *SeaWiFS*, *MODIS*, and *MERIS*).

The Geostationary Ocean Color Imager (GOCI) is the first ocean color observation satellite placed in a geostationary orbit, which allows 1-hour temporal resolution (Choi et al. 2012). This opens new opportunities in studying processes related to submesoscale variability.

A significant advance in sensor technology resulted from subdividing spectral ranges of radiation into bands (intervals of continuous wavelengths), and allowing to form multi-spectral images. A system for remote sensing of the ocean color consists of such sensors with a narrow field of view, aimed at a point on the ocean surface (IOCCG 2000). Special devices allow for the sensor to scan the ocean surface (also due to the motion of the satellite with respect to the Earth's surface). The data acquired from different points on the ocean surface constitute its color image. The information content of the signal depends on the spectral resolution and the number of selected wavelengths. For example, on the *SeaWiFS* satellite, several bands cover the blue, green, and red parts of the visible spectrum and the near-IR range.

Higher spectral resolution potentially leads to more informative remote-sensing systems. The so-called *hyperspectral* remote sensing involves systems with very fine spectral resolution and many wavelengths. Hyperspectral remote sensing has improved the interpretation of the complex biophysical processes controlling optical properties of the coastal ocean.

IOCCG (2012) identified new directions in remote sensing of ocean color. One of the new approaches is remote sensing of phytoplankton functional types, grouping phytoplankton according to their biochemical function but not necessarily by the common phylogeny (Nair et al. 2008; Thingstad et al. 2008).

Identifying the surfactant-associated functional group could help to establish a connection between color, temperature, and SAR satellite remote sensing. Natural surface-active materials result from biochemical and biophysical processes in the near-surface layer of the ocean. These processes involve bacteria (see Chap. 2). Surfactants are among the major factors controlling the marine aerosol production and, thus, have connection to climate and its changes (as well as including feedback to phytoplankton productivity).

7.5.2 Remote Sensing of Ocean Color

Remote sensing of ocean color is a passive method, since the sun is the source of light. The photons from the sun follow different pathways before reaching the remote sensor. The light entering the sensor originates from scattering of photons by the atmosphere, reflection of direct sunlight from the sea surface (specular reflection), and the upwelling light that is back-scattered from below the sea surface (Fig. 7.34).

The upwelling light scattered from below the sea surface carries useful information in relation to the water-body properties. This light is, however, attenuated on its pathway from the sea surface to the remote sensor because of absorption and scattering by the atmosphere.

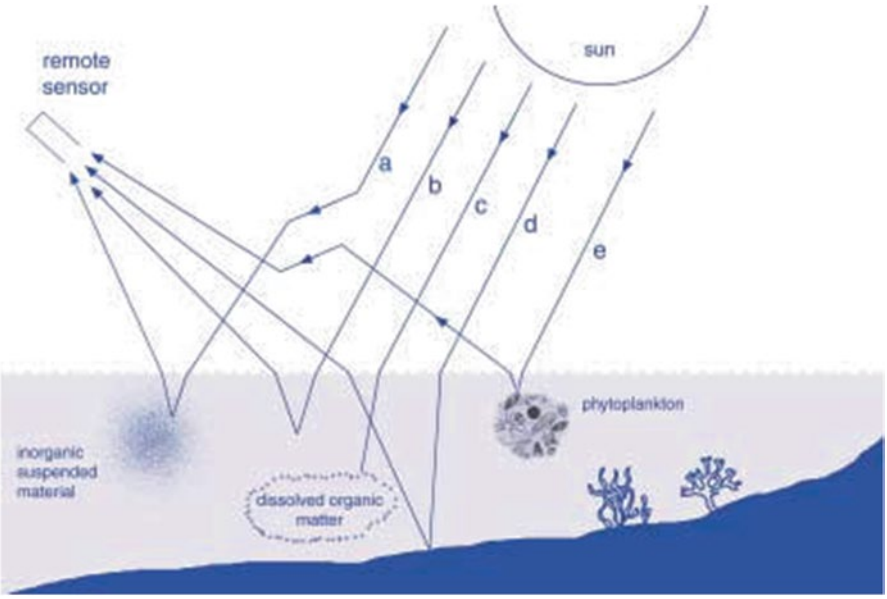

Fig. 7.34 Schematic representation of the factors that influence upwelling light leaving the sea surface: **a** upward scattering by inorganic suspended material; **b** upward scattering from water molecules; **c** absorption by the yellow-substance component; **d** reflection from the bottom; and **e** upward scattering from phytoplankton. (After IOCCG 2000. Courtesy of Shubha Sathyendranath)

The specular reflection at the sea surface and atmospheric attenuation represent noise for remote sensing of ocean water properties using color. Specular reflection from the sun can be avoided by changing the orientation of the detector with respect to the position of the sun. This, nevertheless, does not help in eliminating the flux scattered from the atmosphere that reaches the sensor at many angles. More than 80% of the light reaching satellite sensors may be of atmospheric origin (Morel 1980). Techniques for atmospheric correction are therefore an essential component of remote sensing of the ocean color (Gordon 1997; Sathyendranath and Platt 2010).

Figure 7.34 illustrates the main factors that influence upwelling light back-scattered from below the sea surface. (This diagram is a bit simplified, because it does not show multiple reflections and scattering.) Direct and scattered (diffuse) solar radiation penetrating the sea surface is absorbed and scattered by the water molecules and suspended and dissolved materials contained in the near-surface water. In coastal areas, sunlight may reflect from the ocean bottom.

Ocean color imagery is affected by properties of a thicker near-surface layer than the microwave and IR imagery. Color is therefore a more conservative characteristic of the water mass (*i.e.,* less dependent on very short timescale processes) than the surface roughness or SST, and it may better define dynamical ocean features. These features are often very clearly seen in the chlorophyll-α band (Yentisch 1984); however, strictly speaking, phytoplankton is not a conservative tracer. In coastal regions,

other color-imagery products such as the yellow substance and suspended sediment may be even better tracers than chlorophyll (Kopelevich et al. 1998).

The intrinsic color of the ocean is defined by spectral variations in reflectance R_s which according to IOCCG (2000) is defined as follows:

$$R_s(\lambda, z) = \frac{E_u(\lambda, z)}{E_d(\lambda, z)} \tag{7.1}$$

where $E_u(\lambda, z)$ is the spectral irradiance in all the upward directions, or upwelling spectral irradiance, at wavelength λ and depth z; and $E_d(\lambda, z)$ is the spectral irradiance in all the downward directions, or the downwelling spectral irradiance, at the same wavelength and depth. Irradiance E_u or E_d is the flux received by a flat collector facing downward or upward, respectively (see definitions of E_u or E_d in Sect. 1.4.1).

The upwelling spectral irradiance E_u is a measure of all the light that leaves the sea surface. The remote sensor with a narrow field of view receives only a small fraction of this flux. The description of the light field should hence include information on directional distribution of the light. Spectral radiance $L(\theta, \phi, \lambda, 0)$, introduced in Sect. 1.4.1 and defined as the spectral radiant energy with wavelength λ per unit area and per unit solid angle, can provide this information.

A parameter closely related to the sea surface reflectance is the remote-sensing reflectance, which is defined in the following way (IOCCG 2000):

$$R_{rs}(\theta, \phi, \lambda, 0) = \frac{L(\theta, \phi, \lambda, 0)}{E_d(\lambda, 0)} \tag{7.2}$$

The remote-sensing reflectance makes use of upwelling radiance rather than irradiance. It decomposes the reflectance R_s into its component radiances as a function of the viewing angles θ (zenith angle) and ϕ (azimuth angle).

Note that the definition of the remote-sensing reflectance by IOCCG (2000) differs from the traditional definition of the reflectance coefficient of the sea surface given in Sect. 1.4.5. The latter does not include the upwelling light back-scattered from below the sea surface, which is the essential component of the ocean color signal. Since the color imagery of the ocean is a rapidly evolving area of science, we have decided to keep both definitions in this book.

According to Sect. 1.4.6, the ocean color, or remote-sensing reflectance, is an apparent optical property, because it can be modified by the zenith-angular structure of the incident light field as well as by the nature and quantity of substances present in the medium. Variations in the spectral form and magnitude of the ocean-color signal potentially contain quantitative information on the types of substances present in the water and on their concentrations. In order to obtain this information it is necessary to express remote-sensing reflectance in terms of inherent optical properties, which are independent of the incident light field, and are determined entirely by the type and concentration of substances present in the upper ocean water. The relationship between ocean color and inherent optical properties of seawater is

consequently of great interest for the interpretation of remote sensing data. The inherent optical characteristics of the ocean in application to remote sensing are discussed in more detail in the next section.

7.5.3 Inherent Optical Characteristics of the Upper Ocean Water

Remote sensing of ocean color requires understanding the optical properties in the upper ocean water. Optical properties of the near-surface ocean water can be separated into the properties of pure water and the properties of the dissolved and suspended matter. The presence of dissolved salts in the water only slightly modifies its optical properties, which, nevertheless, can make a difference for certain applications. Suspended matter can influence the light propagation in a more significant way.

Three main components influencing the optical properties of seawater in addition to pure water itself and the light reflection off the bottom (in coastal areas) are as follows (IOCCG 2000):

- phytoplankton (which also includes other phytoplankton microscopic organisms);
- inorganic suspended material; and
- yellow substances represented by colored, dissolved, organic substances and "detail" particulate material (the latter generally has absorption characteristics similar to yellow substances).

Jerlov (1976) proposed an optical classification of oceanic surface waters by distinguishing three major water types (I, II, and III), two intermediate types (IA and IB), and coastal turbidity types (1, 3, 5, 7, and 9). Morel and Priuer (1977) partitioned the oceanic waters into Case 1 and Case 2 water. They defined Case 1 waters as those waters in which phytoplankton and an accompanying biochemical and particulate environment are mainly responsible for variations in optical properties of the water. Case 2 waters, according to their classification, are the waters that are also influenced by inorganic particles in suspension and yellow substances.

The inherent optical properties of the water that are relevant to remote sensing of the ocean color are the absorption and scattering coefficients, which describe the exponential rate of decay of flux per unit path length of light in the water due to absorption and scattering of light, respectively. The observed color of the ocean results from the interaction of incident flux (downwelling, direct-solar and diffuse-sky, and irradiances) with water and with its organic and inorganic substances. The processes of absorption and scattering control the manner in which impinging photons propagate through a natural water body and substantially determine the color of the ocean. The process of absorption is simply the removal of photons from the light field, while scattering changes the direction of photon propagation. Scattering of photons can occur in both an elastic and inelastic manner. Elastic scattering does not change the photon wavelength, while inelastic scattering does. Fluorescence of dissolved organic matter or phytoplankton is an example of inelastic scattering (IOCCG 2000).

The absorption and scattering coefficients are defined for the idealized conditions of collimated, monochromatic flux incident normally on the water, and traversing an infinitesimally thin layer of the water. (Scattering coefficients are defined separately for elastic and inelastic scattering processes.) Unlike the apparent optical properties (e.g., diffusive attenuation coefficient for downwelling irradiance K_d defined in Sect. 1.4.6), the inherent properties do not depend on natural-light conditions. A complete description of the scattering process requires knowledge of the distribution of the scattered light as a function of scattering angle.

Inherent optical properties of Case 1 waters primarily depend on phytoplankton populations and accompanying materials. In Case 2 waters, suspended particulate material and dissolved organic matter of aqueous or terrestrial origins can influence inherent optical properties (in addition to and independently on phytoplankton). The optical properties of substances other than phytoplankton often dominate the bulk-optical properties of Case 2 waters (Siegel and Michaels 1996). In order to retrieve quantitative information on the constituents of the water body from ocean color, information on the inherent optical properties of each of major constituents is required.

The Marine Optical Buoy (MOBY) project supports the validation of satellite ocean color imagery data collected by *SeaWiFS* and *MODIS*. An extended study of optical properties of the near-surface layer of the ocean has been conducted during the Radiance in a Dynamic Ocean (RaDyO) program (Dickey et al. 2012).

The development of techniques for the interpretation of ocean color in the remote-sensing context has been focused on the theoretical modeling of ocean color as a function of inherent optical properties and on the cataloguing of the inherent optical properties of substances encountered in the near-surface ocean waters, as well as their variations with the concentrations of the substances (IOCCG 2000). Remarkably, the inherent optical properties allow a simple addition of the contributions of the individual components that can constitute a multicomponent medium (which may not work for apparent optical properties, especially in highly scattering media). It is therefore feasible to resolve individual components and their concentrations from remote sensing of the ocean color. Detailed cataloguing of the inherent optical properties of the near-surface ocean waters is important for development of the most sophisticated inverse algorithms that also take into account the natural variability in the optical signatures of these substances, especially due to the influence of air bubbles populating the near-surface layer of the ocean.

7.5.4 *Influence of Bubbles on Optical Scattering in the Upper Ocean*

The top few meters of the ocean are most important for remote sensing of ocean color. The traditional classification into Case 1 and Case 2 waters does not include the presence of bubbles (Morel and Prieur 1977). Air bubbles efficiently scatter light in water because their refractive index is considerably less than that of the surrounding

water, and their size is typically large compared to wavelengths of light. The intermittent nature of bubble entrainment depending on near-surface turbulence and, to some extent, biochemical processes leads to strong fluctuations in light scattering near the ocean's surface (Terrill et al. 2001).

Air-bubble concentration and size distribution (*i.e.*, major determinants of optical scattering) vary greatly in time and space as a function of wind and wave conditions. Part of the error in the data products generated by existing ocean color algorithms can be related to variable concentrations of air bubbles in the near-surface layers; the existing parameterizations of backscattering coefficient in the semi-analytical algorithms for inverting reflectance measurements are most likely biased by the presence of the wind–wave-dependent bubble backscatter. In addition, submerged bubbles can influence the validation of atmospheric correction, which is based on the comparison of in situ and satellite-derived water-leaving radiances (Terrill et al. 2001).

Stramski (1994) assessed the significance of bubbles for the scattering of light in the ocean in quiescent seas (no breaking waves). He found that even the biologically formed and stabilized bubbles that dominate the bubble population during quiescent sea states can contribute to the total scattering and backscattering coefficients of seawater on the order of 1–10 %.

Zhang et al. (1998) studied the optical properties of bubbles coated with an organic film. The coatings exerted a small influence on total light scattering by bubbles larger than 10 μm in size. The estimated effect on backscattering was found as being much more significant: the backscattering efficiency enhanced by as much as a factor of 4 for coated bubbles.

Terrill et al. (2001) performed light-scattering calculations for acoustically measured bubble size distributions and size-dependent scattering efficiencies in rough weather conditions. Light scattering from a single air bubble in water was determined from the Mie theory (Chandraesekhar 1950), which allowed for the solution of the angular distribution of light scattered from the bubble when illuminated by a monochromatic source. The Mie solution to the angular distribution of light scattering from a sphere operates with the radiant energy either completely scattered into all directions, Q_b, or the energy backscattered, Q_{bb}, as a fraction of radiant energy intercepted by the projected area of the sphere. The backscattering efficiency, Q_{bb}, is relevant to the bubble-mediated effects in remotely sensed ocean color.

The bulk scattering coefficient and backscattering coefficient, respectively, for a given bubble size distribution are calculated in the following way (Terrill et al. 2001):

$$b(bubbles) = \int Q_b \pi r^2 N(r)\, dr \tag{7.3}$$

$$b_b(bubbles) = \int Q_{bb} \pi r^2 N(r)\, dr \tag{7.4}$$

where $N(r)$ is the bubble size distribution function (see Sect. 6.2.3). Equations (7.3) and (7.4) treat the bubbly water as a mixture of random, single-scattering particles.

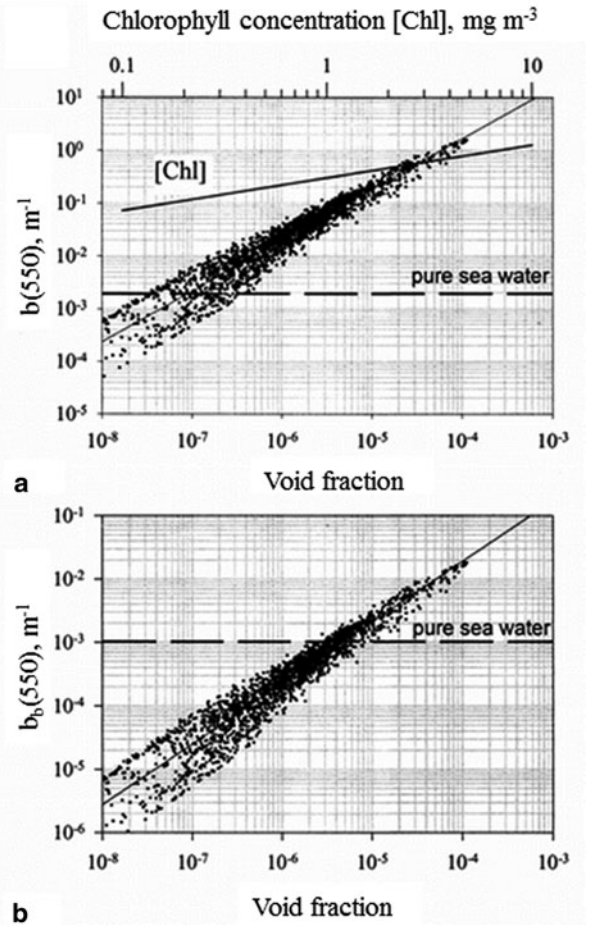

Fig. 7.35 Scatterplots of **a** b and **b** b_b calculated from acoustic data and Mie theory versus the void fraction of the bubble density. The data suggest that the optical effects of the bubbles on b_b, and hence the remote-sensing reflectance, are significant at void fractions above 10^{-6}. Reference values for pure seawater scatter at 550 nm are from Smith and Baker (1981). The empirical relationship between scatter at 550 nm and [Chl] for Case 1 waters presented in plate (a) is taken from Loisel and Morel (1998). (Reproduced from Terrill et al. (2001) by permission of American Geophysical Union)

The inherent bulk properties are the sum of the contributions by the individual bubbles (Mobley 1994).

The range of bubble radii present in the near-surface layer of the ocean defines the limits of the integrals. Small bubbles with radii less than $r = 4$ μm, however, have practically no contribution to the integrals and thereby to light scattering. Larger bubbles, which do contribute to the light scattering, practically do not depend on the wavelength of photons. Hence, bubble mediated effects on the scattering and backscattering coefficients are expected to have little spectral dependence.

Figure 7.35 showing scatterplots of b and b_b versus the void fraction indicates the correspondence between the bubble densities and the bubble contribution to the bulk light-scattering properties. The void fraction of entrained air is defined as $\beta = 4/3\,\pi \int r^3 N(r)\,dr$.

According to Fig. 7.35, scattering levels span a range of four to five decades. Backscatter coefficients b and b_b vary from 10^{-5} m^{-1} to over 1 m^{-1} and 10^{-6} m^{-1} to over 10^{-2} m^{-1}, respectively. (Note that this is for only 20 min of observations.) The level of bubble contribution to the total backscatter becomes significant compared to the pure seawater scattering at bubble densities with void fractions above 10^{-6}.

Terrill et al. (2001) evaluated the contribution of entrained bubbles to optical scattering in the open ocean by comparison with commonly accepted relationships between the light-scattering coefficient b and chlorophyll-α concentration [Chl] (Fig. 7.35a). For oligotrophic (Case 1) waters the bubble contribution to total scatter may be a significant fraction of the contribution by chlorophyll. At low chlorophyll concentrations, the errors in the bio-optical interpretation of measured optical properties may be very large due to surface-wave breaking. For example, at a void fraction of 10^{-6}, scatter from bubbles can be almost as large as the scatter by particles at a low chlorophyll [Chl] of 0.02 mg m^{-3}, while in more productive waters with [Chl] levels at 0.5 mg m^{-3}, scatter from the same bubble density is only 10 % of the scatter from particles (the chlorophyll). For the void fraction of order 10^{-5} (note that average void fractions of 10^{-5} are observed at wind speed of ~12 ms^{-1}), the bubble scatter is about equal to that of chlorophyll for 0.5 mg m^{-3} concentration.

The remote-sensing relevant parameter is the backscatter parameter b_b. The bubble backscatter exceeds the backscatter for pure water at average void fractions of 10^{-5} (Fig. 7.35b). Terrill et al. (2001) unfortunately do not provide the corresponding backscatter parameter for chlorophyll-α. It is therefore impossible to make quantitative estimates of the distortion of color imagery by bubbles from their results. The effect of bubbles is most likely strong under high wind speed conditions, especially if the assumption of Zhang et al. (1998) regarding the role of organic films in coating the bubbles and enhancing their ability to scatter the light is correct.

7.6 Marine Chemistry and Biology

Chemical and photochemical reactions in the near-surface layer of the ocean ensure the growth and accumulation of phytoplankton and neuston. Some of the chemical processes in the upper ocean do not require light (*dark* chemical processes). Other chemical processes are excited by chemical absorption of sunlight (photochemical processes). The biological cycling and supply of inorganic and organic elements necessary for phytoplankton growth can depend on both dark chemical and photochemical reactions (Bissett et al. 2001). The cycling of dissolved inorganic macronutrients (nitrogen, phosphorous, silica, etc.) is mostly related to biological activity in the water, with plant-growth removal and microbial regeneration, rather than to photochemical reactions. In some situations, upwelling and mixing processes can lead to substantial redistribution of chemical properties in the upper ocean, overshadowing in situ bio-chemical reactions. The supply of materials such as cobalt, iron, manganese, vitamins, and some other essential micronutrients depends on biological, dark chemical, and photochemical reactions as well as atmospheric processes.

The majority of ultraviolet irradiance ($\lambda < 400$ nm) in the sea is absorbed by chromophoric (colored) dissolved organic matter (CDOM). This absorbed energy drives photochemical reactions in the near-surface layer of the ocean. The photochemical reactions include photo-destruction of chemical bonds and fragmentation of complex molecules into smaller compounds; both reactions are of fundamental importance for bio-productivity in the upper ocean (Plane et al. 1997; Bissett et al. 2001). These photochemical reactions can both promote (by breaking down complex molecules and increasing accessibility of organic carbon and some inorganic nutrients) and retard (by damaging cellular constituents) biological processes. In addition, secondary reactions between energized organic molecules and dissolved oxygen in seawater form highly reactive chemical compounds including hydrogen peroxide and hydroxyl radicals. Another type of secondary reaction occurs between "excited" CDOM and other chemical compounds such as trace metals and sulfur compounds. Since CDOM strongly absorbs the solar ultraviolet (UV) radiation, it regulates the penetration depth of the biologically harmful UV radiation into the ocean (Zepp et al. 1995).

A complex mixture of photochemical-reaction products (reactive oxygen species, inorganic nutrients, and trace gases) accumulates in the near-surface layer of the ocean affecting the biological availability of dissolved organic matter as well as the optical properties of surface water. Remotely sensed spectral radiance can therefore provide estimates of CDOM absorption and concentration (Bissett et al. 2001).

An interesting phenomenon, sometimes observed in the upper ocean, is the formation of thin biologically active layers. The layers of phytoplankton, zooplankton, and *marine snow* ranging from a few centimeters to a few meters thick, extending up to many kilometers horizontally, and lasting for days have been reported in estuaries, fjords, and coastal shelves (Donaghay et al. 1992; Rines et al. 2002). These thin layers may have elevated levels of nutrient uptake, increased intensity of competition and predation, higher accumulation of chemical waters and toxins, and higher levels of microbial degradation and remineralization than found in the seawater immediately above and below them (Sieburth and Donaghay 1993). The thin layers also affect optical and acoustical characteristics of the upper ocean.

Alldredge et al. (2002) observed thin layers of phytoplankton and marine snow and the distributions of associated zooplankton in the near-surface layer of a shallow fjord (Fig. 7.36). Four days before the measurements shown in Fig. 7.36, strong winds advected a plume of fresher and warmer water (generated by a river) into the experimental area. The wind speed then dropped to 1–1.5 m s^{-1}.

Profiles of physical and optical structure suggest that the position of thin biota layers was related to the near-surface pycnocline. There are two distinct thin layers in Fig. 7.36. The thin layer associated with phytoplankton fluorescence is at the bottom of the near-surface mixed layer (~ 3 m depth). There is also a layer of marine snow, an accumulation of microscopic aggregates of detritus particulate matter > 0.5 mm in diameter, which occurred about 1.5–2 m below the layer of high fluorescence.

The data shown in Fig. 7.36 are obtained under low wind speed conditions. When wind increased later, the snow layer and phytoplankton layers merged.

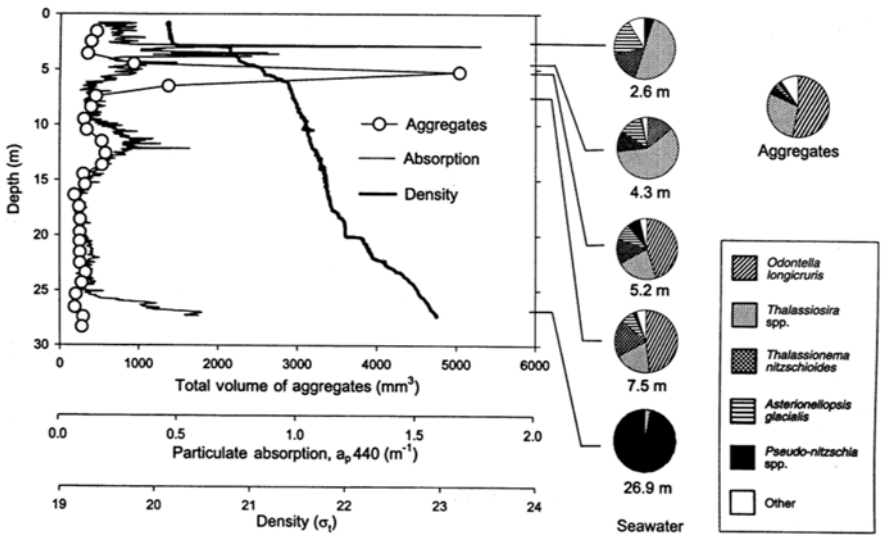

Fig. 7.36 Thin biological layers as indicated in absorption and by the accumulation of microscopic aggregates in relationship to seawater density (σ_t), and particulate absorption at 440 nm in a shallow Pacific fjord. The phytoplankton thin layer is observed about 2 m above the marine snow thin layer. Diatom community composition is shown in the pie diagrams. (Reproduced from Alldredge et al. (2002) by permission of Inter-Research Science Publisher)

There was a pattern of maximum zooplankton abundance in the surface layer and minimum abundance within the marine snow layer. Zooplankton (measured acoustically) concentrated in the layer from 0 to 5 m, which was above the marine snow layer (there was 4 times more zooplankton at 2 m than within the marine snow layer at 6 m). Total zooplankton abundance below the snow layer was increased compared to the marine snow layer but still at about 1/3 to 1/2 of the abundance in the near-surface layer.

Both the layer of high plankton concentration at ~3 m depth and the marine snow layer at ~5 m depth tended to occur at small discontinuities in the density profile (Fig. 7.36). Marine snow contains a significant fraction of nonliving organic matter. The mechanism by which the nonliving matter accumulates into thin layers is supposedly different from that for living organisms (plankton). Plankton presumably concentrates in the turbulent entrainment zone, which is at the bottom of the near-surface mixed layer, while the marine snow aggregates sink until they reach neutral density.

The turbulence measurements made simultaneously with biological and optical observations by Alldredge et al. (2002) revealed relatively low dissipation rates within the marine snow layer, which indicated that the latter is below the actively mixed layer. According to Asper (1987), aggregates of 0.5 mm in diameter sink at rates of 40–50 m d^{-1}. It would require only a few hours for a 0.5-mm aggregate formed at the surface to reach a depth of 5 m (and much less time for larger, more

rapidly sinking aggregates). Aggregates collide and form larger aggregates. The large aggregates sink until they reach neutral density. If this does not occur, then the thin layer will never form because the aggregates will continue sinking and no accumulation will occur. Attainment of neutral density is a requirement for the persistence of any layer of passively sinking particles. Alldredge and Crocker (1995) proposed that neutral buoyancy of an aggregate sinking from a lower salinity surface layer into a halocline could be attained if some proportion of the aggregate's interstitial volume was occupied by lower density mucus, which is resistant to the diffusion of salts and water. Interstitial mucus would form from the gelatin and aggregation of polysaccharides exuded by the diatoms in the lower salinity layer (Alldredge et al. 1993). The sharp salinity gradient in the fjord created the sharp density interfaces that accumulated marine snow in the form of thin layers observed in Fig. 7.36.

The thin biologically active layers have mostly been observed in the coastal zones of the ocean. Terrestrial runoff and river outflows provide organic-rich waters to the coastal ocean. In the open ocean, observations of biological and chemical thin layers near the surface are nevertheless quite rare. The importance and the frequency of occurrence of this phenomenon in the open ocean are therefore largely unknown (which can, in part, be explained by the absence of proper techniques for the measurement of biochemical parameters near the air–sea interface).

Theoretical studies indicate that thin near-surface layers of biota can change remote-sensing reflectance R_{rs} defined by (7.2) up to several percent (Petrenko et al. 1998). The color-imagery methods described in Sect. 7.5. are based on the assumption of a vertically homogeneous ocean. Further development of remote-sensing techniques may enable identification of thin biological layers in the upper ocean.

7.7 Ocean Acoustics

The sea surface is an important element of the acoustic environment of the ocean (Brekhovskich and Lysanov 1978). In contrast to other types of ocean boundaries such as the sea bottom or ice cover, the free sea surface by itself practically does not absorb acoustical energy—it predominately scatters it. The scattering of sound at the wave-disturbed surface leads to space and time fluctuations of the propagating sound; as a result, spectral and statistical characteristics of the sound change. Sound scattered from the ocean surface may represent a serious disturbance to the effectiveness of hydro-acoustical systems.

In addition to scatter from the ocean surface, the acoustic signal may scatter due to near-surface turbulence, microstructure, and fine structure, depending on frequency. Sound refraction due to internal waves in the near-surface thermocline or rain-formed halocline may lead to a distortion of the acoustic signal and to its intensity fluctuations. In the process of sound scattering by the fine structure and

microstructure, the contribution of temperature inhomogeneities usually dominates over the effects of salinity and velocity fluctuations. The sound-speed dependence on salinity and velocity (though, Doppler shift depends on velocity) are second-order effects in the ocean compared to that of temperature.

Thin, concentrated layers of phytoplankton and zooplankton sometimes occurring in the near-surface layer of the ocean (see Sect. 7.6) can effectively scatter and absorb acoustic signals. Air bubbles also substantially contribute to sound scatter, absorption, and noise generation. High concentrations of bubbles are observed in the near-surface layer of the ocean below breaking waves and in ship wakes. The actions of wave breaking and bubble production generate easily detectable ambient noise that has been used as a signal to determine variables such as wind speed and rain rate. This noise can strongly degrade the performance of systems that attempt to detect unnatural acoustic signatures or map objects using acoustics.

7.7.1 Effects of Stratification

Under light winds, fine structure and microstructure can develop in the near-surface layer of the ocean due to solar warming and rainfalls. Local gradients of temperature and salinity may have significant magnitudes (see Chap. 4). In such a medium, sound speed may fluctuate along the acoustic path. Orbital motions due to surface-wave action cause undulation of inhomogeneities in temperature and salinity, which cause phase changes in the sound propagation near the surface. (The orbital motions also cause Doppler shifts.) The near-surface stratification is believed to affect the horizontal propagation more than vertical propagation of sound in the ocean.

The speed of sound at 10 dbar pressure, 36 psu salinity, and 19°C is $c = 1520$ m s^{-1}. The fluctuation of the speed of sound due to temperature and salinity changes is, respectively, as follows:

$$\left(\Delta c / \Delta T\right)_{S=36\,psu, T=19^{o}C} = 2.83\text{m s}^{-1\text{o}}\text{C}^{-1}, \tag{7.5}$$

$$\left(\Delta c / \Delta S\right)_{S=36\,psu, T=19^{o}C} = 1.13\text{m s}^{-1}\text{psu}^{-1} \tag{7.6}$$

The maximum temperature difference in the diurnal thermocline of 5°C corresponds to a 14 m s^{-1} difference in the sound speed. Statistics of near-surface salinity anomalies in the ocean are, however, poorly known. During rainfalls, sea surface salinity depressions of a few psu have been reported (Paulson and Lagerloef 1993; Soloviev and Lukas 1997), which corresponds to a few m s^{-1} difference in the speed of sound.

Significant surface salinity (as well as temperature) changes have been observed near icebergs. Lugt and Ugincius (1964) estimated that the sound propagating horizontally through the cool and freshwater in the vicinity of an iceberg could refract up to about 18°.

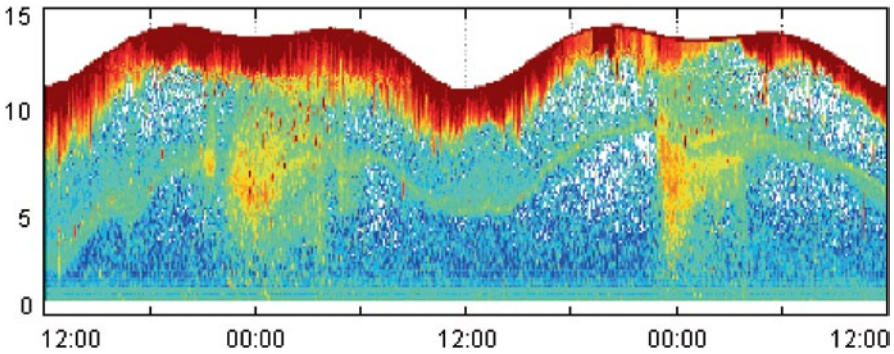

Fig. 7.37 An example of a thin layer of zooplankton, as visualized with acoustical scattering at 265 KHz in East Sound, WA. Here: *X* axis = time, 24–26 June 1998, *Y* axis = depth, in meters, bottom referenced. (After McManus et al. 2003. D.V. Holliday http://www.gso.uri.edu/criticalscales/about/index.html)

7.7.2 Biological Scattering Layers

Objects containing internal gas volumes may resonate at certain frequencies and produce very intense scatter of sound. Fish swim bladders are an example. Thin, concentrated layers of phytoplankton and zooplankton in the near-surface layer have episodically been observed in the coastal ocean (Sect. 7.6). These thin layers range from only a few tens of centimeters to a few meters in vertical extent (Cowles et al. 1998; Hanson and Donaghay 1998). Biota in these layers are often highly concentrated. Layers can be horizontally continuous for kilometers or more and persistent for days to weeks, strongly affecting the optical and acoustical properties of the water column (Donaghay and Osborn 1997; Rines et al. 2002).

Figure 7.37 reveals the persistence of a thin layer of zooplankton (green line, about 65 dB) over a 48-hour period. The nighttime disruption of this layer is presumably due to convection. However, the layer regenerates in the morning hours when the convection is inhibited due to the absorption of solar radiation. Note that the near-surface layer of intense scatter (red regions in Fig. 7.37) is due to bubbles generated in the process of wave breaking. Under high wind speed conditions, wind–wave turbulence destroys biological scattering layers in the near-surface layer.

The data illustrated in Fig. 7.37 were taken in a fjord in the Pacific Northwest. Evidence of thin layers has also been reported in Monterey Bay, in the South Atlantic Bight, as well as on the shelf off west Florida, Oregon, and southern California. The frequency of the appearance of sound-scattering biological layers in the near-surface layer of the open ocean is practically unknown. In the open ocean, these layers can supposedly appear during algae blooms. One of the authors of this book (Soloviev) observed a thin layer of biota in the North Atlantic Ocean (39°N, 20°W) during a calm weather period in July 1982. This layer produced an appreciable

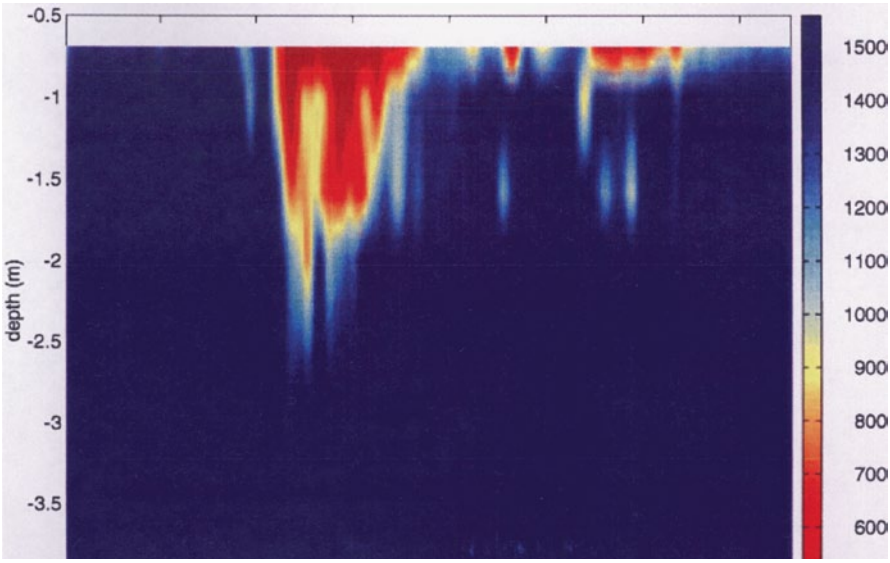

Fig. 7.38 The response of the sound-speed field to a single large wave-breaking event. A region of very low sound speed exists near the surface for about half a minute, while the reductions are smaller but dissipate more quickly at depth. Orbital motions of the waves advecting the bubble cloud past the sensors produce high-frequency oscillations visible in this figure. (Reproduced from Terrill and Melville (1997) by permission of the Journal of the Acoustical Society of America)

disturbance to the electromagnetic velocity sensor (this type of sensor is described in Chap. 3) during measurements with a free-rising profiler. The layer was first detected at about 20 m depth and was gradually moving toward the ocean surface.

The nature of the influence on the electromagnetic velocity sensor by the individual types of plankton is not completely clear. The interference signal from plankton was of significantly higher frequency than that from the turbulent velocity signal. The plankton layer did not affect the microstructure conductivity sensor signal. Professor Percy Donaghay (URI) (private communication) suggested that this disturbance might be caused by plankton species accumulating iron (magnetic material).

7.7.3 Effects of Bubbles on Sound Propagation

Wave breaking at the surface of the ocean entrains air and produces bubbles. Raindrops can also generate bubbles. Bubbles represent a great disturbance to sound propagation in the ocean. Populated with bubbles, the near-surface layer under high wind speed conditions represents a two-phase medium, which significantly modifies the phase speed (Fig. 7.38), scattering, and absorption of acoustic waves (Farmer and Lemon 1984). Intense near-surface bubble layers formed during heavy rains

may also effectively absorb sound energy (see Sect. 6.4.6). Bubbles also change the value of the buoyancy frequency in the near-surface layer of the ocean, which can result in the so-called *bubble mode* of the internal wave field (Grimshaw and Khusnutdinova 2004).

The big difference in density and compressibility between an air bubble and the surrounding water provides a mechanism for bubbles to both generate and interact with acoustic (pressure) waves. Bubbles resonate at characteristic frequencies that are determined by their radius. The lowest eigenfrequency of a single bubble oscillation is known from the work of Minnaert (1933):

$$\omega_0 = \frac{1}{r_0}\left(\frac{3\gamma p_0}{\rho}\right)^{1/2}, \tag{7.7}$$

where ρ is the water density, $\gamma = c_p / c_v \approx 1.4$ is the polytropic index for air (c_p and c_v are the specific heat capacity of water under constant pressure and volume, respectively), and p_0 is the ambient pressure.

Resonant bubbles cause especially strong scatter and absorption effects. For acoustic frequencies at or near its lower resonant frequency, a bubble has a scattering cross section up to three orders of magnitude larger than that of a solid particle of the same dimension. For acoustic frequencies much less than the resonant frequencies of the bubbles, the speed of sound depends solely on the volume of air present in the water. At higher frequencies, bubble resonances cause the sound speed to become dependent on the bubble size distribution.

A complex dispersion relationship for linear wave propagation and attenuation through a population of bubbles of variable size is as follows (Commander and Prosperetti 1989):

$$\frac{c^2}{c_m^2} = 1 + 4\pi c^2 \int_0^\infty \frac{r_0 N(r_0)\, dr_0}{\omega_0^2 - \omega^2 + 2ib\omega}, \tag{7.8}$$

where c is the bubble-free sound speed, c_m is the complex sound speed in the mixture, ω_0 is the radian resonant frequency of a bubble of radius r_0 defined from equation (7.7), ω is the radian frequency of the sound, b is the damping coefficient, and $N(r_0)dr_0$ is the number of bubbles per unit volume in the range (r_0, $r_0 + d\,r_0$).

The real and imaginary parts of the complex sound-speed dispersion relationship (7.8) describe the phase speed and attenuation of sound propagating through the medium, respectively. This bubble acoustics model compares well with a number of historical measurements that contain a wide range of radii at void fractions up to 1 % (Commander and Prosperetti 1989). Relationship (7.8) may no longer be valid at higher void fractions because of the effect of multiple scattering ignored in the model. High void fractions of the order of 10 % that exist directly beneath breaking waves in the ocean quickly degas over timescales of a wave period or less to bubble densities suitable for acoustic sizing techniques (the latter neglect multiple scattering). The typical mean void fractions in the upper ocean, depending on depth, range from 10^{-7} to 10^{-4} in winds of 10–13 m s^{-1} (Table 6.3).

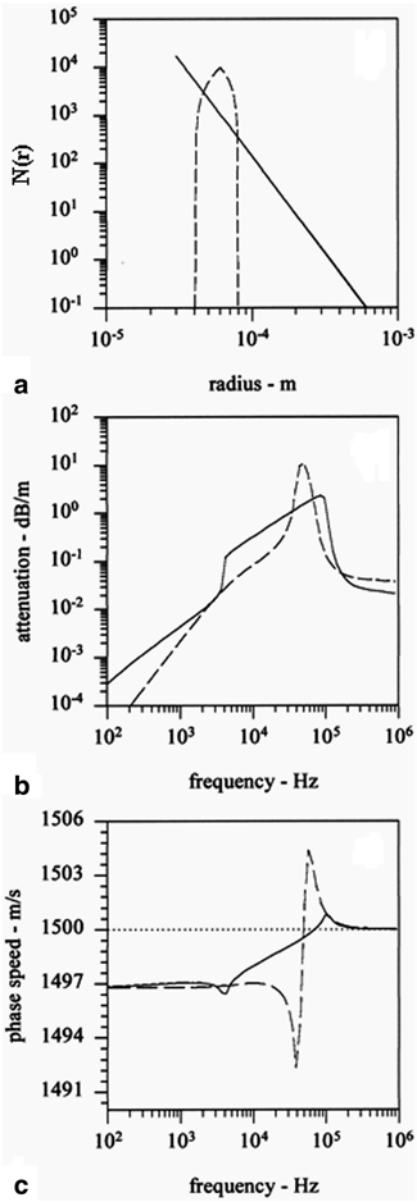

Fig. 7.39 **a** Two sample bubble size distributions and the corresponding **b** frequency-dependent attenuation, and **c** dispersion curves calculated from (7.8). Solid line represents a power law size distribution with a slope of 3.5 (between radii r_0=30 and 600 μm); dashed line corresponds to a narrow distribution centered at r_0=60 μm. (Note that the *x* axis in subplots b and c is the frequency rather than the bubble radius as in subplot a.). (Reproduced from Terrill and Melville (2000). Copyright © 2000 American Meteorological Society. Used with permission)

Figure 7.39 shows the attenuation and phase speed as a function of frequency calculated from (7.8) for two different idealized bubble size distributions. These two distributions (Fig. 7.39a) are a power law with a slope of 3.5 (solid line) between r_0=30 and 600 μm and a narrow peaked distribution centered at 60 μm radius (dashed line). The number densities of the bubble populations are normalized by setting void fractions for both distributions to $\beta = 1.91 \times 10^{-7}$.

Figure 7.39b shows the resulting frequency-dependent attenuation curves. The narrow size distribution (dashed line) results in large attenuation in a narrow frequency band centered at the resonant frequency of a 60-μm bubble. The power-law size distribution yields attenuation across a wider frequency band. This is consistent with the wider range of radii present in the power-law size distribution.

It is remarkable that there are three different regimes for the phase speed, which are common to both distributions (Fig. 7.39c). The phase speed becomes nondispersive at frequencies much lower than the resonant frequencies of the bubbles. The phase speed also asymptotes to the value for bubble-free water at frequencies much greater than the resonant frequencies of the bubbles. Strong frequency dependence is observed in the intermediate region where the dispersion varies according to the range of bubble sizes and the shape of the size distributions.

Figure 7.38 shows the sound-speed field disturbed by a large bubble cloud from a wave-breaking event. For this particular event, the sound speed was dramatically reduced at the surface (to approximately 500 m s^{-1}) for 30–40 s. At a depth of a few meters, the sound speed was reduced by only about 100 m s^{-1} and for a shorter time period. Short-lived events like this one are primarily responsible for injecting air into the water column and lowering the mean sound speed.

The average sound-speed reduction is at a maximum near the ocean surface and monotonically decreases with depth (because the average bubble concentration does so). The flux of bubbles into the surface waters apparently increases as the incidence of wave breaking increases, further reducing the sound speed in the near-surface layer.

In order to describe the depth dependence of the layer of reduced sound speed, Terrill and Melville (1997) calculated a contour representing the depth, $z_{0.99c}$, at which the mean sound speed is 99 % of the bubble-free value. They derived a linear relationship between the depth of the reduced sound-speed layer and the significant wave height H_s:

$$z_{0.99c} = 0.26H_s + 0.31, \tag{7.9}$$

with the correlation coefficient, r^2=0.97. Since the significant wave height is approximately four times the root mean square (RMS) wave amplitude (Sect. 3.4.2, eq. 3.48.), the results suggest that the 99 % contour depth has a characteristic length that scales with the RMS wave amplitude. Note that formula (7.9) is an interpolation of the field data taken within the range of significant wave heights from 1 to 7 m and may not be applicable outside of this range.

Significant wave height and the wind speed have often been used for obtaining correlations with bubble-driven acoustic phenomena such as backscatter and ambient noise, though with limited success. The correlation between $z_{0.99c}$ and significant wave height in the experiment of Terrill and Melville (1997) was high; however, under certain conditions, it could be disturbed. The presence of swell can significantly alter the measured significant wave height only contributing second-order effects to the wave breaking, or the acoustically active portion of the wave field (Felizardo and Melville 1995). Some other factors can also affect the wave-breaking process. For example, Terrill and Melville (1997) report the effect of strong surface currents (due

to the passage of an eddy that spun off the nearby Gulf Stream) on the small-scale wave breaking and the sound speed pattern in the near-surface layer of the ocean.

7.7.4 Acoustic Technique for Measuring Bubble Size Distributions

Vagle and Farmer (1998) published a fine review of acoustical methods to measure bubble size distributions in the near-surface layer of the ocean including the acoustical resonator (Breitz and Medwin 1989; Farmer et al. 1998; Su et al. 1994), acoustic pulse-propagation sensor (Lamarre and Melville 1994; Terrill and Melville 2000), and backscatter measurement with multiple- and single-frequency sonars (Thorpe 1982; Vagle and Farmer 1992). We discuss here in detail only the acoustic pulse-propagation approach.

The sound speed, c_m, in the low-frequency limit of dispersion relationship (7.8) is a function of the density ρ_m and compressibility K_m of the bubble mixture, and is determined from the formula:

$$c_m = \left(\rho_m K_m\right)^{-1/2} \tag{7.10}$$

where $\rho_m = \beta\rho_a + (1-\beta)\rho_w$ and $K_m = \beta K_a + (1-\beta)K_w$. K_a and K_w are the compressibility of air and water, respectively. In the low-frequency limit, the sound speed is simply a function of the void fraction β.

Asymptotic relationship (7.10) has provided the basis for the development of a single-frequency sound velocimeter for measurement of entrained air beneath breaking waves. Lamarre and Melville (1995) measured propagation times of a narrowband acoustic pulse across a fixed path length, which provided a direct measurement of the sound speed and determination of the void fraction. This method, however, does not provide information about the size distribution of bubbles constituting the void fraction. (Remember that the size distribution of bubbles has emerged as an important factor in many practical applications including air–sea gas exchange and production of marine aerosols.)

In order to calculate the size distribution of bubbles, the dispersion relationship (7.8) should be inverted, which requires sound velocity measurement in a range of frequencies. Terrill and Melville (2000) developed a broadband sound velocimeter that simultaneously measured sound speed and attenuation over a wide range of frequencies. Their velocimeter measured the attenuation and dispersion of a broadband acoustic pulse over frequencies ranging from 4 to 100 kHz across a fixed pathlength using a two-transducer system. The acoustic data were inverted to derive the bubble size distributions over the range from 30 μm to 800 μm.

The results of laboratory tests of the Terrill and Melville (2000) method are shown in Fig. 7.40. Bubbles with radii in the range of 60–90 μm contribute most to the total void fraction. This bubble size range corresponds to a peak in the acoustic attenuation at frequencies of 36–54 kHz. Similar numbers of bubbles exist at the smaller radii; significant differences in the number of larger bubbles are, however, observed. The rise velocity of the bubbles is proportional to the square of the ra-

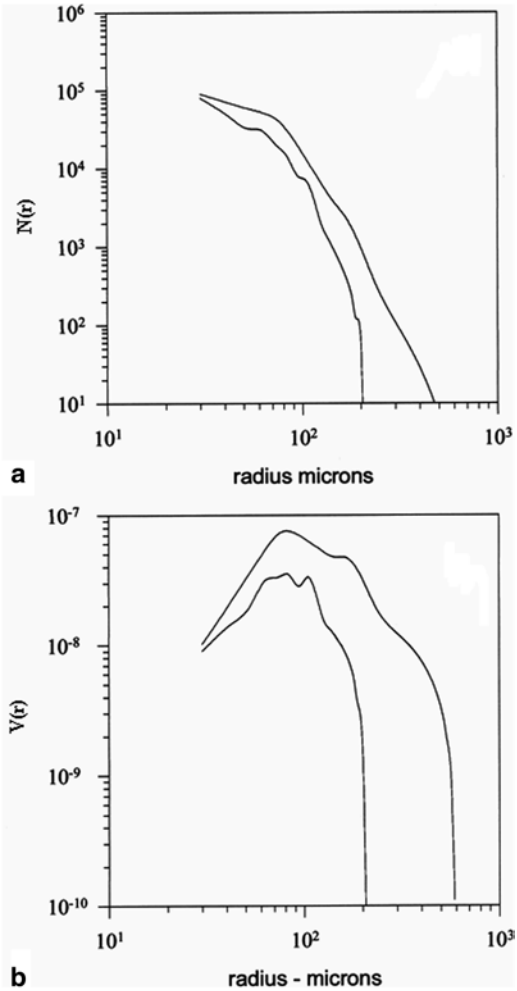

Fig. 7.40 **a** The mean bubble-size distributions and **b** the resulting mean volume-scaled distributions for the two measurement locations in the laboratory tank with different wave-breaking intensity. Each mean is calculated using $O(100)$ size distributions that were inverted on a per-ping basis for $t = 18$–42 s and $t = 31$–50 s at the two locations. The upper solid line is the 1 m downstream location and the lower solid line is the 2 m downstream location in the wave tank. (Reproduced from Terrill and Melville (2000). Copyright © 2000 American Meteorological Society. Used with permission)

dius; as a result, the larger bubbles reach the surface at a significantly faster rate. The terminal rise velocity of an air bubble (see Sect. 6.2.2) with a 30-µm radius is 0.0008 m s^{-1}, while the rise velocity for an 800-µm air bubble is approximately 0.3 m s^{-1}, an increase of over 350 times. This provides a plausible explanation of the difference for large bubbles.

7.7.5 Ambient Noise Produced by Bubbles

The fundamental problem of identifying an underwater sound source by its acoustical signature requires knowledge of the ambient noise (background) spectra under different hydrometeorological conditions. The first studies of ambient noise were undertaken in relation to the development of underwater acoustics after World War

II, revealing the dependence of ambient noise on the wave height and wind velocity (Knudsen et al. 1948). Since that time many efforts have been made to develop qualitative and quantitative descriptions of the processes that contribute to ambient noise (marine mammals, earthquakes, rain, breaking wind waves, etc.).

Wind is indirectly responsible for the ambient noise generation, namely via breaking wind waves (Kerman 1984; Medwin and Beaky 1989). The fraction of dissipated wave energy radiated as sound waves is of the order 10^{-8} (Loewen and Melville 1991a). Two approaches to understanding the nature of the sound radiated by oscillating air bubbles in a bubble cloud under breaking waves have been formulated. Medwin and Daniel (1990) and Loewen and Melville (1991b) assume that individual bubbles radiate sound, while Carey and Bradley (1985) and Prosperetti (1985) focus on collective oscillations.

The bubbles of radius from 30 to 1,000 μm, which are less than the Hinze scale (see Sect. 6.2.3 for definition), are believed to dominate the spectrum of bubbles produced by breaking waves. According to (7.7) a bubble within this size interval must have a natural frequency within 3–100 kHz. The available data, however, indicate that the ambient noise produced by breaking waves has much lower frequencies. The collective oscillation mode can explain the observed shifting of the ambient noise to lower frequencies compared to the noise that could be produced by individual bubbles. Tkalich and Chan (2002) developed a theoretical model for the prediction of ambient noise level due to collective oscillations of air bubbles under breaking wind waves. The model predicts the sound-intensity spectra from wind speed or wave height of breaking waves as an environmental input. The model is also able to explain the main observed features of ambient noise produced by breaking waves, including the slope and frequency range of the spectra.

Crum (1995) and Kolaini et al. (1995) suggested that the bubbles could change their oscillation mode from individual to collective in a transition from a less violent to more violent type of wave breaking. The question of which mode, individual or collective, is most important in the process of noise generation has not yet been answered.

7.7.6 Ambient Noise Produced by Rain

Rainfall generates sounds in the ocean, caused by the ensemble of individual raindrop splashes on the water surface. These splashes represent a loud and distinctive sound, allowing detection, classification, and estimation of rainfall parameters in the ocean (Shaw et al. 1978; Nystuen et al. 2000).

The acoustic sensor (hydrophone) collects data from a relatively large area on the ocean surface, which is proportional to the depth of the hydrophone. Since the area of averaging for an acoustic sensor can be orders of magnitude larger than for other types of rain gauges, much higher temporal resolution of the rainfall measurement can be achieved. The acoustic measurement of rainfall with a 5-s temporal resolution has revealed instantaneous rain rates exceeding 1,000 mm/hr during an ex-

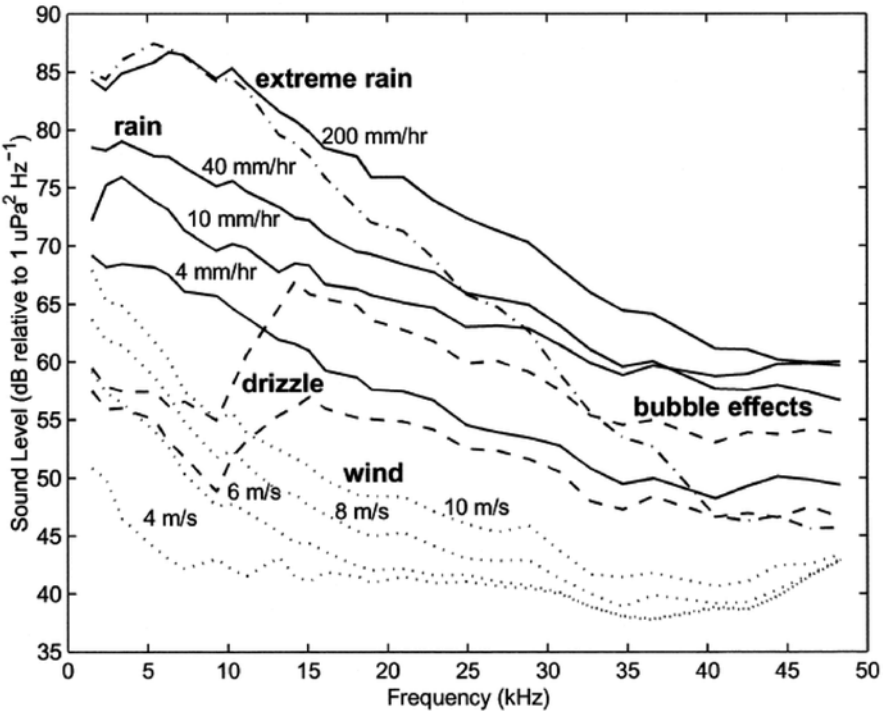

Fig. 7.41 Examples of the sound spectra generated by geophysical sources during an experiment in the South China Sea: periods of wind only (*dotted line*), drizzle (*dashed line*), rain (*solid line*), and extreme rain (*top solid line*). Five minutes after the start of an extreme rain, the sound levels above 20 kHz dropped to substantially lower values (*dash-dot line*), which is an indication of bubble layer formation by the rainfall. (Reproduced from Nystuen et al. 2000. Copyright © 2000 American Meteorological Society. Used with permission)

tremely strong rain event (>100 mm/hr, according to conventional rain gauges). These extreme rain rates could not be detected with conventional rain gauges typically using the longer temporal resolutions (Nystuen and Amitai 2003).

Acoustic analysis of underwater sound applied to identifying and quantifying geophysical processes consists of two steps (Nystuen et al. 2000): (1) the source of sound is identified from the spectral characteristics of the sound and (2) the geophysical quantity of interest is quantified.

Typical distinctive spectral shapes for different geophysical, biogenic, or anthropogenic noise sources aid the first step. Figure 7.41 shows examples of the sound spectra generated by geophysical sources during an experiment in the South China Sea. The spectral shape of wind-generated sound is attributed to breaking wind waves (see Sect. 7.7.8). A relatively uniform negative spectral slope from a peak near 500 Hz to over 25 kHz characterizes the wind-generated sound. It is remarkable that 5 min after the start of an extreme rainfall event (rainfall rate at 200 mm h^{-1}), the sound level at 40 kHz dropped 15 dB relative to the start of the

downpour. This is presumably because of sound absorption by the intense bubble layer formed due to heavy rain. Farmer and Lemon (1984) observed the deviations at frequencies over 10 kHz that were caused by acoustic absorption by bubbles (but for sea-state conditions with $U_{10} > 10$ m s^1 with high levels of wave breaking).

Sound levels in the surface layer of the ocean due to precipitation are much higher relative to the wind-generated sound level. Moreover, the variance of sound intensity within different acoustic frequency bands can be used as an aid to classify rainfall type and wind–wave conditions (Nystuen and Selsor 1997).

In addition to the known geophysical sounds created by air–sea interaction (wind, precipitation, subsurface bubbles), the ocean is also full of natural and anthropogenic noise sources. Shipping is one the most common anthropogenic noises in the ocean. Human activities other than shipping can also create loud sounds. Marine mammals produce significant acoustic signals. In addition, snapping shrimps can produce a very loud, broadband sound that can dominate the underwater sound field. Fortunately, these shrimp live on hard substrata in shallow tropical water and are not present in the open ocean. There are also unidentified sources of sound in the ocean. Altogether, 7.1 % of the noise recorded by Nystuen et al. (2000) in the South China Sea was contaminated by unrelated sounds. Removal of contaminating sounds is an important part of identifying acoustical signals produced by wind, precipitation, and subsurface bubbles. Fortunately, the spectral properties of these sounds are usually distinctively different from the other (contaminating) sounds.

For a sound source at the free ocean surface modeled as an acoustic dipole radiating sound energy downward in a $\cos^2\theta$ pattern, the intensity of sound at some depth h below the surface is expressed as follows (Nystuen 2001):

$$I(h) = \int I_0 \cos^2\theta \,\mathrm{atten}(p)\; dA, \tag{7.11}$$

where I_0 is the sound intensity distribution at the surface, θ is the zenith angle, and atten(p) is the function describing the attenuation due to geometric spreading and absorption along the acoustic path p.

Absorption of sound in the ocean depends on its frequency. The frequency dependence varies with the water properties (salinity, pressure, chemical composition) and the bubble density. Large diurnal warming events and freshwater flux due to rain can produce appreciable stratification in the near-surface layer of the ocean (Chap. 4). If the speed of sound varies along the path, acoustic refraction occurs. For short distances, acoustic refraction is a minor effect; as a result, a p^{-2} (spherical) law can well approximate the spreading of sound. Vagle et al. (1990) found that even in strongly refracting environments only a minor correction is required, since most of the acoustic energy arrives at steep angles.

For straight acoustic paths, equation (7.11) can be rewritten in the following way:

$$I(h) = \int I_0 \cos^2\theta \frac{\exp(-\alpha p)}{4\pi\rho^2} dA, \tag{7.12}$$

where α is the sound absorption coefficient. According to Medwin and Clay (1998), α is a strong function of frequency, ranging from 0.5 dB km^{-1} at 1 kHz to 10 dB km^{-1} at 40 kHz. It is much higher in seawater than in freshwater. (The change of α for a small salinity change at a fixed frequency in the range from 0.1 to 100 kHz can be approximated as $\Delta\alpha/\alpha \approx \Delta S/S$.)

For acoustic rain estimation, it is important to know the effective listening area of the hydrophone. Rainfall measurements are needed on relatively large temporal or spatial scales, because rainfall is randomly (exponentially) distributed in space and time. Larger inherent sampling area should produce better temporal mean rainfall statistics. The sound spectrum of any single raindrop is variable in spectral character (except for small raindrops). The inversion techniques aimed at determination of rain parameters from its acoustic signature are based on the mean spectrum. It is therefore important to integrate over many discrete events (individual splashes) to obtain a smooth mean spectrum.

Equation (7.12) can provide an estimate for the effective listening area. Nystuen (2001) concluded from the analysis of (7.12) that for a uniform source of sound on the ocean surface (and absorption neglected), 50 % of the sound energy arrives from an area equal to πh^2 over the hydrophone, while 90 % of the sound energy arrives from an area equal to $\pi(3h)^2$, where h is the depth of the hydrophone.

7.7.7 Passive Acoustic Monitoring of Sea Surface Processes

Several air–sea interaction processes are responsible for the production and modification of underwater sound in the ocean as discussed in the previous section. Passive monitoring of the underwater sound field thus offers a means to make measurements of these processes. In particular, breaking wind waves and precipitation are the natural sources of underwater sound in the frequency range from 500 Hz to 50 kHz. Unique spectral characteristics of these sound sources allow them to be identified and then quantified (Nystuen 2001). Distortion of these acoustic signals by subsurface ambient bubbles in principle permits the detection and quantification of the near-surface bubbles, which are a potential indicator of the gas transfer velocity and sea-state condition.

Since the resonant frequency depends on the bubble radius, it is important to know the bubble size distribution and its dependence on depth and environmental conditions, especially on surface wave parameters. The surface wave characteristics depend on several factors including wind speed and its history, fetch, etc. For the interpretation of acoustical data, it is important to know the spectral and other statistical characteristics of surface waves. The dissipation of wave energy into turbulence appears to be a convenient integral parameter for characterizing the bubble field and related sound generation (Gemmrich and Farmer 1999).

As stated in Sect. 7.7.5, inversion of the underwater ambient sound field consists of identifying the source of the sound, and then quantifying it. Nystuen and Selsor (1997) identify the following four ocean surface features producing distinctive

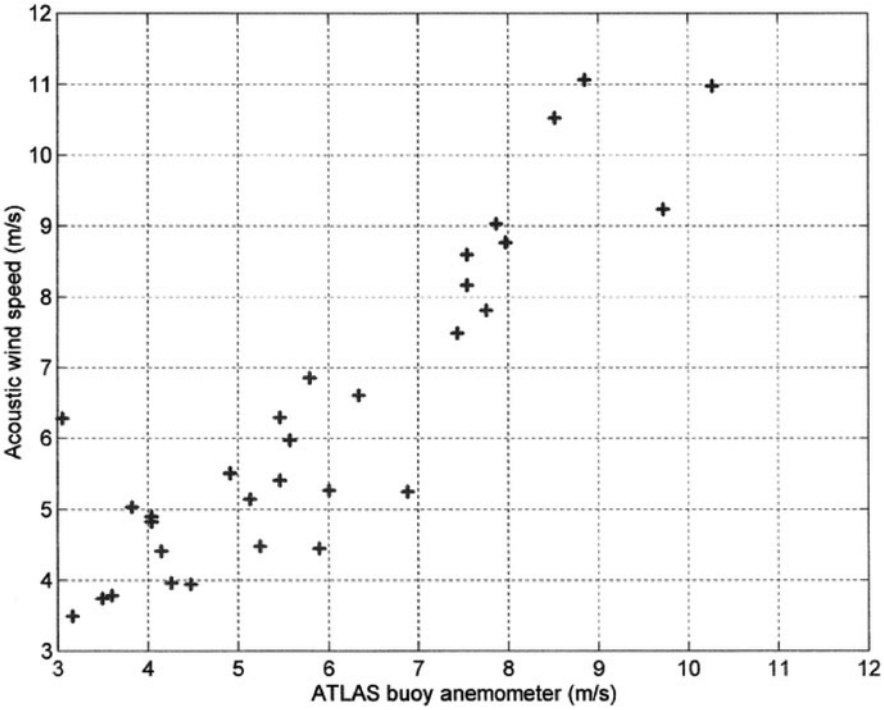

Fig. 7.42 Wind speed measured by the anemometer at 4 m height versus the acoustic estimate of wind speed from equation (7.13). (Reproduced from Nystuen (2001). Copyright © 2001 American Meteorological Society. Used with permission)

features in the sound spectrum from 1 to 50 kHz: wind, drizzle, heavy rain, and ambient bubbles present (Fig. 7.41). Once the acoustic classification is done, several algorithms are available to quantify wind speed and precipitation.

(a) Acoustical wind-speed measurements Vagle et al. (1990) developed an empirical algorithm for the acoustic estimation of wind speed using 8 kHz data from the North Atlantic Ocean. The sound level is empirically related to 10-m-height wind speed by the following formula:

$$U_{10} = \left(10^{SL_8/20} + 104.3\right)/53.91, \tag{7.13}$$

where SL_8 is the sound level at 8 kHz, and U_{10} is the 10-m wind speed. This method is valid for wind speeds $U_{10} > 2.2$ m s^{-1} (without wind–wave breaking, there is practically no acoustic signature of the wind field).

Figure 7.42 shows a comparison of wind speed observations from the buoy anemometer and from the acoustic data. The acoustic wind speed is in reasonable agreement with the anemometer record, although the acoustic estimates appear to be biased high above 7 m s^{-1}. This algorithm, however, is not capable of providing accurate wind speed data under rainy conditions.

Table 7.1 Raindrop-size categories for acoustic estimation. The raindrop size categories are identified by different physical mechanisms associated with the drop splashes (Medwin et al. 1992; Nystuen 1996. (After Nystuen 2001.)

Drop size	Diameter, mm	Sound source	Frequency range, kHz	Splash character
Tiny	<0.8	Silent		Gentle
Small	0.8–1.2	Loud bubble	13–25	Gentle, with bubble every splash
Medium	1.2–2.0	Weak impact	1–30	Gentle, no bubbles
Large	2.0–3.5	Impact	1–35	Turbulent, irregular bubble entrainment
		Loud bubble	2–35	
Very large	>3.5	Loud impact	1–50 kHz	Turbulent, irregular bubble entrainment penetrating jet
		Loud bubbles	1–50 kHz	

(b) Acoustic rain-rate measurements Several types of acoustic rainfall-rate algorithms are available in the literature. An acoustic estimate of rainfall rate can be made from an empirical relationship between the sound level within a particular frequency band and the rainfall rate. For instance, Nystuen (2001) derived the following relationships:

$$\log_{10} P = \left(SPL_{2-5} - 51.5\right)/17 \tag{7.14}$$

$$\log_{10} P = \left(SPL_{4-10} - 50\right)/17 \tag{7.15}$$

that were tuned to match the total rainfall accumulation from a disdrometer. Here SPL_{2-5} and SPL_{4-10} are the sound levels in the frequency bands 2–5 kHz and 4–10 kHz in decibels relative to 1 $\mu\mathrm{Pa}^2\ \mathrm{Hz}^{-1}$, respectively. While these relationships are easy to apply, they lead to outliers and also may overestimate rainfall when the rain contains relatively more large drops.

Since raindrops of different sizes have distinctive acoustic signatures underwater (Table 7.1), the underwater sound can be decomposed into components associated with each drop size. The sound field can be "inverted" to estimate the drop size distribution in the rain (Nystuen 2001).

According to equation (7.12), the observed sound intensity at the hydrophone is associated with the sound intensity at the surface, modified by attenuation. The sound intensity, I_0, at the surface can be related to the drop size distribution in the rain as follows (Nystuen 2001):

$$I_0\left(f\right) = \int A\left(D, f\right) V_T\left(D\right) N\left(D\right) dD, \tag{7.16}$$

where f is the frequency, $A(D, f)$ is the transfer function (which is supposed to be known) describing the radiated sound as a function of frequency for a given drop size D, V_T is the terminal velocity of the drop, and $N(D)$ is the drop size distribution in the rain. A discrete version of this equation can then be solved in order to estimate the drop size distribution in the rain from the ambient noise measurements. Once

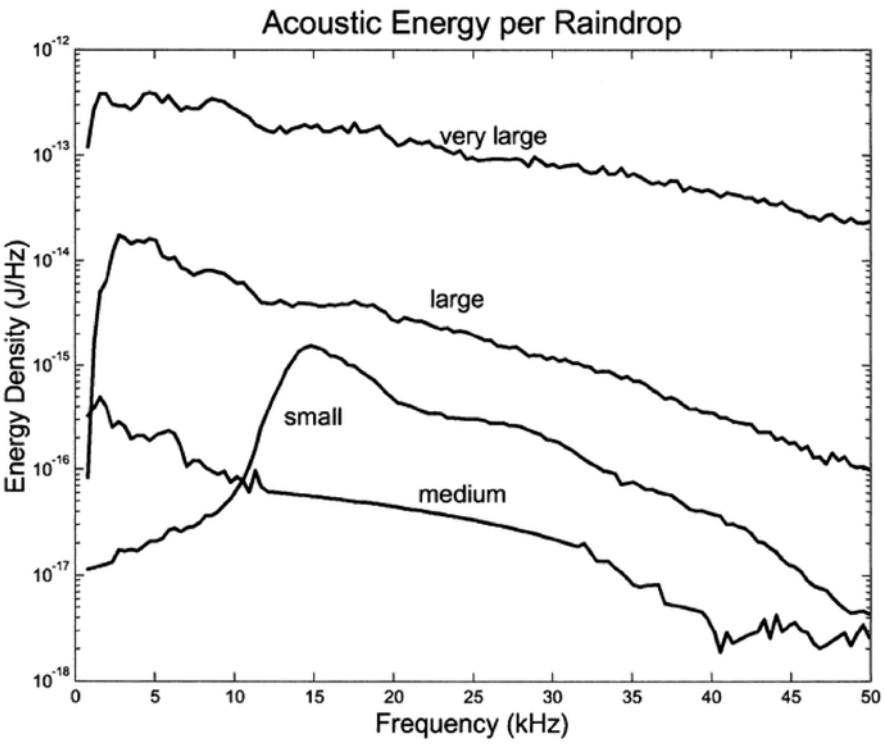

Fig. 7.43 The acoustic signature of individual drop size categories. This forms the basis for the inversion of the sound field to obtain the drop size distribution. (Reproduced from Nystuen (2001). Copyright © 2001 American Meteorological Society. Used with permission)

a drop size distribution is derived, the rain rate is calculated by integrating overall drop sizes.

The sound spectrum produced by different sizes of droplets has some specific features (Fig. 7.43), which makes a straightforward application of the inversion technique unrealistic. Nystuen (2001) proposed a constrained inversion technique to address this problem. It takes into account the following spectral features of the rain-generated sound:

1. The sound of drizzle, which has a peak at 13–25 kHz (Fig. 7.41), is only detected when raindrops larger than 0.8-mm diameter are present in the rain, because drops smaller than 0.8 mm do not produce a detectable sound signal and cannot be measured acoustically. This sets the lower size limit for small raindrops. The upper size limit for small raindrops is set to 1.2 mm (see Table 7.1) based on laboratory studies.
2. Medium drop splashes, which do not generate bubbles (Table 7.1), are relatively quiet. Whenever the rain contains drops larger than 2.0 mm, the sound levels below 10 kHz are much increased. Thus, the lower size limit for large rain-

drops is set at 2.0 mm. Table 7.1, therefore, defines the medium drop size to be 1.2–2.0 mm diameter. The small drops are so much louder than the medium drops from 13 to 30 kHz that the sound signature for the medium drops had to be interpolated through this frequency range. The signal from the medium drops is small, although it appears to be louder than expected from laboratory studies. Presumably, this sound is from the impact of the drop onto the water surface and thereby is a broadband signal.

3. Large drops sound loud underwater. The sound generated by any individual large drop is, however, at the very narrow bands associated with any bubbles that are generated plus a broadband signal from the impact. According to laboratory results, larger drops produce, on average, larger bubbles. The largest bubbles tend to be loudest, producing a spectral peak in the mean spectrum at the resonance frequency of these sound-dominating bubble sizes. The "large" drops produce the spectral peak between 2 and 5 kHz, while the peak for the very large drop category extends down to 1–2 kHz.

The sound energy radiated by very large raindrops is relatively large compared to their water volume. In order to address this situation, Nystuen (2001) developed a constrained algorithm, which performs an iterative inversion. If the number of very large drops per square meter of sea surface per second appears to be greater than a chosen value, 10 m^{-2} s^{-1}, then very large drops are assumed to be present. If very large drops are not present, the second iteration of the inversion is repeated with the very large drop population set to zero.

Since the medium raindrops have a weak acoustic signal, another constraint is imposed. The medium raindrops are difficult to hear, especially against the background of very large raindrops. Unrealistic values of the medium drop category produced by inversion algorithms are unfortunately common. Medium-sized raindrops, however, often comprise a significant part of the liquid content of rainfall; accurate estimates of their populations are very important. In order to address this problem, Nystuen's (2001) algorithm assumes that if very large raindrops are detected within the rain, then the medium drops that might be present cannot be heard. In the case of very large drops present, the algorithm therefore makes no attempt to acoustically invert for the medium drop population; instead, the medium drop population is set based on the small drop population count. If during the initial iteration very large raindrops are not detected, then the next iteration of the acoustic inversion estimate for the medium drop population is obtained from the singular value decomposition with the very large drop population set to zero. The resulting drop size distribution is also additionally constrained to be monotonically decreasing with drop size above the medium drop size category. In addition, the medium drop count is not allowed to be greater than twice the small drop population. Although the last two constraints are artificial, they are nevertheless consistent with most of the observed drop size distributions recorded by a conventional disdrometer (Fig. 7.44).

Figure 7.44 demonstrates the performance of the inversion to obtain rainfall rate with a limited data set obtained in a mangrove-lined pond near Miami. For this data set, the acoustic rain accumulation total is 900 mm, which compares well to 969 mm from the disdrometer, 963 mm from the capacitance rain gauge, and

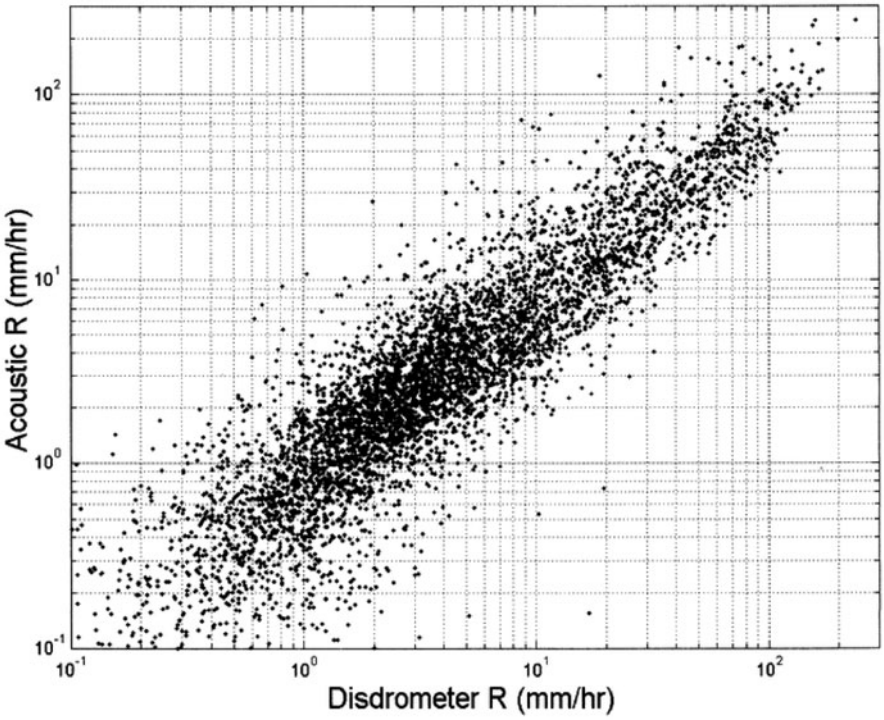

Fig. 7.44 Acoustic rainfall rate versus disdrometer rainfall rate for over 6000 min of rainfall from Apr to Dec 1994. (Reproduced from Nystuen (2001). Copyright © 2001 American Meteorological Society. Used with permission)

1031 mm from the optical rain gauge. Although there are some outliers, the overall correlation between the logarithms of the disdrometer rainfall rate and the acoustic inversion rainfall rate is 0.90.

The acoustic inversion based on equation and the additional constraints mentioned above represents an improvement over the direct acoustic methods (7.14) and (7.15) because it makes an optimal use of the available information. The inversion method has the additional advantage of being used to calculate other rainfall parameters such as the size distribution of rain droplets. This acoustic inversion technique is still pending full validation for oceanic conditions, although some important steps in this direction have already been done. A comparison of the acoustically derived wind speed and rainfall rate estimates with the QwikScat winds and TRMM rain estimates in the Bay of Bengal showed encouraging results (Riser et al. 2008). Acoustical measurements of rainfall reported from passive aquatic listeners (PALs) from a mooring in the Ionian Sea off the southwestern coast of Greece were consistent with collocated high-resolution X-band dual-polarization radar rainfall measurements (Anagnostou et al. 2008). A modification of Argo floats has been equipped with PAL technology to monitor the ocean ambient sound during the drift phase of the Argo float mission (Nystuen et al. 2011).

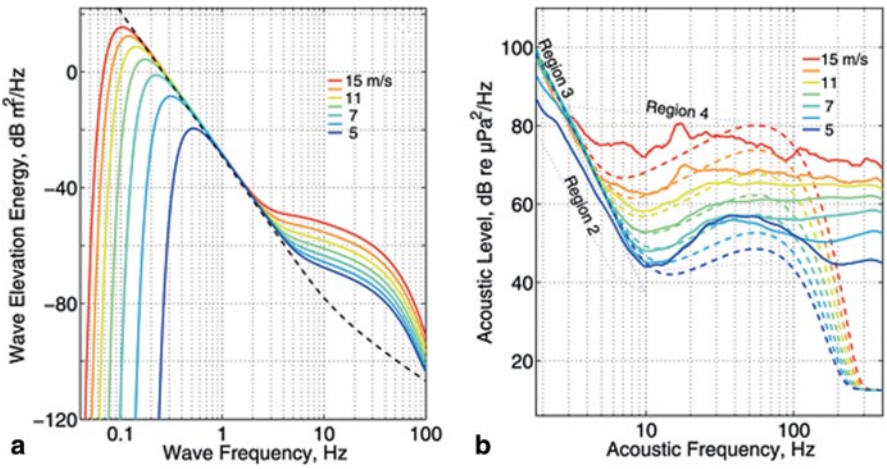

Fig. 7.45 **a** Model energy spectra for the surface wave elevation. The dashed line is the Phillips' saturation spectrum. **b** Acoustic spectrum model is shown by dashed lines and the observed acoustic spectra (rotated by f^8 are represented by solid lines. (Reproduced from Duennebier et al. (2012) by permission of American Geophysical Union)

(c) Acoustic classification of rainfall type Black et al. (1997) proposed an acoustic classification of the two general rainfall types, convective and stratiform, based on the physics of sound generation. Small raindrops (0.8–1.1 µm diameter) effectively produce sound in the HF band, while, the rain containing large raindrops (diameter >2.0 mm) produces sound in both frequency bands. The ratio of the sound intensity in a HF band (10–30 kHz) to a lower frequency band (4–10 kHz) can therefore serve as a characteristic of the raindrop distribution and, hence, of the rainfall type.

Atlas et al. (1999) extended the Black et al. (1997) acoustic classification of rainfall types by using additional features of the sound field. They proposed to link systematic variations in the raindrop size distribution to four different rainfall categories: convective, transition convective, and two types of stratiform rain (type 1 and type 2).

7.7.8 Passive Acoustic Monitoring of Surface Waves from Seafloor Pressure Fluctuations in the Deep Ocean

Surprisingly, important information about the state of the sea surface can be obtained from seafloor pressure fluctuations associated with nonlinear interactions between oppositely traveling surface waves of half their frequency (Farrell and Munk 2008; Munk 2009; Duennebier et al. 2012). The acoustic measurements in the deep ocean shown in Fig. 7.45b are consistent with the model surface wave spectra shown in Fig. 7.45a.

The two-scale wave model of the Elfouhaily et al. (1997) and Hwang (1997) type appears to be qualitatively consistent with acoustic measurements in the deep ocean by Duennebier et al. (2012). The results shown in Fig. 7.47b suggest that there is also a good quantitative agreement between this wave model transformed into the Longuet-Higgins (1950) pressure spectrum and the acoustic data up to about 80 Hz for the wind speed range from 7 to 11 m s^{-1}. There were fewer than 0.1 % of time during the 20 months of observations when wind speed was above 12.5 m s^{-1}; as a result, the levels in Fig. 7.47b associated with wind speeds higher than 12.5 m s^{-1} are less certain than those at lower wind speeds. At lower than 7 m s^{-1} wind speeds and higher frequencies, the observed acoustic levels were higher than predicted by the model, which is possibly due to other noise sources. Note that the acoustic background above approximately 80 Hz is probably generated by sources other than the Longuet-Higgins mechanism.

The acoustic measurements of this type provide important insight into the directional spreading of surface wave spectra. The Longuet-Higgins pressure available at the ocean floor $F_p\left(\omega_p\right)$ in terms of the surface wave elevation wave number spectrum $F_\zeta\left(k\right)$ and the overlap function I is as follows (Hughes 1976; Farrell and Munk 2008; Duennebier et al. 2012):

$$F_p\left(\omega_p\right)=\frac{\pi}{8}\left(\frac{\rho}{c}\right)^2\omega_p^6\frac{kF_\zeta^2\left(k\right)}{d\omega_\zeta/dk}I\left(k\right) \tag{7.17}$$

where $\omega_p=2\omega_\zeta$ and ω_p and ω_ζ are the angular acoustic and surface wave frequency, respectively;

$$I\left(k\right)=\int_{-\pi}^{\pi}H\left(k,\theta\right)H\left(k,\theta+\pi\right)d\theta \tag{7.18}$$

where ρ is the water density, c the speed of sound in water, k the wave number, and θ the angle from the downwind direction. The wave directionality function, H, must satisfy the following conditions:
$\left\langle\zeta^2\right\rangle=\iint kF_\zeta\left(k\right)H\left(k,\theta\right)d\theta dk$ and $\int_{-\pi}^{\pi}H\left(k,\theta\right)d\theta=1$, where $\left\langle\zeta^2\right\rangle$ is the mean-squared wave elevation.

It is easy to see from (7.17) and (7.18) that the amount of acoustic energy transformed from surface waves into deep ocean by the Longuet-Higgins mechanism is substantially determined by the spreading function, H, and the resulting overlap integral I. Duennebier et al. (2012) parameterized the overlap integral as the following:

$$I_{dB}\left(k\right)=9.5\tan^{-1}\left[0.04\left(k/k_p\right)^{1.7}\right]-2.9, \tag{7.19}$$

where $k_p=4\pi^2f_p^2/g=4\pi^2\left(1.56/U_{10}\right)^2/g=9.8/U_{10}^2$. Figure 7.46 compares empirical function (7.19) with the overlap integral derived from (7.17) with measured acoustic spectrum F_p and model wave spectrum F_ζ.

For an isotropic surface wave field, the overlap integral I = 1/(2π) corresponds to a—8 dB level in Fig. 7.46. According to Farrell and Munk (2010), for wind-driven

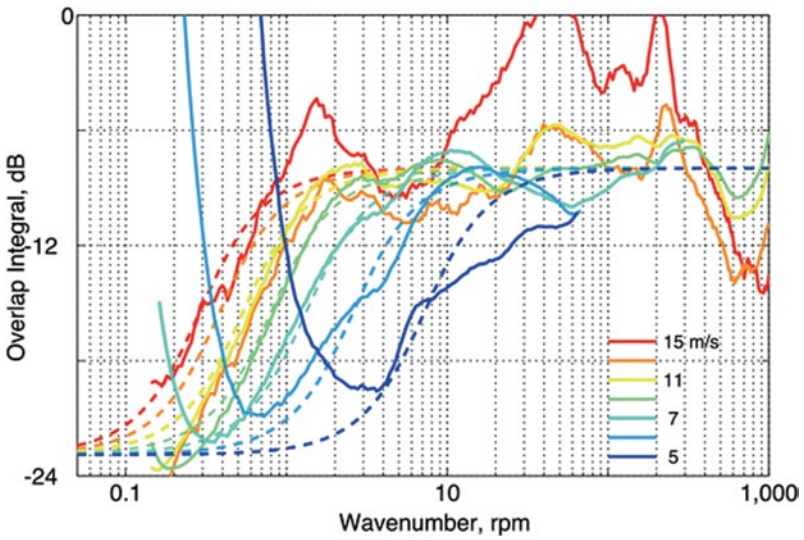

Fig. 7.46 Comparison of empirical formula (7.19) (dashed) to the overlap integral estimated from the acoustic spectrum F_p and wave model F (solid). Colored curves correspond to different wind speeds. (Reproduced from Duennebier et al. (2012) by permission of American Geophysical Union)

seas the overlap integral is not likely to be appreciably larger than $1/(2\pi)$. Nevertheless, higher overlap integral values are possible when the seas are dominated by opposing surface wave systems. For the case of bimodal seas, the overlap integral may increase to values of less than 0.5 (−6 dB) near $f/f_p = 10$ and then decrease to the isotropic level of $1/(2\pi)$ at higher frequencies (Ewans 1998). Here, f is the surface wave frequency and f_p is the frequency of the wave energy peak.

Acoustic data of Duennebier et al. (2012) shown in Fig. 7.46 indicate that surface wave field directionality significantly determines the acoustic spectrum at frequencies below approximately 2 Hz (which is equivalent to $f = 1$ Hz in surface wave frequency), above which the acoustic levels imply close to isotropic surface wave directionality. Note that Duennebier et al. (2012) used an empirical coefficient 0.12 in the model wavenumber spectrum for the saturation range of surface waves. Later, Ardhuin et al. (2013) revised this coefficient to 0.18. The ultra-gravity wave range ($f > 1$ Hz), which is the main interest of this analysis, is not affected by this difference in any significant way.

7.7.9 3D Sonar Technology for Near-Surface Studies

Soloviev et al. (2012a) demonstrated capabilities of 3D sonar technology for near-surface studies on the example of the turbulent wake of a ship. For tests in the wakes of ships of opportunity, they employed a real-time 3D imaging system, CodaOctopus Echoscope-Underwater Inspection System (UIS). The sonar has a working

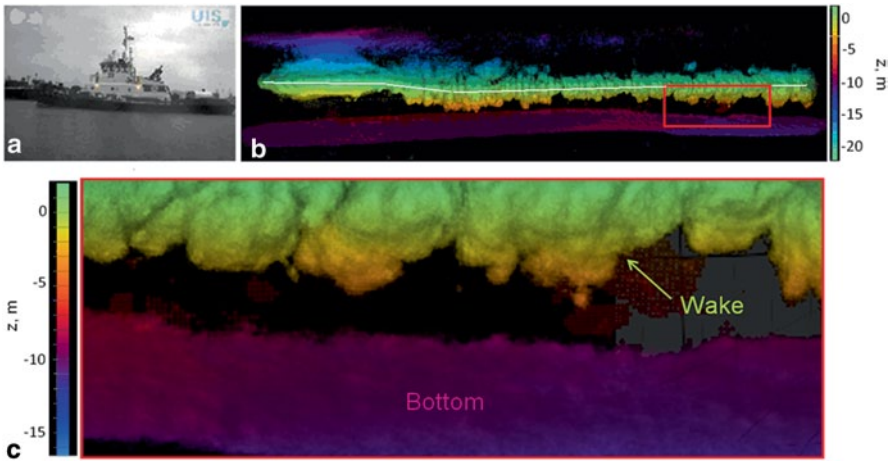

Fig. 7.47 **a** Snapshot of the tugboat taken from the video and **b** its hull surrounded by the bubble curtain and wake in 3D sonar, with surface reflections. Position of the sea surface is indicated by the white line. The image above the white line, including a purple-blue color above the ship hull, is an artifact due to surface reflections. The red box indicates the area of **c**, the enlarged view of the wake with surface reflections removed. Color scales are provided as depth in meters relative to mean sea level. In this color scale, the ocean bottom appears in a purple color. (After Soloviev et al. (2012a). Copyright © 2012 American Meteorological Society. Used with permission)

frequency of 375 kHz with a 128×128 (16,384) array of beams, which provide an angular coverage of 50 x 50° and a beam spacing of 0.39°. The maximum range is 150 m with a range resolution of 3 cm and a ping rate of 12 Hz.

Sonar data during the passage of a tugboat in the Tampa Bay Port Channel are shown in Fig. 7.47. The survey vessel equipped with the sonar system was moving on an opposite course relative to the tugboat at approximately 2.6 m s^{-1}. The sonar image of the tugboat wake is shown in Fig. 7.47b with surface reflections not removed.

A segment of the tugboat wake visualized with the 3D sonar is shown in more detail in Fig. 7.47c. This image displays a strong intermittency of the wake shape, while turbulent features are resolved starting from centimeter scale.

Note that surface reflections (as well as signatures of the survey vessel wake) have been removed from Fig s. 7.47c and 7.48, which was possible due to the 3D aspect of this instrument. The 3D aspect of the sonar view of the ship wake allows quantitative estimation of the characteristics of the wake segment shown in Fig. 7.47.

A more sophisticated approach may include geometric properties of boundaries, such as fractal dimensions, which provide clues to the distribution of physical scales in turbulent flows (Sreenivasan et al. 1989; Catrakis 2000). The power spectral density of turbulence can be related to the image fractal dimension (Voss 1988; Meneveau and Sreenivasan 1991). An effective method for evaluating the fractal dimension from images of turbulent clouds has been developed by Zubair and Catrakis (2009). This method is applicable to the analysis of CodaOctopus Echoscope

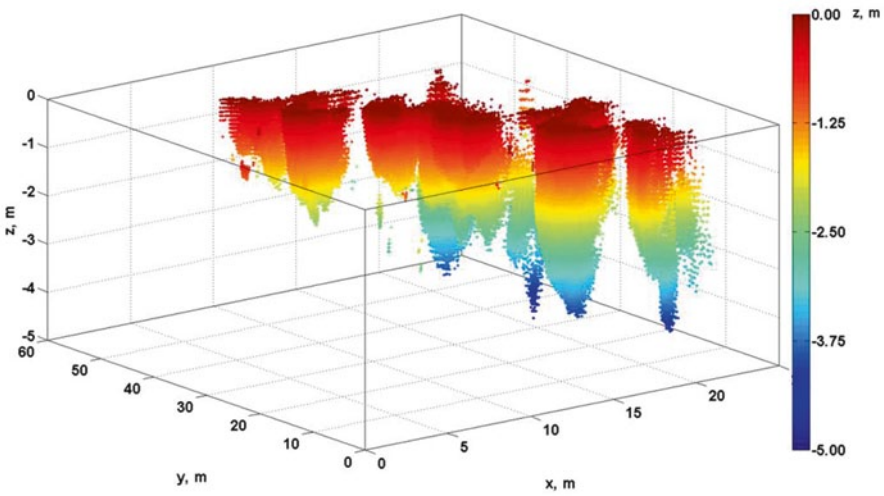

Fig. 7.48 Segment of the tugboat wake shown in Fig. 7.46. Color scales are provided as depth in meters relative to mean sea level. (After Soloviev et al. (2012a). Copyright © 2012 American Meteorological Society. Used with permission)

sonar images due to the capability of this 3D sonar to produce quantitative measurements of length scales. A method similar to the particle imaging velocimetry (PIV), utilizing the 3D sonar imagery of the bubble cloud boundary, may also be developed in the future for extraction of 3D vector fields. These approaches can also be useful to measure turbulence in breaking wind waves.

7.8 Ocean State Estimation, Climate Modeling, and Prediction

Accurately modeling the air–sea interface and near-surface layer of the ocean is important for a number of reasons. The near-surface layer is the portion of the ocean that humans are most affected by, and which humans affect most. The fluxes of energy, momentum, and buoyancy into and through the near-surface ocean are responsible for driving the general circulation of the ocean. The heat and freshwater fluxes into and through this layer are responsible for the stratification of the ocean and for the formation of water masses that fill the ocean. The distribution of heat in the near-surface ocean affects the overlying atmosphere on a variety of time and space scales. The exchanges of gases with the near-surface ocean, and fluxes of aerosols and salt into the atmosphere are crucial elements of the climate system as well.

The ocean plays a vital role in the Earth's climate and its variations. Thus, numerical models of the ocean are essential tools for understanding, assessing, and predicting climate variability and change, along with the associated impacts. For

example, understanding the relative roles of different ocean processes during El Niño-Southern Oscillation (ENSO) events has depended strongly on experiments with forced ocean models and coupled ocean–atmosphere models. Ocean models are now used routinely to assimilate observations to provide initial conditions for coupled ocean–atmosphere models that are used to predict seasonal-to-interannual climate variability. Global climate models that are used in greenhouse gas scenarios of future climates depend significantly not only on accurate representation of ocean physics, but also on representation of ocean biogeochemistry because the absorption and sequestration of CO_2 in the ocean is a very important element of global change projections.

Ocean models are important in their own right as tools for managing marine transportation, for search and rescue efforts, to support coastal engineering, for marine hazards mitigation, and for management of marine ecosystems, among other applications. The international Global Ocean Data Assimilation Experiment (GODAE) is underway as this is written, aimed at significantly advancing our ability to assess the state of the oceans, with these and other applications as objectives.

Successfully modeling the ocean requires adequate boundary conditions (usually expressed in the form of air–sea fluxes) and accurate parameterization of the grid-scale impacts of processes that are not resolved by the model numerical grid. Forcing and parameterization errors may accumulate unevenly in the model domain, and in coupled models they may be amplified considerably by positive feedback mechanisms. For oceanic GCMs on global and regional scales, the near-surface processes discussed throughout this book cannot be resolved. Global parameterizations of such processes are sought, but in many cases this is an elusive goal.

Another approach to parameterization is to incorporate submodels that can be used to provide a statistical representation of the grid-scale impacts of physics that cannot be resolved by the main model. An example of such an enhanced-resolution submodel is the non-hydrostatic cloud-resolving model embedded in an atmospheric GCM (Randall et al. 2003).

Submodels may be needed to represent variables that cannot easily be represented in the main model. For example, growing recognition of the important role of waves in determining the momentum fluxes across the air–sea interface motivated the inclusion of spectral wave submodels in operational numerical weather prediction models at NOAA/National Centers for Environmental Prediction (NCEP) (Tolman et al. 2002) and European Centre for Medium-Range Weather Forecasts (ECMWF) (Janssen 2007). For some applications, such as ship routing and storm surge forecasting, the modeled wave fields are of direct utility. Another example is the use of a biological submodel to predict near-surface optical properties for an ocean GCM. However, biogeochemical processes and their interaction with physics near the air–sea interface represent a fundamental challenge for modeling climate variability and change because the appropriate equations are not yet fully developed.

Another fundamental challenge of long-term predictions is that the nonlinear equations describing the ocean and atmosphere are known to be a deterministic chaotic system (Lorenz 1963). A characteristic feature of such systems is that small errors introduced in the initial conditions grow exponentially with time until they

"saturate." The exponential error growth fundamentally limits the predictability skills of numerical models (Liu et al. 2009). This problem relates to dynamics of nonlinear systems and is beyond the scope of this monograph.

Below, we discuss the representation of near-surface processes in the context of surface boundary conditions and near-surface subgrid-scale parameterizations for numerical ocean models, and the possible roles of these processes in ocean and climate simulation, state estimation, and prediction.

7.8.1 Air–Sea Fluxes

Air–sea fluxes depend not only on the conditions in the atmosphere, but also on processes in the upper ocean boundary layer. Surface gravity waves are only the most obvious example. Thus, there is a coupled nature to ocean surface boundary conditions, and ocean models that are driven by specified fluxes cannot take these feedbacks into account. Coupled ocean–atmosphere models can, in principal, take them into account, but they generally do not have the vertical resolution to do so. Thus, these effects must be parameterized.

(a) Wave-mediated momentum fluxes At the present time, neither ocean GCMs nor coupled climate models explicitly include the effects of surface waves, except as crudely parameterized by a wind-speed (and may be wave-spectral) dependent drag coefficient. The flux of momentum from the atmosphere to the ocean (or vice versa under calm winds) intimately involves the surface wave field, which depends on the history of the wind locally and at remote locations. A major challenge is that the surface wind stress depends on the wave roughness, and the accurate partitioning of atmospheric momentum into the wave field and near-surface currents and turbulence is a poorly posed problem. Properly accounting for these influences includes consideration of the Stokes drift due to wave radiation stress and spray effects (see below), and of the turbulence created when waves break.

(b) Rain-mediated fluxes Section 1.5 discussed the heat, freshwater, and momentum fluxes associated with rainfall. These effects are generally ignored in ocean and coupled models, even though they can have substantial impacts in some regions and at some times. Even on climate timescales, the net effects can be significant. For example, for the 4 months of the TOGA COARE intensive observing period there was a net sensible heat flux of 6 W m^{-2} due to rainfall (Weller and Anderson 1996). This may seem insignificant, but the net heat flux for the same period was only about 20 W m^{-2}.

Parameterization of rainfall contributions to air–sea fluxes is moot at this time because obtaining accurate estimates of rain rates, which vary strongly in time and space, is so problematic. Even in atmospheric analyses and coupled models, where rain rates must be known for grid-scale averages, the errors for rain-modulated fluxes are large. Because of the small spatial scales and large temporal variability of rainfall, and the nonlinearity of the rainfall-mediated processes, parameterization using grid-scale rain rates is not likely to be successful.

(c) Spray-mediated fluxes Under the very high winds in tropical and midlatitude cyclones, momentum, heat, and moisture fluxes are significantly altered from those estimated from Monin–Oboukhov similarity profiles, due to the presence of spray. Spray redistributes air–sea energy fluxes from sensible to latent heat, and it alters the momentum flux from the atmosphere to the ocean (Sect. 6.4). Both positive and negative feedbacks are involved with spray modification of heat and momentum fluxes (Zhang and Perrie 2001). Because the effects of spray are not completely understood and well modeled, it remains undecided whether tropical cyclones may become more intense due to spray (Andreas and Emmanuel 2001; Wang et al. 2001); while, Chapter 6 provides a new perspective in this direction.

Air–sea fluxes within extratropical cyclones are apparently altered by spray effects, leading to changes in surface winds and rainfall within the storms. Meirink (2002) compared latent and sensible heat fluxes in modeled North Sea storms with and without spray effects using a parameterization based on Makin (1998) and Andreas (1998). Maximum differences of latent fluxes were over 100 W m^{-2}, while sensible heat flux differences were reduced by comparable amounts. The net heat flux difference was as large as 50 W m^{-2}. Because of enhanced evaporation, the inclusion of spray effects resulted in an increase in rainfall by as much as 7 mm d^{-1} in some parts of the storm-affected area.

(d) Solar absorption and turbidity The volume absorption of penetrating solar radiation in the ocean plays an important role in determining the temperature and density structure of the upper ocean. Changes of turbidity alter the profile of shortwave radiation, and episodic or seasonal changes of productivity may significantly affect turbidity (Lewis et al. 1990; Siegel et al. 1995; Ohlmann et al. 1996). The impact of altered penetration of shortwave radiation can be significant for climate models (Schneider and Zhu 1998; Murtugudde et al. 2002; Miller et al. 2003). Biological influences on turbidity are not amenable to parameterization at this time. Biogeochemical submodels are required (Christian et al. 2002). Though for the upper ten centimeters of the open ocean (where mostly the red part of the radiation spectrum is absorbed), the effect of turbidity on the absorption of solar radiation is nevertheless relatively "small" (see Sect. 1.4.6).

(e) Air–sea gas exchange The fluxes of gases like carbon dioxide (CO_2), dimethylsulfide (DMS), and ozone (O_3) gases across the air–sea interface are an important part of the global climate and its changes (Tans et al. 1990; Takahashi 2000; Huebert et al. 2004). The global ocean is a significant sink for anthropogenic carbon; approximately a third of the human CO_2 emitted over the industrial period has been taken up by the oceans (Khatiwala et al. 2013). DMS produced by marine plankton and emitted to the atmosphere is involved in the formation of cloud condensation nuclei, which are a factor in direct and indirect climate forcing (Kettle and Andreae 2000).

Soloviev and Schlüssel (2002) suggested that local estimates of air–sea gas exchanges can be derived from interfacial, bubble-mediated, and mixed-layer parameterizations and model components and extended to global scale with the help of remote-sensing techniques. Estimates of local air–sea gas fluxes critically depend on the parameterization for the gas transfer velocity. Empirical approach has result-

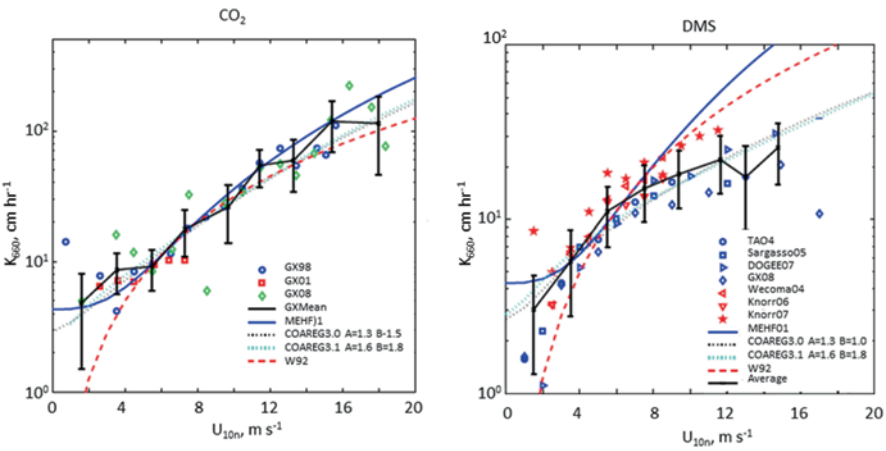

Fig. 7.49 (*left*) Gas transfer coefficient for CO_2 as a function of 10 m neutral wind speed from direct surface-based observations and COAREG parameterization. (*right*) DMS gas transfer coefficient as a function of 10 m neutral wind speed from direct surface-based observations and COAREG parameterization. (After Fairall et al. (2011) by permission of John Wiley and Sons)

ed in a number of useful gas transfer parameterizations (Wanninkhof et al. 2009). Modeling and parameterization of the air–sea gas transport is, however, a turbulent boundary layer problem, which is inherently linked to physics of the air–sea interface and near-surface layers (Soloviev and Schlüssel 1994; Fairall et al. 1996) and involves multi-phase physics (Woolf and Thorpe 1991). A potential advantage of physically based versus empirical parameterizations is that the former can potentially provide global coverage, while the latter will require adjustment of their empirical coefficients for specific climatic regions, seasons, and, perhaps, even for single weather events (Soloviev et al. 2007). At the same time, it is still a long way for producing a robust parameterization scheme for air–sea gas exchange providing global coverage. Such areas of the air–sea gas-exchange physics as bubble-mediated transport, and gravity-capillary and surfactant effects have not yet been completely understood.

An important step toward physically based parameterization for the air–sea gas exchange has been made by Fairall et al. (2011). Their parameterization (COAREG) incorporates the physics of the turbulent boundary layer and the properties of the sea surface. It takes into account resistance from both water and air sides of the air–sea interface, bubble-mediated transfer, gas solubility, and possible chemical reactions. An example of an application of this parameterization to the CO_2 and DMS gases is given in Fig. 7.49.

A broader view of the air–sea exchange processes and their spatial and temporal variability in the vicinity of the experimental area and beyond can be obtained from satellite data. IR and microwave images from the AVHRR and from the SSM/I have been used to retrieve boundary layer variables for the time period corresponding to *GasEx-98* (Fig. 7.50). These variables include the SST, surface friction velocity, low-level atmospheric humidity, near-surface stability, and the atmospheric back

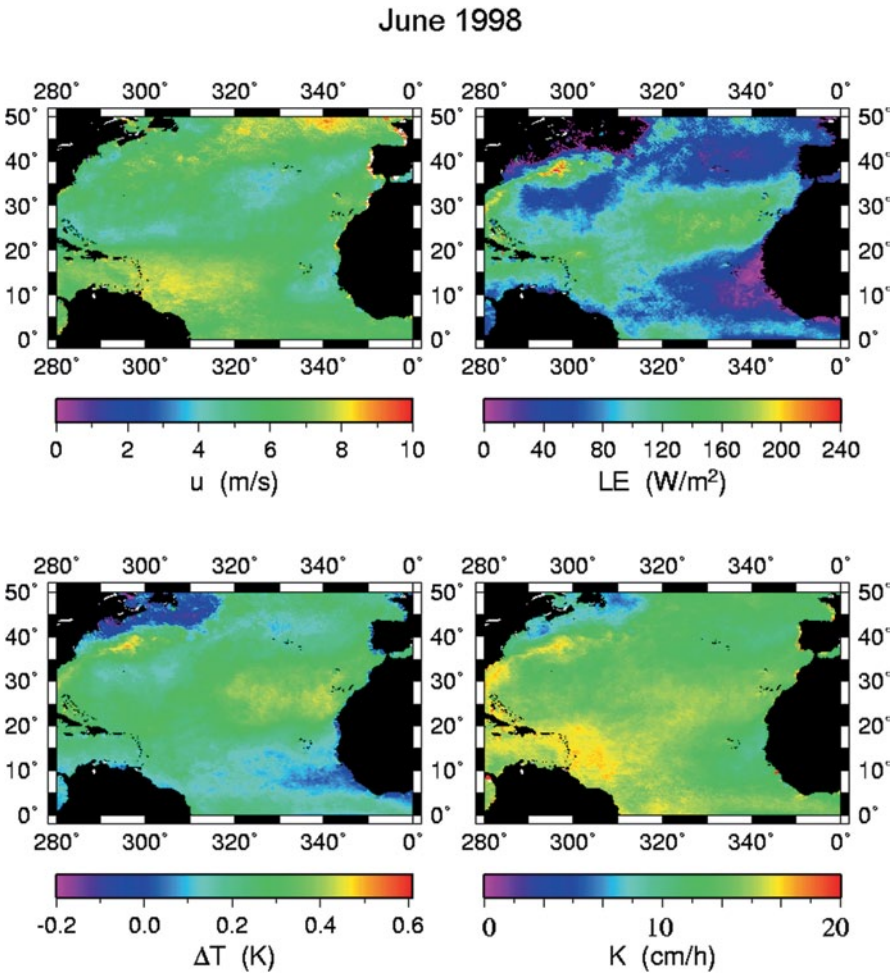

Fig. 7.50 Wind speed (u), cool skin (ΔT), latent heat flux (LE), and total ($K=K_{int}+K_b$) air–sea gas transfer velocity for the *GasEx-98* period of June 1998 as calculated from satellite data and parameterizations. (After Schlüssel and Soloviev 2002)

radiation. They are used to calculate energy and momentum fluxes which, in turn, are used together with a surface renewal model to parameterize the temperature difference across the thermal molecular boundary layer of the upper ocean and the air–sea gas exchange coefficient.

Oceanic whitecaps (spilling wave crests) are the sea surface features detectable from satellites in the microwave emissivity signal. The bubble-mediated component of the air–sea gas exchange can be linked to the fraction of sea surface covered by whitecaps (Monahan 2002).

Surface films can dramatically reduce the air–sea gas exchange through modification of capillary waves (Frew et al. 1995). According to Bock et al. (1999) and

Jaehne et al. (1987), regardless of the surfactant concentrations, the gas transfer velocity shows a reasonable correlation with the mean square slope of the sea surface. Due to the fact that the remotely sensed wind velocity (like that shown in Fig. 7.1) is determined from the mean square slope, this substantially reduces (but does not completely eliminate) the dependence of the gas transfer coefficients on surface films.

An independent approach including database of dissolved organic radiocarbon, measurements and a suite of ocean GCMs in an inverse mode has been used to quantify air–sea gas exchange on a global scale (Sweeney et al. 2007). This approach is, however, based on GCMs, which still contain uncertainties.

(f) Vertical mixing The projection of momentum from the surface wind into the interior of the ocean depends strongly on the vertical structure of turbulence, which is only crudely parameterized in coupled climate models, and in many ocean GCMs. Turbulence from wave breaking is presently not considered in ocean models; yet this is a large source of turbulent kinetic energy in the near-surface layer.

One of the approaches to parameterizing the vertical mixing coefficient in the ocean is the so-called K-Profile Parameterization (KPP) scheme proposed by Large et al. (1994). A further development of this approach undertaken in Chap. 3 of this monograph provides a robust and computationally effective mixing parameterization scheme. However, use in GCMs is sensitive to grid size and resolved vertical shear.

In some situations (like nighttime convective mixing), nonlocal processes dominate transport of properties within the upper ocean mixed layer. This transport is performed by coherent structures considered in Chap. 5 of this monograph. Incorporation of coherent structures into parameterization schemes has not yet been done in a systematic way.

(g) Horizontal mixing Horizontal mixing is a complex process including multiscale nonlinear interactions. On the submesoscale, horizontal pressure gradients due to spatially varying buoyancy fields produce quite intensive mixing. Influx of buoyancy through the air–sea interface is an important component of this process. In the tropical ocean, rainfalls substantially contribute to the spatial inhomogeneity of buoyancy flux at the air–sea interface. The horizontal mixing coefficient therefore appears to be intimately linked to freshwater cycling and salinity effects (Chap. 5).

As the spatial resolution of numerical ocean models increases, processes that were completely unresolved may become partially resolved. Horizontal mixing is a case in point: when the model grid fully resolves mesoscale eddies, then smaller scales on which rotational effects are less effective become more important to parameterize.

7.8.2 Interactions

While some subgrid processes have been parameterized, the interactions among these processes are generally not considered. For example, due to freshwater cycling

and salinity effects, a salt-stratified barrier layer (Lukas and Lindstrom 1991) may exist over a broad region covering many grid points in a numerical model. But the barrier layer is maintained by the interaction of resolved processes and unresolved processes acting on subgrid scales (Vialard and Delecluse 1998b). The subduction process that plays a role in barrier layer maintenance involves large-scale advection, but also involves small-scale frontal processes including subgrid vertical and horizontal mixing.

The barrier layer favors the growth and eventual displacement of the warm pool into the central Pacific by isolating the mixed layer from entrainment cooling and by confining the response of westerly wind events to a relatively shallow mixed layer (Vialard and Delecluse 1998a). This process is an important part of the ENSO cycle (Maes et al. 2002; see Sect. 1.7.4). It can also be important in the dynamics of coastal regions with river run-off (like the Bay of Bengal) and in the marginal polar seas under conditions of ice melting.

Vinayachandran et al. (2002) captured the formation of a barrier layer at 17°30'N, 89°E in the northern Bay of Bengal. On 28 July 1999, the upper 30 m layer was homogeneous in both temperature and salinity (Fig. 7.51). Subsequently, a freshwater plume from river discharge and rainfall was advected to the experimental area. The arrival of the freshwater plume caused the depth of the mixed layer to decrease to about 10 m and the salinity in the surface layer to drop by about 4 psu. As a result, a new halocline and thus a barrier layer formed within the upper 30 m of the ocean (Fig. 7.52). Air–sea interaction was then restricted to this thinner mixed layer; a 0.5 °C temperature inversion just below the mixed layer provided evidence that the surface cooling was restricted to this thin layer.

Such a thin surface layer is more strongly coupled to the atmosphere. The salt-stratified barrier layer may thus be involved in the processes of deep atmospheric convection and cyclogenesis by reducing the entrainment cooling from below the mixed layer (Murty et al. 2002; Subrahmanyam et al. 2005). The barrier layer inhibition of entrainment cooling delays the development of the cold wake, thus reducing the source of negative feedback on the enthalpy flux to the storm. The relative importance of this effect depends on the strength of the storm when it encounters the barrier layer region, and how fast the storm moves (Balaguru et al. 2012).

7.8.3 Ocean State Estimation and Prediction

A major area of near-surface ocean science application involves assessing the current state of the ocean and forecasting its future evolution, both of which have had important impacts on modern society. It was clearly recognized in the 1970s that numerical weather prediction skill benefited from improved specification of SST—the lower boundary condition over the oceans in bulk-flux formulations—and this helped provide motivation for the building of a global array of geostationary and polar-orbiting satellites. However, specification of SST does not provide sufficient information to ocean models. Subsequent research has overwhelmingly shown that

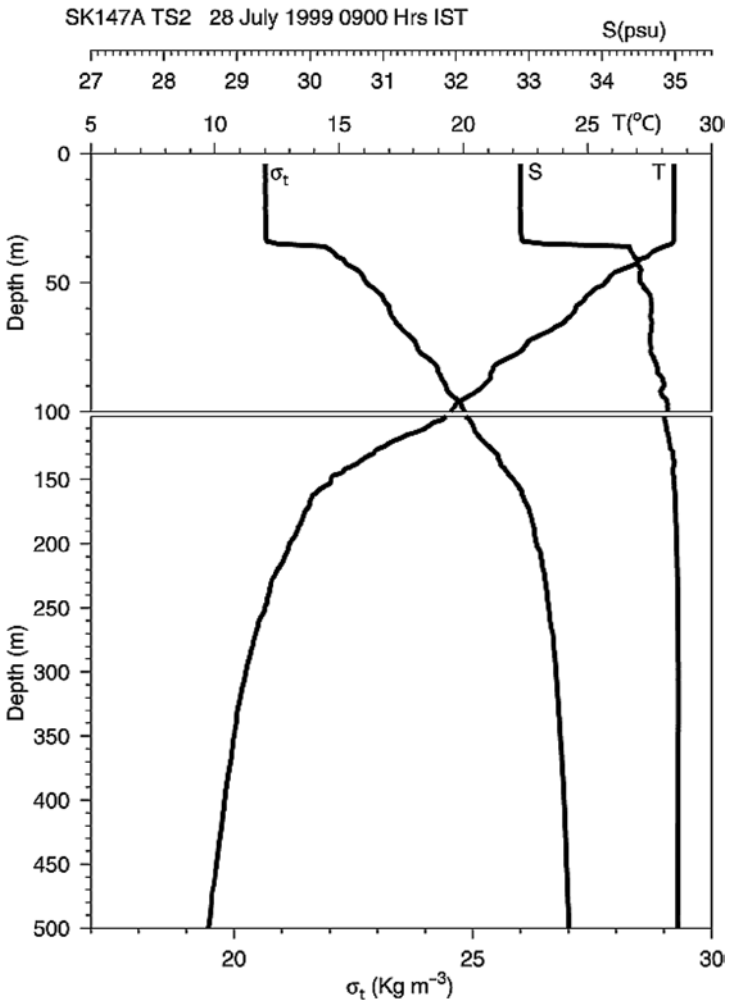

Fig. 7.51 Vertical profiles of temperature, salinity, and density measured at 17°30N, 89°E in the northern Bay of Bengal. (Reproduced from Vinayachandran et al. (2002) by permission of American Geophysical Union)

short-term numerical weather prediction skill benefits from improved air–sea interaction physics (especially surface waves) and better specification of ocean initial conditions (especially upper ocean heat content).

The air–sea fluxes of heat, moisture, momentum, and gases are the fundamental coupling variables for the ocean–atmosphere system (see Chap. 1). These fluxes are hard enough to measure well over the ocean for limited times at one location. Satellites do not observe these fluxes. Buoys and drifters do not directly measure them, but can observe changes of ocean and atmospheric state variables, flow, temperature, and salinity/humidity. Bulk formulations have been traditionally used to

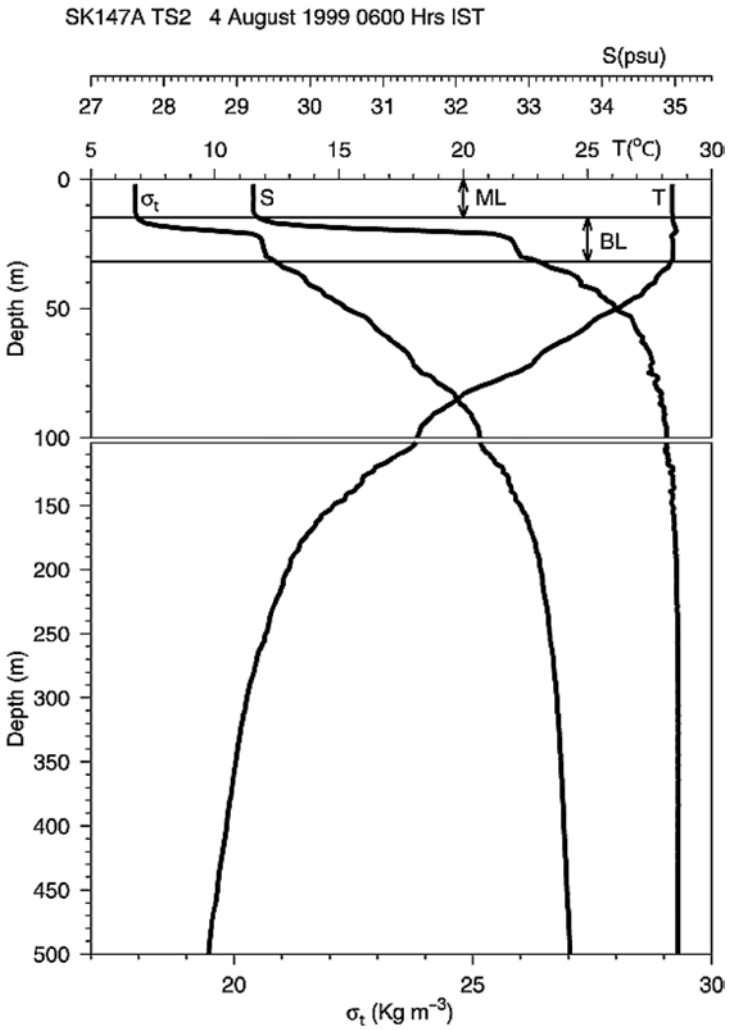

Fig. 7.52 Vertical profiles of temperature, salinity and density after arrival of the freshwater plume. ML and BL indicate mixed layer, and barrier layer respectively. (Reproduced from Vinayachandran et al. (2002) by permission of American Geophysical Union)

estimate fluxes, but the accuracy of these estimates in ocean and atmospheric analysis products depends on the quality of the dynamics models, and on the quantity and types of observations used to constrain them.

Because of the nonlinearities of air–sea interaction on a variety of space and timescales discussed throughout this book, rectified effects influence the evolution of the coupled system on climate timescales (Webster and Lukas 1992; Meehl et al. 1994). Climate prediction models require prediction of the coupled evolution of the atmosphere and ocean starting from an initial estimate of the state of the system,

with the initial ocean state having more influence over longer timescales due to the high heat capacity of seawater, and due to the ocean's integration of atmospheric forcing. Even long-term climate projections based on changing atmospheric composition require an initialization of the ocean state, particularly considering that the observations used to verify them include natural multi-decadal variability.

State estimation is complicated by the small vertical and horizontal scales that are not resolved by ocean observations and numerical models. Even with increased resolution, models cannot fill observational holes without adequate representation of the physics on those scales. As learned, small scales processes do not simply generate linear, additive noise, but are tied into the rest of the ocean and climate system. For example, fronts in the mixed layer are fundamental to the maintenance of the thermocline over time.

All elements of ocean–atmosphere state estimation—observations, model physics, and model resolution—have improved notably over the past decade or so. Despite an array of new technology, such as satellite altimeters, scatterometers, moored buoys, and profiling floats, connecting evolving surface characteristics with interior ocean variations remains a challenge. For example, to avoid fouling of sensors and calibration shifts, Argo floats are programmed to stop pumping water through sensors at depths less than 6 m. Shipboard profiling measurements are compromised by ship disturbance of the upper few meters (typically, sometimes more). Development of new instrumentation for studying the near-surface layer of the ocean remains an important task.

References

Alldredge AL, Crocker KM (1995) Why do sinking mucilage aggregates accumulate in the water column? Sci Total Environ 165:15–22

Alldredge AL, Passow U, Logan BE (1993) The abundance and significance of a class of large, transparent organic particles in the ocean. Deep Sea Res 40:1131–1140

Alldredge AL, Cowles TJ, MacIntyre S, Rines JEB, Donaghay PL, Greenlaw CF, Holliday DV, Dekshenieks MM, Sullivan JM, Zaneveld R (2002) Occurrence and mechanism of formation of a dramatic thin layer of marine snow in a shallow Pacific fjord. Mar Ecol Prog Ser 233:1–12

Alpers W (1985) Theory of radar imaging of internal waves. Nature 314:245–247

Alpers W, Huang W (2011) On the discrimination of radar signatures of atmospheric gravity waves and oceanic internal waves on synthetic aperture radar images of the sea surface. IEEE Trans Geosci Rem Sens 49(3):1114–1126

Alpers W, Hühnerfuss H (1989) The damping of ocean waves by surface films: a new look at an old problem. J Geophy Res 94(C5):6251–6265

Alpers W, Mitnik L, Hock L, Chen KS (1999) The Tropical and Subtropical Ocean Viewed by ERS SAR. http://www.ifm.zmaw.de/fileadmin/files/ers-sar

Andreas EL (1998) A new sea spray generation function for wind speeds up to 32 m s-1. J Phys Oceanogr 28:2175–2184

Anagnostou MN, Nystuen JA, Anagnostou EN, Nikolopoulos EI, Amitai E (2008) Evaluation of Underwater Rainfall Measurements during the Ionian Sea Rainfall Experiment. IEEE Trans Geosci Rem Sens 46(10):2936–2946

Andreas EL, Emanuel KA (2001) Effects of sea spray on tropical cyclone activity. J Geophys Res 58:3741–3751
Asper VL (1987) Measuring the flux and sinking speed of marine snow aggregations. Deep-Sea Res 34:1–7
Apel JR (1994) An improved model of the ocean surface wave vector spectrum and its effects on radar backscatter. J Geophys Res 99(16):269–16, 291
Atlas D, Ulbrich CW, Marks FD, Amitai E, Williams CR (1999) Systematic variation of drop size and radar–rainfall relations. J Geophys Res 104:6155–6169
Balaguru K, Chang P, Saravanan R, Leung LR, Xu Z, Li M, Hsieh J-S (2012) Ocean barrier layers' effect on tropical cyclone intensification. PNAS 109(36):14343–14347
Ballabrera-Poy J, Murtugudde R, Busalacchi AJ, (2002) On the potential impact of sea surface salinity observations on ENSO predictions. J Geophys Res 107(C12):8007. doi:10.1029/2001JC000834
Bentamy A, Katsaros KB, Mestas-Nuñez AM, Drennan WM, Forde EB, Roquet H. (2003) Satellite estimates of wind speed and latent heat flux over the global oceans. J Climate 16:637–656
Berger M, Camps A, Font J, Kerr Y, Miller J, Johannessen J, Boutin J, Drinkwater MR, Skou N, Floury N, Rast M, Rebhan H, Attema E (2002) Measuring Ocean Salinity with ESA's SMOS Mission. ESA Bulletin 111:113f
Biao Z, Perrie W (2012) Cross-Polarized Synthetic Aperture Radar: A New Potential Measurement Technique for Hurricanes. Bull Amer Meteor Soc 93: 531–541
Bissett WP, Schofield O, Glenn S, Cullen JJ, Miller WL, Plueddemann AJ, Mobley CD (2001) Resolving the impacts and feedbacks of ocean optics on upper ocean ecology. Oceanography 14(3):30–53
Black PG, Proni JR, Wilkerson JC, Samsury CE (1997) Oceanic rainfall detection and classification in tropical and subtropical mesoscale convective systems using underwater acoustic methods. Mon Weather Rev 125:2014–2024
Bock EJ, Hara T, Frew NM, McGillis WR (1999) Relationship between air-sea gas transfer and short wind waves. J Geophys Res 104:25821–25831
Bolin B (1960) On the exchange of carbon dioxide between atmosphere and sea. Tellus 12(3):274–281
Borge JCN, Rodriguez GR, Hessner K, Conza PI (2004) Inversion of marine radar images for surface wave analysis. J Atmos Ocean Technol 21:1291–1300
Boutin J, Martin N, Yin X, Font J, Reul N, Spurgeon P (2012) First assessment of SMOS data over open ocean: part II—Sea surface salinity. IEEE Trans Geosci Rem Sens 50(5):1662–1675
Breitz ND, Medwin H (1989) Instrumentation for in-situ acoustical measurements of bubble size distributions. J Atmos Ocean Tech 86:739–743
Brekhovskich LM, Lysanov YP (1978) Acoustic of the ocean. In: Voitov VI (eds) Physics of the ocean 2, Nauka, Moscow, pp 49–145
Broecker WS (1991) The great ocean conveyor. Oceanography 4:79–89
Brusch S, Lehner S, Fritz T, Soloviev A, van Schie B (2011) Ship surveillance with TerraSAR-X. IEEE Trans Geosci Rem Sens 49(3):1092–1103
Bulatov MG, Kravtsov Yu A, Lavrova O Yu, Litovchenko K Ts, Mityagina MI, Raev MD, Sabinin KD, Trokhimovskii Yu G, Tchuryumov AN, Shugan IV (2003) Physical mechanisms of aerospace radar imaging of the ocean. Physics-Uspekhi 46(1):63–80 (in Russian)
Carey WM, Bradley MP (1985) Low-frequency ocean surface noise sources. J Acoust Soc Amer 78:S1–S2
Catrakis HJ (2000) Distribution of scales in turbulence. Phys Rev E 62:564–578
Chandraesekhar S (1950) Radiative Transfer. Oxford University Pressreprinted by Dover Publications, New York, pp. 393 (1960)
Chapron B, Collard F, Kerbaol V (2004) Satellite synthetic aperture radar sea surface Doppler measurements. Proceedings of the Second Workshop on Coastal and Marine Applications of SAR, 8–12 September 2003. Svalbard, ESA Publications Division, pp. 133–140 (ESA SP–565)

Choi J-K, Park YJ, Ahn JH, Lim H-S, Eom J, Ryu J-H (2012) GOCI, the world's first geostationary ocean color observation satellite, for the monitoring of temporal variability in coastal water turbidity. J Geophys Res 117, C09004. doi:10.1029/2012JC008046

Christian J, Verschell M, Murtugudde R, Busalacchi A, McClain C (2002) Biogeochemical modeling of the tropical Pacific Ocean I: Seasonal and interannual variability. Deep-Sea Res 49:509

Commander KW, Prosperetti A (1989) Linear pressure waves in bubbly liquids: Comparison between theory and experiments. J Acoust Soc Amer 85:732–746

Cox C, Munk W (1956) Measurement of the roughness of the sea surface from photographs of the Sun's glitter. J Opt Soc Am 44:838–850. doi:10.1364/JOSA.44.000838

Cowles TJ, Desiderio RA, Carr M-E (1998) Small-scale planktonic structure: Persistence and trophic consequences. Oceanography 11(1):4–9

Crisp D (2004) The state-of-the-art in ship detection in synthetic aperture radar imagery. Australian Dept. Defense, Canberra, Australia

Crum IA (1995) Unresolved issues in bubble-related ambient noise. In: Buckingham MJ, Potter JR (eds) Proceedings of III Int. Meeting on Natural Physical Processes Related to Sea Surface Sound "Sea Surface Sound'94," University of California, Lake Arrowhead, 7–11 March 1994. 243–269 (World Scientific, Singapore)

Dickey T, Banner ML, Bhandari P et al (2012) Introduction to special section on Recent Advances in the Study of Optical Variability in the Near-Surface and Upper Ocean. J Geophys Res. 117. doi:10.1029/2012JC007964 (C00H20)

Donaghay PL, Osborn TR (1997) Toward a theory of biological-physical control of harmful algal bloom dynamics and impacts. Limnol Oceanogr 42(5):1238–1296

Donaghay PL, Rines HM, Sieburth JM (1992) Simultaneous sampling of fine scale biological, chemical and physical structure in stratified waters. Ergeb Limnol 36:97–108

Donelan MA, Pierson WJ (1987) Radar scattering and equilibrium ranges in wind-generated waves with application to scatterometry. J Geophys Res 92:4971–5029

Duennebier FK, Lukas R, Nosal E-M, Aucan J, Weller RA (2012) Wind, waves, and acoustic background levels at Station ALOHA. J Geophys Res 117. doi:10.1029/2011JC007267 (C03017)

Eldhuset K (1996) An automatic ship and ship wake detection system for spaceborne SAR images in coastal regions. IEEE Trans Geosci Rem Sens 34(4):1010–1019

Elfouhaily T, Chapron B, Katsaros K, Vandemark D (1997) A unified directional spectrum for long and short wind-driven waves. J Geophys Res 102(C7):15,781–15,796. doi:10.1029/97JC00467

Ewans KC (1998) Observations of the directional spectrum of fetchlimited waves. J Phys Oceanogr 28:495–512. doi:10.1175/1520-0485 (1998 028 <0495:OOTDSO> 2.0.CO;2)

Ermakov SA, Sergievskaya IA, Shchegolkov Yu.B (2002) A laboratory study of strong modulation of radar signals due to long waves on the water surface covered with a surfactant film. Radiophy Quant Electron 45(12):942–957

Fairall CW, Bradley EF, Godfrey JS, Wick GA, Edson JB, Young GS (1996) The cool skin and the warm layer in bulk flux calculations. J Geophys Res 101:1295–1308

Fairall CW, Yang M, Bariteau L, Edson JB, Helmig D, McGillis W, Pezoa S, Hare JE, Huebert B, Blomquist B (2011) Implementation of the COARE flux algorithm with CO2, DMS, and O3. J Geophys Res 116. doi:10.1029/2010JC006884

Farmer DM, Lemon D (1984) The influence of bubbles on ambient noise in the ocean at high wind speeds. J Phys Oceanogr 14:1761–1777

Farmer DM, Vagle S, Booth AD (1998) A free-flooding acoustical resonator for measurement of bubble size distributions. J Atmos Ocean Tech 15(5):1132–1146

Farrell WE, Munk W (2008) What do deep sea pressure fluctuations tell about short surface waves? Geophys Res Lett 35:L19605. doi:10.1029/2008GL035008

Farrell WE, Munk W (2010) Booms and busts in the deep. J Phys Oceanogr 40: 2159–2169, doi:10.1175/2010JPO4440.1

Fedorov KN (1991) Salinity as Cinderella of Physical Oceanography. Selected Works in Physical Oceanography by K.N. Fedorov. 292–299 (in Russian)

Felizardo FC, Melville WK (1995) Correlations between ambient noise and the ocean surface wave field. J Phys Oceanogr 25:513–532

Flores-Vidal X, Flament P, Durazo R, Chavanne C, Gurgel K-W (2013) High Frequency Radars: beam forming calibrations using ships as reflectors. J Atm Ocean Tech 30:638–648
Frew NM, Bock EJ, McGillis WR, Karachintsev AV, Hara T, Muensterer T, Jaehne B (1995) Variation of air-water gas transfer with wind stress and surface viscoelasticity. In: Jaehne B, Monahan EC (eds) Air-Water Gas Transfer. AEON Verlag & Studio, Hanau, pp 529–541
Fu LL, Holt B (1982) Seasat views oceans and sea ice with synthetic aperture radar. NASA JPL Publication, Pasadena
Fujimura A, Soloviev A, Kudryavtsev V (2010) Numerical simulation of the environmental effects on SAR imagery of ship wakes. IEEE Geosci Rem Sens Lett 7:646–649
Fujimura A, Soloviev A, Rhee SH, Romeiser R (2013) Coupled model simulation of wind stress effect on far wakes of ships in sar images (Manuscript in revision)
Gade M, Alpers W, Huhnerfuss H, Masuko H, Kobayashi T (1998) Imaging of biogenic and anthropogenic ocean surface films by the multifrequency/multipolarization SIR-C/X-SAR. J Geophys Res 103(C9):18851–18866
Gade M, Hühnerfuss H, Korenowski G (Eds) (2006) Marine Surface Films: Chemical Characteristics, Influence on Air-Sea Interactions and Remote Sensing. Springer, The Netherlands, 341 pp
Garbe CS, Jähne B, Hauβecker H (2002) Measuring the sea surface heat flux and probability distribution of surface renewal events. In: Saltzman ES, Donealn M, Drennan W, Wanninkhof R (Eds) AGU Monograph Gas Transfer at Water Surfaces. pp 109–114
Garrett WD, Smith PM (1984) Physical and chemical factors affecting the thermal IR imagery of ship wakes.NRL Memorandum Report 5376. Naval Researcj Lab, Washington DC 20375, p. 30
Geiser PW (2004) The WindSat space borne polarimetric microwave radiometer: sensor description and early orbit performance. IEEE Trans Geosci Remote Sens 42(11):2347–2361
Gemmrich JR, Farmer DM (1999) Observations of the scale and occurrence of breaking surface waves. J Phys Oceanogr 29:2595–2606
Gentemann CL, Wentz FJ, Brewer M, Hilburn K, Smith D (2010) Passive microwave remote sensing of the ocean: an overview. In: Barale V, Gover JFR, Alberotanza L (eds) Oceanography from Space revisited. Springer, pp 19–44
Gilman M, Soloviev A, Graber H (2011) Study of the Far Wake of a Large Ship. J Atmos Ocean Technol 28:720–733
Gordon HR (1997) Atmospheric correction of ocean color imagery in the earth observing system era. J Geophys Res 102:17,081–17,106
Greidanus H, Kourti N (2006) Findings of the DECLIMS project—Detection and classification of marine traffic from space. SEASAR: Advances in SAR oceanography from envisat and ERS missions. Eur. Space Agency, Roma
Grimshaw RHJ, Khusnutdinova KR (2004) The effect of bubbles on internal waves. J. Phys. Oceanogr 34:477–489
Grodsky SA, Reul N, Lagerloef G, Reverdin G, Carton JA, Chapron B, Quilfen Y, Kudryavtsev VN, Kao H-Y (2012) Haline hurricane wake in the Amazon/Orinoco plume: AQUARIUS/SACD and SMOS observations. Geophys Res Lett 39:L20603. doi:10.1029/2012GL053335
IOCCG (2000) Remote sensing of ocean colour in coastal, and other optically-complex waters. In: sathyendranath S (eds) Reports of the international ocean colour coordinating group, No. 3. IOCCG, Dartmouth
IOCCG (2012) Mission requirements for future ocean-colour sensors. In: McClain CR, Meister G (eds) Reports of the international ocean-colour coordinating group, No. 13. IOCCG, Dartmouth, p. 106
Jaehne B, Muennich O, Boesinger R, Dutzi A, Huber W, Libner P (1987) On the parameters influencing air–water gas exchange. J Geophys Res 92:1937–1949
Janssen PAEM (2007) Progress in ocean wave forecasting. J. Comp. Phys. doi:10.1016/j.jcp.2007.04.029, 23 p.
Jerlov NG (1976) Marine Optics. Elsevier, Amsterdam
Jo Y-H, Yan X-H, Pan J, Liu WT (2004) Sensible and latent heat flux in the tropical Pacific from satellite multi-sensor data. Remot Sens Environ 90:166–177

Johannessen JA, Kudryavtsev V, Akimov D, Eldevik T, Winther N, Chapron B (2005) On radar imaging of current features: 2. Mesoscale eddy and current front detection. J Geophys Res 110:C07017. doi:10.1029/2004JC002802

Hanson AK Jr, Donaghay P.I (1998) Micro- to fine-scale chemical gradients and layers in stratified coastal waters. Oceanography 11(1):10–17

Hare JE, Fairall CW, McGillis WR, Edson JB, Ward B, Wanninkhof R (2004) Evaluation of the national oceanic and atmospheric administration/coupled-ocean atmospheric response experiment (NOAA/COARE) air-sea gas transfer parameterization using GasEx data. J Geophys Res 109:C08S11. doi:10.1029/2003JC001831

Hennings IR, Alpers RW, Viola A (1999) Radar imaging of Kelvin arms of ship wakes. Int J Remot Sens 20(13):2519–2543

Huebert B, Blomquist B, Hare JE, Fairall CW, Bates T, Johnson J (2004) Measurements of the sea-air DMS flux and transfer velocity using eddy correlation. J Geophys Res Lett 31:L23113. doi:10.1029/2004GL021567

Huhnerfuss H, Alpers W, Dannhauer H, Gade M, Lange PA, Neumann V, Wismann V (1996) Natural and man-made sea slicks in the North Sea investigated by a helicopter-borne 5-frequency radar scatterometer. Int J Remot Sens 17(8):1567–1582

Hughes B (1976) Estimates of underwater sound (and infrasound) produced by nonlinearly interacting ocean waves, J Acoust Soc Am 60(5):1032–1038. doi:10.1121/1.381203

Hwang PA (1997) A study of the wavenumber spectra of short water waves in the ocean. Part II: Spectral model and mean square slope. J Atmos Oceanic Technol 14:1174–1186

Katsaros KB, DeCosmo J (1990) Evaporation at high wind speeds, sea surface temperature at low wind speeds: examples of atmospheric regulation. proceedings, workshop on modeling the fate and influence of marine spray. Marseille, France, pp. 1–11 (June 5–7, 1990)

Katsaros KB, Soloviev AV (2003) Vanishing horizontal sea surface temperature gradients at low wind speeds. Bound-Layer Meterol 112:381–396

Katsaros KB, Fiuza A, Sousa F, Amann V (1983) Surface temperature patterns and air-sea fluxes in the German Bight during MARSEN 1979, Phase 1. J Geophys Res 88:9871–9882

Katsaros KB, Soloviev AV, Weisberg RH, Luther ME (2005) Reduced horizontal sea surface temperature gradients under conditions of clear sky and weak winds. Bound.-Layer Meterol (in press)

Kerman BR (1984) Underwater sound generation by breaking wind Waves. J Acoust Soc Am 75:149–165

Kettle AJ, Andreae MO (2000) Flux of dimethylsulfide from the oceans: a comparison of updated data sets and flux models. J Geophys Res 105:26793–26808

Khatiwala S, Tanhua T, Mikaloff Fletcher S, Gerber M, Doney SC, Graven HD, Gruber N, McKinley GA, Murata A, Ríos AF, Sabine CL (2013) Global ocean storage of anthropogenic carbon. Biogeosciences 10:2169–2191

Klemas V (2012) Remote sensing of coastal and ocean currents: an overview. J Coast Res 28(3):576–586. (West Palm Beach, Florida, ISSN 0749–0208)

Knudsen VO, Alford RS, Emling JW (1948) Underwater ambient noise. J Mar Res 3:410–429

Kolaini AR, Dandeault P, Ruxton AD (1995) Passive and active acoustical measurement of laboratory breaking waves. In: Buckingham MJ, Potter JR (eds) Proceedings of III Int. Meeting on Natural Physical Processes Related to Sea Surface Sound "Sea Surface Sound'94,". University of California, Lake Arrowhead, pp. 229–240 (7–11 March 1994, World Scientific, Singapore)

Kopelevich OV, Sheberstov SV, Burenkov VI, Evdoshenko MA, Ershova SV (1998) New data products derived from SeaWIFS ocean color data: examples for the mediterranean basin. International symposium satellite-based observation: a tool for the study of the mediterranean basin. Tunis, pp. 23–27 (November, 1998)

Lagerloef G (2012) Satellite mission monitors ocean surface salinity, Eos Trans. AGU 93(25):233. doi:10.1029/2012EO250001

Lagerloef GSE, Swift CT, Le Vine DM (1995) Sea surface salinity: the next remote sensing challenge. Oceanography 8:44–50

Lagerloef GSE, Lukas R, Bonjean F, Gunn JT, Mitchum GT, Bourassa M, Busalacchi AJ (2003) El Niño tropical pacific ocean surface current and temperature evolution in 2002 and outlook for early 2003. Geophys Res Lett 30(10):1514

Large WG, McWilliams JC, Doney SC (1994) Oceanic vertical mixing: A review and a model with a nonlocal boundary layer parameterization, Rev Geophys 32:363–403

Lee T, Lagerloef G, Gierach MM, Kao H-Y, Yueh S, Dohan K (2012) Aquarius reveals salinity structure of tropical instability waves, Geophys Res Lett 39:L12610. doi:10.1029/2012GL052232

Lamarre E, Melville WK (1994) Sound-speed measurements near the ocean surface. J Acoust Soc Amer 96:3605–3616

Lamarre E, Melville WK (1995) Instrumentation for the measurement of sound speed near the ocean surface. J Atmos Ocean Technol 12:317–329

Le Vine DM, Kao M, Garvine RW, Sanders T (1998) Remote sensing of ocean salinity: results from the Delaware coastal current experiment. J Atmos Ocean Tech 15:1478–1484

Lee T, Lagerloef G, Gierach MM, Kao H-Y, Yueh S, Dohan K (2012) Aquarius reveals salinity structure of tropical instability waves. Geophys Res Lett 39:L12610. doi:10.1029/2012GL052232

Lehr WJ, Simecek-Beatty D (2000) The relation of Langmuir circulation processes to the standard oil spill spreading, dispersion, and transport algorithms. Spill Science & Technology Bulletin 6: 247–253

Leifer I, Lehr B, Simecek-Beatty D, Bradley E, Clark R, Dennison P, Hu Y, Matheson S, Jones C, Holt B, Reif M, Roberts D, Svejkovsky J, Swayze G, Wozencraft J (2012) State of the art satellite and airborne marine oil spill remote sensing: application to the bp deepwater horizon oil spill. Remot Sens Environ 124:185–209

Lewis MR, Carr M-E, Feldman GC, Esaias W, McClain C (1990) Influence of penetrating solar radiation on the heat budget of the equatorial Pacific Ocean. Nature 347:543–545

Liu WT, Tang W, Xie X, Navalgund R, Xu K, (2008) Power density of ocean surface wind-stress from international scatterometer tandem missions. Int J Remote Sens 29(21):6109–6116

Liu H-L, Sassi F, Garcia RR (2009) Error growth in a whole atmosphere climate model. J Atmos Sci 66:173–186

Liu Y, Weisberg RH, Hu C., Zheng L (2011) Tracking the Deepwater Horizon oil spill: A modeling perspective. Eos Trans. AGU, 92(6): 45–46.

Loewen MR, Melville WK (1991a) Microwave backscatter and acoustic radiation from breaking waves. J Fluid Mech 224:601–623

Loewen MR, Melville WK (1991b) A model of the sound generated by breaking waves. J Acoust Soc Am 90:2075–2080

Loisel H, Morel A (1998) Light scattering and chlorophyll concentration in case 1 waters: a reexamination. Limnol Oceanogr 43(5):847–858

Longuet-Higgins MS (1950) A theory of microseisms, Philos Trans R Soc London Ser A 243:1–35. doi:10.1098/rsta.1950.0012

Lorenz EN (1963) Deterministic nonperiodic flow. J Atmos Sci 20:130–141

Lugt H, Ugincius P (1964) Acoustic rays in an ocean with heat source or thermal mixing zone. J Acoust Soc Am 36(4):258–269

Lukas R, Lindstrom E (1991) The mixed layer of the western equatorial Pacific Ocean. J Geophys Res C96 (Supplement): 3343–3358

Lyden JD, Hammond RR, Lyzenga DR, Schuchman RA (1988) Synthetic aperture radar imaging of surface ship wakes. J Geophys Res 93:12293–12303

Maes C, Picaut J, Belamari S (2002) Salinity barrier layer and onset of El Niño in a Pacific coupled model. Geophys Res Lett 29(24):2206. doi:10.1029/2002GL016029

Makin VK (1998) Air-sea exchange of heat in the presence of wind waves and spray. J Geophys Res 103:1137–1152

Martin M, Dash P, Ignatov A, Banzon V, Beggs H, Brasnett B, Cayula J-F, Cummings J, Donlon C, Gentemann C, Grumbine R, Ishizaki S, Maturi E, Reynolds RW, Roberts-Jones J (2012) Group for High Resolution Sea Surface temperature (GHRSST) analysis fields inter-comparisons. Part 1: A GHRSST multi-product ensemble (GMPE), Deep Sea Research Part II: Topical Studies in Oceanography. (ISSN 0967–0645, 10.1016/j.dsr2.2012.04.013)

Matt S, Soloviev A, Rhee S (2011) Modification of turbulence air-sea interface due to the presence of surfactants and implications for gas exchange. Part II: numerical simulations. Gas transfer at water surfaces, Kyoto University Press, pp. 299–312

Matt S, Fujimura A, Soloviev A, Rhee SH, Romeiser R (2012a) Fine-scale features on the sea surface in SAR satellite imagery—Part 2: numerical modeling. Ocean Sci Discuss 9:2915–2950

Matt S, Soloviev A, Brusch S, Lehner S (2012b) Numerical simulation of wind shadow type wakes in SAR Imagery. IEEE Geosci Remot Sens Sympisium (IGARSS 2012) 22–27 (July 2012, Minich, Germany)

McManus MA, Alldredge AL, Barnard A, Boss E, Case J, Cowles TJ, Donaghay PL, Eisner L, Gifford DJ, Greenlaw C, Herren D.V. Holliday D, Johnson S, MacIntyre CF, McGehee D, Osborn TR, Perry MJ, Pieper R, Rines JEB, Smith DC, Sullivan JM, Talbot MK, Twardowski MS, Weidemann A, Zaneveld JRV (2003) Changes in characteristics, distribution and persistence of thin layers over a 48-hour period. Mar Ecol Prog Ser 261:1–19

McNeil CL, Merlivat L (1996) The warm oceanic surface layer: implications for CO2 fluxes and surface gas measurements. Geophys Res Lett 23:3575–3578

Medwin H, Beaky MM (1989) Bubble sources of the Knudsen sea noise spectra. J Acoust Soc Am 86:1124–1130

Medwin H, Clay CS (1998) Fundamentals of Acoustical Oceanography. Academic Press, San Diego, p. 712

Medwin H, Daniel AC (1990) Acoustical measurements of bubble production by spilling breakers. J Acoust Soc America 88:408–412

Medwin H, Nystuen JA, Jacobus PW, Ostwald LH, Synder DE (1992) The anatomy of underwater rain noise. J Acoust Soc Amer 92:1613–1623

Meehl GA (1994) Coupled Land-Ocean-Atmosphere Processes and South Asian 30 Monsoon Variability. Science 266: 263–267

Meirink JF (2002) The role of wind waves and sea spray in air–sea interaction. Ph.D. dissertation, Technische Universiteit Delft, p. 168

Meneveau C, Sreenivasan KR (1991) The multifractal nature of turbulent energy dissipation. J Fluid Mech 224:429–484

Migliaccio M, Nunziata F, Gambardella A (2009) On the copolarised phase difference for oil spill observation. Int J Remote Sens 30(6):1587–1602

Milgram JH, Skop RA, Peltzer RD, Griffin OM (1993) Modeling short sea wave energy distribution in the far wakes of ships. J Geophys Res 98(C4):7115–8370

Miller AJ, Alexander MA, Boer GJ, Chai F, Denman K, Erickson DJ III, Frouin R, Gabric AJ, Laws EA, Lewis MR, Liu Z, Murtugudde R, Nakamoto S, Neilson DJ, Norris JR, Ohlmann JC, Perry RI, Schneider N, Shell KM, Timmermann A (2003) Potential feedbacks between Pacific Ocean ecosystems and interdecadal climate variations. Bull Am Met Soc 84:617–633. doi:10.1175/BAMS-84-5-617

Minnaert M (1933) On musical air bubbles and the sound of running water. Philos Mag 16: 235–248

Minchew B, Jones C, Holt B (2012) Polarimetric L-band SAR signatures of oil from the Deepwater Horizon spill. IEEE Trans Geosci Remot Sens. 50(10): 3812–3830 doi.org/10.1109/TGRS.2012.2185804

Mobley CD (1994) Light and water: radiative transfer in natural waters. Academic Press, San Diego

Monahan EC (2002) Oceanic whitecaps: Sea surface features detectable via satellite that are indicators of the magnitude of the air-sea gas transfer coefficient. Proc Indian Acad Sci (Earth Planet Sci) 111(3): 315–319

Monahan EC, Torgersen T (1990) The enhancement of air-sea gas exchange by oceanic whitecapping. In: Wilhelms SC, Gulliver JS (eds) Air-Water Mass Transfer. American Society of Civil Engineers, New York, pp. 608–617

Morel A (1980) In-water and remote measurement of ocean color. Bound-Lay Meteorol 18:177–201

Morel A, Prieur L (1977) Analysis of variations in ocean color. Limnol Oceanogr 22:709–722
Munk W (2009) An inconvenient sea truth: spread, steepness, and skewness of surface slopes. Annu Rev Mar Sci 1:377–415
Murtugudde R, Beauchamp J, McClain CR, Lewis M, Busalacchi A (2002) Effects of penetrative radiation on the upper tropical ocean circulation. J Climate 15:471–487
Murty VSN, Subrahmanyam B, Sarma MSS, Tilvi V, Ramesh Babu V (2002) Estimation of sea surface salinity in the Bay of Bengal using Outgoing Longwave Radiation. Geophys Res Lett 29. doi:10.1029/2001GL014424
Nair A, Sathyendranath S, Platt T, Morales J, Stuart V, Forget M-H, Devred E, Bouman H (2008) Remote sensing of phytoplankton functional types. Remot Sens Environ 112(8):3366–3375
Nash JD, Moum JN (2005) River plumes as a source of large-amplitude internal waves in the coastal ocean. Nature 437:400–403
NRC (2003) Oil in the sea III: Inputs, fates, and effects (pp. 65). Washington, D.C.: National Academy of Sciences
Nunziata F, Migliaccio M, Gambardella A (2011) Pedestal height for sea oil slick observation IET Radar, Sonar & Navigation 5(2): 103–110 doi:10.1049/iet-rsn.2010.0092
Nystuen JA (1996) Acoustical rainfall analysis: rainfall drop size distribution using the underwater sound field. J Acoust Soc Amer 13:74–84
Nystuen JA (2001) Listening to raindrops from underwater: an acoustic disdrometer. J Atmos Ocean Tech 18:1640–1657
Nystuen JA, Selsor HD (1997) Weather classification using passive acoustic drifters. J Atmos Ocean Tech 14:656–666
Nystuen JA, Amitai E (2003) High temporal resolution of extreme rainfall rate variability and the acoustic classification of rainfall. J Geophys Res 108:8378. doi:10.1029/2001JD001481
Nystuen JA, McPhaden MJ, Freitag HP (2000) Surface measurements of precipitation from an ocean mooring: the acoustic log from the South China Sea. J Appl Meteorol 39:2182–2197
Nystuen J, Riser S, Wen T, Swift D (2011) Interpreted acoustic ocean observations from Argo Floats. J Acoust Soc Am 129(4):2400–2400
Ohlmann JC, Siegel DA, Gautier C (1996) Ocean mixed layer radiant heating and solar penetration: A global analysis. J Climate 9: 2265–2280
Özgökmen TM, Fischer PF (2012) CFD application to oceanic mixed layer sampling with Lagrangian platforms. International Journal of Computational Fluid Dynamics 26: 6–8
Paduan J, Graber H (1997) Introduction to high-frequency radar: reality and myth. Oceanography 10:36–39
Paulson CA, Lagerloef GSE (1993) Fresh surface lenses caused by heavy rain over the western Pacific warm pool during TOGA COARE. EOS Trans AGU 74, Suppl. to No. 43:125
Peltzer RD, Griffin OM, Barger WR, Kaiser JAC (1992) High-resolution measurement of surface-active film redistribution in ship wakes. J Geophys Res 97(C4):5231–5252
Peters NJ, Skop RA (1997) Measurements of Ocean Surface Currents from a Moving Ship Using VHF Radar. J Atmos Oceanic Technol 14: 676–694
Petrenko AA, Zaneveld JRV, Pegau WS, Barnard AH, Mobley CD (1998) Effects of a thin layer on reflectance and remote-sensing reflectance. Oceanography 11(1):48–50
Pichel WG, Clemente-Colon P, Wackerman CC, Friedman KS (2004) Ship and wake detection. In: Jackson CR, Apel JR (eds) Synthetic aperture radar marine User's Manual. NOAA, pp. 277–303
Plane JMC, Blough NV, Ehrhardt MG, Waters K, Zepp RG, Zika RG (1997) Report Group 3—Photochemistry in the sea-surface microlayer. In: Liss PS, Duce RA (eds) The Sea Surface and Global Change. Cambridge University Press, UK, pp. 71–92
Prosperetti A (1985) Bubble-related ambient noise in the ocean. J Acoust Soc Am 78:S2
Purkis S, Klemas V (2011) Remote sensing and global environmental change. Wiley-Blackwell, Oxford
Randall D, Khairoutdinov M, Arakawa A, Grabowski W (2003) Breaking the cloud parameterization deadlock. Bull Amer Meteor Soc 84(11):1547–1564

Reed AM, Milgram JH (2002) Ship wakes and their radar images. Annu Rev Fluid Mech 34(1):469–502

Rines JEB, Donaghay PL, Dekshenieks MM, Sullivan JM, Twardowski MS (2002) Thin layers and camouflage: hidden Pseudo-nitzschia populations in a fjord in the San Juan Islands, Washington, USA. Mar Ecol Prog Ser 225:123–137

Riser S, Nystuen J, Rogers A (2008) Monsoon effects in the Bay of Bengal inferred from profiling float-based measurements of wind speed and rainfall. Limnol Oceanogr 53:2080–2093

Romeiser R (2008) M4S 3.2.0 User's Manual, University of Hamburg, Hamburg

Romeiser R, Johannessen J, Chapron B, Collard F, Kudryavtsev V, Runge H, Suchandt S (2010) Direct surface current field imaging from space by along-track InSAR and Conventional SAR. In: Barale V, Gover JFR, Alberotanza L (eds) Oceanography from Space: Revisited. Springer, pp. 73–91

Sabins FF (1987) Remote Sensing Principles and Interpretation, 2nd ed. W.H. Freeman, New York, pp. 449

Sathyendranath S, Platt T (2010) Ocean-colour radiometry: achievements and future perspectives. In: Barale V, Gover JFR, Alberotanza L (eds) Oceanography from Space: Revisited. Springer, pp. 349–359

Schneider EK, Zhu Z (1998) Sensitivity of the simulated annual cycle of the sea surface temperature in the equatorial Pacific to sunlight penetration. J Climate 11:1932–1950

Schlüssel P, Soloviev A (2002) Air-sea gas exchange: cool skin and gas transfer velocity in the North Atlantic Ocean during GasEx-98. Adv Space Res 29(1):107–11

Schlüssel P, Emery WJ, Grassl H, Mammen TC (1990) On the bulk-skin temperature difference and its impact on satellite remote sensing of the sea surface temperature. J Geophys Res 95:13341–13356

Shaw PT, Watts DR, Rossby HT (1978) On the estimation of oceanic wind speed and stress from ambient noise measurements. Deep Sea Res 25:1225–1233

Shay LK, Cook TM, Peters H, Mariano AJ, Weisberg RH, An PE, Soloviev AV, Luther ME (2002) Very high-frequency radar mapping of surface currents. IEEE J Ocean Eng 27:155–169

Sieburth JM, Donaghay PL (1993) Planktonic methane production and oxidation within the algal maximum of the pycnocline: seasonal fine scale observation in an anoxic estuarine basin. Mar Ecol Prog Ser 100: 3–15

Siegel DA, Ohlmann JC, Washburn L, Bidigare RR, Nosse CT, Fields E, Zhou YM (1995) Solar-radiation, phytoplankton pigments and the radiant heating of the equatorial Pacific warm pool. J Geophys Res 100:4885–4891

Siegel DA, Michaels AF (1996) Quantification of non-algal light attenuation in the Sargasso Sea: implication for biogeochemistry and remote sensing. Deep Sea Res II 43:321–345

Smith RC, Baker KS (1981) Optical properties of the clearest natural waters (200-800 nm). Appl Opt 31: 177–184

Soloviev A, Donelan M, Graber HC, Haus B, Schlussel P (2007) An approach to estimation of near-surface turbulence and CO_2 transfer velocity from remote sensing data. J. Marine Syst 66: 182–194

Soloviev AV, Schlüssel P (1994) Parameterization of the temperature difference across the cool skin of the ocean and of the air-ocean gas transfer on the basis of modelling surface renewal. J Phys Oceanogr 24:1339–1346

Soloviev A, Schlüssel P (2002) A model of the air-sea gas exchange incorporating the physics of the turbulent boundary layer and the properties of the sea surface. In: AGU Monograph Gas Transfer at Water Surfaces. E.S. Saltzman, M. Donelan, W. Drennan, and R. Wanninkhof, Eds., pp 141–146

Soloviev A, Lukas R (1997) Observation of large diurnal warming events in the near-surface layer of the western equatorial Pacific warm pool. Deep Sea Res 44 Part I:1055–1076

Soloviev AV, Gilman M, Young K, Brusch S, Lehner S (2010) Sonar measurements in ship wakes simultaneous with TerraSAR-X overpasses. IEEE Trans Geosci Remot Sens 48:841–851

Soloviev A, Matt S, Gilman M, Hühnerfuss H, Haus B, Jeong D, Savelyev I, Donelan M (2011) Modification of turbulence at the air-sea interface due to the presence of surfactants and impli-

cations for gas exchange. Part I: laboratory experiment. Gas Transfer at Water Surfaces. Kyoto University Press, pp. 245–258
Soloviev A, Maingot C, Agor M, Nash L, Dixon K (2012a) 3D Sonar Measurements in Wakes of Ships of Opportunity. J Atmos Oceanic Technol 29:880–886
Soloviev A, Maingot C, Matt S, Dodge RE, Lehner S, Velotto D, Brusch S, Perrie W, Hochberg E (2012b) Fine-scale features on the sea surface in SAR satellite imagery—Part 1: Simultaneous in-situ measurements. Ocean Sci Discuss 9:2885–2914
Sorooshian S, Gao X, Hsu K, Maddox RA, Hong Y, Gupta HV, Imam B (2002) Diurnal variability of tropical rainfall retrieved from combined GOES and TRMM satellite information. J Climate 15:983–1001
Sreenivasan K, Ramshankar R, Meneveau C (1989) Mixing, entrainment and fractal dimensions of surfaces in turbulent flows. Proc Roy Soc London 421A:79–108
Stramski D (1994) Gas microbubbles: an assessment of their significance to light scattering in quiescent seas. Proc SPIE Ocean Opt XII(2258):704–710
Su M-Y, Todoroff D, Cartmill J (1994) Laboratory comparisons of acoustic and optical sensors for microbubble measurement. J Atmos Ocean Tech 11:170–181
Subrahmanyam B, Murty VSN, Sharp RJ, O'Brien JJ (2005) Air-sea coupling during the tropical cyclones in the Indian Ocean: a case study using satellite observations. J Pure Appl Geophys 162: 1643–1672
Sweeney C, Gloor E, Jacobson AR, Key RM, McKinley G, Sarmiento JL, Wanninkhof R (2007) Constraining global air-sea gas exchange for CO_2 with recent bomb 14^C measurements. Glob Biogeochem Cycles 21:GB2015
Synthetic Aperture Radar (SAR). Marine User's Manual. Washington, DC. September 2004. U.S. DEPARTMENT OF COMMERCE. National Oceanic and Atmospheric Administration, Technology & Engineering, pp. 464
Takahashi T (2000) Distribution of surface water pCO2 and the net sea-air CO2 flux over the global oceans. Paper presented at the Ewing Symposium, Lamont Doherty Earth Observatory, October 27–28
Tans PP, Fung IY, Takahashi T (1990) Observational constraints on the global atmospheric CO2 budget. Science 247:1431–1438
Terrill EJ, Melville WK (1997) Sound-speed measurement in the surface-wave layer. J Acoust Soc Am 102(5):2607–2625 (Part 1)
Terrill EJ, Melville WK (2000) A broadband acoustic technique for measuring bubble size distributions: laboratory and shallow water measurements. J Atmos Ocean Tech 17:220–239
Thingstad TF, Strand E, Larsen A (2008) Stepwise building of plankton functional type (PFT) models: a feasible route to complex models? Progress Oceanography 84(1–2):6–15
Thorpe SA (1982) On the clouds of bubbles formed by breaking wind-waves in deep water, and their role in air–sea gas transfer. P Trans Roy Soc Lon Ser A 304:155–210
Tkalich P, Chan ES (2002) Breaking wind waves as a source of ambient noise. J Acoust Soc Am 112(2):456–463
Tolman HL, Balasubramaniyan B, Burroughs LD, Chalikov DV, Chao YY, Chen HS, Gerald VM (2002) Development and implementation of wind generated ocean surface wave models at NCEP. Weather and Forecasting 17:311–333
Vagle S, Farmer DM (1992) The measurement of bubble size distributions by acoustical backscatter. J Atmos Ocean Tech 9(5):630–644
Vagle S, Farmer DM (1998) A Comparison of four methods for bubble size and void fraction measurements. IEEE J Ocean Eng 23:211–222
Vagle S, Large WG, Farmer DM (1990) An evaluation of the WOTAN technique for inferring oceanic wind from underwater sound. J Atmos Ocean Tech 7:576–595
Velotto D, Migliaccio M, Nunziata F, Lehner S (2010) Oil-slick observation using single look complex TerraSAR-X dual-polarized data, IEEE Int Geosci Remot Sens Symposium (IGARSS) 3684–3687
Vialard J, Delecluse P (1998a) An OGCM study for the TOGA decade. Part I: role of salinity in the physics of the western Pacific fresh pool. J Phys Oceanogr 28:1071–1088

Vialard J, Delecluse P (1998b) An OGCM study for the TOGA decade. Part II: Barrier-layer formation and variability. J Phys Oceanogr 28:1089–1106
Vinayachandran PN, Murty VSN, Ramesh Babu (2002) Observations of barrier layer formation in the Bay of Bengal during summer monsoon. J Geophys Res 107. doi:10.1029/2001JC000831
Voronovich AG, Zavorotny VU (2001) Theoretical model for scattering of radar signals in Ku- and C-bands from a rough sea surface with breaking waves. Wave Random Media 11(3):247–269
Voss R (1988) Fractals in nature: from characterization to simulation. In: Peitgen H, Saupe D (eds) The science of fractal images. Springer-Verlag, pp. 21–70
Wang Y, Kepert JD, Holland GJ (2001) The effect of sea spray evaporation on tropical cyclone boundary-layer structure and intensity. Mon Weather Rev 129(10): 2481-2500
Wanninkhof R, Asher WE, Ho DT, Sweeney C, McGillis WR (2009) Advances in Quantifying Air-Sea Gas Exchange and Environmental Forcing. Annual Review of Marine Science 1: 213–232
Webster, P. J., and R. Lukas, 1992: TOGA COARE: The Coupled Ocean-Atmosphere Response Experiment. Bull Amer Met Soc 73: 1377–1416
Weller RA, Anderson SP (1996) Surface meteorology and air-sea fluxes in the western equatorial Pacific warm pool during the TOGA Coupled Ocean-Atmosphere Response Experiment. J Climate 9: 1959–1992
Woolf DK, Thorpe SA (1991) Bubbles and the air-sea exchange of gases in near-saturation conditions. J Mar Res 49: 435–466
Yentisch CS (1984) Satellite representation of features of ocean circulation indicated by CZCS colorimetry. In: Remote Sensing of Shelf Sea Hydrodynamcis, J.C.J. Nihoul, Ed., Elsevier, Amsterdam: 336–354
Yueh SH, Dinardo SJ, Fore AG, Li FK (2010) Observations and modeling of ocean surface winds," IEEE Trans Geosci Remote Sens. 48(8): 3087–3100
Zepp RG, Callaghan TV, Erickson DJ (1995) Effects of increased solar radiation on biogeochemical cycles. Ambio 24: 181–187
Zhang X, Lewis M, Johnson B (1998) Influence of bubbles on scattering of light in the ocean. Appl Opt 37: 6525–6536
Zhang Y, Perrie W (2001) Feedback mechanisms for the atmosphere and ocean surface. Bound -Layer Meterol 100: 321–348
Zubair FR, Catrakis HJ (2009) On separated shear layers and the fractal geometry of turbulent scalar interfaces at large Reynolds numbers. J Fluid Mech 624: 389–411

Index

A. Soloviev, R. Lukas, *The Near-Surface Layer of the Ocean,* Atmospheric and Oceanographic Sciences Library 48, DOI 10.1007/978-94-007-7621-0,

C

D

T